



# LAGUNA-LBNO

---

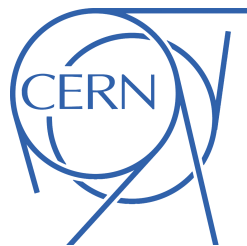
## **A Long-Baseline Neutrino Beam Facility from CERN to a Far Detector Site at 2300 km Distance**

---

CONCEPTUAL DESIGN REPORT

May 29, 2015

LAGUNA-LBNO WP4 DELIVERABLE REPORT



GRAND AGREEMENT 284518

Project Acronym : LAGUNA-LBNO

Project full title: "Design of a pan-European Infrastructure for Large Apparatus studying Grand Unification, Neutrino Astrophysics and Long Baseline Neutrino Oscillations"

# THE CERN NEUTRINO BEAM TO PYHASALMI - CN2PY

## Conceptual Technical Design

J. Alabau-Gonsalvo, A. Alekou, F. Antoniou, W. Bartmann,  
M. Benedikt, D. Berthoux, B. Biskup, L. Bottura, M. Calviani,  
N. Charitonidis, J.M. Cravero, I. Efthymiopoulos, L. Faisandel,  
B. Ferral, R. Garodby, F. Gerigk, S. Gilardoni, B. Goddard, M. Jones, A.  
Huschauer, A. Lachaize, C. Lazaridis, M. Manfredi, D. Missiaen,  
J. Osborne, Y. Papaphilippou, A. Parfenova, F. Sanchez-Galan,  
E. Shaposhnikova, D. Smargianaki, R. Steerenber, C. Strabel, F. Velotti,  
P. Velten, V. Venturini, H. Vincke, P. Vojtyla,  
*CERN - Geneva Switzerland*

A. Curioni, F. Petrolo, F. Resnati, A. Rubbia  
*ETHZ - Zurich, Switzerland*

A. Blondel, E. Noah, Y. Karadzhov  
*University of Geneva - Geneva, Switzerland*

T. Stainer  
*University of Liverpool - Liverpool, UK*

C. Densham, M. Fitton  
*RAL - Oxford, UK*





# Copyright

Copyright © LAGUNA-LBNO Consortium, 2014 and CERN. For more information on LAGUNA-LBNO, its partners and contributors please see [www.laguna.ethz.ch](http://www.laguna.ethz.ch). For CERN please see in [www.cern.ch](http://www.cern.ch).

The LAGUNA-LBNO Design of a pan-European Infrastructure for Large Apparatus studying Grand Unification, Neutrino Astrophysics and Long Baseline Neutrino Oscillations is a project co-funded by the European Commission under FP7 Research Infrastructures, grant agreement no 284518. LAGUNA-LBNO began in September 2011 and run for 3 years.

The information herein only reflects the views of its authors and not those of the European Commission and no warranty expressed or implied is made with regard to such information or its use.

CERN reserves literary and scientific copyrights in all countries of the world. This report or any part of it, may not be reprinted or transmitted without written permission of the copyright holder, the Director General of CERN. However permission may be freely granted for appropriate non-commercial use.

If any patentable invention or registrable design is described in the report, CERN makes no claim to properly rights in it, but offers it for the free use of research institutions, manufacturers and others. CERN, however, may oppose any attempt by a user to claim an proprietary or patent rights in such inventions or designs as may be described in the present document.



# Executive Summary

This report describes the design study for a future long-baseline neutrino beam from CERN to a far detector located underground at the Pyhäsalmi mine in Finland (CN2PY). The design of the beam covers two operation phases: a first phase, using a proton beam from the CERN SPS with protons at 400 GeV and a beam power of 750 kW, and a second phase using a proton beam at 50 GeV with 2 MW of beam power produced by a new High-Power Proton Synchrotron (HP-PS). The focus of the design study has been to address the key issues for the neutrino and proton beam, proving the fundamental validity of the concept. The report includes conceptual and basic technical description of the proton beam transfer, HP-PS accelerator and neutrino beam components studied within the available resources in the project. The physics motivation and expected performance for measuring the neutrino oscillation parameters with this facility are described in a separate document of the LAGUNA-LBNO project.

This design study is greatly inspired by the CNGS neutrino beam facility that was successfully operated at CERN until 2012, reaching a world-record beam power operation of approx. 360 kW. Emphasis is given to address the new challenges of the beam arising from the steep 18% slope due to the longer baseline and the foreseen operation at high beam power. The optimisation of radiation and environmental impact aspects for the beam operation have been the guiding factors for the design. Solutions for the civil engineering and handling of beam components, conventional during installation but also activated in future interventions and maintenance operations, have been studied and presented. Further, the R&D to further develop the design concepts presented here are outlined, in particular those required to operate the injectors (PS and SPS) at the foreseen high power of 750 kW and the assumed magnets for the transfer lines and HP-PS accelerator. Finally, the design concept of a near detector located at 800 m distance from the target is presented. The report includes a possible project structure and schedule timeline with assumptions on the budget profile and resources from similar projects at CERN.



# Contents

<b>Copyright</b>	<b>iii</b>
<b>Executive Summary</b>	<b>v</b>
<b>List of Figures</b>	<b>xv</b>
<b>List of Tables</b>	<b>xxxiii</b>
<b>Acronyms, Abbreviations</b>	<b>xxxix</b>
<b>1 Introduction</b>	<b>1</b>
1.1 Physics requirements and beam design criteria . . . . .	3
1.2 Overview of the Neutrino Beam . . . . .	5
1.2.1 Upgrade path with the HP-PS . . . . .	8
1.3 Layout Implementation Options . . . . .	10
1.3.1 Option A: extraction from LSS6 of SPS . . . . .	11
1.3.2 Option B: extraction from LSS2 of SPS . . . . .	11
1.4 The Near Detector . . . . .	11
<b>2 High-Intensity beams with present CERN Accelerators</b>	<b>15</b>
2.1 HI Beams in the PS . . . . .	16
2.1.1 Beam production schemes . . . . .	16
2.1.2 Injection losses . . . . .	17
2.1.3 Injection Oscillations . . . . .	17
2.1.3.1 The injection process . . . . .	18
2.1.3.2 Measurements . . . . .	18
2.1.3.3 Simulation studies with the HEADTAIL code . . . . .	19
2.1.4 Acceleration . . . . .	23
2.1.5 Transition Crossing . . . . .	24
2.1.6 Extraction . . . . .	24
2.1.7 Tunnel shielding . . . . .	25
2.1.8 Machine operability . . . . .	25
2.1.9 Exotic scenarios . . . . .	26
2.2 HI Beams in the SPS . . . . .	26
2.2.1 Introduction . . . . .	26
2.2.2 Main Limitations and Studies of high intensity CNGS-type beams in the SPS . . . . .	27
2.2.2.1 High intensity beams in the SPS after LIU . . . . .	30

<b>3</b>	<b>Proton Beam Transfer</b>	<b>33</b>
3.1	Introduction and assumptions . . . . .	33
3.2	400 GeV/c proton beam from SPS . . . . .	34
3.2.1	400 GeV/c beam extraction from SPS LSS2 to target near North Area . . .	34
3.2.1.1	Non-Local extraction simulations and tests at 440 GeV . . . . .	34
3.2.1.2	LSS2 extraction elements . . . . .	39
3.2.1.3	Transport through TT20 . . . . .	39
3.2.1.4	Switching from TT20 into new beamline . . . . .	40
3.2.1.5	New beamline from TT20 to LAGUNA neutrino target . . . . .	42
3.2.2	400 GeV/c extraction from SPS LSS6 to target near LSS1 . . . . .	46
3.2.2.1	Switching from TT60 into new beamline . . . . .	46
3.2.2.2	Transport to LAGUNA target . . . . .	46
3.3	50 GeV/c proton beam transfer for Phase II with HP-PS . . . . .	50
3.3.1	Transfer of 50 GeV/c beams to North Area target location . . . . .	51
3.3.2	Transfer of 50 GeV/c beams to LSS1 area target location . . . . .	54
3.4	4 GeV/c H- transfer line from SPL to HP-PS injection . . . . .	57
3.4.1	Beam line optics . . . . .	58
3.5	Summary and conclusions . . . . .	60
3.6	Secondary yield and target design . . . . .	60
3.6.1	Primary beam energy . . . . .	61
3.6.2	Target segmentation . . . . .	63
3.6.3	Material . . . . .	63
3.6.4	Target dimensions . . . . .	64
3.7	Beam Optimization . . . . .	64
3.7.1	Horn shapes . . . . .	66
3.7.2	Monte-Carlo simulation . . . . .	67
3.7.3	Genetic Algorithm . . . . .	68
3.7.4	Selected configurations and corresponding neutrino fluxes. . . . .	70
3.8	Decay pipe configuration . . . . .	71
3.9	Muon shielding configuration . . . . .	72
3.9.1	Presentation of the WANF facility and comparison with CN2PY. . . . .	72
3.9.2	Purely passive shielding. . . . .	76
3.9.3	The "dipole-like" toroid magnet shield. . . . .	77
<b>4</b>	<b>The CN2PY Neutrino Beam Design</b>	<b>81</b>
4.1	The CNGS experience and lessons learned . . . . .	81
4.1.1	The proton beam . . . . .	81
4.1.2	The neutrino beam . . . . .	84
4.1.3	Operational Performance . . . . .	87
4.2	Overview . . . . .	96
4.2.1	General radiation protection guidelines . . . . .	97
4.3	Geology and Metrology . . . . .	98
4.3.1	Physics Constraints . . . . .	99
4.3.2	Geodesy . . . . .	99
4.3.2.1	Determination of the Beam Line Parameters . . . . .	99
4.3.3	Geodetic Networks . . . . .	100
4.3.4	Civil Engineering . . . . .	100
4.3.5	Metrology . . . . .	101
4.3.6	Survey and Alignment . . . . .	101
4.3.6.1	Primary Beamline . . . . .	101
4.3.6.2	Secondary Beamline . . . . .	101

4.3.6.3	Monitoring . . . . .	101
4.3.7	As-built Measurements . . . . .	102
4.4	The target cavern . . . . .	102
4.4.1	The He tank . . . . .	102
4.4.2	Shielding . . . . .	104
4.4.2.1	Energy deposition and cooling . . . . .	105
4.5	Target configuration . . . . .	110
4.5.1	The beam window . . . . .	110
4.5.2	Target and Horn integration and assembly . . . . .	110
4.5.3	Remote Maintenance and Test Area . . . . .	110
4.5.4	Graphite target for 400 GeV beam . . . . .	112
4.5.4.1	Energy deposition study . . . . .	113
4.5.4.2	Design proposals . . . . .	113
4.5.4.3	Engineering studies . . . . .	115
4.5.4.4	Summary . . . . .	117
4.5.5	Helium cooled graphite target for 50 GeV beam . . . . .	117
4.6	Focusing elements . . . . .	126
4.6.1	Design overview . . . . .	127
4.6.2	Electric circuits . . . . .	127
4.6.3	General Mechanical concept . . . . .	127
4.6.3.1	Electrical systems . . . . .	131
4.6.3.2	Water and He systems . . . . .	137
4.6.3.3	FE Analysis of the horn structure . . . . .	137
4.7	The Horn Power Converters . . . . .	147
4.7.1	Introduction and requirements . . . . .	147
4.7.2	Topology and parameters . . . . .	147
4.7.2.1	Regulation and control . . . . .	150
4.8	The decay pipe . . . . .	150
4.8.1	Thermal analysis . . . . .	153
4.8.2	Mass flow considerations . . . . .	158
4.8.3	Decay pipe accessories . . . . .	158
4.9	The hadron stop . . . . .	158
4.9.1	Design overview . . . . .	159
4.9.2	Thermal calculations . . . . .	163
4.10	The muon stations . . . . .	166
4.11	Critical beam instrumentation . . . . .	167
4.12	Handling issues . . . . .	167
4.13	Shielding elements . . . . .	167
4.14	General Services . . . . .	167
4.14.1	Cooling networks . . . . .	167
4.14.2	Ventilation systems . . . . .	167
4.14.3	Electrical networks . . . . .	168
<b>5</b>	<b>The High-Power Proton Synchrotron Accelerator Feasibility Study</b>	<b>169</b>
5.1	Design requirements and choices . . . . .	169
5.1.1	Average beam power . . . . .	169
5.1.2	Circumference . . . . .	170
5.1.3	Repetition rate . . . . .	171
5.1.4	Intensity . . . . .	171
5.1.5	Electrical Power . . . . .	172
5.1.6	Losses control . . . . .	172



5.1.7	Optics and layout . . . . .	172
5.1.8	Machine parameters . . . . .	172
5.2	Ring optics and beam dynamics . . . . .	174
5.2.1	Lattice . . . . .	174
5.2.1.1	Linear optics and layout . . . . .	174
5.2.1.2	Space-charge and aperture considerations . . . . .	177
5.2.1.3	Tune working point adjustment . . . . .	180
5.2.1.4	Chromaticity correction . . . . .	180
5.2.2	Orbit Correction Studies . . . . .	182
5.2.3	Non-linear optics and machine imperfections . . . . .	185
5.2.4	Multipole field errors . . . . .	186
5.2.4.1	Frequency maps . . . . .	186
5.2.5	Space-charge studies for the HP-PS . . . . .	187
5.3	Beam transfer . . . . .	190
5.3.1	$H^-$ injection . . . . .	192
5.3.1.1	Optics requirements . . . . .	192
5.3.1.2	Foil Stripping . . . . .	192
5.3.1.3	Beam loss control . . . . .	193
5.3.1.3.1	Inelastic nuclear scattering . . . . .	194
5.3.1.3.2	Elastic nuclear scattering . . . . .	194
5.3.1.3.3	Multiple Coulomb Scattering . . . . .	194
5.3.1.3.4	Fringe Field Deflection . . . . .	195
5.3.1.4	Laser Stripping . . . . .	196
5.3.2	Longitudinal painting for $H^-$ injection . . . . .	198
5.3.2.1	Basic assumptions . . . . .	199
5.3.2.2	Injection with energy offset and single harmonic RF system . . . . .	200
5.3.2.3	Summary . . . . .	200
5.3.3	Extraction Systems . . . . .	203
5.3.3.1	50 GeV extraction . . . . .	203
5.3.3.2	75 GeV extraction . . . . .	205
5.3.4	The LP-SPL design . . . . .	205
5.3.4.1	Fulfilling the HP-PS beam requirements . . . . .	207
5.4	Longitudinal parameters during acceleration . . . . .	207
5.4.1	Acceleration cycles . . . . .	207
5.4.2	Beam stability . . . . .	210
5.4.2.1	Stability at injection . . . . .	211
5.4.2.2	Constraints from optics . . . . .	211
5.4.2.3	Stability during acceleration . . . . .	212
5.4.3	Optimum cycle . . . . .	215
5.4.4	Injection into SPS . . . . .	220
5.4.5	Summary . . . . .	221
5.5	Collimation . . . . .	223
5.5.1	Introduction . . . . .	223
5.5.2	Collimators and halo settings . . . . .	224
5.5.2.1	Collimator-placement and jaw opening size . . . . .	224
5.5.2.2	Collimator-material . . . . .	225
5.5.2.3	Halo settings . . . . .	227
5.5.3	Length and material of primary collimators . . . . .	230
5.5.3.1	Inefficiency . . . . .	230
5.5.3.2	Absorptions . . . . .	231
5.5.3.3	Losses in the collimation-LSS . . . . .	232

5.5.3.4	Losses downstream the collimation-LSS . . . . .	247
5.5.4	Impact parameter and material of secondary collimators . . . . .	247
5.5.4.1	Inefficiency . . . . .	247
5.5.4.2	Absorptions . . . . .	247
5.5.4.3	Losses in the collimation-LSS . . . . .	259
5.5.4.4	Losses downstream the collimation-LSS . . . . .	259
5.5.5	Power deposition . . . . .	259
5.5.6	Higher statistics . . . . .	273
5.5.7	Both H and V halo . . . . .	279
5.5.8	Summary . . . . .	282
5.6	Magnetic Elements . . . . .	282
<b>6</b>	<b>Implementation</b> . . . . .	<b>287</b>
6.1	Civil engineering considerations . . . . .	287
6.1.1	Overview . . . . .	287
6.1.2	Civil Engineering . . . . .	291
6.1.2.1	Location . . . . .	291
6.1.2.2	Land Features . . . . .	293
6.1.2.3	Geology . . . . .	293
6.1.2.4	Site Development . . . . .	296
6.1.2.5	Construction Methods . . . . .	296
6.1.2.6	Junction Cavern . . . . .	297
6.1.3	Proton Beam Tunnel . . . . .	297
6.1.4	Neutrino Beam Tunnels . . . . .	299
6.1.4.1	The transfer area . . . . .	300
6.1.4.2	The service cavern - TCV . . . . .	304
6.1.5	Decay and Hadron Stop tunnels . . . . .	306
6.1.5.1	The hadron stop tunnel . . . . .	306
6.1.6	Near Detector Area . . . . .	307
6.1.7	Civil Engineering Cost Considerations . . . . .	307
6.1.8	Civil Engineering Scheduling and Resource Considerations . . . . .	307
6.2	Handling and transport . . . . .	307
6.2.1	Standard cranes . . . . .	308
6.2.1.1	Main access shaft crane . . . . .	308
6.2.1.2	The near detector shaft surface crane . . . . .	308
6.2.1.3	The near detector tunnel overhead crane . . . . .	312
6.2.2	Remotely operated cranes . . . . .	312
6.2.2.1	Transport tunnel overhead crane . . . . .	312
6.2.2.2	Beam tunnel crane . . . . .	315
6.2.2.3	Remote operations . . . . .	319
6.2.3	Remotely operated Omni-wheel platform . . . . .	323
6.2.4	Lifts . . . . .	323
6.3	Installation scenarios . . . . .	325
6.3.1	Hadron stop . . . . .	327
6.3.2	Decay pipe . . . . .	328
6.3.3	Target cavern installation . . . . .	330
6.3.3.1	Horn (Refelctor) installation and exchange . . . . .	331
6.3.3.2	Installation of Near Detector . . . . .	332

<b>7</b>	<b>The Near Detector</b>	<b>335</b>
7.1	General Considerations . . . . .	335
7.2	Beam at the ND . . . . .	335
7.2.1	ND Placement . . . . .	336
7.2.2	Spectra at the ND for a $\nu_\mu$ Run . . . . .	336
7.3	LBNO ND Layout . . . . .	336
7.4	Sub-detectors . . . . .	337
7.4.1	The Argon Gas Time Projection Chamber: TPC . . . . .	337
7.4.2	The Totally Active Scintillating Detector: T ASD . . . . .	337
7.4.3	The Electromagnetic Calorimeter: ECAL . . . . .	340
7.4.4	The Magnetised Iron Neutrino Detector: MIND . . . . .	340
7.4.5	The Air Magnet Around the Pressure Vessel . . . . .	340
7.5	LBNO ND Study Plan . . . . .	341
7.5.1	Phase 0 . . . . .	341
7.5.2	Phase 1 . . . . .	341
7.5.3	Phase 2 . . . . .	341
7.5.4	Phase 3 . . . . .	342
7.5.5	Phase 4 . . . . .	342
7.5.6	Phase 5 . . . . .	342
7.6	Software framework . . . . .	342
7.6.1	Third Party Dependency Software Versions . . . . .	343
7.7	Simulations . . . . .	343
7.7.1	The Near Detector Implementation in the Software . . . . .	343
7.7.1.1	The Time Projection Chamber . . . . .	343
7.7.1.2	The Scintillator Bars . . . . .	345
7.7.1.3	The Vessel . . . . .	345
7.7.1.4	The Magnetic Field . . . . .	345
7.7.1.5	The Magnet . . . . .	345
7.7.1.6	The Surrounding Environment . . . . .	345
7.7.2	Simulation of the Beam . . . . .	347
7.7.3	Expected TPC Rates . . . . .	347
7.7.4	Neutrino Interactions in the TPC . . . . .	348
7.7.5	Particles leaving the TPC . . . . .	350
7.7.6	TPC Momentum Reconstruction Techniques . . . . .	350
<b>8</b>	<b>Radiation and Environmental Aspects</b>	<b>357</b>
8.1	Radiological aspects . . . . .	357
8.1.1	FLUKA studies . . . . .	358
8.1.2	Prompt dose rates . . . . .	361
8.1.3	Residual dose rates . . . . .	362
8.1.4	Air activation . . . . .	377
8.1.5	Helium activation . . . . .	383
8.2	Environmental aspects . . . . .	383
8.2.1	Releases of radioactive substances to the ambient air . . . . .	386
8.2.1.1	Generic dose coefficients for atmospheric releases . . . . .	386
8.2.1.2	Target Chamber . . . . .	387
8.2.1.3	Hadron Stopper . . . . .	390
8.2.1.4	Helium volumes . . . . .	390
8.2.1.5	Summary and constraints . . . . .	393
8.2.1.6	Releases of radioactive substances to surface water . . . . .	396
8.2.1.7	Stray radiation at the surface of the facility . . . . .	397

8.2.1.8	Activation of soil, rock and groundwater . . . . .	397
<b>9</b>	<b>Acknowledgements</b>	<b>399</b>
<b>A</b>	<b>LAGUNA-LBNO Parameter List</b>	<b>401</b>
<b>B</b>	<b>Engineering drawings</b>	<b>403</b>
B.1	3-D model references in SmarTeam . . . . .	403
B.2	2-D model references in SmarTeam and EDMS . . . . .	403
	<b>Bibliography</b>	<b>407</b>



# List of Figures

1.1	Schematic view of the CERN to Pyhäsalmi long-baseline neutrino beam. . . . .	1
1.2	Oscillation probability for $(\nu_a \rightarrow \nu_b)$ as a function of the neutrino energy from eq. ?? for a 2300 km long baseline. . . . .	4
1.3	Oscillation probability for $\nu_\mu \rightarrow \nu_e$ (in blue) and $\bar{\nu}_\mu \rightarrow \bar{\nu}_e$ (in red) for four different values of $\delta_{CP}$ and for the normal hierarchy $\Delta m_{32}^2 > 0$ (NH) and $\sin^2(\theta_{13} = 0.09$ . The spectral information with the distinct positions of the first and second oscillation maxima and amplitude variations, provide an unambiguous determination of oscillation parameters and allows in principle to distinguish the two CP-converging scenarios. . . . .	5
1.4	Same as Fig. 1.3 but for inverted hierarchy $\Delta m_{32}^2 < 0$ (IH). . . . .	6
1.5	Integrated pot per year as a function of the overall efficiency of the accelerators and for 200 days of operation. For SPS this is a combination of the net efficiency of the accelerators combined with the beam sharing fraction with the fixed target physics program. . . . .	7
1.6	Schematic layout of the proposed CN2PY neutrino beam. The main elements of the neutrino beam and approximate distances from the target are indicated. . . .	8
1.7	Average current versus kinetic energy for a number of existing (blue) and future (red) high power machines [?]. . . . .	9
1.8	CN2PY layout Option A: Layout of the CN2PY beam in the CERN area using the SPS extraction channel in LSS6. The long proton beam transfer line is shown in blue. The second phase HP-PS is also shown with its transfer lines from LP-SPL and connection to the proton line (in green) . . . . .	12
1.9	CN2PY layout option B, with the facility located in the vicinity of the TCC2 target area in the CERN Preveessin site. The CN2PY beam line will be pointing downwards by 10.4 deg. The decay pipe and the two near detector locations at 800 m distance from the primary target is also shown. . . . .	13
2.1	SPS super-cycle configuration with five 6 s CNGS cycles, or 100% duty cycle of the neutrino beam. The intensity per cycle is $3.8 \cdot 10^{13}$ protons, corresponding to a beam power of <b>405 kW</b> . . . . .	15
2.2	Schematic representation of the PS injection region. The dashed line indicates the deviation from the design closed orbit due to the horizontal injection bump, which is created by the dipoles BSM40 - 44 (adapted from [?]). The elements are labeled using a combination of device-specific letters and two figures, indicating the straight section they are located in. . . . .	18
2.3	Horizontal difference signals on the CNGS (left) and TOF (right) beams on different turns after injection. . . . .	20
2.4	Vertical difference signals on the CNGS (left) and TOF (right) beams on different turns after injection. . . . .	20

2.5	Vertical signals of turns 20, 40 and 60 after injection of the TOF beam (left). The figure on the right shows the power spectrum computed every single turn. The trend of increasing oscillation frequencies is evident. . . . .	20
2.6	Top: The blue bar indicates a single bin of the measured data of the TOF beam. The vertical oscillations performed by this bin over the first 20 turns are represented by the black dots. In order to obtain the vertical tune of this respective bin a sinusoidal fit considering a window of five turns only (indicated by the red area) is computed. The window slides from turn 1 to turn 16 and the average over the obtained frequencies is considered as vertical tune of this bin. Bottom: A detuning following the line density is revealed and the maximum tune shift is found at the peak density of the bunch. The error bars represent the standard deviation, which increases significantly at the head and the tail of the bunch as the signal is dominated by the noise. . . . .	21
2.7	Simplified model of the PS vacuum chamber. The dashed line indicates the geometry of the cylindric chamber that was used as input for ImpedanceWake2D. . . . .	21
2.8	Simulation results for the TOF beam depicted in the same way as in Fig. 2.5. The intra-bunch oscillations as well as the increase in frequency are very well reproduced. . . . .	22
2.9	Tune shift along the bunch as deduced via simulations, which depends, likewise to the measurements shown in Fig. 2.6, on the local intensity of the bunch. The maximum vertical tune shift is similar to what was measured in the PS. . . . .	22
2.10	Simulation results for a single CNGS bunch with an intensity of $350 \cdot 10^{10}$ p at the current injection energy. . . . .	23
2.11	Simulation results for a future high-intensity single bunch with an intensity of $500 \cdot 10^{10}$ p at a kinetic energy of 2 GeV. The increase of the intra-bunch frequency is slower compared to the case shown in Fig. 2.10, leading to reduced requirements for the transverse damper system. . . . .	23
2.12	The 200 MHz voltage programme during the CNGS cycle together with available bucket area (left figure). The RF power required during acceleration cycle for nominal ( $4.4 \times 10^{13}$ ) and ultimate ( $7.0 \times 10^{13}$ ) CNGS intensities. . . . .	28
2.13	The voltage programmes tested during MD studies in 2012 (left figure). Corresponding BCT (intensity) signals after beam capture in the nominal voltage of 0.8 MV (black trace) and tested 0.6 MV (blue trace). . . . .	29
2.14	Left figure: typical example of the measured beam structure (a.u.) after capture in the SPS with 0.8 MV voltage. Right figure: average and minimum-maximum bunch length evolution during the CNGS cycle for Batch 1 (blue color) and Batch 2 (red color). . . . .	29
2.15	Left figure: average bunch length from 1400 ms till 1500 ms cycle time for Batch 1 (blue) and Batch 2 (red). Right figure: relative bunch length (with respect to the reference bunch length at 1450 ms) at 1457 ms (green), 1480 ms (magenta, transition crossing), 1490 ms (red), and 1501 ms (blue). . . . .	29
2.16	Studies of particle loss reduction during MD in 2012. Left figure: nominal (grey) and modified (blue) voltage. Right figure: beam intensity (orange) and bucket area in nominal (grey) and modified (blue) voltage. . . . .	30
2.17	Total 200 MHz voltage as a function of the RF current, available in the SPS for acceleration with maximum RF power per cavity limited to 700 kW for different RF configurations: present situation with 4 cavities and 18 sections (black curve), 6 cavities with 18 sections (magenta) and approved upgrade for 6 cavities with 20 sections (blue). The RF current of 0.73 A corresponds to bunch intensity $N = 4.8 \times 10^{13}$ (dashed vertical line) and 1.06 A to $N = 7 \times 10^{13}$ (4200 bunches spaced by 5 ns). Horizontal dashed line indicates the present limit of 7.5 MV. . . . .	31

2.18	The slip factor $\eta$ during the CNGS acceleration cycle for the two SPS optics: the present Q26 optics with $\gamma t = 22.8$ (solid line) and the Q20 optics with $\gamma t = 18$ used for the LHC beams from 2012 (dashed line). . . . .	31
2.19	The 200 MHz voltage programmes designed for acceleration of beams with various longitudinal emittance with constant momentum filling factor (0.95) of the RF bucket are shown for the present Q26 optics (left figure) and the new Q20 optics used for LHC beams (right). . . . .	32
3.1	Bumped (blue) and kicked (red) 440 GeV/c beam horizontal envelopes for non-local extraction over 2.5 km between SPS LSS6 and LSS2, with the SPS aperture. . . . .	35
3.2	Extraction bump (blue) and kicked (red) 440 GeV/c beam envelopes for non-local extraction in LSS2, showing MST and MSE septa (solid black) and extraction quadrupole field limits (orange). . . . .	35
3.3	Bumped (blue) and kicked (red) 440 GeV/c beam horizontal envelopes for non-local extraction in SPS LSS1, showing orbit bump to avoid TIDP. . . . .	36
3.4	Histograms of minimum aperture available in 1000 seeds for circulating and extracted 440 GeV/c beam. . . . .	36
3.5	Non-local fast extracted beam on the BTV screen in the TT20 transfer line, October 2012. . . . .	37
3.6	Measured last-turn trajectory of 440 GeV/c SPS beam kicked from LSS6 and extracted in LSS2, from beam tests in October 2012. . . . .	37
3.7	Losses at extraction septum as a function of extraction bump amplitude, with two slightly different beam emittances. The losses at low bump amplitude are the extracted beam on the outer edge of the septum, while those at high bump amplitude are the circulating beam on the inner edge of the septum. . . . .	38
3.8	Schematic of SPS extraction permit interlock loops which would be required for the non-local extraction. . . . .	38
3.9	Examples of possible TT20 locations for new BPMs and BLMs for fast extracted beam - a total of 12 new locations are needed and have been identified. . . . .	40
3.10	Location of new LAGUNA beamline just downstream of MSSB splitter-switch magnets. . . . .	40
3.11	Existing MSSB splitter magnets at the top of TT20, which would need to be replaced by a new bipolar laminated design. . . . .	41
3.12	Cross-sections of the existing MSSB and new MSSB-S magnets. . . . .	41
3.13	Switch region in TDC2, showing branch off of new beamline to LAGUNA and switch with proposed SHiP beamline. . . . .	42
3.14	Geometry of TT20 and new normal-conducting LAGUNA transfer line from SPS LSS62 including TT20 line to T2. The new beamline starts after the splitters, at around 630 m . . . . .	43
3.15	Cross sections of the QTG and MBG main magnets used for the 400 GeV/c TT41 transfer line from the SPS to the CNGS target. . . . .	44
3.16	Typical short straight section in the 400 GeV/c CNGS beamline, showing corrector and BPM located between the dipole and quadrupole. The tunnel slope at this location is 5.7%, to be compared to 18% for LAGUNA. . . . .	44
3.17	Optics of new beamline from SPS LSS2 to the LAGUNA target, including re-matched TT20, for fast extracted 400 GeV/c beam. . . . .	45
3.18	Minimum half-aperture (m) needed for beam acceptance in the line from LSS2 to the LAGUNA target, not including mechanical tolerances, sagitta or vacuum chamber. . . . .	46
3.19	Halfcell for new superconducting beamline from TT66 to the LAGUNA target. Dipoles are short to keep the sagitta small. . . . .	47



3.20	Geometry of new superconducting LAGUNA transfer line from SPS LSS6, including SPS ring and TT10 injection line, and TT20. . . . .	47
3.21	Optics of modified TT66 and new LAGUNA beamline, for fast extracted 400 GeV/c beam from LSS6. . . . .	48
3.22	Minimum half-aperture (m) needed for beam acceptance in the line from LSS6 to the LAGUNA target, not including mechanical tolerances, vacuum chamber or cold-bore. . . . .	49
3.23	Minimum half-aperture (m) needed for beam acceptance in the new beamlines to the LAGUNA target for 50 GeV/c beams, not including mechanical tolerances, vacuum chamber or cold-bore, and assuming the 400 GeV/c optics. . . . .	50
3.24	Cross-section of SPS tunnel (at a QF quadrupole), showing a 600x600 mm quadrupole and 1000x500 mm dipole for comparison. . . . .	52
3.25	Optics of 1.2 km long 50 GeV/c transfer line accommodated within the SPS tunnel, with a dipole field of 0.23 T. . . . .	53
3.26	Minimum half-aperture (m) needed for beam acceptance in the 50 GeV/c line inside the SPS tunnel from LSS1 to LSS2, not including mechanical tolerances, vacuum chamber or sagitta. . . . .	54
3.27	Optics of new 50 GeV/c beamline from HP-PS to the LAGUNA target. . . . .	55
3.28	Minimum half-aperture (m) needed for beam acceptance in the 50 GeV/c line from HP-PS to the LAGUNA target, not including mechanical tolerances, or vacuum chamber. . . . .	56
3.29	Slope of HP-PS to LAGUNA target transfer line, as a function of position in the line. The line has a maximum slope of about 26%, with most of it constant at 25%. . . . .	57
3.30	Longitudinal section of 4 GeV/c HP-PS H <sup>-</sup> injection line, showing the various crossing tunnels. The actual beam line must be bent more smoothly than indicated due to the Lorentz stripping limit. . . . .	57
3.31	Power loss from Lorentz stripping for the different SPL options. For the 4 GeV LP-SPL the dipole field in the injection line to the HP-PS is limited to 0.115 T, to keep beam losses below 0.1 W/m. . . . .	58
3.32	Beta and dispersion functions along the 4 GeV/c transfer line from SPL to HP-PS. . . . .	58
3.33	Calculated beam half-apertures along the 4 GeV/c transfer line from SPL to HP-PS. . . . .	59
3.34	Initial energy (left) and angular (right) distributions of perfectly focused $\pi^+$ giving rise to neutrinos at the FD within the first and second maximum oscillation energy ranges. $\theta_z$ is the relative angle between the beam axis and the pion. . . . .	61
3.35	Left (resp. right): Secondary $\pi^+$ yield of the target for a 400 GeV (resp. 50 GeV) primary proton beam in the $\{E_\pi, \theta_\pi\}$ space. $\theta_\pi$ is the momentum angle of the pion relative to the beam axis. . . . .	62
3.36	Angular distributions of the pion yield from the target for 400 GeV and 50 GeV primary energy. Left (resp. right): Selection of pions generating neutrinos at the first (resp. second) oscillation maximum: $E_\pi \approx 11$ GeV ( $E_\pi \approx 4$ GeV). . . . .	62
3.37	Energy (left) and angular (right) distributions of $\pi^+$ yield from the target for 400, 350 and 280 GeV primary beam energy. . . . .	62
3.38	Energy weighted relative yield of $\pi^+$ emitted at $\theta_\pi < 0.1$ rad for different gap lengths (left) and different densities (right). Red: $20 < E_\pi < 50$ GeV, corresponding to the energy range of interest in CNGS. Black: $2.5 < E_\pi < 25$ GeV, corresponding to the energy range of interest in LAGUNA/LBNO. . . . .	63

3.39	Kinematics of neutrinos from pion decays. The red horizontal line is the maximum angle with respect to the beam axis, $\theta_\nu^{\max} = 0.87 \times 10^{-5}$ rad, for a neutrino produced in the decay pipe to reach an on-axis 400 m diameter FD distant of 2300 km. The two red vertical lines are the position of the two first oscillation maxima for 2300 km long baseline. If the pions above 14 GeV are focused at an off-axis angle $\theta_\pi \sim 7.5 \times 10^{-3}$ rad, their decays can contribute to the FD neutrino flux near the first oscillation maximum energy. . . . .	65
3.40	Visual description of beam parameters. . . . .	68
3.41	CN2PY description in FLUKA for the beam optimization. Left: Target and horns chambers. Right: Beam Dump . . . . .	68
3.42	Left: Spatial distribution of the $\nu_\mu$ beams at 2300 km from the target between 0 and 50 km distance from the beam axis. Right: Same distribution but extending only up to $r = 10$ km. Perfect and unfocused beams are shown for comparison. . . . .	69
3.43	Fitness evolutions during the second round of optimization. Left: GLB400 optimization. Right: LE50 optimization. . . . .	70
3.44	Beam optics configurations in the LE-GLB space. The configurations above the red line that connects the maximum LE and the maximum GLB ever obtained is the sample is which the final configuration will be chosen. Left: GLB400 optimization. Right: LE50 optimization. . . . .	70
3.45	$\nu_\mu$ flux at FD of the selected configurations for both optimization iterations. Left: GLB400 optimization. Right: LE50 optimization. Fluxes that would be obtained assuming a perfect focusing of all the secondary particles are also shown. . . . .	71
3.46	2D cut views of horn (left) and reflector (right) corresponding to the selected configurations for the phase I at 400 GeV. . . . .	71
3.47	2D cut views of horn (left) and reflector (right) corresponding to the selected configurations for the phase II at 50 GeV. . . . .	73
3.48	Neutrino flux at the FD with an optimised focusing configuration and for different decay pipe configurations. . . . .	73
3.49	Relative $\nu_\mu$ flux at FD with respect to the decay tunnel length and radius. Left: "1st max" neutrino energy selection, right: "2nd max" neutrino energy selection. The flux of the $\{l_d = 300 \text{ m}, r_d = 1.5 \text{ m}\}$ configuration is set as reference. . . . .	74
3.50	Layout of the WANF facility after 1979. . . . .	74
3.51	Left: Concept of the toroidal magnet to shield the detectors from high energy muons (taken from [?]). Right: The toroidal magnet used in WANF [?]. . . . .	75
3.52	Muon fluence in the beam dump and near detector area with a 400 GeV primary beam. Please note the very different scale used on the y and z axes. The black lines on the left represent the layout of the end of the decay tunnel and the beam dump. The thin rectangular box at $z=800$ m represents the near detector volume. . . . .	76
3.53	Muon fluence along the beam axis in the area of the near detector for a passive iron shielding of 100 m long and for different diameters. The solid (resp. dashed) lines represent the average (resp. maximum) fluence at a given z position. The vertical red line indicates the position of the near detector and the horizontal ones shows the maximum level of muon background tolerable at the detector. . . . .	77
3.54	Layout of the beam dump with the active shield. The length $l$ , the radius $r$ and the shift position from the beam axis $s$ have been optimized with MC calculations. . . . .	78
3.55	Muon trajectories from secondary decays (400 GeV primary beam energy) into the active shield (left) and the earth before the near detector location (right). . . . .	78
3.56	Muon fluence along the beam axis in the area of the near detector for different configurations of the active muon shield. The distribution corresponding to the selected passive configuration is also shown for comparison. . . . .	79

4.1	Schematic representation of the production of an accelerator-made neutrino beam.	81
4.2	Layout of the CNGS underground structures at CERN where the neutrino beam is produced.	82
4.3	Photo of the 800 m proton beam transfer line for CNGS with the tilted magnets.	83
4.4	Photo of the CNGS target cavern with the target station in the forefront. The slope of the tunnel required to point to Grand Sasso is visible.	84
4.5	Sketch showing the vertical arrangement of the CNGS neutrino beam tunnels.	85
4.6	The CNGS target. Left: detail of a target head with the graphite rods the support structure and the external aluminium cylinder. Right: photo during the installation of the target unit with the five heads in its place in the beam. The side iron and marble shielding and the forced-air duct at the bottom are visible. In the final installation a top shielding with remotely movable blocks is installed.	86
4.7	Photo of the horn during its installation in the tunnel.	87
4.8	The hadron stop during its construction.	88
4.9	Integrated number of protons delivered from SPS to the CNGS target.	89
4.10	SPS super-cycle configuration with five 6 s CNGS cycles, or 100% duty cycle of the neutrino beam. The intensity per cycle is $3.8 \cdot 10^{13}$ protons, corresponding to a beam power of <b>405 kW</b> .	90
4.11	Plot showing the beam position in $x$ (left) and $y$ in front of the target as measured for almost the entire CNGS operation.	90
4.12	Expected $\nu_\mu$ fluence spectrum at Gran Sasso, compared to the product of oscillation probability times $\nu_\tau$ cross section.	91
4.13	The Muon monitoring station with 18 BLM detectors.	92
4.14	Central muon detector signal during the five years of physics for CNGS.	93
4.15	Cut view of the experimental area. The target chamber, surrounded by grey concrete blocks placed inside the helium vessel (in green) includes shielding elements (red iron blocks), cooling plates (blue aluminium plates) and elements as target, horn, reflector and its ancillaries and services.	97
4.16	View of the Helium tank showing the two openings for maintenance of the horn and reflector and the connection with the decay pipe. During operation, shutter is open and enclosed in the rectangular box situated over the vessel.	103
4.17	Downstream view of the Helium tank showing the flanged connection to the decay pipe and the stepped shape to compensate the slope. Openings for maintenance of the horn and reflector and decay pipe shutter enclosure can be appreciated.	103
4.18	Cut view of the target chamber. Shielding elements (red iron blocks), cooling plates (blue aluminium plates) and elements as target, horn, reflector and its ancillaries and services are placed inside the helium vessel (in green). The helium vessel is surrounded by concrete blocks.	104
4.19	Model of the Target chamber. One quarter of the chamber (1 m-length sector) is simulated. Iron thickness is 800 mm, while aluminium blocks are 200 mm thick. Water pipes (14 mm ID are also modelled).	106
4.20	Model of the Target chamber. Detail of the cooling channels imbedded in the aluminium blocks.	107
4.21	Detail of the boundary conditions. Heat was deposited as internally generated (volumetric heating) averaged over 80 mm thick layers, water pipes considered water at constant temperature (no temperature increase along the walls).	107
4.22	Profile temperature for an ideal case. A constant temperature of 25 was imposed at the external walls of the aluminium plates. Cooling is made by pure conductivity. Due to the peaked heat deposition, internal walls maximum temperature is 75 °C.	108

4.23	Heat deposition profile at the target chamber [50 GeV configuration]. Water cooling [20 °C, hf 2000 W/m <sup>2</sup> K] and He cooling [22 °C, hf 5 W/m <sup>2</sup> K] considered. Maximum temperatures at the roof iron blocks are around 70 °C. . . . .	108
4.24	Target and horn assembly. . . . .	111
4.25	View of the hot cell nearby the target cavern with the horns and the target handling station. . . . .	112
4.26	400 GeV beam structure. . . . .	113
4.27	FLUKA energy deposited study. . . . .	114
4.28	Target design proposal. In the cross-section view on the right, the inner graphite rod is shown at the venter. The outer structure with cocentring Graphite and Be tubse such to allow the He to flow through. The volume between the graphite rods and the Be structure will be in vacuum. . . . .	114
4.29	He flow circulation. . . . .	115
4.30	Graphite rod steady state temperature profile. . . . .	116
4.31	Graphite (up) and Beryllium (down) pipe steady-state temperature profile. . . . .	116
4.32	Thermal transient analysis for the first pulse (a): 1st pulse, (b): pause, (c): 2nd pulse. . . . .	116
4.33	Structural transient analysis for the first pulse. . . . .	117
4.34	Deformation of the structure due to its own weight. . . . .	118
4.35	Energy deposition in the target head as simulated by FLUKA. . . . .	119
4.36	Graphite head parameters. . . . .	119
4.37	Steady state heat load of the target head. . . . .	120
4.38	Stresses of the target head. . . . .	121
4.39	Thermal conductivity of the target. . . . .	122
4.40	Thermal conductivity of the target. . . . .	122
4.41	Von-mise stresses. . . . .	123
4.42	Heat deposition. . . . .	123
4.43	Target head internal stress. . . . .	125
4.44	Downstream view of the horn. . . . .	128
4.45	Drawing of the horn showing its main dimensions. . . . .	128
4.46	Cut view of the horn showing the integrated target, striplines, water noozles, feedings and striplines. . . . .	129
4.47	Cut view of the horn showing the integrated target, and its helium feeds . . . . .	130
4.48	Industrial nozzles used for cooling of metal castings. . . . .	130
4.49	Current parameters for the phase-I (left) and phase-II(right) operation. . . . .	131
4.50	Overall view of the striplines. A fast coupling is foreseen under the horn while standard couplings are used elsewhere.Total length is around 25 m. . . . .	132
4.51	View of the aluminium plates attached to the shells of the horn.. . . .	132
4.52	Cut view of the target chamber showing the striplines insertion. . . . .	133
4.53	CDetail of the striplines fast coupling connection. Left: Cut view showing the Cu plates on both sides during the vertical insertion. Right: Detail of the striplines-fast coupling connection showing the principle of the clamping mechanism. . . . .	133
4.54	Narrow clearance hydraulic torque wrenches. . . . .	134
4.55	Geometry and materials used in the thermal analysis of the striplines. . . . .	135
4.56	Boundary condition of the model. Phase 2 (left), Phase-1 (right). . . . .	136
4.57	Temperature map of the stripline submitted to the beam and current pulse. Left: for the phase 1 (400 GeV beam), Right: for the phase 2 (50 GeVbeam) and with an HTC set to a value close to natural convection (12 W/cm <sup>2</sup> /K). . . . .	137
4.58	Maximum and minimum temperature of the striplines submitted to the current and beam pulse against the heat transfer coefficient resulting from the helium flow cooling. . . . .	138

4.59	Cut view of the horn. The water quick connector is situated at the downstream part. It feeds the nozzles (situated at the top part of the horn via the rails and collects the water from the bottom pipe. . . . .	138
4.60	Cut view of the quick plug-in water connector. . . . .	139
4.61	The horn model used for the FE analysis. . . . .	140
4.62	Overall view of the horn structure used for the structural analysis. The whole structure has been simulated, although a cut is shown. . . . .	141
4.63	Mesh detail showing the cables used to support the internal conductor. Cables were considered prestressed (pre-stress force 20 kg). . . . .	141
4.64	Main vibration modes of the horn structure. Frequencies range between 93 and 117 Hz and concern mainly the internal conductor and the horn exit. . . . .	142
4.65	Details of the mesh used for the thermoelectrical analysis. . . . .	142
4.66	Details of the mesh used for the thermoelectrical analysis. . . . .	143
4.67	Detail of the boundary conditions and the geometry. Internal conductor is 2mm thick while external conductor is 20 mm thick. Connections are made through a massive flange. . . . .	143
4.68	Vertical (top) and Lateral (bottom) of the internal conductor. . . . .	145
4.69	Von Mises stress at the global model of the horn. Values are low except in the support regions. . . . .	146
4.70	Detail of the maximum stresses. They are reached in a non-critical area and are BC dependant. Can be reduced with slight modifications in the shape or thickness of the support. . . . .	146
4.71	Horn and Reflector power converters topology. . . . .	148
4.72	Simulated current waveform for the Horn (Phase I). . . . .	149
4.73	Simulated capacitor bank waveforms for the Horn (Phase I). . . . .	149
4.74	Top: Cut view of the entrance of the Decay pipe showing the water cooling channels and He shutter (depicted in transparent blue). Bottom:Detail of the decay pipe exit window. A 50 mm thick water edge-cooled plate closes the He volume and separates it from the hadron stop volume. . . . .	151
4.75	Example of Hydra-cool type cooling channels adapted to a circular geometry as the one present at the decay pipe.. . . .	152
4.76	Detail of the boundary conditions applied to the model of the decay pipe (0.5 m slice). Heat generation is applied to the pipe and the concrete, while no heat load is applied to the molasses. Water pipes were considered in the internal pipe and a constant temperature of 25 °C at the molasses was imposed. . . . .	153
4.77	Temperature in the first sector of the decay pipe above 600 °C. 25 °C imposed in the molasse . Total heat 118 kW . . . . .	154
4.78	Temperature profile in the first sector of the decay pipe around 190 °C. 25 °C imposed in the molasses and 10 cooling channels (20 mm width) . Heat @ BC=86 kW removed by water, 32 kW removed by conductivity to the molasses. . . . .	155
4.79	Detail of temperature profile in the first sector of the decay pipe around 190 °C. 25 °C imposed in the molasses and 10 cooling channels (20 mm width) . Heat @ BC =86 kW removed by water, 32 kW removed by conductivity to the molasses. Due to the temperature gradient along the circumference, more cooling channels are required. . . . .	155
4.80	Temperature in the decay pipe around 85 °C, maximum temperature in the concrete 93 °C. 25 °C imposed in the molasses and 16 cooling channels (20 mm width). This would be the minimal requirements . . . . .	156

4.81	Detail of the temperature profile in the decay pipe with a 16 cooling channels (20 mm width around 85 °C, maximum temperature in the concrete 93 °C. 25 °C imposed in the molasses). This would be the minimal requirements for water cooling. . . . .	156
4.82	With 32 cooling tubes, internal temperature of the decay pipe is below 50 °C. Maximum temperature is reached in the region concrete-molasses that surrounds the decay pipe. . . . .	157
4.83	Detail of the water cooling channels in the decay pipe. Water temperature set to 20 °C, convection coefficient to 2000 W/m <sup>2</sup> K. . . . .	157
4.84	View of the connection between the helium tank and the decay pipe. The helium shutter is placed vertically on the top of the tank and separates the volume of the He tank (2100 m <sup>3</sup> ) from the helium volume of the target chamber (105 m <sup>3</sup> ) . . . .	159
4.85	TVIEW of the Hadron stop. The graphite block is situated upstream, following the decay pipe. Iron dumps are shown in red. . . . .	160
4.86	Cut view showing details of the start of the Hadron stop section and the decay pipe exit with two helium inlets and a water cooled window. . . . .	161
4.87	View of the CNGS Hadron Stop. Graphite blocks, aluminium cooling plates and CERN Standard Iron blocks are shown. . . . .	161
4.88	View of the aluminium cooling blocks and the integrated cooling tubes. . . . .	162
4.89	View of the energy deposition profile at the hadron stop considered for the AN-SYS calculations for the 50 GeV beam. Top: $y - z$ plane, Bottom: $x - z$ plane. . . . .	163
4.90	Heat deposition profile at the hadron stop - 50 GeV configuration. . . . .	164
4.91	Heat deposition profile at the hadron stop - 400 GeV configuration. . . . .	164
4.92	Cut view showing the temperature profile for a water cooled hadron stop. 50 GeV beam, maximum temperature is 110 °C at the centre of the graphite block. . . . .	165
4.93	63 Cut view showing the temperature profile for a water cooled hadron stop. - 400 GeV beam, maximum temperature is 118°C at the centre of the graphite block.165	165
4.94	6Graphite reaction temperatures in different gases. (Data from Toyo Tanso USA).Maximum temperature of the graphite at the LAGUNA hadron stop is 120 °C. . . . .	166
5.1	Average current versus kinetic energy for a number of existing (blue) and future (red) high power machines [?]. . . . .	170
5.2	Possible CERN accelerator complex with LINAC4, LP-SPL and HP-PS . . . . .	173
5.3	Optics functions for the LSS considering foil injection (top left), LSS with laser injection (top right), NMC cell (bottom left) and one sixth of the full ring (bottom right). . . . .	176
5.4	Incoherent space charge detuning for the laser injection option. The 50 GeV and 75 GeV versions correspond to the top and bottom plots. The colour code shows the horizontal and vertical detuning (left and right, respectively). . . . .	178
5.5	Parametrisation of maximum dipole half-gap (top left), quadrupole aperture (top right), pole tip field (bottom left) in the plane of the emittances for the 75 GeV HP-PS with laser injection. The bottom right plot shows the radius along one sixth of the lattice. . . . .	179
5.6	Working points of the two injection options, foil (left) and laser (right), in the tune map. . . . .	180
5.7	Tunability plots for the foil injection option (left) and laser injection option (right). The colour code represents the maximum horizontal (top) and vertical (bottom) beta functions. . . . .	181
5.8	Off-momentum beta beating along one sixth of the machine for the foil injection scheme (left) and for the laser one (right). . . . .	181

5.9	Distribution of the maximum orbit deviation at the horizontal (left) and vertical (right) planes for the foil optics scheme, before (red) and after (blue) correction. . . . .	182
5.10	Distribution of the maximum required kicker-strength for 500 random seeds, in the horizontal (red) and vertical (blue) planes, in the foil (left) and laser (right) schemes. . . . .	183
5.11	Horizontal (left) and vertical (right) orbit deviations for the foil scheme, before (red) and after (blue) correction. . . . .	184
5.12	Horizontal (left) and vertical (right) orbit deviations for the laser scheme, before (red) and after (blue) correction. . . . .	184
5.13	Maximum orbit deviation for different percentages of used horizontal (red) and vertical (blue) correctors. For each case, a different set of correctors is used by MICADO. . . . .	185
5.14	On and off-momentum average transverse dynamic aperture measured in beam sizes for the HP-PS ring with foil injection (left) and laser injection (right) for 1000-turns tracking, using 100 random seeds of misalignment and correction. . . . .	185
5.15	On and off-momentum average transverse dynamic aperture measured in beam sizes for the HP-PS ring with foil injection (left) and laser injection (right) for 1000-turns tracking, using 100 random seeds of misalignment and correction and applying systematic multipole components. . . . .	187
5.16	Frequency and diffusion maps of the HP-PS for the foil injection option. In columns: -0.6% momentum deviation particles, on-momentum particles and 0.6% momentum deviation particles. The diffusion parameter is colour-coded in all plots. . . . .	188
5.17	Frequency and diffusion maps of the HP-PS for the laser injection option. In columns: -0.6% momentum deviation particles, on-momentum particles and 0.6% momentum deviation particles. The diffusion parameter is colour-coded in all plots. . . . .	189
5.18	Tune-spread (green) of $\sim(-0.22)$ created due to the space-charge effect . . . . .	191
5.19	Horizontal (top) and vertical (bottom) normalised emittance increase for 5,000 turns due to the space-charge effect, with (red) and without (blue) closed orbit errors. . . . .	191
5.20	Phase space distribution after painting over 600 turns. The particles in red represent the last injected bunch. . . . .	193
5.21	Total beam loss from stripping inefficiency and scattering. The optimum foil thickness is $1500 \mu\text{g}/\text{cm}^2$ . . . . .	195
5.22	Particle flow through the $\text{H}^-$ injection line . . . . .	196
5.23	Combined foil and laser $\text{H}^-$ injection system. The chicane bumpers are indicated in blue and red, the painting bumpers in green. Two foils are shown, one for the stripping of the injected ions and one for the waste beam. The laser equipment consists of a wiggler, an excitation laser and a specifically designed third chicane magnet. . . . .	197
5.24	Stripping scheme with neutralisation in a wiggler magnet or by photodissociation (left) and excitation with final stripping (right). . . . .	197
5.25	Required angle between ion and laser beam to reach the respective excited ion states for three different ion energies. . . . .	198
5.26	<i>LP-SPL bunches at injection in the HP-PS. Bunches that are represented by dashed lines are injected one turn later than the bunches represented by solid lines. The ellipses denote the full beam for an elliptical density, hence a parabolic profile is assumed for the simulations.</i> . . . . .	199

5.27	Example of the longitudinal phase space (bottom) and bunch density (top), for first injected turn (left) and after 10 turns (right) where the filamentation process of the LP-SPL bunches in the HP-PS bucket is clearly visible. . . . .	201
5.28	Longitudinal phase space (left) and bunch density (middle and right) for the 50 GeV baseline and foil injection, at the end of the painting process (top) and at the end of flat-bottom when beam is ready for acceleration (bottom) . . . . .	201
5.29	Longitudinal phase space (left) and bunch density (middle and right) for the 50 GeV baseline and laser injection, at the end of the painting process (top) and at the end of flat-bottom when beam is ready for acceleration (bottom) . . . . .	202
5.30	Longitudinal phase space (left) and bunch density (middle and right) for the 75 GeV option with foil injection, at the end of the painting process (top) and at the end of flat-bottom when beam is ready for acceleration (bottom) . . . . .	202
5.31	Longitudinal phase space (left) and bunch density (middle and right) for the 75 GeV option with laser injection, at the end of the painting process (top) and at the end of flat-bottom when beam is ready for acceleration (bottom) . . . . .	203
5.32	Betatron and dispersion functions for the 50 GeV foil option of the long straight section in the top plot and beam envelopes at extraction on the bottom. The elements in green denote dipoles, in red quadrupoles and in turquoise the kicker magnets. The septum blades are indicated in magenta. . . . .	204
5.33	Betatron and dispersion functions for the 75 GeV laser option of the long straight section in the top plot and beam envelopes at extraction on the bottom. The elements in green denote dipoles, in red quadrupoles and in turquoise the kicker magnets. The septum blades are indicated in magenta. . . . .	205
5.34	<i>Magnetic field and dB/dt during acceleration for the 50 GeV baseline (left) and 75 GeV option (right)</i> . . . . .	208
5.35	<i>Synchronous momentum (left) and synchronous voltage (right) for 50 GeV (blue line) and 75 GeV (red line).</i> . . . . .	208
5.36	<i>Accelerating voltage function for a constant filling factor of 80% and various longitudinal emittances for the 50 GeV baseline (left) and the 75 GeV option (right).</i> . . . . .	209
5.37	<i>Full momentum spread for a constant filling factor of 80% and various longitudinal emittances for the 50GeV baseline (left) and the 75GeV option (right).</i> . . . . .	209
5.38	<i>Bunch length for a constant filling factor of 80 % and various longitudinal emittances for the 50GeV baseline (left) and the 75GeV option (right).</i> . . . . .	209
5.39	<i>Narrow-band threshold during acceleration for a constant filling factor of 80% and various longitudinal emittances for the 50 GeV baseline (left) and the 75 GeV option (right).</i>	210
5.40	<i>Broad-band threshold during acceleration for a constant filling factor of 80%and various longitudinal emittances for the 50GeV baseline (left) and the 75 GeV option (right).</i> . . .	211
5.41	<i>Broad-band threshold at injection as a function of longitudinal emittance together with space charge impedance at injection for the 50 GeV baseline (left) and the 75 GeV option (right).</i> . . . . .	212
5.42	<i>Broad-band threshold during acceleration for various longitudinal emittances blow up schemes together with the space charge impedance for the 50 GeV baseline in case of foil injection (left) or laser injection (right).</i> . . . . .	216
5.43	<i>Broad-band threshold during acceleration for various longitudinal emittances blow up schemes together with the space charge impedance for the 75 GeV option in case of foil injection (left) or laser injection (right).</i> . . . . .	216
5.44	<i>Narrow-band threshold during acceleration for various longitudinal emittances blow up schemes together with the space charge impedance for the 50 GeV baseline in case of foil injection (left) or laser injection (right).</i> . . . . .	216



5.45	Narrow-band threshold during acceleration for various longitudinal emittances blow up schemes together with the space charge impedance for the 75 GeV option in case of foil injection (left) or laser injection (right).	217
5.46	Emittance blow-up during acceleration corresponding to values given in table 5.29 for the 50 GeV baseline in case of foil injection (left) or table 5.30 for laser injection (right).	217
5.47	Emittance blow-up during acceleration corresponding to values given in table 5.31 for the 75GeV option in case of foil injection (left) or table 5.32 for laser injection (right).	217
5.48	Voltage program and emittance program during the optimum cycle, both calculated for the 50 GeV baseline (left) and the 75GeV option (right).	218
5.49	Longitudinal emittance evolution and corresponding bunch length for all options considered (50 GeV, 75GeV, laser and foil injection).	218
5.50	Bunch full momentum spread (left) and synchrotron tune (right) during the optimum cycle, both calculated for all options considered (50 GeV, 75GeV, laser and foil injection).	218
5.51	Broad-band threshold together with the space-charge impedance (left) and the narrow-band threshold (right) during the optimum cycle both calculated for all options considered (50 GeV, 75GeV, laser and foil injection).	219
5.52	Required voltage to compress the bunch to 4 ns as a function of the longitudinal emittance at extraction for the 50 GeV baseline (blue dots) and the 75 GeV option (red dots)	220
5.53	Voltage program (left) and emittance program (right) during the cycle for injection into SPS, both calculated for all options under consideration.	221
5.54	Full bunch momentum spread (left) and full bunch length (right) during the cycle for injection into SPS, both calculated for all options under consideration.	221
5.55	Narrow-band and broad-band thresholds during acceleration together with space charge impedance for SPS injection calculated for 50GeV top energy (left) and 75GeV top energy (right).	222
5.56	Variation of the minimum difference between the broad-band threshold and the space charge impedance at extraction for injection into the SPS as a function of the beam intensity.	222
5.57	Halo particles could impact the magnets (grey rectangle), depositing energy that could lead to quenching (red dashed arrow). At a two-stage collimation system the halo particles (red arrow) will get a kick from a thin primary collimator (green rectangle) which will increase the possibility that they will subsequently impact a thick secondary collimator (blue rectangle) where they could get absorbed. The blue arrow represents the case of halo particles that escaped the collimation system and deposited their power in the aperture (purple colour).	223
5.58	Secondary collimators location (TCS1 and TCS2) as a function of the phase advance from the primary collimator (TCP). The dashed lines represent the extremum scattered trajectories that reach their maximum amplitude at the location of the two secondary collimators, and $d_s$ stands for the relative retraction between the primary and secondary collimators' jaws. Figure taken from [?].	224
5.59	$\beta(s)_x$ (continuous line) and $\beta(s)_y$ (dashed line) in the collimation-LSS. The location of the collimators is indicated (red: horizontal, blue: vertical)	226
5.60	$\alpha(s)_x$ (continuous line) and $\alpha(s)_y$ (dashed line) in the collimation-LSS. The location of the collimators is indicated (red: horizontal, blue: vertical)	226
5.61	Scattering angle (r.m.s.) for Graphite (red), Tungsten (green), and Copper (blue) collimators at injection energy (4 GeV).	227
5.62	Halo horizontal (red) and vertical (blue) phase-space when generating only horizontal or only vertical halos respectively.	228
5.63	Initial distribution of $x, x'$ (red) and $y, y'$ (blue) of generated H/V halos.	228
5.64	The impact parameter, $b_{x,y}$ is defined as the transverse offset between the impact location of a halo particle (red arrow) on the primary collimator (green rectangle) and the edge of its jaw.	229

5.65	Impact parameter on the primary collimators when generating a purely horizontal (red) or vertical (blue) halo at $3\sigma$ with $0.01\sigma$ thickness. Fewer particles interact with the primary collimators when a vertical halo is generated due to the value of $\alpha_y$ directly upstream the primary collimators. . . . .	229
5.66	Global inefficiency with respect to the thickness of the primary collimators for horizontal (round markers) and vertical (diamond markers) halos, for Graphite (red), Tungsten (green) and Copper (blue) primaries. . . . .	230
5.67	Global inefficiency with respect to the thickness of the primary collimators for horizontal (left) and vertical (right) halo, for Graphite (red), Tungsten (green) and Copper (blue), with and without additional $90^\circ$ collimators (round and diamond markers respectively). . . . .	231
5.68	Number of halo particles absorbed by each collimator over the the total number of particles that impacted at least once a collimator (in percentage), for different primary collimator material and thickness. . H: Horizontal, V: Vertical, P: Primary, S: Secondary. . . . .	234
5.69	Number of horizontal halo particles absorbed by each collimator over the the total number of particles that impacted at least once a collimator (in percentage), with and without additional $90^\circ$ collimators (round and diamond markers respectively), for different primary collimator material and thickness. H: Horizontal, V: Vertical, P: Primary, S: Secondary. . . . .	237
5.70	Number of vertical halo particles absorbed by each collimator over the the total number of particles that impacted at least once a collimator (in percentage), with and without additional $90^\circ$ collimators (round and diamond markers respectively), for different primary collimator material and thickness. . H: Horizontal, V: Vertical, P: Primary, S: Secondary. . . . .	240
5.71	Number of particles lost per m in the collimation-LSS, when using Graphite primary collimators . . . . .	242
5.72	Number of particles lost per m in the collimation-LSS, when using Tungsten primary collimators . . . . .	244
5.73	Number of particles lost per m in the collimation-LSS, when using Copper primary collimators . . . . .	246
5.74	$x$ - and $y$ -coordinates of particles lost per m between the first 45-51 m of the collimation-LSS when no additional collimators are used. . . . .	250
5.75	Number of particles lost per m outside the collimation-LSS, when using Graphite primary collimators; the arcs are the areas in yellow colour and the horizontal axis starts at 81.5 m. . . . .	252
5.76	Number of particles lost per m outside the collimation-LSS, when using Tungsten primary collimators; the arcs are the areas in yellow colour and the horizontal axis starts at 81.5 m. . . . .	254
5.77	Number of particles lost per m outside the collimation-LSS, when using Copper primary collimators; the arcs are the areas in yellow colour and the horizontal axis starts at 81.5 m. . . . .	256
5.78	$x$ - and $y$ -coordinates of particles lost per m between the first 81.5-110.0 m from the primary collimator. . . . .	257
5.79	Change of impact parameter with the halo size for both horizontal and vertical halos (round and diamond markers respectively). . . . .	257
5.80	Global inefficiency with respect to the impact parameter of horizontal (top) and vertical (bottom) halo, for Graphite (red), Tungsten (green) and Copper (blue) secondaries. . . . .	258

5.81	Number of horizontal halo particles absorbed by each collimator over the the total number of particles that impacted at least once a collimator (in percentage), for different secondary collimator material and impact parameters. H: Horizontal, V: Vertical, P: Primary, S: Secondary. . . . .	262
5.82	Number of vertical halo particles absorbed by each collimator over the the total number of particles that impacted at least once a collimator (in percentage), for different secondary collimator material and impact parameters. H: Horizontal, V: Vertical, P: Primary, S: Secondary. . . . .	265
5.83	Number of particles lost per m in the collimation-LSS, when using Graphite primary collimators . . . . .	266
5.84	Number of particles lost per m in the collimation-LSS, when using Tungsten primary collimators . . . . .	267
5.85	Number of particles lost per m in the collimation-LSS, when using Copper primary collimators . . . . .	268
5.86	Number of particles lost per m outside the collimation-LSS, when using Graphite secondary collimators; the arcs are the areas in yellow colour and the horizontal axis starts at 81.5 m. . . . .	269
5.87	Number of particles lost per m outside the collimation-LSS, when using Tungsten secondary collimators; the arcs are the areas in yellow colour and the horizontal axis starts at 81.5 m. . . . .	270
5.88	Number of particles lost per m outside the collimation-LSS, when using Copper secondary collimators; the arcs are the areas in yellow colour and the horizontal axis starts at 81.5 m. . . . .	271
5.89	$x$ - and $y$ -coordinates of particles lost per m within the first $\sim 30$ m from the end of the collimation-LSS when vertical halo is generated. . . . .	273
5.90	Number of particles lost per m within the collimation-LSS, when 20,000 horizontal (top) and vertical (bottom) halo particles were generated; each lost particle corresponds to a maximum power of 0.08 W. . . . .	274
5.91	H halo, first $\sim 70$ m from the end of the collimation-LSS . . . . .	275
5.91	Number of particles lost per m downstream the collimation-LSS, when 20,000 horizontal and vertical halo particles were generated (bottom plot: first $\sim 70$ m from the end of the collimation-LSS); each lost particle corresponds to a maximum power of 0.08 W. The arcs are the areas in yellow colour; top two plots are for horizontal halo, and bottom two plots for vertical halo. . . . .	276
5.92	Losses of halo in W/m outside the collimation-LSS, given that each lost particle corresponds to 0.08 W. The red line corresponds to the 1 W/m radiation limit and the arcs are the areas in yellow colour; top two plots are for horizontal halo, and bottom two plots for vertical halo. . . . .	278
5.93	Number of particles lost per m within and downstream the collimation-LSS, when both H and V halos were generated (bottom plot only extends to $s = \sim 200$ m as there were no losses downstream this position); the yellow colour represents the arc. . . . .	280
5.94	$x$ - and $y$ -coordinates of particles lost per m between the first 93-98 m from the primary collimator. . . . .	281
5.95	Horizontal (top) and vertical (bottom) tracks of particles lost within 150 m from the primary collimator. . . . .	283
5.96	Horizontal (top) and vertical (bottom) tracks of the absorbed particles. . . . .	284
6.1	Overall CERN environmental view with the two Options foreseen . . . . .	288
6.2	Schematic layout of the civil engineering complex for the Meyrin Option A . . . . .	289
6.3	Schematic layout of the civil engineering complex for the Preveessin Option B . . . . .	290

6.4	Tram stop outside CERN Meyrin Site . . . . .	292
6.5	Simplified cross section of the LHC housed mostly in Molasse Rock . . . . .	293
6.6	Typical geological borehole log and long profile for the area. . . . .	294
6.7	Typical $\odot$ Moraine $\odot$ borehole log. . . . .	295
6.8	$\odot$ Cut-and-Cover $\odot$ excavation technique at LINAC4 (left) and the road header machine (right) . . . . .	296
6.9	$\odot$ Cut-and-Cover $\odot$ excavation technique at LINAC4 (left) and the road header machine (right) . . . . .	297
6.10	New Junction Cavern in the existing TN-TT61 complex. . . . .	298
6.11	New Junction Cavern in the existing TDC2 complex (SHIP Project source). . . . .	298
6.12	Typical machine Extraction Tunnel cross section. . . . .	298
6.13	Plan view of surface buildings for the target cavern. . . . .	299
6.14	General 3D view of the neutrino beam underground structures. . . . .	299
6.15	2D cross-section of the main access shaft. . . . .	303
6.16	2D cross-section of the transport and morgue tunnels. . . . .	304
6.17	2D cross-section of the target cavern before (left) and after the side concrete walls are constructed (right). . . . .	306
6.18	3D top view of the hadron stop with the position of the muon detectors. . . . .	306
6.19	CE planning. . . . .	307
6.20	The target cavern shaft and the surface crane. . . . .	309
6.21	Detail on the target cavern access shaft crane. . . . .	310
6.22	The ND access shaft surface crane. . . . .	311
6.23	Detail of the ND access shaft crane. . . . .	312
6.24	The ND access shaft surface crane. . . . .	313
6.25	The transport tunnel overhead crane. . . . .	314
6.26	Detail of the transport tunnel overhead crane. . . . .	315
6.27	Layout of the gantry crane in the beam tunnel. . . . .	317
6.28	Detail of the layout and coupling of the gantry crane to the travelling trolley. . . . .	317
6.29	Detail of the handling of the horn and shielding blocks with the gantry crane. . . . .	318
6.30	3D drawing (left) and photo (right) of the electrical double twist lock hook used for the handling of shielding blocks. . . . .	320
6.31	3D drawing of the electrical single twist lock hook used for the handling of shielding blocks. . . . .	320
6.32	3D drawing indicating the location of the remote control operations cubical. . . . .	321
6.33	Photo showing the CNGS remotely operated overhead crane after the onboard camera and lighting upgrade. . . . .	322
6.34	Photo showing the CNGS remotely operated overhead crane after the onboard camera and lighting upgrade. . . . .	322
6.35	Cut view showing the access shafts and corresponding depths. . . . .	325
6.36	3D drawing showing the access shaft lift for the near detector site. . . . .	326
6.37	3D drawing showing the completed target cavern and service area. . . . .	330
6.38	Sequence of operations for the Near Detector installation. . . . .	333
7.1	Oscillation probabilities at the LBNO far detector and beam optimisation for $\nu_\mu$ . . . . .	336
7.2	$\nu_\mu$ and $\bar{\nu}_\mu$ spectra for horns set to $\nu_\mu$ run. Two primary proton beam configurations are given: the 400 GeV option operates with the target outside the horn, the 50 GeV option operates with the target inside the horn. Both beams are normalized to equivalent beam power. . . . .	336

7.3	$\nu_e$ and $\bar{\nu}_e$ spectra spectra for horns set to $\nu_\mu$ run. Two primary proton beam configurations are given: the 400 GeV option operates with the target outside the horn, the 50 GeV option operates with the target inside the horn. Both beams are normalized to equivalent beam power. . . . .	337
7.4	Schematic layout of the LBNO ND. . . . .	338
7.5	Plastic scintillator coverage within the pressure vessel. . . . .	338
7.6	Comparing quasi-elastic charged current interactions in liquid and gas argon. The three protons from the interaction vertex are apparent in the GAr TPC, but cannot be resolved in the LAr. . . . .	340
7.7	Sketch of the LBNO ND pressure vessel, showing its main features: the TPC, plastic scintillator modules surrounding the TPC, large flanges, feedthroughs. . .	341
7.8	Top: Images of the ND geometry in the ROOT display for closed (left), partly open (middle) and cross section (right). Bottom: A fully labelled image showing dimensions in cm with detector chambers labelled. . . . .	344
7.9	Left: The muon neutrino energy spectra expected at the ND for placements of 800, 900 and 1000 m from the target. Right: The muon neutrino energy spectra expected at the ND for various radius cuts. . . . .	346
7.10	The neutrino energy spectra, for flavour breakdown, expected at the ND of 800 m. Showing 4 flavours, $\nu_\mu$ in solid black, anti $\nu_\mu$ in solid red, $\nu_e$ in dashed black and anti $\nu_e$ in dashed red. . . . .	346
7.11	An illustration of the ND in the rock environment showing the potential muon tracks that would reach the TPC. The beam is incident from the left and the detector cross section is perpendicular to the beam axis. . . . .	348
7.12	The kinetic energy spectrum for muons in the TPC for neutrino interactions originating in (blue) and outside (red) the TPC. . . . .	349
7.13	The kinetic energies for particles leaving the TPC are shown for each face of the TPC. Upper left shows all types, upper right shows protons, lower left shows muons and lower right shows pions. . . . .	351
7.14	The kinetic energy as a function of angular distribution for particle type breakdown. Clockwise from the top left we have all particles, muons, protons, electrons, gammas and pions. . . . .	352
7.15	Event displays output from the simulation. Left image shows a well reconstructed CCQE event, while the right shows a poorly reconstructed CCQE event. . . . .	353
7.16	Left: The comparison of truth vs reconstructed muon neutrino momentum on an event by event binning. Right: The comparison of truth vs reconstructed muon momentum on an event by event binning. Upper plots show all neutrino interaction types, with only CCQE events shown in the lower plots. . . . .	354
7.17	Upper: The (truth - reconstructed)/truth neutrino momentum for all interaction types. Lower: The (truth - reconstructed)/truth neutrino momentum for CCQE events only, with equation ?? used in black histogram and equation ?? for the red histogram. For neutrino truth energies $\leq 10$ GeV . . . . .	355
7.18	The comparison of reconstructed neutrino momentum with truth values. The black histogram corresponds to truth values while the red histogram is for all reconstructed events. Using only CCQE events, the dotted red is using the momentum sum of the proton and muon and the dotted blue is using only the muon momentum. . . . .	355
8.1	Side view of the LAGUNA – LBNO target chamber as implemented in FLUKA showing the He-vessel with the secondary beam-line elements and the central shielding blocks. Iron is displayed in red, concrete in grey, aluminium in light blue and graphite in yellow. . . . .	358

8.2	Back view of the LAGUNA – LBNO target chamber, the connection tunnels and the service gallery as implemented in FLUKA. Iron is displayed in red, concrete in grey, aluminium in light blue. . . . .	359
8.3	Back view of the LAGUNA – LBNO target chamber showing the shielding inside and around the He-vessel, the connection tunnels and the access shafts to the water sumps. Iron is displayed in red, concrete in grey, aluminium in light blue. . . . .	359
8.4	Side view of the LAGUNA – LBNO hadron stopper area as implemented in FLUKA. Iron is displayed in red, concrete in light grey and graphite in yellow. . . . .	359
8.5	Prompt (left) and residual (right) dose rates (in $\mu\text{Sv/h}$ ) for the 50 GeV (blue) and 400 GeV (red) beam scenario. Note that the given results were based on a preliminary version of the LAGUNA – LBNO target chamber geometry and are only shown for comparative purposes. . . . .	361
8.6	Prompt ambient dose equivalent rates (in $\mu\text{Sv/h}$ ) in the target chamber (top: side view, bottom: front view at horn). . . . .	363
8.7	Prompt ambient dose equivalent rates (in $\mu\text{Sv/h}$ ) in the target chamber (top: along the y-axis at the horn, bottom: along the x-axis at the access to the first sump). . . . .	364
8.8	Prompt ambient dose equivalent rates (in $\mu\text{Sv/h}$ ) in the duct connecting the target chamber and the service gallery (top: top view, middle: side view, bottom: along the x-axis). . . . .	365
8.9	Prompt ambient dose equivalent rates (in $\mu\text{Sv/h}$ ) in the morgue room and the transport tunnel (top: top view, middle: side view, bottom: along the x-axis). . . . .	366
8.10	Prompt ambient dose equivalent rates (in $\mu\text{Sv/h}$ ) in the morgue room and the transport tunnel for the case of an accidental beam loss in the upstream part of the target chamber (top: top view, middle: side view, bottom: along the x-axis). . . . .	367
8.11	Side view of the residual dose rates (in $\mu\text{Sv/h}$ ) in the target chamber for different cooling times (1 hour, 1 day, 1 week). . . . .	369
8.12	Side view of the residual dose rates (in $\mu\text{Sv/h}$ ) in the target chamber for different cooling times (1 month, 6 months). . . . .	370
8.13	Front view of the residual dose rates (in $\mu\text{Sv/h}$ ) at the level of the horn for different cooling times (1 hour, 1 day, 1 week). . . . .	371
8.14	Front view of the residual dose rates (in $\mu\text{Sv/h}$ ) at the level of the horn for different cooling times (1 month, 6 months). . . . .	372
8.15	Residual dose rates (in $\mu\text{Sv/h}$ ) along the x- (top) and the y-axis (bottom) at the level of the horn for different cooling times (1 hour, 1 day, 1 week, 1 month, 6 months). . . . .	373
8.16	Residual dose rates (in $\mu\text{Sv/h}$ ) around the iron shielding located inside of the He-vessel for 1 week of cooling time (top) and along the height of the iron shielding above the horn for different cooling times (1 hour, 1 day, 1 week, 1 month, 6 months, 1year) (bottom). . . . .	374
8.17	Residual dose rates (in $\mu\text{Sv/h}$ ) around the concrete shielding located above the He-vessel for 1 week of cooling time (top) and along the height of the concrete shielding above the horn for different cooling times (1 hour, 1 day, 1 week, 1 month, 6 months, 1year) (bottom). . . . .	375
8.18	Residual dose rates (in $\mu\text{Sv/h}$ ) around the graphite target for 1 week of cooling time (top) and along the length of the graphite target for different cooling times (1 hour, 1 day, 1 week, 1 month, 6 months, 1year) (bottom). . . . .	376
8.19	Side view of the residual dose rates (in $\mu\text{Sv/h}$ ) in the hadron stopper tunnel for different cooling times (1 hour, 1 day, 1 week). . . . .	378
8.20	Side view of the residual dose rates (in $\mu\text{Sv/h}$ ) in the hadron stopper tunnel for different cooling times (1 month, 6 months). . . . .	379

8.21 Activity (in Bq) per radio-nuclide in the air of the target chamber (above) and the first part of the hadron stopper area (below) at the end of an operational year and no cooling time as a function of half-life (in s). Note that no air exchange was assumed. . . . . 382

# List of Tables

1.1	Major parameters and integrated beam intensities considered for the LBNO physics program. . . . .	6
1.2	Indicative depths of the CN2PY caverns worth respect to the target. . . . .	9
1.3	Design parameters of five ring options for the HP-PS, as compared to the PS2. . .	10
2.1	Main beam and RF parameters for the LHC and CNGS-type beams in the SPS under different conditions (operation, special studies and future plans). . . . .	27
3.1	Assumed beam characteristics for LAGUNA-LBNO transfer lines. . . . .	33
3.2	Parameters of the existing MSSB and new MSSB-S magnets. . . . .	42
3.3	Parameters of new normal conducting magnets and converters needed for the 400 GeV/c beamline from TT20 to the neutrino target . . . . .	44
3.4	Parameters of new superconducting magnets and converters needed for the 400 GeV/c beamline from TT60 to the neutrino target, using superconducting main magnets	49
3.5	Parameters of new low field magnets and converters needed for the 50 GeV/c beamline contained in the SPS tunnel, from SPS LSS1 to LSS2. . . . .	52
3.6	Parameters of new normal conducting magnets and converters needed for the 50 GeV/c beamline from HP-PS to the neutrino target. . . . .	56
3.7	Parameters of new normal conducting magnets and converters needed for the 4 GeV/c $H^-$ beamline from SPL to HP-PS. . . . .	59
3.8	Comparison of beam design parameters between T2K and LAGUNA/LBNO . .	64
3.9	Allowed ranges for the parameters describing the beam optics configuration and modifications for the second round of optimizations. . . . .	67
3.10	Parameter values of the selected configurations of the two rounds of optimizations.	72
3.11	Comparative table between WANF and LBNO facility. The WANF parameters have been taken from [?]. . . . .	73
3.12	Indicative values summarizing the WANF muon shielding . . . . .	75
3.13	Indicative values comparing passive vs magnetic shielding in LBNO. The contribution coming from the hadron stopper has been explicitly indicated in each case. . . . .	80
4.1	Key parameters of the CNGS proton beam at 400 GeV/c. . . . .	83
4.2	Estimates of annual proton beam delivery for different scenario of SPS operation used for the design of the CNGS facility, as explained in the text above. The estimates are for injection of two PS batches per SPS cycle of 6 s. . . . .	86
4.3	Helium required flow rates. Values in $m^3/h$ . . . . .	103
4.4	Heat loads at the Target chamber elements for the 50 GeV and 400 GeV operation. (values from FLUKA) . . . . .	105
4.5	Typical values of the heat transfer coefficients. Note that conservative values of 2000 W/( $m^2$ K) for cooling channels (water) and 5 W/( $m^2$ K) for He boundaries have been considered. . . . .	105



4.6	Summary of main results for a water cooled target chamber. Iron bock thickness is 800 mm, water tubes are imbedded in 200 mm thick aluminium plates. Maximum temperatures are reached at the internal walls. . . . .	106
4.7	Energy density and power on target components. MUST CHECK IF THE NUMBERS ARE PER PROT OR PER CYCLE! . . . . .	114
4.8	Key design parameters for the 400 GeV target option. . . . .	115
4.9	Model parameters for the target He cooling. . . . .	120
4.10	Stress distributions in the target versus time. Units are in MPa. . . . .	124
4.11	Stress distributions in the irradiated target versus time. Units are in MPa. . . . .	124
4.12	default . . . . .	132
4.13	Power density calculation according to FLUKA input data. . . . .	136
4.14	Total power deposition in the real structure. . . . .	136
4.15	Horn fatigue calculations according to RCC-MRx . . . . .	147
4.16	Horn and Reflector parameters and requirements for Phase I and Phase II. . . . .	147
4.17	Parameters of the Horn and Reflector power converters for Phase I and Phase II . . . . .	149
4.18	Energy deposition in the Decay Pipe for the 50 GeV case. Values are in kW . . . . .	153
4.19	Results of maximum temperatures for the second sector of the decay pipe. He was assumed at constant temperature (20 °C) along the whole length. . . . .	154
4.20	Minimal thermal properties required for the graphite blocks at the hadron stop. . . . .	162
4.21	Energy deposition in the Hadron stop for the 50 GeV case. Values are in kW. . . . .	162
5.1	Parameters of the LP-SPL relevant to the design of the HP-PS. . . . .	170
5.2	Required HP-PS proton intensity for the three extraction energies discussed, assuming a repetition rate of 1 Hz and a required beam power of 2 MW. . . . .	173
5.3	Machine parameters of the HP-PS. . . . .	175
5.4	Beam parameters chosen for the different HP-PS scenarios. . . . .	177
5.5	Assumed machine imperfections of the HP-PS lattice (RMS values). . . . .	182
5.6	Mean maximum closed orbit distortion for the foil and laser optics, before and after correction. . . . .	183
5.7	Mean maximum kicker-strength. . . . .	183
5.8	Maximum closed orbit distortion for both optics schemes, before and after correction when assuming 10% corrector and 5% monitor failure. . . . .	184
5.9	Relative multipole components in units $10^{-4}$ at the reference radius R. . . . .	186
5.10	Initial beam parameters . . . . .	190
5.11	Assumed machine imperfections of the HP-PS lattice (RMS values) . . . . .	190
5.12	Laser characteristics for $H^0$ to proton stripping . . . . .	198
5.13	Bunch length and full momentum spread after injection for the foil injection . . . . .	200
5.14	Bunch length and full momentum spread after injection for the laser injection . . . . .	200
5.15	Longitudinal emittance and RF voltage after injection for foil injection . . . . .	200
5.16	Longitudinal emittance and RF voltage after injection for laser injection . . . . .	201
5.17	Kicker and septum parameters for a 50 GeV fast extraction. . . . .	204
5.18	Kicker and septum parameters for a 75 GeV fast extraction. . . . .	206
5.19	Main LP-SPL beam characteristics, relevant for the injection into the HP-PS, based on the present LP-SPL design. . . . .	206
5.20	The required main LP-SPL beam characteristics. . . . .	207
5.21	Magnetic field at injection and extraction in the HP-PS together with the maximum dB/dt. . . . .	208
5.22	Longitudinal emittances at injection for all options . . . . .	212
5.23	Blow-up parameters at injection and extraction for constant voltage and energy dependance for foil injection . . . . .	213

5.24	Blow-up parameters at injection and extraction for constant voltage and energy dependance for laser injection . . . . .	213
5.25	Blow-up parameters at injection and extraction for variable voltage and energy dependance for foil injection . . . . .	213
5.26	Blow-up parameters at injection and extraction for variable voltage and energy dependance for laser injection . . . . .	214
5.27	Blow-up parameters at injection and extraction for the "Blow-up 2" scheme for both energies and injection options . . . . .	214
5.28	Blow-up parameters at injection and extraction for the "Blow-up 3" scheme for both top energies and injection options . . . . .	214
5.29	Summary of the emittance blow-up scheme optimisation for the 50 GeV baseline and Foil injection . . . . .	215
5.30	Summary of the emittance blow-up scheme optimisation for the 50 GeV baseline and Laser injection . . . . .	215
5.31	Summary of the emittance blow-up scheme optimisation for the 75 GeV option and Foil injection . . . . .	215
5.32	Summary of the emittance blow-up scheme optimisation for the 75 GeV option and Laser injection . . . . .	216
5.33	Positions and phase advances (H: Horizontal, V: Vertical, P: Primary, S: Secondary; phase advances are given with respect to the primary collimators) . . . . .	225
5.34	Positions and phase advances of the additional 90% collimators; phase advances are given with respect to the primary . . . . .	225
5.35	Collimator jaw opening-size and $\sigma_{x,y}$ at the centre of the collimators . . . . .	225
5.36	Summary of results for higher statistics . . . . .	273
5.37	Summary of results when generating H and V halos . . . . .	279
5.38	Dipole parameters for every HP-PS option. . . . .	285
5.39	Quadrupole parameters for every HP-PS option. . . . .	286
6.1	default . . . . .	301
6.2	Region volumes for the underground structures. The units are in $m^3$ . . . . .	302
6.3	Air or He volumes in the underground structures. . . . .	302
6.4	Key design parameters for the Target Cavern access shaft crane. . . . .	308
6.5	Key design parameters for the ND shaft crane. . . . .	310
6.6	Key design parameters for the ND overhead crane. . . . .	313
6.7	Key design parameters for the ND overhead crane. . . . .	314
6.8	Key design parameters for the beam tunnel crane. . . . .	316
6.9	Key design parameters for the beam tunnel trolley. . . . .	316
6.10	Sequence of operations for the Omni-wheel platform for the handling of the horn. . . . .	324
6.11	Key parameters of the ND shaft lift. . . . .	325
7.1	<i>Geometrical preliminary parameters for the detector layers.</i> . . . .	339
7.2	<i>Particle parameters relevant to the LBNO ND. Interactions in the sub-detectors are shown with a *.</i> . . . .	339
7.3	An extensive table showing all third party software and versions used for current simulation studies . . . . .	343
7.4	<i>Material Parameters.</i> . . . .	345
7.5	A table showing the number of muons per spill reaching the TPC from neutrino interactions inside and outside the TPC. Inside the TPC corresponds to a signal muon and outside corresponds to a sand muon. Errors are statistical only. . . . .	348
7.6	A table showing the number of primary particles generated at in the TPC from neutrino interactions. . . . .	349

7.7	A table showing the number of muons per spill reaching the TPC from neutrino interactions inside and outside the TPC. Inside the TPC corresponds to a signal muon and outside corresponds to a sand muon. Errors are statistical only. . . . .	350
8.1	Elemental composition of the shielding materials as defined in the FLUKA studies.	360
8.2	Parameters of the two standard beam scenarios as employed in the FLUKA studies.	361
8.3	Target area: Radionuclide yield (nuclide per primary proton), total activity at the end of an operational year (in Bq), CA values (in Bq/m <sup>3</sup> ) and ratio of the activity concentration to the CA values. Note, that the Swiss legislation does not include the CA values for some of the short-lived radionuclides, which are however irrelevant for the given studies. . . . .	380
8.4	Hadron stopper area (first 32 m): Radionuclide yield (nuclide per primary proton), total activity at the end of an operational year (in Bq), CA values (in Bq/m <sup>3</sup> ) and ratio of the activity concentration to the CA values. Note, that the Swiss legislation does not include the CA values for some of the short-lived radionuclides, which are however irrelevant for the given studies. . . . .	381
8.5	Activation of helium (top) vs. air (bottom) in the He-vessel: Radionuclide yield (nuclide per primary proton), total activity at the end of an operational year (in Bq), CA values (in Bq/m <sup>3</sup> ) and ratio of the activity concentration to the CA values. Note, that the Swiss legislation does not include the CA values for some of the short-lived radionuclides, which are however irrelevant for the given studies. . .	384
8.6	Activation of helium (top) vs. air (bottom) in the decay pipe: Radionuclide yield (nuclide per primary proton), total activity at the end of an operational year (in Bq), CA values (in Bq/m <sup>3</sup> ) and ratio of the activity concentration to the CA values. Note, that the Swiss legislation does not include the CA values for some of the short-lived radionuclides, which are however irrelevant for the given studies. . .	385
8.7	Dose coefficients for atmospheric releases at three receptor places with the most probable wind directions from the source location and the generic set used in dose calculations for long-term releases and short-term releases . . . . .	388
8.8	Production and releases of radioactivity from the Target Chamber as well as resulting effective doses for the mean residence time of air inside the compartment of 3600 s. . . . .	389
8.9	Production and releases of radioactivity from the Hadron Stopper as well as resulting effective doses for a leak with the mean residence time of air inside the compartment of 2 days. . . . .	391
8.10	Production and releases of radioactivity from the Hadron Stopper as well as resulting effective doses for a flush of the compartment after the annual operation period (a short-term release scenario). . . . .	392
8.11	Production and releases of radioactivity from the He volumes as well as the resulting annual effective doses for the scenario of leaking volumes for one annual operation period. . . . .	394
8.12	Production and releases of radioactivity from the He volumes as well as the resulting annual effective doses for the scenario of the perfectly tight volumes flushed at the end of the annual operation period (a short-term release). . . . .	395
8.13	Summary of the maximum annual effective doses incurred to a member of the public due to releases of radioactive substances to the ambient air from the four most activated compartments. . . . .	396
8.14	Production of the four radionuclides most relevant for groundwater pollution during one 180-day operation period with $2.4 \times 10^{14}$ p/second. . . . .	398
B.1	Total Model of CN2PY facility . . . . .	403
B.2	Part Model - CN2PY Target Area. . . . .	403

B.3	Part Model - CN2PY Service Area. . . . .	403
B.4	Part Model - CN2PY Morgue Area. . . . .	404
B.5	Part Model - CN2PY Beam Areas. . . . .	404
B.6	Part Model - CN2PY Hot Cell Area. . . . .	404
B.7	Part Model - CN2PY Near Detector Area. . . . .	404
B.8	3-D Part Model - CN2PY Area. . . . .	405
B.9	2-D Total Model - CN2PY Layouts . . . . .	405



# Acronyms, Abbreviations

<b>CERN</b>	European Center for Nuclear Research
<b>CN2PY</b>	CERN Neutrinos to Pyhasalmi
<b>CNGS</b>	CERN Neutrinos to Gran Sasso
<b>FT</b>	Fixed Target
<b>FCC</b>	Future Circular Collier
<b>HP-PS</b>	High-Power Proton Synchrotron
<b>IDS-NF</b>	International Design Study for a Neutrino Factory
<b>LBNO</b>	Long Baseline Neutrino Oscillaiton Experiment
<b>LP-SPL</b>	Low-power Superconducting Proton Linac
<b>LHC</b>	CERNs Large Hadron Collider
<b>LINAC4</b>	CERNs Linear Accelerator 4
<b>SPS</b>	CERNs Super Proton Synchrotron
<b>PMNS</b>	The PMNS neutrino model
<b>pot</b>	protons on target



# Chapter 1

## Introduction

A design study for a Long Baseline Neutrino Oscillation Experiment (LBNO) with a new conventional neutrino beamline facility at CERN was initiated in September 2011, supported by EC/FP7 funds. The beam will serve a next generation deep-underground neutrino observatory located at the Pyhäsalmi (Finland) mine at a distance of 2300 km from CERN. The code name CN2PY is given to the beam configuration shown Figure 1.1.

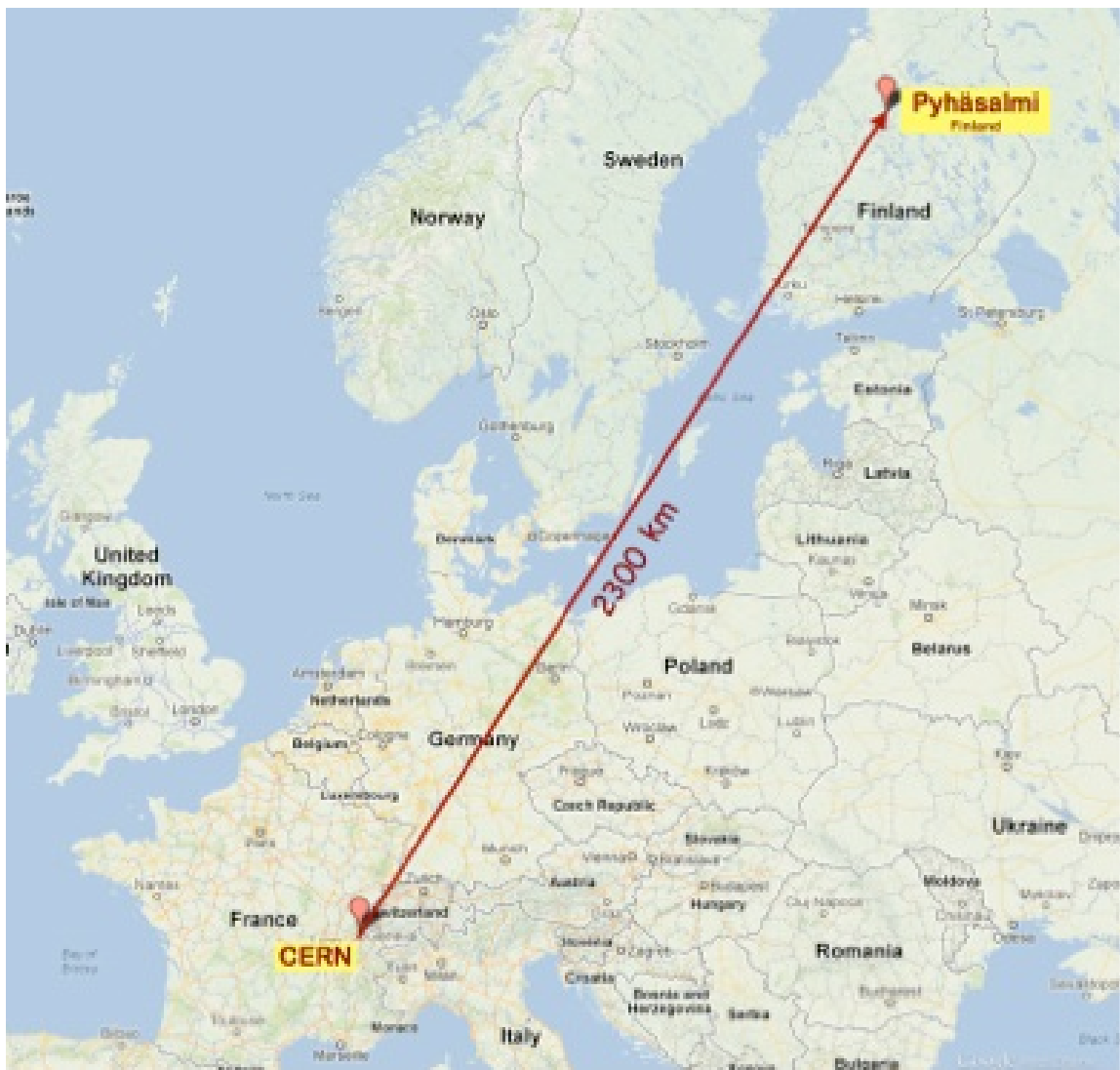


Figure 1.1: Schematic view of the CERN to Pyhäsalmi long-baseline neutrino beam.



CERN presently offers a high-intensity beam from SPS with nominal beam power of 510 kW, that was used until 2012 for CERN Neutrinos to Gran Sasso (CNGS). The beam from SPS will remain in the horizon of 10-15 years, among the highest intensity source of protons. With some limited effort, the beam intensity from SPS could be further increased in the coming years, also profiting from the planned improvements of the CERN accelerators as part of the planned LHC luminosity upgrade, to reach 750 kW. The study presented here, concerns the development of a conventional long-baseline broad-band neutrino beam facility with proven and affordable technologies based on the existing CNGS expertise. The new beam will be exploited in two phases:

**Phase-I** : In an initial phase the facility will use the beam from SPS at 400 GeV, aiming for a power of 0.7 MW following upgrades in the accelerator complex.

**Phase-II** : On a longer timescale new CERN proton accelerators could become available, allowing more intense neutrino beams to be considered. In this study, the option of using the Low-power Superconducting Proton Linac (LP-SPL) extension of LINAC4 feeding the beam to a new High-Power Proton Synchrotron (HP-PS) that provides proton beam in the range of 50-75 GeV of 2 MW in beam power is presented.

Alternative scenarios for Phase-II, like using higher energy or intensity beams from SPS or other injectors build in the framework of the new Future Circular Collider (FCC) recently proposed by CERN [?] could be envisaged, along with the option of building a Neutrino Factory at CERN, where the chosen baseline is among the ones considered in the International Design Study for a Neutrino Factory (IDS-NF) study [?].

This report outlines the conceptual design of the CERN Neutrinos to Pyhasalmi (CN2PY) neutrino beam facility, addressing the key design parameters and technical challenges for this MeagWass-class facility within the available resources and duration of the study. It is organised as follows:

- In the next sessions the physics requirements and an overview of the proposed implementation in the CERN area is presented.
- The availability of high-intensity proton beam using the existing CERN accelerators for the initial phase of the program is discussed next. The required R&D and technical issues to provide such beams in an operational mode for a possible neutrino program are presented.
- The following three chapters focus on the conceptual technical design for the proton beam transfer, the neutrino beam optimisation and design are presented.
- The key design features for the new HP-PS accelerator are discussed in Chapter ??
- Chapter ?? includes the engineering study of the implementation of the beam. The required civil engineering and handling activities and proposed solutions are presented.
- In Chapter ?? the radiation and environmental issues involved in the design and operation of this high-power facility are discussed.
- In the last chapter a possible project structure and timeline are presented.

Further information and drawings on specific topics is included in the appendix sections.

## 1.1 Physics requirements and beam design criteria

Proton accelerators are used to create controlled and intense neutrino  $\nu_\mu$  beams in the so-called "conventional" method as tertiary particles with a tunable mean energy. In this scheme, an intense proton beam is directed towards a target where secondary charged mesons ( $\pi$  and  $K$ ) are produced. A set of toroidal magnets capture and focus these secondary particles to produce a parallel beam that enters a long volume where they decay to neutrinos:

$$\begin{aligned}\pi^{+(-)} &\rightarrow \mu^{+(-)} + \nu_\mu(\bar{\nu}_\mu), \\ K^{+(-)} &\rightarrow \mu^{+(-)} + \nu_\mu(\bar{\nu}_\mu)\end{aligned}$$

A massive absorber at the end of the decay volume stops all remaining particles (including the fraction of non-interacting protons from the primary beam) leaving only muons and the neutrino beam through. The muon beam is measured in muon detectors before it is stopped in the earth. The produced neutrino beam consists mainly from muon neutrinos  $\nu_\mu$  with a small ( $\sim 2\%$ ) contamination of electron neutrinos ( $\nu_e$ ) from the Kaon and muon decay. The whole setup of the primary and the secondary beam elements is directed towards the far large-volume detector located underground few hundreds of kilometres away to detect the  $\nu_\mu \rightarrow \nu_x$  oscillations, where  $x$  is  $e$  or  $\tau$ . A near detector located at a near distance to the hadron stop measures the initial flux of the neutrino beam used to normalize the measured flux.

Neutrino oscillations are, at present, the only experimental evidence for physics beyond the Standard Model. In the framework of the three neutrino family scenario, the weak observable eigenstates  $\nu_\alpha$  ( $\alpha = e, \mu, \tau$ ) are defined as linear combinations of the mass eigenstates  $\nu_i$  (each having a defined mass  $m_i$ ,  $i = 1, 2, 3$ ) via the PMNS [?] matrix  $U$  as  $\nu_\alpha = \sum_i U_{\alpha i} \cdot \nu_i$ . The probability of oscillation from a flavor state  $\alpha$  to  $\beta$  is then given by the equation:

$$P(\nu_\alpha \rightarrow \nu_\beta) = \delta_{\alpha\beta} - 4 \sum_{i>j} \Re(U_{\alpha i}^* U_{\beta i} U_{\alpha j} U_{\beta j}^*) \sin^2(\hat{\Delta}_{ij}) + 2 \sum_{i>j} \Im(U_{\alpha i}^* U_{\beta i} U_{\alpha j} U_{\beta j}^*) \sin(2\hat{\Delta}_{ij}) \quad (1.1)$$

with

$$\hat{\Delta}_{ij} = \frac{(m_i^2 - m_j^2)L}{4E_\nu} = \frac{\Delta_{ij}L}{4E_\nu} \cong \frac{1.27\Delta_{ij}^2 L(\text{km})}{E_\nu(\text{GeV})} \quad (1.2)$$

$L$  the distance between the source and the detector (i.e the neutrino baseline), and  $E_\nu$  the neutrino energy. Equation ?? can be further simplified to:

$$P = \sin^2 2\theta \sin^2(1.27 \times (L/E) \times \Delta m^2) \quad (1.3)$$

where  $L$  is the baseline distance km,  $E$  is the average neutrino energy in GeV,  $\theta$  is the mixing angle for the two flavours concerned, and  $\Delta m^2$  the neutrino mass difference squared in  $\text{eV}^2$  that determines the oscillation wavelength. For a given distance  $L$  from the source, the energy of the neutrino beam, or the energy of the focused mesons, can be varied to address a  $\Delta m^2$  range and vice-versa, within the allowed values for the detector capabilities and particle flux. In Figure 1.2 the oscillation probability for the CN2PY baseline is plotted. The first and second oscillation maximum is shown at approx. 5 and 1.6 GeV respectively.

The  $3 \times 3$  unitary matrix  $U$  of eq. ?? is generally parameterized using the three mixing angles  $\theta_{12}, \theta_{23}$ , and  $\theta_{13}$ , the complex phase  $\delta_{CP}$ , and the two Majorana phases  $\alpha_{21}$  and  $\alpha_{31}$ . Past and ongoing solar or oscillation experiments allowed measuring most of these parameters in good precision [?]. The neutrino mass hierarchy, or the sign of  $\Delta m_{32}^2$  and the CP-violation phase  $\delta$  are the remaining unknown parameters and the focus of the Long Baseline Neutrino Oscillation Experiment (LBNO) experiment. Using the exact formulae the oscillation probabilities for the transition  $\nu_\mu \rightarrow \nu_e$  and  $\bar{\nu}_\mu \rightarrow \bar{\nu}_e$  can be estimated for the CN2PY baseline, shown in Figures 1.3 and 1.4 for different values of the CP violation phase and hierarchy.

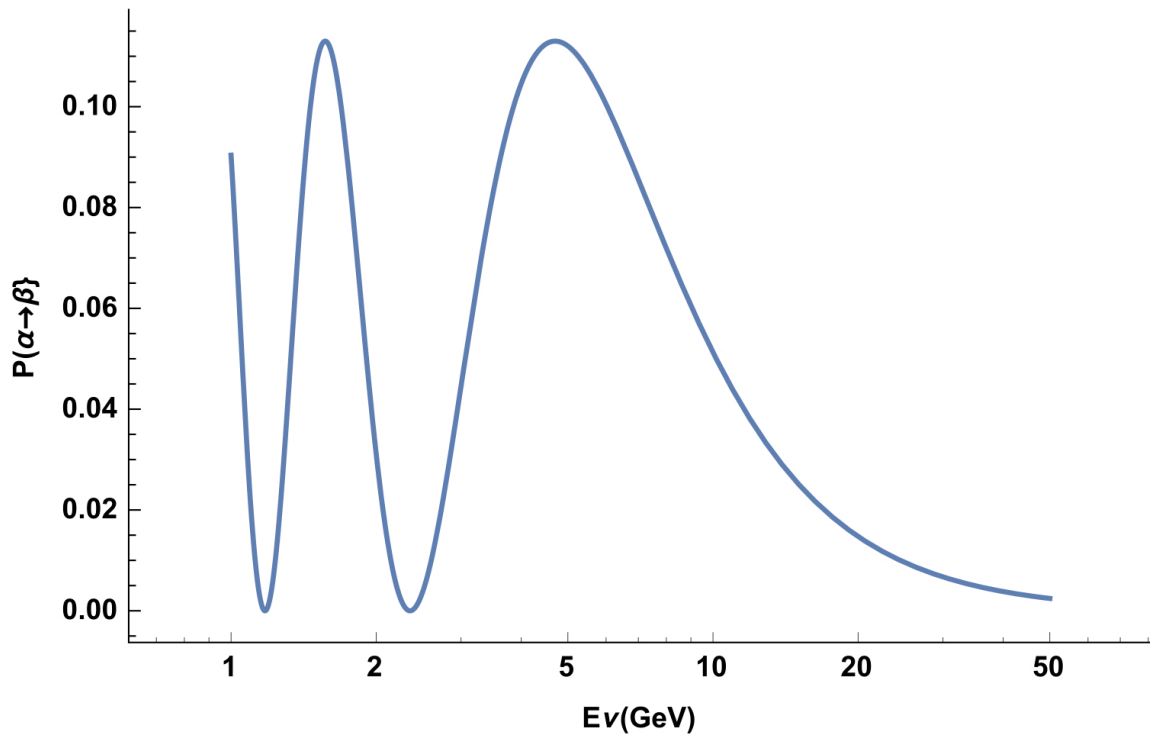


**Figure 1.2:** Oscillation probability for  $(\nu_\alpha \rightarrow \nu_\beta)$  as a function of the neutrino energy from eq. ?? for a 2300 km long baseline.

The LBNO experiment adopts a combination of methods to determine the mass hierarchy and CP-violation phase, based on precise measuring the disappearance and appearance energy spectrum shapes. As show in in Figures 1.3 and 1.4, by measuring with high-resolution the peak position and amplitude of the 1st and 2nd oscillation maximum and minimum and by comparing the data for neutrino and anti-neutrino induced oscillations, the missing parameters can be unambiguously determined. The Liquid Argon and magnetized iron detectors can provide complementary studies for all three active transitions  $\nu_m u \rightarrow \nu_\mu, \nu_\mu \rightarrow \nu_e$ , and  $\nu_\mu \rightarrow \nu_\tau$ , charged current events over the optimised energy range from approx. 1 to 10 GeV. Further, the precise measurement of the full oscillation spectrum would allow to verify the PMNS model and be sensitive to variations in neutrino or antineutrino oscillations beyond those originating from the  $\delta_{CP}$  and the mass hierarchy parameters.

In summary for the LBNO experiment the requirements for the neutrino beam design are:

- neutrino beam production in the range of 1 to 10 GeV
- optimised capture around the 1st and 2nd oscillation probability maxima, i.e. in the energy range [3.0,6.0] and [1.0,2.0] GeV respectively, with emphasis for enhanced rate for the second to compensate for the lower interaction cross-section.
- operation on both neutrino and antineutrino mode should be envisaged.

The physics program for the first phase of LBNO is based on a total of  $1.5 \times 10^{21}$  protons on target (pot) or approx. 7 times of the CNGS approved program. In Table ?? the expected integrated intensities along with the main beam parameters is shown.

The integrated pot estimates assume 200 days of operation per year and 80% efficiency and for the case of SPS 60% beam sharing with other users. In Figure 1.5 the integrated intensity in pot-per year is shown as a function of the overall efficiency of the injectors. From the CNGS experience, such increased SPS beam operation would be achievable should the improvements

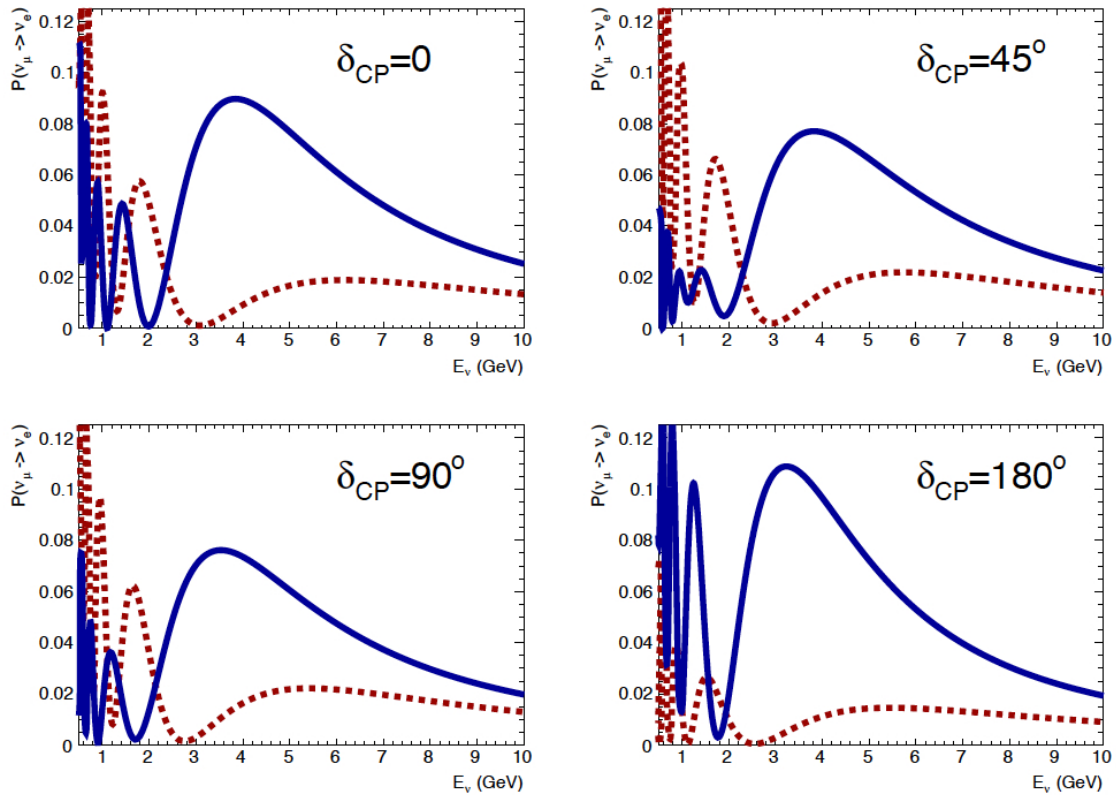


**Figure 1.3:** Oscillation probability for  $\nu_\mu \rightarrow \nu_e$  (in blue) and  $\bar{\nu}_\mu \rightarrow \bar{\nu}_e$  (in red) for four different values of  $\delta_{CP}$  and for the normal hierarchy  $\Delta m_{32}^2 > 0$  (NH) and  $\sin^2(\theta_{13}) = 0.09$ . The spectral information with the distinct positions of the first and second oscillation maxima and amplitude variations, provide an unambiguous determination of oscillation parameters and allows in principle to distinguish the two CP-converging scenarios.

described in detail in the following chapters are realised, and careful planning and sharing between this and other Fixed Target (FT) programs will be agreed.

In summary, a 10 years of operation for Phase-I is assumed to complete the planned physics program, that should be followed with similar period of exposure for Phase-II that could be further adopted and extended depending on the findings of Phase-I operation.

## 1.2 Overview of the Neutrino Beam

CERN has a long-standing experience in building neutrino beams from the early 60's, with the first at PS, followed by two generation of beam lines in the SPS, the WANF and recently the CNGS that resumed operation end of 2012. All facilities have achieved remarkable performance achieving record intensities for their time. The CN2PY design builds upon the technology developed for CNGS and the experience gained by its operation, that is further extended to match the expected increase in the primary beam power delivered by SPS and the future HP-PS synchrotron. CN2PY would be a conventional, third generation neutrino beam facility designed from the beginning to a maximum beam power of 2 MW. The key design considerations can be summarised as follows:

- the secondary beam components should be designed to maximise the physics reach of the experiment with optimised neutrino fluxes in the full energy range of interest,

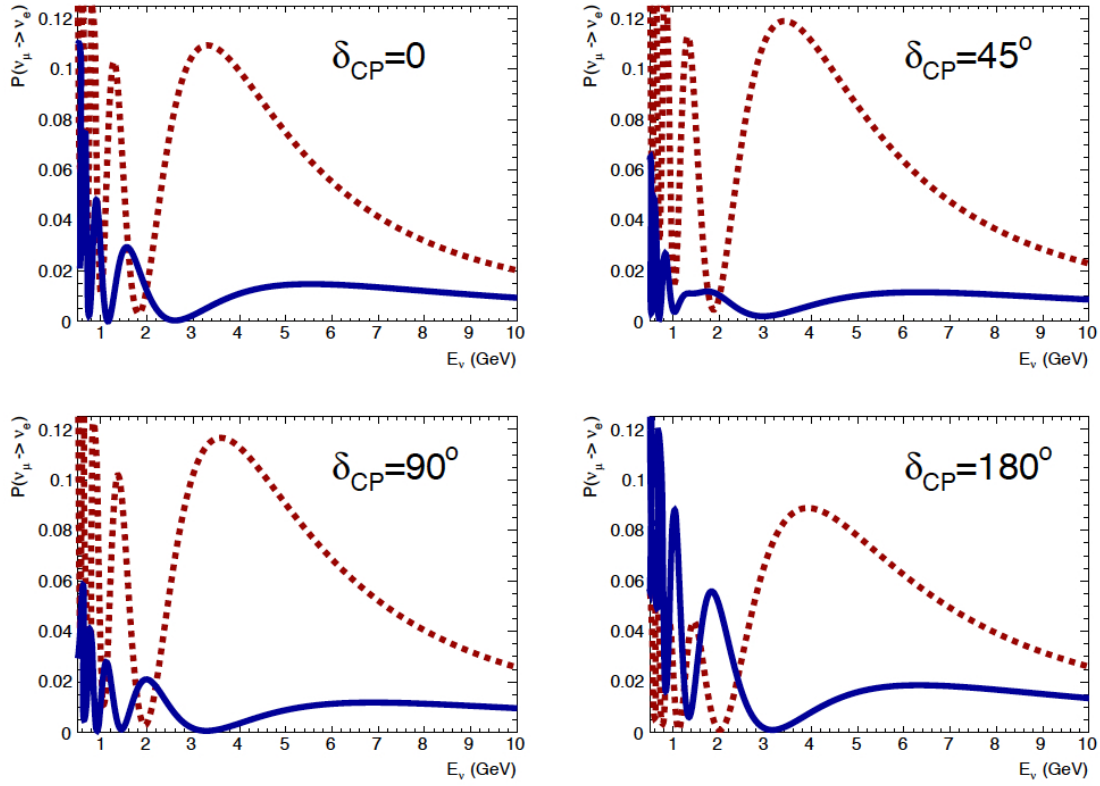


**Figure 1.4:** Same as Fig. 1.3 but for inverted hierarchy  $\Delta m_{32}^2 < 0$  (IH).

**Table 1.1:** Major parameters and integrated beam intensities considered for the LBNO physics program.

Parameter	Unit	Phase-I	Phase-II
Proton injector		<b>SPS</b>	<b>HP-PS</b>
Proton beam Energy - $E_{beam}$	GeV	400	50 ÷ 75
Pulse intensity - $I_{ppp}$	$10^{14}$	0.7	2.5 ÷ 1.7
Cycle length - $t$	s	6	1
Nominal beam power - $P_{beam}$	kW	750	2000
Expected integrated intensity - $pot_{year}$	$10^{21}$	0.10	3.46

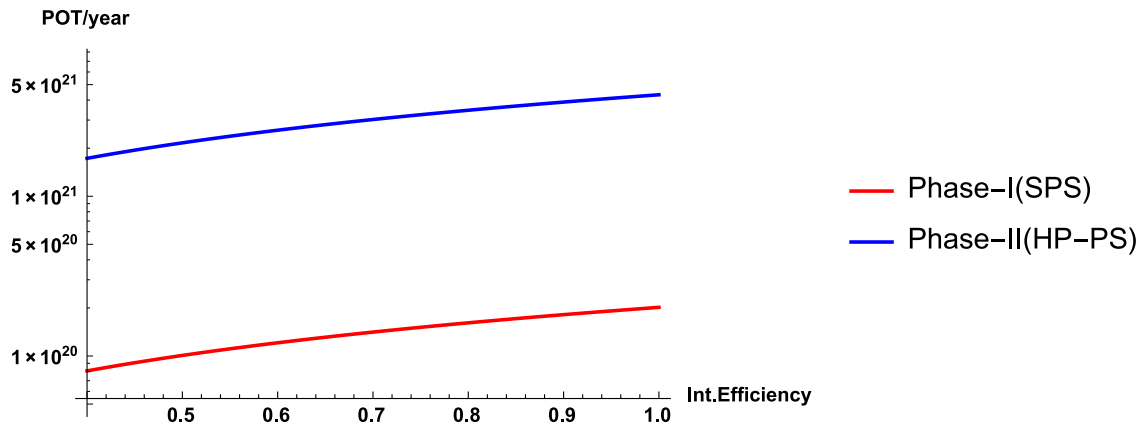


**Figure 1.5:** Integrated pot per year as a function of the overall efficiency of the accelerators and for 200 days of operation. For SPS this is a combination of the net efficiency of the accelerators combined with the beam sharing fraction with the fixed target physics program.

- the facility shielding and infrastructure should be designed from its startup considering the engineering and RP constraints for the later 2 MW beam operation,
- the proton and neutrino beam infrastructure should be designed such to allow an easy transition from the first to the second phase of operation,
- the location of a near on-axis detector should be considered in the design. In the baseline configuration of the facility, the near detector cavern is at 800 m from the target such to guarantee a maximum muon rate of  $\leq 1\mu$  per  $m^2$  per beam pulse, required for the proper operation of the proposed detectors,
- to minimise the produced radioactivity, the target region and decay pipe will be embedded in a helium gas environment,
- provisions for remote handling of the activated components of the neutrino beam (target, horns) will be made, including a hot cell, and a space for temporary storage of damaged components before evacuation.

The CN2PY beam location and layout should take advantage as far as possible from existing infrastructures and installations. In its initial phase, CN2PY will use fast extracted protons from SPS by a system of kicker magnets into a beam transfer line. At the end of this beam line, the protons are bent 10.4 deg, or 18%, downwards to the direction of the Pyhasalmi mine at 2'300 km, shortly before hitting the primary target. A schematic layout of the key neutrino beam components is shown in Figure ??:

- The fast extracted beam from SPS or HP-PS is directed towards a thin low-Z material target of adequate length, where secondary mesons (pions, Kaons) are produced. The beam spot at the target entrance should be circular and its horizontal and vertical sizes will be optimized together with the target radius with the goal to minimize the thermo-mechanical stresses without reducing the mesons and hence the neutrino yield. The resulting beam sigma will be of the order of a few mm, approx. 30% of the target radius. The beam divergence at the target has negligible impact on the mesons yield: it will be determined given the emittance of the extracted beam by the required horizontal and vertical sizes at target entrance. However it will have to be limited such that a significant amount of primary beam could not strike the material of the horn or miss the core of the hadron absorber. A reasonable value should be a divergence smaller or equal than 1 mrad (to be compared with the CNGS of 0.053 mrad). The beam should be steerable

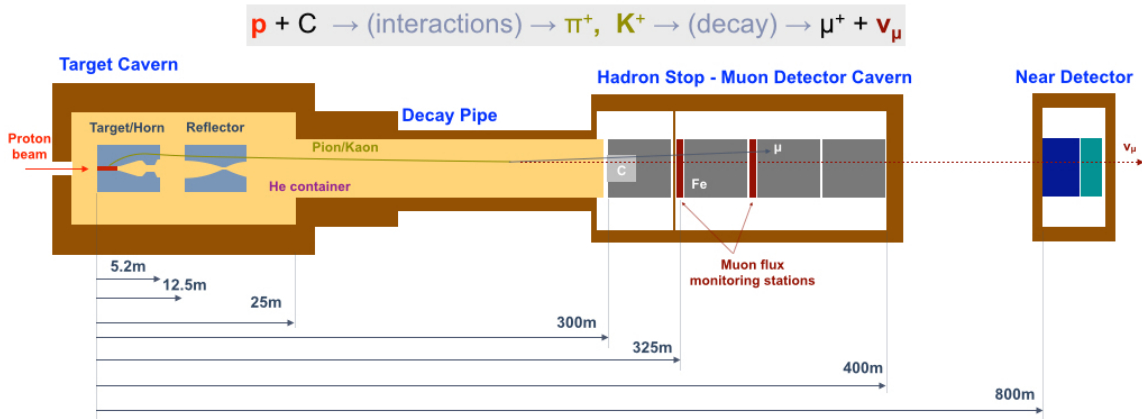


**Figure 1.6:** Schematic layout of the proposed CN2PY neutrino beam. The main elements of the neutrino beam and approximate distances from the target are indicated.

in position and direction and suitable instrumentation should be provided to monitor its intensity and shape.

- A two-stage focusing system with two horns (or following the CERN tradition a horn and a reflector), focuses the generated pions, Kaons of a chosen momenta and charge state to form a parallel beam.
- The focused beam is guided to a 300 m long decay pipe where a large fraction of the focused mesons decay to produce a high-intensity  $\nu_\mu$  beam.
- A massive assembly of iron blocks at the end of the decay pipe, the hadron stop, absorbs the non-interacting part of the primary beam as well as all secondary hadrons produced at the target that did not decay.
- Two monitoring stations embedded after 25 and 50 m in the hadron stop allow monitoring of the flux of muons produced at the decay of the mesons that provide information on the neutrino beam quality and alignment.
- The experimental cavern located at 400 m from the end of the hadron stop that houses the first (near) detector of the experiment. The distance is such that the earth in between provides sufficient shielding to absorb the muons and minimise the background to the near detector.

CERN has a vast experience in building tunnels and big caverns underground in the rock (molasse); the present CERN accelerator complex is close to 50 km of tunnels some in steep slopes and some deep underground, including the large experimental caverns for the LEP/LHC machine. The required slope for the CN2PY beam would be a new challenge, combined with the resulting depth for the hadron stop and near detector caverns indicated in Table ??.

The baseline layout and design parameters presented in this document refer to a particular choice to define a reference design for both operational phases that can be further optimised when the detailed engineering is done.

### 1.2.1 Upgrade path with the HP-PS

In the second phase of CN2PY an increase of the beam power to 2.0 MW using a dedicated injector is foreseen. The new injector under study is a High-Power Proton Synchrotron (HP-PS) using the Low-Power Superconducting Proton Linac (LP-SPL) as low-energy injector at



**Table 1.2:** Indicative depths of the CN2PY caverns worth respect to the target.

Target	Distance [m]	Depth [m]
Target	-	0
Hadron stop - start	300	-54.3
Hadron Stop - end	400	-72.0
Near Detector	800	-144.8

4 GeV [?]. The findings of the PS2 design study [?] which was considered a few years ago as a possible replacement of the actual PS, in view of the LHC injector upgrade, is used as a baseline for the new machine. The HP-PS should be able to deliver beam with energies of above 30 GeV and average beam power of 2 MW on target. In a synchrotron the average beam power  $P$  in the machine is given by the expression:

$$P = qf_r N_p E_k$$

where  $q$  is the particle charge,  $f_r$  the repetition rate,  $N_p$  the number of charged particles, and  $E_k$  the kinetic energy of the beam. The design of such a machine is rather challenging and requires crossing frontiers in all of the parameters. The first three parameters define the average current per machine pulse

$$\bar{I} = qf_r N_p$$

. In Fig. 5.1, the average current is plotted versus the kinetic energy in logarithmic scale for a number of high power accelerators under operation or in the design phase. The average power is represented by straight lines starting from the bottom left part and moving to upper right. It is interesting to observe that most existing high-power accelerators operate at energies of less than 5 GeV, with the exception of the J-PARC main ring (50 GeV). The HP-PS should be also in that area, i.e. high energy with average current of a few tens of  $\mu\text{A}$ .

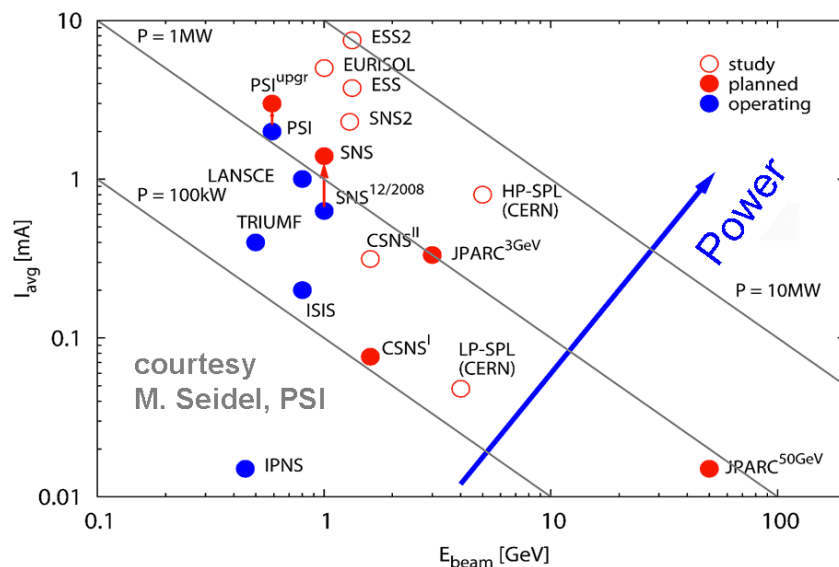


**Figure 1.7:** Average current versus kinetic energy for a number of existing (blue) and future (red) high power machines [?].

In contrast to PS2, the HP-PS would be dedicated as injector to CN2PY therefore does not have strict layout requirements apart from positioning the injection area parallel to the SPL. A three or four-fold symmetric ring would be desirable in order to accommodate in separate



straight sections beam transfer equipment, RF and collimation. In Table 1.3 a preliminary list of parameters for the machine are listed, in comparison to those of PS2.

**Table 1.3:** Design parameters of five ring options for the HP-PS, as compared to the PS2.

Parameters	PS2	HP-PS-V
Circumference [m]	1346.4	1256
Symmetry	2-fold	3 / 4-fold
Beam Power [MW]	0.37	2.0
Repetition rate [Hz]	0.42	1
Kinetic Energy @ inj./ext. [GeV]	4/50	4/50
Protons/pulse [ $10^{14}$ ]	1.1	2.5
pulse length [ms]	0.9	2.0
Dipole ramp rate [T/s]	1.4	3.1
Bending field @ inj/ext. [T]	0.17/1.7	0.17/1.7
Fractional beam loss [ $10^{-4}$ ]	35.1	6.5
Space-charge tune-shift H/V	-0.13/-0.2	-0.2/-0.2
Lattice type	NMC arc, doublet LSS and DS	Resonant NMC arc, doublet LSS
Norm. emit. H/V [ $\mu\text{m}$ ]	9/6	13.7/13.4
Max. beta H/V [m]	60/60	
Max. dispersion [m]	3.2	5
Dipole gap height [mm]	80	120
RMS electrical Power [MW]	5.2	17.0

In the presented list, among many others under consideration, the required high-power is achieved by increased beam intensity and stretching the linac pulse to 2.0 ms. Detailed studies of the HP-PS design are presented in the following chapters.

### 1.3 Layout Implementation Options

For the geographical location of the facility within the CERN accelerator complex two options are considered, exploiting alternative options for the SPS extraction with the additional constraints:

- The length of the proton beam transfer from the SPS extraction point is minimised considering the bending radius to produce the required downwards slope and the resulting depth of the target cavern is optimised, that further determines the depths of the other structures and shafts.
- The location of the access shafts, in particular that of the target cavern, is far from densely populated areas such to minimise possible radiological impact.
- The access shafts for the neutrino beam, hadron stop and near detector should be located within the CERN reserved area, or close to it, and preferably close to existing areas and infrastructure to minimise costs.
- The target location should allow the injection from the HP-PS machine whose location is fixed close to the CERN Meyrin site.

- The layout of the underground structures and transfer lines must be at adequate distance from existing tunnels to avoid any interference during construction and operation.

Both options have positive and negative aspects and a choice among them cannot be done at this stage. Having the target and near detectors close to the Preveessin area (or BA2) is preferred from the radiological issues and reuse of infrastructure. With this constraint Option A comes with probably an initial increased cost due to the long proton transfer line, however at the same time assures minimal interference with the operation of SPS, and the proton line will be anyhow needed in the second stage to transfer the beam from the HP-PS to the target. Option B maximizes the use of existing infrastructures in the initial phase, however it requires a modification to the SPS LSS2 extraction. A technical solution is found, with re-engineering of some kicker magnets and reshuffling of the LSS2 equipment [?]. In the second stage with the HP-PS operation the beam would have to be transferred to the CN2PY target in the North Area using a new proton transfer line.

### 1.3.1 Option A: extraction from LSS6 of SPS

In this scenario, the existing fast extraction channel of SPS to LHC in LSS6 and the TT60/TI2 transfer line is used. The LSS6 extraction channel could be with minor modifications become identical to that of LSS4, specially designed to accept the high-brightness beam for LHC and the high-intensity beam for CNGS [?]. The same extraction point was used in the past for the West Area and WANF neutrino beams. The CN2PY beam branches off the TT60 transfer line using a set of fast switching magnets in the BA7 area. A new approx. **800 m** long transfer line brings the beam close to the BA2 access point of SPS where the target cavern would be located. The layout of this option is shown in Figure 1.8.

### 1.3.2 Option B: extraction from LSS2 of SPS

In this scenario, the SPS extraction in LSS2 presently used for the FT resonant extracted beams to the North Area is modified to accommodate a fast extraction. The existing TT20 transfer line is used to transport the primary proton beam up to the TDC2 cavern where the CN2PY beam branches off using fast switching magnets and directed towards the target cavern located underground on the southern side of the existing TCC2 cavern. The layout is shown in Figure 1.9. The two near detectors are located just outside the fenced area of the Preveessin site and can be easily accessible.

## 1.4 The Near Detector

The proposed Near Detector (ND) is based on the pressurised gas TPC detector described in this report [94].

Pressurised gas Time Projection Chambers (TPC) are a well proven detector technology. For LBNO, we propose to include several layers of plastic scintillator modules within the pressure vessel that encloses a 20 bar Argon TPC in order to provide good tracking of secondaries from neutrino events occurring in the TPC fiducial volume. This small technological step defined mainly by the inclusion of plastic scintillator modules in a pressurised inert environment is considered feasible, and represents the novelty in our approach. We plan to use silicon photomultipliers (SiPM) first used at the T2K ND280 ND on a large scale from 2006 as the light sensing instrumentation for plastic scintillators. This choice is motivated by the high light yields, low after pulsing, and low cross-talk of the latest generation SiPMs, combined with their intrinsic compactness, robustness and magnetic field immunity. The pressure vessel in our scenario is enclosed in a magnetic field.

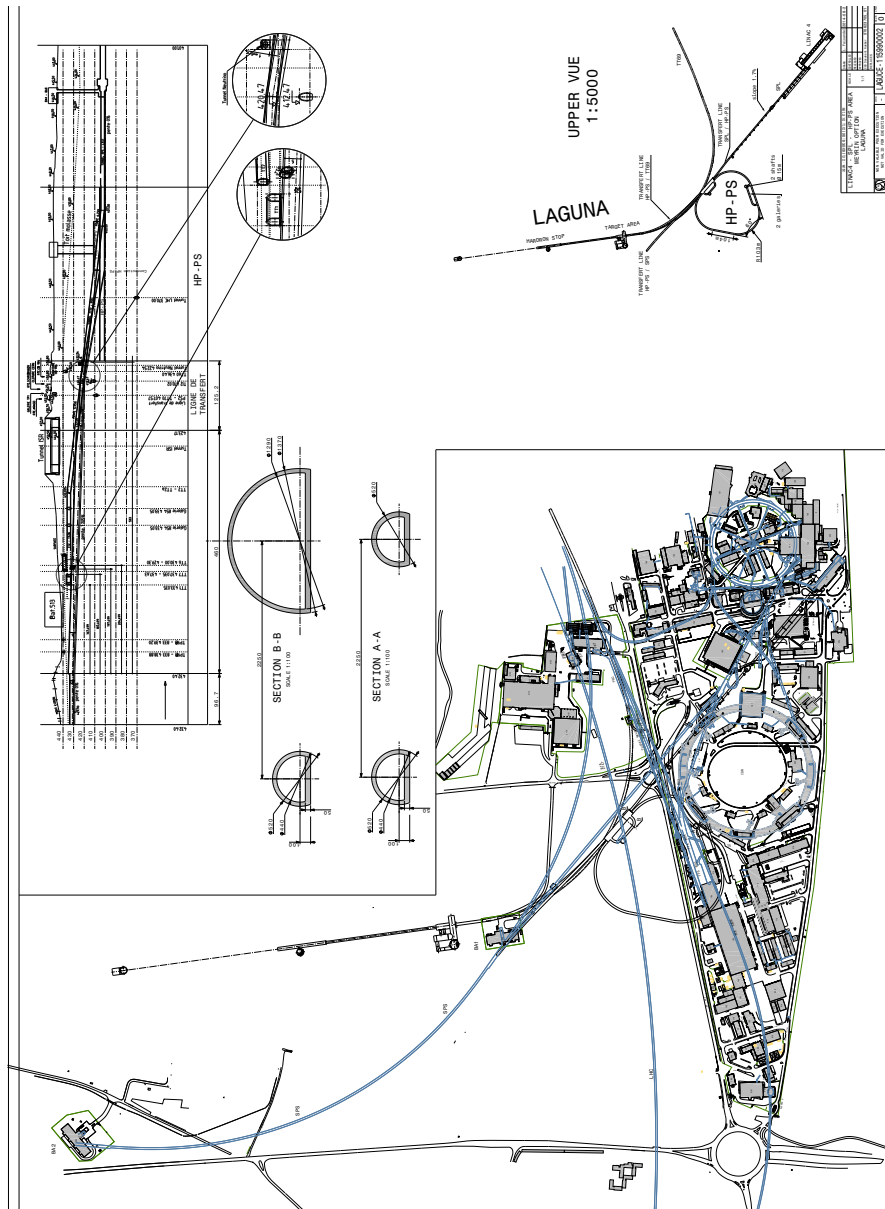


**Figure 1.8:** CN2PY layout Option A: Layout of the CN2PY beam in the CERN area using the SPS extraction channel in LSS6. The long proton beam transfer line is shown in blue. The second phase HP-PS is also shown with its transfer lines from LP-SPL and connection to the proton line (in green)

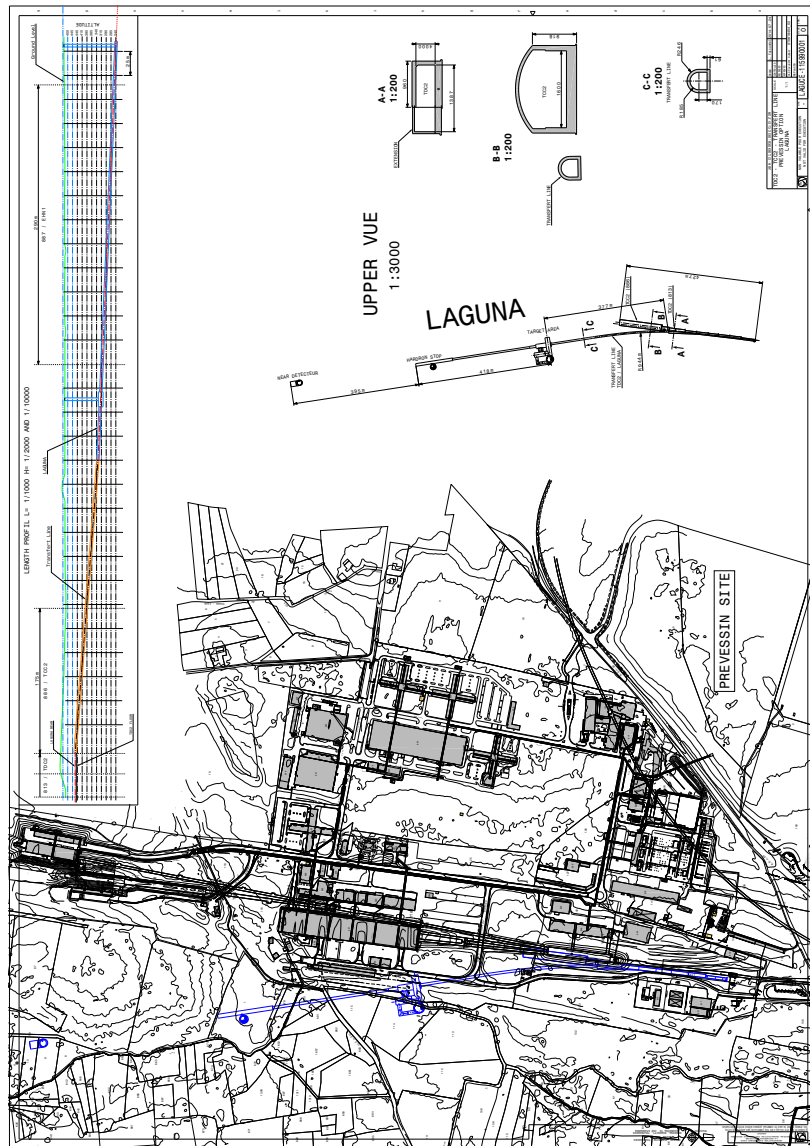


**Figure 1.9:** CN2PY layout option B, with the facility located in the vicinity of the TCC2 target area in the CERN Prevezsin site. The CN2PY beam line will be pointing downwards by 10.4 deg. The decay pipe and the two near detector locations at 800 m distance from the primary target is also shown.

Although Liquid Argon (LAr) can resolve events with one nucleon (range of a 20 MeV proton in LAr is  $\sim 4$  mm), e.g. 1p1h events, reconstruction of events with more than one nucleon from the vertex is much more challenging. These multi-nucleon events are known to be significant for medium-to-high Z targets such as Argon. At the ND location for LBNO, 800 m from the target, the high energy muon background ( $10 \mu/m^2/spill$ ) from the target would saturate a LAr detector, leading to pile-up of events. A high pressure Argon TPC, although a factor  $\times 40$  less dense than LAr, would nevertheless provide a significant sample of events, whilst being less susceptible to pile-up. The vertexing capabilities of pressurised gas TPCs are well matched to the requirements of precision measurements of neutrino cross-sections. Moreover, the pressure vessel can be designed to provide an additional safety barrier so that small volumes of nuclear targets (such as a hydrogen cask) can be introduced in the pressure vessel. This type of near detector concept is also considered to a number of planned future facilities such as: LBNE and  $\nu$ STORM in US, T2HyperK in Japan.

## Chapter 2

# High-Intensity beams with present CERN Accelerators

The SPS accelerator is the key asset of CERN in producing competitive neutrino beams in the sub-MW range for neutrino oscillation experiments. The fast extracted 400 GeV proton beam from SPS operates with a 6 s cycle with two to bursts of 10.5 s per cycle with up  $2.25 \times 10^{13}$  protons each, corresponding to a maximum beam power of 510 kW. During the CNGS operation, the SPS machine achieved world-wide record performance at that time, reaching for few-hours peak operation power of 405 kW, and sustained daily average operation of 380 kW of beam power (see Figure 2.1) in periods where dedicated running for CNGS was scheduled. In

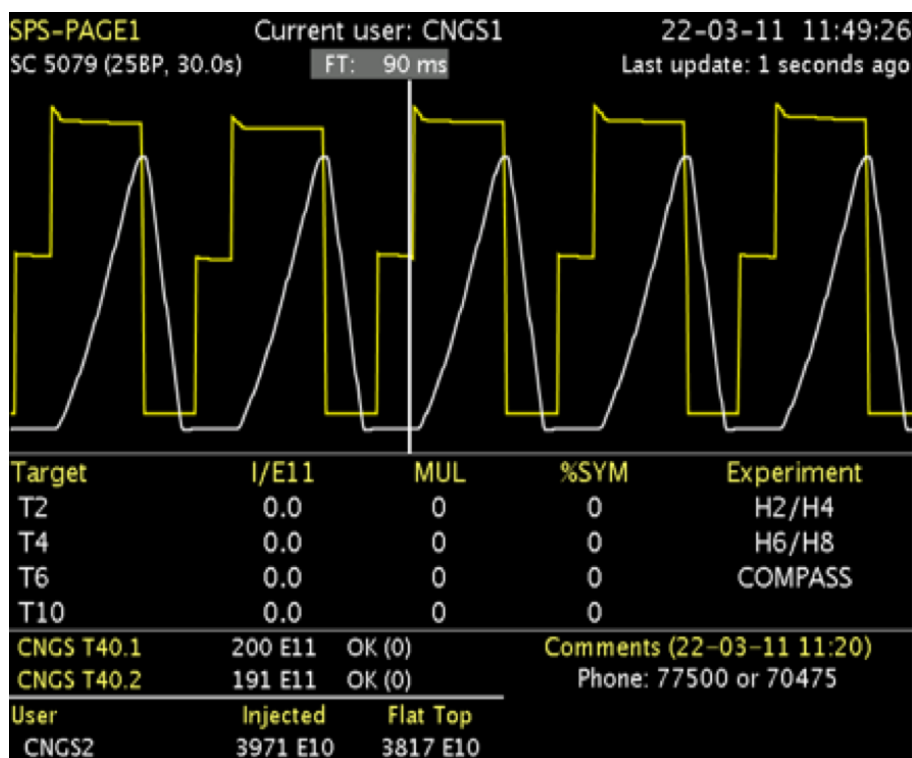


**Figure 2.1:** SPS super-cycle configuration with five 6 s CNGS cycles, or 100% duty cycle of the neutrino beam. The intensity per cycle is  $3.8 \cdot 10^{13}$  protons, corresponding to a beam power of 405 kW.

normal operation conditions, the average beam power for CNGS is approximately of 300 kW, because of

- Intensity limitations due to beam loss in the PS in producing, accelerating and extracting

towards SPS high-intensity beams.

- Intensity limitations at SPS to capture and accelerate with minimal losses high-intensity large duty factor beams.
- Competition for beam time sharing with LHC, the Fixed Target Physics program and Machine Developments.

The CNGS has been a source of very valuable operational experience that is a good starting point. Studies to understand the full performance potential of the machines have been performed and will be reported in the next sections, along with the bottlenecks, required R&D, and mitigation solutions mandatory to reach the high-intensity beam parameters required for the CN2PY physics program in both PS and SPS.

## 2.1 HI Beams in the PS

The CERN Proton Synchrotron (PS) is now reaching his 55 years, being built initially for a maximum intensity of some  $10 \times 10^{11}$  proton per pulse (ppp) [5]. The impressive intensity increase achieved during the last few decades (see for example [6]) required major upgrades, like the increase of the injection energies, done twice in the past and planned again in the future [7], as the introduction of two new extraction techniques, namely the Continuous Transfer (CT) [8] and Multi-Turn Extraction (MTE) [9] to provide beams to the SPS for fixed target physics.

Some tests done in preparation of the CNGS [10] run for high intensity beam production successfully showed the possibility to deliver more than  $3 \times 10^{13}$  ppp to the SPS (see [11] and reference therein), and previous analysis tended to indicate as a bit too optimistic the possibility to deliver it regularly.

The experience acquired during the CNGS run revealed, however, that large losses during regular operation with high intensity finally limited the deliverable intensity to a more moderate  $2.8 \times 10^{13}$  ppp, and even less during the last year of operation due to stray radiation induced outside of the PS tunnel, in particular in the injection and extraction regions.

The analysis performed in the framework of the Beam Loss Radiation Working Group [12] (BLRWG) and more recently in the PS Radiation Working Group [13] (PSRWG) also enlighten some concerns for the high intensity runs.

Some specific studies and interventions were done in recent years for high-intensity beams, some of them implemented in the framework of the PS - LHC injector upgrade [14] (PS-LIU) programme. Part of the activities already foreseen for the injector upgrades will also be beneficial for the neutrino production beams, while other interventions were optimized taking into account the production of both LHC and high-intensity beams.

Main PS limitations could be identified based on the experience from CNGS operation and other high-intensity beam runs, such as for the TOF experiment [15] in particular, in the injection, acceleration and extraction processes. Preliminary analysis identified the main areas where studies should be carried out to push the beam intensity beyond the CNGS values, at the same time keeping reasonably low losses, as suggested by the guidelines expressed by the PSRWG [13].

To-date, it is not clear what would be the maximum intensity achievable even after solving all issues already identified. Nevertheless it is assumed that the intensity for a LAGUNA-type beam [16] should be at least of  $4 \times 10^{13}$  ppp.

### 2.1.1 Beam production schemes

The working hypothesis for neutrino beam production is to assume the same SPS injection scheme as today, namely two consecutive 1.2 s long PS cycles with 5-turn extraction each, based

on the MTE scheme [9], which are used to fill the 10/11th of the SPS circumference. Concerning the beam transfer from the PSB, two bunches per PSB ring, operating on  $h = 2$ , are injected into buckets at harmonic  $h=8$ . After a first acceleration, a double bunch splitting takes place at 3.5 GeV/c and acceleration to the final 14 GeV/c extraction momentum is done on  $h = 16$  harmonics. Finally, prior to extraction, the beam is debunched to allow imposing a 200 MHz structure (rebunching) before extraction for the recapture in the SPS. A 200 MHz longitudinal structure is imprinted on the de-bunched beam to allow beam detection by the pick-ups in the PS-SPS transfer line and during the first SPS turns. For the time being, no plans are envisaged to change this production scheme even for the 2 GeV injection energy upgrade foreseen for the PS-LIU.

### 2.1.2 Injection losses

Extensive studies realized in past years [17, 18] showed that the high beam losses observed during the first few hundred turns, which are limiting the maximum intensity that can be injected into the PS ring, are due to two different mechanisms. Fast losses observed during the first turn are caused by the reduced aperture of the injection septum, considering the transverse emittances that the PSB can deliver at 1.4 GeV with the typical Linac2 beam. Slow losses, lasting for few hundred turns, are caused by intrabunch injection oscillations, resulting from the effect of indirect space combined with the presence of unavoidable injection errors. Furthermore, the presence of the horizontal injection bump reduces also the available aperture in the injection region.

A careful re-design of the injection optics, both for the injection line as well as for the ring, the enlargement of vacuum chambers, and an increase of the injection septum apertures, are planned in the framework of the LIU project, as described in [14]. The injection oscillations should not constitute a major issue, as they can be effectively eliminated by the transverse damper, as described in Ref. [18], which also will be upgraded [19]. Injection oscillations are also described in details in section[].

Clearly, the introduction of the Linac4 as PSB injector and the 2 GeV injection upgrade should be beneficial, thanks to the reduction of the physical beam transverse emittances, thus leading to an increase of the available aperture. The final gain in terms of losses and equipment activation remains to be assessed, since it is still not clear what will be the final transverse emittances delivered by the PSB in the Linac4-2 GeV era, and thus what will be the resulting injection losses, in particular for very high beam intensities. In a conservative re-design of the injection region, necessary for the 2 GeV upgrade, the mechanical aperture of the various elements will be kept in any case as during the 1.4 GeV operation, to include sufficient margin for any future scenario of high intensity beam production.

### 2.1.3 Injection Oscillations

Beam loss during the injection process of high-intensity proton beams into the CERN Proton Synchrotron (PS) constitutes one of the current limitations to the production of high-intensity beams, as they will be required for neutrino production in the future. During the routine machine operation vertical intra-bunch oscillations, which contribute to these injection losses, were observed on high-intensity beams. In order to understand the mechanism causing these oscillations measurements and simulation studies were conducted and revealed that indirect space charge forces cause a coherent tune shift, which depends on the local particle density of a bunch. Therefore, different parts of a bunch start oscillating at different frequencies, which are determined by the local tune shift, leading to the observed intra-bunch oscillations.

Currently, the transverse damper system of the PS [?] allows to damp these oscillations. However, a detailed understanding of the underlying mechanism is indispensable in order to



predict the efficiency of the system for future high-intensity beams and, therefore, the experimental results and simulation studies are summarized in this section.

### 2.1.3.1 The injection process

The PS is composed of 100 combined-function magnets, which are interleaved by 100 straight sections. This arrangement results in a FOFDOD lattice and the numbering of the straight sections is done according to the respective downstream main magnet unit (MU). The proton bunches are created in the Proton Synchrotron Booster (PSB) [?] and sent towards the PS injection septum, which is located in straight section (SS) 42. A single-turn injection process is adopted at a kinetic energy of 1.4 GeV and four dipole magnets create a horizontal injection bump, which brings the orbit of the circulating particles close to the blade of the magnetic septum. Subsequently, the injection kicker in SS45 puts the beam on the closed orbit (see Fig. 2.2).

The large negative excursion of the beam in SS43 constitutes the major horizontal aperture restriction in the PS. According to simulation studies presented in [?], the  $3\sigma$  envelope of the circulating beam almost touches the mechanical aperture at the beginning of MU43. Due to the elliptic geometry of the vacuum chamber at this location, a horizontal excursion of the beam also constitutes a vertical aperture restriction. Therefore, losses at injection are caused by a beam, which is, due to the vertical closed orbit and the injection error, circulating off-center.

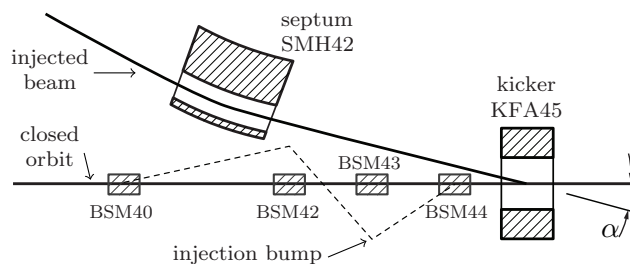


**Figure 2.2:** Schematic representation of the PS injection region. The dashed line indicates the deviation from the design closed orbit due to the horizontal injection bump, which is created by the dipoles BSM40 - 44 (adapted from [?]). The elements are labeled using a combination of device-specific letters and two figures, indicating the straight section they are located in.

### 2.1.3.2 Measurements

The transverse stability of particle beams in the PS can be investigated with high bandwidth instrumentation such as a wide band pick up (WBPU), which provides three different output channels, i.e. the horizontal and vertical difference signals and the sum signal. The transverse signals are proportional to the bunch displacement and the line density, while the sum signal is proportional to the line density only. This instrument allows to measure high frequency oscillations within a bunch.

Measurements were performed on the high intensity TOF and CNGS beams (reference?), which are both operated at harmonic number  $h = 8$  at injection. However, the total intensities vary significantly as only a single bunch of, at maximum,  $850 \cdot 10^{10}$  protons is sent to nTOF facility (reference?), while eight bunches, resulting in up to  $2800 \cdot 10^{10}$  protons per pulse (ppp), are accelerated for CNGS-type beams.

In Figs. 2.3 and 2.4, the horizontal and vertical difference signals measured on both beams are depicted. The oscillatory behavior of the bunches is clearly much more pronounced in the vertical plane. However, horizontal oscillations are also observed, which are, due to the closed orbit in this plane, more difficult to interpret. These observations were reproducible each time the beams were injected. Apparently, these vertical oscillations build up rapidly after injection,

in a time span which is short compared to the synchrotron period (between 400 and 600 turns at injection).

Instead of considering consecutive turns, if one looks at every 20th turn for example, as the number of turns increases, the oscillation frequency is also found to increase. By means of an FFT the power spectrum of each single turn is computed, allowing the turn-by-turn evolution of the oscillation frequency to be obtained. Although this approach is limited in resolution (signals for single turns consist of only 500 data points), a trend is clearly visible: each turn the intra-bunch frequency increases (see Fig. 2.5).

Additional information about the local oscillation frequency can be extracted from the measured data by regarding the bunch as an accumulation of independent, coherently oscillating slices. Each slice is considered to be represented by a single bin of the measurement data and the applied procedure is explained in Fig. 2.6: looking only at the first 20 turns after injection and assuming a linear machine, as is usually the case at injection energy, the harmonic motion of each slice is obtained. Subsequent application of a sinusoidal fit allows computation of the tune of the different slices. Apparently, these slices are subject to a tune shift depending on their position within the bunch, proportional to the line density. Therefore, particles oscillate with a transverse frequency, which depends on the particle's longitudinal position, causing the observed intra-bunch oscillations. Due to the fact that the motion of the centroid does not exhibit any growth the observations are described as oscillations rather than instabilities.

### 2.1.3.3 Simulation studies with the HEADTAIL code

The effect of the vacuum chamber on the ensemble of particles forming a bunch was simulated using the HEADTAIL code, whose physical concepts are based on [?], in combination with the analytic code ImpedanceWake2D [?]. With the latter the wake functions can be computed from the beam coupling impedance of a flat or a cylindrical structure. The resulting dipolar and quadrupolar wake functions then serve as input for the HEADTAIL simulations, in which the bunches are longitudinally sliced and the macroparticles within these slices experience kicks based on the provided wake functions.

In order to determine the wall impedance of the PS vacuum chamber a simplified model was used, consisting of a single geometry made of stainless steel all along the  $2 \cdot \pi \cdot 100$  m circumference of the ring (see Fig. 2.7). In reality this type of chamber accounts for about 70% of the installed vacuum chambers, while the remaining beam pipes differ in size and/or material.

Simulations using this simple description of the PS lead to results, which reproduce the measurements extremely well. In order to compare the results of the simulations to the measured data, Fig. 2.8 is produced identically to Fig. 2.5. The simulations show that, after applying an initial offset to the bunch, vertical intra-bunch oscillations are obtained. The spectrum of these oscillations, which was again computed turn by turn, shows an overall increase of the frequency for an increasing number of turns, which is also in agreement with the measurements. Likewise, this applies to the vertical tune shift, which is depicted in Fig. 2.9. Only minor differences between the measurements and the simulations are observed, which can be explained by the incomplete modeling of the machine.

At low energy, the wall impedance is basically dominated by the indirect space charge impedance rather than the contribution of the finite conductivity of the wall. Therefore, the effects of particles within a certain slice on themselves are mainly driving the presented intra-bunch oscillations. One possibility to reduce this effect is to reduce the injection error by carefully adjusting the particle trajectory in the transfer line between the PSB and the PS.

In the framework of the LIU project [?] an upgrade of the PS injection kinetic energy from 1.4 to 2 GeV is currently being investigated. By increasing the injection energy the importance of the indirect space charge forces is reduced and, therefore, also the vertical tune shift. However, future beams for neutrino production will require bunch intensities of  $500 \cdot 10^{10}$  p (compared

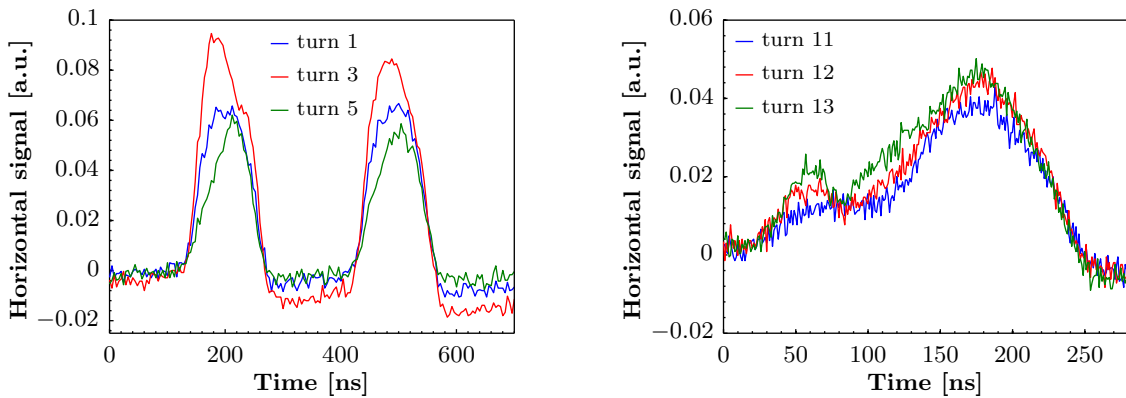


**Figure 2.3:** Horizontal difference signals on the CNGS (left) and TOF (right) beams on different turns after injection.

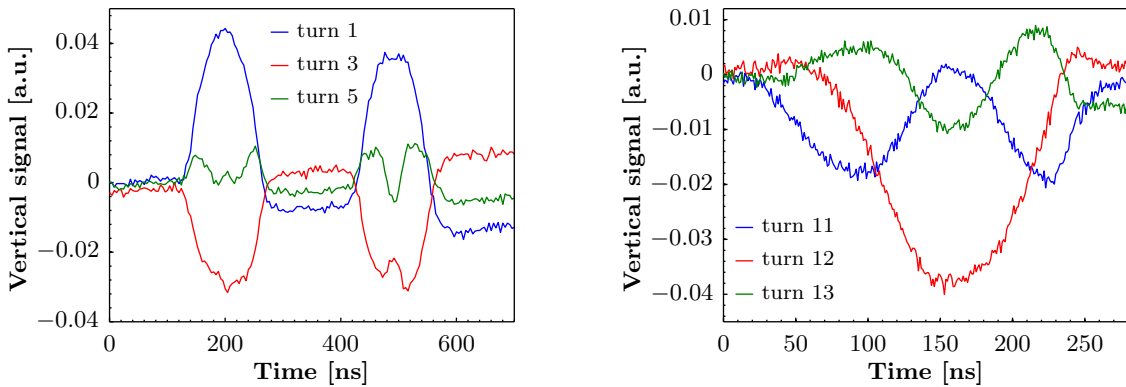


**Figure 2.4:** Vertical difference signals on the CNGS (left) and TOF (right) beams on different turns after injection.

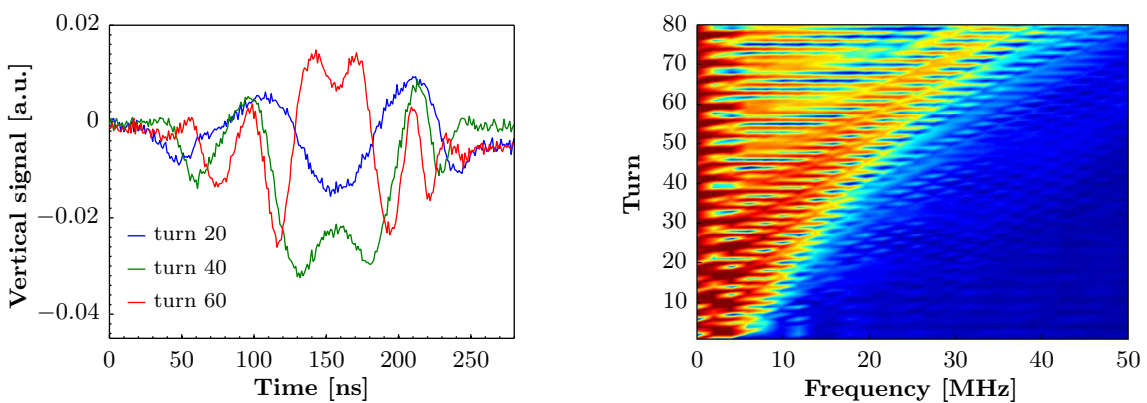


**Figure 2.5:** Vertical signals of turns 20, 40 and 60 after injection of the TOF beam (left). The figure on the right shows the power spectrum computed every single turn. The trend of increasing oscillation frequencies is evident.

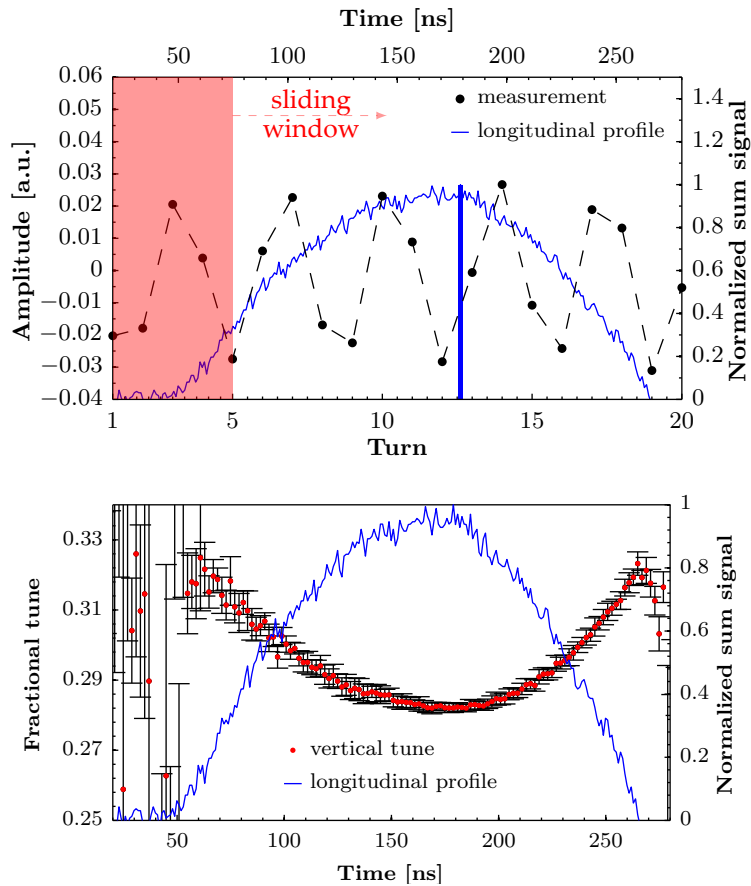


**Figure 2.6:** Top: The blue bar indicates a single bin of the measured data of the TOF beam. The vertical oscillations performed by this bin over the first 20 turns are represented by the black dots. In order to obtain the vertical tune of this respective bin a sinusoidal fit considering a window of five turns only (indicated by the red area) is computed. The window slides from turn 1 to turn 16 and the average over the obtained frequencies is considered as vertical tune of this bin. Bottom: A detuning following the line density is revealed and the maximum tune shift is found at the peak density of the bunch. The error bars represent the standard deviation, which increases significantly at the head and the tail of the bunch as the signal is dominated by the noise.

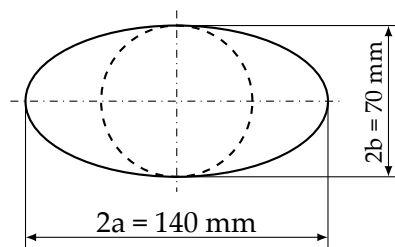


**Figure 2.7:** Simplified model of the PS vacuum chamber. The dashed line indicates the geometry of the cylindrical chamber that was used as input for ImpedanceWake2D.

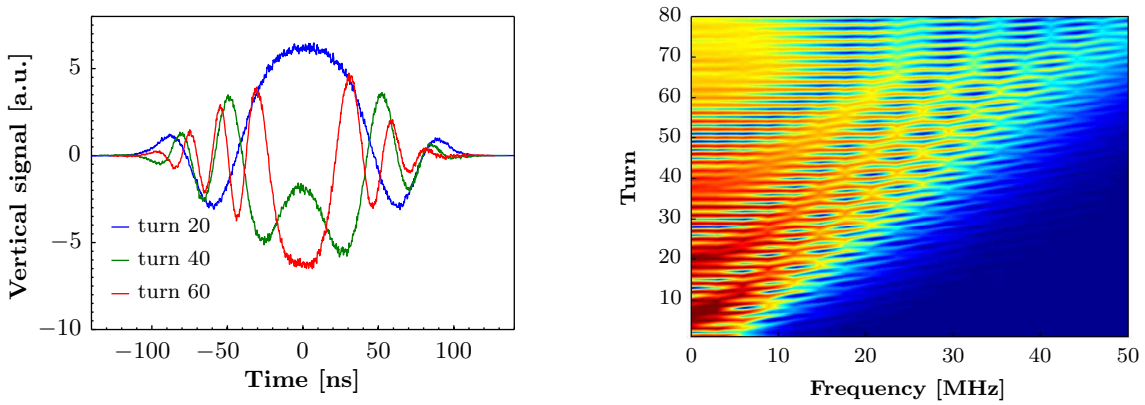


**Figure 2.8:** Simulation results for the TOF beam depicted in the same way as in Fig. 2.5. The intra-bunch oscillations as well as the increase in frequency are very well reproduced.

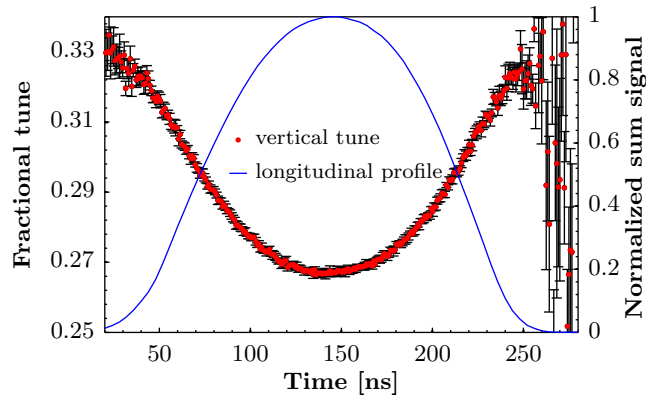


**Figure 2.9:** Tune shift along the bunch as deduced via simulations, which depends, likewise to the measurements shown in Fig. 2.6, on the local intensity of the bunch. The maximum vertical tune shift is similar to what was measured in the PS.

to  $350 \cdot 10^{10}$  p for CNGS-type beams), which increases the tune shift. In Figs. 2.10 and 2.11 simulations at both the current and the proposed injection energy are depicted, which show that an overall reduction of the tune shift can be expected for future beams. This reduces the requirements in terms of bandwidth for the transverse damper and, therefore, the system should remain effective for this type of future high-intensity beams.

The availability of LINAC4 (reference?) as well as new injection optics (reference?) will also contribute to a reduction of the losses at injection by reducing the physical beam size.

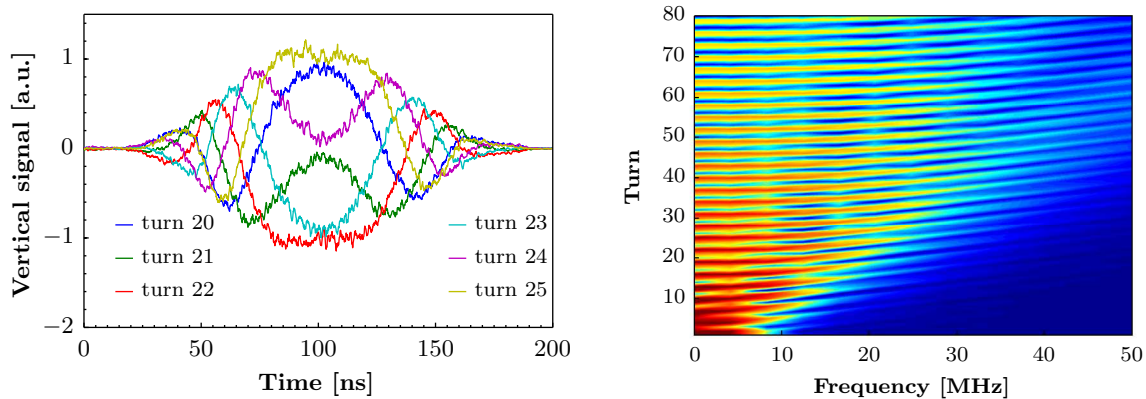


**Figure 2.10:** Simulation results for a single CNGS bunch with an intensity of  $350 \cdot 10^{10}$  p at the current injection energy.

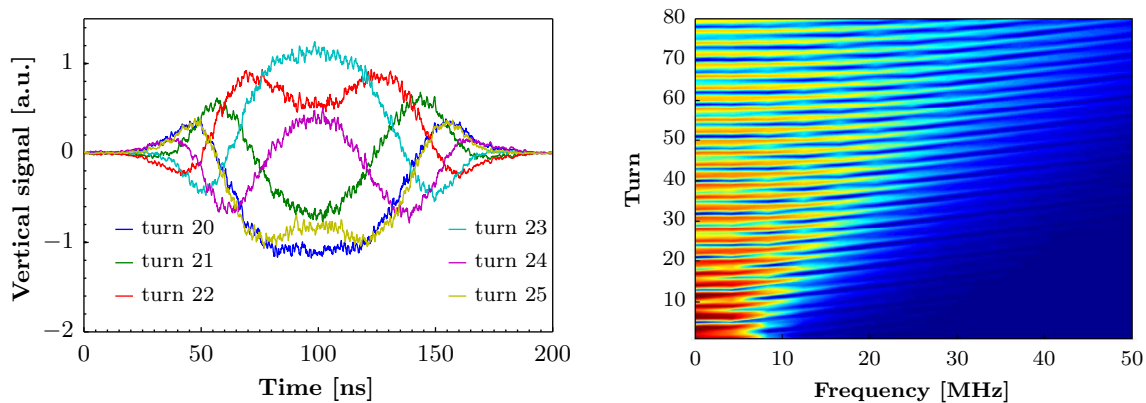


**Figure 2.11:** Simulation results for a future high-intensity single bunch with an intensity of  $500 \cdot 10^{10}$  p at a kinetic energy of 2 GeV. The increase of the intra-bunch frequency is slower compared to the case shown in Fig. 2.10, leading to reduced requirements for the transverse damper system.

### 2.1.4 Acceleration

The main RF system of the PS is composed of ferrite loaded cavities tunable from 2.8 MHz to 10 MHz which was installed in the early 1970s [20]. During the preparatory high intensity runs for the CNGS, significant longitudinal losses were identified during acceleration. In particular, the maximum RF power available at transition crossing, where the RF-phase jump takes place, and during acceleration, turned out to be insufficient for intensities above  $3.5 \times 10^{13}$  ppp. On top of this, frequent tripping of the cavities was observed, probably due to the continuous overload of the RF tubes.

Preliminary investigations done in the framework of the LIU upgrade [21] showed that there is still some margin left for the power amplifiers. However, such a margin risks to insufficient considering the huge intensity increase required by the LAGUNA-type beam. For this reason,

a specific study should be performed to assess the limit of the existing system for high intensity beams, similarly to what has been done for the LHC-type beams [22, 23].

Preliminary investigations will be carried out to scrutinize alternative and more modern RF systems, based for example on Finemet© technology [24].

### 2.1.5 Transition Crossing

Extensive studies on single bunch instabilities at transition crossing were performed in [17, 25]. Particular attention was given to a vertical Transverse Mode Coupling Instability (TMCI) appearing for single bunch intensities of about  $6 \times 10^{12}$  ppp and causing losses of the order of few percent [17]. TMCI appears as an intrabunch vertical oscillation with a central frequency of 700 MHz driven by a broadband impedance source. This frequency range is well beyond the capabilities of the existing transverse damper, whose bandwidth is limited today to about 23 MHz and in the future to 100 MHz [19]. According to preliminary results [26], and thanks to the development of a new impedance model [14], the driving impedance has been identified as generated by the several kickers installed in the PS ring.

Different mitigation measures have been proposed for future high intensity operations. The first one, today in operation, is the increase to the maximum allowed of the longitudinal emittance during transition crossing [27]. If this would reveal to be insufficient, some attempt could be done to reduce the impedances driving the instability. It is worth mentioning that in the SPS and in the LHC the serigraphy technique has been successfully applied to the kickers [28]. However, even if this solution was not properly studied yet in the context of the PS machine, it seems to be pretty difficult to implement because of the very short length of the PS kicker modules.

Other different techniques could be tried, like introducing a chromaticity jump synchronous with the already implemented gamma jump [17], a different or faster gamma jump scheme, the use of octupoles to introduce some transverse Landau damping [29].

An active system to combat the instability might also be studied, inspired by the 1 GHz transverse damper proposed in the LARP framework to counteract the electron-cloud driven instabilities appearing in the SPS [30].

### 2.1.6 Extraction

MTE should definitely replace during the 2014 run the CT extraction, thus reducing significantly the losses at the extraction, from a maximum of 10% to about 1-2%, as proven during a brief part of the CNGS run. The MTE extraction is based on beam trapping in stable islands of the transverse phase-space [9]: the beam is split in five beamlets by crossing of a fourth-order resonance and, once sufficiently separated in the horizontal plane, each beamlet is extracted on five consecutive PS turns. The adiabaticity of the trapping process requires a long extraction flat top.

The losses during the MTE extraction are produced, as predicted, by the fact that the beam has to be transferred de-bunched from the PS and SPS. A portion of the beam intercepts the blade of the extraction septum during the kicker rise time. This caused in the past run a too large activation of the extraction septum, which was considered not compatible with the reliable operation of the PS as LHC injector [31]. For this reason, and despite the drastic reduction of the overall PS ring activation observed during the MTE operation compared with an equivalent operation period realized with the CT extraction [31], MTE was left on stand-by during the last part of the CNGS run. The mitigation of the extraction septum activation has been implemented by installing a so-called dummy septum, as described in Ref. [32]. This solution will be tested during the 2014-2015 run, and it should drastically improve the activation in the extraction region, but, of course, it would not eliminate the extraction losses.



A revision of this scheme is planned after the SPS 200 MHz upgrade [33], since at that time a bunched beam transfer, as proposed in [9], would be possible, which clearly would completely eliminate the beam losses at extraction. Alternatively, studies will be performed to test whether a stable and empty gap in the longitudinal beam distribution could be created in the PS, for example by injecting seven bunches from the PSB with the PS set on  $h = 8$ . Moreover, such a gap could be synchronised with the kickers<sup>®</sup> rise time, thus highly reducing or even removing the losses at extraction.

It is worth stressing that the MTE extraction has been successfully tested only with CNGS-like intensities, i.e., up to  $2.8 \times 10^{13}$  ppp. Considering that intensity-dependent effects, like space-charge [34], have been already observed, it is clear that further studies should be carried out when increasing further the beam intensities, as it cannot be excluded that new collective effects would appear and change the islands<sup>®</sup> properties. In particular the larger space charge-induced tune shift and tune spread will enhance the coupling between the transverse and longitudinal degrees of freedom, possibly impacting on the trapping efficiency.

Some speculations were made to about the possibility to extract LAGUNA-type beams at beam momenta higher than 14 GeV/ $c$ , to avoid transition crossing in the SPS, and to profit from a reduced physical beam size at SPS injection. Albeit interesting from the point of view of the SPS performance, such a scenario implies the complete replacement of all the MTE extraction kickers as their strength is exactly matching what is needed at 14 GeV/ $c$ . Furthermore, also the magnetic elements (sextupoles and octupoles) might need an upgrade in terms of strength. For both kickers and magnets, the technological challenge of designing and building upgraded versions should not lead to underestimating an apparently simpler challenge, i.e., finding space for the new extraction elements in the overcrowded PS straight sections. On top of this limitation, a careful analysis of the magnetic cycle should be realized. The PS, in fact, is currently capable of accelerating from 1.4 GeV to 20 GeV in one basic period, corresponding to 1.2 s, and to fast extract the beam, but without any flat top at high energy. If the MTE transverse gymnastics would be realized at momentum higher than 14 GeV/ $c$ , and leaving the accelerating part of the magnetic cycle unchanged, a cycle 2.4 s long instead of the standard one of 1.2 s used today would be needed. Of course, the duty cycle of the SPS would be considerably reduced and hence also the average beam power delivered to the target. A further optimisation could be made by assessing the minimum beam momentum beyond 14 GeV/ $c$  for which the SPS performance would not be affected by the transition crossing. This beam momentum could be used to design a PS magnetic cycle still of 1.2 s, but possibly with a long enough magnetic flat top to perform an optimal adiabatic trapping. Of course, all this requires further studies at the level of the SPS, first, and then of the PS.

### 2.1.7 Tunnel shielding

The PS external shielding has been improved during the Long Shutdown 1 (LS1), occurring during 2013-2014, in the injection and extraction regions. The interventions were required in any case in the framework of the 2 GeV injection upgrade and for fixed target normal operation. However, the tunnel shielding has been increased taking already into account a routine LAGUNA-like operation and considering some conservative values for the beam losses [14].

### 2.1.8 Machine operability

Of some concern is that, with high intensity beams and absolute losses larger than today, more down time due to cool-down should be expected before repairing any equipment in the PS tunnel. In particular, in case of failures in very radioactive zone, there is a certain risk of very long LHC down-time (weeks). The various devices installed in the PS ring, such as the main PS magnets, were in fact not built with modern techniques for fast removal or remote handling.



Mechanical parts with fast removal in critical zones have been considered only for newly installed equipment, like for the dummy septum mentioned in the previous section [32].

Also, aging of materials due to stray radiation should be assessed. Of particular concern is the aging of the main magnets and their auxiliary circuits due to radiation in the high-losses areas, considering also the limited number of spares available (only 4 spares in total, one per magnet type).

### 2.1.9 Exotic scenarios

Some different filling schemes of the SPS could be proposed to circumvent the limitation of the maximum intensity per cycle that could be delivered by the PS. Under the assumption that 10/11<sup>th</sup> of the SPS circumference should be filled, an alternative filling scenario could envisage two consecutive 3 PS-turns extraction plus a cycle with a 4 PS-turns extraction, each using the MTE technique. While the first two cycles could generate the three-turn extraction by crossing the third-order resonance, the last one would require crossing the fourth-order resonance made unstable by an appropriate setting of the octupoles, as described in Ref. [35]. The advantage of this scheme would be a more moderate intensity per cycle to be accelerated in the PS. For example, for a total intensity injected in the SPS of  $8 \times 10^{13}$  p, and supposing the same intensity per islands in each PS cycle, this would correspond to a total intensity of  $2.4 \times 10^{13}$  p for the two three-turn extraction cycles and  $3.2 \times 10^{13}$  p for the four-turn extraction cycle. Moreover, the different kick to extract the last turn would not be needed for any of the cycles proposed here.

A clear disadvantage would be the loss of 1.2 s due to the extra cycle, impacting on the duty cycle of the SPS experiment, but also on the reduced beam availability for the PS physics users.

It is worth mentioning that experimental studies carried out in the PS already showed that it is possible to capture the beams in three islands [36], even if their extraction was not realized as for MTE.

Further studies should also concern the islands transverse emittances resulting from the capture process, since resonances of different order (third and fourth) create islands of different surface. More than this, the island of different resonances could feature different orientation in phase space, thus inducing different optical mismatch at injection into the SPS.

The difference in beam emittance used to be considered acceptable in terms of SPS performance in the case of the CT, as it was shown that slices of equal intensity, i.e., the nominal case during standard operation, feature rather different horizontal emittances [9]. Nevertheless, the difference between the resulting properties of the extracted beams should be quantified before drawing any further conclusion.

As a last remark, it is worth mentioning that other schemes could be envisaged, e.g., based on three consecutive three-turn extractions, but in this case the filling fraction of the SPS circumference would be of only 9/11<sup>th</sup> and the performance of the corresponding scenario should be carefully quantified.

## 2.2 HI Beams in the SPS

### 2.2.1 Introduction

The beam required by LBNO project is very similar to the one used by the CNGS. Beam power of 750 kW considered by the LAGUNA-LBNO corresponds to the total intensity of  $7 \times 10^{13}$  pp (ultimate CNGS intensity which was never achieved) extracted from the SPS every 6 s or to  $8.4 \times 10^{13}$  pp per 7.2s, see Table ??.

During this operation mode two PS batches are injected into the SPS. The maximum (record) PS intensity achieved at 14 GeV/c in the past (see Section??) was around  $3 \times 10^{13}$  using a single

**Table 2.1:** Main beam and RF parameters for the LHC and CNGS-type beams in the SPS under different conditions (operation, special studies and future plans).

		OPERATION		SPS RECORD		AFTER LIU (2020)	
		LHC	CNGS	LHC	CNGS	LHC-targ.	CN2PY
SPS beam energy	[GeV]	450	400	450	400	450	400
Bunch spacing	[ns]	50	5	25	5	25	5
Bunch intensity	$10^{11}$	1.6	0.105	1.3	0.13	2.2	0.17
number of bunches		144	4200	288	4200	288	4200
SPS intensity	$10^{13}$	2.3	4.4	3.75	5.3	6.35	7.0*
PS intensity	$10^{13}$	0.6	2.3	1.0	3.0	1.75	4.0*
PS cycle length	[s]	3.6	1.2	3.6	1.2	3.6	1.2/2.4*
SPS cycle length	[s]	21.6	6.0	21.6	6.0	21.6	6.0/7.2
PS beam momentum	[GeV/c]	26	14	26	14	26	14
Average current	[ $\mu$ A]	0.17	1.17	0.28	1.4	0.47	1.9/1.6
Beam power	[kW]	77	470	125	565	211	747/622

PSB batch injection with a 1.2 s PS cycle and was around  $4 \times 10^{13}$  using a double PSB batch injection leading to the 2.4 s long PS cycle (1.2 s more due to the length of the PSB cycle). This gives maximum (potential) SPS intensity at 14 GeV/c (no losses) of  $6 \times 10^{13}$  pp with injection plateau of 1.2 s and of  $8 \times 10^{13}$  pp injected during 2.4 s. Therefore maximum intensity accelerated by the SPS to 400 GeV/c with a 3 s acceleration time (present situation), 5% losses (optimistic assumption) and no limitations (see below) can be  $7.6 \times 10^{13}$  pp with a 7.2 s cycle or  $5.7 \times 10^{13}$  pp with a 6.0 s cycle. This corresponds to a 680 kW beam in the first case and to a 610 kW in the second. Taking into account that relative beam losses increase with intensity and reliability of accelerator is reducing for high intensity operation, the second option is the preferred one.

As one can see from Table 2.1 high total beam intensity is also required for the High Luminosity LHC (HL-LHC) project. However the acceleration cycle for the LHC beams is significantly longer (more than a factor 3) and correspondingly 3 times less beam power can be delivered in this case. The main difference of the CNGS-type beam from the LHC beams accelerated in the SPS, see also Table 2.1, is related to the shorter PS cycle, only possible with beam injection at 14 GeV/c and therefore transition crossing in the SPS. The CNGS beam fills the whole SPS ring and the LHC beam ? less than a half leading to very different requirements for limited RF power (continuous and pulsed regimes). The CNGS-type beam has smaller bunch spacing (5 ns) and lower bunch intensity. As a result these beams have different beam control (LLRF) and suffer from different intensity effects (beam loading, instabilities, beam-induced heating, ?). The main intensity and performance limitations of the CNGS-type beam are discussed below.

## 2.2.2 Main Limitations and Studies of high intensity CNGS-type beams in the SPS

In 2004 the intensity record of  $5.3 \times 10^{11}$  protons was reached at the end of a 3 week beam test after a careful tuning of all accelerators [?]. The aim of this test was to identify and study the intensity limitations as well as to investigate possible improvements. The main limitations for high intensity CNGS-type beam in the SPS are

- Beam losses due to many different reasons
- Longitudinal beam stability (leading to uncontrolled longitudinal emittance blow-up)
- Maximum available power at 200 MHz (750 kW for full ring) and therefore voltage (7.5 MV) due to beam loading

- Beam induced heating of equipment
- Large transverse (vertical) emittance at injection
- Injection below transition
- No bunch-to-bucket transfer, debunched beam component at injection
- Transverse damper (LHC beams: 40 MHz bandwidth)

The main limitation for further intensity increase during high intensity operation in 2004 was the beam loss leading to radiation issues. Indeed the relative beam loss for whole accelerator chain increased from 24% to 38% for the SPS intensity increase from  $4.4 \times 10^{13}$  to  $5.3 \times 10^{13}$ . Possible improvements for the CNGS-type beam were studied in the special WG on Beam Loss and Radiation. Being also at the limit in the PS, the last CNGS operation in 2012 was with reduced total intensity of  $4 \times 10^{13}$ .

At the moment maximum available voltage is used during the cycle (see Fig ??) due to uncontrolled emittance blow-up during transition crossing followed by beam instabilities during ramp. Any voltage reduction at given moment in the cycle leads to beam losses.

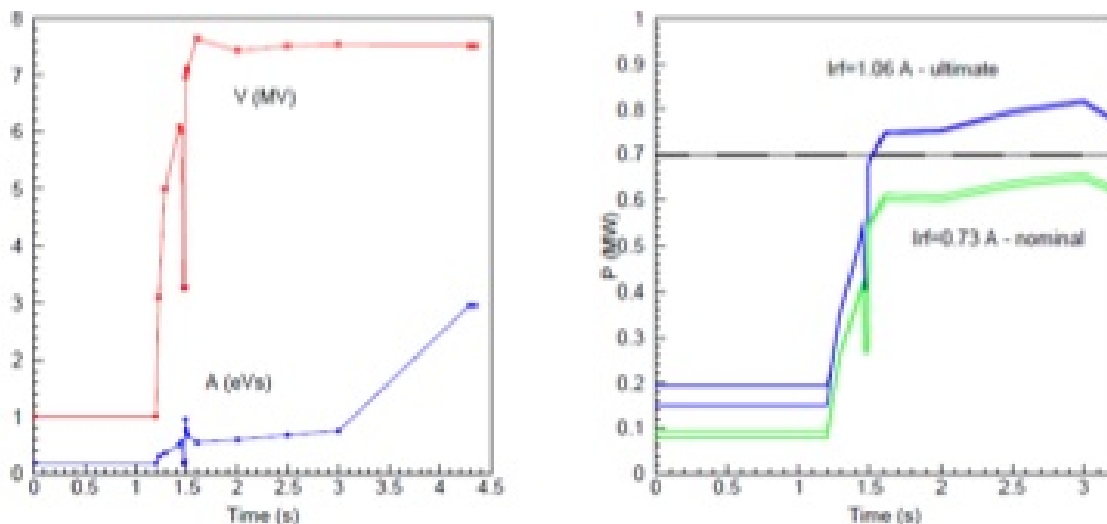


**Figure 2.12:** The 200 MHz voltage programme during the CNGS cycle together with available bucket area (left figure). The RF power required during acceleration cycle for nominal ( $4.4 \times 10^{13}$ ) and ultimate ( $7.0 \times 10^{13}$ ) CNGS intensities.

In 2012 studies of the CNGS beam stability were performed during three half-day MD sessions to verify existing intensity limitations in light of the performance required by LAGUNA-LBNO [?]. Voltage programme on the flat bottom was modified to see the effect on beam quality and losses. It was confirmed that operational programme is practically optimum for this beam intensity (injected  $3.6 \times 10^{13}$ ), see Fig 2.13.

Typical beam structure after capture is shown in Fig. 2.14 (left). Average and minimum-maximum bunch length variation is presented in Fig. 2.14 (right) where significant emittance blow-up can be seen after transition crossing together with growing bunch oscillations at the end of the cycle.

Average bunch length oscillations after transition crossing are well visible in Fig. 2.15(left), while in Fig. 2.15 (right) one can see bunch length variation along the batch for different moment in the cycle.

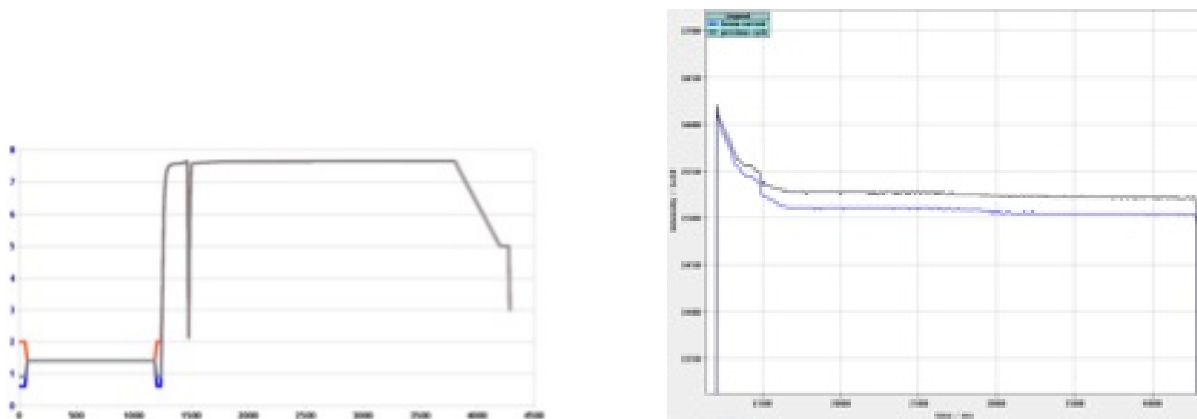


**Figure 2.13:** The voltage programmes tested during MD studies in 2012 (left figure). Corresponding BCT (intensity) signals after beam capture in the nominal voltage of 0.8 MV (black trace) and tested 0.6 MV (blue trace).

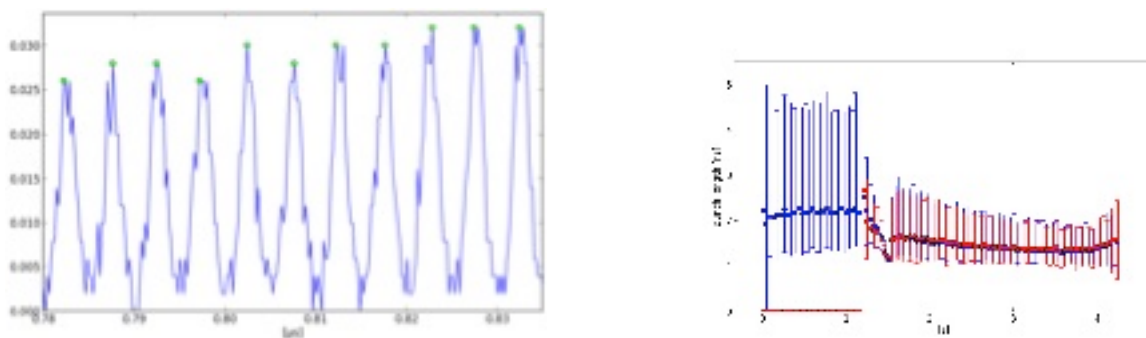


**Figure 2.14:** Left figure: typical example of the measured beam structure (a.u.) after capture in the SPS with 0.8 MV voltage. Right figure: average and minimum-maximum bunch length evolution during the CNGS cycle for Batch 1 (blue color) and Batch 2 (red color).

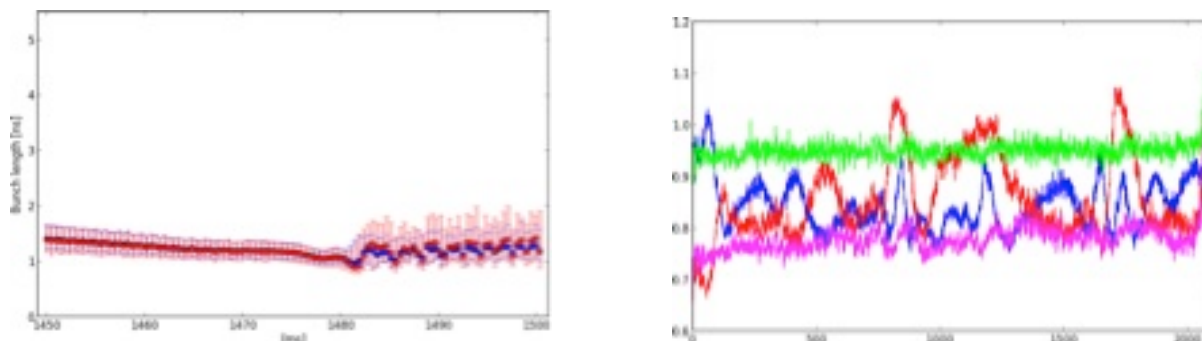


**Figure 2.15:** Left figure: average bunch length from 1400 ms till 1500 ms cycle time for Batch 1 (blue) and Batch 2 (red). Right figure: relative bunch length (with respect to the reference bunch length at 1450 ms) at 1457 ms (green), 1480 ms (magenta, transition crossing), 1490 ms (red), and 1501 ms (blue).

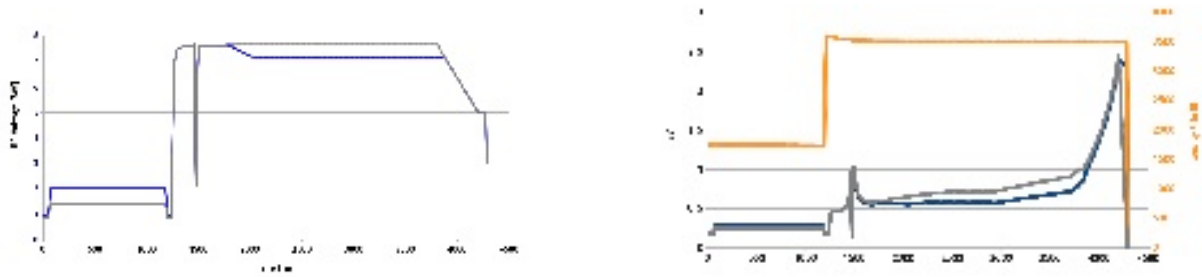


**Figure 2.16:** Studies of particle loss reduction during MD in 2012. Left figure: nominal (grey) and modified (blue) voltage. Right figure: beam intensity (orange) and bucket area in nominal (grey) and modified (blue) voltage.

### 2.2.2.1 High intensity beams in the SPS after LIU

After upgrades foreseen for the LHC beams by the LIU project (to be completed by 2020) [LIU], potentially higher intensity CNGS-type beam can also be accelerated in the SPS. However this potential can be fully realised only after many studies and probably additional upgrades, not planned by the LIU project.

The following LHC Injectors Upgrade (LIU) will be also beneficial for the CNGS-type beam:

1. Upgrade of the 800 MHz (to be completed in 2015). This RF system is used for stabilisation of the LHC beam during the whole cycle and on the flat top. Only one cavity is operational at the moment. After the upgrade two cavities will be available with RF power of 300 kW at the cavity input. The new FB and FF systems around the cavities will allow their impedance to be significantly reduced as well as beam loading effect.
2. Upgrade of the 200 MHz RF system (2020): 4 existing cavities (2 with 4 section and 2 with 5 sections) will be re-arranged into 6 cavities using 2 additional spare sections. New digital beam control (LLRF) will be commissioned in 2020.
3. Impedance reduction:
  - (by 20% for 200 MHz RF, from 2020);
  - serigraphy of extraction kickers, from 2015;
  - search for unknown impedance sources and their modifications
4. Improved beam instrumentation
5. e-cloud mitigation (by scrubbing or using Amorphous Carbon coating)

Presently both voltage and power are at the limit: 7.5 MV used after transition crossing (due to uncontrolled longitudinal emittance blow-up). Significant improvement for CNGS and fast LHC cycle are expected with 6 cavities using 20 sections (2 additional sections), see Fig.6.

New SPS optics with  $\eta_t=18$  was deployed for the LHC beams in the SPS in 2012. The main motivation is increase in the transverse instability (TMCI) threshold at injection. For the CNGS-type beams this change in transition energy would give an increase of the slip factor  $\eta = 1/\gamma^2 - 1/\gamma_t^2$  above transition in respect to the nominal optics ( $\eta_t=22.8$ ), see Fig. 2.18.

The threshold of the longitudinal instability scales as  $N_{th} \sim |\eta|$ . Longitudinal instability threshold (single RF) scales as  $N_{th} \sim |\eta|\epsilon^2/E$ , so probably one can expect less uncontrolled emittance blow-up after transition. However, for the same bucket area, required RF voltage also scales as  $V_{rf} \sim |\eta|$  as can be seen in Fig. 2.19.

Possible LLRF improvements in the SPS (identified during the high intensity run [2]):

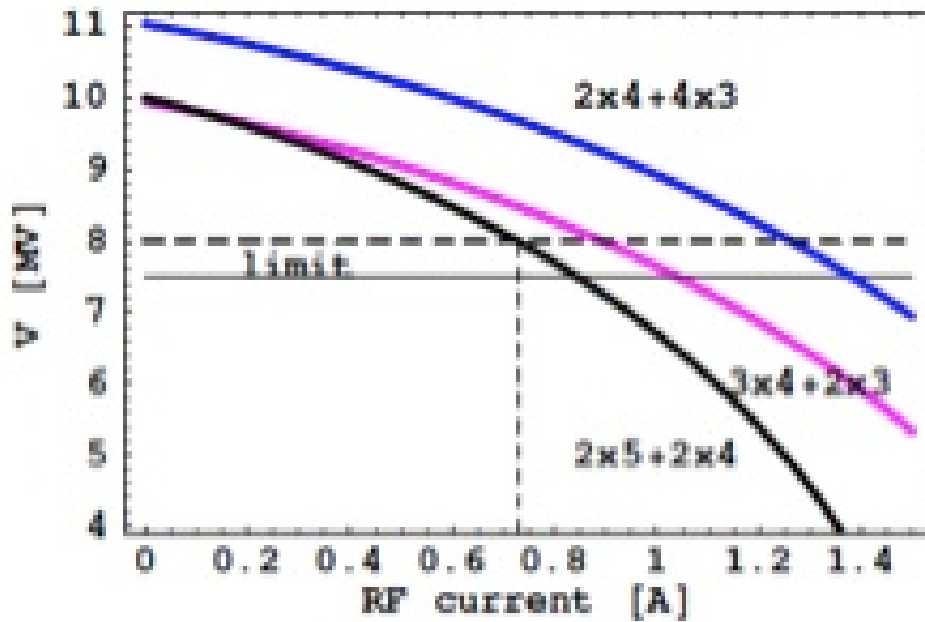


**Figure 2.17:** Total 200 MHz voltage as a function of the RF current, available in the SPS for acceleration with maximum RF power per cavity limited to 700 kW for different RF configurations: present situation with 4 cavities and 18 sections (black curve), 6 cavities with 18 sections (magenta) and approved upgrade for 6 cavities with 20 sections (blue). The RF current of 0.73 A corresponds to bunch intensity  $N = 4.8 \times 10^{13}$  (dashed vertical line) and 1.06 A to  $N = 7 \times 10^{13}$  (4200 bunches spaced by 5 ns). Horizontal dashed line indicates the present limit of 7.5 MV.

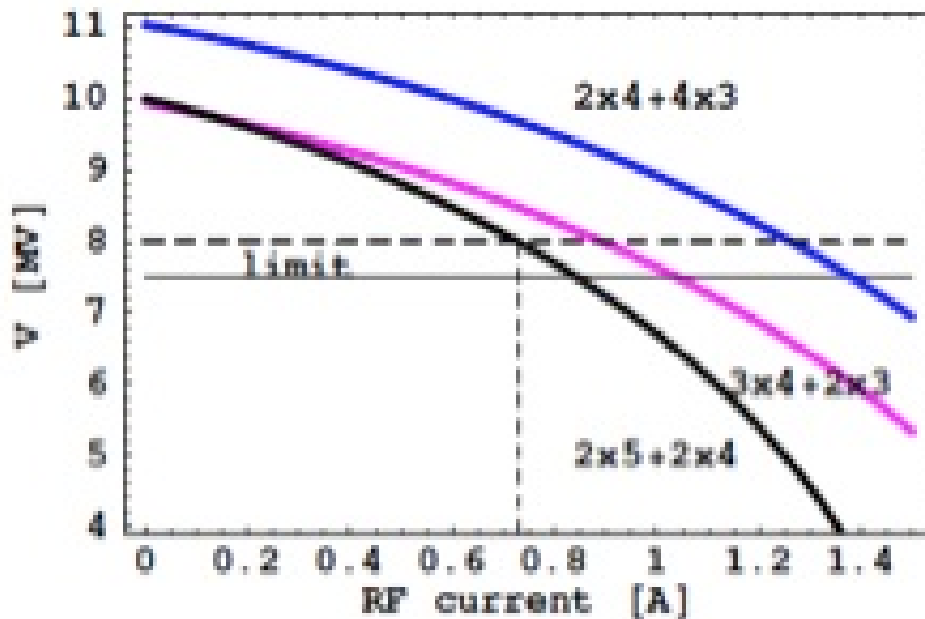


**Figure 2.18:** The slip factor  $\eta$  during the CNGS acceleration cycle for the two SPS optics: the present Q26 optics with  $\gamma t = 22.8$  (solid line) and the Q20 optics with  $\gamma t = 18$  used for the LHC beams from 2012 (dashed line).

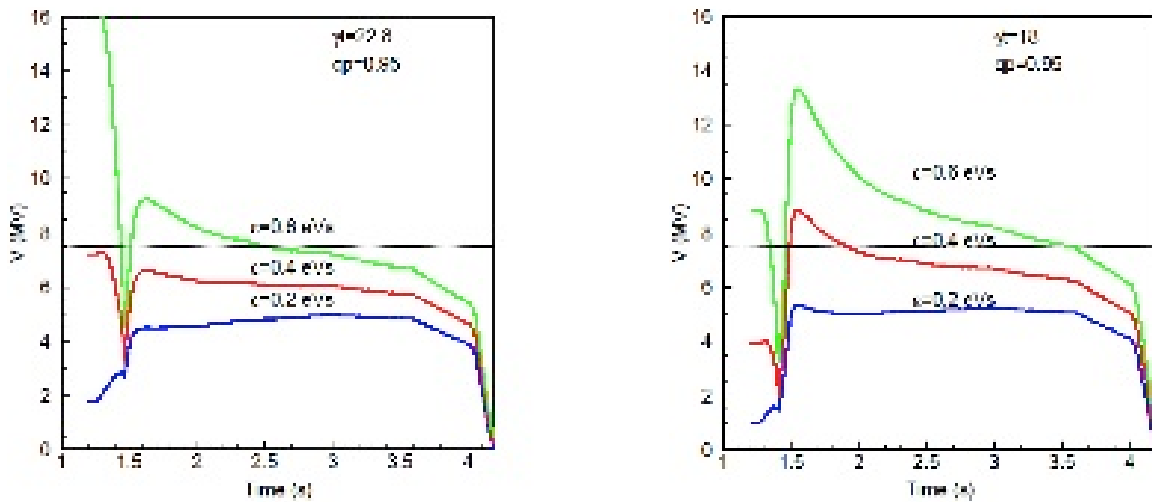


**Figure 2.19:** The 200 MHz voltage programmes designed for acceleration of beams with various longitudinal emittance with constant momentum filling factor (0.95) of the RF bucket are shown for the present Q26 optics (left figure) and the new Q20 optics used for LHC beams (right).

- Separate capture of each PS batch in the SPS (possible due to large bandwidth of the main 200 MHz TW RF system) would allow voltage capture modulation (0.8 MV increased to 2.5 MV) ? optimum for beam loss reduction.
- Variable gain of 1-turn-delay feedback.
- Upgrade of the frequency range of the feed-forward system below 26 GeV/c; will be implemented during the 200 MHz RF upgrade (after LS2, 2020).
- Use of the 800 MHz RF system during cycle should be possible after LS1, in 2014.

Open questions which require additional beam studies are:

- Use of the 800 MHz RF system (Landau cavity) for beam stability
- Optimum transition crossing
- Need for collimation system for loss localisation
- Use of the new optics (Q20) with lower transition energy ( $\gamma_t=18$  instead of present 22.8) *f*.

## Chapter 3

# Proton Beam Transfer

### 3.1 Introduction and assumptions

The first phase of LAGUNA-LBNO at CERN will use the SPS to produce 400 – 700 kW beams of between 4 and  $7 \times 10^{13}$  protons per cycle, which will be transferred to the neutrino production target, using fast extraction and new beam lines. The options for extraction and beam transfer lines from SPS to the target are presented in the first section.

For the second phase of the project, a new 50 – 75 GeV/c synchrotron is foreseen to increase the beam power on the target to around 2 MW. The second section presents the options for the beam transfer lines from this HP-PS to the target, including a discussion on the staging and the path from phase 1 to phase 2.

The final section presents the 4 GeV/c H- injection beamline from the SPL to the HP-PS. The injection and extraction systems for the HP-PS machine are described separately in Chapter xx.

For all the beam lines described the assumptions used to calculate required magnet apertures for the different beams are given in Table 3.1. The equation used to estimate the required aperture is

$$A_{x,y} = N \cdot \sqrt{\beta_{x,y} \cdot \epsilon_{x,y}} \cdot 1.1 + |D_{x,y}| \cdot \frac{\Delta p}{p} \cdot 1.1 + co \cdot \sqrt{\frac{\beta}{\beta_{max}}} \quad (3.1)$$

for calculation of the beam envelopes  $A_x$  and  $A_y$ , where  $\epsilon$  is the r.m.s. emittance,  $D$  and  $\beta$  are the dispersion and beta functions,  $\Delta p/p$  is the momentum spread and  $co$  the maximum allowed trajectory excursion. For these studies, a  $5 \sigma$  beam size, a 4 mm trajectory excursion and a beta beating factor of 1.1 have been used.

**Table 3.1:** Assumed beam characteristics for LAGUNA-LBNO transfer lines.

Parameter	Unit	Beam from SPS	Beam from HP-PS	Beam to HP-PS
Particle type		p <sup>+</sup>	p <sup>+</sup>	H <sup>-</sup>
Momentum	GeV/c	400	50	4.0
Rigidity	Tm	1336.5	169.8	16.16
Beam power	kW	700	2000	200
Norm. emittance H	$\mu\text{m}$	10	8	0.35
Norm. emittance V	$\mu\text{m}$	8	5	0.35
Momentum spread		5e-4	5e-4	5e-4
Max. trajectory offset	mm	4	4	4
Beta beating factor (on $\beta$ )		1.21	1.21	1.21



## 3.2 400 GeV/c proton beam from SPS

The options for extraction and transfer of the 400 GeV/c high-power proton beam from the SPS have been compared for the LAGUNA-LBNO study [?]. One important assumed constraint is that the SPS impedance (about 20 M $\Omega$ /m effective impedance in the vertical plane, of which around 60% is from the kickers) cannot be significantly increased with respect to its present levels [?], in order not to degrade the performance of the SPS for high intensity, high power beams for LAGUNA-LBNO and also for the existing and future LHC beams [?]. In addition the existing capacity should be retained for extraction of different beams in the three extraction systems in SPS Long Straight Sections (LSS) 2, 4 and 6. These constraints essentially preclude the addition of a new extraction kicker system for LSS2, and has resulted in the concept of non-local extraction [?] being developed for LSS2, using the existing kickers from LSS6. In the following sections the different options of extraction from either LSS2 or LSS6 are explored, together with the related requirements and first design considerations for the beam transfer line geometries and magnet systems.

### 3.2.1 400 GeV/c beam extraction from SPS LSS2 to target near North Area

For a target facility located near the existing SPS North Area infrastructure, an extraction from SPS LSS2 is needed. The extraction in LSS2 would allow the reuse of the existing TT20 transfer line, up to a dedicated switch section into the new transfer line arc which takes the beam to the LAGUNA target. A fast extraction of LAGUNA beams from SPS LSS2 has requirements similar to the extraction used for CNGS [?]. The lack of fast kickers in LSS2 and the difficulties of integrating such a system with the present layout, together with the impedance considerations mentioned above, have led to the development of non-local extraction where another kicker in a different region of the SPS is used to excite a large betatron oscillation in the beam, re-using the magnetic extraction septa in LSS2 at a suitable phase advance to remove the beam from the SPS aperture. The concept has been checked in simulation and tested in the SPS with low intensity beam, and has been shown to be conceptually feasible [?] using a modified version of the present MKE kicker system. This solution is also relatively inexpensive with a low impact on the SPS ring, which would allow nearly beam tests and validation, although it requires particular attention on the interlocking and machine mode configuration since many machine parameters over two arcs of the SPS (more than 2 km) could affect the extraction trajectory stability and envelope.

#### 3.2.1.1 Non-Local extraction simulations and tests at 440 GeV

Madx was used to carry out tracking simulations to determine the optimum SPS configuration for the LAGUNA non-local extraction. To extract the beam in SPS LSS2, the MKE kickers in LSS6 were chosen, and the simulations carried out at a beam energy of 440 GeV, which was fixed by practical considerations on the interlocking of the extraction for the beam tests. The nominal machine tune of  $Q_x = 26.62$  gives a poor MKE – TPST phase advance of 24°, and so a new machine tune of 26.87 was deployed, to give a suitable phase advance of close to 90°. For a real deployment the MKE6 to TPST phase advance can be controlled by a redeployment of the so-called Q-split powering of the SPS main quadrupoles, and is not considered as a limitation for the concept.

One important limitation, however, is that the ZS septa have to be retracted from the beam during the non-local fast extraction, as the location of the septum wires in the beam aperture is not compatible with the extraction trajectory in LSS2. This places limitations on the beam types which can be operated simultaneously in the SPS.

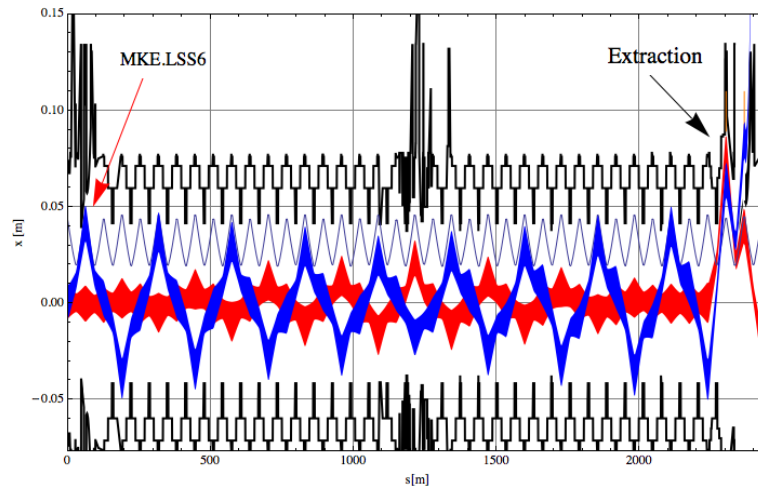


**Figure 3.1:** Bumped (blue) and kicked (red) 440 GeV/c beam horizontal envelopes for non-local extraction over 2.5 km between SPS LSS6 and LSS2, with the SPS aperture.

Figure 3.1 shows the bumped beam envelope (red) and the kicked beam envelope (blue), together with the SPS aperture model. Of note are the large oscillations in the arc, for the last turn before extraction, excited by the MKE kicker in LSS6, and the bumps in the closed orbit prior to extraction, at the extraction septum in LSS2, Fig. 3.2 and also in the region of the internal beam dump TIDP in LSS1, to overcome a local aperture limitation, Fig. 3.3.

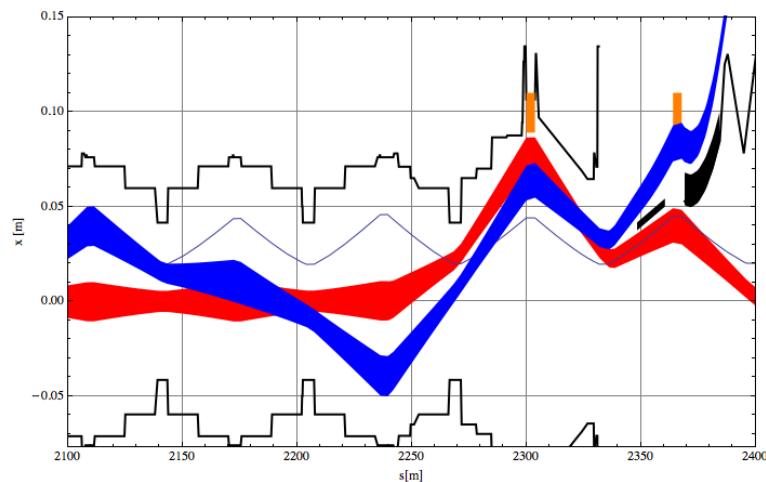


**Figure 3.2:** Extraction bump (blue) and kicked (red) 440 GeV/c beam envelopes for non-local extraction in LSS2, showing MST and MSE septa (solid black) and extraction quadrupole field limits (orange).

The circulating beam opening at the entrance of the extraction septum (TPST) was simulated for an ensemble of SPS machine configurations, with different random errors and orbit corrections applied and an horizontal emittance of 8.0 microns (normalised). The results are shown in Fig. 3.4(a) and show that there is no significant aperture limitation at the extraction septum, even for the worst combination of random machine errors. The average clearance is 8.9 sigma, with a standard deviation of 1.4 sigma.

Another important concern is the aperture available for the extracted beam, with the large betatron oscillations in the SPS sextants 6 and 1. Figure 3.4(b) shows the minimum aperture at extraction, again for 1000 random machine configurations. The average clearance is 10.4 sigma, with a rather large standard deviation of 5 beam sigmas.

The beam tests were held in October 2012, with a special SPS cycle with  $Q_x = 26.87$  and low

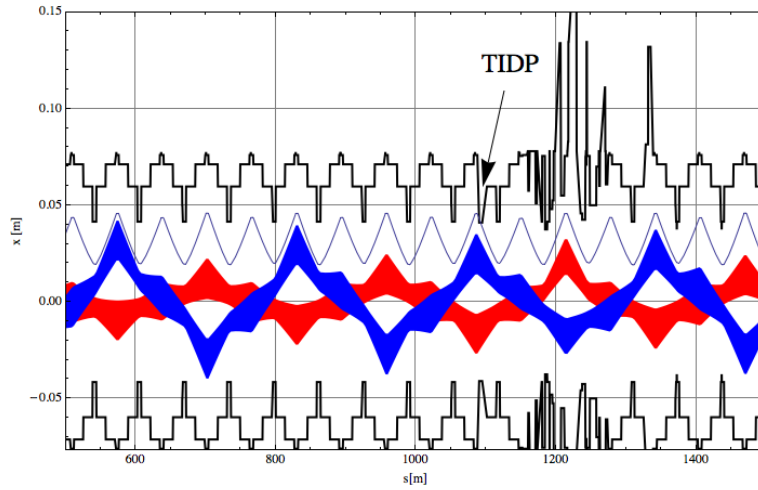


**Figure 3.3:** Bumped (blue) and kicked (red) 440 GeV/c beam horizontal envelopes for non-local extraction in SPS LSS1, showing orbit bump to avoid TIDP.

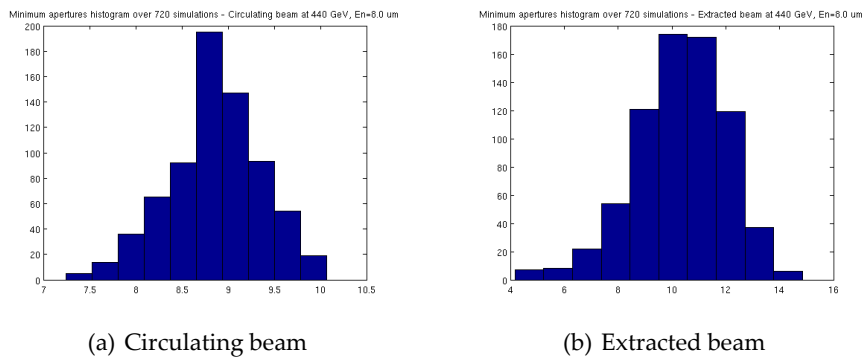


**Figure 3.4:** Histograms of minimum aperture available in 1000 seeds for circulating and extracted 440 GeV/c beam.

intensity configuration with a single bunch of  $10^{11}$  p+. Horizontal emittances were measured at 5.0 and 6.5 microns (normalised), with the increase being made deliberately to approach the operational high intensity values which are between 8 and 10 microns. The beam was successfully extracted with the calculated extraction element settings, and optimisations performed to check the calculated trajectories. The last turn of the beam positions in the SPS could be captured using the orbit system in a manual mode, and show the  $\sim 30$  mm oscillations in the arcs in sextants 6 and 1, Fig. 3.6. The beam was recorded on the BTV screen in the TT20 beamline, Fig. 3.5. A scan of the beam position at the extraction septum was performed by varying the bump height and measuring losses at the septum - the results shown in Fig. 3.7 show that the clearance at the septum is ample, with at least 3-4 mm clearance each side of the optimal position. No losses in the machine arcs were recorded at the moment of extraction, even with the addition of orbit bumps of up to 5 mm at expected aperture limits, which is another important result. The optimum bump amplitude was found in the MD tests to be at 28 mm at the TPST entrance.

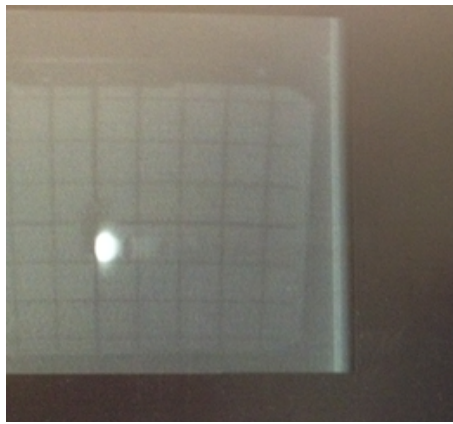


**Figure 3.5:** Non-local fast extracted beam on the BTV screen in the TT20 transfer line, October 2012.

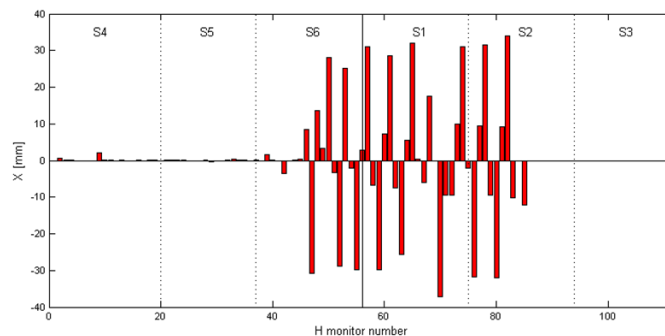


**Figure 3.6:** Measured last-turn trajectory of 440 GeV/c SPS beam kicked from LSS6 and extracted in LSS2, from beam tests in October 2012.

The linearity of the phase advance between LSS6 and LSS2 with kick oscillation amplitude was checked in MD and no measurable variation was found up to the maximum amplitude tested. In addition the phase advance was not dependant on the single bunch intensity – however, with full beam intensity there is expected to be a tune variation which will need to be corrected, and which may require an interlock on the range of allowed intensity which can be extracted, similar to the Beam Quality Monitor (BQM) system presently in use for the LHC beam.

It is also to be noted that the working point of the SPS may change in the future for opti-

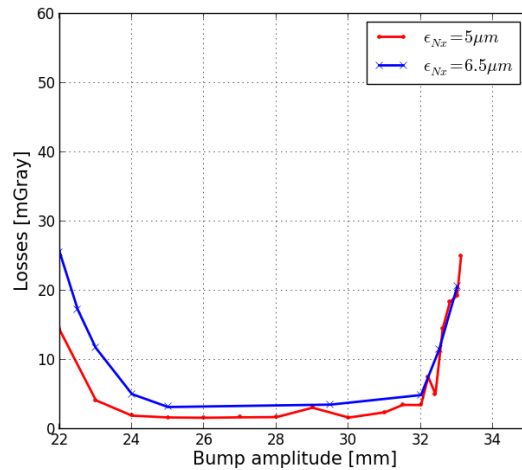


**Figure 3.7:** Losses at extraction septum as a function of extraction bump amplitude, with two slightly different beam emittances. The losses at low bump amplitude are the extracted beam on the outer edge of the septum, while those at high bump amplitude are the circulating beam on the inner edge of the septum.

misation of the cycle – in order to be able to still fix the phase advance from the MKE in LSS6 to the TPST in LSS2 at or near  $90^\circ$ , the ‘Q-split’ powering of the main QF chain needs to be re-commissioned. This allows the horizontal tune of half of the SPS (between LSS3 and LSS6) to be varied independently while keeping the overall machine tune constant, which allows the phase advance between LSS1 and LSS2 to be fixed. A concern for the re-use of this system is the possible perturbation of the LHC machine tune during the rise time of the Q-split current, an effect which plagued LEP in the past [?].

For the non-local extraction, a rather important change to the SPS interlocking would be required, with the addition of a separate beam permit loop for the extraction, which would have inputs from different clients around the SPS ring, Fig. 3.8. Although conceptually simple, replicating existing technology, the lengths of fibre involved (at least 20 km to be pulled) means this is likely to be relatively expensive. Inputs would include orbit correctors, extraction bumpers, main bends, main quadrupoles, main sextupoles, extraction quadrupoles and sextupoles, Q-split power supplies and the Beam Quality Monitor.

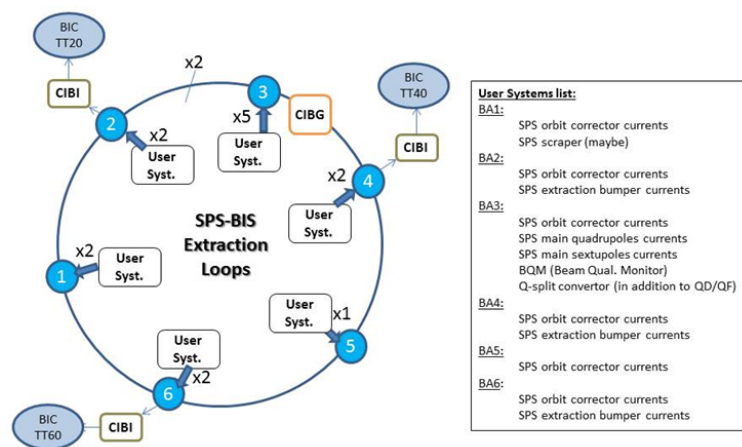


**Figure 3.8:** Schematic of SPS extraction permit interlock loops which would be required for the non-local extraction.

As a result of the simulations and beam tests the non-local extraction concept was demon-

strated to work, and seems to be quite robust - for other potential applications, the extraction using this technique was also tested at 110 GeV/c, where the physical beam size is a factor two larger than at 440 GeV/c - again, the beam was extracted from the SPS without any problems.

### 3.2.1.2 LSS2 extraction elements

The LSS2 magnetic extraction elements can basically remain as they are now for operation with the non-local extraction. As mentioned above, the only major issue is the need to retract the ZS wires (and hence the full ZS girder) from the beam while performing the non-local fast extraction, to avoid beam loss and damage of the ZS. This mechanical movement is slow, of the order of a minute, and also requires a subsequent beam set up of the slow extraction to re-optimize the losses in the extraction channel. These elements preclude fast cycle changes between LAGUNA and the North Area Fixed target beams for extraction through LSS2, and mean that an alternate time-sharing operational model will be needed which is clearly sub-optimal. Potential ideas to alleviate this problem have been investigated but no solution has been found to date.

A closed orbit extraction bump will be produced using the existing LSS2 bumper magnets. These will need additional interlocking, as for the fast extractions in LSS4 and LSS6. There are no issues of bumper strength or rise time, as the systems are dimensioned for 450 GeV/c rigidity. The only changes to the system will be the addition of interlocks for the power converters.

The copper current-carrying conductor of the MST septum is presently protected by a 5 mm thick TPST diluter. This will certainly need upgrading for the 400 GeV/c fast extracted beam, with replacement of the aluminium/copper diluter element by graphite or carbon-composite, as for the TPSG elements in LSS6 [?]. A validation of the new TPS design will be needed, with FLUKA simulations based on the beam parameters and on the assumed geometry. No major issues are expected, given that the beam intensity and brightness are well below the requirements of the HL-LHC beams in the SPS, which pose similar problems in LSS4 and LSS6.

The extraction specific instrumentation will need upgrading. A large 206 mm aperture BPCE coupler will be needed at SPS main quadrupole 219, for interlocking of bumper beam position prior to extraction, and the BTVE extraction screens at entrance and exit of MST and MSE girders need upgrading (4 units in total, although possibly only the screens at the septum entrances are essential). The locations and designs of the new screens must be compatible with the existing instruments for the slow extraction.

### 3.2.1.3 Transport through TT20

The present TT20 beamline needs to be equipped to accept high-intensity fast extracted beams. The powering scheme for the line will remain unchanged to the switch region, and all magnet supplies and apertures are compatible with 400 GeV/c beam with a new optics.

A significant extension to the present beam instrumentation is needed, with the addition of Beam Position Monitors (120 mm diameter BPCK couplers) at about 12 existing quadrupoles. Space has been identified in the lattice for all BPMs and BLMs, for example Fig. 3.9. A few integration issues exist in some locations; it is not apparent where to locate a BPM near QNFL210400, as the TED vacuum chamber and downstream dipoles leave little space. The electronics for these monitors can possibly be recuperated from the CNGS TT41 line. The BPMs should be cabled to BA2, with the maximum cable length to the bottom of the BA2 shaft is about 550 m, and the minimum length about 70 m. Beam loss monitors based on ionisation chambers will also be needed at each TT20 quadrupole. A total of about 15 new BLMs will be needed. These should be cabled to BA2 if possible. Again the cable lengths range between about 70 and 550 m, to the bottom of the BA2 shaft. In addition the existing BTV screens BTV210026 and BTV210352 need upgrading, with the addition of interlocking on the screen positions, and the addition of

OTR screens for accurate profile measurements (CNGS beamline specification). An addition BTV screen will be needed in the early part of TT20, upstream of the TED if possible, e.g. near QTLF210200. A new fast Beam Current Transformer will be needed at the start of TT20, before the TED. This should be cabled to BA2. This could possibly be located just before QTLD210300, in the test region for beam instrumentation.

The interlocking of the line also needs to be upgraded with the addition of a Beam Interlock (BIC) system and probably a Warm Magnet Interlock system (WIC).

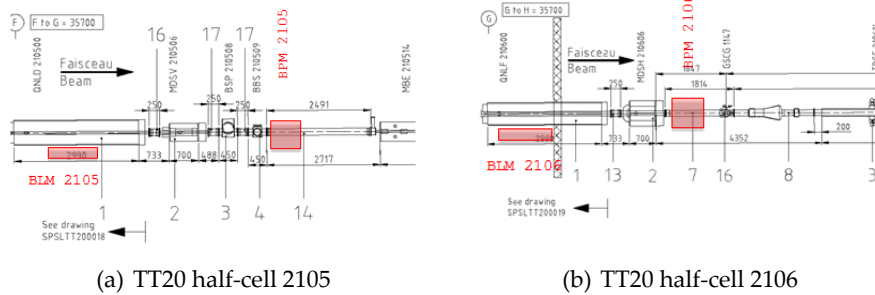


**Figure 3.9:** Examples of possible TT20 locations for new BPMs and BLMs for fast extracted beam - a total of 12 new locations are needed and have been identified.

The large beam emittance and low extraction energy mean that the TT20 optics will need to be rematched to provide sufficient aperture. The normal design criteria is taken as an half-aperture sufficient to accept a minimum number beam sigma, typically 6, taking into account dispersion, peak trajectory, beat beating and mechanical and alignment tolerances.

### 3.2.1.4 Switching from TT20 into new beamline

The new beam line branches off at the top of the existing TT20, in the TDC2 cavern. One of the main challenges of using TT20 is the 400 GeV/c switch to the new beam line, due to the high beam rigidity and absence of space in the present beam line. An elegant suggestion is to replace the three existing MSSB2117 splitter magnets, with newly built splitters, which allow negative polarity powering. This would provide an elegant way of doing this without sacrificing the full slow spill to one of the existing North Area beam lines. With a two-polarity splitter magnet, an extra beam line is possible, symmetric to the T6 beam line but to the left of the T2/T4 line instead of to the right, see Fig. 3.10.



**Figure 3.10:** Location of new LAGUNA beamline just downstream of MSSB splitter-switch magnets.

The three existing MSSB magnets 211713, 211723 and 211732, Fig. 3.12, need to be replaced by similar magnets (termed MSSB-S) which allow enough aperture for the beam deflected in the opposite direction. The main requirements for the new magnets are:

- Replicate existing splitter functionality for present NA beams;
- Polarity reversal possible within about 2 seconds;
- Adequate good-field region around both sides of field-free septum hole;





**Figure 3.11:** Existing MSSB splitter magnets at the top of TT20, which would need to be replaced by a new bipolar laminated design.

- Same  $\int B \cdot dl$  and physical length as present MSSB.

The present MSSB design [?] is an in-vacuum Lambertson septum, with a vacuum separation to keep the coils and water connections in air, built with radiation robust materials and low-maintenance assembly. The magnets operate with 0.8 T in the gap, and have a limit  $B_{max}$  of 1.6 T in the steel at the point of the septum element. Interestingly, for today's North Area splitter design, the wedge angle  $\theta$  of the septum is  $36^\circ$ , and since  $B_{max} \sin \theta \approx B_{gap}$ , it is therefore possible by running at higher current to increase the gap field to about 0.95 T without a major effect on the field quality. The alternative of using a higher saturation steel like FeCo would gain something, but would be much more expensive, mechanically tricky and lead to activation issues.

The gap is 75 mm high, which requires about 48 kA.turns at 0.8 T. The present coil scheme of 48 turns and 1 kA can be retained. The coil technology is special, using compacted MgO powder around a central copper current carrying water-cooled tube, mechanically supported by an external grounded copper sheath. The MgO is evacuated to avoid moisture degradation and the maximum voltage to earth is 1 kV.

The present MSSB are built with solid yokes, assembled from several precision machined pieces. Because of the need to switch the polarity between SHIP and normal FT cycles a laminated yoke is essential for the MSSB-S. A possible technology would be 1.5 mm punched laminations, blue-steamed for insulation and assembled with a stacking factor of 98%. This technology is routinely used in the SPS for the extraction septa MSE/T that are also exposed to high radiation doses. The drive current (or the magnetic length, in case the power convertors are really limited to 1000 A) might need to be increased by 2% compared to the existing magnet to compensate for slight reduction in  $\int B \cdot dl$ .

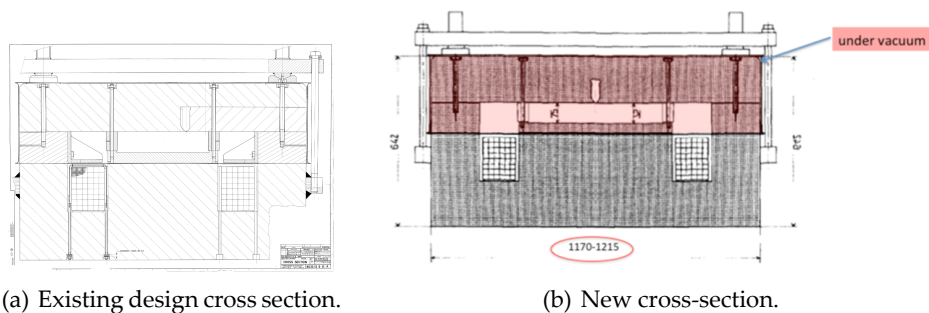


**Figure 3.12:** Cross-sections of the existing MSSB and new MSSB-S magnets.



The MSSB-S cross-section can be a simple variation of the present MSSB, Fig. 3.12, with the good field region extended to the other side of the septum hole. Here some advantage can be taken of the operation at 400 GeV/c. the maximum offset for the switched beam at the exit of the 3rd MSSB is around 90 mm. Allowing another 40 mm for the beam size and orbit, alignment tolerances, the good field region (and pole width) needs to be extended by 130 mm only, although an extra 150 mm would make the septum hole symmetric to the pole. The overall yoke width is likely to increase from 1042 mm to approximately 1170 mm, and the weight will increase from the present 24 tonnes to about 27 tonnes. Main parameters are compared to the existing MSSB in Table 3.2. The inductance and resistance are scaled from the existing magnet, with the preliminary pole width and coil size.

**Table 3.2:** Parameters of the existing MSSB and new MSSB-S magnets.

Parameter	Unit	MSSB	MSSB-S
Magnetic length	m	4.7	4.7
Gap field	T	0.8	0.8
Stacking factor	%	100	98
Coil turns		48	48
Current	A	9947	1014
Vertical gap	mm	75	75
Pole width	mm	400	530
Magnet inductance	H	0.11	0.14
Coil resistance	mΩ	65	66
Number of magnets in series		3	3
Minimum rise-time	s	10	2
Maximum voltage to ground (3 magnets in series)	V	~250	400

### 3.2.1.5 New beamline from TT20 to LAGUNA neutrino target

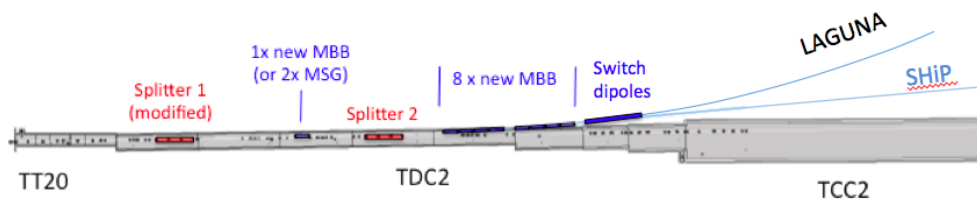


**Figure 3.13:** Switch region in TDC2, showing branch off of new beamline to LAGUNA and switch with proposed SHiP beamline.

A maximum deflection angle to exit the TDC2 tunnel is beneficial to reduce the longitudinal extent of the civil engineering works in the crucial junction region. Large bends of type MBB or MBN will be needed, which can run at almost 2 T and are 6.2 m or 5.0 m long, respectively. It must be noted that the MBN magnets are highly inductive, so pulsing rapidly a large series of magnets would require a converter with an unrealistically large voltage rating. The first version of the initial part of the beamline configuration is shown in Fig. 3.13, below. New dipole and quadrupole locations are indicated along the new beamline. In the version produced, 9 MBB type (or similar) main dipoles are needed as early as possible in the line to move beam out of TDC2.

Overall, an angle of at least 80-100 mrad is needed with respect to TT20. In the first optics checks this was obtained with the 8 mrad from the three MSSB switch magnets, plus 9× MBB

magnets running at a conservative field of 1.73 T giving 8 mrad each. A total of about 11 MBN magnets would be needed to reach the same deflection.

In the initial configuration studied, the MBBs are grouped into a single dipole as early as possible, and two standard half-cells of 4 dipoles each. It is to be noted that no new dipoles are located near the second splitter, for reasons of installation, maintenance and radiation dose during operation.

Once in the new extraction tunnel where the main tilted dipole string is used to provide the vertical and horizontal deflection to the neutrino target. In the first design, the first bending elements are switch dipoles, designed to allow a straight-on beamline to the proposed SHiP experiment [?], with the remaining dipoles of MBB type.

The transfer line to the LAGUNA-LBNO target is a regular FODO with normal conducting dipoles with 6.2 m magnetic length, 1.85T peak field and a vertical aperture of 30 mm, not including vacuum chamber. These are very similar to the dipoles used in the TT41 transfer line to the CNGS target. The dipoles are installed with a large tilt angle to provide both vertical and horizontal deflection, to meet the geometrical contrasts of the neutrino beam to Finland. The line geometry is shown in Fig. 3.15, together with the existing SPS and TT20 beam lines for reference. Focussing is accomplished with 2.2 m long quadrupoles, using parameters for the quadrupoles in the TT41 transfer line to the CNGS target with a 35 mm aperture and 30 T/m gradient. The parameters for the transfer line magnets, including the numbers and required power converter families, are shown in Table 3.3. Correctors have been assumed at all regular quadrupoles, which is probably generous, and the integrated strength has been dimensioned by scaling from similar lines, without detailed trajectory correction studies made at this stage. Cross sections of the quadrupole and dipole used in the CNGS TT41 beamline are shown in Fig. ??, and a typical CNGS short straight section in Fig. 3.16.

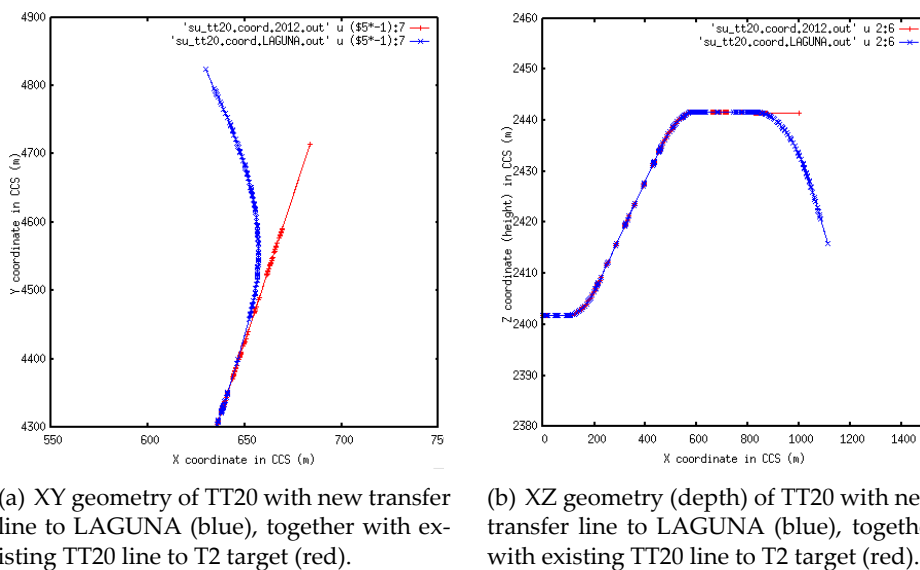


**Figure 3.14:** Geometry of TT20 and new normal-conducting LAGUNA transfer line from SPS LSS62 including TT20 line to T2. The new beamline starts after the splitters, at around 630 m

The preliminary optics of the new section of the full beamline including TT20 is shown in Fig. 3.17. Maximum beta functions and dispersion values are reasonable given the beam energy and physics emittance - the vertical dispersion in the line is significant due to the large bends at the bottom and top of TT20 - at this stage no major effort has been made to match this away in the new beamline. No space has been allocated yet in the lattice for any collimation, which from CNGS experience is not required for fast-extracted beams. The final focus to the neutrino production target is accomplished with a triplet of quadrupole magnets, each of

**Table 3.3:** Parameters of new normal conducting magnets and converters needed for the 400 GeV/c beamline from TT20 to the neutrino target

Parameter	Unit	Main dipoles	Main quadrupoles	Dipole correctors
Magnetic length	m	6.2	1.4	0.5
Gap field	T	1.8		0.2
Gradient	T/m		30	
Bend angle	mrاد	8.4		0.075
Sagitta	mm	6.5		0.005
Vertical good field region	mm	30	35	35
Horizontal good field region	mm	50	35	35
Installed magnets		41	15	13
Magnets powered in series		41	8	1
Installed converters		1	7	13

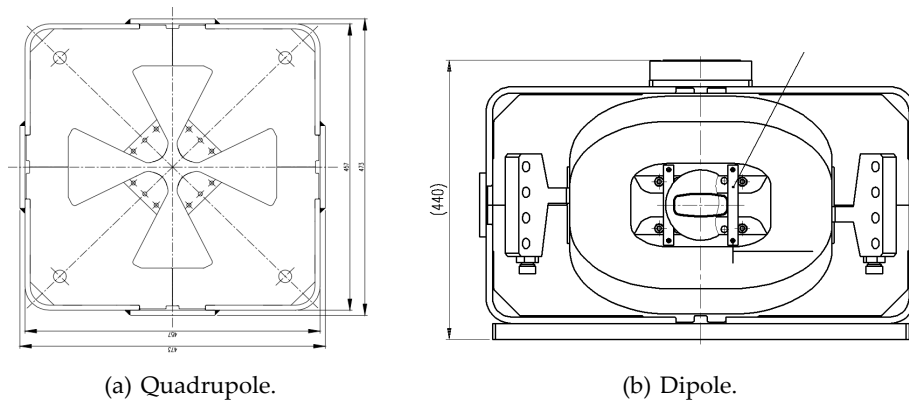


**Figure 3.15:** Cross sections of the QTG and MBG main magnets used for the 400 GeV/c TT41 transfer line from the SPS to the CNGS target.

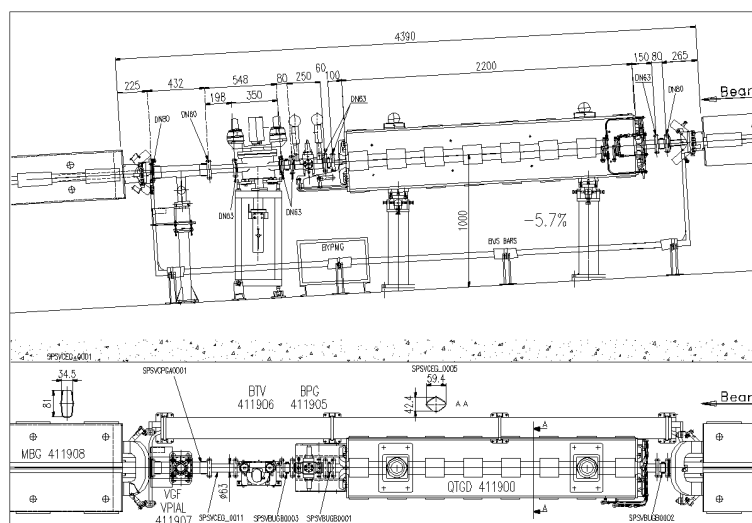
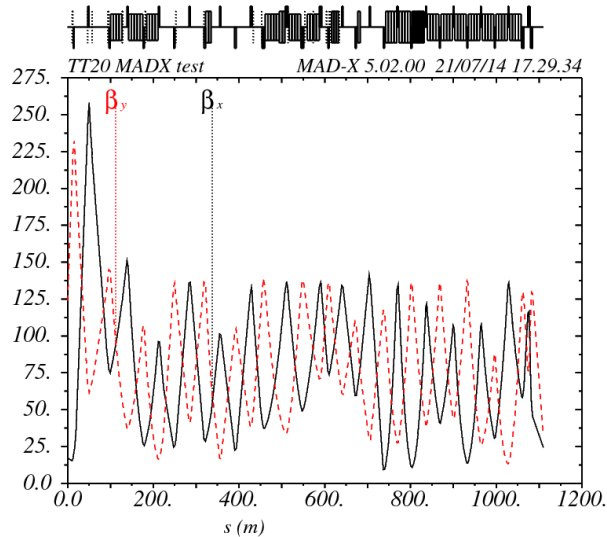
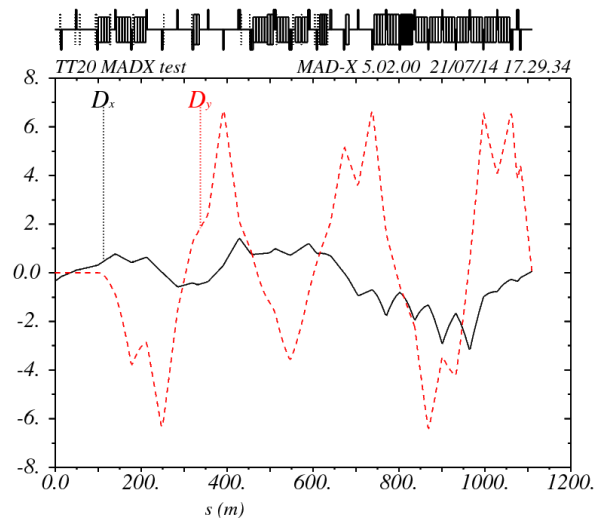


**Figure 3.16:** Typical short straight section in the 400 GeV/c CNGS beamline, showing corrector and BPM located between the dipole and quadrupole. The tunnel slope at this location is 5.7%, to be compared to 18% for LAGUNA .

which is composed of two standard quadrupoles to achieve the required integrated gradient. The space between the exit of the final quadrupole and the target is 25 m, which should be adequate for beam instrumentation, a vacuum window, shielding and the target mechanism. The dispersion at the target is matched to less than 5 cm in both planes, and the beta functions are 24 m in the horizontal plane and 32 m in the vertical plane.



(a) Beta functions



(b) Dispersion functions

**Figure 3.17:** Optics of new beamline from SPS LSS2 to the LAGUNA target, including re-matched TT20, for fast extracted 400 GeV/c beam.

The required aperture for the beam was calculated from the optics. Taking conventional assumptions on the momentum spread, number of sigma required, orbit and beta-beating, the minimum half apertures in the X and Y planes were calculated along the line, Fig. 3.18. It can be seen that around 40 mm is needed for the beam, with mechanical tolerances, beam vacuum system, sagitta and cold bore to be added to give the free aperture. With a bend angle of 8.5 mrad and a length of 6.2 m the sagitta is 6.5 mm. A total of 41 new long dipoles are needed, and 15 quadrupoles, together with around 13 correctors for trajectory correction and steering on the target.

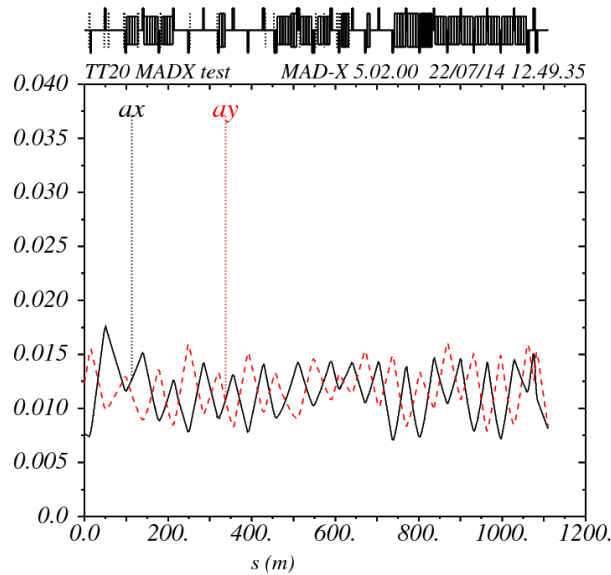


**Figure 3.18:** Minimum half-aperture (m) needed for beam acceptance in the line from LSS2 to the LAGUNA target, not including mechanical tolerances, sagitta or vacuum chamber.

### 3.2.2 400 GeV/c extraction from SPS LSS6 to target near LSS1

For a target facility located near the existing SPS LSS1 infrastructure, an extraction from SPS LSS6 is proposed. The extraction in LSS6 would allow the reuse of the existing TT60 transfer line, up to a dedicated switch section into the new transfer line section past the present HiRadMat facility [?] and into an arc which takes the beam to the LAGUNA target. The transfer line would need to use superconducting dipoles to achieve the required geometry, with fields below 5 T.

Fast extraction of LAGUNA beams from SPS LSS6 again has requirements similar to the extraction used for CNGS [?]. LSS6 is equipped with a fast extraction system for the LHC beam, which can easily be adapted to the required rise time and flat-top duration for LAGUNA, simply by mirroring the installation used for CNGS. This will add two kickers to the ring and hence impedance, but the system in LSS4 which was used for CNGS in the past can be reduced in scope to cope with just the LHC beams, and the total number of extraction kickers in the SPS can remain at 8, as at present. Other minor changes may be necessary in the extraction channel instrumentation, but essentially the system is already able to provide 400 GeV/c beams to the TT60 beamline.

#### 3.2.2.1 Switching from TT60 into new beamline

The new beam line has been considered as a replacement of the existing TT66 line used for HiRadMat, which branches off at the end of the existing TT60, after a part common to LHC and HiRadMat. At this stage no study of the compatibility with HiRadMat has been made - this is not expected to pose any conceptual problems, and in reality should be relatively straightforward to add a switch and new beamline section to provide the additional line for LAGUNA (space was left in the TT66 beamline explicitly for such a purpose [?]).

#### 3.2.2.2 Transport to LAGUNA target

The initial beam transport uses the existing TT60 transfer line, with the addition of a dedicated switch section to maintain compatibility with beams for LHC and for the HiRadMat facility [?]. A new section of transfer line is foreseen using superconducting dipoles and quadrupoles,

with a tentative concept based on the GSI-FAIR SIS300 design [?, ?]. Dipoles are 4.0 m long with 4.6 T field, and quadrupoles 1.4 m with 40 T/m maximum gradient. The geometry of the new beamline, together with the SPS is shown in Fig. 3.20. It can be seen that the new beamline passes under the existing TT10 tunnel for the injection into the SPS, and under the SPS ring itself, at a distance of more than 15 m in both cases. The depth of the target below the SPS is about 100 m, corresponding to around 150 m below the surface of the earth. The required dipole bending field is around 4.6 T, and the magnets are split into two families, with tilts of 166 and 280 mrad respectively, to accomplish the simultaneous horizontal and vertical bend. It is worth noting that the strong inclined bends produce a large rotation of the beam frame of reference [?], such that at the target the XY plane is rotated by 220 mrad, which needs to be followed with the alignment of the quadrupoles and correctors to maintain orthogonality between the two planes. A 35 m long half-cell has been constructed with 6 dipoles (the dipoles are short to keep the effect of the beam sagitta on the aperture small), Fig. 3.19.

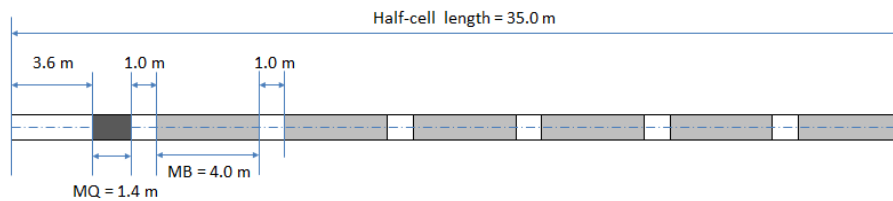
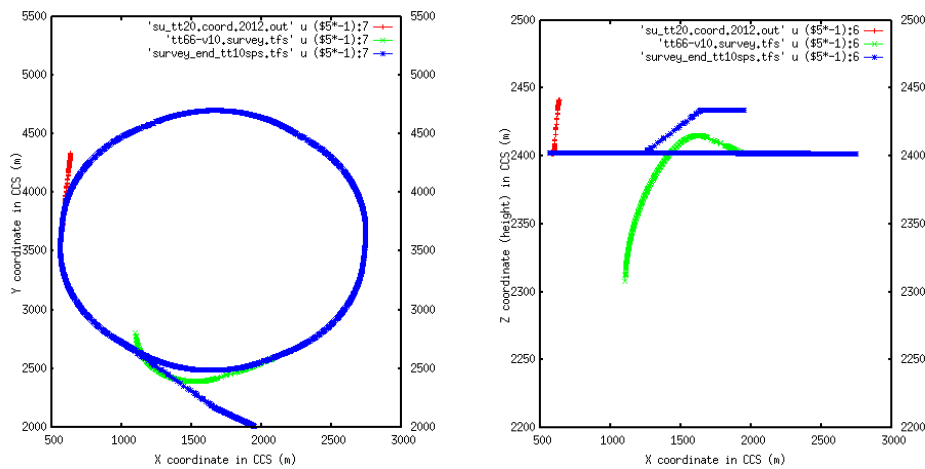


**Figure 3.19:** Halfcell for new superconducting beamline from TT66 to the LAGUNA target. Dipoles are short to keep the sagitta small.

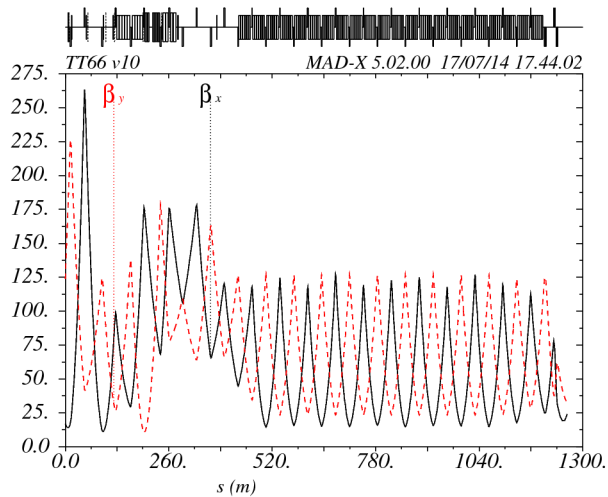


(a) XY geometry of new transfer line (green), together with SPS and TT10 injection line (blue) and TT20 line (red).

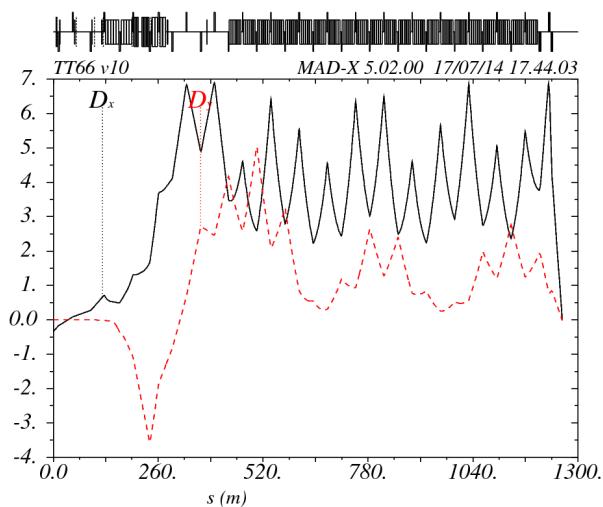
(b) XZ geometry of new transfer line (green), together with SPS and TT10 injection line (blue) and TT20 line (red).

**Figure 3.20:** Geometry of new superconducting LAGUNA transfer line from SPS LSS6, including SPS ring and TT10 injection line, and TT20.

The beamline has been matched to give beta functions of around 125 m in both planes. More difficult is the control of the dispersion in this line, given the large dispersion in both planes coming from the TT60 bends, plus the fact that the bends in the arc are tilted with large angles. A first solution has been found with a phase advance of around  $90^\circ$  in the horizontal plane and  $80^\circ$  in the vertical, and optics of the modified TT66 and the new beamline are shown in Fig. ???. The numbers and parameters of the new magnets needed are shown in Table 3.4. The larger beta functions (up to 260 m) at the start of the line occur in the normal conducting TT60 and TT66 magnets, which are of larger aperture.



(a) Beta functions (m)



(b) Dispersion functions (m)

**Figure 3.21:** Optics of modified TT66 and new LAGUNA beamline, for fast extracted 400 GeV/c beam from LSS6.

An important derived parameter for the superconducting magnet system is the required aperture for the beam. Taking conventional assumptions on the momentum spread, number of sigma required, orbit and beta-beating, the minimum half apertures in the X and Y planes were calculated along the line, Fig. 3.22. It can be seen that around 40 mm is needed for the beam, with mechanical tolerances, beam vacuum system, sagitta and cold bore to be added to give the coil aperture. With a bend angle of 13.5 mrad and a length of 4.0 m the sagitta is 6.8 mm - as this scales with the square of the magnet length, it is clear that longer magnets may need to be of curved construction, or significantly larger aperture.

A total of 132 superconducting dipoles are needed, and 28 quadrupoles, together with around 24 correctors for trajectory correction and steering on the target. It is expected that the correctors and all beam instrumentation can be located in the generous 3.6 m of short straight section at the start of every half cell. The spacing between adjacent superconducting main magnets is assumed to be 1.0 m (between the magnetic lengths).

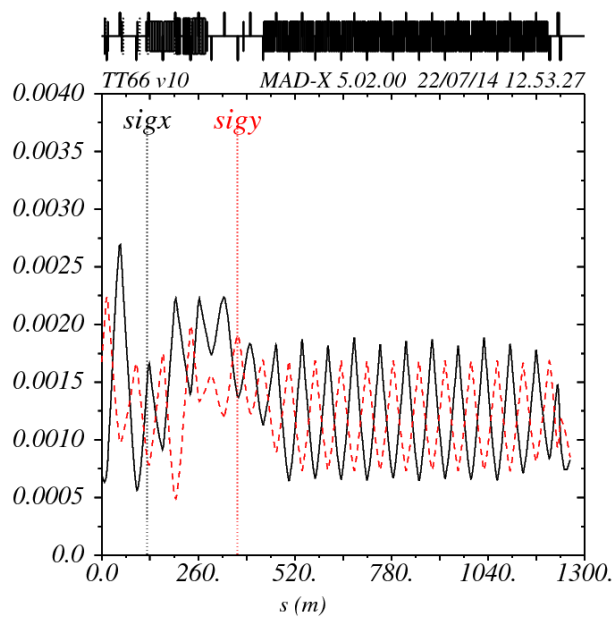


**Figure 3.22:** Minimum half-aperture (m) needed for beam acceptance in the line from LSS6 to the LAGUNA target, not including mechanical tolerances, vacuum chamber or cold-bore.

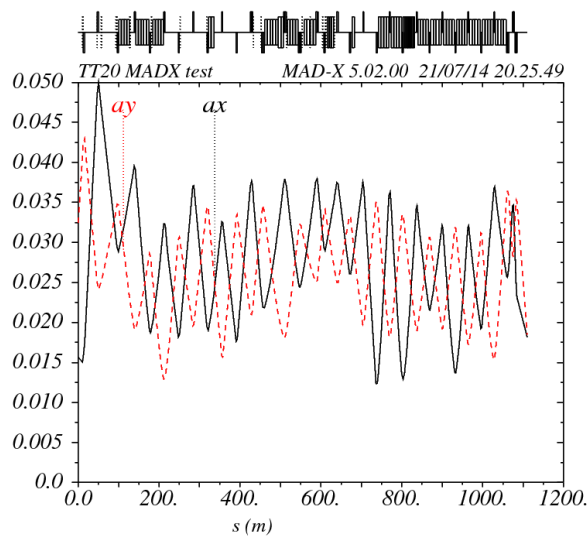
**Table 3.4:** Parameters of new superconducting magnets and converters needed for the 400 GeV/c beamline from TT60 to the neutrino target, using superconducting main magnets

Parameter	Unit	Main dipoles	Main quad.	Dipole corr.
Magnetic length	m	4.0	1.4	0.5
Gap field	T	4.6		0.2
Gradient	T/m		40	
Bend angle	mrad	13.65		0.075
Sagitta	mm	6.8		0.005
Vertical good field region	mm	40	40	40
Horizontal good field region	mm	47	40	40
Number of installed magnets		132	28	26
Max. magnets powered in series		132	6	1
Installed converters (families)		1	15	26

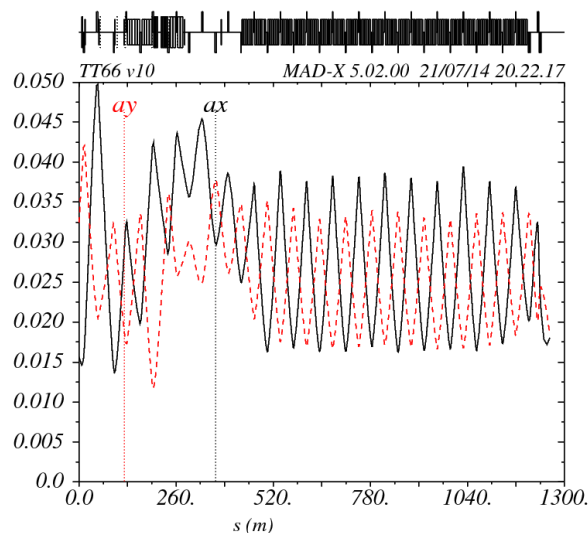


### 3.3 50 GeV/c proton beam transfer for Phase II with HP-PS

The challenges of 50 GeV/c proton beam transfer are different to those of the 400 GeV/c beam. The beam is 8 times less rigid at 170 Tm, which means that smaller bending radii can be achieved in the transfer lines - of the order of 125 m assuming a dipole filling factor of 66%, compared to around 1 km for a 400 GeV/c beamline. However, the physical beam emittance is a factor of  $2\sqrt{2}$  larger, which means that magnet apertures will typically be at least twice as large as for 400 GeV/c, when fixed errors are taken into account. In addition, if strong dipoles are used, the sagitta can increase considerably the horizontal good field region requirement, imposing shorter dipoles or longer, curved units. For illustration, the aperture plots, Figs. ?? and 3.22, have been recalculated for 50 GeV/c beams, Fig. ?? - it can be seen that the magnet aperture required increases from around 40 mm to around 80 mm.



(a) Beamline from LSS2



(b) Beamline from LSS6

**Figure 3.23:** Minimum half-aperture (m) needed for beam acceptance in the new beamlines to the LAGUNA target for 50 GeV/c beams, not including mechanical tolerances, vacuum chamber or cold-bore, and assuming the 400 GeV/c optics.

### 3.3.1 Transfer of 50 GeV/c beams to North Area target location

As mentioned above, the adaptation of the exiting TT20 line and new beam lines to 50-75 GeV beams presents issues of aperture, given that the lines are designed for beams with 5-8 times the energy, and hence physical aperture requirements which are a factor of around 2 smaller. The replacement of the magnets by lower field, larger aperture magnets poses no conceptual problems; however, this will have a very high cost as the full beam lines will need to be completely rebuilt. A study of detailed compatibility for the baseline magnet design should be made to optimise the costs, to try and investigate whether the lower energy beams can be accommodated by magnets which are strong enough for the 400 GeV/c beams, or whether replacement by a new magnet design is the best option.

A more difficult conceptual problem is the connection of the new HP-PS to the start of TT20. Again, in theory and if cost is no issue, a new transfer line tunnel could simply be dug from the HP-PS extraction to join TT20 or the new target beamline; but again, this would be associated with a very high cost and schedule impact. The option of transferring the beam inside the SPS machine using existing SPS magnets in one arc between LSS1 and LSS2 as a transfer line has been discarded, as although it would almost certainly work with little additional equipment, and with minimal changes to the existing SPS lattice, this proposal would essentially block the SPS from running any other beams during the operation of the HL-PS., as even a short magnetic flat-top for the beam transfer would impose a longer (1.2 s) SPS cycle segment, for reasons of minimising the effects of the magnetic history. The tentative baseline is therefore to construct a separate 50-75 GeV/c transfer line between LSS1 and LSS2, inside the SPS tunnel. This line poses some fairly major issues of integration, illustrated in Fig. ??, where another accelerator with similar magnet cross sections needs to be integrated into the tunnel. Possibly permanent dipole (and even quadrupole) magnets can be used, as has been proven at Fermilab in the Recycler ring and the 8 GeV transfer line [?], since the bending radius of the SPS arcs of around 1 km can be accomplished at 50 GeV/c with a dipole field of 0.25 T or so, for the SPS filling factor of 66%. Advantages of such a solution are many, such as no powering or cooling, no electrical interference with the SPS, radiation hardness and low operating cost. In addition the field quality requirements will not be stringent, and more exotic alternatives with combined function magnets could be investigated to minimise the dipole field and hence magnet weight and volume.

The SPS tunnel is relatively generously dimensioned, and space might be available for a transfer line with magnets which are no more than 600 mm in height and around 1000 mm in width might be possible Fig. 3.24, although this would pose considerable engineering challenges for supporting, alignment and maintenance access, in addition to the integration problems with existing and new infrastructure and machine elements.

A first hall-cell for 50 GeV/c beam transport in the SPS tunnel has been designed based on four 3.1 m long 0.23 T dipoles, with a half-cell length of 16 m and a quadrupole length of 1.0 m, to fit to the 32 m long SPS half-cells. A missing magnet dispersion suppresser has been used, as for the SPS, with one half-cell missing all magnets. The beta functions in the arc are 52 m peak, with 5 m horizontal dispersion, Fig. 3.25. The quadrupoles are assumed to be 1.0 m long with a maximum gradient of 8 T/m. The dispersion coming from the HP-PS extraction is essentially transmitted into the start of the TT20 transfer line, which obviously will need adapting completely to the lower beam energy, unless the same idea of a separate, low energy line is also adopted there to keep the present TT20 and North area operational.

The aperture needed for the dipoles and quadrupole is about 50 mm, with maybe 60 mm needed at or near the focussing QFs, without considering vacuum chambers or tolerances. The half aperture required is shown in Fig.?.?. The numbers and parameters of the magnets needed is shown in Table 3.5.

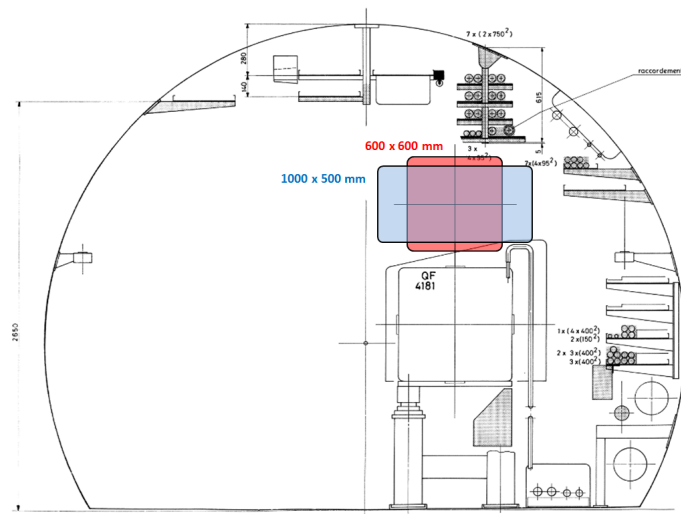
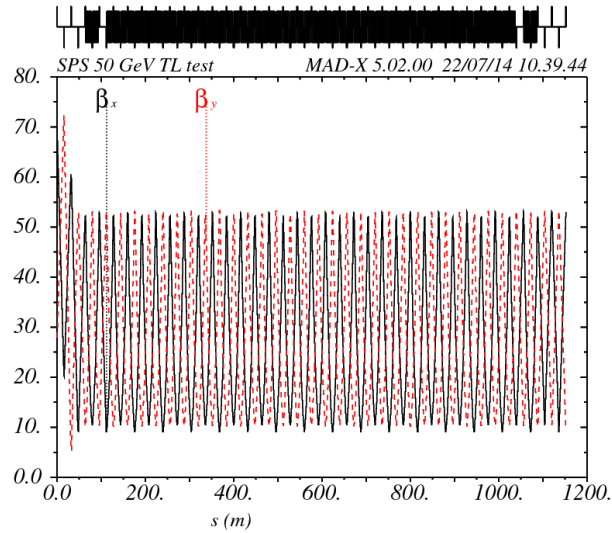


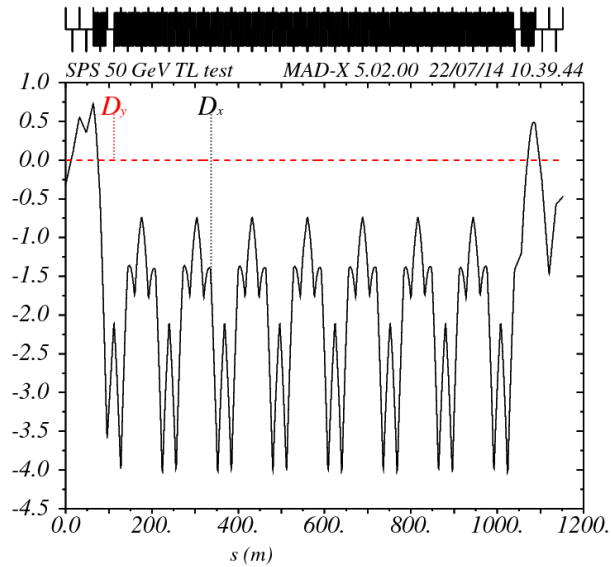
**Figure 3.24:** Cross-section of SPS tunnel (at a QF quadrupole), showing a 600x600 mm quadrupole and 1000x500 mm dipole for comparison.

**Table 3.5:** Parameters of new low field magnets and converters needed for the 50 GeV/c beamline contained in the SPS tunnel, from SPS LSS1 to LSS2.

Parameter	Unit	Main dipoles	Main quad.	Dipole corr.
Magnetic length	m	3.1	1.0	0.15
Gap field	T	0.23		0.1
Gradient	T/m		8	
Bend angle	mrad	4.2		0.09
Sagitta	mm	1.6		
Vertical good field region	mm	50	50	50
Horizontal good field region	mm	60	60	60
Number of installed magnets		248	73	73
Max. magnets powered in series		248	31	1
Installed converters (families)		1	10	73



(a) Beta functions (m)



(b) Dispersion functions (m)

**Figure 3.25:** Optics of 1.2 km long 50 GeV/c transfer line accommodated within the SPS tunnel, with a dipole field of 0.23 T .

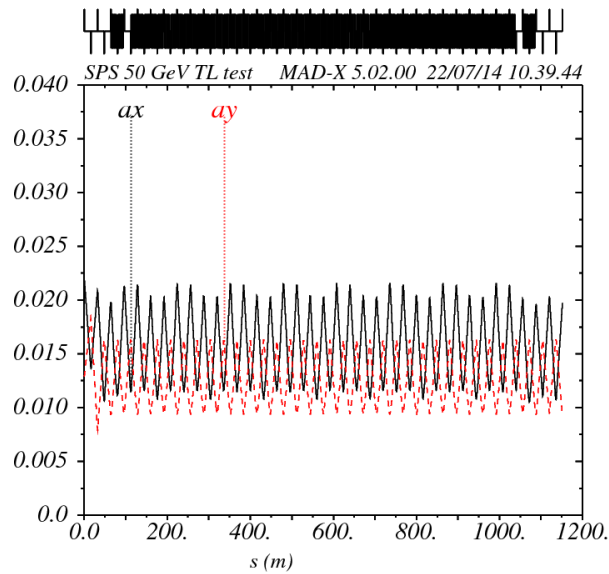


**Figure 3.26:** Minimum half-aperture (m) needed for beam acceptance in the 50 GeV/c line inside the SPS tunnel from LSS1 to LSS2, not including mechanical tolerances, vacuum chamber or sagitta.

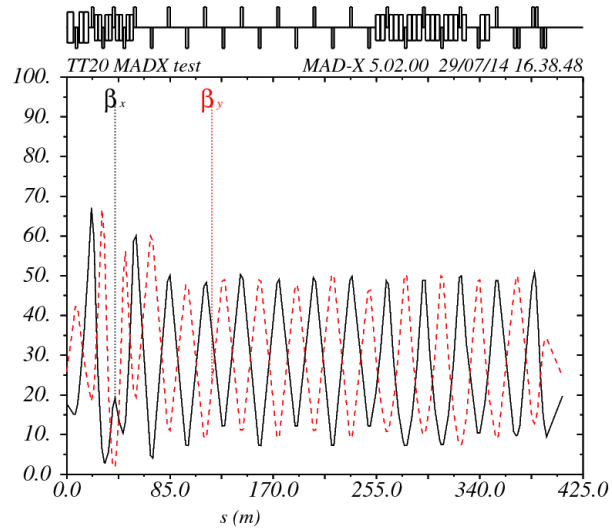
### 3.3.2 Transfer of 50 GeV/c beams to LSS1 area target location

For the option of target location near SPS LSS1, a 410 m section of 50 GeV/c transfer line is required to connect the HP-PS to the superconducting line described above from SPS LSS6 and TT60. The depth and location of the HP-PS are critical in determining the requirements for this transfer line, which will have a large vertical offset to overcome. The minimum bending radius of  $\sim 125$  m is an advantage, but the slope of the tunnel is also a major consideration, and realistically should not exceed 25%, which is already higher than the 18% required at the LAGUNA target. It is to note that this is already rather extreme compared to existing facilities.

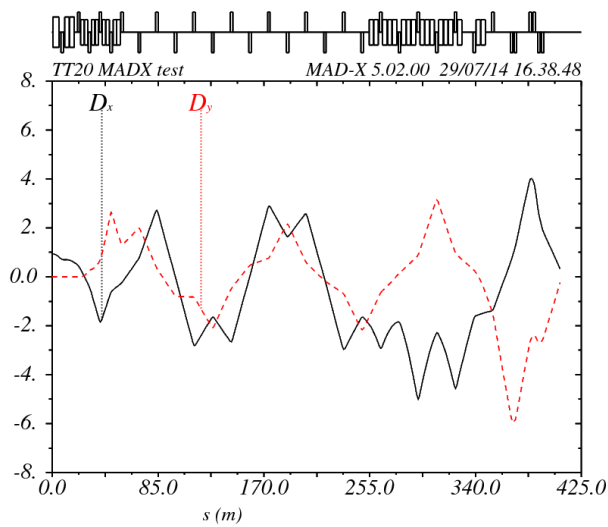
The transfer line has been designed with an initial pseudo-achromat vertical bend to achieve the 25% slope imposed by the geometrical constraints of the HP-PS location and the LAGUNA target depth. This bend is made with 8 dipoles of 2.7 m long and 1.95 T, interspersed with matching quadrupoles to give the large vertical phase advance needed to suppress the vertical dispersion to a sufficient level. The remainder of the line is then constructed with a 15 m long FODO layout, with the horizontal and remaining vertical matching section made with 3.6 m long, 1.95 T dipoles. It will certainly be possible to use 2.7 m long dipoles for these bends as well, in a possible later optimisation to reduce the number of magnet types. All quadrupoles are 2 m long and have a maximum gradient of 17 T/m - this could of course be optimised if the gradient can be increased, to use shorter magnets. A final focus triplet has been used - here the distance from the exit of the last quadrupole to the LAGUNA target is smaller than for the 400 GeV/c line, at 13 m. This distance can probably be increased if necessary, although at the expense of the minimum beta values possible on the target.

The dispersion control in this line is difficult, as the geometry is defined completely by the levels and orientations of the HP-PS and target. In the version studied, both horizontal and vertical dispersion functions reach about 4–5 m, and are not closed - however, the line is matched to give essentially zero dispersion on the LAGUNA target, although the  $D'$  is large in both planes, of the order of 150 mrad. The beta functions have been kept to about 50 m through the line, except in the initial matching section where slightly larger values are needed. The optical functions are shown in Fig. 3.27(b).

Using the standard assumptions for the aperture, the magnets need to have apertures of at least 45 mm, Fig. 3.28, not including sagitta or vacuum chamber. With the 2.7 m long dipoles



(a) Beta functions (m)



(b) Dispersion functions (m)

**Figure 3.27:** Optics of new 50 GeV/c beamline from HP-PS to the LAGUNA target.

the sagitta is already 10.5 mm, and with the 3.6 m dipoles this increases to 18.6 mm, due to the large bend angles of 31 and 41 mrad, respectively. The horizontal aperture (not including vacuum chamber) for the dipoles is then likely to be something like 60-65 mm. The numbers and main parameters for the magnets needed are given in Table 3.6.

Should the extraction momentum of the HP-PS be 75 GeV, there is plenty of free space in the transfer line to accommodate 50% more bending dipoles, with minor changes only in the geometry. The slope and layout of the transfer line will remain unchanged - the magnet apertures will be slightly smaller.

The impressive slope angle  $\Phi$  of the transfer line as a function of the distance is shown in Fig. 3.29. The feature between 250 and 340 m is due to the bends used for the (mainly) horizontal deflection to match the LAGUNA geometry, and is a result of the vertical offset resulting from the horizontal bend with a strong slope - these have been tilted away from the horizontal by 80 mrad, to actually minimise this effect, to avoid exceeding the maximum tunnel floor slope. Clearly, slopes of this magnitude will require very special transport, handling and survey engineering, in particular some good brakes on the vehicles used for installation.

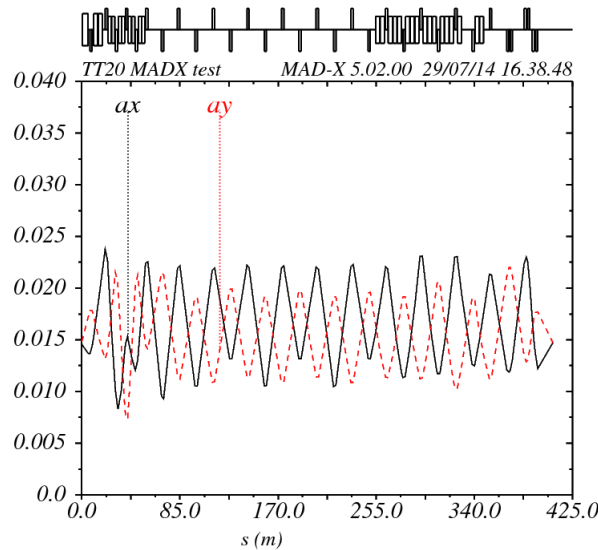


**Figure 3.28:** Minimum half-aperture (m) needed for beam acceptance in the 50 GeV/c line from HP-PS to the LAGUNA target, not including mechanical tolerances, or vacuum chamber.

**Table 3.6:** Parameters of new normal conducting magnets and converters needed for the 50 GeV/c beamline from HP-PS to the neutrino target.

Parameter	Unit	Main dipole 1	Main dipole 2	Main quad.	Dipole corr.
Magnetic length	m	3.6	2.7	2.0	0.5
Gap field	T	1.95	1.95		0.2
Gradient	T/m			40	
Bend angle	mrad	41	31		0.59
Sagitta	mm	18.6	10.5		0.04
Vertical good field region	mm	45	45	45	45
Horizontal good field region	mm	65	55	45	45
Number of installed magnets		17	8	32	30
Max. magnets in series		8	17	8	1
Installed converter families		1	1	15	30

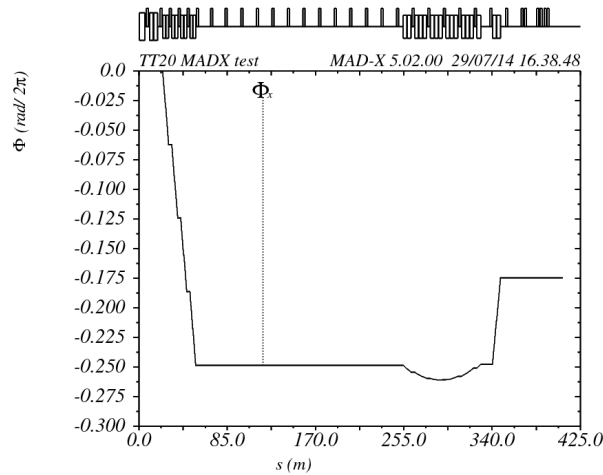


**Figure 3.29:** Slope of HP-PS to LAGUNA target transfer line, as a function of position in the line. The line has a maximum slope of about 26%, with most of it constant at 25%.

### 3.4 4 GeV/c H<sup>-</sup> transfer line from SPL to HP-PS injection

A 4 GeV/c SPL-to-HP-PS transfer line is required for the multi-turn H<sup>-</sup> injection into HP-PS using a stripping foil or laser stripping [?]. This is essentially identical to the requirements for the injection into the PS2 machine previously studied at CERN, and the remainder of this section is based on the work done in this context [?].

Since the HP-SPL could potentially provide 5 GeV/c beams, with power up to 4 MW (by increasing the repetition rate) the injection line geometry in terms of dipole field limits for the early part of the beamline to PS2 was designed to be compatible with high power 5 GeV/c beams. The HP-PS is assumed to be located in the same plane as the SPS, such that the transfer line has to overcome an altitude difference of 21 m over its length of ~250 m between the SPL and the HP-PS. As several existing tunnels, e.g. the TI2 transfer line, cross the injection line in this area, it must pass a fixed point C (Fig. 3.30) to ensure a sufficient distance from these tunnels, to allow civil engineering work without major interference to the existing installations. Furthermore, the strengths of the bending magnets have to be limited to below prevent Lorentz stripping of the H<sup>-</sup> beam [?, ?] and thereby to limit the beam loss below 0.1 W/m. Together with the height difference, this results in a relatively large slope of 8.1% of the beam line.

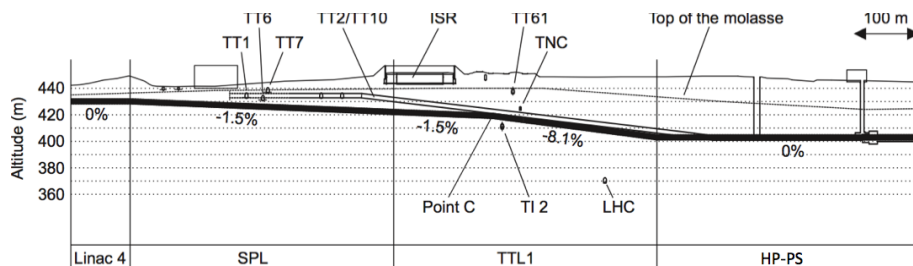


**Figure 3.30:** Longitudinal section of 4 GeV/c HP-PS H<sup>-</sup> injection line, showing the various crossing tunnels. The actual beam line must be bent more smoothly than indicated due to the Lorentz stripping limit.

The maximum field allowed for a power loss of 0.1 W/m (taken as the design figure-of-merit) for the different SPL options are shown in Fig. 3.31. The pessimistic case of the 200 kW, 4 GeV/c HP-SPL has been used to define the final part of the transfer line geometry, which results in a low dipole field of 0.115 T, a minimum bending radius of 141 m and a maximum



quadrupole gradient of 2 T/m, corresponding to a maximum normalised gradient of  $0.25 \text{ m}^{-2}$ .

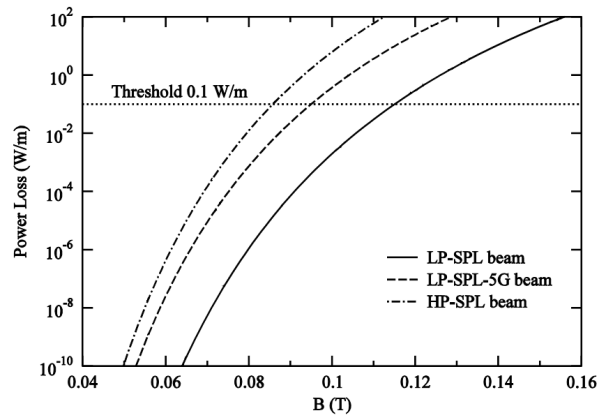


**Figure 3.31:** Power loss from Lorentz stripping for the different SPL options. For the 4 GeV LP-SPL the dipole field in the injection line to the HP-PS is limited to 0.115 T, to keep beam losses below 0.1 W/m.

### 3.4.1 Beam line optics

The beam line layout consists of a FODO lattice with  $90^\circ$  phase advance per cell and a cell length of 25 m [?]. The bending is performed with two combined horizontal and vertical achromats which provide a dispersion-free region in between and easy matching to the required beta function and dispersion value at the stripping foil at the end of the beam line (Fig. 3.32). The strengths of the bending magnets in the entire beam line are compatible with 4 and 5 GeV LP-SPL beams, in case the final injection energy of the HP-PS is eventually increased, e.g. to facilitate efficient laser stripping. The calculated half-apertures for the line are shown in Fig. ??.

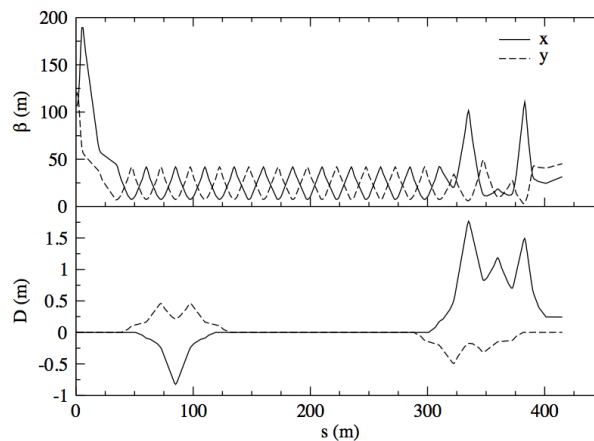


**Figure 3.32:** Beta and dispersion functions along the 4 GeV/c transfer line from SPL to HP-PS.

The magnet and convertor numbers and parameters are shown in Tab. 3.7. For the main bending magnets the reuse of former LEP dipole magnet yokes equipped with new coils is imaginable - this is reflected in the choice of magnet length. Studies on the trajectory correction have been carried out for a previous version of this transfer line [?].

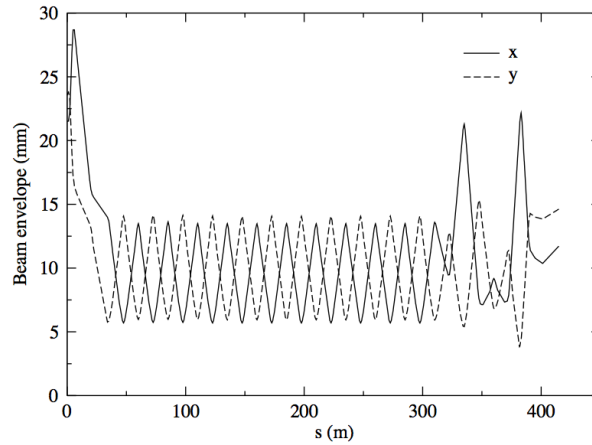


**Figure 3.33:** Calculated beam half-apertures along the 4 GeV/c transfer line from SPL to HP-PS.

**Table 3.7:** Parameters of new normal conducting magnets and converters needed for the 4 GeV/c  $H^-$  beamline from SPL to HP-PS.

Parameter	Unit	Main	Main	Main	Dipole
		V dipole	H dipole		
Magnetic length	m	5.75	5.75	2.0	0.25
Gap field	T	1.95	1.95		0.08
Gradient	T/m			1.6	
Bend angle	mrad	31	31		1.2
Sagitta	mm	22.4	22.4		0.04
Vertical good field region	mm	85	60	60	60
Horizontal good field region	mm	60	85	60	60
Number of installed magnets		8	16	33	33
Max. magnets in series		8	16	12	1
Installed converter families		1	1	11	30

### 3.5 Summary and conclusions

Preliminary designs have been worked out for all transfer lines for the LAGUNO-LBNO study. Two options have been covered, with neutrino targets located either near the SPS North Area (with 400 GeV/c extraction from SPS LSS2), or near the SPS LSS1 infrastructure (with 400 GeV/c extraction from SPS LSS6 and a superconducting transfer line). The extraction from LSS2 would require a new type of non-local beam ejection from SPS, which has been studied in detail for LAGUNA and shown to work perfectly in low-intensity SPS beam tests conducted in 2012. The staging of the project to 2 MW using the 50 GeV/c HP-PS has been studied, with the transfer of 50 GeV/c protons from the HP-PS to both target locations, either by means of a transfer line in the SPS tunnel, or by means of a new, very steeply inclined line to the LSS1 location. Finally, the 4 GeV/c  $H^-$  injection line to the HP-PS is described.

Overall there are no major issues which have been identified for any of the options, and many of the potential issues have been studied in some detailed to ensure their feasibility - these include the non-local extraction, the switching of the 400 GeV/c beam from TT20, the changes to the TT20 beamline, the optics studies and the detailed work on the 4 GeV/c  $H^-$  injection line. The beam transfer concepts all appear to be solid, with no major concerns on the feasibility or required technology.

A conventional wide band beam is envisioned for CN2PY, in which charged mesons generated by a proton beam impinging a solid target are focused by a multi horn focusing device in the direction of the far detector (FD). The mesons, consisting of mostly pions and kaons, are then allowed to decay into a several hundreds of meters long tunnel. The uncollided protons and the remaining secondary particles are stopped in a beam dump at the end of the decay tunnel. Downstream the beam dump sits a large iron shield to prevent the high energy muons emitted along the neutrinos to reach the near detector and cause an intolerable background level.

Two successive phases using a different primary beam are foreseen for CN2PY-LAGUNA/LBNO: a first phase using the upgraded SPS that will deliver a 400 GeV beam at about 750 kW, and at a later stage, a primary beam provided by the HP-PS facility at 50 GeV and 2 MW. Some parts of the CN2PY facility are constrained by the high energy of phase I (the muon shield, for example), when others are constrained by the high power of phase II, especially the design of the target station. Both the primary beam energy and the target geometry have an influence on the secondary yield, and thus on the neutrino spectrum at the FD, therefore it is necessary to perform dedicated beam optics optimizations for each phase.

All the Monte-Carlo calculations were performed with the FLUKA Monte-Carlo code [101, ?] and the experience gained on the design and operation of the now stopped CNGS beam line [?] was used extensively.

### 3.6 Secondary yield and target design

With a 400 GeV primary beam and under the assumption that the momenta of all the pions and kaons produced in the target are made parallel to the beam axis by the focusing system, 95% of the particles exiting the target and giving rise to  $\nu_\mu$  under 10 GeV at the FD consist of  $\pi^+$  ( $\pi^-$  in the case of  $\bar{\nu}_\mu$ ). Therefore, the optimization of the target design should be conducted with the goal of maximizing the yield of those pions.

Figure 3.34 shows the initial energy and angular distributions of such perfectly focused  $\pi^+$  neutrino parents. The pion population was sampled according to two different energy selections for the neutrinos that reached the FD: a "first oscillation maximum" selection:  $3 < E_\nu < 6$  GeV and a "second oscillation maximum" selection:  $1 < E_\nu < 2$  GeV.

With a perfect focusing, the energy of the "first maximum"  $\pi^+$  parents goes from 7 GeV up to 14 GeV and are emitted from the target between 0 and 100 mrad with a most probable angle

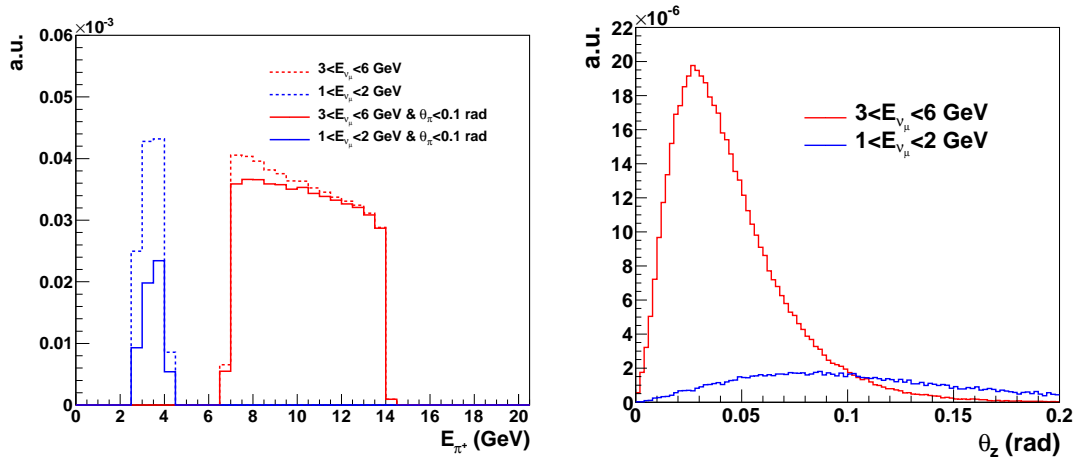


**Figure 3.34:** Initial energy (left) and angular (right) distributions of perfectly focused  $\pi^+$  giving rise to neutrinos at the FD within the first and second maximum oscillation energy ranges.  $\theta_z$  is the relative angle between the beam axis and the pion.

of 27.5 mrad. The energy range of the "second maximum"  $\pi^+$  parents is narrower, between 2.5 and 4.5 GeV but they are emitted in a much broader angle range, to more than 200 mrad and a most probable angle of 80 mrad.

These distributions give an idea of which pions will contribute the most to the neutrino spectrum. However it should be noted that:

- A realistic neutrino spectrum will receive a contribution from secondary particles at higher energy than 14 GeV decaying off-axis. Depending on the beam optics configuration this contribution may not be negligible.
- Because of the very broad angular distribution, the "second oscillation maximum" pions are difficult to efficiently focus, especially if one wants to focus the "first oscillation maximum" pions with the same focusing system.

Figure 3.35 shows the pion secondary yield from the target in the  $\{E_\pi, \theta_\pi\}$  space for both 400 and 50 GeV primary energy. As expected, more low energy secondary particles are produced at lower primary energy but the angular distribution at a given energy is not significantly modified, see fig.3.36. This means that a given beam optics will focus a secondary particle of a given energy the same way independently of the primary beam energy. However, it does not mean that the same beam focusing optimization will maximize the physics potential for both primary energy regime and this is the reason why independent optimizations have been carried out. More details are given in section 3.7.

### 3.6.1 Primary beam energy

The primary beam energy of the upgraded SPS might be slightly reduced if it provides some benefit for the physics program. Figure 3.37 shows the energy and angular distributions of  $\pi^+$  yield for different primary energies. Since the shape of those distributions are similar for the chosen primary energies but the total yield scales with the energy, it appears that from the point of view of the secondary beam production and focalization, the highest available proton energy should be used at a given intensity.

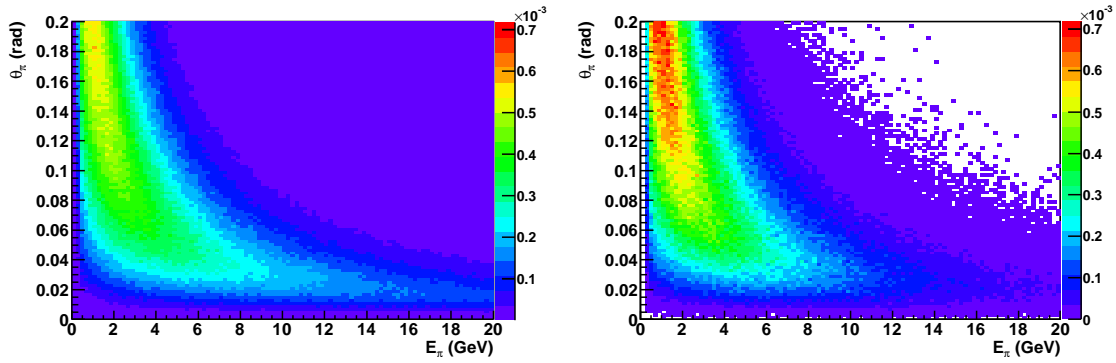


**Figure 3.35:** Left (resp. right): Secondary  $\pi^+$  yield of the target for a 400 GeV (resp. 50 GeV) primary proton beam in the  $\{E_\pi, \theta_\pi\}$  space.  $\theta_\pi$  is the momentum angle of the pion relative to the beam axis.

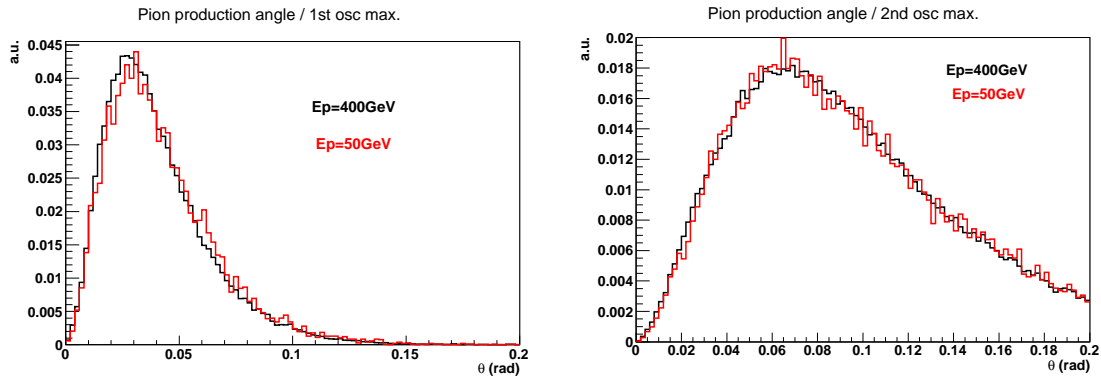


**Figure 3.36:** Angular distributions of the pion yield from the target for 400 GeV and 50 GeV primary energy. Left (resp. right): Selection of pions generating neutrinos at the first (resp. second) oscillation maximum:  $E_\pi \approx 11$  GeV ( $E_\pi \approx 4$  GeV).

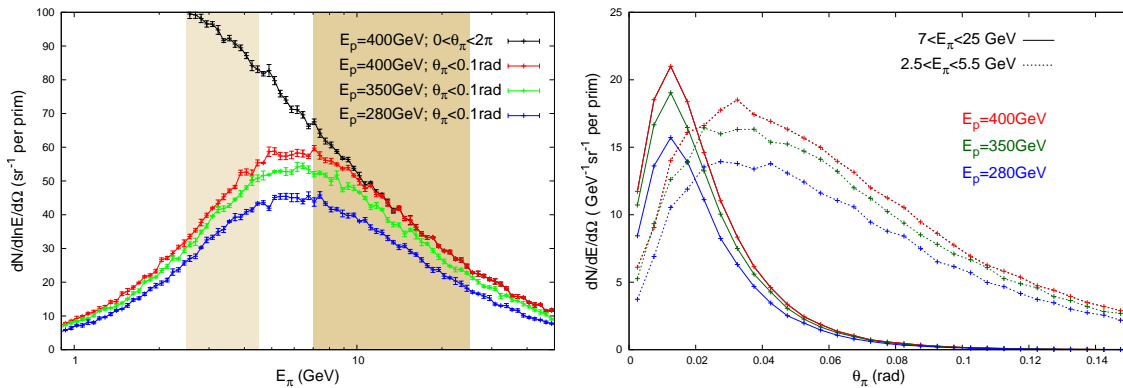


**Figure 3.37:** Energy (left) and angular (right) distributions of  $\pi^+$  yield from the target for 400, 350 and 280 GeV primary beam energy.

### 3.6.2 Target segmentation

Within certain limits, the size of the primary beam can be adapted to the radius of the target. With the requirement of having a full containment of the beam in the target, the largest possible radius is preferred since it helps to reduce the thermal stress of the target. Following the strategy used for the CNGS installation, the following ratio ensures that only 5% of the beam doesn't interact in the target:

$$r_{tgt} = 3.76 \times \sigma_{beam}$$

where  $r_{tgt}$  is the radius of the target rods and  $\sigma_{beam}$  is the gaussian width of the beam. The CNGS facility was dedicated to the production of a  $\nu_{\mu}$  beam of high energy directed to the OPERA and ICARUS detectors. The goal of these experiments was the measurement of  $\nu_{\mu} \rightarrow \nu_{\tau}$  oscillations through the detection of the  $\tau$ s resulting from  $\nu_{\tau}$  interaction in the detector volumes. The segmentation of the target in CNGS favored the emission of high energy pions produced at very forward angles by reducing their probability of reinteraction within the target. This effect has been crosschecked with the FLUKA simulation of CN2PY by selecting the pion yield above 20 GeV (see fig.3.38-left). In the case of CN2PY such a benefit is not observed since the pions of interest are of lower energy and thus emitted at larger angle. For this reason, an unsegmented target is recommended.

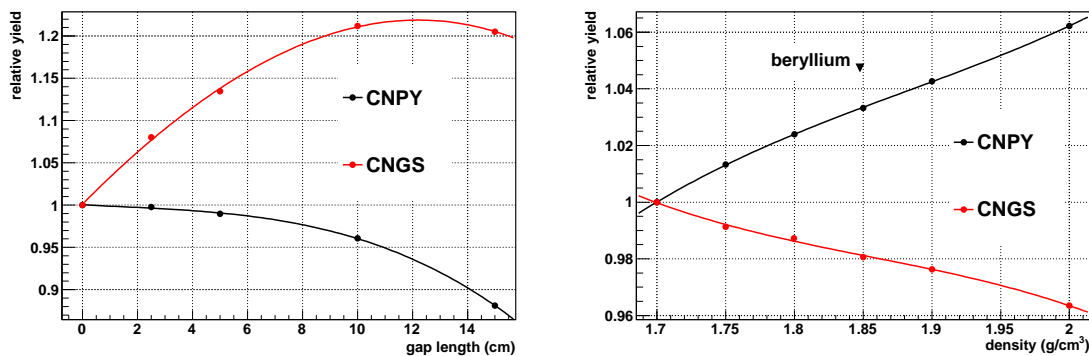


**Figure 3.38:** Energy weighted relative yield of  $\pi^+$  emitted at  $\theta_{\pi} < 0.1$  rad for different gap lengths (left) and different densities (right). Red:  $20 < E_{\pi} < 50$  GeV, corresponding to the energy range of interest in CNGS. Black:  $2.5 < E_{\pi} < 25$  GeV, corresponding to the energy range of interest in LAGUNA/LBNO.

### 3.6.3 Material

Among the low Z solid targets, carbon and beryllium are the two best options. Any higher Z material would suffer from too high energy deposition and dynamical stresses induced by the proton beam, as well as pion reabsorption and scattering. Graphite can be produced with density ranging from 1.7 to 2.2 g/cm<sup>3</sup> whereas the beryllium is only available at 1.85 g/cm<sup>3</sup>. The baseline is to use graphite since it is the best known material. However, radiation damage may be an issue for long term operation depending on the POT requested by the experiments. If graphite is found not to be suitable, beryllium may be a valid alternative if the beam footprint can be made large enough. Figure 3.38-right shows the energy weighted relative yield of  $\pi^+$  with beryllium and carbon at different densities. A slight increase of yield is observed when increasing the density and at equal density, beryllium provides also a slightly higher yield than carbon. If the largest possible density is preferred from the point of view of physics, it will be limited by the energy density and temperature increase. Following the experience acquired from CNGS, which used graphite at 1.75 g/cm<sup>3</sup>, a slightly higher density of 1.85 g/cm<sup>3</sup> has been set as the baseline target material.

### 3.6.4 Target dimensions

Ideally, the length and the radius of the graphite target would be optimized together with the beam optics to maximize the neutrino flux of interest for both phases of the project. However, severe constraints related to the energy deposition and engineering issues need to be taken into account to provide a realistic configuration of the target and horns ensemble.

For this reason, a first round of optimization was performed in which the target parameters were allowed to vary within relatively wide ranges (showed in table 3.9 of next section). Then a second round was performed implementing the recommendations of the target design working groups:

- For the HPPS-50 GeV optimization, according to the experience from T2K [?] a graphite target of no less than 13 mm is needed to sustain the 2MW power delivered by the HPPS primary beam (see table 3.8). The target length should be at least 90 cm but no more than 1.3 m. If a horn with a collector part is used, the inner radius of this collector part should be larger than the target radius by 1.4 cm to allow for enough space for the support framework and the cooling system of the target.
- For the SPS-400 GeV optimization, the proposed values for the length and radius of the target are respectively 1.3 m and 4 mm. The inner conductor radius of the horn collector part is set to 2 cm in this case.

Parameter	Unit	T2K	LBNO (Phase I)	LBNO (Phase II)
Beam power	MW	0.75	0.75	2.2
Beam energy	GeV	30	400	50
Protons per spill		$3.3 \times 10^{14}$	$2 \times 3.5 \times 10^{13}$	$2.7 \times 10^{14}$
Beam cycle	s	2.1	2 (?)	1
Target radius	mm	13	> 4	>13

**Table 3.8:** Comparison of beam design parameters between T2K and LAGUNA/LBNO

## 3.7 Beam Optimization

The neutrino spectrum at the FD is the result of the following chain of events:

- The production of secondary particles from a high energy primary beam colliding into a long cylindrical solid target, resulting in a source of secondary particles that is far from being mono-energetic and well collimated.
- The deflection of the secondary particles in a complex focusing system composed of two horns defined by a large set of inter-correlated parameters.
- The decay of secondary particles more-or-less focused along the decay pipe axis, giving rise to neutrinos that will reach and interact in the FD if emitted just in the right direction (the solid angle of the FD 2300 km away is about  $4 \times 10^{-10}$  sr).

Because of the intrinsic complexity of the physics processes that are taking place between the collision of the primary beam in the target and a neutrino reaching the FD, it is not possible to predict precisely what will be the shape of the neutrino spectrum for a given configuration of the focusing system. MC simulations have thus been used extensively to generate for this purpose.

Concerning the focalization itself, the first observation is that the optimal angle to which each secondary particle should be focused depends on their energy. For pions of low energy ( $< 12$  GeV), a relative angle from beam axis as small as possible after focalization is preferred since all the neutrinos of interest will be emitted in a cone smaller than the FD solid angle. However, pions of higher energy would need to be focused at a small off-axis angle in order to emit neutrinos with energy in the range of interest for oscillation studies ( $\lesssim 6$  GeV), see fig.3.39.

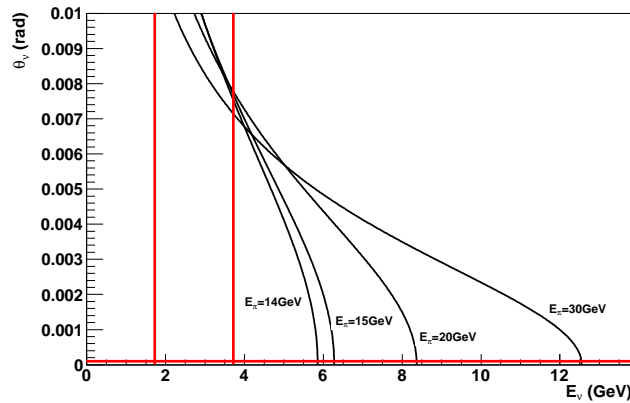


**Figure 3.39:** Kinematics of neutrinos from pion decays. The red horizontal line is the maximum angle with respect to the beam axis,  $\theta_{\nu}^{\max} = 0.87 \times 10^{-5}$  rad, for a neutrino produced in the decay pipe to reach an on-axis 400 m diameter FD distant of 2300 km. The two red vertical lines are the position of the two first oscillation maxima for 2300 km long baseline. If the pions above 14 GeV are focused at an off-axis angle  $\theta_{\pi} \sim 7.5 \times 10^{-3}$  rad, their decays can contribute to the FD neutrino flux near the first oscillation maximum energy.

Ideally, CN2PY should focus the secondary particles emitted from the target in a way to produce the highest possible flux between 1 and 6 GeV in order to cover the two first oscillation maxima. This kind of optimization is challenging because it is well known that a focusing system composed of two horns is not able to focus efficiently secondary particles in such a large energy range [?]. Therefore, the configuration achieving the “best compromise” between each parts of the spectrum would need to be found, ensuring at the same time that the overall flux within the energy range of interest is maximized.

But the neutrino flux shape that would maximize the  $\delta_{\text{CP}}$  coverage for a given total flux is not readily available because it requires additional informations such as the neutrino cross-sections, the detector response and exposure, the various backgrounds, the foreseen systematic effects, etc.

For example, it has been demonstrated that even a few counts located at the energy of the second oscillation maximum would enhance dramatically the CPV coverage, significantly more than the same number of counts near the first oscillation maximum, especially if the latter is already dominated by systematic effects. On the other hand, the very low energy secondary particles required to enhance the neutrino flux at the second maximum are notoriously hard to focus efficiently and, because of the intrinsic limitations of the two horns focalization method, will be achieved only at the expense of the higher energy secondary particles focalization to a point that it may not be profitable from the point of view of the  $\delta_{\text{CP}}$  coverage.

On the other hand, the shape of the neutrino spectrum at the FD also depends on the shape of the secondary yield emitted by the target. This distribution itself depends on the primary beam energy and the target geometry, both being different between the two phases of the project. The 50 GeV primary beam will indeed generate more secondary particles decaying into neutrinos close to the second oscillation maximum (pions of 4 GeV and below, see figs. 3.34 and 3.35) and for this reason, the optimal beam optics configuration for this phase may be



one that focuses mainly those low energy secondaries, contrarily to the 400 GeV primary beam where it may be more profitable to focus as much as possible the larger number of secondaries that decay into neutrinos closer to the first oscillation maximum.

For those reasons, several successive optimizations maximizing different parts of the neutrino flux have been performed independently for the two phases:

- **High Energy optimization (HE):** maximization of the integral of  $\nu_\mu$  flux in a 0-6 GeV energy window. In this case, the optimized beam optics should produce wide band beams covering both first and second oscillation maxima.
- **Low Energy optimization (LE):** maximization of the integral of  $\nu_\mu$  flux in a 1-2 GeV energy window. In this case, the optimized beam optics should produce neutrino fluxes mainly around the second oscillation maximum.
- **CPV based optimization using GloBeS (GLB):** maximization of the total  $\delta_{CP}$  sensitivity as computed by GloBeS [?] with all the systematic uncertainties turned off to save CPU time.

A first iteration of the beam optimization has been performed without taking into account the engineering constraints on the target design. Processing the resulting optimized fluxes through the LBNO analysis software (see xxx of the deliverable and xxx LBNO physics paper), it was concluded that the flux shape generated by the GloBeS-CPV based optimization (labelled as GLB400) was producing the best performance for the measurement of  $\delta_{CP}$  using the SPS-400 GeV beam, whereas the highest sensitivity to  $\delta_{CP}$  with the HPPS-50 GeV beam was obtained by the low energy beam produced by the Low Energy optimization (labelled as LE50). This result confirms that the second oscillation maximum gives the highest sensitivity to  $\delta_{CP}$  measurement providing that a well matching primary beam energy is available. If this is not the case, as with the SPS beam at 400 GeV, the most efficient method is to produce a wider band beam covering also the first oscillation maximum.

For the second iteration, the engineering constraints for the design of the target as presented in section 3.6.4 were implemented and a new round of both GLB400 and LE50 optimizations were performed.

More than 20 inter-correlated parameters are involved to describe the focusing system composed of the two magnetic horns located downstream the target. In order to find the optimal focalization systems for LBNO, a very large number of different configurations needs to be evaluated. To explore efficiently a fraction of the parameter space as large as possible, a dedicated optimization tool based on genetic algorithm has been developed.

In the following sections, the modelization of the horn shapes, the Monte-Carlo simulations, the genetic algorithm and finally the selected configurations of the two rounds of optimization are presented.

### 3.7.1 Horn shapes

It is crucial for LBNO to enhance the low energy part of the neutrino energy spectrum at the FD since the second oscillation maximum, located around 1.5 GeV at 2400 km, enhances drastically the sensitivity to  $\delta_{CP}$  of the whole experiment.

Similarly to the CNGS design, having the target station and the first horn as separated devices would be advantageous to tackle some engineering issues, like the design of the target cooling, the target/horn electrical insulation and the long-term maintenance, especially regarding the target replacement. However, in such a configuration the angular acceptance of any realistic focusing system is limited to about 0.1 rad [?] and in this case about  $\sim 40\%$  of the "second maximum"  $\pi^+$  are not focused, see fig.3.34.

For this reason, the shape of the first horn has a collector part fully enclosing the target whose purpose is to bend the low energy secondary particles emitted at large angle that decays mainly into neutrinos below 2 GeV. The downstream part consists of an elliptical inner shape to focus the secondary particles along the beam axis. This kind of geometry has been adopted in all the neutrino beam lines producing a beam of  $\approx 1$  GeV and below (T2K, MiniBooNE, etc.).

A second horn with a larger aperture is placed downstream and its role is to focus back the secondary particles of interest that would have been under-focused or over-focused by the first horn, thus its traditional name of "reflector".

Table 3.9 shows the full set of parameters used to describe the beam optics configuration in the MC simulation as well as the allowed ranges in which each parameter was allowed to vary during the two rounds of optimization. A visual description is shown in fig.3.40.

Parameter	Symbol	Unit	First round	Second round	
Optimization scheme			LE50 & GLB400	LE50	GLB400
target radius	$r_{tgt}$	cm	0.4-1.5	1.3-2.0	0.4
target length	$l_{tgt}$	cm	80-200	90-130	130
circulating current in horn	$I_H$	kA	150-300	idem	idem
circulating current in reflector	$I_R$	kA	150-250	idem	idem
distance horn-reflector	$d_{HR}$	m	1-20	idem	idem
horn length 1st part	h1_l1	cm	$l_{tgt}$	90-200	90-200
horn length 2nd part	h1_l2	cm	125-208	idem	idem
horn length 3rd part	h1_l3	cm	78-140	idem	idem
horn length 4th part	h1_l4	cm	0-10	idem	idem
horn length 5th part	h1_l5	cm	25-70	idem	idem
horn 1st inner radius	h1_r1	cm	$r_{tgt}+0.6$	$r_{tgt}+1.4$	2
horn 2nd inner radius	h1_r2	cm	7-40	idem	idem
horn 3rd inner radius	h1_r3	cm	2.5-16	idem	idem
horn 4th inner radius	h1_r4	cm	2-20	idem	idem
horn outer radius	h1_r	cm	$h1\_r2+30$	idem	idem
reflector length 1st part	h2_l1	cm	50-300	idem	idem
reflector length 2nd part	h2_l2	cm	3-20	idem	idem
reflector length 3rd part	h2_l3	cm	50-300	idem	idem
reflector 1st inner radius	h2_r1	cm	10-40	idem	idem
reflector 2nd inner radius	h2_r2	cm	2-10	idem	idem
reflector 3rd inner radius	h2_r3	cm	10-40	idem	idem
reflector outer radius	h2_r	cm	$h2\_r1+30$	idem	idem

**Table 3.9:** Allowed ranges for the parameters describing the beam optics configuration and modifications for the second round of optimizations.

At a later stage of the project, more refined optimizations could be performed with additional correlations and/or constraints between the parameters.

### 3.7.2 Monte-Carlo simulation

For the beam optimization, the secondary beam line has been only crudely described in FLUKA. The target is described by a cylinder of graphite. The two horns and the target are suspended into an empty environment representing the target hall. Following the LAGUNA/LBNO expression of interest [3], the decay tunnel, whose entry is located 30 m after the target, is set to be a cylinder of 300 m long and 1.5 m radius. The decay geometry was fixed during the beam optics optimization but a study of the impact of the decay dimensions on the neutrino fluxes

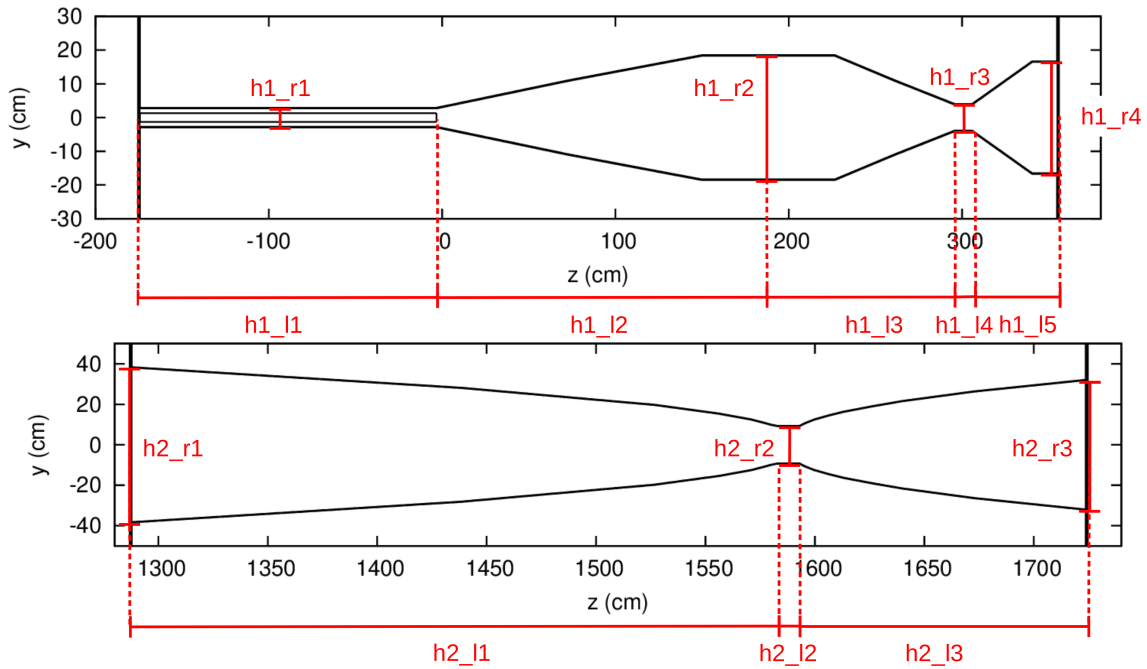


Figure 3.40: Visual description of beam parameters.

is presented in section 3.8. And finally, the vacuum volumes are surrounded by molasse, see fig.3.41.

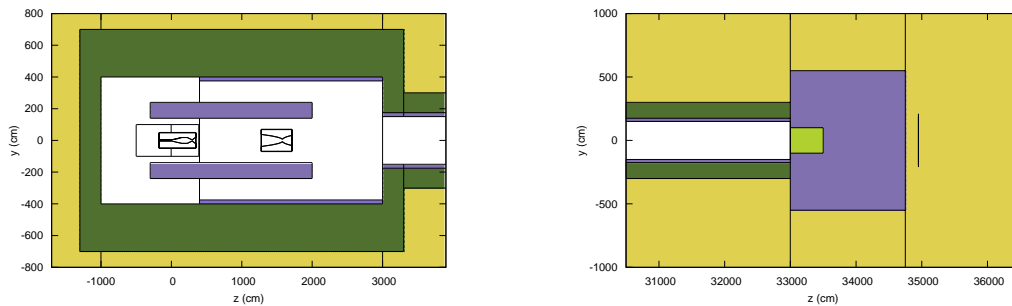
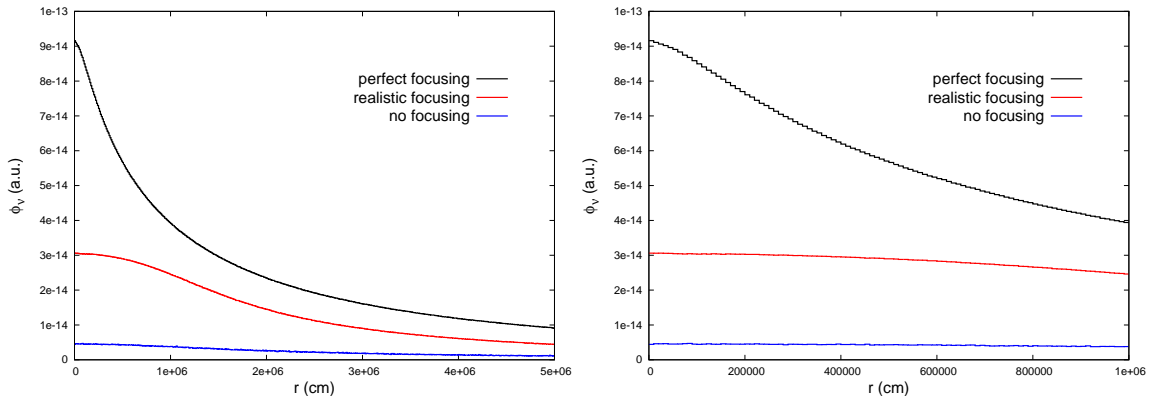


Figure 3.41: CN2PY description in FLUKA for the beam optimization. Left: Target and horns chambers. Right: Beam Dump

To increase the MC statistics, statistical direction biases were used for the secondary decays and the  $\nu_\mu$  flux was scored at 2300 km within a circular surface of 1 km radius. This increased scoring cross-section produces the same spectrum shape than the one produced by a realistic FD cross-section because the neutrino beam at 2300 km remains flat well above 1 km off-axis, see fig.3.42.

### 3.7.3 Genetic Algorithm

Genetic algorithm is a search heuristic that mimics the process of natural selection in order to generate useful solutions to optimization and search problems. A population of candidate solutions called individuals (in our case the beam configurations) is evolved toward better solutions. Each candidate solution has a set of properties, usually called chromosomes (in our case the set of parameters described previously). At each generation, the fitness of each individual



**Figure 3.42:** Left: Spatial distribution of the  $\nu_{\mu}$  beams at 2300 km from the target between 0 and 50 km distance from the beam axis. Right: Same distribution but extending only up to  $r = 10$  km. Perfect and unfocused beams are shown for comparison.

is evaluated and the best performing individuals are stochastically selected to recombine and mutate their chromosomes to produce new individuals. This iterative process is carried out until no further fitness improvements is observed in the population. This kind of algorithm is well suited to optimize solutions of relatively complex problems dealing with many degrees of freedoms and or/constraints where the best solutions cannot be predicted beforehand.

The algorithm code itself is provided by the DEAP toolkit [?] which provides a rich, flexible and easy-to-use environment to implement an algorithm that best suits the problem at hand.

To initialize the algorithm, some tuning parameters have to be defined. Their optimal values depend on each problem and most of the time are difficult to select precisely and efficiently. For this work, trial-and-error runs have been performed using different combinations of values for the parameters. Based on how fast the algorithm was converging and the maximal value obtained for the fitness, the following configuration has been chosen:

- Population of 100 individuals.
- Two-points cross-over method.
- 10% probability of mutation for each gene. If mutation occurs, the mutated value is obtained by a gaussian randomization of  $1\sigma=7.5\%$  around the nominal value, with the condition of staying within the allowed range.
- The selection of best individuals for breeding is the classical "tournament" method with 3 elements.

The critical part when setting up the algorithm is the definition of the fitness since it is the quantity that the algorithm will attempt to maximize during the evolution. One of the limiting factor of this kind of algorithm is that the evaluation function computing the fitness needs to be as fast as possible because it will be called many times (typically, more than 1000 configurations needs to be evaluated to complete one run of optimization).

For CN2PY, the ideal fitness would be the  $\delta_{CP}$  sensitivity of the experiment. However, computing a realistic  $\delta_{CP}$  coverage is a complex and CPU intensive procedure which requires a fit function using the 4 species neutrino spectra ( $\nu_{\mu}$ ,  $\bar{\nu}_{\mu}$ ,  $\nu_e$ ,  $\bar{\nu}_e$ ) at the FD and for both horn polarities with a given  $\nu/\bar{\nu}$  sharing ratio, all the systematic uncertainties and the detector response. This task requires high statistic MC samples and a dedicated analysis package (described in section xxx) that can not reasonably be integrated into the optimization algorithm itself. This is for this reason that the iterative optimization strategy presented before has been adopted instead, setting the fitness to be some part of the  $\nu_{\mu}$  flux, depending of which 'HE', 'LE' or 'GLB' optimizations is performed.

The evolution of the population toward greater fitness is monitored as the algorithm is running in order to terminate it when no more increase of the fitness is observed (see fig. 3.43). All the evaluated configurations are recorded for later analysis. Moreover, not only the quantity set as fitness but all three HE, LE of GLB quantities are systematically evaluated and recorded for each individual. For each optimization run, the final configuration is chosen among a sample of good performing configurations in the LE-GLB phase (see fig. 3.44) by searching for the best compromise between the physics performance and the engineering aspects.

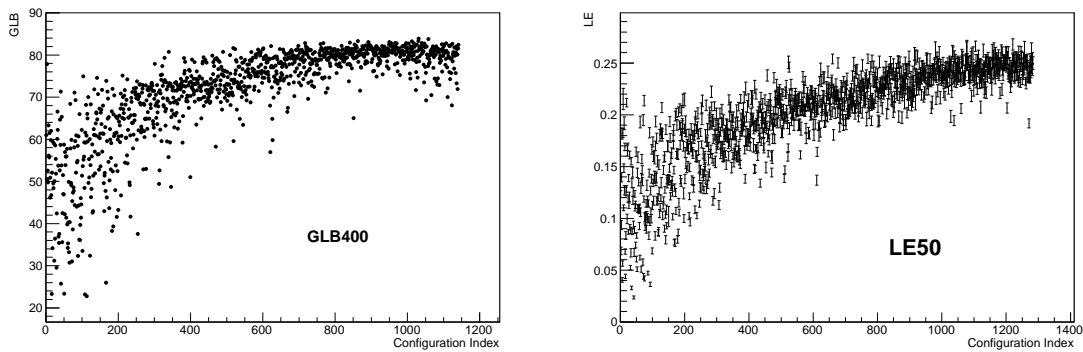


**Figure 3.43:** Fitness evolutions during the second round of optimization. Left: GLB400 optimization. Right: LE50 optimization.

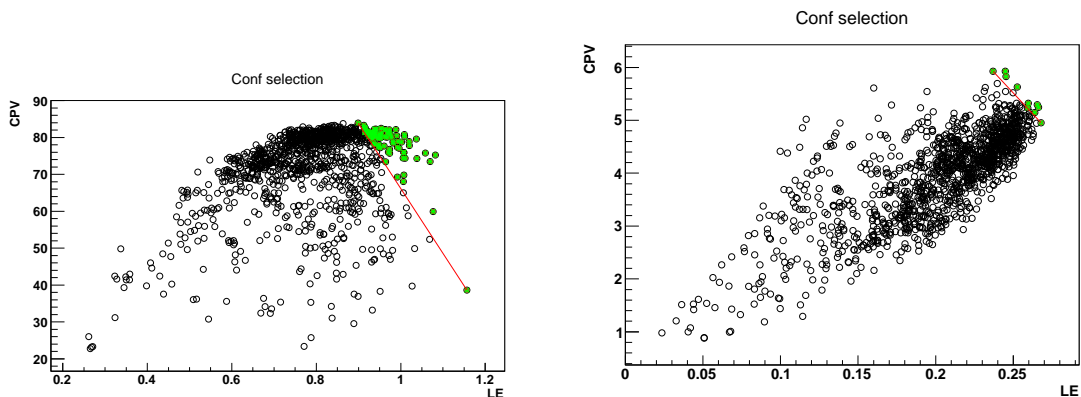
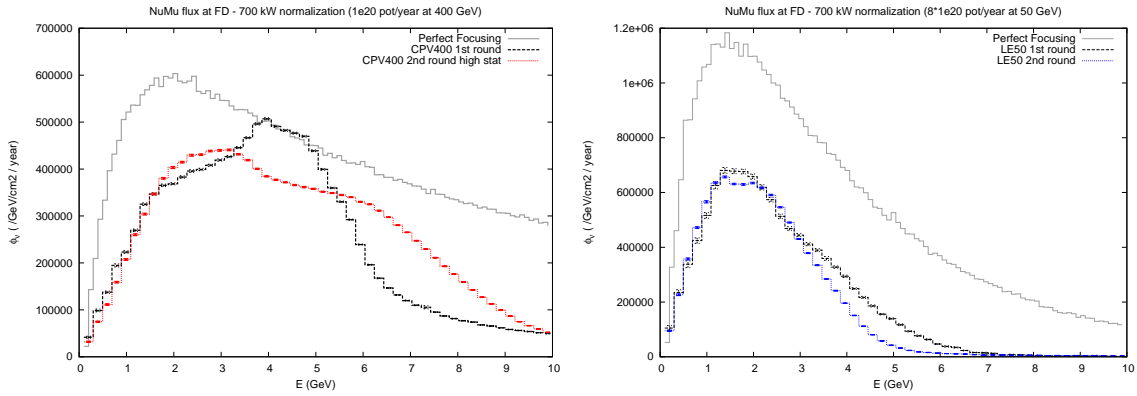


**Figure 3.44:** Beam optics configurations in the LE-GLB space. The configurations above the red line that connects the maximum LE and the maximum GLB ever obtained is the sample in which the final configuration will be chosen. Left: GLB400 optimization. Right: LE50 optimization.

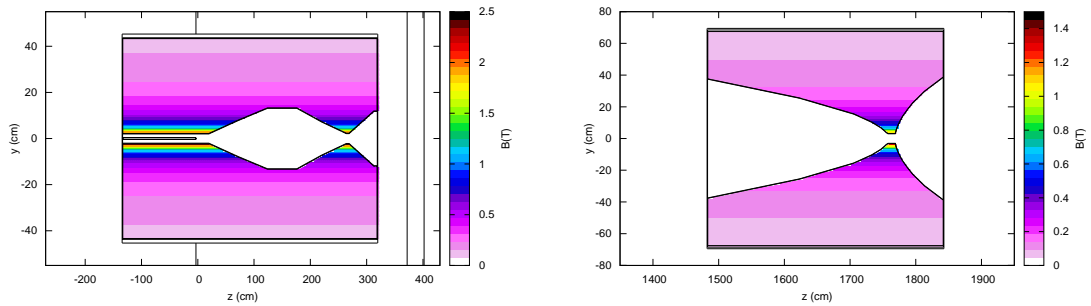
### 3.7.4 Selected configurations and corresponding neutrino fluxes.

Fig.3.45 shows the  $\nu_\mu$  fluxes at the FD of the optimized configurations obtained by the two rounds of LE50 and GLB400 optimizations. Between the first and second iterations, no significant loss of flux is observed despite the added constraints on the target geometry and on the inner conductor radius of the collector part of the horn.

In the table 3.10, the parameter values corresponding to the selected configurations are shown. The figs. 3.46 and 3.47 shows the 2D cut views of both horns as well as the magnetic field intensity for the second iteration.



**Figure 3.45:**  $\nu_\mu$  flux at FD of the selected configurations for both optimization iterations. Left: GLB400 optimization. Right: LE50 optimization. Fluxes that would be obtained assuming a perfect focusing of all the secondary particles are also shown.



**Figure 3.46:** 2D cut views of horn (left) and reflector (right) corresponding to the selected configurations for the phase I at 400 GeV.

### 3.8 Decay pipe configuration

The excavation of the decay pipe will represent a significant fraction of the total cost of the project. For this reason, it is necessary to get a precise idea of the impact of tunnel configuration, i.e. length and radius:  $\{l_d, r_d\}$ , on the neutrino spectra.

Figure 3.48 shows that the variation of the global shape of the spectrum remains limited when changing the decay pipe configuration within a reasonable range. This observation confirms that the beam optics optimization can be performed independently of the decay pipe configuration. In order to quantify the impact of the decay pipe dimensions on the flux around the two oscillation maxima (the brownish areas indicated on the fig.3.48), let's define the integrated flux in these two regions respectively  $\Phi_\nu^{1st}$  and  $\Phi_\nu^{2nd}$ .

The variations of the  $\Phi_\nu^{1st}$  and  $\Phi_\nu^{2nd}$  fluxes with respect to the decay tunnel configuration are shown on 3.49. With the beam optics configuration used to generate these fluxes, the most probable energy of the pions producing "first maximum" neutrinos (respectively "second maximum" neutrinos) is 11 GeV (respectively 4 GeV). The decay length of 11 GeV pions is 623 m whereas it is 231 m for 4 GeV pions. Moreover,  $\Phi_\nu^{1st}$  receives a significant contribution from even higher energy pions, thus longer decay lengths. From those numbers, we expect a larger variation of  $\Phi_\nu^{1st}$  than  $\Phi_\nu^{2nd}$  when going from 200 to 350 m tunnel length and this is indeed what is observed. More precisely,  $\Phi_\nu^{2nd}$  is not sensitive to the decay tunnel length within the indicated range, whereas  $\Phi_\nu^{1st}$  increases almost proportionally to it, getting multiplied by a factor between 1.3 and 1.45 depending on the tunnel radius.

Parameter	Symbol	Unit	First round		Second round	
			LE50	GLB400	LE50	GLB400
target radius	$r_{tgt}$	cm	0.7	0.426	1.3	0.4
target length	$l_{tgt}$	cm	102	147	129.8	130
circulating current in horn	$I_H$	kA	289	281	292	289
circulating current in reflector	$I_R$	kA	187	198	240	232
distance horn-reflector	$d_{HR}$	m	10.0	5.6	6.5	11.6
horn length 1st part	h1_l1	cm	102	147	140	153
horn length 2nd part	h1_l2	cm	130	127	184	130
horn length 3rd part	h1_l3	cm	117	120	130	114
horn length 4st part	h1_l4	cm	0.0	9.4	9.7	4.8
horn length 5st part	h1_l5	cm	54	42.7	40.4	38.6
horn 1st inner radius	h1_r1	cm	1.3	1.03	2.7	2.0
horn 2nd inner radius	h1_r2	cm	10.3	16.8	13.8	13.3
horn 3rd inner radius	h1_r3	cm	3.9	2.94	13.6	2.3
horn 4th inner radius	h1_r4	cm	14.9	7.8	10.9	11.8
horn outer radius	h1_r	cm	40.3	46.8	43.8	43.3
reflector length 1st part	h2_l1	cm	198	268.1	94.7	274.3
reflector length 2nd part	h2_l2	cm	3.79	7.73	7.2	11.07
reflector length 3rd part	h2_l3	cm	88.8	199	173.2	73
reflector 1st inner radius	h2_r1	cm	39.7	33.0	40.0	37.5
reflector 2nd inner radius	h2_r2	cm	5.06	8.5	5.3	3
reflector 3rd inner radius	h2_r3	cm	34.9	22.8	32.5	38.6
reflector outer radius	h2_r	cm	69.7	63.0	70.0	67.5

**Table 3.10:** Parameter values of the selected configurations of the two rounds of optimizations.

Concerning the radius, a roughly proportional increase of 40% per meter is obtained in the [1,2] m range for the  $\Phi_{\nu}^{2nd}$ , independently of the decay pipe length. For  $\Phi_{\nu}^{1st}$ , the increase depends on the length: a gain of  $\sim 18\%$  is obtained at a length of 350 m, whereas it is only of  $\sim 8\%$  at 230 m.

Anyway, the choice of the decay pipe configuration will mainly be driven by the cost, the civil engineering requirements and the muon background issue at the ND.

### 3.9 Muon shielding configuration

Two scenarios have been investigated for the muon shielding: a completely passive shield made of iron and an active shield consisting of a magnetized iron magnet. The experience acquired during the design and running of the now inoperative WANF facility is used since the two facilities share many common points from the point of view of muon shielding issue.

#### 3.9.1 Presentation of the WANF facility and comparison with CN2PY.

During the first phase of the LAGUNA-LBNO project, the beam line would be operated with the 400 GeV proton beam from SPS at  $7 \times 10^{13}$  p/pulse. In the baseline design, the decay tunnel is a 300 m long and 3 m diameter cylinder. The reference position for the near detector is 800 m from the target since it was shown in very preliminary MC studies that placing the Near Detector any closer would lead to background levels several orders of magnitude too high. These features, as well as the level of tolerable muon background in the near detector are quite similar with the conditions of the now dismantled WANF facility (see table 3.11).

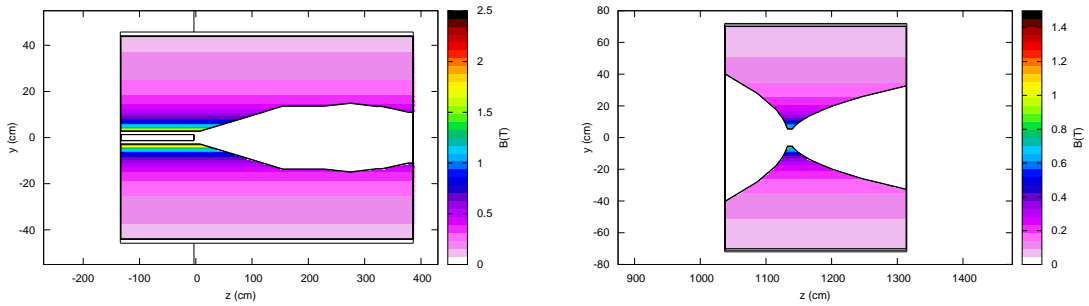


**Figure 3.47:** 2D cut views of horn (left) and reflector (right) corresponding to the selected configurations for the phase II at 50 GeV.

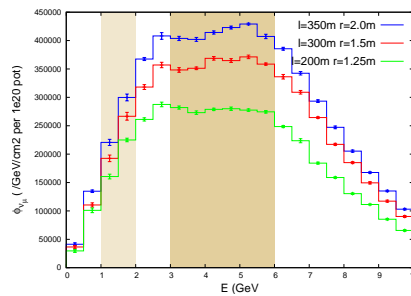


**Figure 3.48:** Neutrino flux at the FD with an optimised focusing configuration and for different decay pipe configurations.

For this reason, a detailed analysis of the muon shielding of WANF brings precious insights on what is required at CN2PY to keep the muon background at the ND to a reasonable level. The initial muon shield of WANF was composed of 425 iron disks of  $\varnothing 2.5\text{m}$  and 40 cm thickness, providing  $123\text{ kg/cm}^2$  of area density [?]. Together with the  $44\text{ kg/cm}^2$  of earth before the detectors, this shield proved inefficient to provide the tolerable level of muon background,  $< 1\mu\text{/m}^2/10^{13}\text{p}$ , at the detectors for the 400 GeV operation. The identified reason was high energy muons coming from  $\theta > 3\text{ mrad}$  relative to the target and interacting into the detectors. These muons, created into the decay pipe inner volume, were bypassing the on-axis passive shield by exiting the decay pipe on its side and then scattering in the rock back to reach the detectors. The primary beam energy was thus lowered to 350 GeV until 1979 when additional passive shielding and an active toroidal magnet were added to deal with those scattered high energy muons (see fig. 3.50 for the post-1979 layout of the whole beam line).

Items	WANF	LBNO phase I
Primary beam	SPS p@350/400 GeV	SPS p@400 GeV
Intensity	$10^{13}\text{p/pulse}$	$7 \cdot 10^{13}\text{p/pulse}$
Distance target/detector	822 m	800 m
Decay tunnel length	290 m	300 m
Decay tunnel diameter	2.2 m (first 32m), 1.2 m (last 258 m)	3 m
End of decay tunnel/detector distance	408 m	470 m
Muon background requirement	$< 1\mu\text{/m}^2/10^{13}\text{p}$	$< 2.5\mu\text{/m}^2/10^{13}\text{p}$

**Table 3.11:** Comparative table between WANF and LBNO facility. The WANF parameters have been taken from [?].



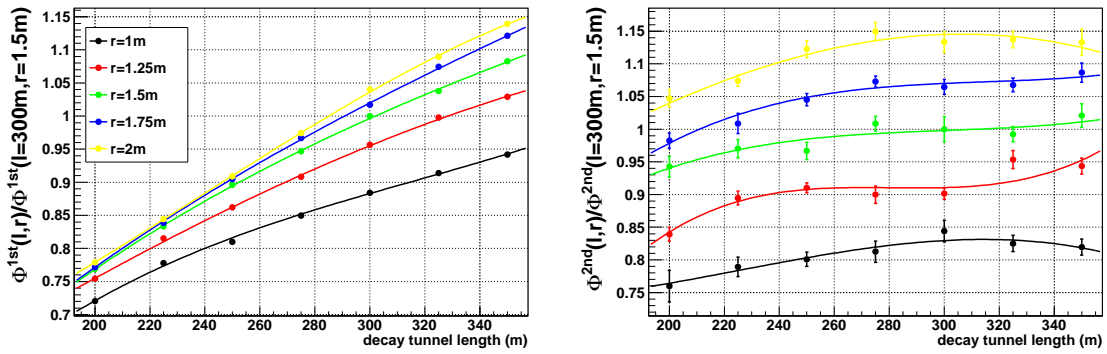


Figure 3.49: Relative  $\nu_\mu$  flux at FD with respect to the decay tunnel length and radius. Left: "1st max" neutrino energy selection, right: "2nd max" neutrino energy selection. The flux of the  $\{l_d = 300\text{ m}, r_d = 1.5\text{ m}\}$  configuration is set as reference.

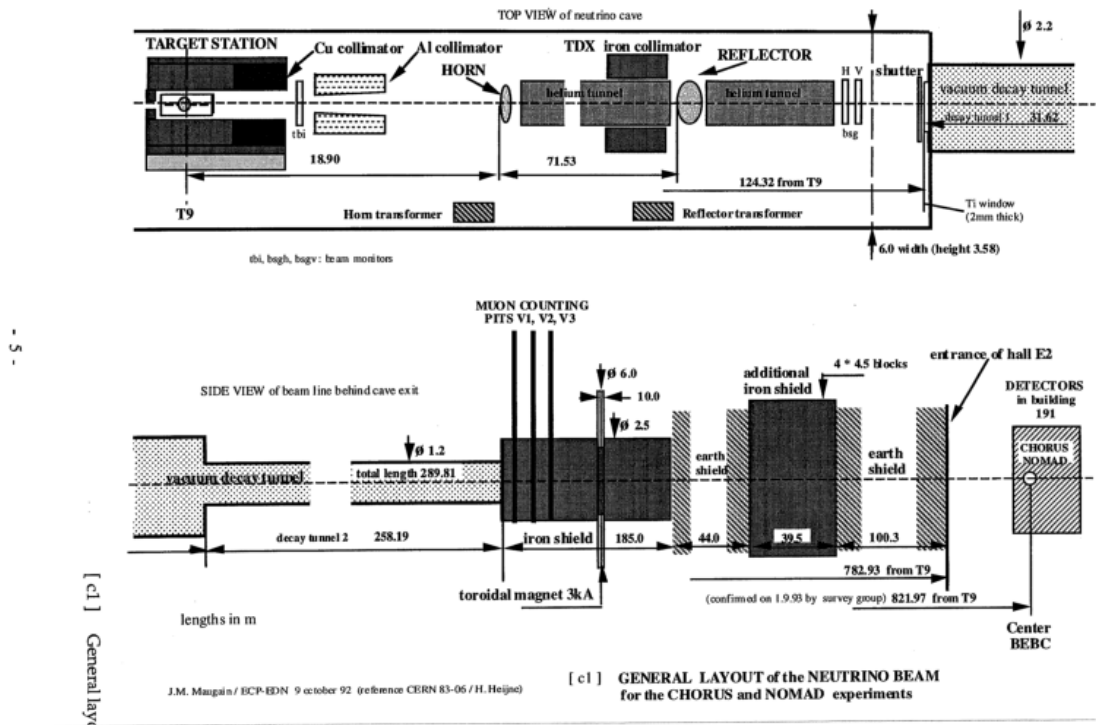
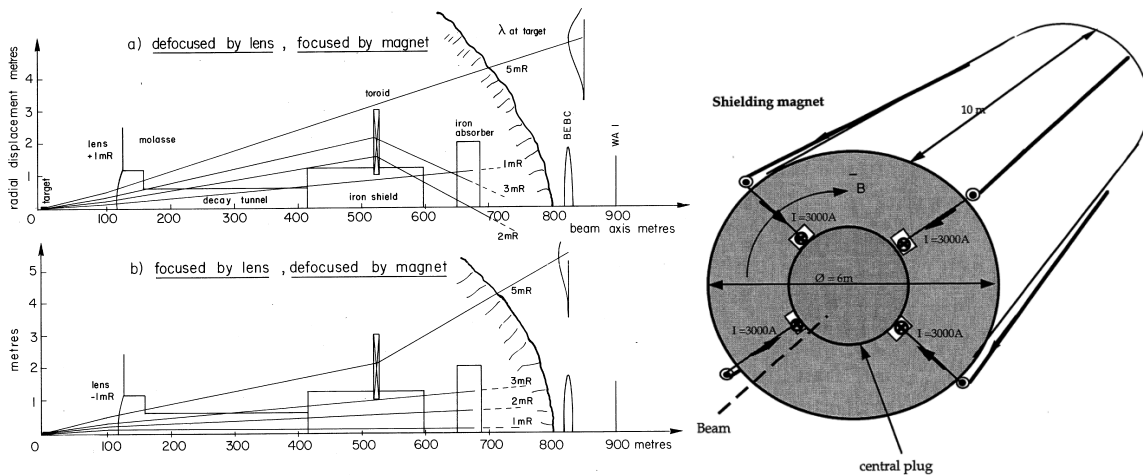


Figure 3.50: Layout of the WANF facility after 1979.

The purpose of the toroidal magnet was to either focus the muons toward the added passive iron or to deflect them away from the detectors, depending on the muon signs (see ??-left). The required bending power of 7.2 Tm and muon solid angle  $\theta > 3$  mrad constrained the size for the toroid magnet: a 10 meter long,  $\varnothing 6$  m with a field free central  $\varnothing 2$  m iron core (see ??-right). The toroidal field was generated by 4 conducting bars with a 3 kA excitation current. Together with the additional passive shielding, this represented a added mass of iron of 4370 t, which nearly doubled the shielding mass, reaching a total value of 10320 t (see ??). This solution was preferred over the purely passive shielding scenario because of the reduced cost [?].



**Figure 3.51:** Left: Concept of the toroidal magnet to shield the detectors from high energy muons (taken from [?]). Right: The toroidal magnet used in WANF [?].

Taking the TOSCA Technical Design Report as reference, a conservative level of  $< 2.5\mu/m^2/10^{13}p$  has been defined for muon background at the CN2PY ND. The issue with the LAr or similar detectors is that a too high level of muons would cause pile-up for the event reconstruction. Ultimately the goal should be to reduce the muon contribution coming from the shield to the same level as the muon contribution coming from the neutrino interactions in the surrounding rocks, for which no study has been performed yet. Due to the common features of the two facilities, a muon shield of comparable size than WANF is expected for CN2PY. However, the  $10.4^\circ$  negative slope required to point the neutrino beam to Finland means that the entire facility will be located underground. Depending on the final configuration of the beamline layout, the end part of the facility, which comprises the hadron stop, the muon station and the muon shield, would be located at a depth between 90 m and 110 m. Moving several ktons of iron at such a depth requires important civil engineering efforts and will come at a significant cost. On the other hand, the efficiency of the shield regarding the muon background suppression at the ND must be studied as precisely as possible to avoid problems similar to those WANF encountered.

Items	WANF<1979	WANF>1979
Area density	123(iron)+44(earth)=167 kg/cm <sup>2</sup>	176.5 kg/cm <sup>2</sup>
Total passive shield length	170 m	200 m
Passive shield diameter	2.5 m	2.5 m (first 160m), 4.5 m (last 40 m)
Passive iron volume	834 m <sup>3</sup>	1443 m <sup>3</sup>
Passive iron mass	5950 t	10320 t
Toroidal shield volume	*	282 m <sup>3</sup>
Toroidal shield mass	*	2200 t

**Table 3.12:** Indicative values summarizing the WANF muon shielding

The range of configurations investigated in this note goes from a purely passive scenario to a mostly purely active ones. The base guideline is to minimize the amount of required material (which is, at first approximation, the parameter driving the cost) while providing a sufficient reduction of muon flux at the near detector position.

### 3.9.2 Purely passive shielding.

Several configurations of the muon shield were tested and the muon fluence along the beam axis were scored with FLUKA with a 400 GeV primary beam and a normalization of  $7 \times 10^{13}$  p/pulse. The earth was assumed to be molasse with a density of  $2.4 \text{ g/cm}^3$  and the shield is composed of pure iron of  $7.2 \text{ g/cm}^3$ . As indication, the average energy loss for high energy muons into those materials is about  $dE/dx \approx 50 \text{ GeV}/100 \text{ m}$  and  $dE/dx \approx 16 \text{ GeV}/10 \text{ m}$  respectively. Figure ?? shows the muon fluence obtained for different length and radius combinations of the passive iron shield. The muon fluence stays at the level of  $100 \mu/m^2/10^{13} \text{ p}$  even with a 132 m long beam dump if the radius of the dump is limited to 1.6 m to barely cover the decay tunnel inner radius. Increasing the radius to 2 m enables to reach much lower muon fluence level even with a shorter length. So similarly to what was experienced with WANF, these MC calculations confirm this qualitative observation that not only the length but also the width of the beam dump is important to decrease the muon fluence at the near detector location.

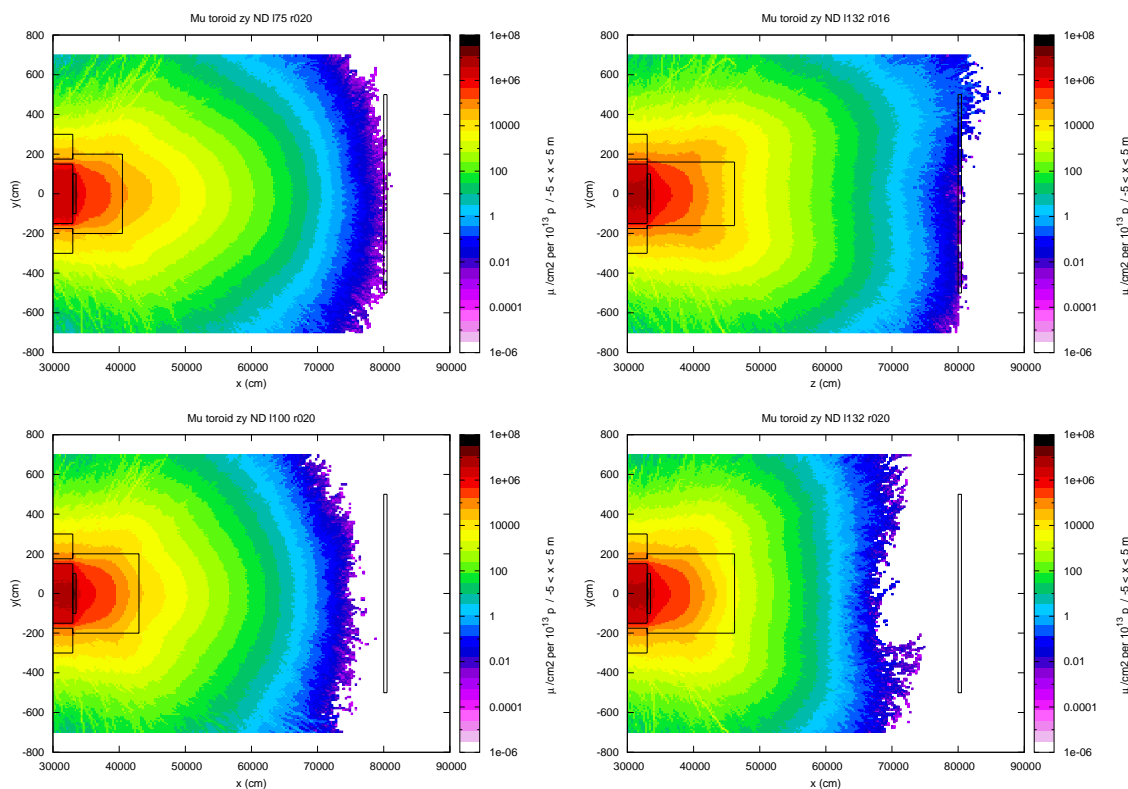


**Figure 3.52:** Muon fluence in the beam dump and near detector area with a 400 GeV primary beam. Please note the very different scale used on the y and z axes. The black lines on the left represent the layout of the end of the decay tunnel and the beam dump. The thin rectangular box at  $z=800 \text{ m}$  represents the near detector volume.

The figure ?? shows the decrease of muon fluence just before the near detector for a 100 m long passive shielding and diameter ranging from 3.2 to 5.2 m. A value of  $d=3.8 \text{ m}$  seems a good compromise between the necessity of minimizing the amount of iron in the shield while at the same time ensuring that the level of muons is low enough at the near detector. A safety

margin has been taken into account to compensate for the limited MC statistics near the end of the distributions and also to account for the possible variation of molasse density. Variations up to 20% have been observed in old molasse samples retrieved and analyzed during the CNGS construction. Therefore, the exact density of the earth between the decay pipe and the near detector will have to be measured to define the exact size of the shield.

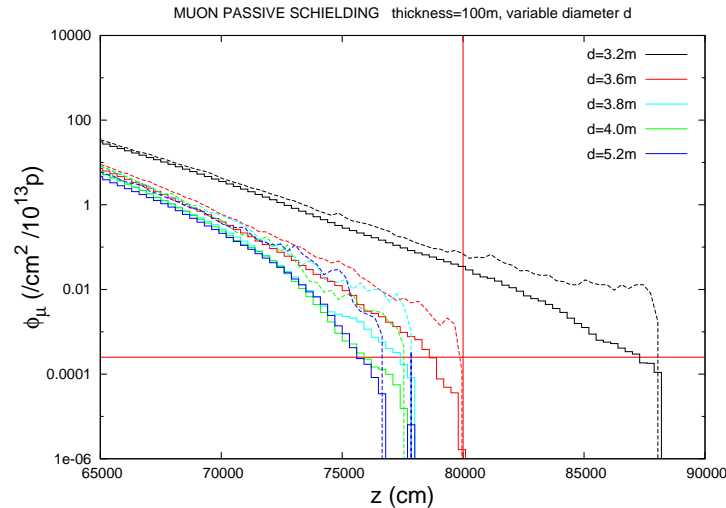


**Figure 3.53:** Muon fluence along the beam axis in the area of the near detector for a passive iron shielding of 100 m long and for different diameters. The solid (resp. dashed) lines represent the average (resp. maximum) fluence at a given  $z$  position. The vertical red line indicates the position of the near detector and the horizontal ones shows the maximum level of muon background tolerable at the detector.

### 3.9.3 The "dipole-like" toroid magnet shield.

Magnetized iron is the only affordable solution to generate enough bending power to deflect the high energy muons. Purely magnetic shields have been considered on previous neutrino facilities but very few have been built because of the complexity of geometry required to ensure that 100% of the muons would be deflected away from the detector [?]. A sizable fraction of the muons created along the neutrinos by secondary decays reach energies up to 350 GeV with a 400 GeV primary beam (and can in theory reach the same energy than the primary beam). Taking into account the size of the decay tunnel (3 m diameter), the volume around the detector that should be free of muons (about 10 m in all directions starting from the center of the detector), the distance between the detector and the beam dump (about 470 m in the present design), and a safety margin to account for scattering in the rock, the minimal bending power required to deflect 350 GeV muons is about 28 Tm.

The first naive idea would be to place large dipole magnets made of magnetized iron just behind the hadron stopper. However, this solution is technically very complex because of the presence of the return yokes which will deflect the muons into the wrong direction. One example of such a purely active shield that has been built is described in [?]. It achieved 23.1 Tm, but the complexity of the design (5 dipoles of different sizes and positions were necessary to avoid any leak) seem incompatible with the constraints of CN2PY where a device as simple and robust as possible is highly desirable.

A more popular way to deflect high energy muons is to use toroidal magnets of iron because strong magnetic fields can be achieved over large volume with a relatively simple design [?]. However, the obvious flaw of such a geometry for a purely active shield is that the central part is completely free of field. In order to solve this issue, a configuration composed of two successive

toroidal magnets placed off-axis and sized as such to shadow completely the cross-section of the decay inner radius has been studied (see figure ?? for schematics of the active shield). The iron would be magnetized to saturation and the two magnets would have inverse polarities so that the deflection produced on the muons by the first magnet would not be cancelled by the second one. The idea is then that on-axis muons of high energy coming from the decay pipe would feel a constant field during all their trajectories into the magnet, effectively acting as a dipole field, hence the name.

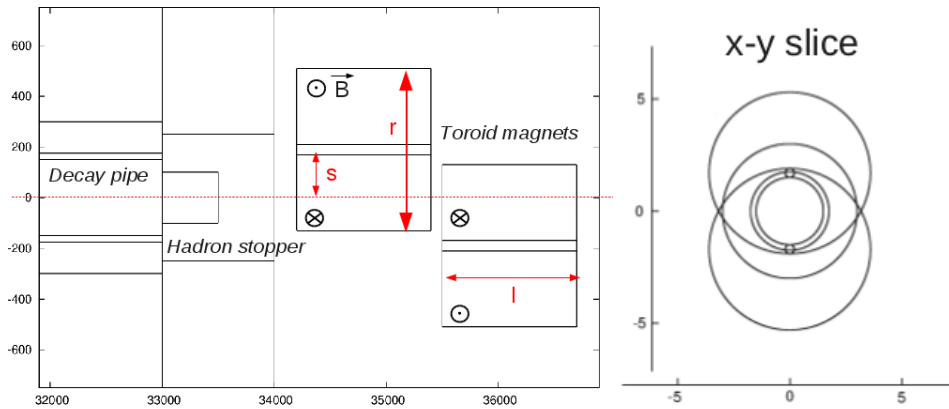


**Figure 3.54:** Layout of the beam dump with the active shield. The length  $l$ , the radius  $r$  and the shift position from the beam axis  $s$  have been optimized with MC calculations.

In order to reach the necessary 28 Tm of bending power and assuming a 1.2 T saturated field, the total thickness of the active shield can be readily estimated to about 24 m (meaning two magnets of 12 m each). The remaining parameters to define are the hole diameter, the radius and the shift distance from the axis of the magnets. The hole diameter should be as small as possible and 40 cm seems a reasonable value since it should give enough space to place the conducting bars and the cooling if the latter proves to be necessary. To avoid creating obvious leaks with the central holes, they should be placed outside of the cross-section of the decay pipe inner radius, which give constraints on the minimal shift distance and, as a consequence, to the radius of the magnets itself. To assess the efficiency of such a design and find the optimal values for the design parameters, muon fluence calculations have been performed. A hadron stopper composed of a 10 m long, 2.5 m radius iron cylinder with a 5 m long and 2 m diameter central graphite core was located at the end of the decay pipe and the active shield just behind it (see ?? for 2D plots showing realistic trajectories of the muons into the active shield and until the near detector position).

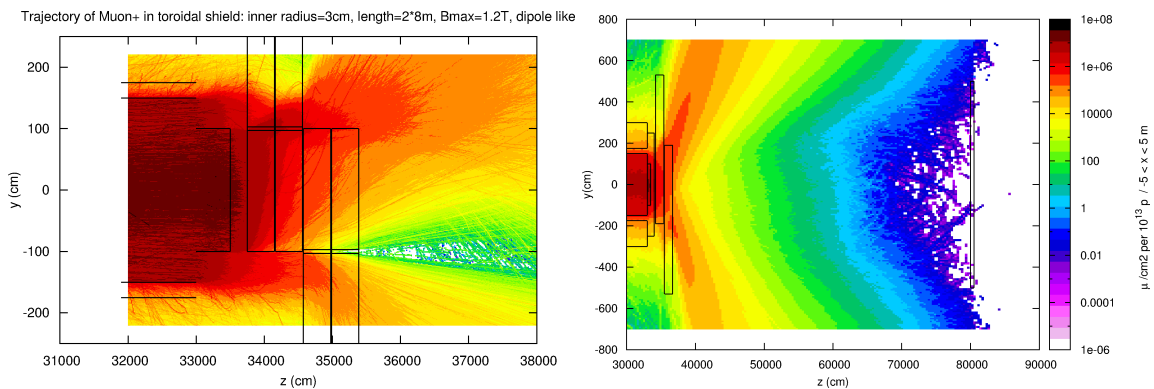


**Figure 3.55:** Muon trajectories from secondary decays (400 GeV primary beam energy) into the active shield (left) and the earth before the near detector location (right).

The results for various configurations with a fixed total length of  $l=2 \times 12$  m are visible on

??,left. As visible, no set of parameters manage to provide a muon fluence suppression similar to the passive configuration selected in the previous section. The computations have thus been repeated with a total length of  $l=2 \times 14$  m. This time (??,right), the efficiency of the passive scenario has been matched by the following configuration:  $\{l=2 \times 14$  m,  $r=3.6$  m, hole diameter=40 cm, shift distance=1.7 m $\}$ .

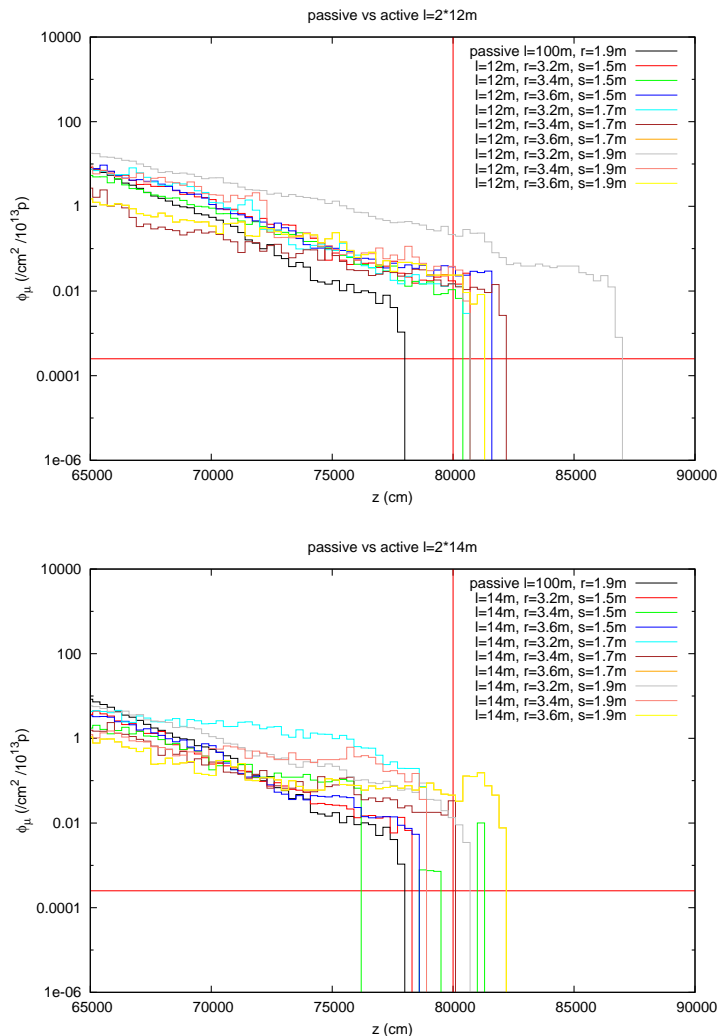


**Figure 3.56:** Muon fluence along the beam axis in the area of the near detector for different configurations of the active muon shield. The distribution corresponding to the selected passive configuration is also shown for comparison.

The table ?? compares the amount of materials required for the selected shield configurations. In the current design, the purely active scenario doesn't compete with the purely passive solution from the point of view of the amount of materials since roughly 600 t more iron is required which represents about 7% of the total mass of the passive shield. But the conclusion might be different if other elements are taken into consideration. For example, the fact that the active shield is more compact along the beamline axis than the passive one may reduce the cost of the underground excavation (in the current layout, the hadron stop would be located about 100 m below surface). The muon counters which would be used to monitor the beam and should be located behind the hadron stopper but before the active shield, have not been taken into account.

Items	Hadron stopper + Passive	Hadron stopper + Active
Total area density	72 (iron)+ 89 (earth)=161 kg/cm <sup>2</sup>	27 (iron)+ 104 (earth)=131 kg/cm <sup>2</sup>
Total length	10+90 m	10+28 m
Diameter	3.8 m	5 / 7.2 m
Volume	78.5+1055.5 m <sup>3</sup>	78.5+1140 m <sup>3</sup>
Mass	565+7600 = 8165 t	565+8208 = 8773 t

**Table 3.13:** Indicative values comparing passive vs magnetic shielding in LBNO. The contribution coming from the hadron stopper has been explicitly indicated in each case.



## Chapter 4

# The CN2PY Neutrino Beam Design

In this chapter the conceptual design of the secondary beam line components and infrastructure is described.

### 4.1 The CNGS experience and lessons learned

The CERN Neutrinos to Gran Sasso (CNGS) project was proposed at the end of the 20th century to study the neutrino oscillations on a long-baseline initiated at CERN with the far detectors located underground at the Gran Sasso Laboratory (LNGS) in Italy, at 730 km [?] distance. The CNGS beam and experiments were proposed to give an indisputable answer to the neutrino oscillations by measuring the transitions  $\nu_\mu \rightarrow \nu_\tau$ .

CNGS profits from the high-intensity and high-energy beam from SPS at 400 GeV/c to produce the required neutrino flux. The neutrino beam layout for CNGS is shown in Figure 4.1. Accelerator neutrino configurations, like CNGS, where  $L \sim 1000$  km, are defined as long-baseline experiments. For CNGS the distance between the source at CERN and the detectors at Grand Sasso lab is measured [?] to be 732 km. In the initial proposal the project consisted

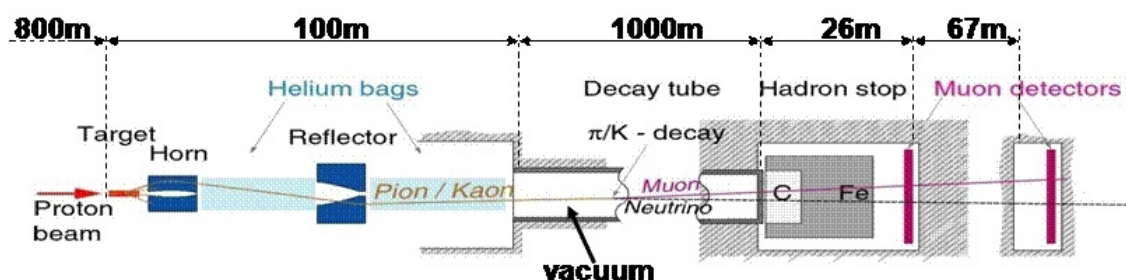


Figure 4.1: Schematic representation of the production of an accelerator-made neutrino beam.

of the neutrino beam at CERN, a near detector located at about 1.5 km from the target and the far detectors at 730 km distance in the underground Grand Sasso Laboratory in Italy. This proposal included in addition a broad physics reach like the possibility using the near detector to seed light into the LSND signal [?] and sterile neutrino search. However mainly due to funding limitations the near detector cavern was later removed from the project, leaving the  $\nu_\tau$  appearance signal the main physics goal for the experiments.

#### 4.1.1 The proton beam

CNGS uses a fast extracted 400 GeV/c proton beam from the CERN SPS. The extraction channel installed at the SPS LSS4 is designed to accept both the high-brightness beam for LHC and the



high-intensity beam for CNGS [?]. The extracted beam is transported over 840 m onto a graphite target located in an underground cavern. A schematic overview of the proton extraction beam and the CNGS neutrino facility underground structures is shown in Fig. 4.2.

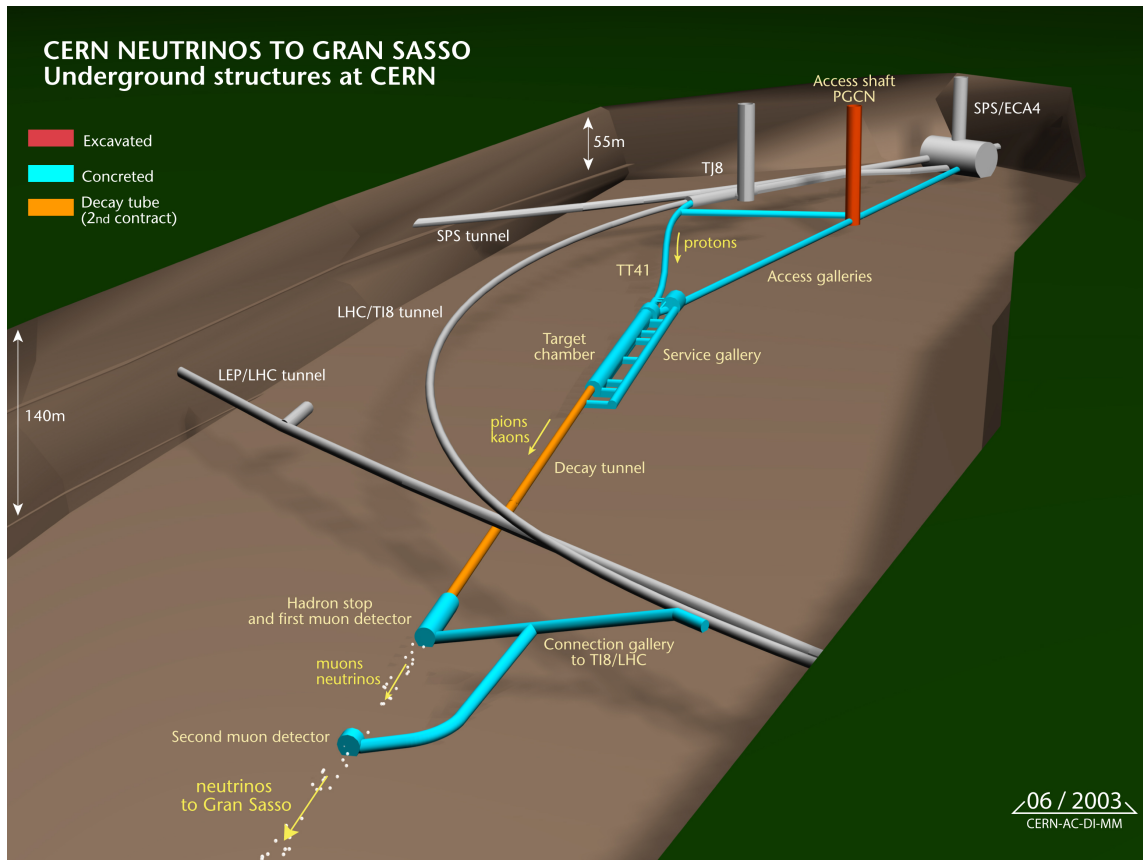


**Figure 4.2:** Layout of the CNGS underground structures at CERN where the neutrino beam is produced.

The extraction channel from SPS is common to CNGS and LHC injection via TI8. After about 100 m from the SPS extraction point, a string of switch magnets is used to direct the beam towards either LHC or CNGS. To direct the beam towards Grand Sasso, a 620 m long arc is needed, followed by a straight section of 120 m for the final focusing to obtain the desired beam size at the target. The last part of the proton beam and the neutrino beam tunnels have a downward slope of 5.6% required to point to the far detector at Grand Sasso. The beam is equipped with steering elements to allow position and angle steering at the target. The final focusing system is also tuneable allowing a variable beam spot at the target from  $\sigma = 0.25$  mm to 1.0 mm with the nominal value of  $\sigma = 0.50$  mm.

In the nominal CNGS operation of SPS, the cycle length is 6 s and the required intensity  $4.8 \times 10^{13}$  protons, making a nominal beam power of 510 kW. The intensity is delivered in two SPS extractions of  $2.4 \times 10^{13}$  protons each lasting for 10.5  $\mu$ s, separated by 50 ms. The beam micro-structure is arranged in bunches with 5 ns bunch spacing and fill the entire circumference of SPS (23  $\mu$ s) except for two  $\sim 1$   $\mu$ s gaps required to accommodate the rise and fall time of the fast extraction system to LSS4. In Tabl. 4.1 the main parameters of the proton beam are listed. For a typical SPS year, with 200 days of operation and 60% beam sharing with other SPS physics users,  $4.5 \times 10^{19}$  protons on target are expected for CNGS.

The magnetic system of the proton beam line consists of 73 dipole magnets (nominal field 1.7 T at 400 GeV/c) [?], 20 quadrupole magnets (nominal gradient of 40 T/m) and 12 corrector magnets (maximum deflection angle of 80  $\mu$ rad). The 5.6% slope of the proton beam is provided by 32 horizontal bending magnets tilted by 12.8°(see Fig. 4.3). Although the nominal



**Figure 4.3:** Photo of the 800 m proton beam transfer line for CNGS with the tilted magnets.

**Table 4.1:** Key parameters of the CNGS proton beam at 400 GeV/c.

Parameter	Nominal Value	Unit
Normalized emittance	H=12, V=7	$\mu\text{m}$
Physical emittance	H=28, V=16	nm
Momentum spread	$0.07 \pm 20$	%
Extraction number per cycle	2	-
$\Delta T$ between extractions	50	ms
Extraction batch length	10.5	$\mu\text{s}$
Number of bunches per extraction	2100	-
Intensity per extraction	$2.4 \times 10^{13}$	protons
Bunch length ( $4\sigma$ )	2	ns
Bunch spacing	5	ns
Beam beta at focus	H=10, V=20	m
Beam sizes at focus (400 GeV - $1\sigma$ )	0.5	mm

beam energy for CNGS is 400 GeV/c, the beam line could operate at a lower energy down to 350 GeV/c, limited by the vertical aperture in the main bending magnets. The beam line is instrumented with beam position, profile and intensity monitors, some of special design due to the high-intensity and radiation environment.

#### 4.1.2 The neutrino beam

The design of the CNGS neutrino (or secondary) beam is based on the successful design of the WANF [?]. In CNGS, a large cavern (TCC4), see Fig. 4.4, contains the target station and the two magnetic focusing elements, called horn and reflector. It extends to 100 m from the target where the 900 m long decay pipe begins. A parallel service tunnel allows direct access to the



**Figure 4.4:** Photo of the CNGS target cavern with the target station in the forefront. The slope of the tunnel required to point to Grand Sasso is visible.

equipment in the target hall for services and interventions. The tunnel structures for CNGS are located deep underground at about 50 m deeper than SPS or about 100 m from the surface due to the angle required directing the 400 GeV/c proton beam to Gran Sasso (Fig. 4.5). A single about 1 km long tunnel gives access to the neutrino beam areas. The design, and in particular the operation of this high-intensity beam facility is optimised for being deep underground mainly for what concerns the handling of the equipment, containment of radiation and environmental impact.

The target used in CNGS is also based on the successful design of the WANF target, but with graphite as prime material due to its thermomechanical properties [?]. A target head consists of 13 graphite rods each 9 cm long interspaced by 9 cm, placed in an aluminium cylinder closed off with beryllium windows. The diameter of the first two rods is 5 mm and of the rest 4 mm. The cylinders are maintained in an inert gas (He) atmosphere and external fins assure the cooling



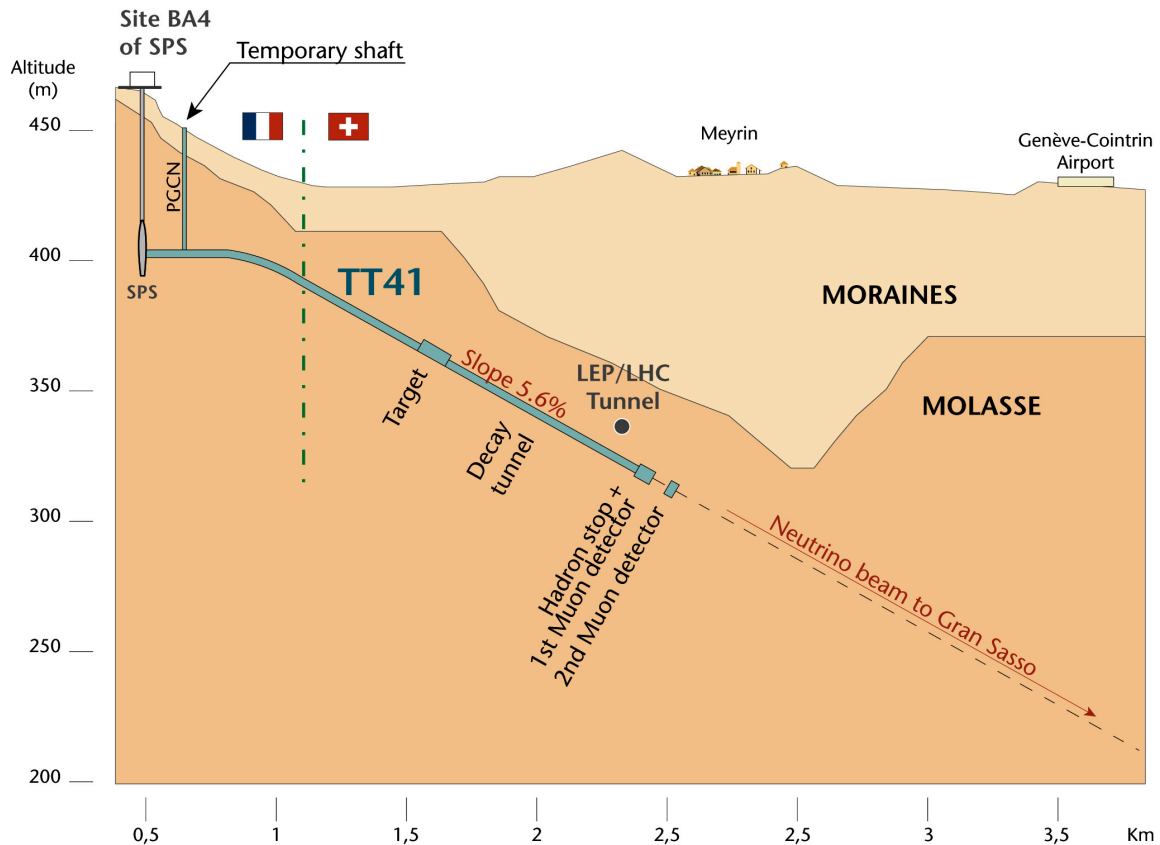


**Figure 4.5:** Sketch showing the vertical arrangement of the CNGS neutrino beam tunnels.

with forced air (Fig. 4.6). Five target heads are mounted on a revolving mechanism to allow for in-situ spares and the whole assembly is aligned, at installation, to  $\pm 0.1$  mm transversally with respect to the proton beam.

Downstream the target the two magnetic focusing elements, namely horn and reflector are installed (Fig. 4.7). They are toroidal coaxial lenses similar in shape and each 7 m long. When pulsed with a high current, a toroidal magnetic field is created between the inner and the outer conductor whose strength varies with the inner conductor shape allowing to focus the particles that traverse. The combined function of the horn and reflector focuses secondary charged particles emerging from the target with a wide range of momenta and angles to produce a parallel beam pointing to the Gran Sasso direction. The horn is pulsed twice in every beam cycle with a current of 150 kA lasting few milliseconds, while the reflector is pulsed with 180 kA. The two pulses are separated by 50 ms, synchronised with the two beam extractions from SPS. A system of sprayers continuously injects water onto the inner conductor to remove the induced heat from the electrical current and from the radiation. As for the target, the horn and reflector design was optimised for remote handling and maintenance operations in the radiation harsh environment of CNGS. By changing the sign of the electric field in the horn and reflector positive or negative hadrons can be focused, producing respectively a neutrino or anti-neutrino beam. Remotely controlled mechanisms allow the re-alignment of the target head and the horn in the transverse plane and relative angle.

The space between the horn and reflector is determined to optimise the wide-band high-energy  $\nu_{\mu}$  beam. It is filled with a 31 m long, 1.2 m diameter tube filled with Helium at 20 mbar overpressure to minimise the particle interactions and radioisotope production in the cavern. A second Helium tube 41 m long is installed downstream the reflector covering the distance to the end of the target cavern where the decay tube starts. The CNGS decay tube is made of steel, 18 mm thick and 994 m long, with a diameter of 2.45 m, surrounded by 50 cm concrete in



**Figure 4.6:** The CNGS target. Left: detail of a target head with the graphite rods the support structure and the external aluminium cylinder. Right: photo during the installation of the target unit with the five heads in its place in the beam. The side iron and marble shielding and the forced-air duct at the bottom are visible. In the final installation a top shielding with remotely movable blocks is installed.

its full length. The decay tube construction was excellent, allowing to easily maintain it under vacuum at less than 1 mbar. The entrance window of the decay pipe is made of a 3 mm thick Titanium foil, while the downstream window is 50 mm carbon steel, water-cooled. At the end of the decay pipe is the hadron stop. It is a massive assembly of blocks 18 m long, the first 3 m of graphite and the rest of cast iron, water-cooled designed to absorb up to 100 kW of power from the non-interacting part of the proton beam and all the secondary hadrons (see Fig. ??). A set of two detection stations separated by 70 m downstream the hadron stop measure the muons in the beam line before they are absorbed further downstream in about 500 m of rock. They can provide the measurement of the beam profile in both the horizontal and vertical plane, thus providing useful information on its direction and quality.

The secondary beam elements are designed to withstand the nominal beam intensity from SPS of  $2 \times 2.4 \cdot 10^{13}$  protons every 6 s protons on target (pot) corresponding to a yearly integrated total of  $4.5 \times 10^{19}$  pot and the harsh radiation environment. In the design phase of the facility it was considered important to provide some margin for possible improvements or upgrades in the accelerator chain and therefore build components - as far as technically and financially affordable - for possible higher intensities than the nominal. In Table 4.2 the expected yearly delivery of protons on target for the different operations modes are described. The "ultimate" beam intensity of  $2 \times 3.5 \cdot 10^{13}$  pot per 6 s cycle, corresponding to a beam power of 750 kW in dedicated operation of SPS for CNGS, is basically to be considered as the limit for the instantaneous beam intensity rather than the continuous operation and integrated intensity. For the

**Table 4.2:** Estimates of annual proton beam delivery for different scenario of SPS operation used for the design of the CNGS facility, as explained in the text above. The estimates are for injection of two PS batches per SPS cycle of 6 s.

Beam type	Protons per PS batch	Protons per SPS cycle	200 days - pot per year			
			efficiency sharing	100% no	55% no	55% 60%
Nominal	$2.4 \times 10^{13}$	$4.8 \times 10^{13}$		$1.38 \times 10^{20}$	$7.6 \times 10^{19}$	$4.56 \times 10^{19}$
Ultimate	$3.5 \times 10^{13}$	$7.0 \times 10^{13}$		$2.02 \times 10^{20}$	$1.11 \times 10^{20}$	$6.65 \times 10^{20}$

design of the target head the ultimate pulse intensity of  $7.0 \times 10^{13}$  protons, corresponding to a maximum of 750 kW of beam power, was used as guideline considering the associated thermal



**Figure 4.7:** Photo of the horn during its installation in the tunnel.

stresses, deposited energy (up to 1.4 kW) and radiation environment.

The concept of the target magazine with the five in-situ spares was also designed for the same intensity, offering the additional possibility to continue even after a single failure without interruption. Since the early stage in the design, optimisation processes for radiation protection issues have been embedded, and followed all along the operation of the facility. Extensive simulations of the facility using the FLUKA code [76] for dose estimates, physics performance and particle fluences have been made, using the maximum nominal integrated intensity of  $7.6 \times 10^{19}$  pot per year. Examples of this optimisation process can be found in the choice of materials, like use of marble shielding, of technical solutions, like the installation of a fully remotely controlled overhead crane with automatic plug-in system for the removal of the shielding blocks and the elements of the neutrino line, and of procedures, as the extensive study of the horn and reflector replacement in case of failure validated with real-life practice sessions before startup. However the operation of such high-intensity beam facilities remains a very challenging task as proven in CNGS but also other neutrino facilities in the past [?].

These design parameters of CNGS correspond to the initial phase of operation of CN2PY beam. The validation of the CNGS design with the five years of beam operation provides a solid bases for the engineering of the CN2PY beam that needs to be further extended to the foreseen operation at 2 MW of beam power.

### 4.1.3 Operational Performance

The construction of the facility started in 2000 and was completed as scheduled in 2006. The beam was successfully commissioned in July 2006 [?], followed by the first physics operations for the experiments. After solving the initial technical problems in 2006 and 2007, the facility had a smooth operation for five years until the end of 2012 delivering  $1.824 \times 10^{20}$  protons on target, corresponding to more than 81% of the approved program [?]. In Fig. 4.9 the development of the integrated yearly and total statistics for the CNGS beam is shown. The record





**Figure 4.8:** *The hadron stop during its construction.*

year for CNGS was 2011, where although running in parallel to LHC and the SPS fixed target program,  $4.84 \times 10^{19}$  protons on target were delivered, slightly beyond the expected  $4.5 \times 10^{19}$  from the project proposal. The nominal beam power of SPS for the CNGS beam of  $4.5 \times 10^{13}$  400 GeV protons every 6 s corresponds to 510 kW in dedicated mode of operation. The actual average beam power during the CNGS operation is lower, approximately 300 kW, primarily due to intensity limitations in order to maintain the beam losses in the Proton Synchrotron (PS) and the SPS within the authorized limits, and secondly due to beam sharing in the SPS with the LHC, the fixed target physics program and machine developments studies. However in certain periods as shown in Fig. 4.10 the SPS was used in dedicated mode for CNGS with an intensity reaching about 85% of the nominal, corresponding to a beam power of 405 kW that is a world record for conventional neutrino beams. The sustained maximum during a day was 330 kW. The efficiency of the accelerator complex increased over the years; the integrated efficiency in the SPS for CNGS was 61% in 2008, 73% in 2009, 80% in 2010, 79% in 2011 and 82% in 2012.

The overall beam performance and the stability of the CNGS primary proton beam line on the target position was excellent throughout the five years of operation. The instrumentation provided in the proton beam line allowed to accurately track the position of the high-intensity beam and monitor its profile and intensity at various locations [?]. The beam position is measured using 23 Beam Position Monitors (BPM); all but the last one equipped with button electrodes for the two planes. The last one is an innovative strip-line coupler pick-up monitor in air, mechanically coupled to the target structure. It provides information on the beam position as seen by the first target rod with a  $\pm 0.35$  mm precision. The beam position stability over the full running period of CNGS was excellent (Figure 4.11) with an rms of 54(77)  $\mu\text{m}$  in the horizontal(vertical) direction for more than 2 million extractions over the five years of operation.

## CNGS: Integrated POT 2006-2012

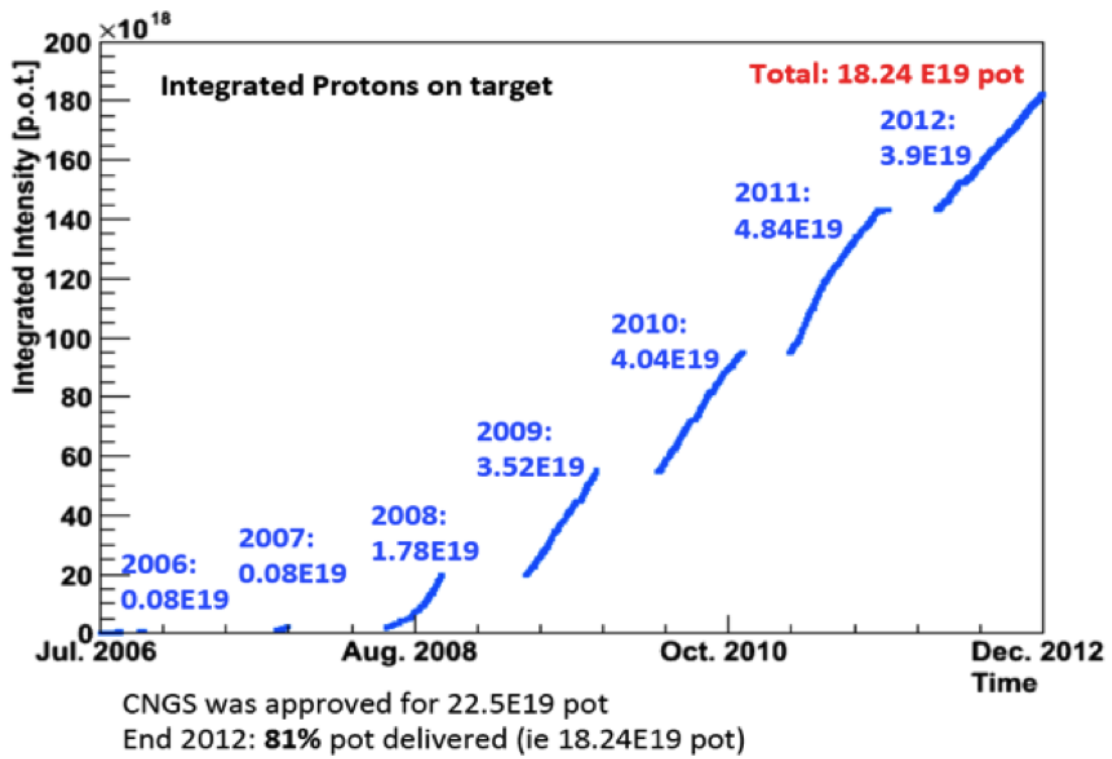


Figure 4.9: Integrated number of protons delivered from SPS to the CNGS target.



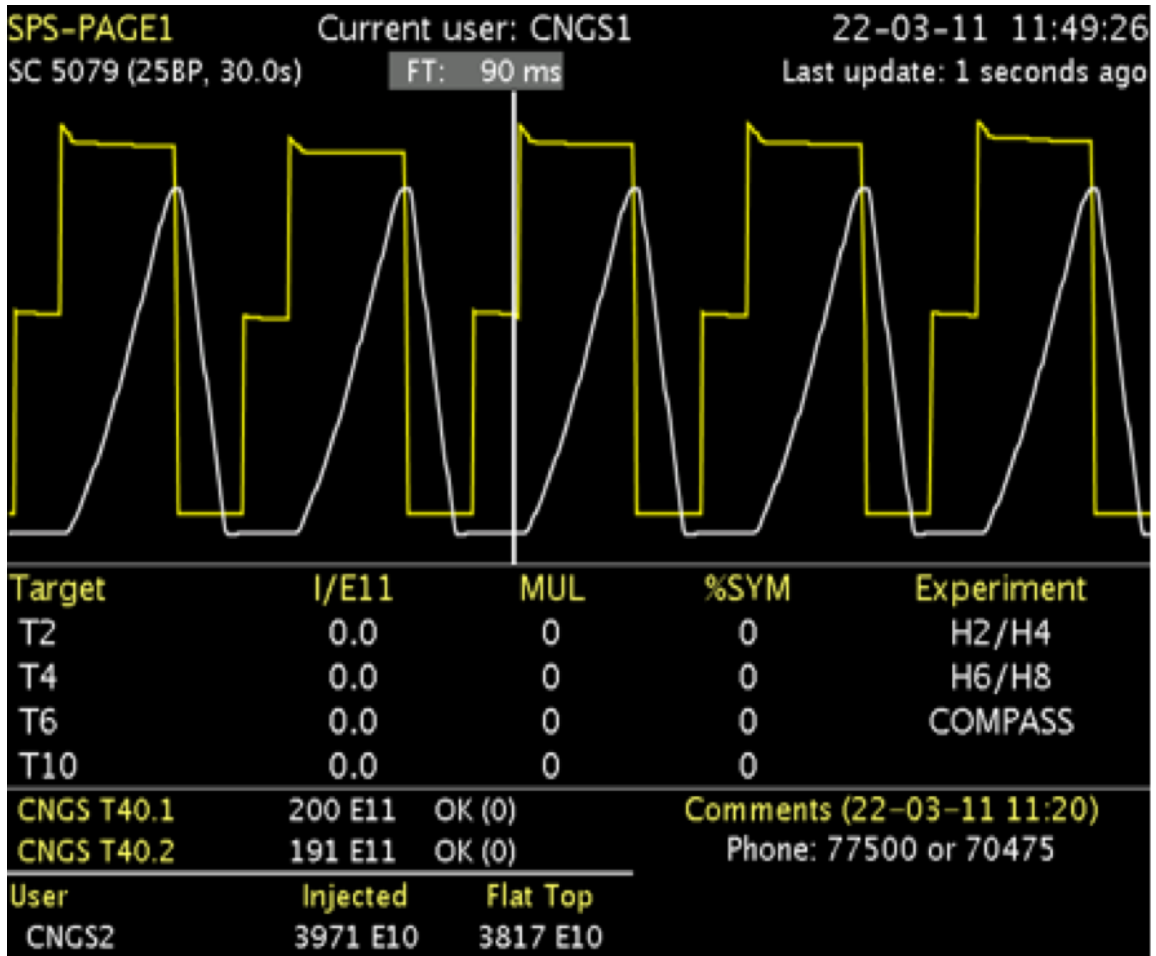


Figure 4.10: SPS super-cycle configuration with five 6 s CNGS cycles, or 100% duty cycle of the neutrino beam. The intensity per cycle is  $3.8 \cdot 10^{13}$  protons, corresponding to a beam power of 405 kW.

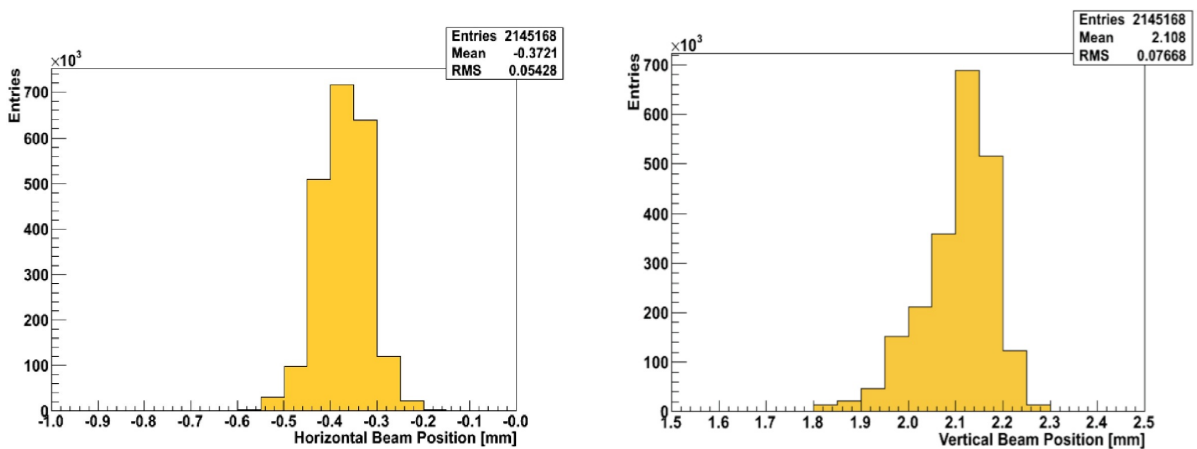
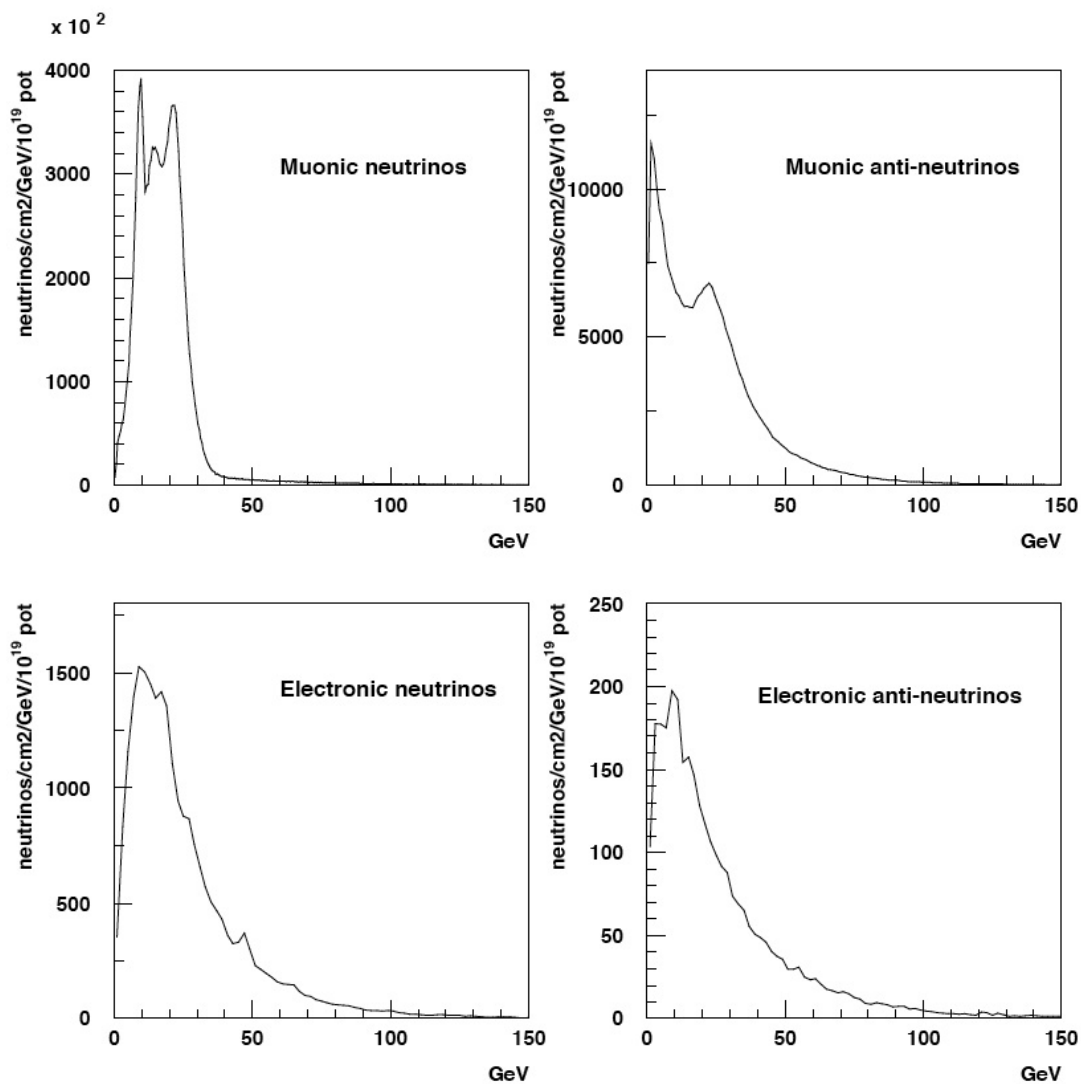


Figure 4.11: Plot showing the beam position in  $x$  (left) and  $y$  in front of the target as measured for almost the entire CNGS operation.

For the proton beam profile, 8 optical transition radiation (OTR) monitors equipped with either a  $7\ \mu\text{m}$  carbon screen for high-intensity operation, or a  $12\ \mu\text{m}$  Titanium screen for a low-intensity beam are used. The OTR radiation at the beam passage is captured by CCD cameras to provide the beam image. To measure the beam intensity, two Beam Current Transformers (BCT) are used at the beginning and end of the proton line. Beam Loss monitors (BLM), ionisation chambers filled with  $\text{N}_2$  are used to monitor the beam losses along the line. Following the initial beam setup at commissioning the beam stayed well tuned and stable throughout the CNGS operation. The maximum beam excursion measured to be well within the  $\pm 4\ \text{mm}$  allowed by the magnet aperture constraints and the losses along the line were minimal. Only small beam steering corrections per week were necessary.

CNGS is a wide-band high-energy neutrino beam. In Figure 4.12 the flux of the four neutrino beam components is shown. The average energy of the  $\nu_\mu$  that are sent to Gran Sasso is



**Figure 4.12:** Expected  $\nu_\mu$  fluence spectrum at Gran Sasso, compared to the product of oscillation probability times  $\nu_\tau$  cross section.

about 17 GeV. The two muon detection stations placed in the forward direction, the first right after the hadron stop and the second at 67 m distance, proven to be the most sensitive and useful instruments in the quality monitoring of the neutrino beam, responding to any misalignment

between the proton beam, the target and the horn, as well as any deterioration of the target and the horns. In each station, 42 muon detectors are installed to measure the muons created in association with the  $\nu_\mu$  in the decay of the secondary hadrons. The muon detectors are assembled in a cross-shaped array to provide the vertical and horizontal muon profiles and the total muon intensity (see Fig. ??) [?]. The distance between two neighbouring detectors is 11.25 cm. The total height/width covered by the detectors is 2.7 m. In addition, an identical monitor is installed on a motorized support, downstream of the fixed ones to allow cross-calibration of the fixed monitors and to probe the muon profile where there is no fixed monitor. The beam profiles from the muon stations provide on-line feedback for the quality control of the neutrino beam. The muon detectors must measure up to  $10^8$  muons/cm<sup>2</sup> during one extraction,

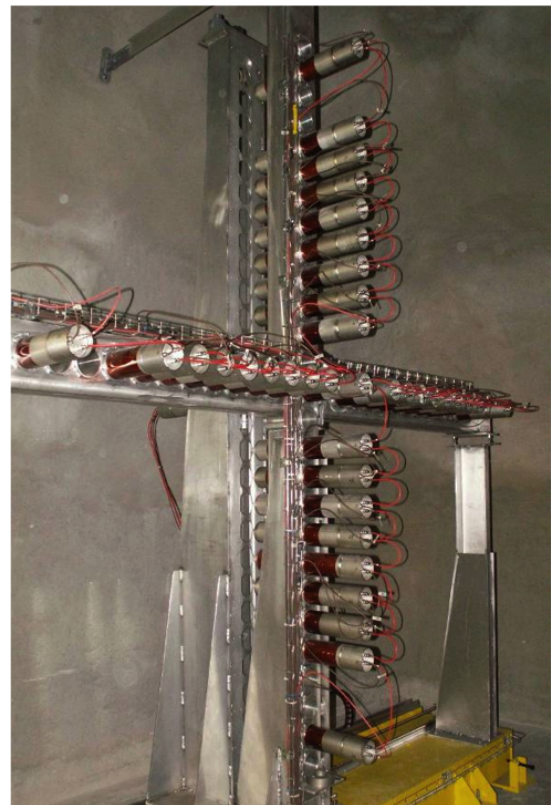


**Figure 4.13:** *The Muon monitoring station with 18 BLM detectors.*

i.e. during  $10.5 \mu\text{s}$ . To cope with such a high instantaneous rate, nitrogen-filled sealed ion-

ization chambers are used. These ionization chambers are also used as beam loss monitors (BLMs) at the Large Hadron Collider (see Fig. ??). Each 48 cm long detector has a diameter of 16 cm, is filled with N<sub>2</sub> at 1.1 bar and has 61 electrodes separated by 5 mm. The bias electric field is set to 2400 ZV/cm [?]. Since the chambers are separated by 67 m of rock, the muon energy spectrum is different in the two chambers. Only muons with an energy above 20 GeV (50 GeV) reach the first (second) muon detector chamber. The first muon detector station is very sensitive to misalignment between the target and the horn, while the second station gives information on proton-target alignment [?]. Hence scanning the proton beam w.r.t. the target and the horn and comparing the muon monitor profiles provides optimal secondary particle production efficiency and a precise alignment of the beam w.r.t the target and the horn [?]. The muon monitor reproducibility for all the detectors was measured to be better than 1% r.m.s. The response of the different muon monitors is identical within less than 1%, as cross-checked with the motorized monitor [?].

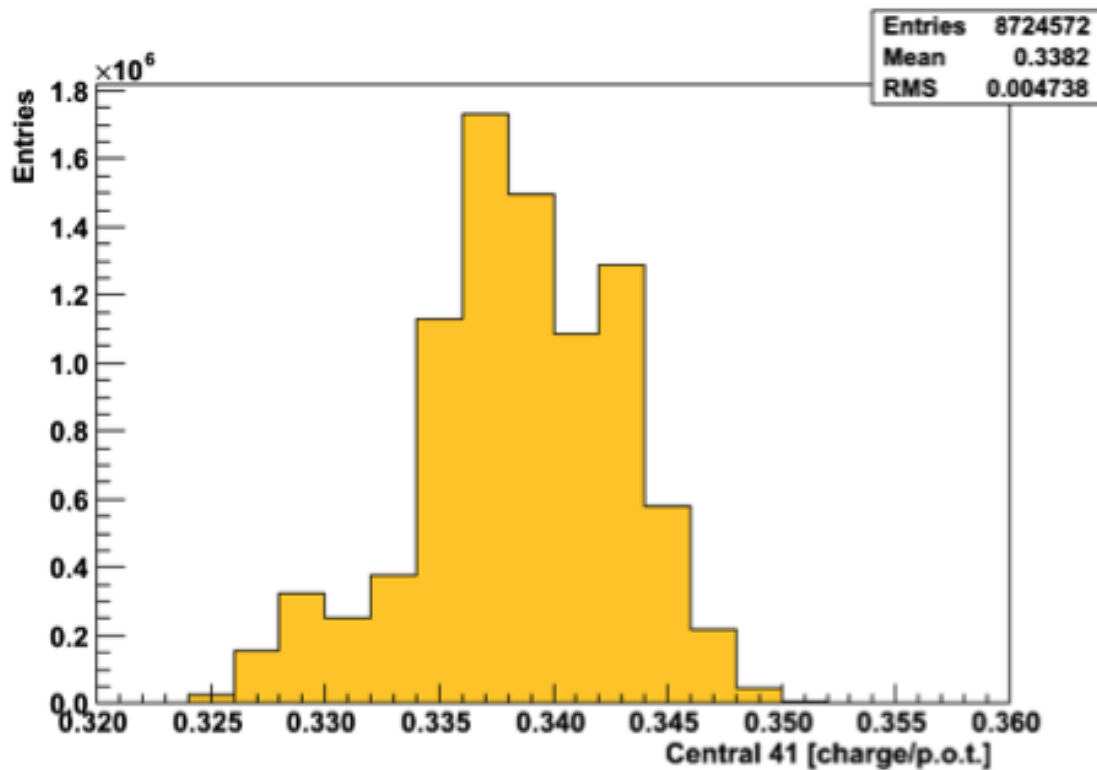


**Figure 4.14:** Central muon detector signal during the five years of physics for CNGS.

Fig. 4.14 shows the signal in the muon detector in the centre of the detector station in the first muon pit during the 5 years of CNGS operation. The mean value is 0.338 charges/pot, with an r.m.s. of 0.005, demonstrating the remarkable stability of the secondary beam line elements. The stability of the signal amplitudes in the muon detectors also shows the target yield remained constant and no deterioration of the target has been observed. The effect of deteriorated horn capacitors was seen in the muon yield, though only at the 1% level.

The careful and optimised design and construction of CNGS paid off during operation, with the facility reaching remarkable high up-times, even when operating at the top intensities provided by SPS:

- the proton beam stability and operation with remarkably minimum losses,
- the target head design was proven very robust and only one head was used during the full operation period,

- the vacuum design of the 1 km long decay pipe performed extremely well keeping the required level at all times, even during long technical stops with the pumps switched off,
- the hadron stop design that required zero interventions, with no signs of any leaks during the whole operation period,
- the design of the target ventilation system assuring the designed minimum humidity levels in the cavern,
- the horn and reflector systems, which apart from some early problems described below, survived well operated with approx.  $10^7$  pulses.

On the other hand, CNGS suffered from initial "teething problems", fortunately not major ones. These provide important lessons learned for the design of future even more challenging facilities like CN2PY:

- Soon after its startup in 2006 the facility had to stop due to a leak in the cooling system of the reflector. Repair activities were not at all foreseen for the CNGS neutrino beam elements. Instead sufficient redundancy and safety factors were applied in the design, and spares were constructed for the target and the horn, considered to be "consumables", that could be exchanged with optimised remote handling procedures. This approach is fine, however as the failure occurred so early, the radiation levels were sufficiently low to allow a repair campaign to be organised in-situ instead of using spares, thus reducing the production of radioactive waste from the facility.

For CN2PY, the similar approach will be followed, i.e. the target and horns will be designed with a safety factor and considered as consumables, to be repaired after failure with spares. A fully equipped hot-cell is envisaged in the design to allow small repairs in the equipment exposed to radiation, and perform a target/horn exchange as the two systems will be coupled together.

- Profiting from the horn repairs, preventive maintenance and improvements were made in the whole cooling circuit of the reflector and the horn.

For CN2PY, special attention is paid in the design of the peripheral systems of the target and horns: design of cooling water and service piping, avoid complicated arrangement, redundant system and verification of all welds before assembly.

- Improvements were made in the powering strip-lines of the horn and reflector because signs of degradation were observed in the flexible parts installed to compensate for the thermal expansion and alignment errors during installation.

A full engineering analysis for the thermal and mechanical constraints due to pulsing for the CN2PY striplines is made, based on the improved CNGS design.

- In 2007, with slightly increased beam intensity, the facility had to stop due to successive failures in the ventilation system due to radiation damage. Although the ventilation units were placed in the side service gallery at 5-6 m distance from the target cavern, the penetrating or streaming radiation, in particular the high-energy hadrons due to the direct view to the target cavern, was sufficient to create single-event effects (SEE) [?] in the commercial electronics components that were used. A general reconfiguration of the ventilation system was organised and all electronics components were relocated in a safe area protected by additional  $60 \text{ m}^3$  of concrete shielding that was installed. On the positive side, this incident in CNGS triggered a large campaign for the CERN LHC that was about to start operation with beam that continues until today, to remove all electronics from the tunnel or other areas where high-radiation fields are expected and introduce additional shielding to limit the radiation from the beams. In addition, the service gallery

of CNGS was converted to an ad-hoc irradiation facility (CNRAD) [?] where extensive tests of electronics components installed in the CEN accelerators as well as raw materials were tested.

For CN2PY the layout and location of the access galleries leading to the service and infrastructure room is optimised to avoid increased radiation levels and need to use radiation graded electronics. No active electronics are foreseen to remain during operations in the target and neutrino beam region, and all materials used will be checked and optimised for their expected activation levels.

- During the maintenance operations for the restart of the facility for 2009, it was discovered that increased torque was required for the rotating mechanism for the target magazine with the five heads. Again an in-situ inspection was organised and the problem was identified in the failure of the ball bearings due to radiation as the material type, although intended to be radiation hard was not! As the target showed no signs of degradation it was decided to re-install it instead of using the spare unit. Since, the target worked beautifully, and survived the whole five years of operation. In the following years, and with the increase in the focus turned to the handling of the radiation in the air volume of the target cavern, in particular the containment of the produced Tritium in the target cavern volume.

For CN2PY the need for movable parts is minimised in the design, and those remaining (like the quick connections for the horn and reflector striplines) all material and components will have to be validated for proper functionality in the expected harsh radiation environment.

- With the continuous operation of the facility the handling of the water collected in the sumps at the target and hadron stop caverns turned out to be a worrying factor. This because the water collected was exposed and in contact with the air of the TCC4 cavern thus easily capturing tritium produced during beam operation.

During the 2010 technical stop, additional sumps were constructed at the end of the proton beam and access tunnels to collect and re-direct the drainage water before reaching the target cavern and come in contact with the tritium environment there. As a result, the quantities of the collected water were drastically minimized to a manageable level, that could be handled by the centralized evaporator of the lab. The use of an evaporator to treat the condensation water from the target cavern ventilation system was envisaged, however not implemented due to the required complexity of the installation and the little gain in view of the imminent stop of the facility.

For CN2PY, the handling of the drainage water in the tunnels will be carefully done to redirect any drainage infiltration water out of the radioactive areas. The installation of an evaporator is proposed to be integral part of the ventilation system design to evaporate the condensation waters as part of the industrial process.

Finally, in the course of operations specialized tools and methods had to be developed to optimise the maintenance interventions and minimize the dose to personnel respecting the ALARA principle. For example,

- a new CERN-made radiation-hard design for the horn/reflector water filter cartridges was developed, that also allows the easy exchange of the filtering material with optimised operations in following the ALARA principle and minimized production of radioactive waste,
- several improvements were made in the remote capabilities of the overhead crane of the target cavern to improve the camera resolution and vision

- 

The design and operation of CNGS facility was a valuable and very rewarding experience. The concepts, ideas and engineering solutions developed for CNGS have inspired greatly this study for the topics mentioned above but also in numerous details that are hard to describe but can be identified in the proposed design. CN2PY would be a third generation neutrino beam for CERN (WANF-CNGS-CN2PY) bringing forward the developed expertise in the MW range.

## 4.2 Overview

The CN2PY secondary neutrino beam line is constituted by the target station cavern (housing the production target, the focusing horns and the target service equipment), the decay pipe and the hadron absorber.

The beam line would be located depth underground at approx. 145 meters below the average surface level in area around SPS BA1, and a bit shallower for the alternative option in the Preveessin North Area. The end of the proton beam and the full neutrino beam, decay pipe and hadron stop, should follow the angle pointing to the far detector at 2'300 km distance, resulting to an 18% slope. The design is made such to minimize the excavation of large caverns that could be both costly and non optimal from air activation at the foreseen high-intensity beam operation. The design of the target cavern is inspired by the "chase" configuration of both NuMi beam at FNAL [?] and T2K at J-PARC [?].

Under this approach, the target and horns are located inside a trench accessible only from the top with remotely operated overhead cranes, at roughly 6 m from the target vault surface level. The "chase" would be approx. 30 m long and enclosed in a He-vessel to reduce air activation. A layer of approx. 2 m of water-cooled iron blocks placed along the whole length of the "chase" inside the He tank should protect the surface of the target vault and reduce the ambient dose equivalent. The decay tunnel is made out of an water cooled 3 m diameter iron pipe approx. 274 m long that is completely embeded concrete. The decay pipe will be also filled with He, and will be on the same volume with the target chase during beam operation. A remotely manipulated shutter window allows separating the target chase He volume from that of the decay pipe in case of interventions to optimise the operation time and cost. The hadron absorber should be constituted by a graphite core – employed to dilute energy deposition of primary and secondary particles - of around 100 cm radius and 200-300 cm in length. An iron shielding of 100 m long follows required to reduce the muon flux to the near detector.

The required services for the neutrino beam will be located in a adjacent cavern located at an optimised distance to minimise the radiation levels thus avoide using radiation classified components. The installation completes with a space for temporary storage for radioactive equipment and a hot-cell to manipulate the target and horn/refector.

The chase design provides an easy way to introduce the required shielding required to absorb the energy deposition of the primary and secondary particles produced at the target and focused through the horn and reflector. The design is based on the following requirements:

- There must be a high density and potentially demountable region where the energy deposition from the intense production at the target are absorbed. The cascade of these particles has to be contained, as there must be minimal deposition of radioactivity in the surroundings.
- In order to steer the beam towards the Pyhäsalmi site, accurately positioned mechanical components must be placed in the volume of the target chamber. The target chamber must be large enough to accommodate such elements (namely, the target, horn, reflector and its auxiliary ancillaries).



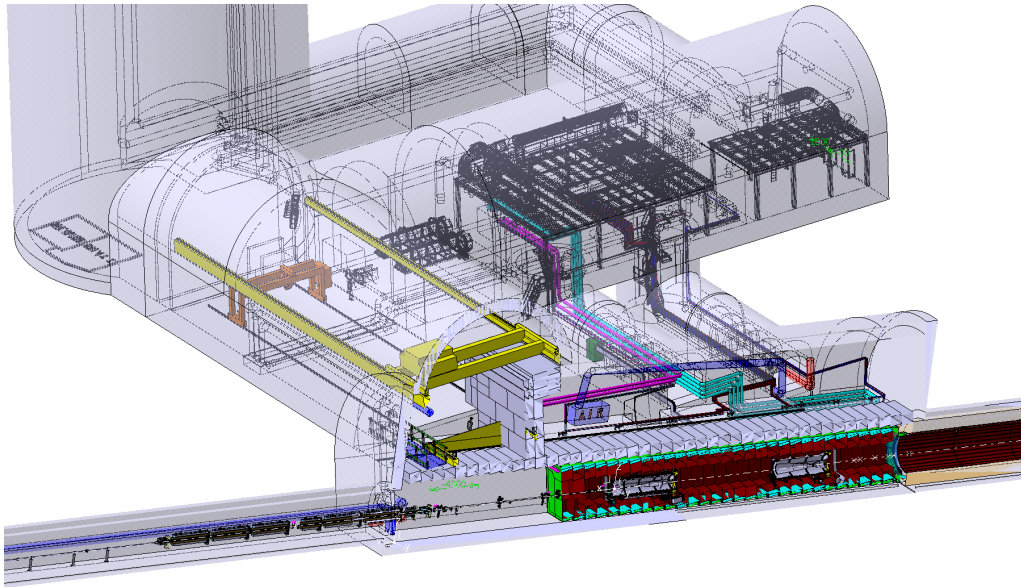


**Figure 4.15:** Cut view of the experimental area. The target chamber, surrounded by grey concrete blocks placed inside the helium vessel (in green) includes shielding elements (red iron blocks), cooling plates (blue aluminium plates) and elements as target, horn, reflector and its ancillaries and services.

In the following sections detailed description of the engineering design of the neutrino beam and its components is describe.

#### 4.2.1 General radiation protection guidelines

According to CERN's radiation protection regulation the exposure of persons to radiation and the radiological impact on the environment should be as low as reasonably achievable (the ALARA principle). To allow for such optimization numerous radiation protection guidelines should be followed from the design phase of a facility onwards. A few of these general guidelines are listed below.

##### Prompt and residual radiation

- The design of the entire facility must not only respect legal dose limits but also satisfy the optimization principle (ALARA) with respect to individual and collective doses for workers and the public. The design goals for individual and collective doses are valid for commissioning, normal beam operation, maintenance and accidents.
- The activation properties of the materials used for the construction of the facility must be considered during the design process as they may have a direct impact on later handling (maintenance and repair) and waste disposal. For this the ActiWiz material catalogue should be consulted [109].
- Only absolutely necessary equipment should be installed in areas of high radiation levels. The higher the activation the more reliable should equipment be.
- Depending on residual dose levels and tasks, manual interventions should partially or completely be replaced by remote maintenance/repair. Any component should be optimized to lower maintenance time and repair needs.



### **Air activation**

- Air volumes should be minimized in areas of high levels of prompt radiation or even better be replaced by a helium or vacuum environment.
- Air volumes in which considerable air activation is expected should be separated from adjacent areas and the outside. Therefore, both static (e.g., sealing of air volumes) and dynamic (e.g., leak extraction) air confinement should be employed.
- A ventilation system should guarantee a pressure cascade from low to high contaminated areas.
- In the target area a “closed” ventilation circuit with HEPA filters should be used. The area should be flushed before access. Also the air exhaust should be equipped with HEPA filters and the airborne radioactivity released into the environment have to be monitored.

### **Water and molasse activation**

- Water cooling circuits for highly radioactive elements like the target and the dump should be closed and separated from others.
- Water sumps should be avoided in areas with high tritium concentration.
- Activation and/or contamination of ground water and earth should be avoided.
- The facility should not be built in a “wet” environment. A hydrological study of the envisaged site should therefore be performed.
- Molasse samples should be taken and analysed for their chemical and radiological composition.

### **Radioactive waste**

- The design must consider minimization, decommissioning and dismantling of radioactive waste.

## **4.3 Geology and Metrology**

Directing a neutrino beam, over a distance of 2300 km, to a remote detector is a long-range sighting problem, the parameters of which are expressed in terms of absolute positions of the origin and of the target. These two positions allow the related azimuth and slope of the vector to be deduced. All computations must, of course, be made in a common reference system but they must also take into account some physical aspects of the Earth, i.e. gravity field anomalies and their effects.

The accuracy with which the direction of the beam line is established, and the beamline elements aligned, at CERN, will be a function of the size of the neutrino beam when it arrives at the detector in the Pyhäsalmi mine, and more importantly the size of the densest part of the beam. This required accuracy value must then be distributed appropriately between the different potential sources of error.

The direction of the beam line will be established by the secondary beamline alignment and the position of the target-horn-reflector. The critical part is the last straight segment of free trajectory, i.e. between the last horizontal/vertical corrector and the axis of the horn. Knowing that the possible deformations and movements can progressively reach millimetres, it becomes a monitoring problem, complicated by the hostile radiation level of the area.

The Laguna-LBNO project foresees a muon detector station at the end of the decay tunnel after the hadron stop, and this reference segment for the control of the final alignment therefore has its origin at the exit axis of the horn and its end at the centre of the muon detector. This is the best way to provide a check of the beam set-up and stability during operation. The following study and discussion for the geodesy and metrology of the project is based on this 330 m long baseline.

### 4.3.1 Physics Constraints

In comparison to the neutrino beam provided for the CNGS project, the CN2PY beam has a lower energy. Although the natural divergence of the proton beam for the Laguna-LBNO project will be similar (0.6 mrad), the lower energy means the divergence of the neutrino beam is greater and has been estimated (**how?**) to be of the order of magnitude of 40 mrad. This divergence leads to a transverse beam size of approximately 100 km in Pyhäsalmi, see Figure ?? . Indeed the neutrino density for the central 10 km of the beam is effectively constant.

A maximum offset must be adopted as a goal, and it has been proposed that the geodetic process must comply with final r.m.s. errors of  $\pm 1000$  m, as far as random errors alone are concerned. This corresponds to  $\pm 4 \times 10^{-4}$  rad r.m.s., i.e. 80 arcsec. Such a specification for the geodetic process is relatively easy. Nevertheless, other uncertainties and various error sources may affect the direction and the slope of the beam during operation, like geo-mechanical forces on the constructed structures, thermal expansion and mechanical constraints on the critical components, etc.

### 4.3.2 Geodesy

The preliminary data for the direction of the neutrino beam line between the CERN site and the Pyhäsalmi mine, came from a CUPP Report (“Prospects for long distance neutrino oscillation searches in Pyhäsalmi underground laboratory”). These geodetic coordinates were transformed into the CERN Coordinate System, to enable the slope and bearing of the beam line in that system to be calculated directly. It is assumed that these preliminary coordinates were either coarse geographic coordinates (latitude  $\phi$  and longitude  $\lambda$ ) interpolated from cartographic maps or, more precisely, issued from transformations between national and global systems. In any case they were taken to be given in the WGS84 reference system. If this were not the case, or there were other approximations linked to the coordinates of the point provided (e.g. discrepancies or distortions in the cartographic systems based on old “historical” data, an accumulation of measurement errors, etc.), the resulting errors could reach the order of metres across large national networks, they can be much more between systems (one arc second error in  $\phi$  or  $\lambda$  leads to an error of 31m in position). Indeed more recent geodetic coordinates provided for the mine showed differences amounting to a few hundred metres.

The link between CERN and Pyhäsalmi does not need to be so accurate in terms of relative positioning, but the orientation parameters remain important. Horizontally, the precise knowledge of the bearing depends only on the angular differences between the local system and the GPS satellite system(s). Vertically, the precise knowledge of the slope is additionally affected by that of a reference equipotential surface, called the ‘geoid’, defined at a presupposed zero level of the coordinate system.

#### 4.3.2.1 Determination of the Beam Line Parameters

The first step required to determine the neutrino beam line is therefore to determine with sufficient accuracy coordinates for the Pyhäsalmi mine. Obtaining the latest coordinates available

for the mine, and in particular the location of the far detector, together with the necessary information regarding the source and the accuracy of the position determination, will allow an assessment to be made as to whether or not Far Detector point needs to be determined more accurately or not.

Simultaneous GPS measurements between geodetic reference pillars on the CERN and Pyhäsalmi site would allow the relative positions of the two sites to be determined in a common reference frame, and a control of the orientation between the two sites. Should the Pyhäsalmi Far Detector point need to be re-determined, this would be achieved by densifying the network (using standard survey techniques) from the geodetic reference pillars measured by GPS to provide points at the top of the mine. The transfer underground could be made by suspending plumb bobs down an access shaft (recently tested at CERN for the CLIC project studies, and used for the construction of the new Gotthard Tunnel –at depths up to 800 m); or by means of Inertial Navigation Systems (as used in the Soudan mine for the MINOS project in the USA). Either an INS or gyro-theodolite could be used to provide the connection between the point established underground from the surface, and the Far Detector point. Knowledge of the local reference system used for the mine and a global geodetic reference system, and the transformations required to pass between them, would also allow the Far Detector coordinates to be transformed into the global geodetic reference system, and from there a link would be established to transform the point coordinates into the CCS.

If necessary the geodetic reference pillars of the CCS could also be re-determined with respect to a global geodetic reference frame, and a new model of the local geoid established for the CERN site in order to minimise any possible error from these sources in the bearing and slope determination of the neutrino beam line. Given the relatively low accuracy required in the beam line direction this would probably not be required. As mentioned before, if the Far Detector point and the CERN target point are both known in the CCS, it is straightforward to determine the bearing and slope of the beam line in the CCS, which can then be used as input into the secondary beam line studies.

### 4.3.3 Geodetic Networks

A network of geodetic pillars across the CERN site already exists, and has been used to provide control for the installation of all the accelerator facilities at CERN. Additional geodetic reference pillars would be established as required, close to the new Civil Engineering works, to provide a reference network for those works.

The Survey team would also establish an underground geodetic reference network in all the new underground areas in which the position or orientation of beam line elements, detectors, or infrastructure needed to be determined. This would be achieved by a densification of the surface geodetic reference network to establish points at the top of each shaft using standard survey techniques. Plumb bobs or optical plumb lines would then be used to transfer point coordinates underground, and finally a gyro theodolite would be used to establish, or control, the orientation of an underground geodetic reference network. This same process would also be used to control the position of points at the start of the secondary beam line.

### 4.3.4 Civil Engineering

For the Civil Engineering works the Survey team will determine the coordinates of the geodetic reference points to be used for the project. Full information will be provided regarding the geodetic reference systems used at CERN, and any necessary transformations. CERN should also control the civil engineering works to assure that they conform to the requirements of the project, in particular the constraint imposed by the machine alignment such as the tunnel diameter, orientation, slope, floor heights and floor smoothness. Before the tunnelling work begins,

a deep reference point in the TT20 should be established to provide a datum with respect to which any movements in the existing tunnel can be monitored.

The secondary beam line can only be attached to points known in the CCS at the start of the line. Vertical access shafts or sight shafts must be provided at the target area, the muon station and the Near Detector cavern such that the Survey team can establish an underground network of points at each of these locations, with coordinates known in the CCS.

### **4.3.5 Metrology**

For all objects too large to be processed by the Metrology Lab, or where otherwise identified, the Survey team would provide dimensional controls and fiducialisation of any beam line or detector elements. This would be achieved primarily through the use of Laser Trackers and Close Range Photogrammetry.

### **4.3.6 Survey and Alignment**

The survey and alignment of the beamline and detector elements will follow the standard methodology employed for all accelerator and detector alignment and assembly work carried out by the Survey team at CERN.

#### **4.3.6.1 Primary Beamline**

A new primary beamline is effectively a new project in itself. Although many of the geodesy and metrology activities to be taken into account are similar to those of the secondary beamline, the primary beamline is not considered in detail here.

#### **4.3.6.2 Secondary Beamline**

The first activity required for the installation of the beam line elements, and the associated infrastructure, is the marking out on the floor of reference points. These will be made using the underground geodetic network as a reference, followed by the first alignment of the beamline elements. Both of these processes would be carried out using total stations and digital levels. The final smoothing of the beamline elements to assure the required accuracy in the relative alignment of the elements will be the final stage of the alignment process and be done using stretched wire offset measurements and digital levels.

#### **4.3.6.3 Monitoring**

Although the initial alignment of the beam line elements, up to the Horn/Reflector, is not difficult to attain, deformations of the tunnel and underground target chamber may lead to a misalignment of the beam line which could exceed the accepted tolerance. The total alignment accuracy of  $4 \times 10^{-4}$  rad translates into a relative lateral movement of 4 mm at a distance of 10 m. During the first few years after construction a movement of this order of magnitude is possible, and in some underground tunnels at CERN millimetric movements are still seen every year.

These movements can be overcome by periodic re-alignment of the beam line elements, but this would quickly become impossible if it involved the intervention of a survey team in the heavily shielded area around the target. The alternative is a remotely controlled survey monitoring and alignment system, although even this might be difficult in the harsh radioactive environment.

Ideally the monitoring system would identify the absolute and relative movements of the elements at the end of the secondary beam line together with the elements in the target chamber. Equipping appropriately shielded areas of the secondary beam line tunnel and the target chamber with electronic tilt meters and extensometers/deep reference points, would already provide useful information regarding the movements and deformations of the civil engineering works. These measurements would need to be supplemented by sensors such as Wire Positioning Systems (WSP), Hydrostatic Levelling Systems (HLS) and Dimensional Offset Measurement Sensors (DOMS) used successfully to monitor the low-beta quadrupole magnets on either side of the LHC experiments, or BCAMs used to monitor the relative positions of the detectors in the LHC Experiments. A system using these sensors would include the beam line elements at the end of the secondary beamline.

Connecting the measurements in the tunnel to those in the target chamber would necessarily involve some holes through the shielding, or dedicated boreholes between them. Measuring the target and horn/reflector components would be more difficult with all the shielding in place. One possibility might be to create a rigid shielding structure in which these components were cradled, and to fiducialise the complete assembly.

Re-aligning the target or horn/reflector assemblies remotely would most likely involve the removal of some of the shielding around them, removing at least the top of the shielding to reveal the assemblies in their shielded trench. Measuring their position and orientation would necessarily involve a system placed on a robotic platform. Realigning them would probably be best done by introducing precisely machine mechanical shims into a specially designed support system.

#### 4.3.7 As-built Measurements

As-built measurements of the civil engineering, the technical infrastructure and the installed accelerator elements and experiment detectors will be made at specified stages of the installation. These measurements will be made using a laser scanner.

### 4.4 The target cavern

#### 4.4.1 The He tank

To reduce particle absorption in air, a 'helium tank' fills the useful secondary beam volume between horn and reflector (approximate length 27 m) and is connected to the decay pipe (approximate length 275 m). The absorption length is  $\lambda_{air} = 800$  m for air and  $\lambda_{He} = 2500$  m for helium. Both ends of the tank are closed by windows, a stainless steel 50 mm thick at the downstream part of the decay pipe and a titanium window at the upstream part of the target chamber. The helium is contained in the tank at a positive differential pressure of less than 20 mbar. An oxygen analyser controls the helium concentration; the exhaust minimum flow rate, to ensure the measurement of the helium concentration with precision, is about 30 l/h (see Table ??). The helium flow is controlled and adjusted by a flowmeter equipped with a needle valve.

The helium tank is manufactured in pieces and welded in position into the cavern (see transport and handling). Two removable covers are situated respectively over the horn and reflector regions, allowing the access of the cranes for maintenance.

The material used for the helium tank is specified to be steel 304-L or P355NH, according to the Euronorm EN10028. At production of the steel plates, the corresponding quality criteria are applied. In particular, ultrasonic tests are to be performed on 20% of the steel plates manufactured (according to standard EN 10160).

**Table 4.3:** Helium required flow rates. Values in  $m^3/h$ .

Element	Volume [ $m^3$ ]	Estimated renewal rate	Flow mass rate [ $m^3/h$ ]
Target chamber	110	5	550
Decay pipe	1950	2	4000
Horn	7	5	35
Reflector	8	5	40
Target	-	Inlet 40 m/s	370

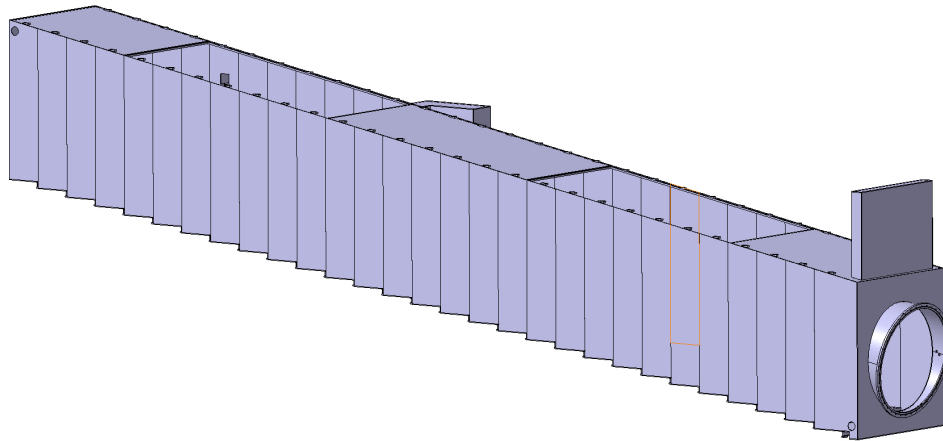


**Figure 4.16:** View of the Helium tank showing the two openings for maintenance of the horn and reflector and the connection with the decay pipe. During operation, shutter is open and enclosed in the rectangular box situated over the vessel.

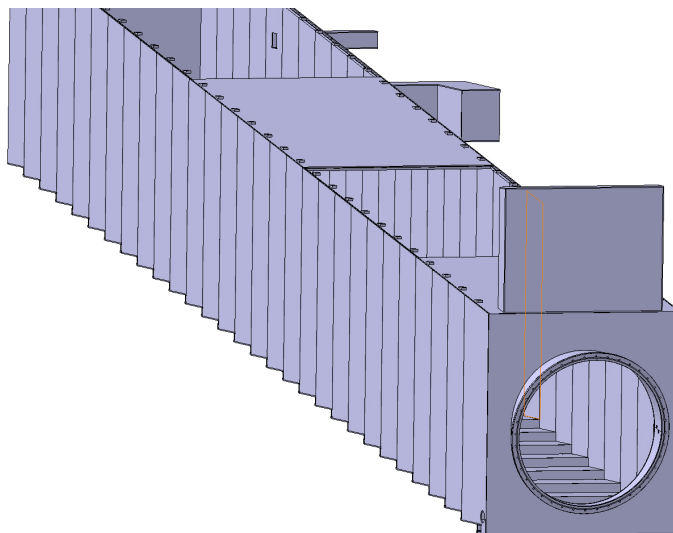


**Figure 4.17:** Downstream view of the Helium tank showing the flanged connection to the decay pipe and the stepped shape to compensate the slope. Openings for maintenance of the horn and reflector and decay pipe shutter enclosure can be appreciated.

#### 4.4.2 Shielding

Unlike the CNGS chamber it is evident that because of its insulation against radiation, heat loss in a bed of poorly conductive mass of iron and concrete blocks, the target chamber has to be actively cooled. Preliminary calculations, discussed in the next section, indicate that in steady-state (equivalent to the situation after 200 days of running with protons per second at 400 GeV/c, the internal sides of the iron wall in the proximity of the target could reach several hundred degrees Celsius (700 °C). These high temperatures would risk destroying the concrete supporting structures, and via radiation heat transfer increase the temperature of the non-cooled internal elements of the horn and the conductor leading to sticking or inducing creeping and permanent deformation of parts of them. Several heat flow calculations [?] with different conditions have been made, indicating that the iron walls have to be actively cooled.

The design requirements for a cooled target chamber are listed below:

- The total power deposited on the target chamber in the worst case of continuous dedicated running is about 900 kW. Most of this deposition is highly localized in the iron blocks. The rest, is relatively diffused over the concrete region.
- The internal walls need to be at a reasonable, constant temperature, in order to allow stable operation of the internal components.
- Water cooling must be demineralized in a closed circuit and be very robust. It should be designed for a 20-year lifetime with no intervention to the heat sink required.
- A monitoring system of the water flow and temperature is necessary. This has to be designed with appropriate redundancy, considering the mechanical and thermal stresses expected in the target chamber region.

Once installed this region is completely sealed from the galleries and muon pits.

The general layout of the civil engineering of the target chamber area is shown in Figure ?? Access to the area is evidently very limited. It not possible when is running. Access to the

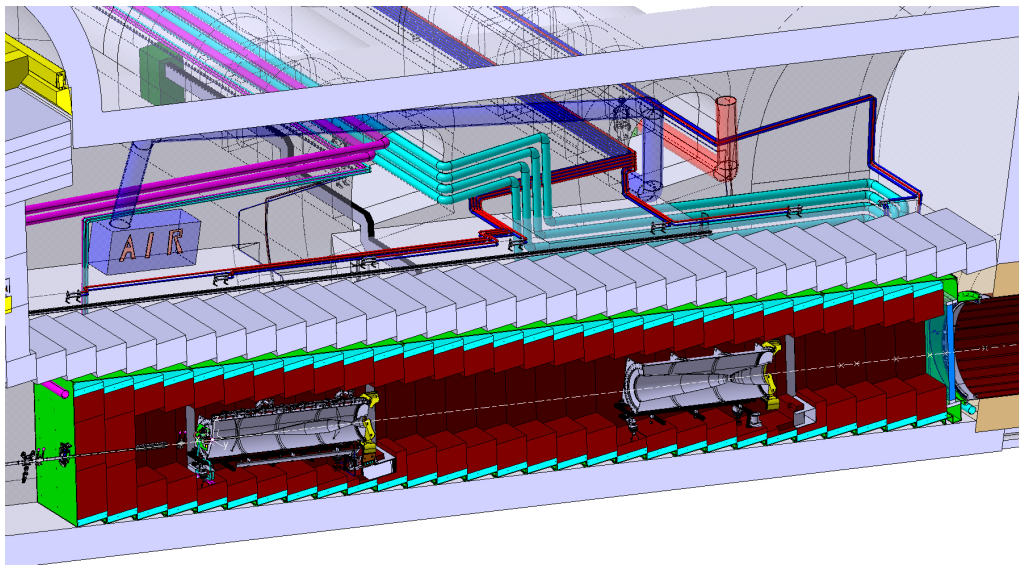


**Figure 4.18:** Cut view of the target chamber. Shielding elements (red iron blocks), cooling plates (blue aluminium plates) and elements as target, horn, reflector and its ancillaries and services are placed inside the helium vessel (in green). The helium vessel is surrounded by concrete blocks.

hot cell is possible via the man shaft. The vessel containing the target chamber is followed

by a 3 m diameter decay pipe welded to it. A gate shutter is foreseen to separate the helium contained in the decay pipe from the one at the target chamber and to minimize the total volume during maintenance operations. All the services feeding each internal component of the target chamber (horn and reflector) are assembled in one of the lateral iron blocks and can be removed remotely.

#### 4.4.2.1 Energy deposition and cooling

Preliminary calculations have been made of the heat flow and final temperatures in the target chamber, though no final optimisation of all the possible parameters has been made. These calculations have, however, given indications of what could be a reasonable, safe design that would satisfy the required conditions. The proposed design is described in the following section.

The calculation of the heat flow in the target chamber was performed in two steps. First the FLUKA program was used to calculate the average energy deposition in the chamber by a fully simulated reference neutrino beam, including primary protons not interacting in the target. The output from this simulation was used as the input to the heat transfer calculation in the target chamber.

**Table 4.4:** Heat loads at the Target chamber elements for the 50 GeV and 400 GeV operation. (values from FLUKA)

Element	400 GeV beam		50 GeV beam	
	Energy [GeV/cm <sup>3</sup> /prot]	Power [kW]	Energy [GeV/cm <sup>3</sup> /prot]	Power [kW]

Several simplifying assumptions were made to ease the calculation problem. A four-fold symmetry was assumed to allow a faster first round of calculations, e.g. the heat sink was taken as 1/4 of the square geometry. A sector of 1 m length (corresponding to the standard length of the blocks) was considered. Although the geometry has symmetry, the heat loads don't because they depend from the distance to the target, which is situated closer to the ceiling wall. The analysis considered the worst case (deposition values to the roof over the horn and to the surrounding walls). Water cooled channels in the aluminium blocks have been considered as the source of the convective sink, with constant values for water temperature and several film coefficients (referenced in Table 4.5 and Table 4.6). Boundary conditions in the helium internal walls were also considered pessimistic, and a heat transfer coefficient of 5 w/m<sup>2</sup> K was assumed while the He reference temperature was set to 22 °C.

**Table 4.5:** Typical values of the heat transfer coefficients. Note that conservative values of 2000 W/(m<sup>2</sup> K) for cooling channels (water) and 5 W/(m<sup>2</sup> K) for He boundaries have been considered.

	Air	Water
	[W/(m <sup>2</sup> K)]	
Free convection	5 - 25	20-100100
Forced Convection	10 - 200 W/(m2K)	50 - 10.000
Boiling Water	-	3.000 - 100.000
Condensing Water Vapor	-	5.000 - 100.000

The heat power deposited during operation is around 950 kW, to be removed with a water system by means of 100 Al cooling plates in contact with the iron blocks of the chamber. As-



**Table 4.6:** Summary of main results for a water cooled target chamber. Iron bock thickness is 800 mm, water tubes are imbedded in 200 mm thick aluminium plates. Maximum temperatures are reached at the internal walls.

Tube diameter	Convection Coefficient		Tmax at iron [C]	Convection Heat	
	Helium Film [W m <sup>-2</sup> C <sup>-1</sup> ]	Water Film [W m <sup>-2</sup> C <sup>-1</sup> ]		Water [W]	Helium [W]
-					
14	5	2000	75	-980203	-44525
14	5	200000	66	-988167	-36561
14	5	10000	68	-986568	-38160
14	5	1000	83	-972621	-52107
14	5	500	98	-958090	-66638
14	20	100	136	-596569	-428159
16	5	2000	73	-981231	-43497
14	1	2000	78	-1015282	-9446
36	5	2000	69	-985442	-39286
36	5	10000	61	-992900	-32800
36	20	10000	55	-918100	-106600

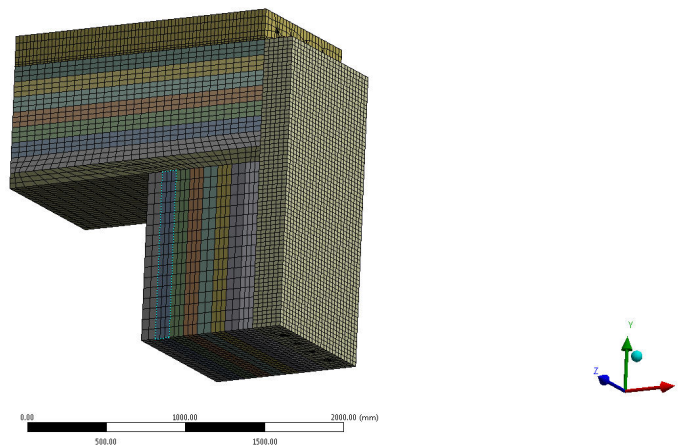


**Figure 4.19:** Model of the Target chamber. One quarter of the chamber (1 m-length sector) is simulated. Iron thickness is 800 mm, while aluminium blocks are 200 mm thick. Water pipes (14 mm ID are also modelled).

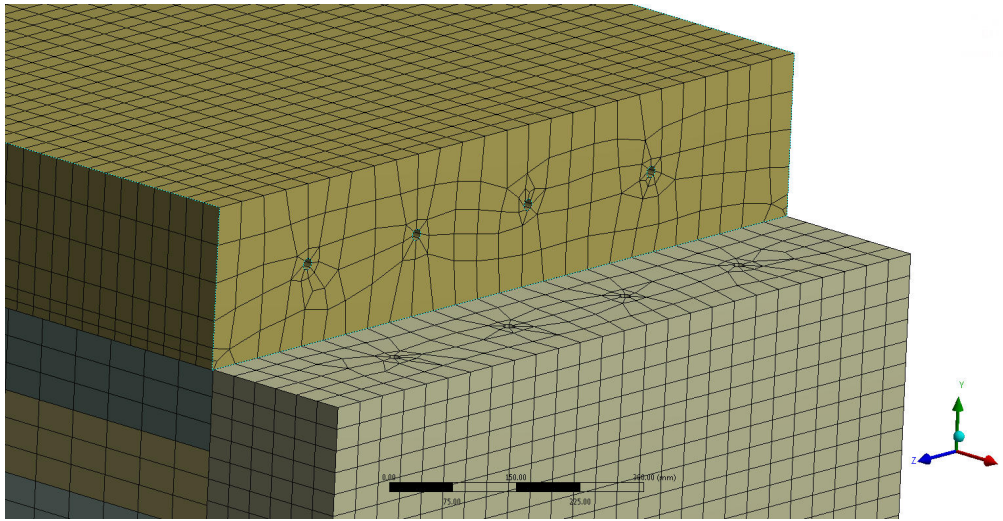


**Figure 4.20:** Model of the Target chamber. Detail of the cooling channels imbedded in the aluminium blocks.

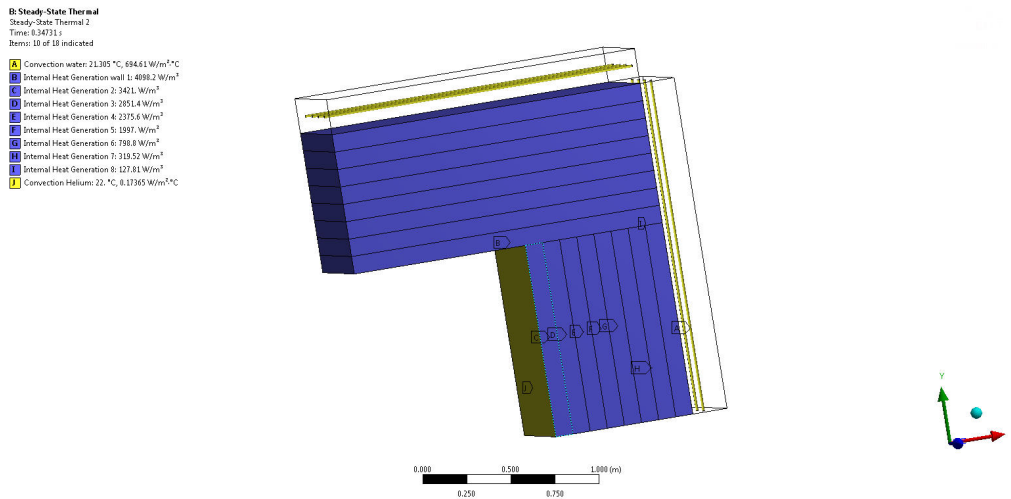


**Figure 4.21:** Detail of the boundary conditions. Heat was deposited as internally generated (volumetric heating) averaged over 80 mm thick layers, water pipes considered water at constant temperature (no temperature increase along the walls).

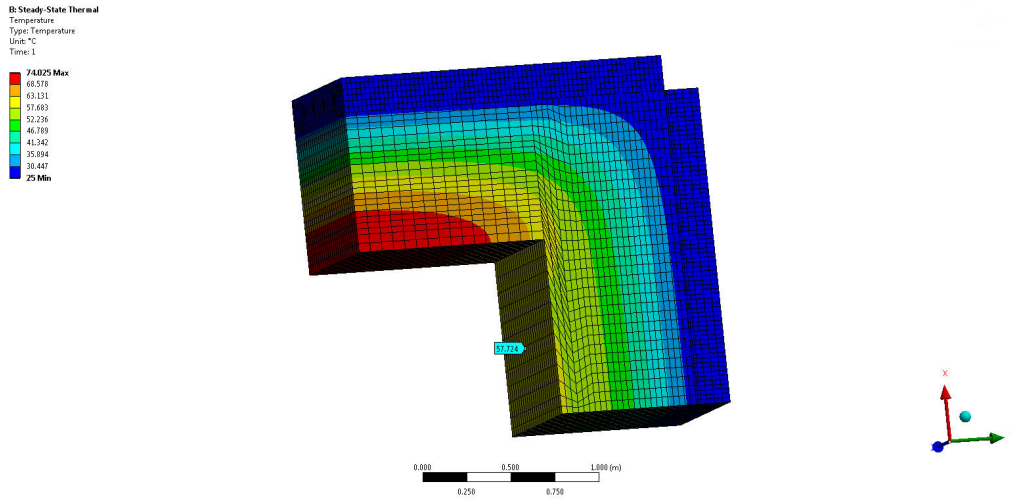


**Figure 4.22:** Profile temperature for an ideal case. A constant temperature of 25 was imposed at the external walls of the aluminium plates. Cooling is made by pure conductivity. Due to the peaked heat deposition, internal walls maximum temperature is 75 °C.

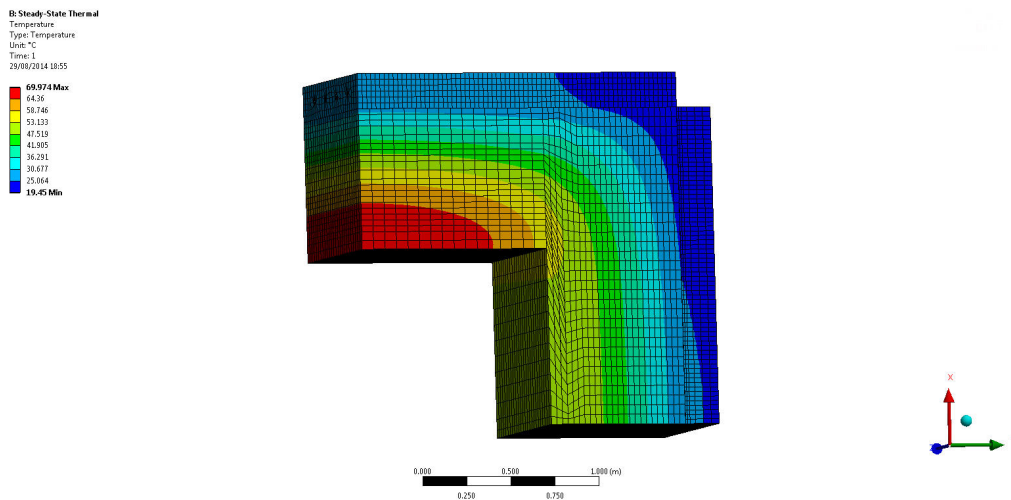


**Figure 4.23:** Heat deposition profile at the target chamber [50 GeV configuration]. Water cooling [20 °C,  $h_f$  2000 W/m<sup>2</sup> K] and He cooling [22 °C,  $h_f$  5 W/m<sup>2</sup> K] considered. Maximum temperatures at the roof iron blocks are around 70 °C.

suming a fluid overheating of 12.5 °C due to the heat removed, the required mass flow for the target chamber aluminium plates would be:

$$\dot{m}_{water} = \frac{\dot{Q}_{cooling}}{q_{water}} = \frac{\dot{Q}_{cooling}}{c_{water} \Delta T} = \frac{(264000 + 265000 + 222000 + 211000)}{4186 \times 12.5} = 18.4 \text{ [kg/s]} \quad (4.1)$$

## 4.5 Target configuration

The target must be able to withstand primary beam intensities very similar to the CNGS case (in the order of  $3.5 \cdot 10^{13}$  p+/pulse). Given that the primary beam energy does not matter too much for a radially thin target, the expected stresses and thermal loads will be very similar to the CNGS target ones for comparable beam sizes. The design will start from the very successful CNGS one: however the lower primary beam energy (larger beam size) and lower energy of the focused pions will likely result in larger rods with little or no spacing between them. As a result of the larger beam size the peak stresses will be somewhat smaller than at CNGS, however the repetition rate will be higher. Only one target will be installed also because the integration with the horn (see next paragraph) would not allow a revolver-like approach like at CNGS. The target will be between 100 cm and 130 cm long with a radius in a range between 4-8 mm. The target assembly should provide alignment capabilities with respect to the beam and with respect to the downstream horn/reflector. The target cooling is still to be defined: in any case a dedicated cooling system needs to be foreseen, potentially separated from the general cooling/ventilation configuration of the target chase.

### 4.5.1 The beam window

The proton beam line vacuum is separated from the target station and decay volume helium at atmospheric pressure by a proton beam window. This will be modelled on the T2K design which comprises two thin skins of Ti6Al4V cooled by helium flowing between the two skins. The window assembly seals between the vacuum pipe and the target station vessel using differentially pumped, inflatable bellows seals that seal to mirror flanges. This arrangement makes it relatively straightforward to replace the beam window when it has reached a pre-determined radiation damage limit.

### 4.5.2 Target and Horn integration and assembly

The integration of the target with the magnetic horn is based on the T2K design and the proposed layout is shown in Figure ???. The target is cantilevered within the bore of the horn from a plate mounted at the upstream end. A target operating with a 2 MW beam power will have a limited lifetime, consequently the target is mounted in such a way that it can be replaced remotely in a remote maintenance area, or a "hot cell" designed for this purpose as described below. Since the LBNO target station will be relatively deep underground, it has been designed to be as compact as possible, resulting in some differences with the shallow T2K target station layout. A key difference is that the secondary beam components will be supported from kinematic mounts in the floor of the target station, and connections to services such as the horn strip lines and the target coolant pipes will be made automatically/remotely when the horn assembly is lowered into place.

### 4.5.3 Remote Maintenance and Test Area

At a primary proton beam power of 2 MW, the target is expected to have a considerably shorter lifetime than the horn, so it is highly desirable to be able to replace a failed target without having to replace the horn. Consequently a target and horn remote maintenance and test area is included in the design of the target station as shown in Figure ???.

This "hot cell" will be equipped with conventional master-slave manipulators and a shielding window for maximum flexibility during replacement and repair operations. In the event of a failure or as a scheduled replacement operation, the complete horn assembly will be lifted out of the target station and installed in the remote maintenance area using the remote crane

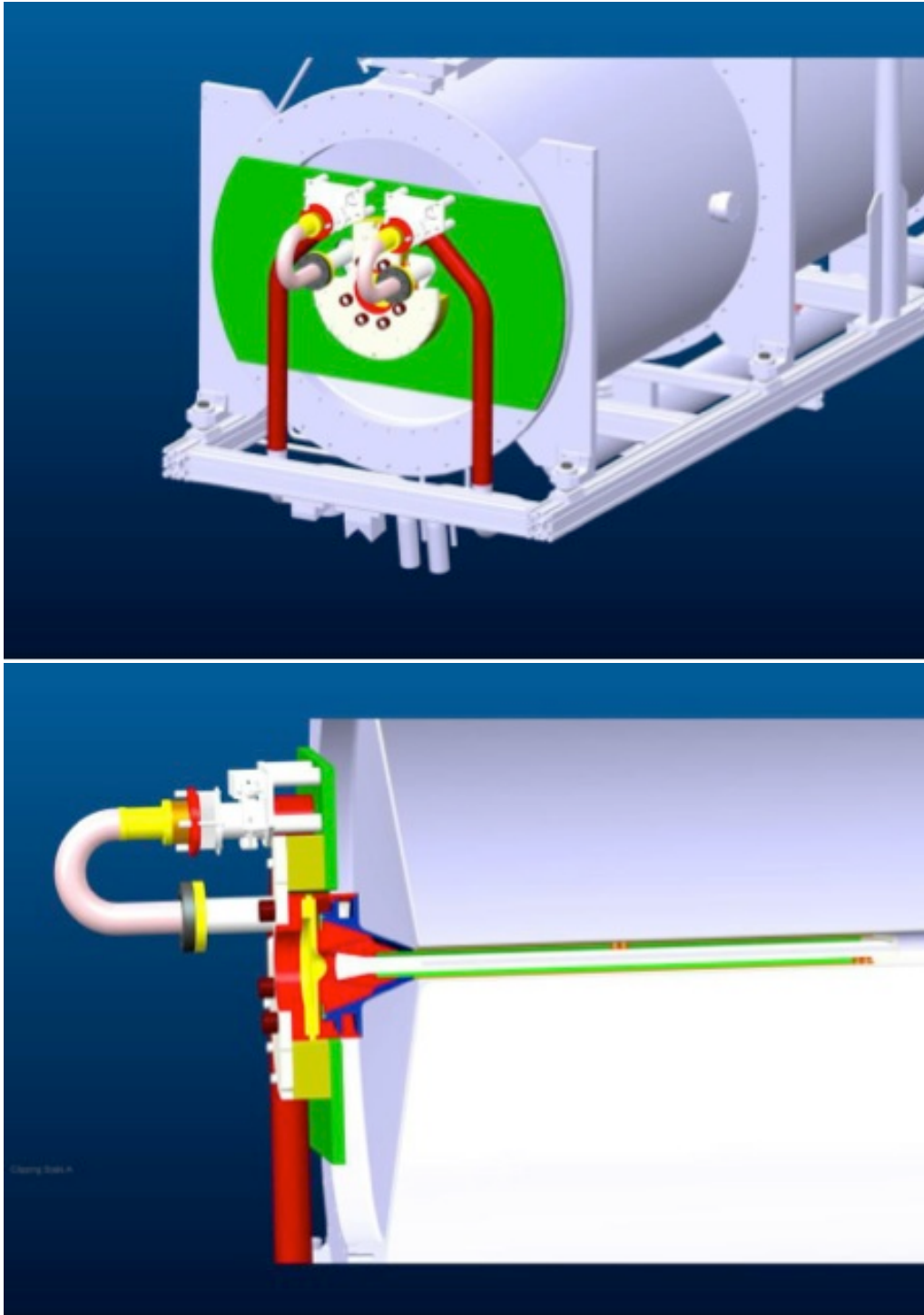


**Figure 4.24:** Target and horn assembly.

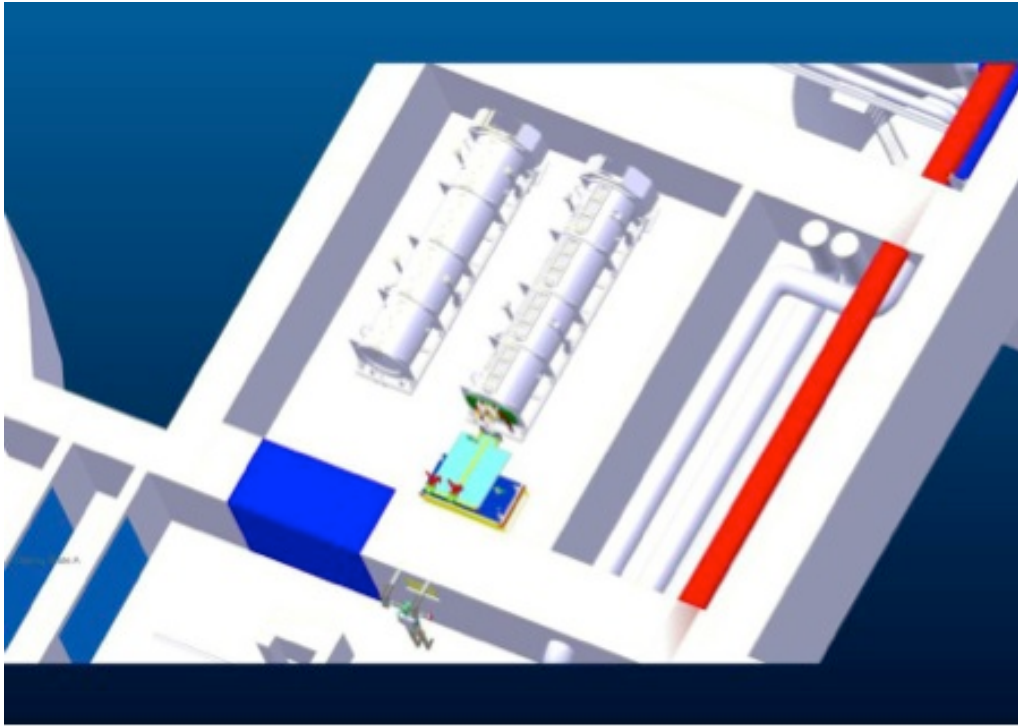


**Figure 4.25:** View of the hot cell nearby the target cavern with the horns and the target handling station.

system described above. A target exchange mechanism modelled on the system developed for T2K will be used to replace a target permitting the horn to be re-used.

Included in the hot cell will be a horn and target test area reproducing all the target station mounts and services connections, and switch gear that will permit horns to be tested using the same pulsed power supply used during operation. Due to air activation when the beam is running, it will only be possible for personnel to access the area during beam shut-downs. In order to minimise the running time lost to maintenance, repair and test operations, the hot cell is designed to permit one horn assembly to be worked on while another is being tested prior to installation.

#### 4.5.4 Graphite target for 400 GeV beam

For the Phase-I operation with the 400 GeV beam, a graphite target is proposed. The structure has to fit in the narrow horn neck (54 mm diameter) and has to include a close circuit for a cooling system. The whole assembly will be approximately 1.3 m long and has to be kept in cantilever in order to avoid touching the horn neck. A graphite bar of 8 mm diameter is used as a target and kept at temperatures of around 1400 °C. The graphite exchanges heat by radiation with an external graphite pipe. The whole structure is supported by a second pipe, made of beryllium that contains the helium cooling circuit.

The material chosen for the target of LAGUNA/LBNO [73] that suits best the physics purposes is graphite. The size of the target core represents a first requirement: a bar of 8 mm diameter and 1.3 meter length would be an optimal solution as discussed in Section ???. The graphite bar is to be placed inside a structure that ensures the correct positioning and has to be kept at some distance from the horn neck, which has an internal diameter of 54 mm. The structure is also hosting the cooling system that has to be dimensioned to ensure the required temperatures. The graphite core optimum temperature is about 1200-1400 °C to minimize the material



properties modification due to radiation damage, while the beryllium structure around should be at no more than 60-80 °C.

The beam characteristics are described below, they are similar to CNGS:

- Primary beam momentum: 400 GeV/c
- Intensity:  $7 \cdot 10^{13}$  p/cycle, ( $3.5 \cdot 10^{13}$  p/pulse, two 2 pulses/cycle)
- Pulse length: 10.5  $\mu$ s
- Time between two extractions: 50 ms
- Repetition rate: 6 s
- Average beam power: 750 kW)

The beam structure is shown in Figure 4.27.

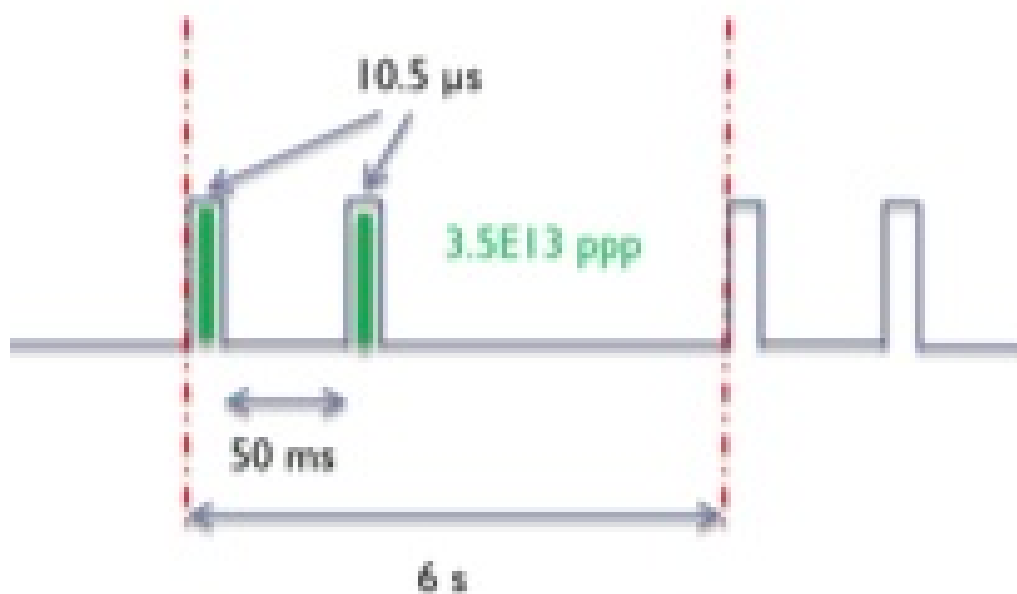


Figure 4.26: 400 GeV beam structure.

#### 4.5.4.1 Energy deposition study

The energy density values were determined by using the FLUKA Monte-Carlo transport code. In the simulation a proton beam with 400 GeV/c momentum was used. The shape of the beam was Gaussian in both planes with a 2 mm FWHM ( $\sigma = 0.85$  mm). A 2D plot of the energy deposition is shown in Figure 3, and the main results summarised in Table ??.

The energy density is interpolated in the finite element calculation performed with the ANSYS FEM code.

#### 4.5.4.2 Design proposals

The proposed solution is a graphite bar positioned inside two concentric pipes: the inner one made of graphite and the outer one made of beryllium as shown in Figure 4.28. For manu-



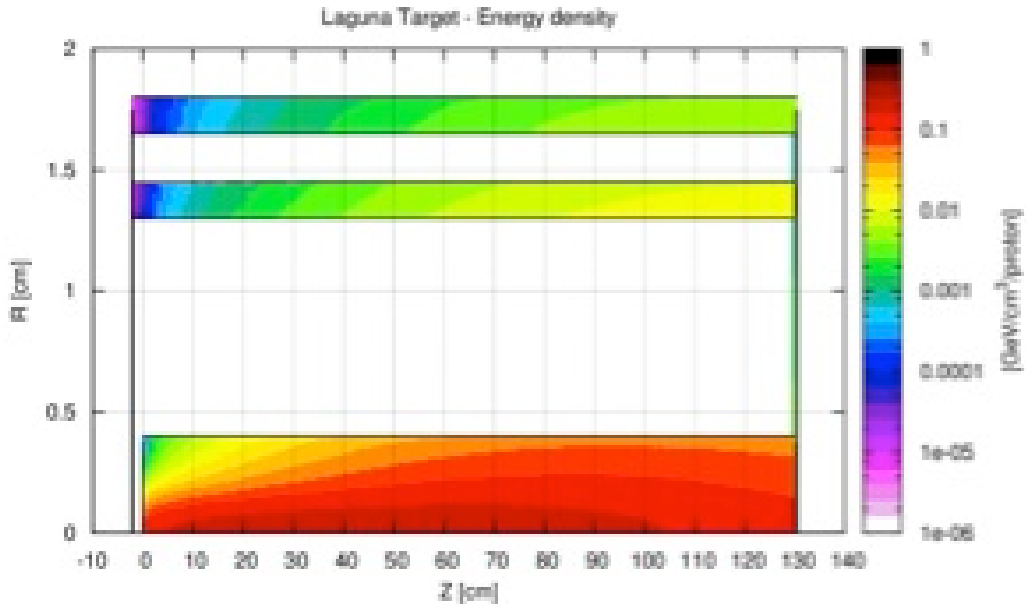


Figure 4.27: FLUKA energy deposited study.

Table 4.7: Energy density and power on target components. MUST CHECK IF THE NUMBERS ARE PER PROT OR PER CYCLE!

Component	Energy deposited [kJ/pulse/prot]	<Power> [W]
Graphite rod	52.7	800
Graphite pipe	12.3	2000
Be pipe	6.7	1100
Upstream Be window	$52.7 \cdot 10^{-4}$	8
Downsteram Be window	$20.2 \cdot 10^{-2}$	33

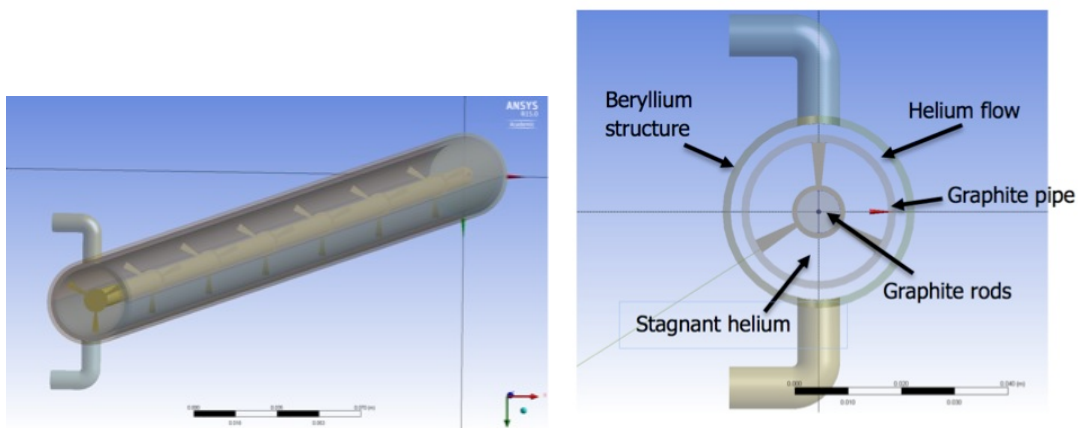


Figure 4.28: Target design proposal. In the cross-section view on the right, the inner graphite rod is shown at the venter. The outer structure with cocentring Graphite and Be tubse such to allow the He to flow through. The volume between the graphite rods and the Be structure will be in vacuum.

facturing reasons, the graphite bar is composed of 6 -7 different parts (20 -25 cm long). The graphite rods are supported and kept aligned with the center of the outer pipes. The first carbon pipe is used to extract heat by radiation to cool down the graphite core. Externally, the pipe is cooled down by helium flow circulating through a 2 mm gap between them.

A thin horizontal surface will be used to force the flow to go through the whole length on the upper half, flow downwards in order to cool down the windows and come back through the lower half (Figure 4.29). The main design parameters are summarised in Table 4.8.

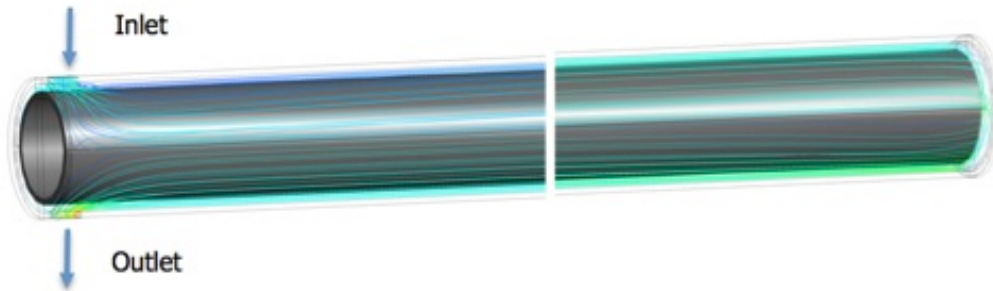


Figure 4.29: He flow circulation.

Table 4.8: Key design parameters for the 400 GeV target option.

Component	Inner diameter [mm]	External diameter [mm]	Length [mm]
Graphite rod	-	8	1300
Graphite pipe	13	14.5	1300
Be pipe	16.5	18	1326

#### 4.5.4.3 Engineering studies

##### FEM simulations

Regarding the graphite rod, a thermal analysis was performed considering radiation cooling with the inner graphite pipe and considering a conservative external film coefficient of  $300 \text{ W K}^{-1} \text{ m}^{-2}$  and an external average temperature of  $50 \text{ }^\circ\text{C}$  for the helium. This boundary condition is taken as a first approach and the relative helium flow has to be evaluated. As a first estimate, a 5-10 g/s helium flow at around 15 bar would be necessary to keep the temperatures of the beryllium pipe relatively low. With these boundary conditions the maximum temperatures reached in steady-state are:  $1387 \text{ }^\circ\text{C}$  for the graphite rod (Figure 4.30),  $202 \text{ }^\circ\text{C}$  for the inner graphite pipe and  $126 \text{ }^\circ\text{C}$  for the beryllium structure (Figure 4.31).

The transient effect of the single pulse was also evaluated for checking the stresses generated on the target core. The pulse is composed by two bunches with intensity  $3.5 \cdot 10^{13}$  protons each with a pulse length of  $10.5 \mu\text{s}$ , separated by 50 ms.

The temperatures reached in sequence starting from room temperature are shown in Figure 4.32.

The sequence shows the temperatures reached:

a - after the 1st pulse

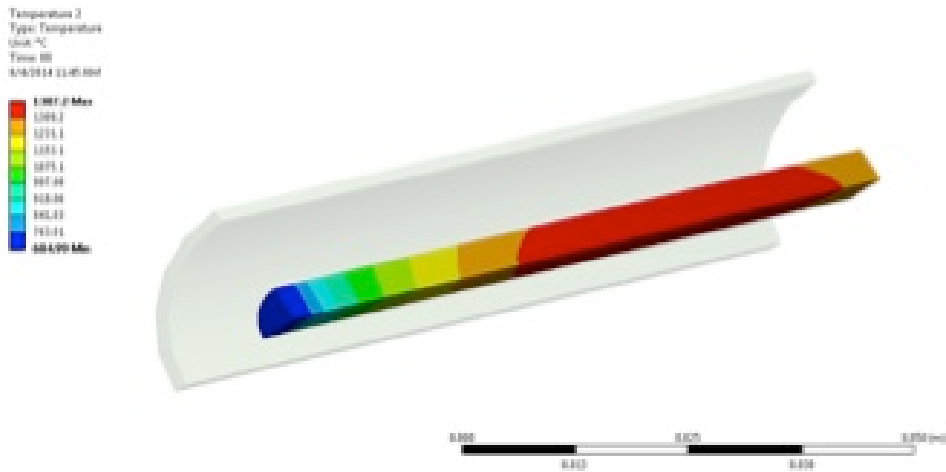


Figure 4.30: Graphite rod steady state temperature profile.

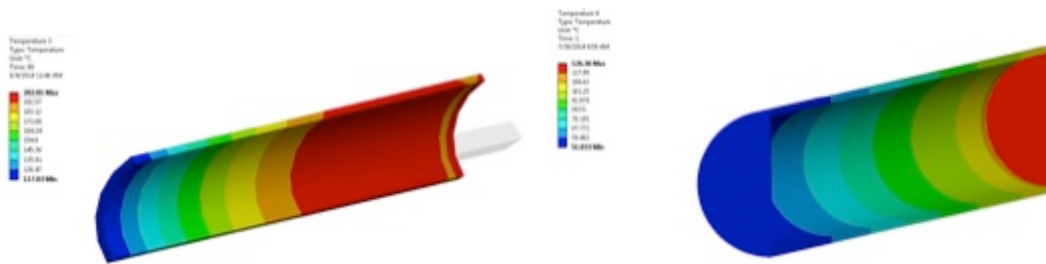


Figure 4.31: Graphite (up) and Beryllium (down) pipe steady-state temperature profile.

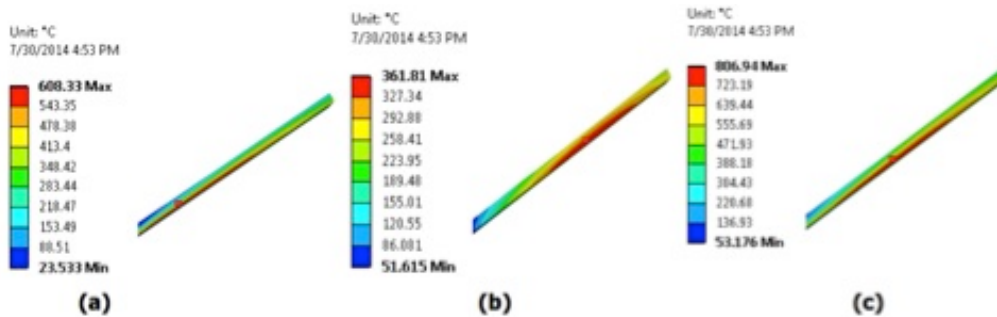
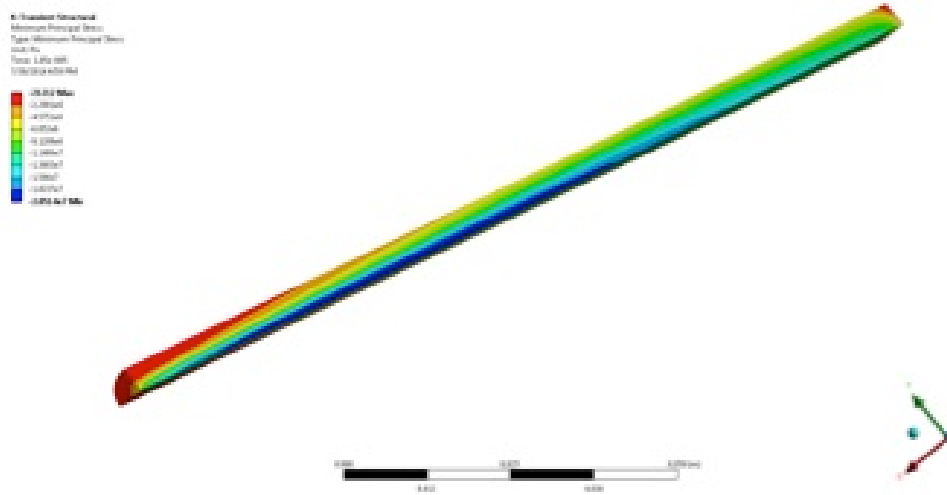


Figure 4.32: Thermal transient analysis for the first pulse (a): 1st pulse, (b): pause, (c): 2nd pulse.

**b** - cool down between 1st and 2nd pulse (50 ms)

**c** - after 2nd pulse

The resulting maximum compressive stresses are 20 MPa (Figure 4.33). When considering



**Figure 4.33:** Structural transient analysis for the first pulse.

a steady-state case the stresses are quite low (0.75 MPa) due to the homogeneity of the temperature field and the value of the stresses when 1 pulse is added is also close to 20 MPa. This value has to be then considered as a cyclic load.

The fatigue limit of pure graphite is ranging between 26.9 and 31.3 MPa [?] so, as a first approach, the rod (even if considered as a full block) seems to be working in safe conditions but close to the material limitations. A structural analysis was performed to evaluate the effect of the helium pressure of 15 bar on the beryllium structure, the resulting maximum stress is 36 MPa in proximity of the window. A bending radius of 1 cm has been taken into account in the design. The maximum displacement was checked for the whole structure kept in cantilever considering the weight of the whole structure. A displacement of 0.43 mm on the free end is found (Figure 4.34). Being the gap available 9 mm, there would be no risk of contact between the target and the horn.

#### 4.5.4.4 Summary

With the proposed design, the target seems to be working in safe conditions from the mechanical point of view. The flow characteristics for the He cooling system could be studied in order to obtain the optimal working condition. This study represents a first approach to the target design.

#### 4.5.5 Helium cooled graphite target for 50 GeV beam

For this study the feasibility of a T2K style helium cooled graphite target [75] has been investigated for use in the higher energy and rep rate beam. The beam parameters used for this target study are:

- Beam energy : 50 GeV
- Sigma : 0.424 cm

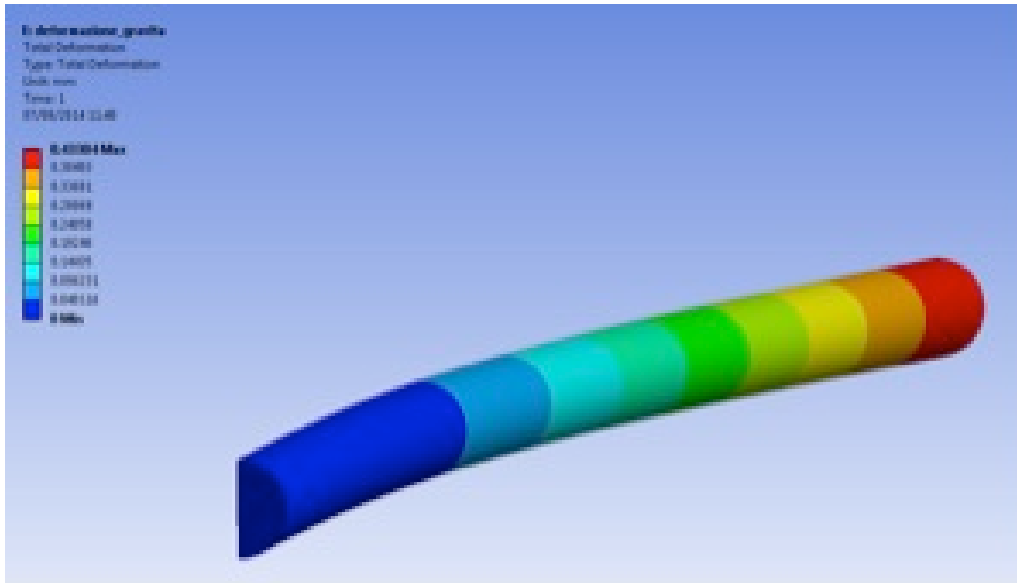


**Figure 4.34:** Deformation of the structure due to its own weight.

- Protons per pulse :  $2.7 \times 10^{14}$
- Pulse repetition rate : 1 Hz (corresponding to approx. 2 MW of beam power)

The target studied has a diameter of 26 mm and a length of 900 mm. The length of a single piece monolithic graphite target is limited by the block size of the graphite. For IG-43 the maximum block size is  $300 \times 540 \times 850$  mm and a 1 metre length is achievable if cut from corner to corner. If required a longer target could be made using a segmented design or by joining the graphite rod. The cooling capacity has been significantly increased from T2K by using a higher helium mass flow rate of 70 g/s and to keep the pressure drops and flow velocity to a reasonable level the operating pressure has increased to 5 bar.

The energy deposition in the target rod has been estimated by FLUKA [?] for a typical high density isotropic nuclear grade graphite such as Toyo-Tanso IG-43 or POCO ZXF-5Q. This is simulated as carbon with a density of 1.85 g/cc.

The total integrated power deposited in the target is estimated to be:

$$8.414357 \cdot 10^{-1} \text{ GeV/primary} \times 1.602 \cdot 10^{-10} \text{ J/GeV} \times 2.7^{14} \implies 36.4 \text{ kJ/pulse@1Hz} = 36.4 \text{ kW} \quad (4.2)$$

which for the foreseen 1 Hz operation corresponds to 36.4 kW of beam power. The peak energy deposition in the target is:

$$5.586 \cdot 10^{-3} \text{ GeV/cc/primary} \times 1.602 \cdot 10^{-10} \text{ J/GeV} \times 2.7 \cdot 10^{14} = 241.6 \text{ J/cc} \quad (4.3)$$

And per gram of material:

$$241.6 \text{ J/cc} / 1.85 \text{ g/cc} = 130 \text{ J/g} \quad (4.4)$$

For this study temperature dependant material properties of the fine grain nuclear grade isotropic graphite, Toyo-Tanso IG-43 were used. These properties are given in the graphs and table below [80].

The cooling fluid for this study is assumed to be helium. Helium has good thermal transport properties as well as being low density which makes it transparent to pions and low activation with tritium being the main product. Helium was treated as an ideal gas with the properties as given in the table below.

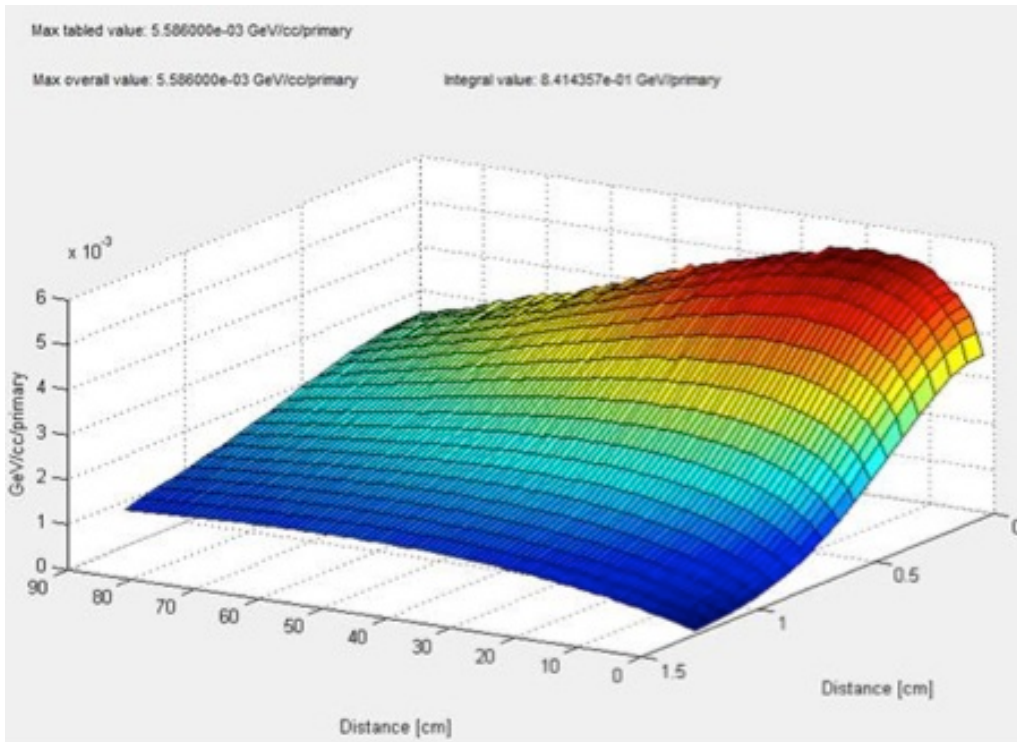


Figure 4.35: Energy deposition in the target head as simulated by FLUKA.

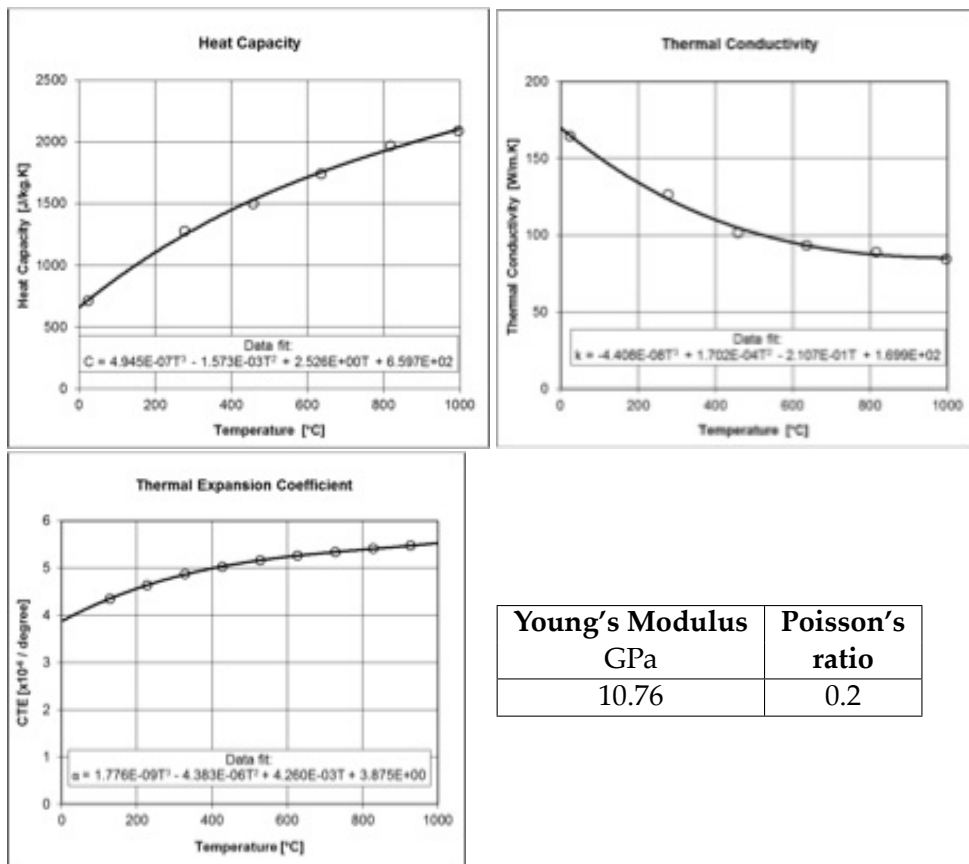


Figure 4.36: Graphite head parameters.



**Table 4.9:** Model parameters for the target He cooling.

Molar Mass	kg/kmol	4.00
Specific heat at constant pressure	J/kg.K	5240
Dynamic viscosity	kg/m.s	1.86E-05
Thermal conductivity	W/m.K	1.42E-01

Using the FLUKA energy deposition, a Conjugate Heat Transfer (CHT) model was created using Ansys CFX [78]. This type of coupled Computational Fluid Dynamics (CFD) and thermal heat transfer model is important for a gas cooled target as the bulk temperature of the cooling fluid rises significantly along the length of the target.

The cooling channel around the target is modelled as an annular duct with a 4 mm gap. The turbulence model used in the analysis was Shear Stress Transport (SST) which is generally recommended for this type of analysis and yields accurate heat transfer coefficients with low grid sensitivity. The reference pressure used in all models was 1 atmosphere and therefore all pressures shown are gauge pressure. Figure ?? shows the results of the analysis assuming a steady state heat load by time averaging the FLUKA results. The maximum core temperature is 767K (494°C).

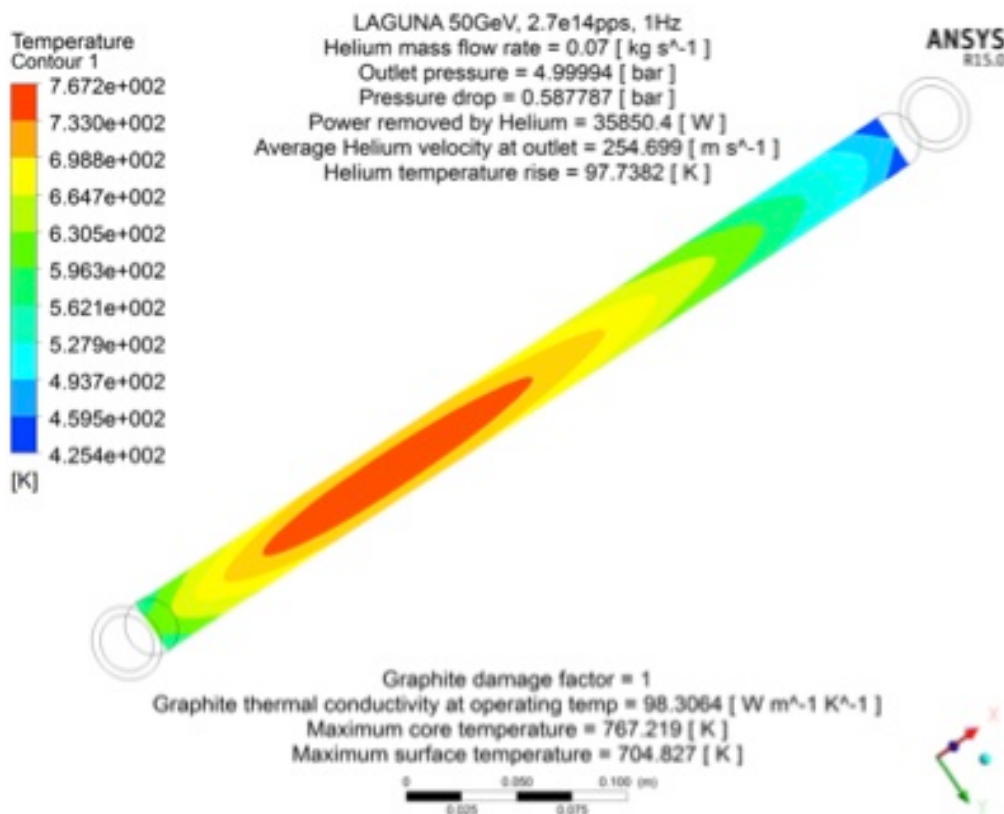


**Figure 4.37:** Steady state heat load of the target head.

The results from the CHT analysis were imported into an ANSYS Mechanical [79] simulation to calculate the thermal stresses in the target. Figure ?? shows that an equivalent stress of 1.8 MPa is predicted which is low compared the strength of IG-43 which is quoted as in tension, 54 MPa in bending and 90 MPa in compression [80].

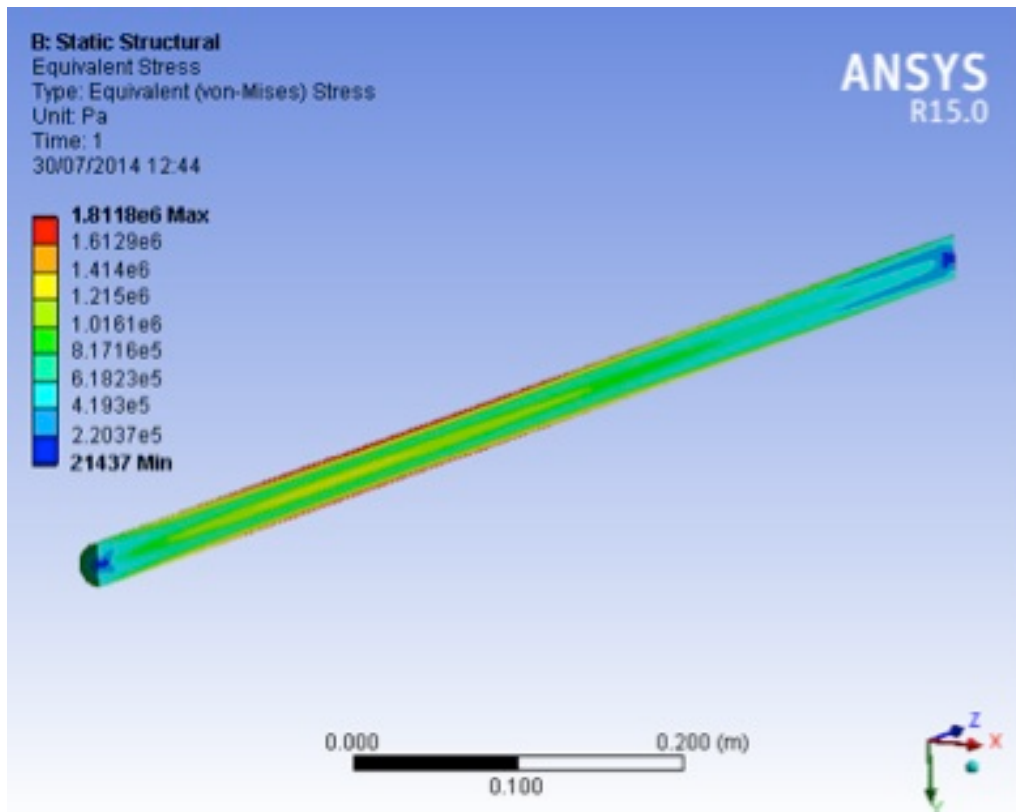


Figure 4.38: Stresses of the target head.

The thermal conductivity of graphite has been shown to significantly degrade with radiation damage. The graph below shows how the thermal conductivity of a similar graphite Toyo-Tanso IG-11 reduces with radiation damage from fast neutrons [81].

The reduction in thermal conductivity is dependent on irradiation temperature and it is seen that irradiation at higher temperatures has a less detrimental effect, possibly because the damage effects are annealed out. This is why the T2K target was designed to run at a high temperature which is possible with helium cooling. To investigate how the potential loss in thermal conductivity might affect the target the same CHT and Mechanical models were run but the thermal conductivity was reduced by a factor of 4, this being the worst case shown in the figure above for fast neutrons and assuming similar radiation damage effects result from high energy protons. Figure ?? shows that with this decrease in thermal conductivity, the core temperature of the target has increased to 971 K (698°C). This is still an acceptable operating temperature for graphite but there is now a much stronger thermal gradient as the surface temperature has not changed. As a result of the increased thermal gradients the Von-mises equivalent stress in the target has increased to 7.6 MPa. However this would still seem to be an acceptable stress level with a factor of safety of 4.9 based on the tensile strength of IG-43.

To study the transient, pulse to pulse (1 Hz) behaviour of the target a transient thermal model was created in ANSYS mechanical. The Heat Transfer Coefficient and near wall temperatures from the ANSYS CFX simulation were mapped onto a 2D axisymmetric model. The heat deposition from FLUKA was applied to the model at a 1 Hz rep rate. Deposited heat was averaged over a 100  $\mu$ s time step which is small enough that no significant conduction takes place. The results of this simulation are shown in Figure ?? and it can be seen that it takes approximately 1 minute for the target to reach a ‘steady state’ operating condition.



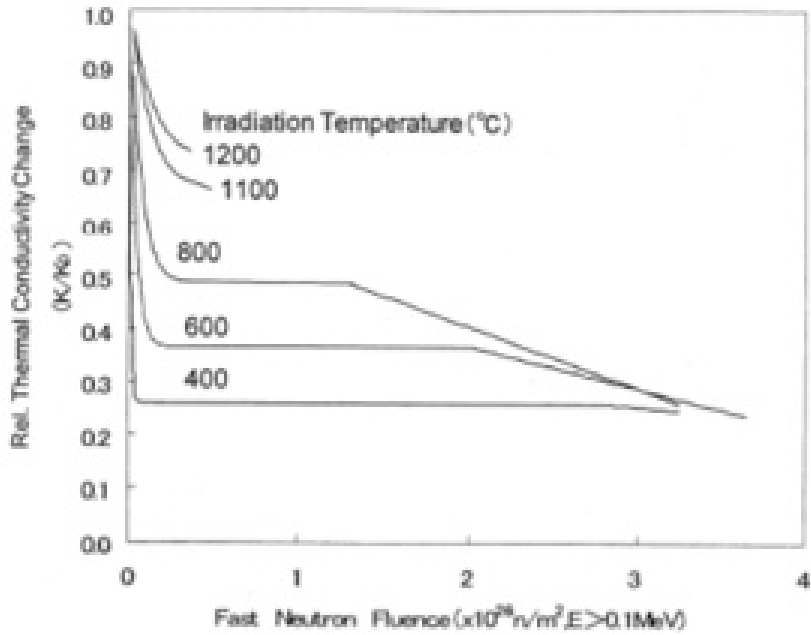


Figure 4.39: Thermal conductivity of the target.

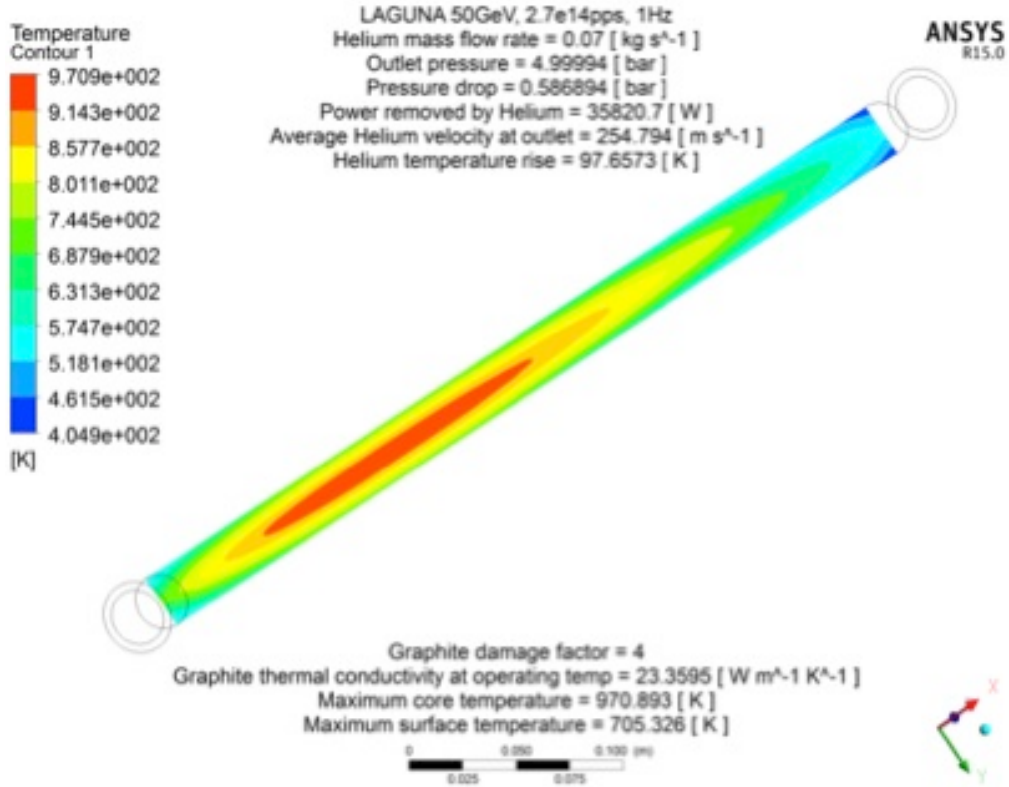


Figure 4.40: Thermal conductivity of the target.

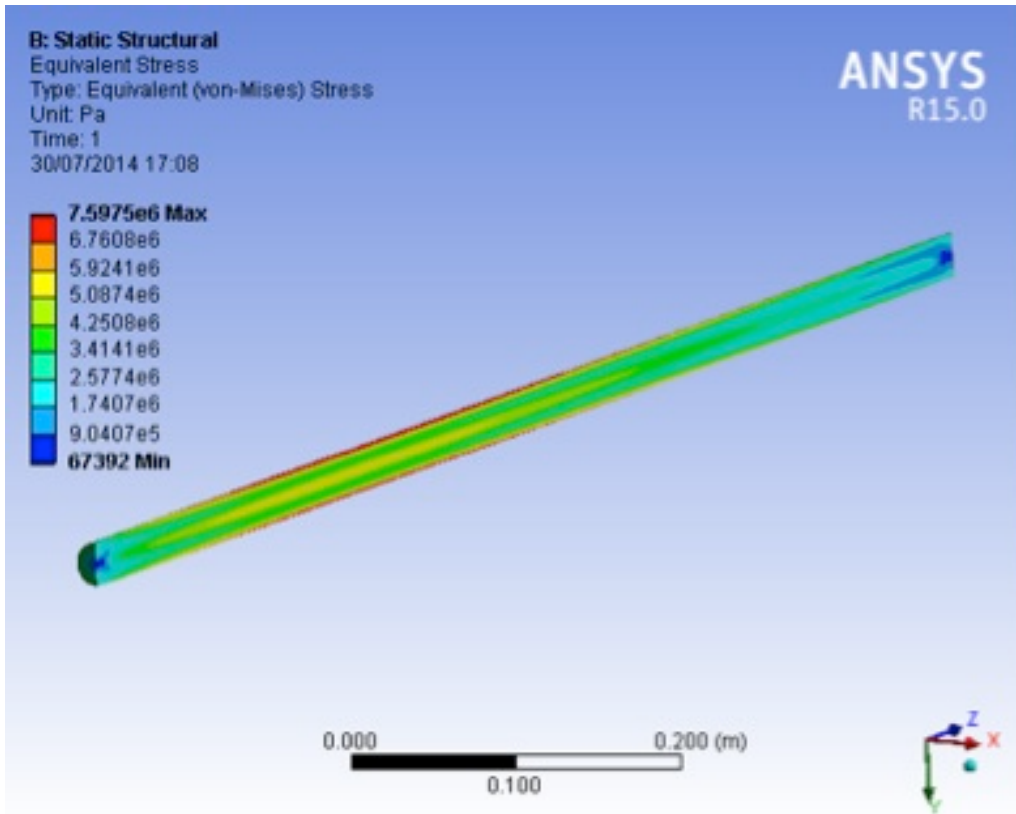


Figure 4.41: Von-mise stresses.

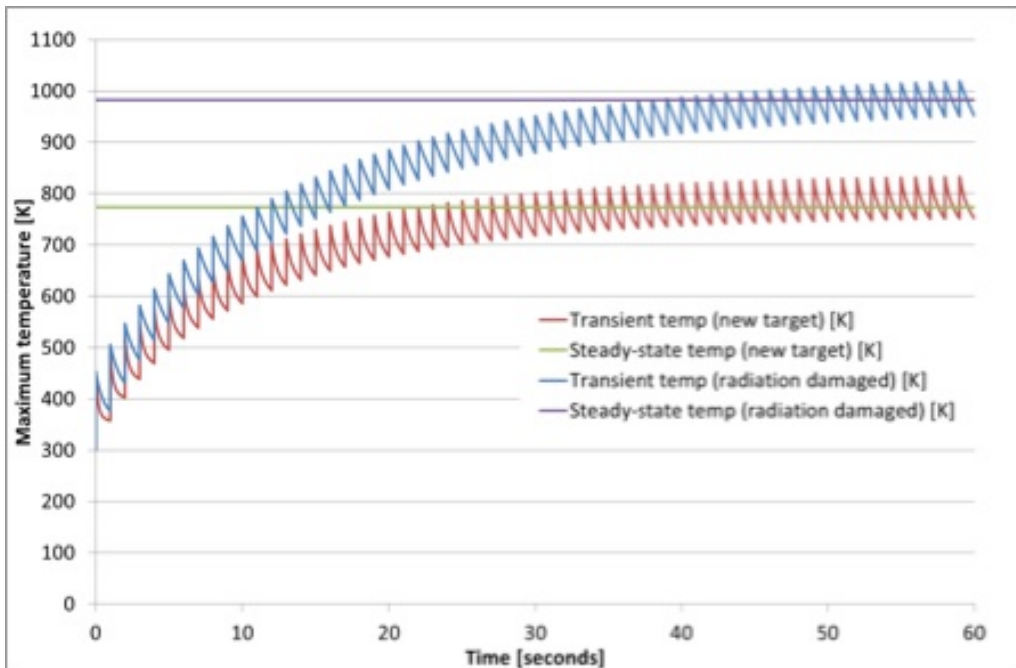


Figure 4.42: Heat deposition.

Using an ambient temperature (23 °C) specific heat capacity of 712 J/kgK the first pulse temperature jump is expected to be:

$$130\text{J/g} / 0.712\text{J/g K} = 182.6\text{ K} \quad (4.5)$$

However in this ANSYS simulation the temperature jump from first pulse is 153 K and this decreases to 81.5 K when the target approaches a steady-state operating condition. This effect is due to the highly non-linear temperature dependant specific heat capacity of graphite which are included in the ANSYS model.

The temperature distributions from the transient simulation were imported into a stress analysis. Table ?? shows the results for a new target at 3 different points in time. The maximum

**Table 4.10:** Stress distributions in the target versus time. Units are in MPa.

New graphite	Hoop stress		Radial stress		Longitudinal stress		
	von-Mises	Max	Min	Max	Min	Max	Min
Just after first pulse	2.89	1.99	-2.90	1.23	-2.90	1.95	-5.72
Just after 59th pulse	2.75	2.75	-2.75	1.08	-2.75	2.76	-5.46
Just after 60th pulse	1.54	1.53	-0.88	0.21	-0.88	1.54	-1.76

von-Mises stress is found to be just after the first pulse for a new target. When the target heats up the specific heat capacity increases which reduces the temperature jump, however this is offset by an increase in thermal expansion and decrease in thermal conductivity of the graphite. The net effect is that the pulse to pulse thermal stress remains almost constant. The thermal stress cycling from pulse to pulse is 1.2 MPa.

For a radiation damaged target the stress after the first pulse is identical as the pulse is too fast for any conduction to take place. However as the target approaches a steady operating condition the equivalent stress increases to 8.33 MPa. The thermal stress cycling from pulse to pulse actually reduces slightly to around 1 MPa (see Table ??).

**Table 4.11:** Stress distributions in the irradiated target versus time. Units are in MPa.

Damaged graphite	Hoop stress		Radial stress		Longitudinal stress		
	von-Mises	Max	Min	Max	Min	Max	Min
Just after first pulse	2.88	1.99	-2.89	1.24	-2.89	1.95	-5.70
Just after 59th pulse	8.33	8.33	-6.65	2.27	-6.65	8.33	-13.25
Just after 60th pulse	7.28	7.28	-5.12	1.43	-5.12	7.29	-10.24

The target is subject to inertial stresses that act in addition to the pulse to pulse transient thermal stress described above. These inertial stresses occur where the beam energy deposition is faster than the characteristic expansion time of the target, where the expansion time is equal to the characteristic target dimension divided by the speed of sound in the material.

If the energy deposition time is very short the heating becomes effectively instantaneous. Where this is the case the material response can be approximated as constant volume heating which gives rise to a stress that is proportional to the temperature jump. This stress then propagates through the target in the form of stress waves. As long as the magnitude of the stress waves is below the point where material yielding occurs then they are elastic waves (not plastic or shock waves) that travel through the target material at the speed of sound. The waves cause stress and strain oscillations in different directions at frequencies defined by the characteristic dimensions of the target and the speed of sound of the target material. As a conservative

start point the analysis that follows is based on the premise that the stress induced in the target is always below the yield stress and all the results presented below are based on a linear relationship between stress and strain.

The inertial stresses generated in the graphite target rod by a single 3 micro-second long beam spill were calculated using a transient structural analysis in ANSYS. Fixed (i.e. not temperature dependent) room temperature material properties were assumed. The rate of energy deposition during the spill was assumed to be uniform such that any bunch structure of the beam was ignored. Once it had been applied in the model the temperature distribution was assumed to be fixed, meaning that the spreading of heat energy by thermal conduction was not included. The target was assumed to be supported from the upstream end as a cantilever.

The inertial stress response on the target axis at the position where the temperature rise is at a maximum is shown in Figure ???. The stresses increase during the beam spill (first 3 micro-seconds) while the temperature is being ramped up, after which many stress oscillations take place. The radial oscillation period of about 16 micro-seconds and longitudinal oscillation period of about 1.4 milli-seconds are clearly visible. Von-Mises stress peaks of around 11 MPa are predicted.

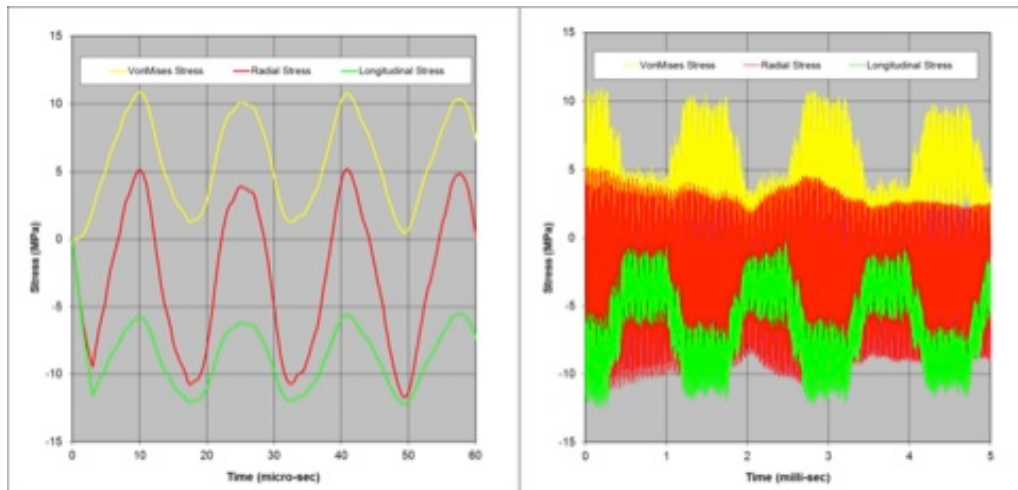


Figure 4.43: Target head internal stress.

## 4.6 Focusing elements

The horn and reflector are composed of two cylindrically symmetric conductors of thin aluminium alloy, specially shaped to produce an azimuthal magnetic field along the beam axis that focuses the secondary mesons emitted from the target into a nearly parallel beam. This field focuses charged particles of the correct sign over the interesting energy range and defocuses the particles of the opposite signs. The experimental requirement is for a neutrino energy peaked around 2 GeV, which corresponds to a pion energy of roughly 5 GeV. The focusing system to be developed in order to achieve these energies will consist of two magnetic lenses, a horn and a reflector. The exact shape, dimensions and current will be determined in close collaboration with the experiment in order to maximize the neutrino yield within reasonable engineering parameters. A critical parameter given the low energy of the focused pions will be to maximize the angular acceptance of the focusing system, possibly up to 100 mrad or more. This requirement will also imply that the target must be very close or partially embedded into the horn. A very preliminary layout with a simple horn and reflector has been used up to now in order to define the basic parameters and to perform the initial radiological estimations. The final horn and reflector current will likely be in the 200-300 kA range depending on the final optimization. The minimum pulsing cycle should be 3.6sec and the flat top duration of few 20 micro-seconds. The current is produced from the discharge of a capacitor bank to the horn/reflector in resonant mode. Key requirements for the construction of both horn and reflector include:

- The shape of the inner conductor must be carefully machined to respect the required geometry, thus maximising particle focusing performances and minimizing the electrical forces, in particular in the thin inner conductor;
- The horn and reflector are electrically pulsed. The conductors must therefore be isolated from the supporting structure using non-organic insulation material.
- The distribution of the electrical current from the striplines to the equipment should be as distributed and equalized as possible;
- The inner conductor and end plates must be as thin as possible to minimize absorption losses from the secondary particles;
- The structure will be subject to ponderomotive forces inducing fatigue effects. In addition, the radiation effects in the conductors may reduce the mechanical strengths of the used material. The system must be build such to allow at least 10<sup>7</sup> pulses, corresponding to about 4 years of operation in the facility at 200 days per year;
- The horn and reflector need to be water-cooled. The circuit can be open on the recuperation tank but must be hermetic on the equipment side to minimize the production of vapour in the beam volume. Under the proposed design, they will be mounted on shielding modules that are then lowered into the steel shielding channel;
- The remote displacement the horn in x,y should be possible for alignment with respect to the target.

Easy exchange of the horn and reflector in case of failure should be foreseen.

In order to protect the neck of the horn and reflector from an incorrectly steered primary beam, a collimator placed upstream the target should be envisaged. It should be able to withstand few shots at maximum intensity without failure.

### 4.6.1 Design overview

Apart from their inner and outer conductor shaping, the horn and reflector systems are conceptually identical. We have chosen two independent systems for reasons of flexibility. Since the horn and reflector are highly irradiated, organic insulation material has to be avoided: the use of an adapting pulse power transformer with low voltage on the horn/reflector solves this problem since the use of glass mica compounds becomes possible. A maximum of components have to be kept outside the target chamber and are located in the service gallery. The inner conductor, end plates and, to a smaller extent, the outer conductor have to be as thin as possible to minimize the absorption losses of secondary particles. Higher currents lead to higher cone angles of the inner conductor, so reducing the path and the corresponding absorption of the secondary particles through the aluminium walls. The horn and reflector are electrically pulsed. Therefore, the structure is submitted to dynamic repetitive forces inducing fatigue effects. The inner conductor is, in first approximation, forced into traction when pulsed. The design goal is to provide full reliability over at least  $10^7$  current pulses. Precise centring of inner and outer conductors and accurate azimuthal thickness of the wall are very important since electromagnetic forces tend to pull the conductor into the centre line, thus creating alternate flexion. The degree of revolution symmetry of the magnetic field distribution has to be as high as possible, especially on the current feeding side of the magnetic volume: a basic condition to be fulfilled is that the currents in the feeding strip-lines be equal. The horn and reflector need to be water-cooled. The high radiation level contributes to the production of a highly corrosive atmosphere, and therefore, the internal space between the inner and outer conductor will be filled with Helium. Based on CNGS experience, metal surface treatment is not needed. Quality and reliability of the electrical contacts is a particularly critical issue. One should keep in mind that contact pressure must not vanish when pulsing. Precise displacement of the remotely controlled horn and reflector is crucial in order to tune the beam position and angle at the muon counters (and thus at Phyasalami). Easy exchange of horn or reflector without human intervention is compulsory. An overhead crane with remote control and video camera is proposed, complemented with special tools for connection/disconnection from the feeding strip-lines.

### 4.6.2 Electric circuits

The maximum operational currents retained are  $I_H = 291$  kA and  $I_R = 198$  kA. Fatigue effects caused by 10 million alternate tractions are taken into account when considering the mechanical stress limit. Stress calculations and experimental results from the CNGS beam operation confirm that the expected lifetime corresponding to typically one year year of operation, is realistic.

DESCRIBE HERE REQUIREMENTS FOR EL SYSTEMS

### 4.6.3 General Mechanical concept

The magnetic horn for the present conceptual design as seen from the electrical connection side is shown in Figure 4.72. The construction of the horn and reflector is very similar. The attachments to the flexible copper grids connected to the feeding strip-lines are visible. The flexibility of these grids allows the horn or the reflector to be moved in the up/down directions as required during the alignment procedure. The copper grids are made of 8 flexible copper bars bolted into the aluminium connection bars. Each grid assembly is then silver-plated.

Figure 4.45 shows the general assembly of the horn station and its overall dimensions. The horn is screwed onto a support frame. This assembly is picked up by two hooks, transported and precisely placed in position by means of the overhead crane onto a base frame. The posi-

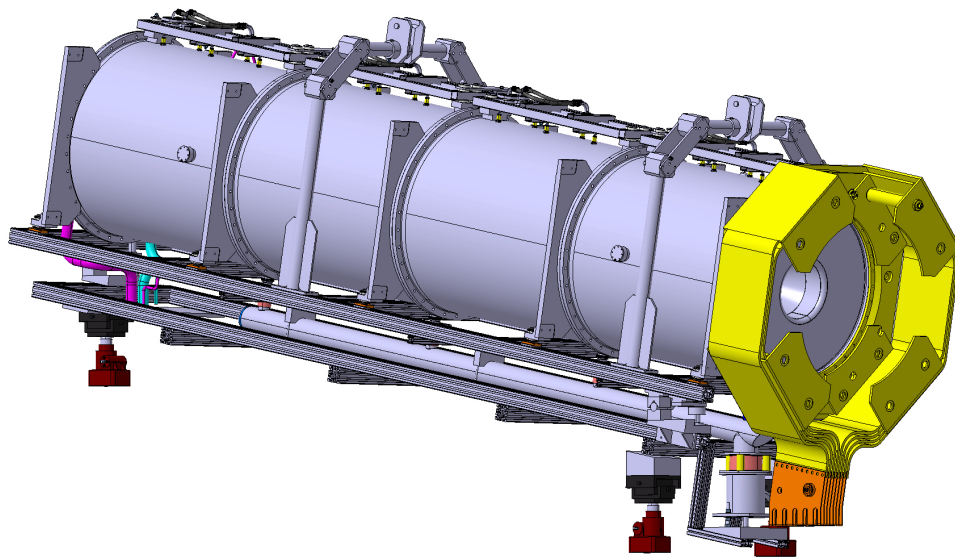


Figure 4.44: Downstream view of the horn.

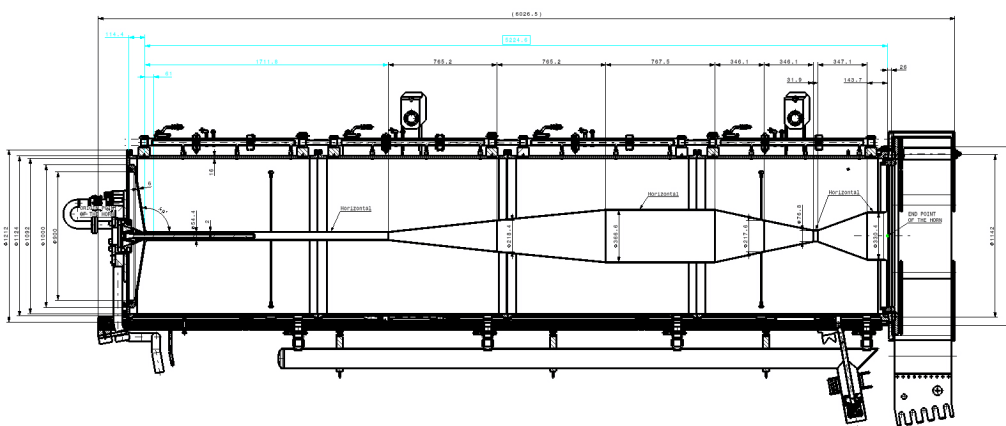


Figure 4.45: Drawing of the horn showing its main dimensions.



tioning is ensured by special vertical girders so that the support frame comes accurately into place when deposited.

### The inner conductor

It is made of several pieces. The neck region is machined out of Al-6061-T6. The remaining part is an assembly of several parts welded (e-beam) together, each one made also out of Al-6061-T6 (2 mm thick metal sheets rolled and welded).

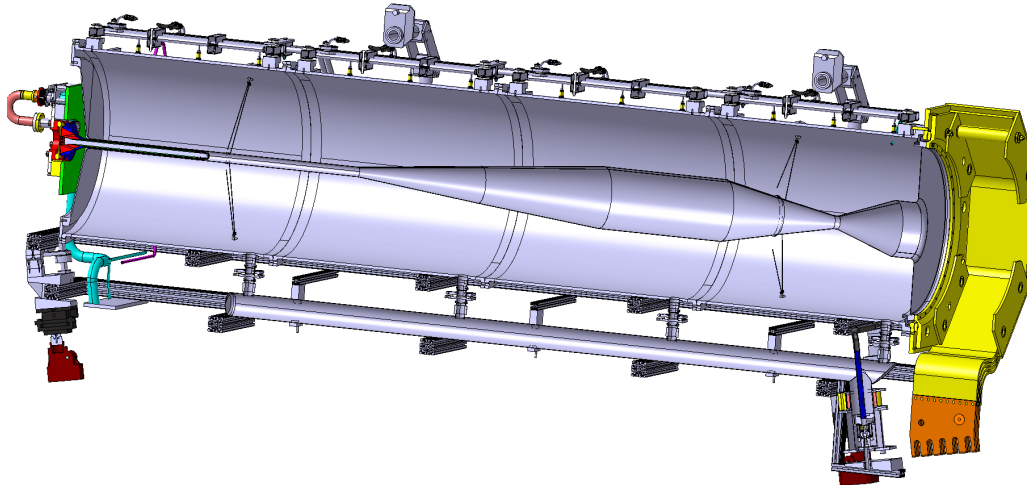


**Figure 4.46:** Cut view of the horn showing the integrated target, striplines, water nozzles, feedings and striplines.

### The outer conductor

This conductor is cylindrical with a wall thickness of 16 mm and is an assembly of several parts screwed together, each one made out of Al-6061-T6. The inner diameter of the outer conductor is machined with a maximum ovality default of 0.2 mm. Inner/outer concentricity is 0.1 mm. Centring of the inner conductor is achieved with adjustable centring appliances using stainless steel cables to hold and precisely centre the inner conductor with respect to the outer conductor. Insulation of the cables with respect to the outer and the inner conductor is obtained by means of Arclex M glass-mica compound spacers.

### Water cooling

The water cooling system of the horns has been designed for both operation phases. An intensity of  $2.5 \cdot 10^{14}$  protons per extraction, (50 GeV, 2 MW nominal power) and an intensity of  $7 \cdot 10^{13}$  protons per extraction, (400 GeV, 750 kW nominal power). The corresponding total power to be evacuated by the horn cooling system at 400 GeV is 25.8 kW and the contribution due to the joule heating has been accounted. For mass-flow estimations the total power dissipated during operation was considered to be around 60 kW. Most of this heat will be removed with a demineralised water spray system by means of 15 nozzles directing the coolant to the inner conductor.



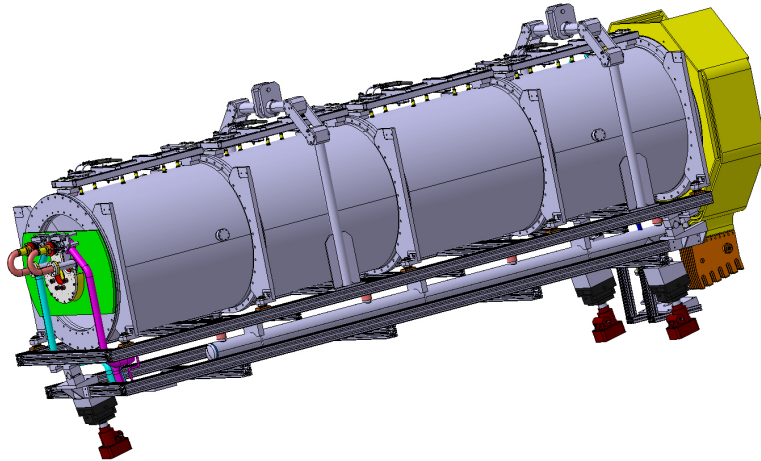


**Figure 4.47:** Cut view of the horn showing the integrated target, and its helium feeds



**Figure 4.48:** Industrial nozzles used for cooling of metal castings.

Assuming a fluid overheating of 8 °C due to the heat removed from the conductor, the required mass flow for the horn is:

$$\dot{m}_{water} = \frac{\dot{Q}_{cooling}}{q_{water}} = \frac{\dot{Q}_{cooling}}{c_{water} \Delta T} = \frac{60000}{4186 \times 8} = 1.8 \text{ [kg/s], or (110 l/min)} \quad (4.6)$$

The cooling systems of horn and reflector are identical. The water circuit is open, with the pump sucking the water from the recuperation tank of the magnetic element and spraying it continuously onto the inner conductor. Industrial sprinklers are distributed along two external pipes located on the upper part of the outer conductor. The water is collected by gravity into the tank located in the strip-line trench. The total amount of cooling water is 165 l/min for both horn and reflector. The flow is monitored with an electronic flowmeter showing the analog flow-value. As additional safety, the water circuit includes a digital flowmeter with an open contact when the flow falls below a predefined threshold. Both flowmeters cut the power supply in case of insufficient flow. The water level in the tank is measured and triggers a warning to refill. It cuts the pump and the power supply when limits are reached.

Two cooling stations running demineralised water will be constructed to cool down the 60 kW and 30 kW of heat load respectively dissipated in nominal conditions by LBNO-LAGUNA horn and reflector. By providing a water overheating of 8C due to the heat removed from the conductor, the required mass flows are respectively is 110 l/min for the horn and 55 l/min for the reflector. A demineralised water network will be available in the operation area, to be used for refilling the cooling system in case of lack of water supply. The water is cooled through a heat exchanger located, with the pump and all auxiliaries, in the services area situated in the vicinity of the hot cell.

#### 4.6.3.1 Electrical systems

The electrical circuits for horn and reflector are identical. The technical requirement is to produce a stable, reproducible field in both focusing elements during the extractions. The precision required is 0.1%. The current cycles are represented in Figure 4.49. for the 400 GeV and the 50 GeV phase respectively.

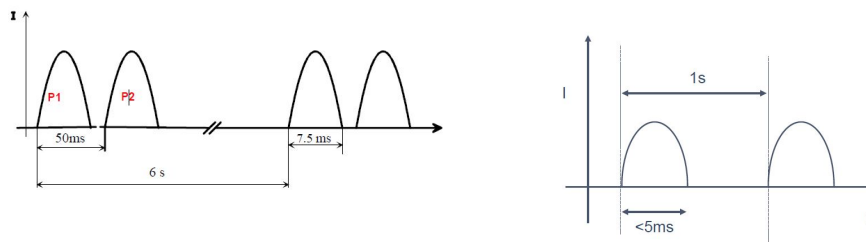


**Figure 4.49:** Current parameters for the phase-I (left) and phase-II(right) operation.

The striplines at the horn region are divided in two parts, one connected to the horn bodies and the second fixed to the auxiliary services block. Figure 4.51 shows the horn side plates, which are connected to the external and internal conductors. The striplines connection is foreseen to be remotely operated. They will be engaged at the end of the vertical positioning stroke, with a contact surface enough to accommodate the electrical connection.

A vise-like system is bolted onto a machined support rigidly fixed to the top surface of the bottom iron blocks, with the face of the fixed jaws just forward of its front edge. The movable

Table 4.12: default

Phase 1 : Beam from SPS @ 400 GeV	Phase 2 : Beam from HP-PS @ 50 GeV
- 6 s cycle	- 1 s cycle
- two extractions/cycle separately by 50 ms	- single extraction per cycle
- beam pulse during $10 \mu\text{s}$ in each extraction	- beam pulse during $4 \mu\text{s}$
- $3.5 \cdot 10^{13}$ protons/extraction ( $7.0 \cdot 10^{13}$ protons/cycle)	$2.5 \cdot 10^{14}$ protons/cycle
- average beam power 750 kW	- average beam power 2.0 MW
Current horn 281 kA	Current horn 291 kA

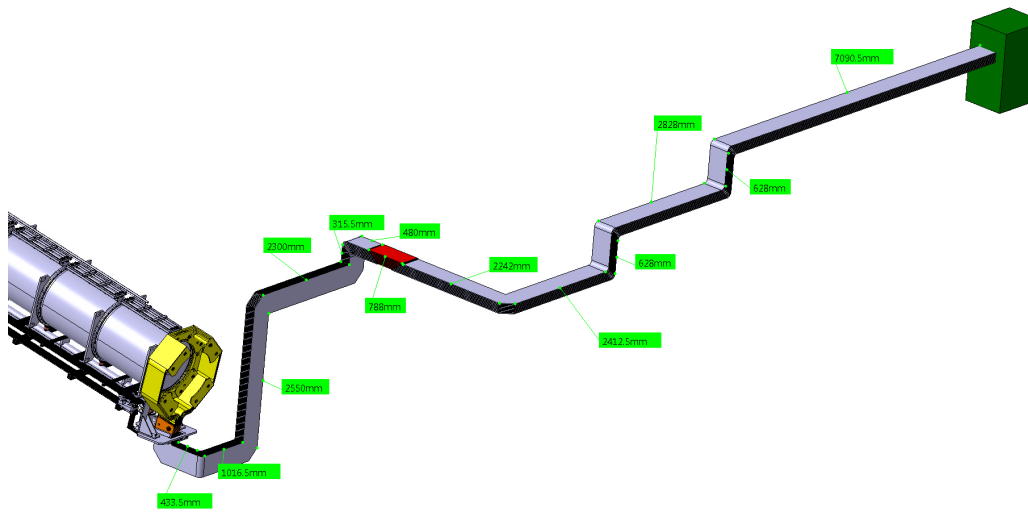


Figure 4.50: Overall view of the striplines. A fast coupling is foreseen under the horn while standard couplings are used elsewhere. Total length is around 25 m.

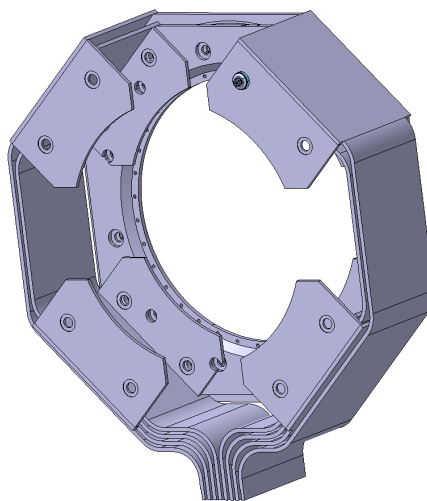
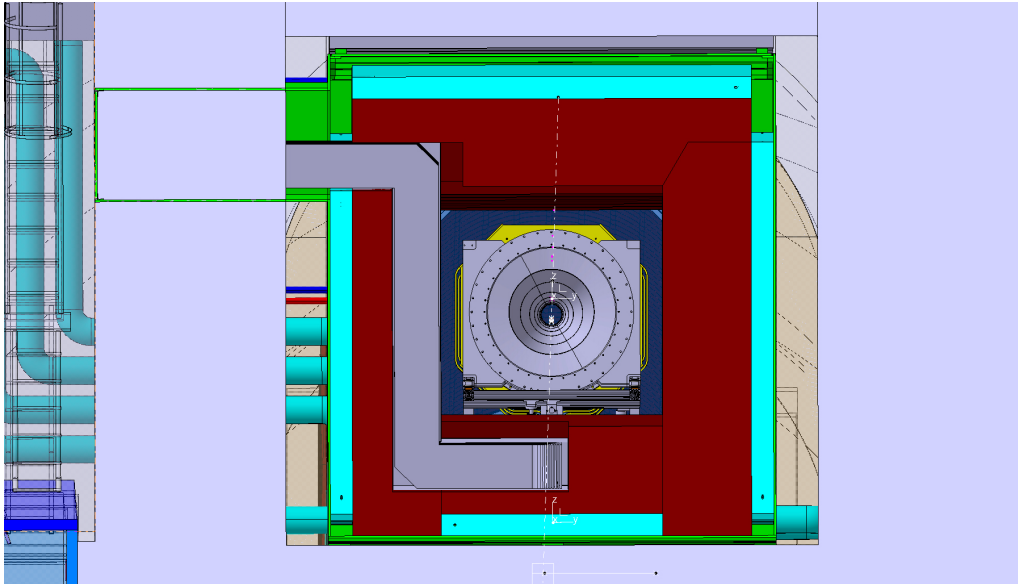
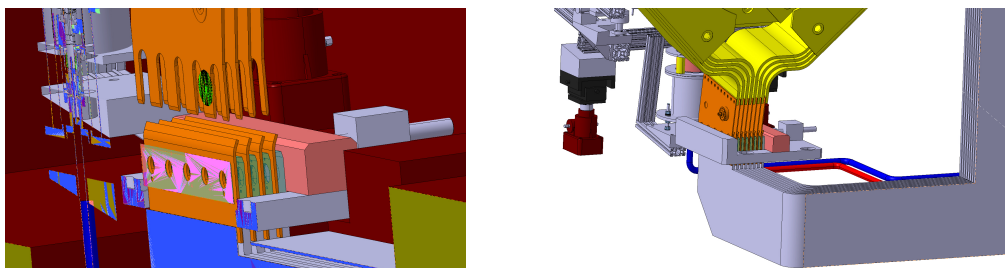


Figure 4.51: View of the aluminium plates attached to the shells of the horn..



**Figure 4.52:** Cut view of the target chamber showing the striplines insertion.



**Figure 4.53:** CDetail of the striplines fast coupling connection. Left: Cut view showing the Cu plates on both sides during the vertical insertion. Right: Detail of the striplines fast coupling connection showing the principle of the clamping mechanism.

jaw may be moved in or out throughout its entire range of motion, vastly speeding up the process of adjustment. A self-locking power square thread screw allows clamping the striplines together. A narrow-clearance hydraulic torque wrench similar to the one depicted in Figure 4.54 will provide the torque required for clamping.



**Figure 4.54:** *Narrow clearance hydraulic torque wrenches.*

The geometry of strip lines was extracted from the model given by CERN. The striplines have a vertical symmetry and therefore only half of the lines were considered. To assess the cooling requirement, only 2 striplines were considered. Figure 4.55 presents the geometry extracted from the CATIA model and imported in ANSYS. It is composed of 2 different materials, namely copper and aluminium. The model was solved in a steady state regime and only the results from the steady state analysis are hereby presented. It was checked that the pulse regime only induced very small raise of temperature in the structure. Therefore the equilibrium temperature reached after several beam and current pulses is dominating the maximum temperature in the structure. This equilibrium temperature is then related to the cooling capacity. It is foreseen to extract the heat by convection, via the helium flow created inside the box. If locally required, small nozzle could enhance locally this cooling capacity. This will have to be defined and analysed in more detail during the full engineering design. To first estimate this cooling requirement a convection boundary condition was used, with a fixed cooling fluid temperature. The temperature in the structure was then assessed against a range of feasible heat transfer coefficient (HTC). For instance one can estimate that the free convection of a flat structure (40 cm long) in an inert Helium environment will be around  $12 \text{ W/cm}^2/\text{K}$ . According to this assessment the HTC range was set from  $5 \text{ W/cm}^2/\text{K}$  to  $500 \text{ W/cm}^2/\text{K}$ .

Figure 4.56 presents the model and boundary conditions as well as the mesh used. Table ?? shows the heat generation rate used according to the data calculated in the FLUKA model. The

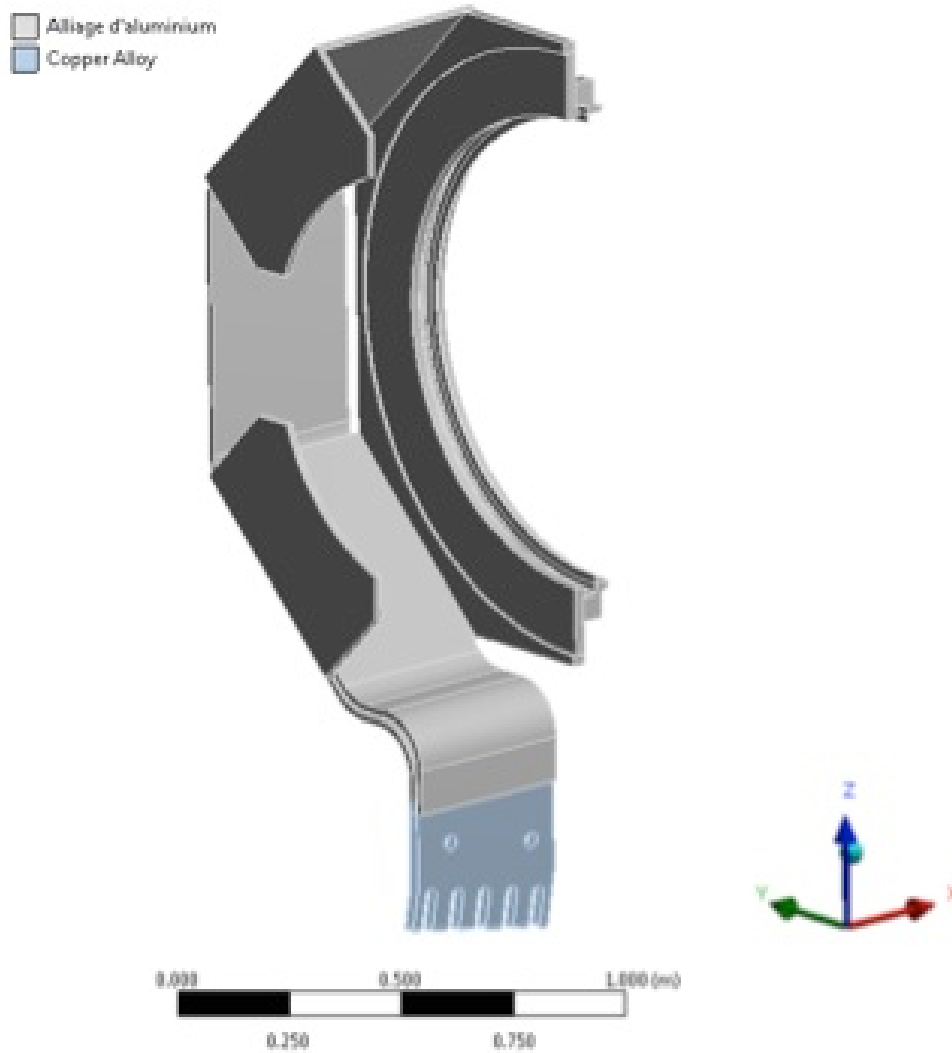


**Figure 4.55:** Geometry and materials used in the thermal analysis of the striplines.

heat density was derived using the total energy deposited in the part and the volume of this part. This analysis is conservative as we have chosen the highest value from the connections part and applied it to the whole structure. Only the copper connector has a separate value also derived from the FLUKA data.

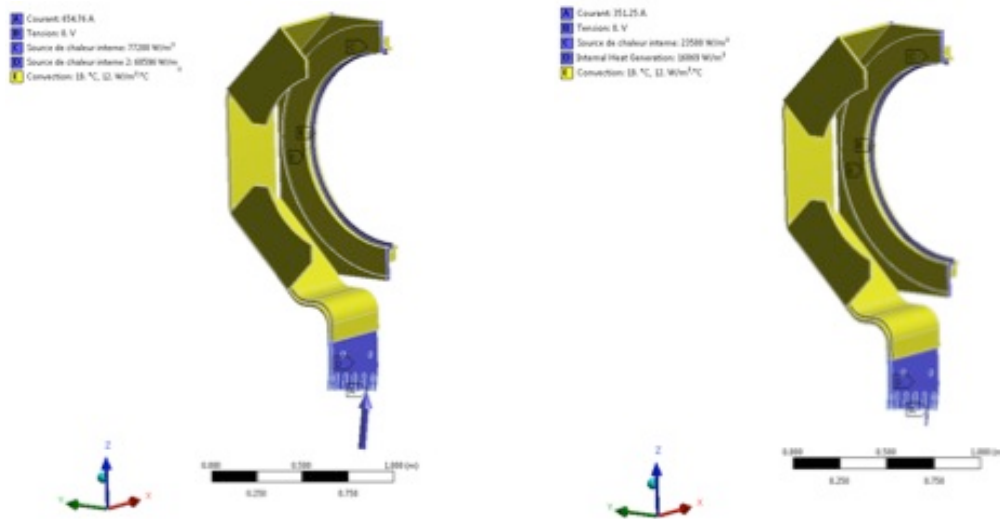


Figure 4.56: Boundary condition of the model. Phase 2 (left), Phase-1 (right).

Table 4.13: Power density calculation according to FLUKA input data.

	Beam Energy (GeV)	Energy per primaries (GeV/p)	Volume (cm <sup>3</sup> )	Energy density (GeV/cm <sup>3</sup> )
Connections	400	3.65	2.90E+05	1.26E-05
Connections	50	5.60E-01	2.90E+05	1.93E-06
Cu-Connector	400	2.06E-02	2.28E+03	9.04E-06
Cu-Connector	50	3.91E-03	2.28E+03	1.71E-06

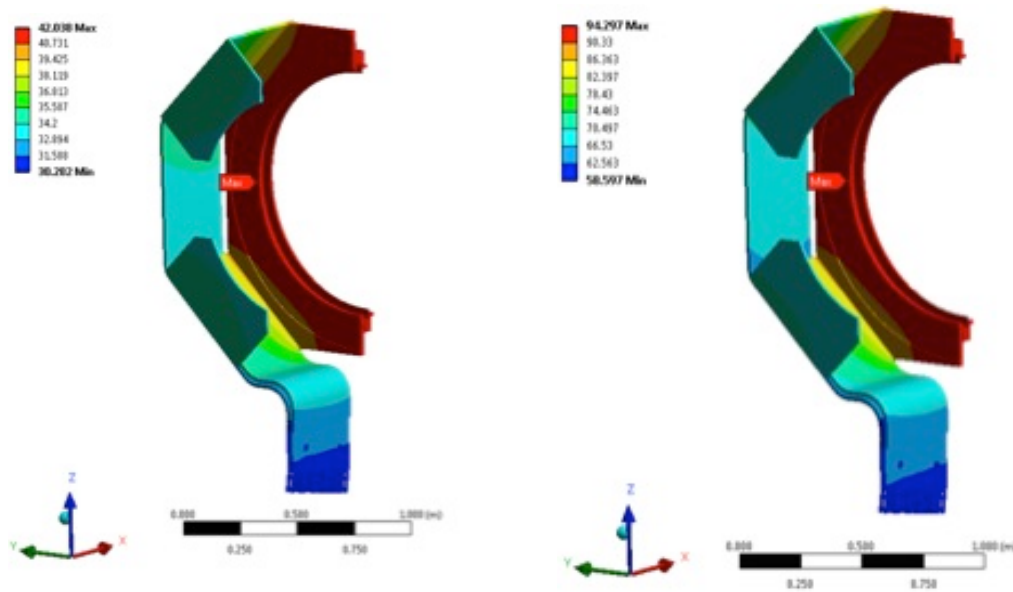
According to Table 4.13, the total power deposited in the overall structure is about 1047.5 W during phase 1 (400 GeV beam) and about 3450.4 W during the phase 2 (50 GeV beam). These values are in good agreement with the finite element calculation, where the reaction probes gave respectively 1044.5 W and 3446.8 W.

Table 4.14: Total power deposition in the real structure.

	Beam energy (GeV)	Part volume (m <sup>3</sup> )	Power density (W/m <sup>3</sup> )	Total power (W)
Connections	400	4.42E-02	23498	1038.4
Connections	50	4.42E-02	77241	3413.3
Cu-Connector	400	5.41E-04	16868.5	9.1
Cu-Connector	50	5.41E-04	68596.5	37.1

Figure 4.57 shows the temperature distribution in the stripline, respectively during phase 1 and 2. The HTC was set to a value close to the natural convection, 12W/cm<sup>2</sup>/K with a fluid temperature of 22 °C.





**Figure 4.57:** Temperature map of the stripline submitted to the beam and current pulse. Left: for the phase 1 (400 GeV beam), Right: for the phase 2 (50 GeV beam) and with an HTC set to a value close to natural convection ( $12 \text{ W/cm}^2/\text{K}$ ).

The maximum temperature during phase 1 reaches  $42 \text{ }^\circ\text{C}$  with this very conservative approach. If for some reason, the HTC was going further down to  $5 \text{ W/cm}^2/\text{K}$  (natural convection in air) the figure 4.58 shows that the maximum temperature during phase 1 will then reach  $70 \text{ }^\circ\text{C}$ . The maximum temperature during phase 2 reaches  $94 \text{ }^\circ\text{C}$  with this very conservative approach. If for some reason the HTC was going further down to  $5 \text{ W/cm}^2/\text{K}$  (natural convection in air) the figure 3 shows that the maximum temperature during phase 2 will then reach  $182 \text{ }^\circ\text{C}$ . Nevertheless, the He inlet at the target chamber is directed towards this region and the forced convection of the helium flow, will keep the structure below these temperatures. According to Figure 4.58, during phase 2 the required HTC will have to be about  $20 \text{ W/cm}^2/\text{K}$ . This kind of value is easily reachable with a forced gas flow (bf see Table 3 - MISSING).

#### 4.6.3.2 Water and He systems

General He and water feeds (inlet and outlets) are foreseen to be maintenance free and remotely operated. They will be engaged at the end of the horn vertical positioning stroke. A push-to-connect design enables quick, simple operation, and no twisting, turning, or wrenching is necessary. The helium pipes feed both the target and the horn, while the water is used for cooling of the horn via the nozzles system.

#### 4.6.3.3 FE Analysis of the horn structure

##### Overview

In order to achieve the calculation, it has been assumed that the mechanical deformation won't have any impact on the heat deposition or the electrical path. Hence, the model is subdivided into one thermal-electrical analysis (transient) and one structural analysis. A one-way coupling has been performed.



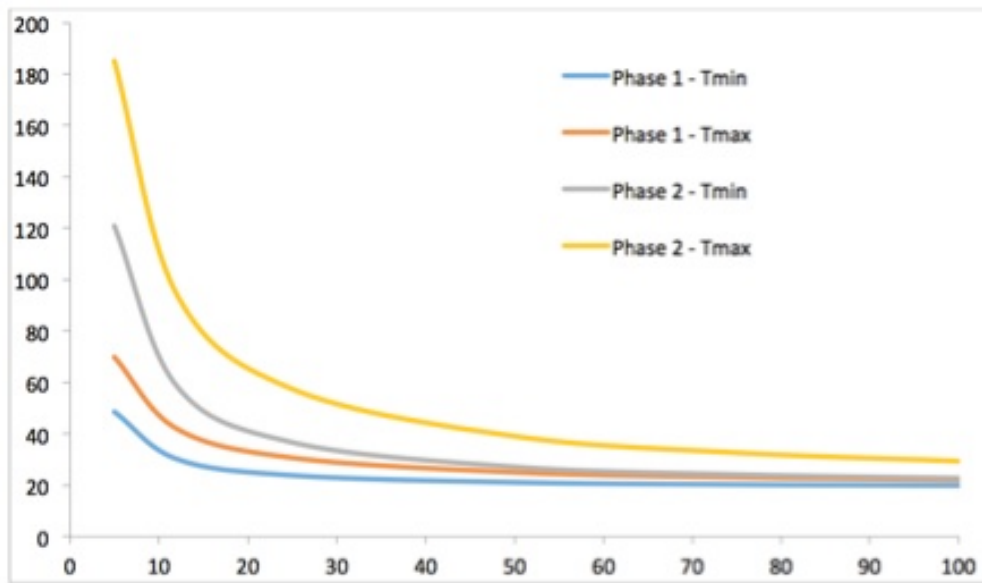


**Figure 4.58:** Maximum and minimum temperature of the striplines submitted to the current and beam pulse against the heat transfer coefficient resulting from the helium flow cooling.

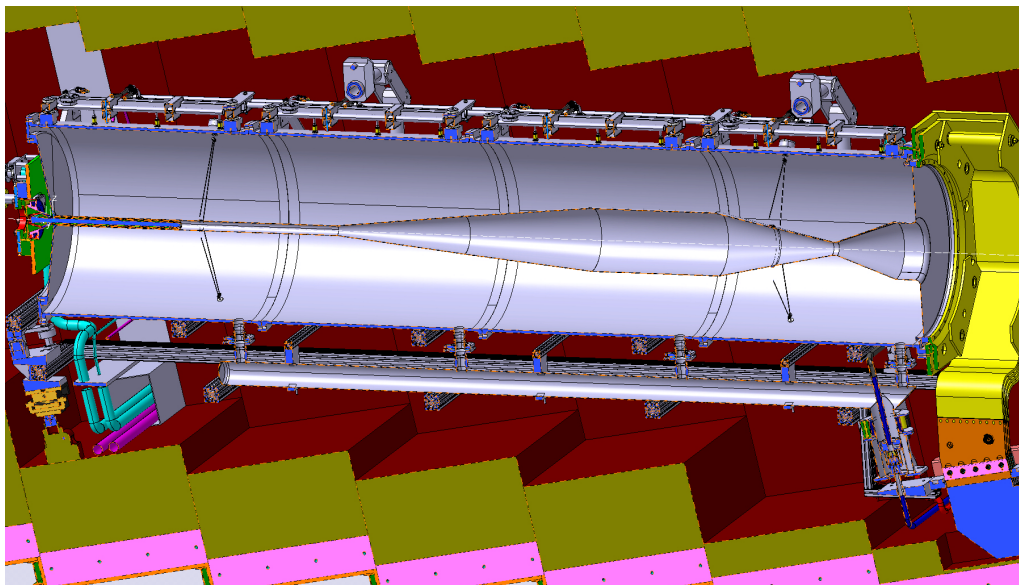


**Figure 4.59:** Cut view of the horn. The water quick connector is situated at the downstream part. It feeds the nozzles (situated at the top part of the horn via the rails and collects the water from the bottom pipe).

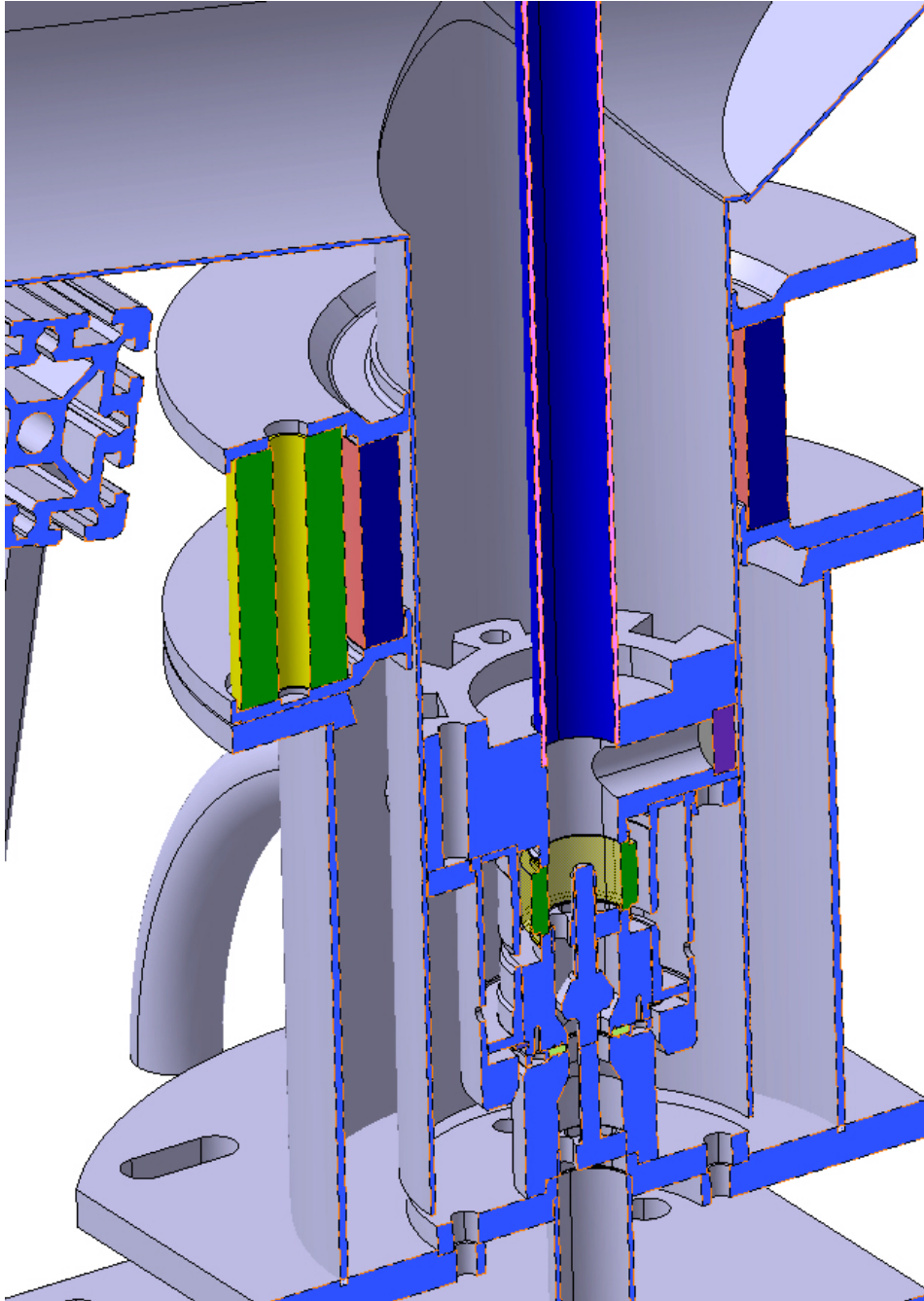


**Figure 4.60:** Cut view of the quick plug-in water connector.

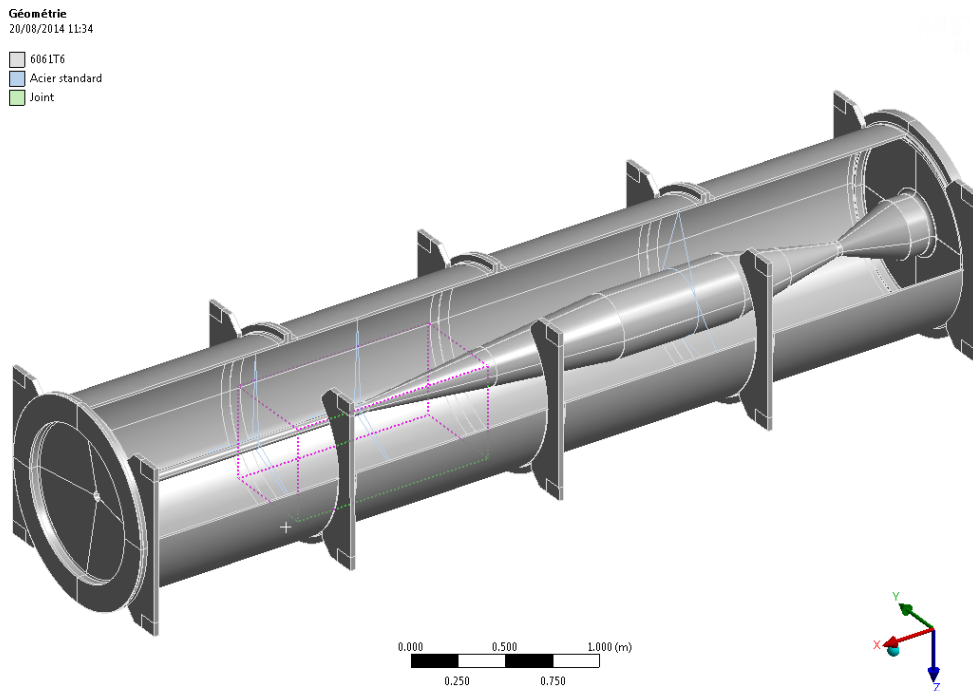


**Figure 4.61:** The horn model used for the FE analysis.

### Thermoelectric model

The loads are considered being uniform over the circumference. The model is hence axisymmetric. Only one slice of the horn is modelled and meshed with plane elements with axisymmetric formulation. First, a steady state analysis is performed (using time-averaged values of current and heat deposition) in order to start the following transient analysis from realistic initial conditions. A transient analysis is then performed, taking both current and heat deposition time history into account. As a heat sink, convection is defined on the outer face of the horn (cooled by water spray) using a conservative heat transfer coefficient of  $10 \times 1000 \text{ W/m}^2\text{K}$  at  $19^\circ\text{C}$ , on the inner faces of the housing (cooled by helium with an assumed heat transfer coefficient of  $100 \text{ W/m}^2\text{K}$  at  $22^\circ\text{C}$ ) and on the outer faces of the housing (cooled by helium) with a conservative heat transfer coefficient of  $5 \text{ W/m}^2\text{K}$  at  $75^\circ\text{C}$ . Those convection boundary conditions are used in both the steady-state and transient analysis.

### Structural model

Due to the gravity, the loads cannot be considered as uniform over the circumference. Furthermore, the geometry (due to the frame attachment and the spiders) does not accept any symmetry except the vertical one. For convenience, it has been however decided to build a full model. The thin parts of the model are meshed using solid-shell elements (solid elements with shell formulation), the massive parts (flanges) of the model are meshed using solid element and the spiders are meshed using cable elements.

In a first step, the cables are pre-stressed (20kg) and the gravity (taking the tunnel slope into account) is acting. The frame is considered as rigid. This analysis is used as a stressed initial state for the upcoming modal analysis.

Then, the maximum temperature profile found in the thermal-electrical analysis is applied on the model and a steady state analysis is performed. The dynamic effects are not taken into account at that point. But this already gives a good idea about the feasibility of it.

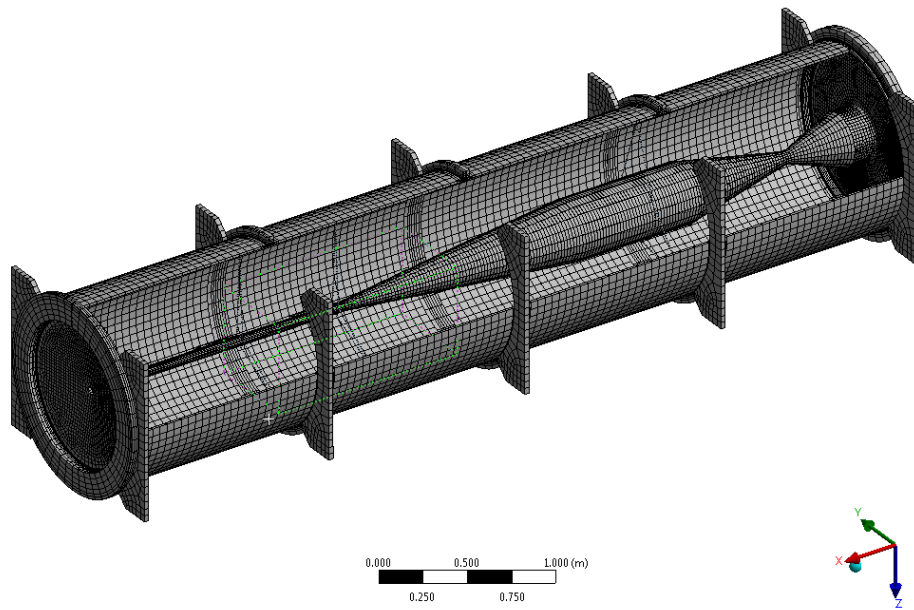


**Figure 4.62:** Overall view of the horn structure used for the structural analysis. The whole structure has been simulated, although a cut is shown.

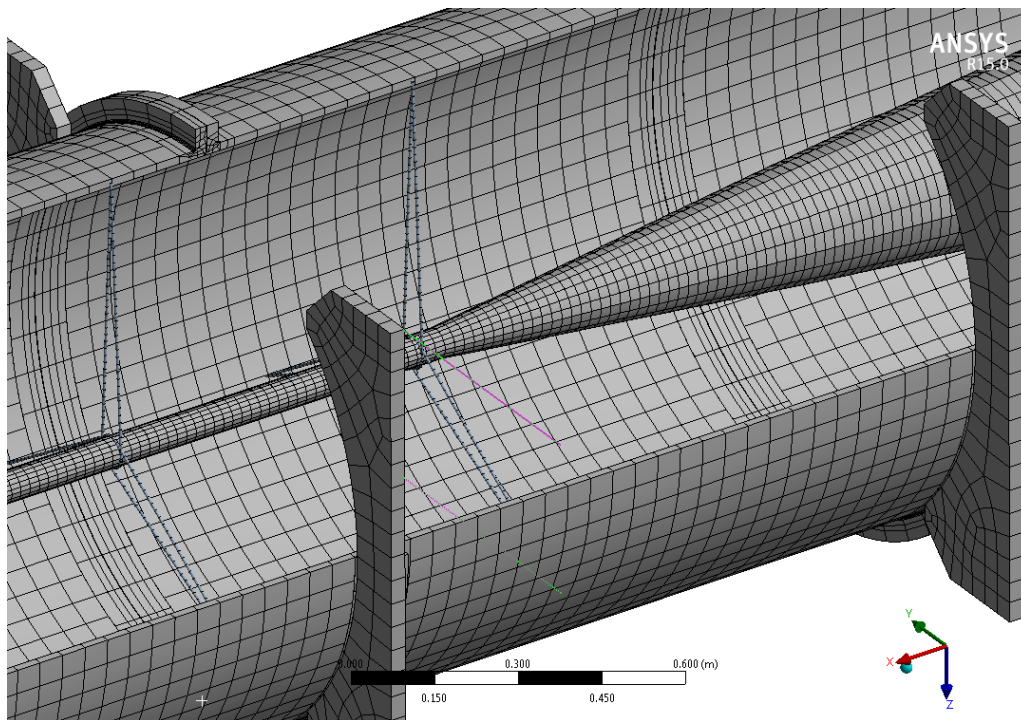


**Figure 4.63:** Mesh detail showing the cables used to support the internal conductor. Cables were considered prestressed (pre-stress force 20 kg).

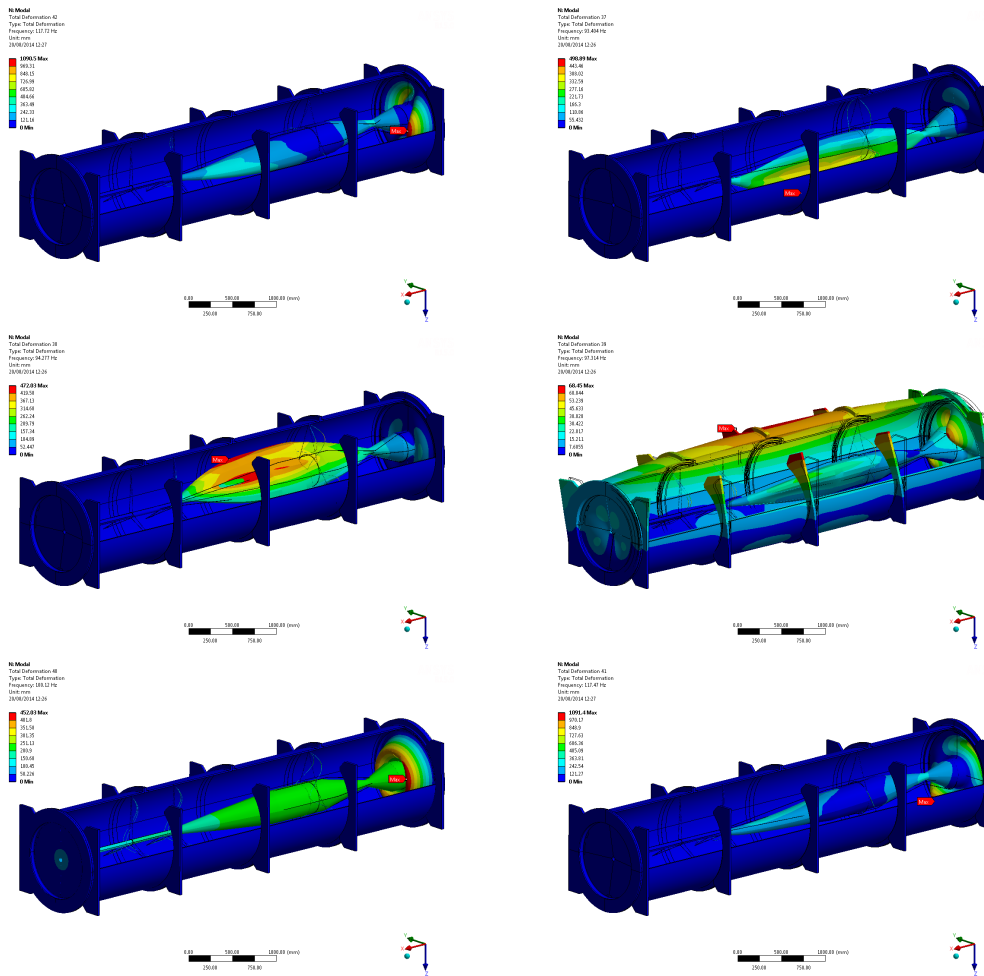


Figure 4.64: Main vibration modes of the horn structure. Frequencies range between 93 and 117 Hz and concern mainly the internal conductor and the horn exit.

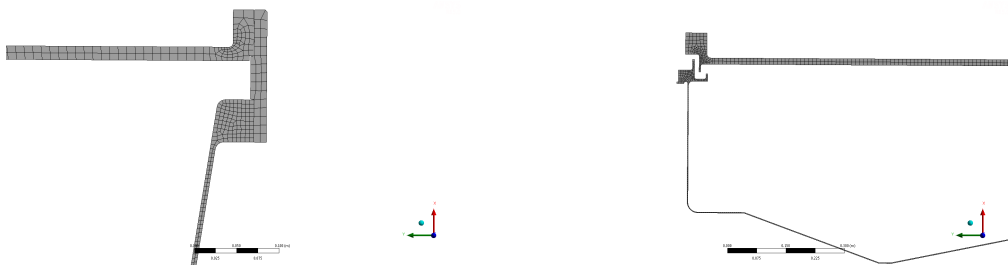


Figure 4.65: Details of the mesh used for the thermo-electrical analysis.

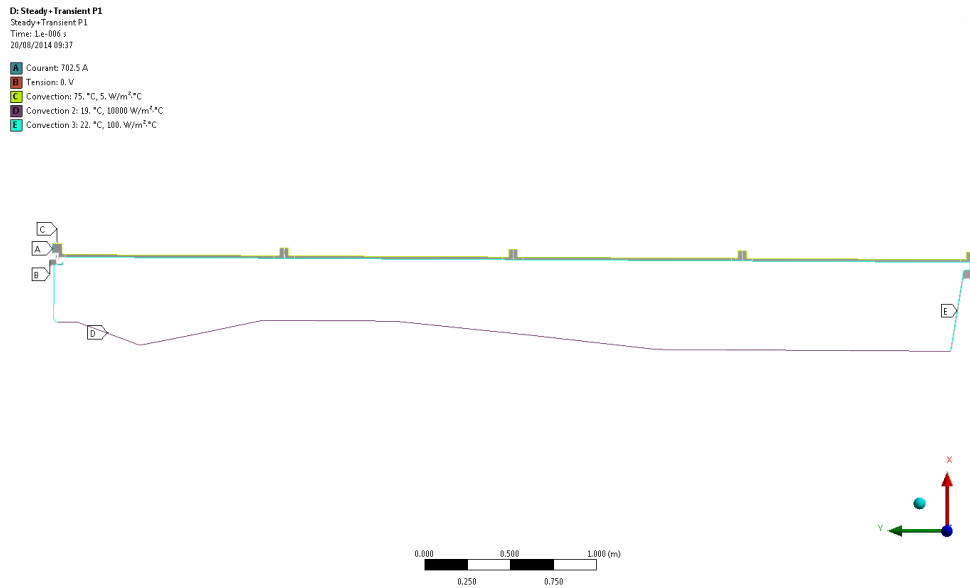


Figure 4.66: Details of the mesh used for the thermoelectrical analysis.

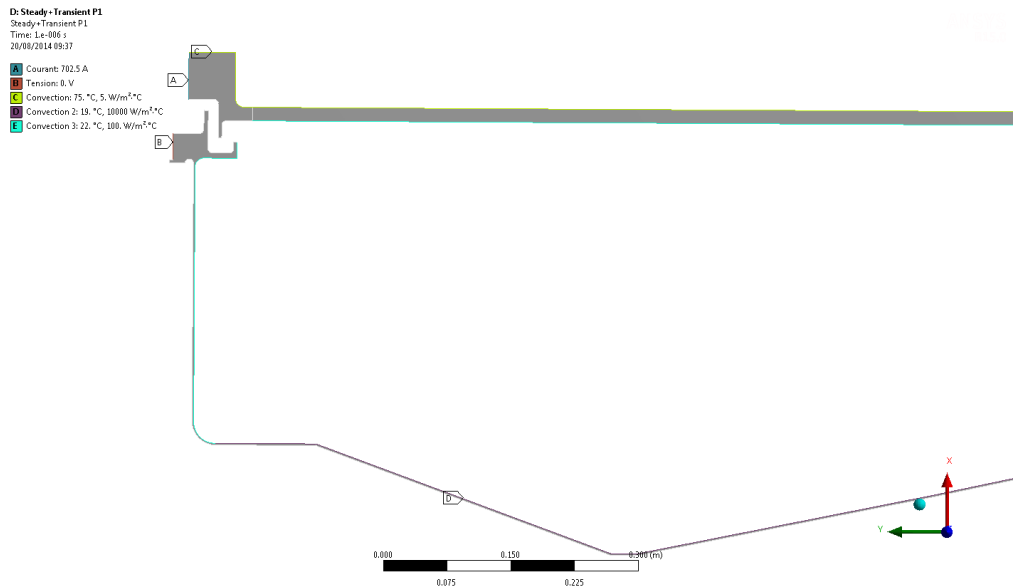


Figure 4.67: Detail of the boundary conditions and the geometry. Internal conductor is 2mm thick while external conductor is 20 mm thick. Connections are made through a massive flange.

## Result interpretation

### *Thermal*

The maximum temperature in steady state is 83 °C for the 400 GeV beam and 73 °C for the 50 GeV beam. Below 75 °C, creep can be neglected for aluminium according to RCC-MRx design standard. The estimated lifetime of the horn is about 1 year (8760 h). This value is less than the limit for creep at 100 °C. Only the pulses will have an impact on this.

For the 50 GeV beam, the temperature remains always below 75 °C, even during a pulse. Hence, creep is not an issue. But for the 400 GeV beam, the temperature reaches 162 °C during a short time. At that temperature, the criteria for negligible creep is 46 h. Considering that the temperature would remain constant at 162 °C during a full pulse, the time at that temperature would be 73 h if no maintenance period is considered. As both those assumptions are very conservative, one can assume that creep, even if non negligible, will have a minor effect on the structure.

### *Structural*

Vertical displacements are below 0.6 mm during pulses, while horizontal displacements are around 3 mm. (The target remains at its position while the downstream part moves).

In the horn (the attachment to the frame are not considered in this discussion as the stress is located at the boundary condition, clearly showing it is a fake stress), the stress reaches for 400 GeV 100 MPa in the internal part of the horn, 275 MPa in the housing, 132 MPa in the exit cover and 30 MPa in the front cover. At 50 GeV, those values are much smaller (31 MPa, 245 MPa, 119 MPa and 28 MPa respectively). For primary and secondary stress, the allowable stress set at 100 °C and highest fluence provided by the standard ( $1151e21 \text{ n}_{th}/\text{cm}^2$ ) is 127 MPa. The stress in the housing and exit cover are above this value. However, the maximum stress is located in fillet close to the flange. No function is associated to it. Hence, increasing the radius would easily decrease the stress in that region. With such a change, one can assume that the stress can be reduced to fit the maximum allowable stress.

### *Fatigue*

Using the current model, one can assess the fatigue in the structure. A simplification of the RCC-MRx methodology has been used using non-irradiated material curves.

#### 1. Assumption:

- ¥ Wished life-time: 1 year ¥ Operating days/year: 200 (full-time) ¥ No maintenance during this operating period. Maintenance occurs during horn replacement ¥ No beam trips considered

#### 2. Cycles definition

For the phase 1 (400 GeV), the strain increase up to the maximum value reached during a cycle of 6 s (steady-state has been already reached). This strain range is noted ?1. During 2,88e6 cycles, there is an oscillation between the maximum value reached during a cycle and the minimum one. This strain range is noted ?2. The full cycles is not subdivided into 2 pulses in this simplified analysis. For the phase 2 (50 GeV), the strain increase up to the maximum value reached during a cycle of 1 s (steady-state has been already reached). This strain range is noted ?1. During 2,88e6 cycles, there is an oscillation between the maximum value reached during a cycle and the minimum one. This strain range is noted ?2.

#### 3. Calculation

Using the simplified RCC-MRx methodology, following results is calculated (Table 7):

In both cases (400 GeV or 50 GeV), the usage factor is well below 1. Hence, fatigue is not an issue.



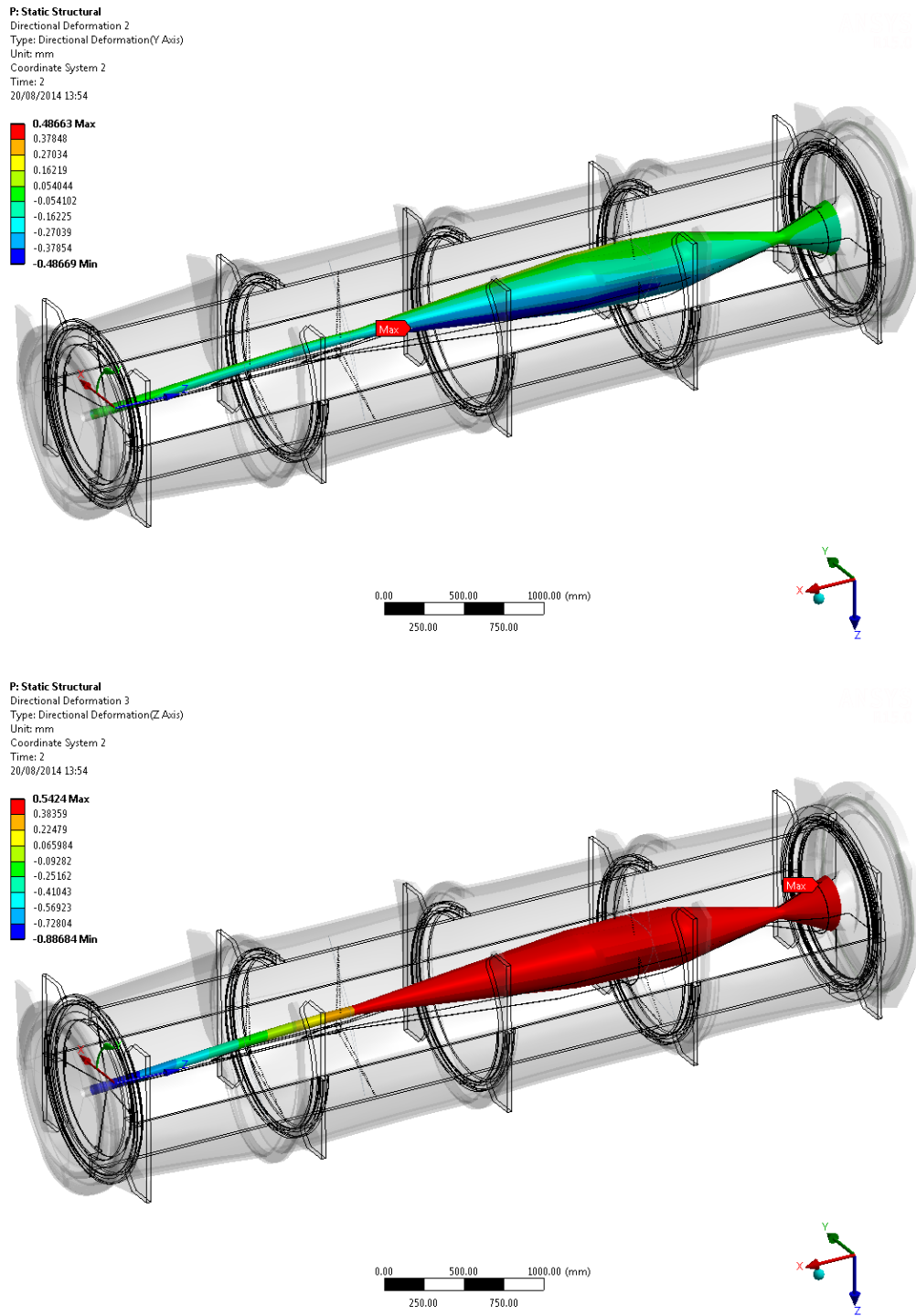


Figure 4.68: Vertical (top) and Lateral (bottom) of the internal conductor.



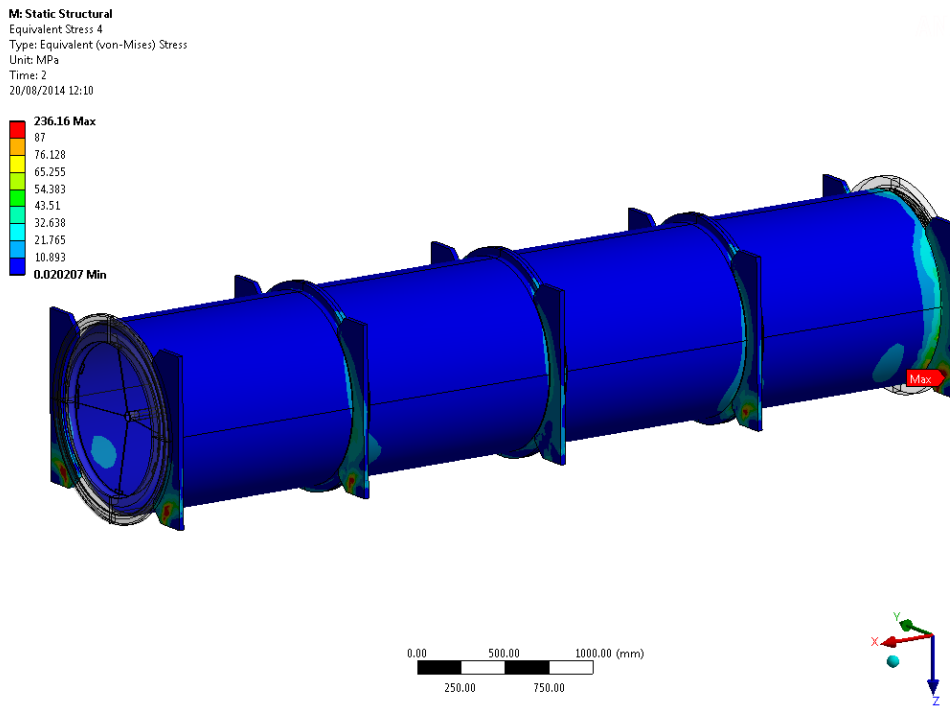


Figure 4.69: Von Mises stress at the global model of the horn. Values are low except in the support regions.

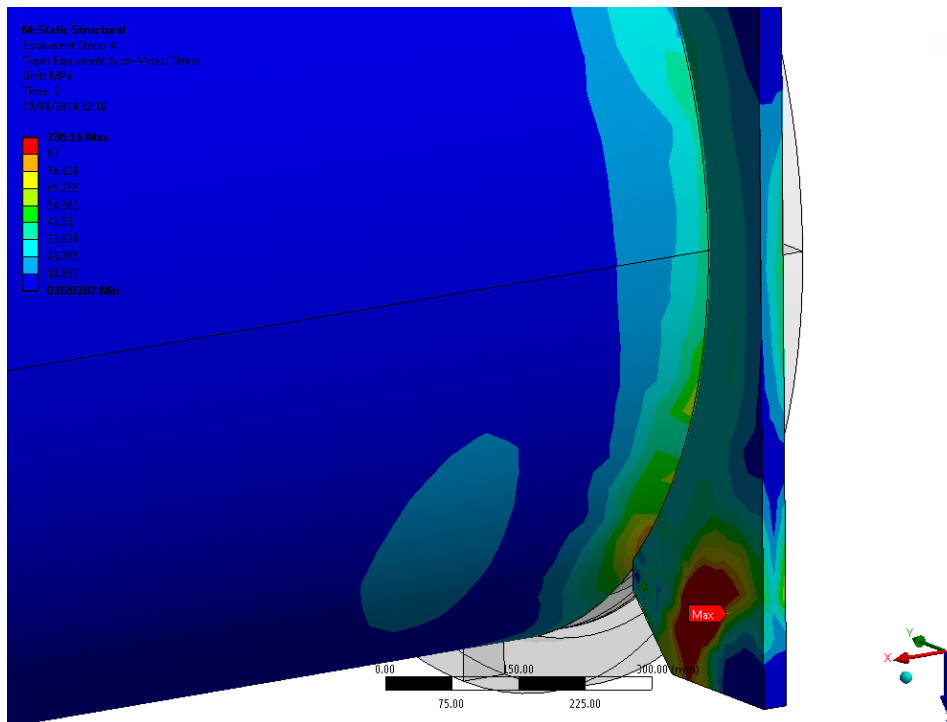


Figure 4.70: Detail of the maximum stresses. They are reached in a non-critical area and are BC dependant. Can be reduced with slight modifications in the shape or thickness of the support.

**Table 4.15:** Horn fatigue calculations according to RCC-MRx

	400 GeV	50 GeV
$\epsilon_1$ (FE, %)	0,37	0,33
$\epsilon_2$ (FE, %)	0,13	0,11
$\epsilon_1$ (RCC-MRx, %)	0,38	0,34
$\epsilon_2$ (RCC-MRx, %)	0,13	0,11
$\epsilon_1$ : allowable cycles	5320	10556
$\epsilon_2$ : allowable cycles	1,04e7	4,4e10
Usage factor	2,78E-01	4,88E-04

## 4.7 The Horn Power Converters

### 4.7.1 Introduction and requirements

The Horn and Reflector are large magnetic elements that require to be operated with very high current pulses. For the first phase of the project (400 GeV), two beam extractions are implemented and, consequently, the power converters need to produce two current pulses spaced by 50 ms. For the Phase II of the project (50 GeV), a single beam extraction is implemented and the converters are used in single pulse mode. The requirements and parameters for the Horn and Reflector are given in Table 4.16.

**Table 4.16:** Horn and Reflector parameters and requirements for Phase I and Phase II.

Parameter	Horn		Reflector	
	Phase I	Phase II	Phase I	Phase II
Peak discharge current	281kA	291kA	198kA	167kA
Maximum repetition rate	6s	1s	6s	1s
Time between 2 pulses	50ms	single pulse	50ms	single pulse
Current precision	<3%			
Load inductance	2.37 $\mu$ H		1.25 $\mu$ H	
Load resistance	0.132 mOhm		0.101 mOhm	

For this project, the powering scheme for the Horn and Reflector has been kept similar to the one that was used for CNGS [82]. The Horn and Reflector are powered using a capacitor discharge power converter, installed in a surface building, and an adaptation transformer installed in the tunnel gallery. The cables length, between the converter and the matching transformer, has been estimated to 200 m and the striplines length, between the transformer and the Horn/Reflector, is 23 m

### 4.7.2 Topology and parameters

The converter topology is based on the charge of a capacitor bank that is then discharged in the inductive load. When the charged capacitor bank is connected to the load, an RLC resonant circuit is formed and, if the circuit is underdamped ( $\zeta < 1$ ), the equation of the discharge current is given by:

$$I_{out}(t) = \frac{U_{co}}{L} e^{-\zeta \omega t} \sin(\omega t) \quad (4.7)$$

with:

$$\zeta = \frac{R}{2} \sqrt{\frac{C}{L}} \quad (4.8)$$

$$\omega_0 = \frac{1}{\sqrt{LC}} \quad (4.9)$$

For the first phase of the project, two capacitor banks and associated discharge switches are installed and for the second phase, one discharge circuit will be removed and will be used as a spare. The topology of the converters is represented in Figure 4.72.

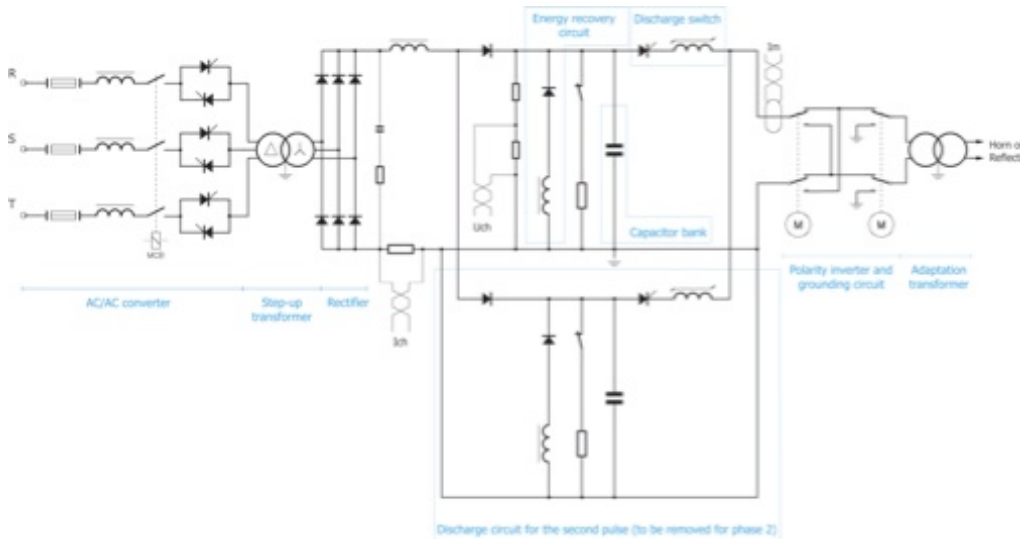


Figure 4.71: Horn and Reflector power converters topology.

When the double pulse mode is used (Phase I), the capacitance value of the two capacitor banks has to be tuned to compensate the effect of the magnetising inductance of the adaptation transformer in order to obtain the same peak current for both pulses during the discharge.

The discharge switches are implemented using serially connected thyristors with RC snubbers and DC voltage sharing resistors. The switches are sized to withstand 20 kV and a surge current of 45 kA (10ms at 25 °C). Their trigger is realised using optic fibres and pulse transformers. A saturable inductor is also installed in order to limit the  $dI/dt$  during the discharge.

The discharge current is monitored using a high current capability DCCT that has a bandwidth close to 100 kHz and exhibits no current droop compared to current transformers. In this case, the current measurement precision for the second pulse and for the phase II operation, with 1 second repetition rate, is maintained.

The adaptation transformers are step-down in voltage and their ratios are selected as a trade-off between the maximum current at the primary, in order to minimize the current in the discharge switch, and the capacitor bank value and charging voltage. Their mechanical construction has to take into account the high electromechanical forces that are produced during the current pulse. In order to reduce the design and production costs, the transformer for the Reflector is considered to be identical as the one for the Horn. The parameters of the discharge circuit for the Horn and Reflector are given in Table 4.17.

For the Phase I of the project, the beam length is 10  $\mu$ s and 4  $\mu$ s for the Phase II. Considering a perfect beam/peak discharge current synchronisation, the Reflector (Phase I) current varies of 1.1 A during the beam passing. For this specific point, the Reflector in Phase I is the more critical because its discharge current pulse duration is 4.6ms and 7.2 ms for the Horn.

For the case of the Horn in the Phase I of the project, the simulated current and voltage waveforms are given in Figure ?? and Figure ?. For the dimensioning of the AC/DC convert-

**Table 4.17:** Parameters of the Horn and Reflector power converters for Phase I and Phase II

Parameter	Horn		Reflector	
	Phase I	Phase II	Phase I	Phase II
Peak discharge current	281kA	291kA	198kA	167kA
Adaptation transformer ratio	20	20		
Discharge switch peak current	14.4kA	14.9kA	10.0kA	8.46kA
Load inductance at converter output	1.024mH	0.576mH		
Load resistance at converter output	81.8mOhms	69.3mOhms		
Capacitor bank value	2?4760uF	1?4760uF	2?3400uF	1?3400uF
Pulse duration	7.2ms	4.6ms		
Energy recovery inductor value	4.8mH	3.6mH		
Charging voltage	7.51kV	7.77kV	4.65kV	3.93kV
Recovered voltage	5.70kV	5.90kV	3.56kV	3.01kV

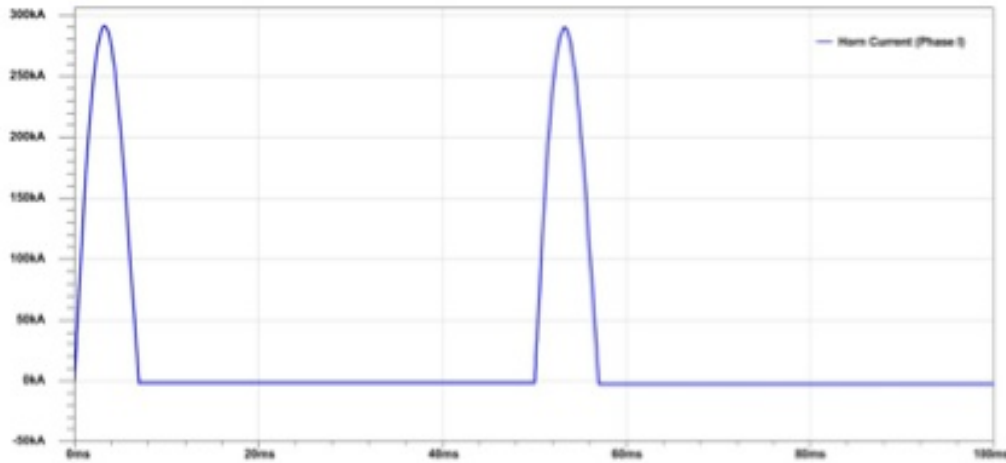


**Figure 4.72:** Simulated current waveform for the Horn (Phase I).

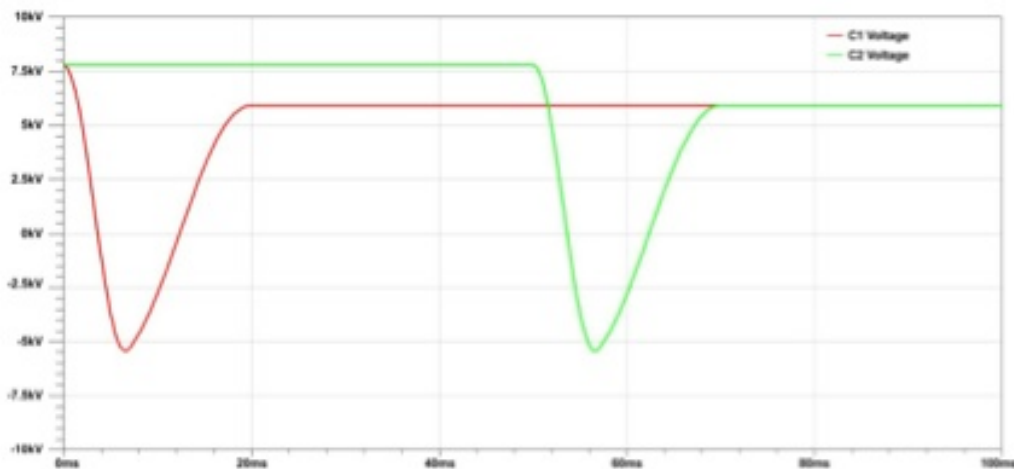


**Figure 4.73:** Simulated capacitor bank waveforms for the Horn (Phase I).

ers, that is used to load the capacitor banks, the more demanding case is the power converter for the Horn in Phase 2 where the repetition rate is 1 second. In this case, the apparent power of the stepping-up transformer, for AC/DC conversion, is 140 kVA. For the CNGS power converters, the apparent power of the charging units was 280 kVA with 10 kV maximum capacitor charging voltage. Consequently, it can be considered that these units, even if they are oversized, are perfectly suitable to be used for this new application without any modification.

#### 4.7.2.1 Regulation and control

The operation of the converters can be split in two phases: one phase for the capacitor charging and one for the discharge and the energy recovery. During the second phase, the thyristors of the AC/DC converter are kept in an off state.

In order to control the peak discharge current value, the regulation system regulates the charging voltage of the capacitor banks. The capacitor charging current is also controlled so as to keep the charging time constant and to obtain a high precision on the charging voltage at the end of the charging process.

This basic regulation system, that operates in open loop as the peak current value is not controlled in real time, can be affected mainly by thermal and capacitance value variations. During the operation, thermal variations will modify the resistive value of the load and introduce an error on the peak discharge current value. Secondly, the capacitor bank value will certainly be subject to variations due to ageing and thermal variations. These effects have a large time constant and they can easily be compensated by an additional (compared to the regulation scheme that is presented in [1]) external current loop that monitors the peak current value and compensate, according to the measured error, the charging voltage for the next discharge pulse.

## 4.8 The decay pipe

The decay region provides a space where secondary particles produced by the target decay to yield muon neutrinos. The decay tunnel length and radius are still under optimization. The radius will be in the 100-200 cm range, and the overall length in the 100-150 m range as counted from the target. The optimization shall be carried out by the experiment in order to maximize the sensitivity within the space constraints given by the North Area layout. As already explained in the layout section, a suitable shielding must surround the decay tunnel in order to reduce the soil activation to acceptable levels. The exact thickness of such a shielding as well as the material (concrete or iron) will be determined in close collaboration with DGS/RP. A water cooling system ? at least for the first section of the decay volume ? might need to be foreseen due to the significant amount of energy deposited by the secondary beam.

The decay pipe is a 270 m long circular pipe, 3 m diameter, 20 mm thick.

The material used for the decay pipe is specified to be steel P355NH, according to the Euro norm EN10028. At production of the steel plates, the corresponding quality criteria are applied. In particular, ultrasonic tests are to be performed on 20% of the steel plates manufactured (according to standard EN 10160).

The pipe is connected to the helium tank that surrounds the target chamber, and thus no entrance window is required.

The decay pipe will be subject to heating from the secondary particles. Its cooling has been investigated in detail and in particular the options of a helium cooled pipe were addressed (the baseline being a single wall pipe). Although it could be a feasible solution, due to the large amount of heat to be removed (around 520 kW along the whole pipe), our choice is the water cooling of the whole pipe. Several standard methods are available for the connection of the pipes, one of them (hydro-formed channels) is shown in Figure 4.75

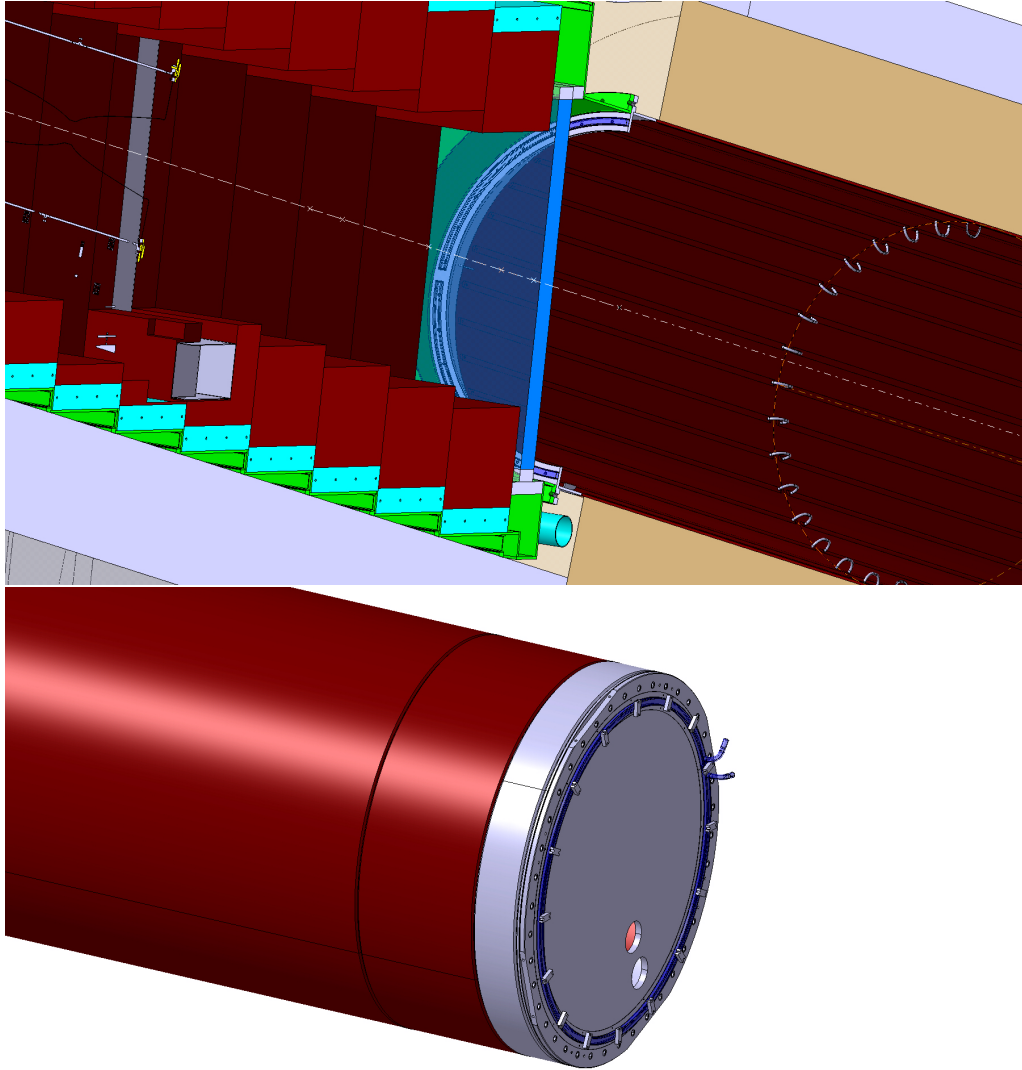


**Figure 4.74:** Top: Cut view of the entrance of the Decay pipe showing the water cooling channels and He shutter (depicted in transparent blue). Bottom: Detail of the decay pipe exit window. A 50 mm thick water edge-cooled plate closes the He volume and separates it from the hadron stop volume.



**Figure 4.75:** Example of Hydra-cool type cooling channels adapted to a circular geometry as the one present at the decay pipe..



Hydra-Cool is a technically superior and cost effective method of water cooling vacuum chambers. It is made by welding a trace to a chamber and then using water pressure to hydro-form the water channel. By utilizing radius bends instead of square corners, it improves water flow and eliminates low flow and stagnant areas. When coupled to a full penetration weld, this reduces the chances of crevice crack corrosion and extends the working life of the chamber.

One of its main advantages is that gives the ability to approximately double the surface area being cooled over conventional  $\odot C \odot$  channel style water cooling. This high surface area coverage possible with this method also makes it an affordable alternative to double walled cooling. It is then well suited to the decay pipe cooling case. The junction between the channels could be via welded U tubes, as was made for T2K or with flexible pipes between insertions added to the hydro-formed channels. Both solutions are well known and technically feasible.

### 4.8.1 Thermal analysis

Starting with the inputs of the FLUKA calculations, thermal analysis were performed with ANSYS to investigate the adequate cooling requirements. The ANSYS model considered a

**Table 4.18:** Energy deposition in the Decay Pipe for the 50 GeV case. Values are in kW

Element	Deposited Energy [GeV/cm <sup>3</sup> /prot]	Power [kW]
concrete shielding		
iron part-1		
irony part-2		
total		
hline		

slice of 1 m length, and included the decay pipe, the concrete surrounding it and the molasses enclosing the concrete. Temperature of the molasses was set to 25 °C and several cooling cases were simulated in order to represent the cooling of the pipe.

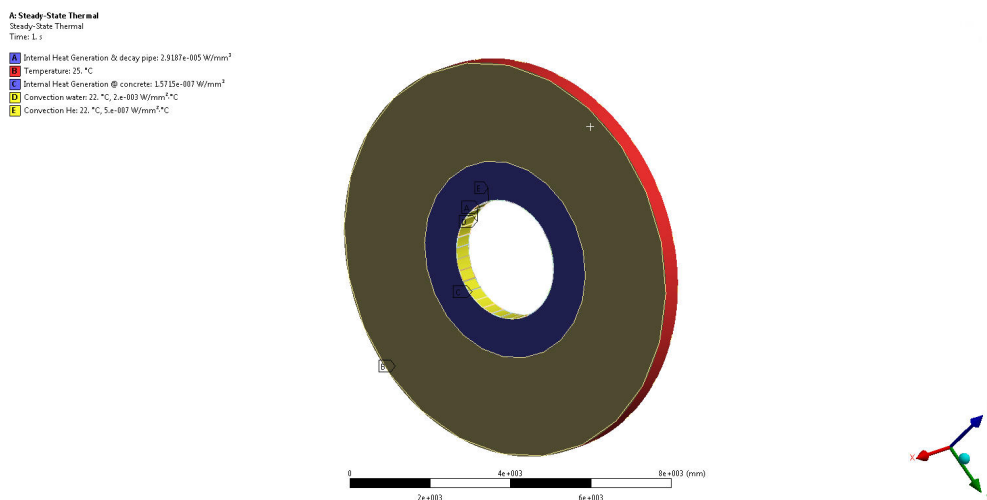


**Figure 4.76:** Detail of the boundary conditions applied to the model of the decay pipe (0.5 m slice). Heat generation is applied to the pipe and the concrete, while no heat load is applied to the molasses. Water pipes were considered in the internal pipe and a constant temperature of 25 °C at the molasses was imposed.



Figure 4.77 shows the temperature profile results for the first case considered: An uncooled decay pipe (a global temperature of 25 °C was set to the molasses as only heat sink source). This led to unacceptable temperatures above 600 °C. The second sector of the decay pipe

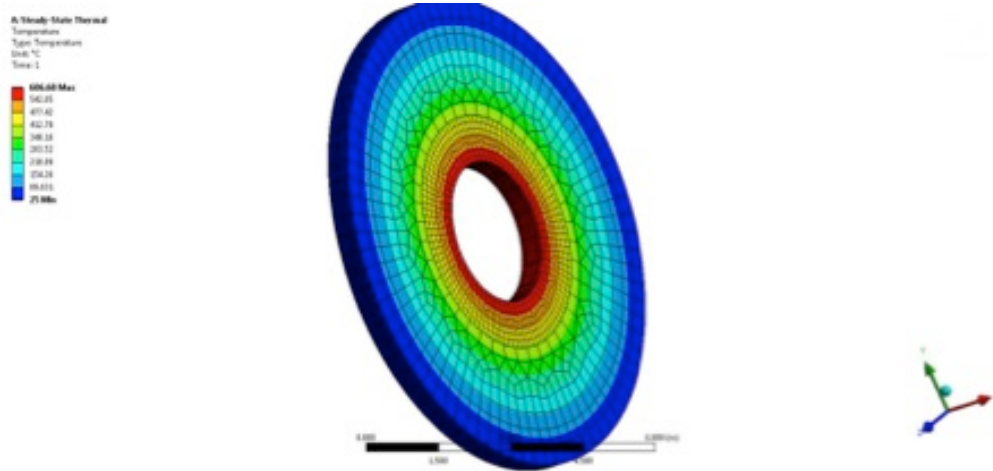


**Figure 4.77:** Temperature in the first sector of the decay pipe above 600 °C. 25 °C imposed in the molasse . Total heat 118 kW

is subject to a lower energy deposition (see Table 4.18)). Results of the ANSYS analysis are summarised in showed that with an adequate He cooling water cooling would not be required. Nevertheless, the analysis assumed a constant He temperature along the length of the pipe, and in the case of the decay this would require an enormous volume of circulating He.

**Table 4.19:** Results of maximum temperatures for the second sector of the decay pipe. He was assumed at constant temperature (20 °C) along the whole length.

He Convection Film Coefficient $W m^{-2} C^{-1}$	Maximum Temperature			Dissipated heat	
	Decay pipe C	Concrete C	Molasse C	He kW	Rock kW
0	210.8	210.8	146.8	0	425
1	104.7	104.7	85.4	214.2	210.8
2	75	77.1	68.2	274.2	150.8
3	61	65.7	60.1	302.6	122.4
5	47.5	55.6	52.3	329.8	95.2
10	35.7	47.3	45.5	353.6	71.4
15	31.4	44.3	42.3	363.3	62.7
20	29.2	42.8	41.7	366.8	58.2

Figures 4.78 to Figure 52 show the temperature profile results for different cases of water cooling: from 10 20 mm contact cooling channels around the circumference to 32 cooling channels. At the chosen configuration, maximum temperatures of 73 C are reached in the concrete/-molasses region, while 45 C are reached in the decay pipe. Note that all these calculations were made assuming a homogeneous heat deposition across the regions. Although it is valid for the decay pipe itself due to its reduced thickness, it is a conservative approach for the surroundings and its values can be assumed as a maximum.

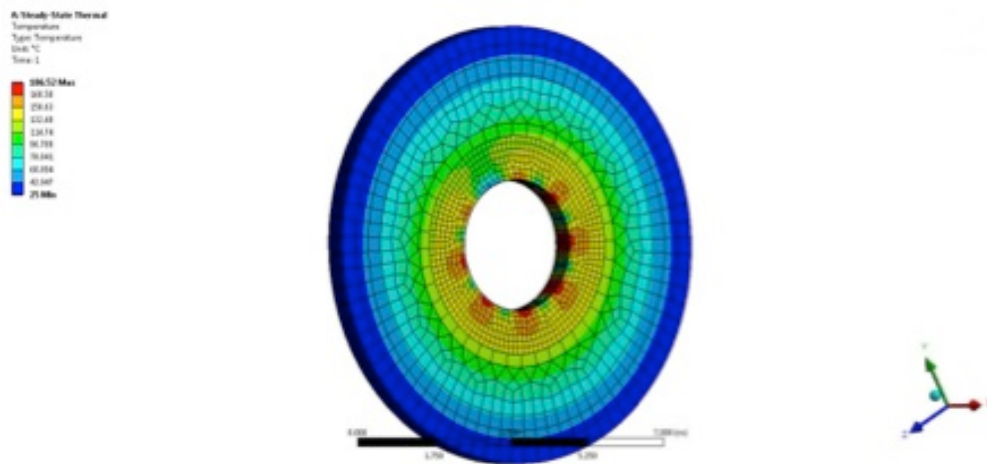


**Figure 4.78:** Temperature profile in the first sector of the decay pipe around  $190^{\circ}\text{C}$ .  $25^{\circ}\text{C}$  imposed in the molasses and 10 cooling channels (20 mm width). Heat @ BC=86 kW removed by water, 32 kW removed by conductivity to the molasses.

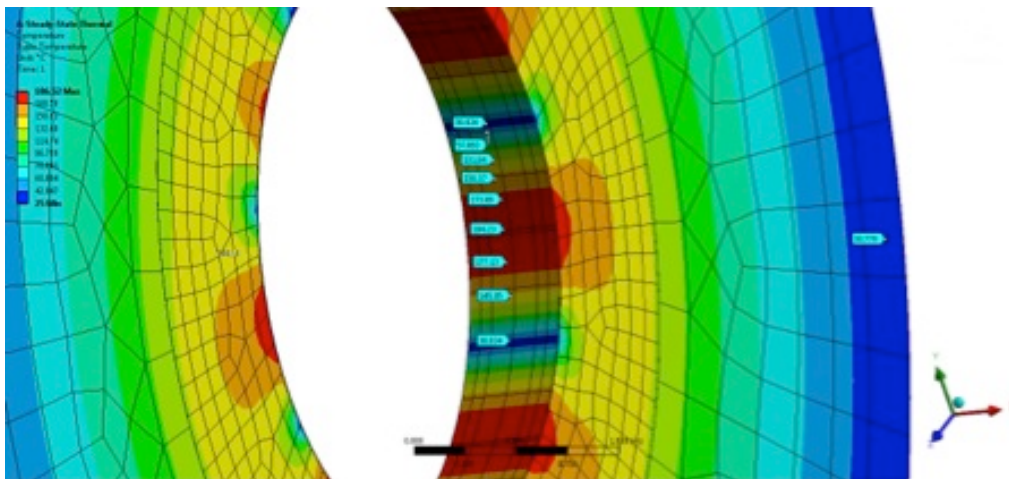


**Figure 4.79:** Detail of temperature profile in the first sector of the decay pipe around  $190^{\circ}\text{C}$ .  $25^{\circ}\text{C}$  imposed in the molasses and 10 cooling channels (20 mm width). Heat @ BC =86 kW removed by water, 32 kW removed by conductivity to the molasses. Due to the temperature gradient along the circumference, more cooling channels are required.

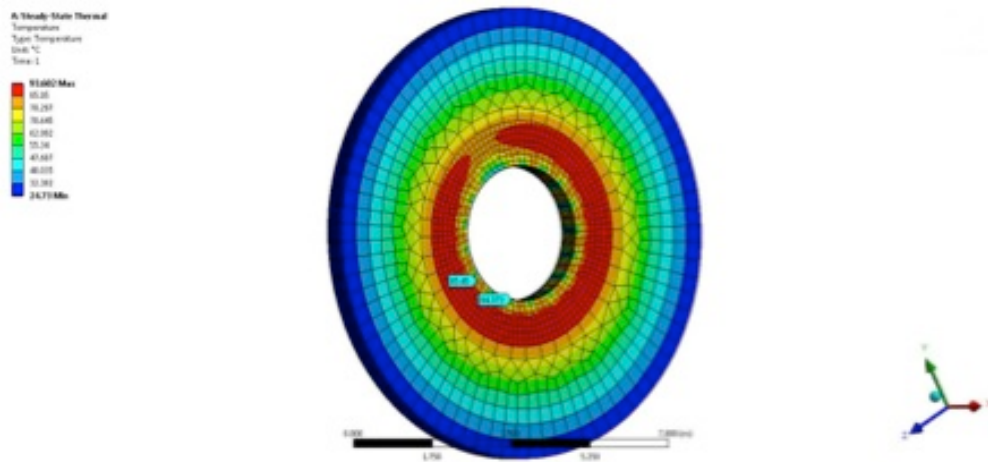


**Figure 4.80:** Temperature in the decay pipe around 85 °C, maximum temperature in the concrete 93 °C. 25 °C imposed in the molasses and 16 cooling channels (20 mm width). This would be the minimal requirements

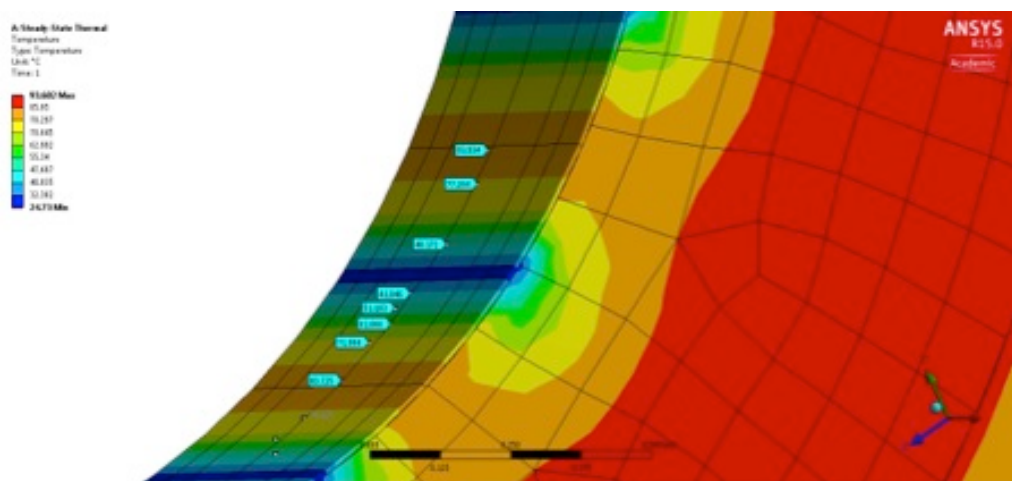


**Figure 4.81:** Detail of the temperature profile in the decay pipe with a 16 cooling channels (20 mm width around 85 °C, maximum temperature in the concrete 93 °C. 25 °C imposed in the molasses). This would be the minimal requirements for water cooling.

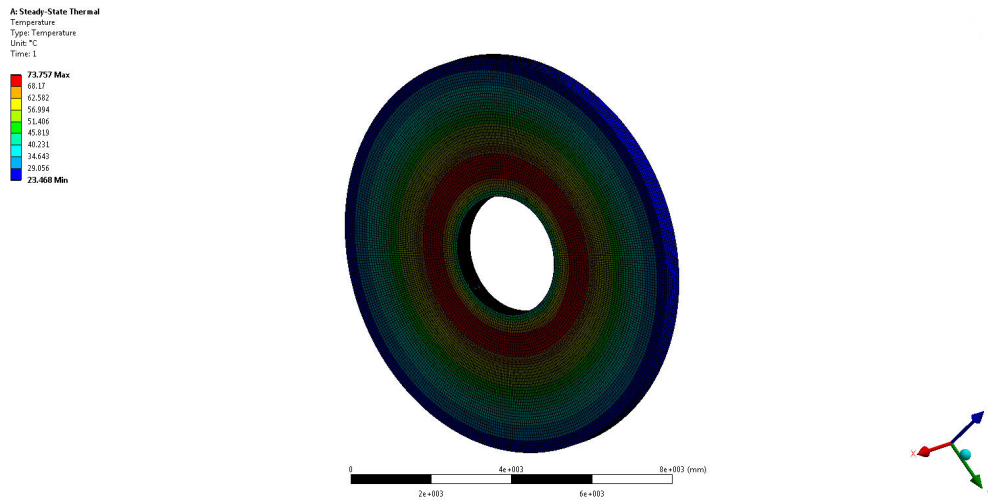


**Figure 4.82:** With 32 cooling tubes, internal temperature of the decay pipe is below 50 °C. Maximum temperature is reached in the region concrete-molasses that surrounds the decay pipe.

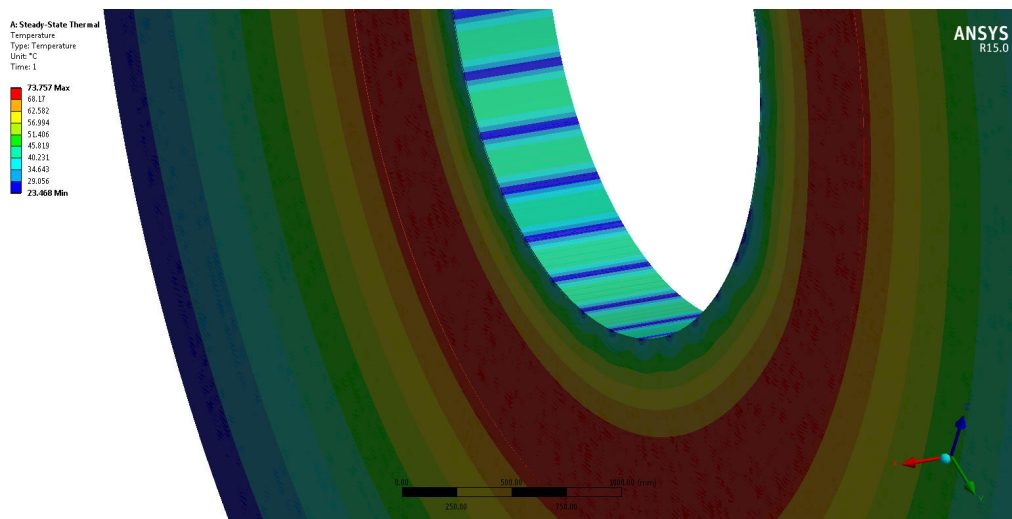


**Figure 4.83:** Detail of the water cooling channels in the decay pipe. Water temperature set to 20 °C, convection coefficient to 2000 W/m<sup>2</sup>K.

### 4.8.2 Mass flow considerations

The heat power deposited during operation is around 69 kW, to be removed with a water system by means of 32 cooling channels in contact with the pipe. Concrete around the decay pipe gets 49 kW, and it has been considered totally removed by the same water cooling system. Assuming a fluid overheating of 12.5 °C due to the heat removed, the required mass flow for the 1st sector of the decay pipe is:

$$\dot{m}_{water} = \frac{\dot{Q}_{cooling}}{q_{water}} = \frac{\dot{Q}_{cooling}}{c_{water} \Delta T} = \frac{(69000 + 49000)}{4186 \times 12.5} = 2.4 \text{ [kg/s]} \quad (4.10)$$

The heat power deposited in the pipe during operation is around 222 kW, to be removed with a water system by means of 32 cooling channels in contact with the pipe. Concrete around the decay pipe gets 203 kW, and it has been considered totally removed by the same water cooling system.

Assuming a fluid overheating of 12.5 °C due to the heat removed from the conductor, the required mass flow for the 2nd sector of the decay pipe is:

$$\dot{m}_{water} = \frac{\dot{Q}_{cooling}}{q_{water}} = \frac{\dot{Q}_{cooling}}{c_{water} \Delta T} = \frac{(222000 + 203000)}{4186 \times 12.5} = 8.2 \text{ [kg/s]} \quad (4.11)$$

### 4.8.3 Decay pipe accessories

The decay pipe consists of welded steel pipes of 3 m diameter, with a total length of 275 m (see Section 4.1). The volume of the pipe is 2120 m<sup>3</sup>, the inner surface amounts to 2600 m<sup>2</sup>. The thickness of the steel pipes is 20 mm, solid enough to withstand the pressure under He provided the surrounding spaces are filled with concrete.

The decay pipe is closed at the hadron stop end by a massive steel plate, 5 cm thick. For safety and economy reasons, i.e. to avoid the circulation of the entire volume of helium when the target chamber is opened, it was decided to install a shutter which is moveable along vertical rails in the connection region to the helium tank. When run conditions are established, the plate is automatically driven out of the beam into a 'run position'. When access to the target area is requested, the shutter is automatically driven in front of the decay pipe. This shutter must be interlocked with the access conditions for the LAGUNA target area.

## 4.9 The hadron stop

The hadron absorber is placed at the end of the decay pipe. It is a massive object to absorb the energy deposition of the primary and secondary beam particles arriving at the end of the decay pipe. Its design would be similar to that of CNGS, i.e. with a graphite core surrounded by iron blocks. The graphite core should cover an area of 1×1 m<sup>2</sup> and the overall shielding should mask the decay pipe volume, i.e. about 3.5×3.5 m<sup>2</sup>. The graphite core should be about 2-3 m long, and the overall hadron stop at least 10 m, leaving at least 7 m of iron shield behind the graphite. The thickness of the iron layer depends significantly on the overall geometry of the installation and in particular on the distance between the end of the decay pipe and the location of the near detector. The design study should make sure that the iron thickness is sufficient to ensure that no muon reaches the near detector position. The hadron absorber will need to be water cooled (with a "sandwich" configuration similar to the CNGS one); the cooling water pipes could be routed via the vertical shaft envisaged for the muon monitoring station.

The hadron stop is placed at the end of the decay tunnel. The purpose of this object is to absorb the energy deposition of the primary and secondary particles arriving at the end of the decay region. The design is based on the following requirements:



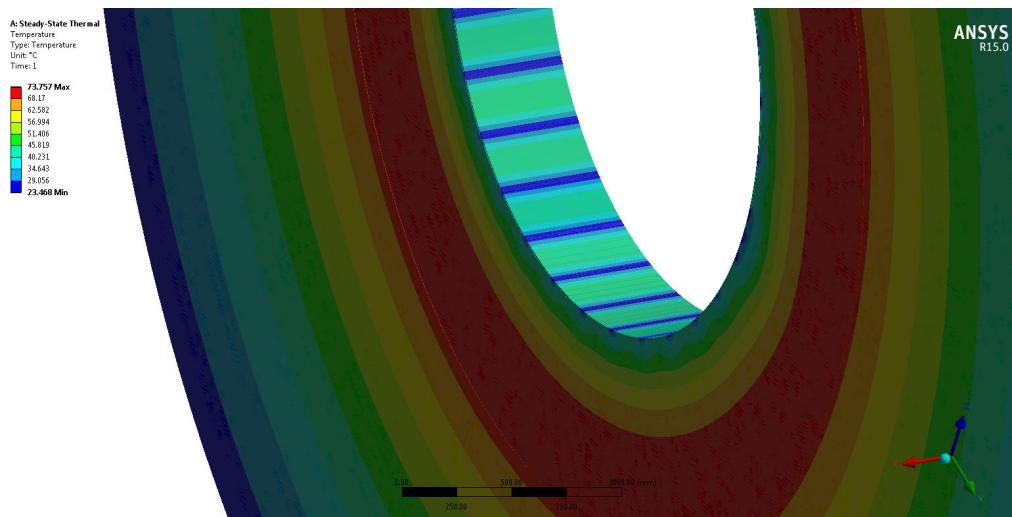


**Figure 4.84:** View of the connection between the helium tank and the decay pipe. The helium shutter is placed vertically on the top of the tank and separates the volume of the He tank ( $2100 \text{ m}^3$ ) from the helium volume of the target chamber ( $105 \text{ m}^3$ )

- There must be a high density and potentially demountable region where the energy deposition of the primary and secondary hadrons from the intense production at the target is absorbed. The cascade of these particles interacting in the dump has to be contained, as there must be minimal deposition of radioactivity in the molasse.
- The hadron stop must be considerably larger than any protection required to absorb the hadrons as there is a need to provide additional material for muon attenuation at the SBL detector to give a direct muon background less than the irreducible background induced by neutrino interactions in the molasses in front of the detector.
- In order to steer the beam towards the Phyasalami site, accurately positioned detectors must be placed behind the hadron stop. In practice, experience has shown that at least two detector pits are required to provide angular and very rough energy information to control any misalignment of the horn and reflector with respect to the target. The two pits should be separated by sufficient material to give an energy difference of the muons sampled of about 40 GeV.

It is evident that because of its insulation against heat loss, buried deep underground in a bed of poorly conductive molasses, the hadron stop has to be actively cooled. Preliminary calculations, discussed in the next section, indicate that after 200 days of running with  $5 \cdot 10^{12}$  protons per second at 400 GeV/c, parts of a simple iron dump could reach several hundred degrees Celsius ( $700 \text{ }^\circ\text{C}$ ). These high temperatures would risk destroying the concrete supporting structures, excluding further access to the muon detector pits. Several heat flow calculations with different conditions have been made, indicating that the dump should be actively cooled. Also, it is clearly advantageous to have a lower density insert at the start of the dump to diffuse the hadronic cascade over a larger volume to improve the heat flow and minimize exceptional hot spots due to non-interacting primary protons on the beam axis.

The general layout of the civil engineering of the hadron stop area is shown in Figure 4.85

#### 4.9.1 Design overview

The design requirements for a cooled hadron stop are listed below:

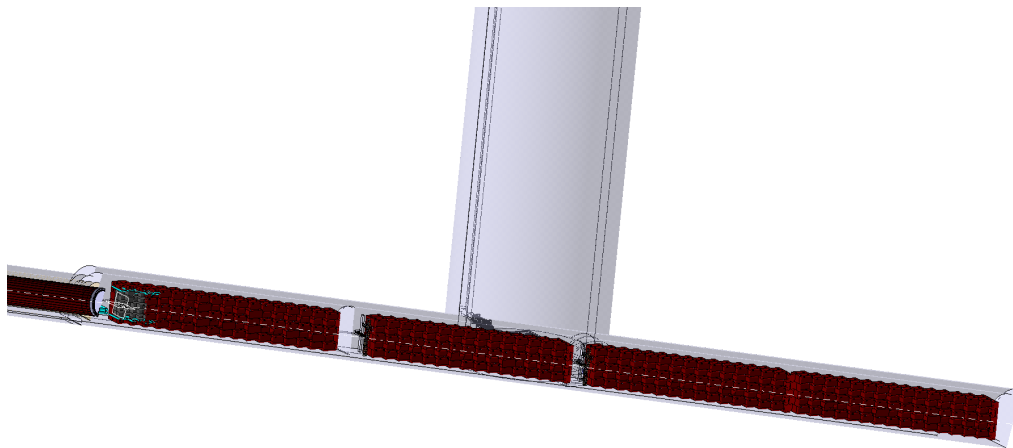


**Figure 4.85:** TView of the Hadron stop. The graphite block is situated upstream, following the decay pipe. Iron dumps are shown in red.

- The total power deposited on the hadron stop in the worst case of continuous dedicated running is about 50 kW. Half of this deposition comes from non-interacting protons, and is highly localized in the centre of the dump. The rest, coming from secondary hadrons, is relatively diffused over a region of 2.6 m in diameter.
- The back end of the hadron stop needs to be at a reasonable, constant temperature, 20/25 °C, in order to allow stable operation of the solid-state detectors and electronics.
- Water cooling must be demineralized in a closed circuit and be very robust. It should be designed for a 20-year lifetime with no intervention to the heat sink required.
- A monitoring system of the water flow and temperature is necessary. This has to be designed with appropriate redundancy, considering the mechanical and thermal stresses expected in the hadron stop region.

Access to the area is evidently very limited. It is only possible when the LAGUNA is not running. The hadron stop is installed in a cavern 6.5m in diameter and 115m long, divided in 4 subsections. A preliminary design of the hadron stop is shown in Figure 4.86 .

The decay tunnel pipe is terminated by a water cooled 50 mm thick steel plate welded to it. An insulating air gap, 20 to 25 cm, is left to separate the plate from the hadron stop and to minimize the heating of the end plate by the dump. Once installed this region is completely sealed from the galleries and muon pits.

The design of the hadron stop is similar to the one used at CNGS. The first component of the stop is a block of graphite (around 9 m<sup>3</sup>) which is used to diffuse the hadron cascade over a large volume to reduce the temperature gradient in the dump and take advantage of the better heat conductivity.

A high density graphite will be used, its minimal required properties are presented in Table 4.20

The graphite block and the first 1.6 m of iron after it is surrounded by aluminium plates at the top and bottom, with a wall thickness of 200 mm. This provides some continuity of cooling to the final mass of iron and ensures a good heat conductivity over the whole surface to the heat sink on which the box sits. This heat sink of cross section 200 × 2400 mm and 4800 mm

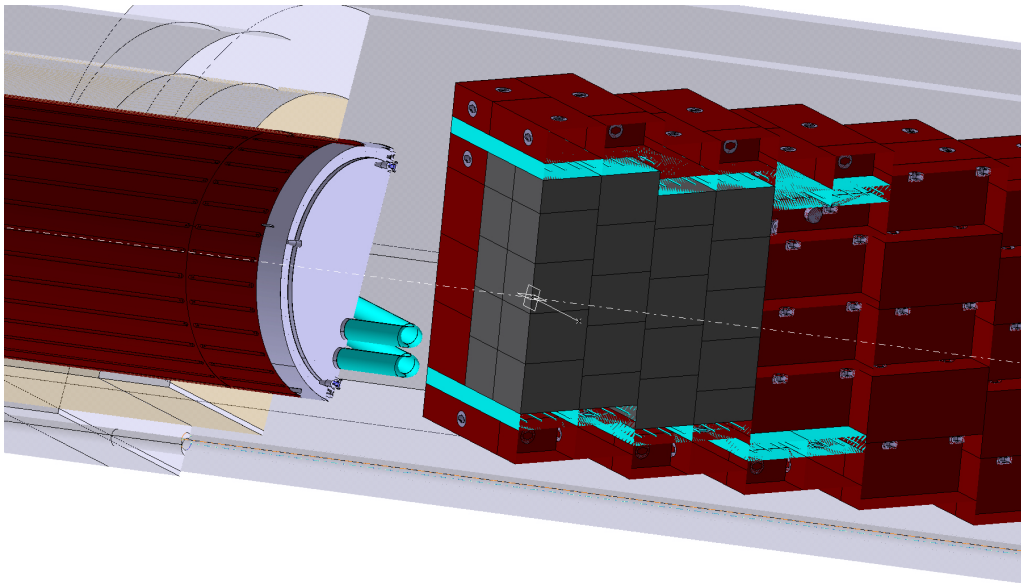


**Figure 4.86:** Cut view showing details of the start of the Hadron stop section and the decay pipe exit with two helium inlets and a water cooled window.



**Figure 4.87:** View of the CNGS Hadron Stop. Graphite blocks, aluminium cooling plates and CERN Standard Iron blocks are shown.



**Table 4.20:** Minimal thermal properties required for the graphite blocks at the hadron stop.

Parameter	Value
Density	1.7 g/cm <sup>3</sup>
Thermal conductivity	125 W/(m K)
Admissible temperature	400 °C

long is water-cooled by 12 independent circuits, each of 4 cm diameter mild steel pipes leading to the back of the hadron stop. Each circuit is independently attached to a general manifold and can be turned off in case of internal leaks or breakage. A schematic drawing of the heat sink is shown in Figure 4.88

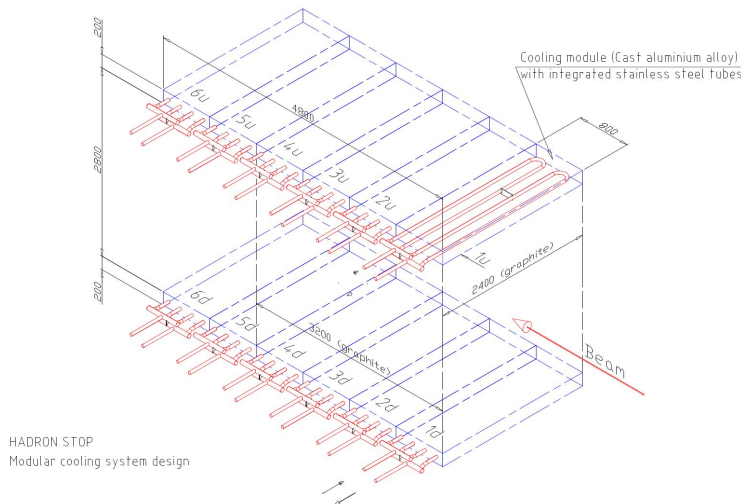


**Figure 4.88:** View of the aluminium cooling blocks and the integrated cooling tubes.

**Table 4.21:** Energy deposition in the Hadron stop for the 50 GeV case. Values are in kW.

Element	Energy [Gev/cm <sup>3</sup> /prot]	Power [kW]
---------	------------------------------------	------------

The whole water-cooled module is encased in standard CERN steel blocks, as shown in Figure 4.86, and all gaps to the cavern walls filled with concrete. As it is impossible to transport the aluminium box filled with graphite as a complete structure down to the cavern, one possibility is to build it in five 60 cm segments, each weighing about 10 tons. These segments are bolted together in situ, as shown in Figure 4.88. The water-cooled module is followed by a mass of 240 m<sup>3</sup> of iron blocks. The cross section of 4 × 4 m<sup>2</sup> is sufficient to attenuate any muons that would multiple-scatter around the hadron stop, and the length of 4 × 27 m along the beam axis should provide enough attenuation to give a safety margin to prevent muons from reaching the near detector.

## 4.9.2 Thermal calculations

Some preliminary calculations have been made of the heat flow and final temperatures in the hadron stop, though no final optimization of all the possible parameters has been made. These calculations have, however, given indications of what could be a reasonable, safe design that would satisfy the required conditions. The proposed design is described in the following section.

The calculation of the heat flow in the hadron stop was performed in two steps. First the FLUKA program was used to calculate the average energy deposition in the hadron stop by a fully simulated reference neutrino beam, including primary protons not interacting in the target. The output from this simulation was used as the input to the heat transfer calculation in the hadron stop.

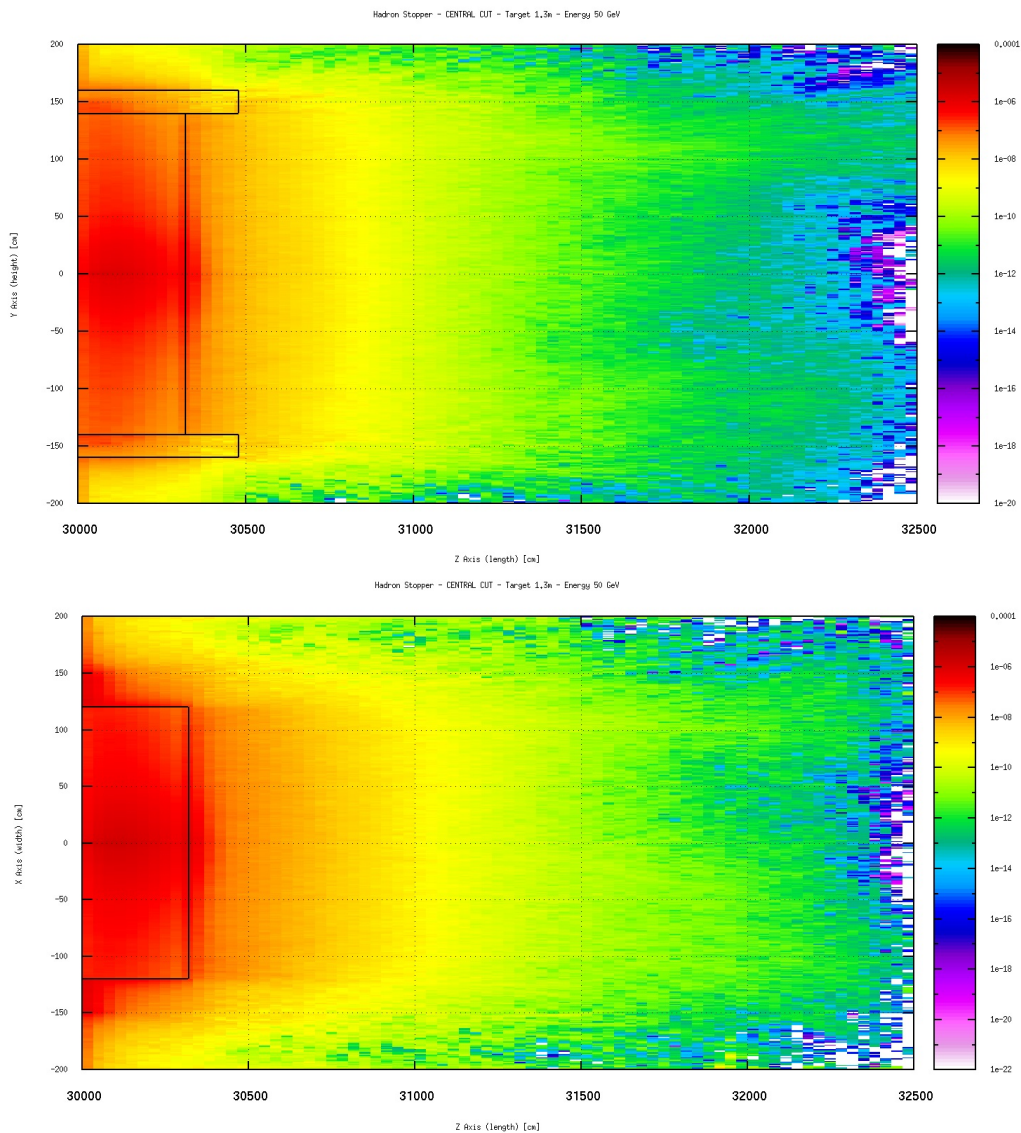


**Figure 4.89:** View of the energy deposition profile at the hadron stop considered for the ANSYS calculations for the 50 GeV beam. Top:  $y-z$  plane, Bottom:  $x-z$  plane.

Several simplifying assumptions were made to ease the calculation problem. A rotational symmetry was assumed to allow a faster first round of calculations, e.g. the heat sink was taken as a 3 m long cylinder of aluminium with an inside radius of 1.46 m and a thickness of 10 cm.

To compensate for this global coverage of the heat sink, which is in reality only at the bottom of the hadron stop (see Figure 4.92), the cooling power was reduced to a quarter of the expected one, i.e. to 12.5 kW. Boundary conditions in the molasses surrounding the hadron stop were fixed at 14 °C at a reasonable distance of 20 m.

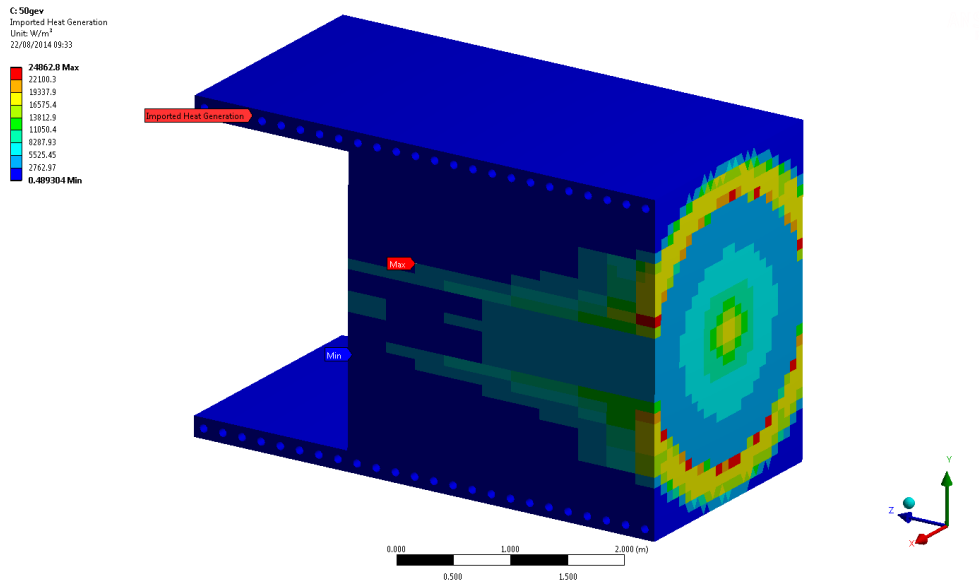


Figure 4.90: Heat deposition profile at the hadron stop - 50 GeV configuration.

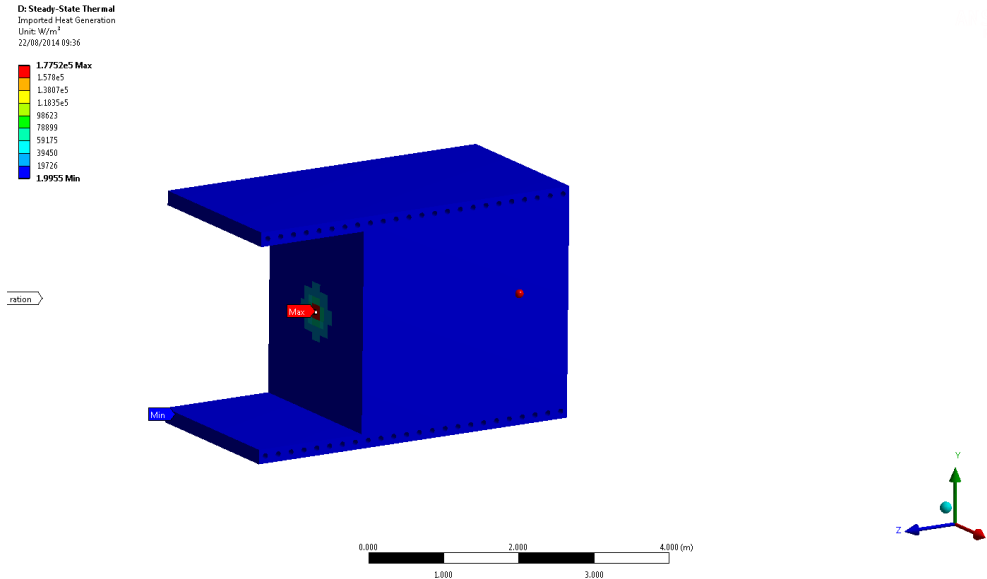
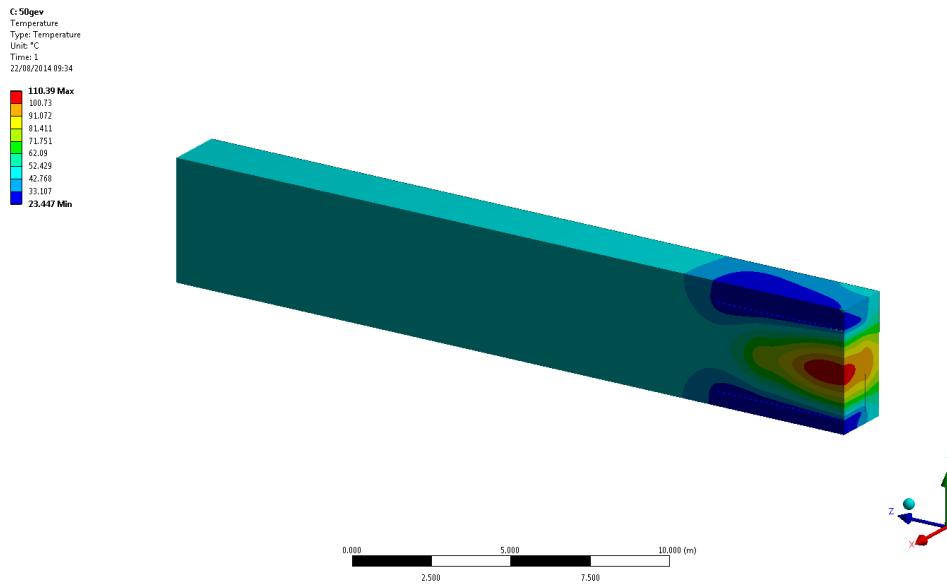
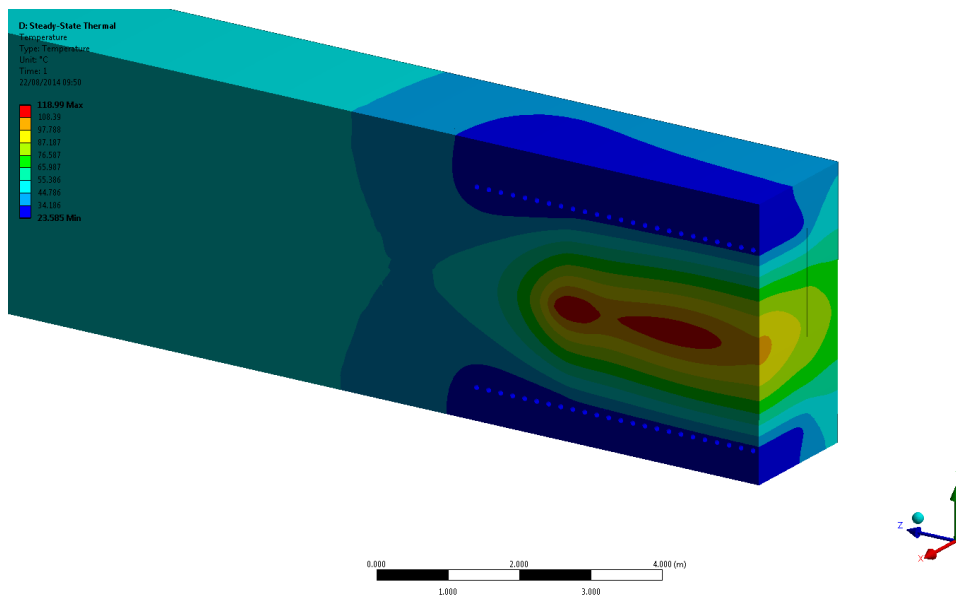


Figure 4.91: Heat deposition profile at the hadron stop - 400 GeV configuration.

The temperature profile due to the impact of the hadron cascade along the beam axis is shown in Figure ?? and Figure 4.93, for the hottest region assuming a continuous operation of beam on target. The maximum temperature on axis in the hadron stop, after 200 days continuous running, rises to 118 °C, partly due to non-interacting protons. The peak in temperature at 3 m is reduced with the foreseen longer heat sink of 5 m. The maximum temperature at the end of the dump is still about 55 °C, but can be easily reduced with additional water cooling.



**Figure 4.92:** Cut view showing the temperature profile for a water cooled hadron stop. 50 GeV beam, maximum temperature is 110 °C at the centre of the graphite block.



**Figure 4.93:** 63 Cut view showing the temperature profile for a water cooled hadron stop. - 400 GeV beam, maximum temperature is 118°C at the centre of the graphite block.

The calculation shows that the temperature in the hadron stopper is not an issue, even with reduced thermal conductance. The temperature in the graphite is far below 400 °C (maximum acceptable temperature for the graphite) and the temperature in the aluminium plates remains around 30 °C, fully acceptable operating temperature. Even with a low water cooling (heat transfer coefficient 100 W/m<sup>2</sup> K for water at 20 °C), the margin would be large enough to accommodate a low thermal conductance between graphite and the aluminium plates.

### ■ Initial Reaction Temperatures in Gas

※Extracted from other publications

Atmospheric Gas	Initial Reaction Temperature	Reaction
Air	380~400℃	Oxidization
Water vapor	700~750℃	Oxidization
Carbon dioxide	800~900℃	Oxidization
Hydrogen	1000~1200℃	Methanation
Nitrogen	2000~2500℃	Cyaniding
Chlorine	2500℃	Graphite sublimation
Argon	3000℃	Graphite sublimation
Vacuum	2200℃	Graphite sublimation

In an oxidizing atmosphere, graphite reacts with oxygen at a relatively low temperature. However, in a non-oxidizing atmosphere, graphite is chemically and thermally an extremely stable material, enabling a broad range of applications.

Figure 4.94: Graphite reaction temperatures in different gases. (Data from Toyo Tanso USA). Maximum temperature of the graphite at the LAGUNA hadron stop is 120 °C.

## 4.10 The muon stations

In order to steer the neutrino beam direction towards the experiments, muon monitor detectors will be installed. Ideally three such stations should be foreseen: a. The first one will be practically embedded in the hadron stop at about 2 m downstream the graphite core, or about 5m from the front face. This to allow observing the low energy muons directly related to the interesting neutrinos for the experiment. b. A second one at about 5 m downstream the hadron stop to observe the penetrating high-energy muons c. Optionally a third one at about 20 m further downstream for improved steering capabilities and redundancy. All stations should be able to measure discretely the horizontal and vertical profile of the beam, preferentially of the same technology or inter-calibrated. The construction could be similar as in CNGS. In the first muon pit the detectors shall be highly resistant to radiation (such as diamond detector) as the

yearly cumulated dose will be extremely high, likely reaching 1 MGy/y; a more precise figure depends on the final position of the 1st muon pit with respect to the graphite core. This installation should be serviced from the top (surface) level through a vertical pit filled with shielding plugs during the operation of the facility. Because of that, careful attention needs to be put in the design phase to shield the surface from prompt radiation. The surface building could also house the cooling station for the hadron absorber.

## 4.11 Critical beam instrumentation

Based on the CNGS experience, in addition to the muon pit already described, well calibrated BCT detectors should be adopted to precisely know the intensity of the beam for each extraction; due to the non-trivial access to the target zone, remote calibration systems should be envisaged. In order to measure the beam footprint close to the target, dedicated beam screens should be adopted right before the beam window. Beam loss monitors (preferably diamond detector-like) should be placed possibly laterally-symmetric with respect to the target. An interlocked beam position monitor right upstream the target should be present (similar to the CNGS BPKG), to avoid sending more than 1 off-axis pulse for target protection.

## 4.12 Handling issues

Discussed in detail in the following chapter.

## 4.13 Shielding elements

The present design offers a minimum quantity of movable shielding blocks. Details of installation and handling given in the next Chapter.

## 4.14 General Services

All the standard stuff

### 4.14.1 Cooling networks

- cooling demin. water for the shielding blocks,
- cooling demin. water for the decay pipe,
- He flow for the target chase and decay volume
- cooling demin. water for horn/reflector

For the shielding blocks

### 4.14.2 Ventilation systems

- air for proton beam tunnel, target cavern, hot-cell and service area

Will work with controlled humidity in close loop and small leak to outside through filters.

### **4.14.3 Electrical networks**

Not particulare requirements. Key clients:

- horn/refelctor - discussed in a separate section below
- services, cranes, ventilation system, lighting

## Chapter 5

# The High-Power Proton Synchrotron Accelerator Feasibility Study

The High-Power Protons Synchrotron (HP-PS) is aimed at providing a new very high power (2 MW) and high energy (30 - 50 GeV) proton source for the CN2PY facility as a potential longer term upgrade. The feasibility study of the new HP-PS, which is largely inspired from the PS2 design study, but dedicated to CN2PY, uses the Low Power Superconducting Protons Linac (LP-SPL) at 4 GeV as injector.

In the next section, the main design constraints together with the basic machine layout and parameters are provided, including the required modifications in the parameters of the LP-SPL for meeting the beam requirements for the new synchrotron. The ring optics is discussed in section 5.2. This section also provides the requirements in terms of magnets and summarises the studies made for orbit correction schemes, non-linear optics, machine imperfections and space charge effects. Section 5.3 summarises the studies performed for the beam transfer systems of the ring, including the charge exchange injection, using the foil stripping method as a baseline, but also the optional laser assisted stripping scheme. It also describes the longitudinal painting scheme, used to fill efficiently the longitudinal phase space, taking into account beam stability criteria, while limiting the required RF voltage. The section finally discusses the extraction of the high energy proton beam together with the required systems. The cycling of the HP-PS together with the longitudinal beam parameters and stability criteria are discussed in section 5.4. Since beam loss management in the HP-PS is mandatory the feasibility study also addresses in section 5.5 extensively a collimation scheme in order to control and localise the losses in specific and well defined places. Section 5.6 discusses the required magnetic elements, as specified in section 5.2 together with the technological challenges to meet the requirements of the magnets proposed in this feasibility study. The minimum required beam instrumentation is summarised in section ???. In case this feasibility study is, sooner or later, converted into a conceptual or technical design study many more details will be required. Section ??? briefly discusses the areas that at least deserve more study or even R&D.

## 5.1 Design requirements and choices

### 5.1.1 Average beam power

The average beam power

$$P = qf_r N_p E_k \quad (5.1)$$

is the product of the charge  $q$ , the repetition rate  $f_r$ , the number of charged particles  $N_p$  and the kinetic energy of the beam  $E_k$ . The first three parameters define the average current per machine pulse  $\bar{I} = qf_r N_p$ . High average beam power, implies both large average current (number



of particles and/or repetition rate) and kinetic energy.

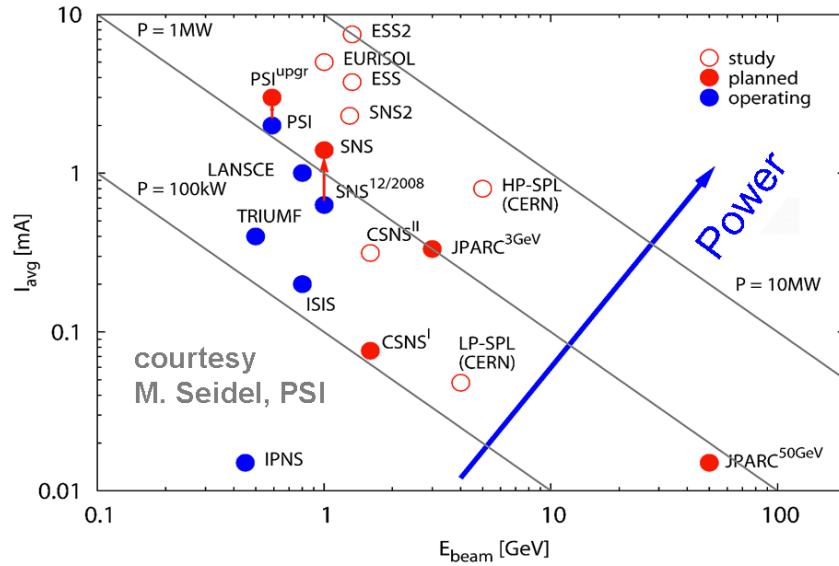


**Figure 5.1:** Average current versus kinetic energy for a number of existing (blue) and future (red) high power machines [?].

In Fig. 5.1, the average current is plotted versus the kinetic energy in logarithmic scale for a number of high power accelerators under operation or in the design phase. The average power is represented by straight lines starting from the bottom left part and moving to upper right. It is interesting to observe that most existing high-power accelerators based on Rapid Cycling Synchrotrons (RSC) operate at energies of less than 5 GeV. In these cases the ratio between the extracted and injected beam energy is often rather low (e.g. 1 to 5). For the HP-PS feasibility study the extracted beam energy is requested to range between 30 and 50 GeV, similar to the J-PARC main ring. With an injected beam energy of 4 GeV, the energy ratio of the HP-PS is between 7.5 and 12.5, which, in combination with the high extraction energy, is beyond the reach of today's RCSs and puts constraints on both number of particles and repetition rate. Note that the actual CNGS beam coming from the SPS at 400 GeV is found out of the figure scale in the bottom right corner, i.e. very high energy but with very low average current, due to the very low repetition rate. All these impact a number of parameter choices, briefly described in the following paragraphs. The parameters of the PS2 ring [?], which was considered a few years ago as a possible replacement of the actual PS, in view of the LHC injector upgrade, are used as a base for comparison.

**Table 5.1:** Parameters of the LP-SPL relevant to the design of the HP-PS.

Parameters	LP-SPL
Rep. rate [Hz]	2
No of protons [ $10^{14}$ ]	1.1
pulse length [ms]	0.9
Kin. Energy [GeV]	4
Beam Power [MW]	0.14

### 5.1.2 Circumference

The PS2 circumference was fixed to 15/77 of the SPS for increasing the flexibility in the choice of the injected bunch patterns [?]. Neglecting RF beam transfer arguments, the circumference

$C$  can be determined by

$$C \approx 3.335 \frac{2\pi\beta E_k}{Bk} ,$$

i.e. the kinetic energy  $E_k$ , the bending field at extraction  $B$ , and the filling (or packing) factor  $k$ , representing the ratio between the total bending length over the ring circumference. For pure FODO rings like the PS or SPS, this parameter is approximately equal to 2/3, but for the PS2 which employs Negative Momentum Compaction (NMC) arc cells, the filling factor is smaller and equal to around 1/2. This may be considered as an upper limit for the filling factor for this type of cells, due to the nature of the optics, which impose variable bending strength (cells with no or reduced number of dipoles) for modulating dispersion. Considering iron dominated magnets, the bending field should not exceed 1.7 T. In this respect, the circumference depends solely on the energy, i.e. the higher the extraction energy the longer the rings.

### 5.1.3 Repetition rate

The repetition rate is imposed by the source or linac. On the other hand, the linac may be shared with other users, so this value should be considered as an upper limit. In order to estimate the magnet ramp rate, it is assumed a linear ramp and fall of the field and equal length among the injection and extraction plateaux. This length is slightly depended on the linac pulse. Considering an extraction bending field of 1.7 T, the injection field can be scaled with the ratio between injection and extraction energy. The ramp rates can be then estimated and can be pretty unprecedentedly high (several T/s). These high magnet ramp rates are translated to high voltage ratings for the main power supply, which themselves lead to high electrical power consumption. Note that the SIS synchrotron design for FAIR project consider super-ferric magnets with 4 T/s ramp rate [?], which is a good option for reducing electrical power with an extra cost and power for cryogenics. Finally, the rapidly varying field generates Eddy currents in the vacuum chambers which themselves attenuate and distort the accelerator magnets fields, alter the field or gradient uniformity and affect beam stability.

### 5.1.4 Intensity

The intensity is limited by space-charge and other collective effects and instabilities, especially at injection. In particular, the incoherent space-charge tune shift

$$\Delta Q_{x,y} = \frac{r_0 N p C}{2(2\pi)^{3/2} \sigma_z \beta \gamma^2 \epsilon_{x,y}}$$

can be used as the parameter through which the transverse beam emittances can be determined. Note that this expression assumes Gaussian bunches which correspond to the higher tune-shift and can be considered as a pessimistic estimate. In order to get the single bunch beam characteristics and for the sake of comparison with PS2, a 25ns bunch structure was considered. The ring is assumed to be fully filled with bunches leaving only a gap for kicker rise/fall time and the bunch length can be used as a fixed parameter. Although this may seem arbitrary, especially in the case of high intensity beams, for which the bunches are much longer and the harmonic number reduced, the ratio between single bunch intensity and bunch length remains almost constant. For keeping space-charge tune-shift below a target value, and for fixed circumference, the transverse emittances have to be increased. A reduced circumference may be interesting especially if it is followed by an increased bunch length, but then for reaching the higher energy cryogenic magnets will be necessary.

### 5.1.5 Electrical Power

The electrical power consumption for ramped magnets depends on the power supply voltage, which itself depends on the maximum magnetic field, the magnet physical characteristics (length, aperture gap and height) and the ramp rate. Considering fixed optics, with maximum betas of 60m and dispersion of 6m and an energy spread of 0.6% (as for PS2), the gap height can be computed. The total dipole length is simply given by the imposed filling factor of 0.5. The electrical power estimated is more than a factor of three higher than the one of PS2 [?], reaching tens of MW. The larger emittances, needed for keeping space charge tune-shift low, impose larger gaps. The high electrical power consumption of iron dominated magnets makes the choice of super-ferric magnets very attractive.

### 5.1.6 Losses control

Considering the average uncontrolled losses' canonical limit of 1 W/m around the ring, and assuming the pessimistic scenario that all losses occur at extraction, the fractional beam loss limit is set to a few  $10^{-4}$  for any ring in that energy range, almost an order of magnitude lower than PS2. This is consistent with requirements of other high-power synchrotrons (e.g. the SNS accumulator ring [?]) and becomes more stringent for shorter rings, as there is less space for distributing the losses. These strict loss limits require an efficient collimation system in a dedicated straight section, in combination with momentum collimation in the arcs.

### 5.1.7 Optics and layout

In contrast to PS2, the HP-PS does not have strict layout requirements, apart from positioning the injection area parallel to the SPL. A three or four-fold symmetric ring would be desirable in order to accommodate in separate straight sections beam transfer equipment, RF and collimation. NMC cells are necessary in order to avoid transition and associated losses. A resonant arc cell can further increase the filling factor and presents very good non-linear dynamics performance [?].

### 5.1.8 Machine parameters

Using the above-mentioned simple scaling laws, several flavours of parameters for the HP-PS were obtained [?], leading to the final nominal parameters.

Assuming that the HP-PS should become part of the CERN accelerator complex with the LP-SPL [?] as injector, which itself is a linear post-accelerator of the LINAC4 that is being commissioned at CERN, a possible schematic integration is given in fig. 5.2. The existing accelerator complex (PSB, PS, SPS) can receive beam at a repetition rate of close to 1 Hz, however, LINAC4 is capable to pulse at a rate of 2 Hz, allowing beam production for the LP-SPL and the HP-PS at a 1 Hz rate too. With the 1 Hz repetition rate and the requested energy range, the number of protons that needs to be accelerated in the HP-PS in order to produce the 2 MW proton beam can be deduced from eq.(??). This results in a beam intensity of  $4.2 \cdot 10^{14}$  protons per pulse for the lower energy in the requested range of 30 GeV and  $2.5 \cdot 10^{14}$  protons per pulse for high end of the specified range 50 GeV. A beam intensity of  $4.2 \cdot 10^{14}$  for the 30 GeV variant is unprecedented in any of the machines presently running, making the option of 50 GeV rather obvious, also taking into account that  $2.5 \cdot 10^{14}$  is a challenging, but feasible beam intensity.

Therefore a beam energy of 50 GeV with a repetition rate of 1 Hz and a beam intensity of  $2.5 \cdot 10^{14}$  protons is considered as the baseline for this HP-PS feasibility study.

By further increasing the extracted beam energy of the HP-PS to 75 GeV, not only the intensity can be further reduced, as indicated in Table 5.2, but the HP-PS also could become an attractive alternative as injector into the existing SPS for filling the LHC. Although the latter is not a requirement for this feasibility study and the energy lies beyond the requested beam energy range of 30 to 50 GeV, the design of the 50 GeV HP-PS was adapted to allow possible compatibility with a machine producing 2 MW beam power at 75 GeV. Although both rings are based on the same optics and layout, in the following sections the 50 GeV design is considered as the baseline, while the 75 GeV option is being described too, indicating clearly where the potential bottlenecks are and where further study might be required, provided the 75 GeV option is deemed interesting.

In case followup will be given to this feasibility study, a choice for the extraction energy should be made, as it will allow optimising the machine design further, removing some of the constraints that were introduced in order to keep the same design for both energies.

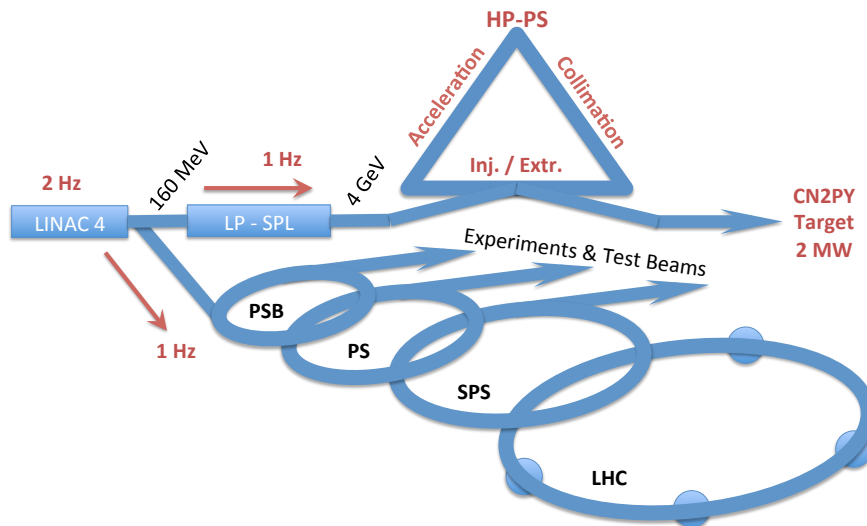


**Figure 5.2:** Possible CERN accelerator complex with LINAC4, LP-SPL and HP-PS

**Table 5.2:** Required HP-PS proton intensity for the three extraction energies discussed, assuming a repetition rate of 1 Hz and a required beam power of 2 MW.

HP-PS extraction energy	Required proton intensity
30 GeV	$4.2 \cdot 10^{14}$
50 GeV	$2.5 \cdot 10^{14}$
75 GeV	$1.7 \cdot 10^{14}$

The LP-SPL accelerates  $H^-$  ions that upon injection in the HP-PS need to be stripped of the electrons, only keeping the protons for further acceleration. The classical scheme of eliminating the electrons is a stripping scheme using carbon or titanium foils. Due to the high intensity of the injected beam, loss management and control at injection is important. The unstripped or

partly stripped ions will be lost in the injection process and needs careful study. Laser assisted stripping could possibly be an attractive alternative to the stripping foil system, but comes with its own requirements. The foil stripping is considered as the baseline in this feasibility study, while the laser stripping option has been studied too and as a consequence a dedicated optics design based on the same machine layout, but with different magnet parameters has been developed.

Although the parameter space of the HP-PS is very different this feasibility study benefited greatly from the PS2 [?] study that was undertaken several years ago at CERN, aiming at replacing the existing CERN PS. This design principally aimed at the production of the LHC beams, hence lower intensities, but smaller beam sizes with the aim to provide high brightness beams for the LHC, whereas the HP-PS focuses on high intensities, higher repetition rates and is not principally concerned by the beam brightness. Another major difference is the proposed shape of the HP-PS, triangular with 3-fold symmetry, providing three Long Straight Sections (LSS) to accommodate in separate straight sections the Injection & Extraction, Beam collimation and the RF accelerating cavities, as indicated in fig. 5.2. One major advantage of this machine geometry is that the majority of the losses will be concentrated in a single LSS where adequate shielding can be applied, leaving the remainder of the machine with low loss levels, hence easing hands-on interventions.

The design of the HP-PS is based on a 3-fold symmetric lattice and has a total circumference of 1256.6 m, which has been adapted to allow also optimal filling of the SPS if this might be required in the future [?]. While the low energy scenario foresees more conventional, but nevertheless super-ferric magnets of 2.1 T peak field, it requires higher bunch population and is therefore more demanding in terms of beam dynamics. On the opposite side the high energy scenario has a lower beam intensity, while the magnet technology is more challenging in terms of peak field (3.1 T) and ramp rate (5.4 T/s). The design parameters of the two energy options are summarised Table 5.3.

The machine does not have strict layout requirements, apart from positioning the injection point such that it is compatible with the requirement for a large bending radius of the LP-SPL to HP-PS transfer line in order to avoid the undesired Lorentz stripping.

## 5.2 Ring optics and beam dynamics

### 5.2.1 Lattice

#### 5.2.1.1 Linear optics and layout

The HP-PS arcs are made out of five Negative Momentum Compaction (NMC) cells for avoiding transition and reducing losses. They are composed of two FODO cells and an insertion of quadrupole doublets in the middle along with 9 dipoles in between the quadrupoles, with a total cell length of 64.7 m. The space between magnets ranges from 0.9 m between consecutive dipoles until 1.6 m between dipoles and quadrupoles in the middle of the cell and is dedicated to install sextupoles, correctors, BPMs and other instrumentation. The full arc becomes achromatic by imposing the horizontal tune to be a multiple of  $2\pi$  ( $4 \times 2\pi = 8\pi$ ), thus avoiding the use of a dispersion suppressor module. As compared to previous design stages, a particular effort was made to reduce the transition gamma to a value of  $15i$ , thereby maximising the momentum compaction factor and increasing instability thresholds.

The LSS lattice is based on quadrupole triplets which allow more space for installing the corresponding equipment. The five families are used for achieving optics constraints especially

Table 5.3: Machine parameters of the HP-PS.

	Unit	50GeV		75GeV	
		Foil	Laser	Foil	Laser
<b>Basic parameters</b>					
Circumference, $C$	[m]		1256.6		
Super-periodicity	-		3-fold		
Beam power inj. / extr.	[MW]	0.19 / 2		0.13 / 2	
Kinetic energy at injection	[GeV]		4		
Repetition rate	[Hz]		1		
RF frequency	[MHz]		40		
$f_{rev} / f_{RF}$ @ injection	[MHz]		0.234 / 39.31		
$f_{rev} / f_{RF}$ @ extraction	[MHz]		0.238 / 40.08		
RF harmonic	-		168		
Number of bunches	-		157		
Protons per pulse	[ $10^{14}$ ]	2.5		1.7	
Intensity per bunch	[ $10^{12}$ ]	1.6		1.1	
<b>Optics parameters</b>					
Betatron horizontal tune, $Q_x$	-	14.24	14.24	14.24	14.24
Betatron vertical tune, $Q_y$	-	11.84	12.22	11.84	12.22
Max. horizontal beta function, $\hat{\beta}_x$	[m]	58.2	77.7	58.2	77.7
Max. vertical beta function, $\hat{\beta}_y$	[m]	62.2	64.6	62.2	64.6
Natural horizontal chromaticity, $Q'_x$	-	-18.1	-19.3	-18.1	-19.3
Natural vertical chromaticity, $Q'_y$	-	-18.9	-19.8	-18.9	-19.8
Min. / Max. dispersion, $\hat{D}_x / \check{D}_x$	[m]		-5.9/5.5		
Transition gamma, $\gamma_t$	-		15.1 <i>i</i>		
<b>Dipole magnets</b>					
Number of dipoles	-		135		
Bending radius, $\rho$	[m]		80.9		
Length, $l$	[m]		3.76		
Min. drift space between dipoles	[m]		0.9		
Main B field inj. / extr.	[T]	0.17 / 2.1		0.17 / 3.13	
Max. beam rigidity, $\hat{B}\rho$	[Tm]	169.9		253.3	
Dipole ramp rate, $\frac{dB}{dt}$	[T/s]	3.5		5.5	
Gap height	[mm]	106		92	
<b>Quadrupole magnets</b>					
Number of quadrupoles	-		138		
Number of independent families	-		9		
Number of types	-		6		
Length, arc	[m]		2		
Length, LSS	[m]		1.81, 2.06, 4		
Max. pole tip field	[T]	0.97	1.22	1.26	1.47
<b>Chromatic sextupole magnets</b>					
Number of sextupoles	-		60		
Number of independent families	-		2		
Number of types	-		1		
Length	[m]		0.3		
Max. normalized sextupole strength	[ $m^{-3}$ ]	1.03		1.09	

for beam transfer equipment and general tuning. During the optimisation process several iterations were performed for the the LSS optics, with the solution of four triplets being the one satisfying all constraints. Two different injection optics are considered for the requirements of foil or laser stripping. For both options the arc optics and layout are the same in order to maintain the negative momentum compaction and the same transition gamma. On the other hand, different requirements are imposed in the LSS by the two different injection methods. The foil option demands round beams in order to minimise the energy deposition, while the laser option requires a very low vertical beam size.

The optics of the LSS for both foil and laser stripping options, together with the optics of a NMC cell and one sixth of the full ring are shown in Fig. 5.3. The horizontal and vertical beta functions are shown in black and red lines respectively, while the horizontal dispersion in green.

The horizontal and vertical beta functions in the arcs are limited below 50 m, while the dispersion oscillates between  $\pm 6$  m, having a big impact on the aperture of the magnetic elements. This unavoidable though for targeting low imaginary transition gamma. For the foil injection option, the maximum beta function in the straight sections rises slightly until 62 m. In the middle of the central drift (the injection point), the beta functions were chosen to be 21 m horizontally and 25 m vertically in order to have a round beam. For the laser injection option there is a maximum of the horizontal beta function of 78 m as a consequence of the low vertical beta (5.6 m) at the injection point. The horizontal dispersion is zero in both cases due to the achromaticity of the arcs.

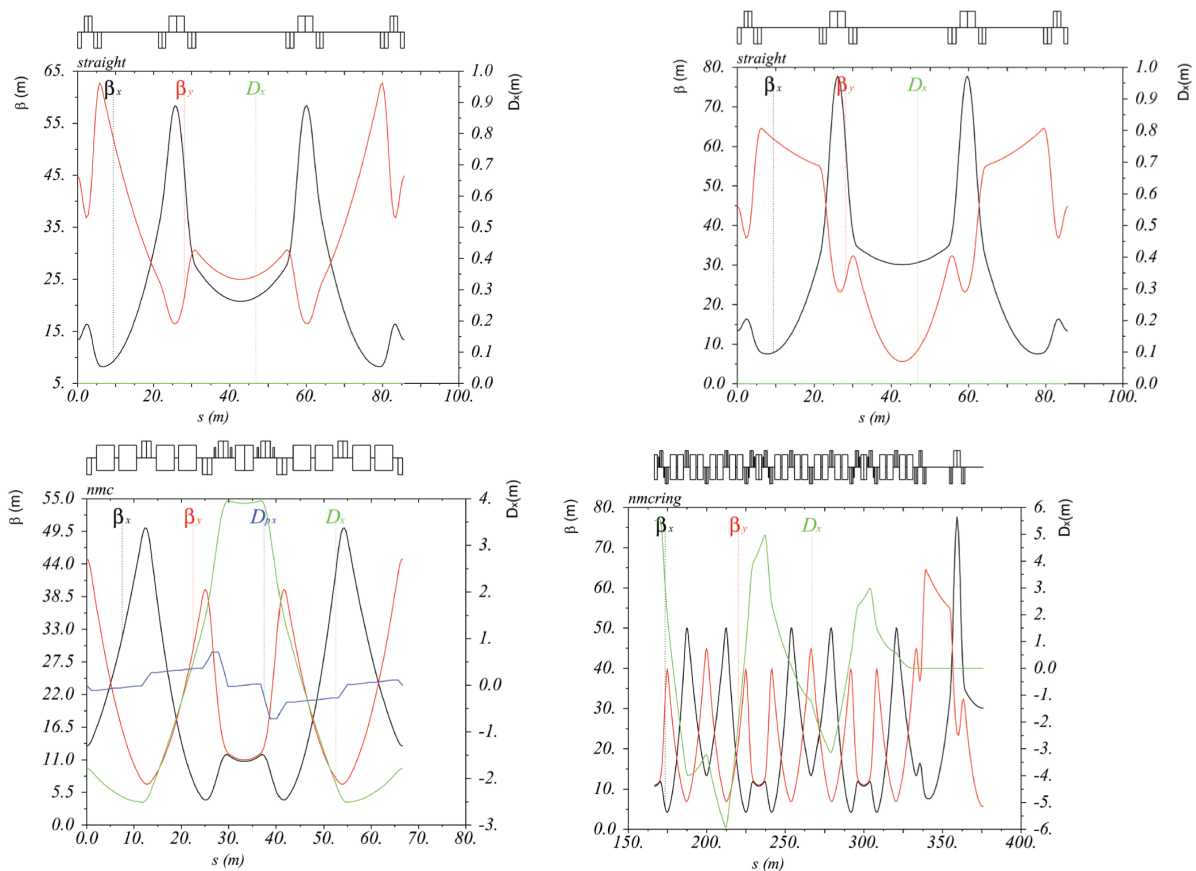


**Figure 5.3:** Optics functions for the LSS considering foil injection (top left), LSS with laser injection (top right), NMC cell (bottom left) and one sixth of the full ring (bottom right).

### 5.2.1.2 Space-charge and aperture considerations

In order to reach the 2 MW nominal beam power, a high beam intensity is required, giving rise to strong collective effects. In particular, the incoherent space-charge tune shift has to be taken into account in the tune working point choice and the determination of the transverse emittances. For this, the incoherent space-charge tune shift formula can be used:

$$\Delta Q_{x,y} = -\frac{r_0 N_b}{(2\pi)^{3/2} \sigma_z \beta^2 \gamma^3} \oint \frac{\beta_{x,y}}{\sigma_{x,y}(\sigma_x + \sigma_y)} ds \quad (5.2)$$

This expression assumes Gaussian bunches which produce larger tune-shifts and is a pessimistic consideration, since for the HP-PS the beam will be painted to a quasi-uniform distribution during the multi-turn injection process. A reasonable space-charge limit is set to -0.25 for both planes. The choice of the transverse emittance, working point and the longitudinal parameters, such as energy spread and bunch length, have an important impact on the machine performance, as they define the space charge detuning and the transverse beam size. The latter will then define the magnet apertures and through these the pole tip magnetic fields, which have to be within the feasibility and cost limits. Finally, in order to minimise the effect of coupling resonances, round beams are desired. In order to find a suitable emittance working point, a parametrisation of the maximum pole tip field and the maximum quadrupole and dipole apertures has been performed, for a range of normalised emittances between  $3 - 25 \mu\text{m rad}$  in both planes, energy spreads between  $4.5 - 7.5 \cdot 10^{-3}$  and bunch lengths between  $10 - 15 \text{ ns}$ , for the four combinations of energy and injection options. The solutions verifying all the requirements have been filtered according to longitudinal constraints and the final chosen working points are presented in Table 5.4.

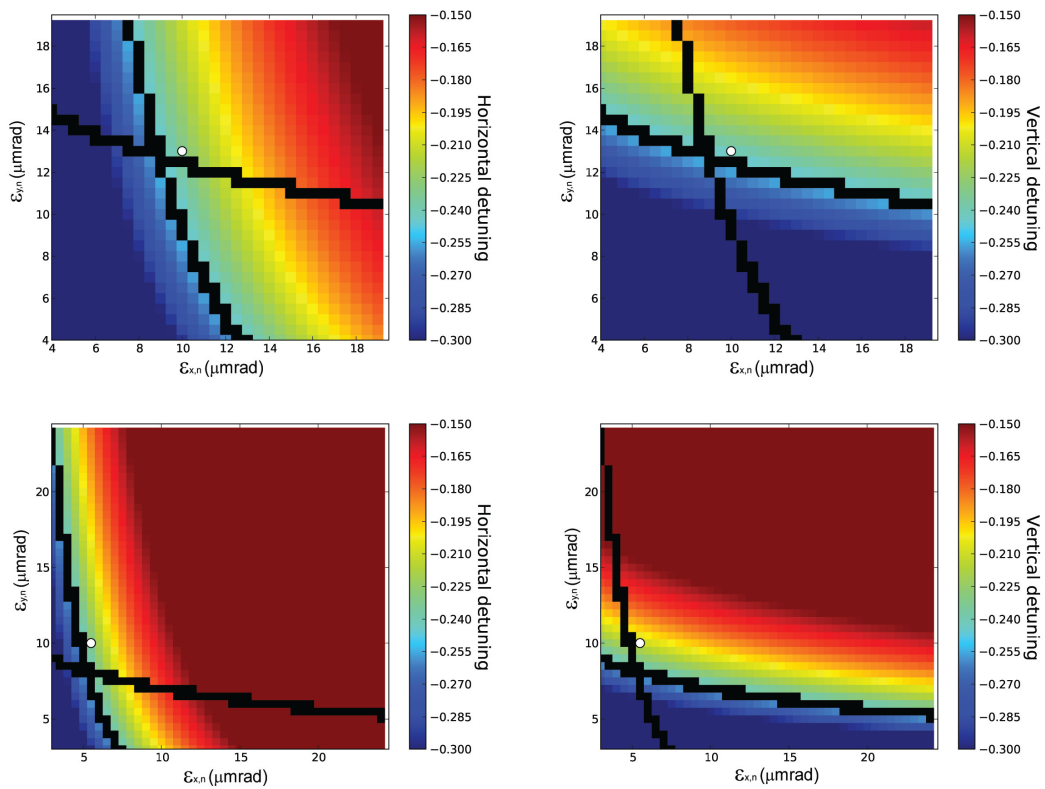
**Table 5.4:** Beam parameters chosen for the different HP-PS scenarios.

Parameter	Unit	50 GeV		75 GeV	
		Foil	Laser	Foil	Laser
Normalised horizontal emittance, $\epsilon_{x,n}$	$[\mu\text{mrad}]$	10.5	10	5.5	5.5
Normalised vertical emittance, $\epsilon_{y,n}$	$[\mu\text{mrad}]$	13.5	13	10	10
Full momentum spread at injection, $dp/p_{\text{inj}}$	$[10^{-3}]$	6.62	7.32	7.33	7.38
Full bunch length at injection, $\tau_{\text{inj}}$	$[\text{ns}]$	12.52	13	13.51	13.76

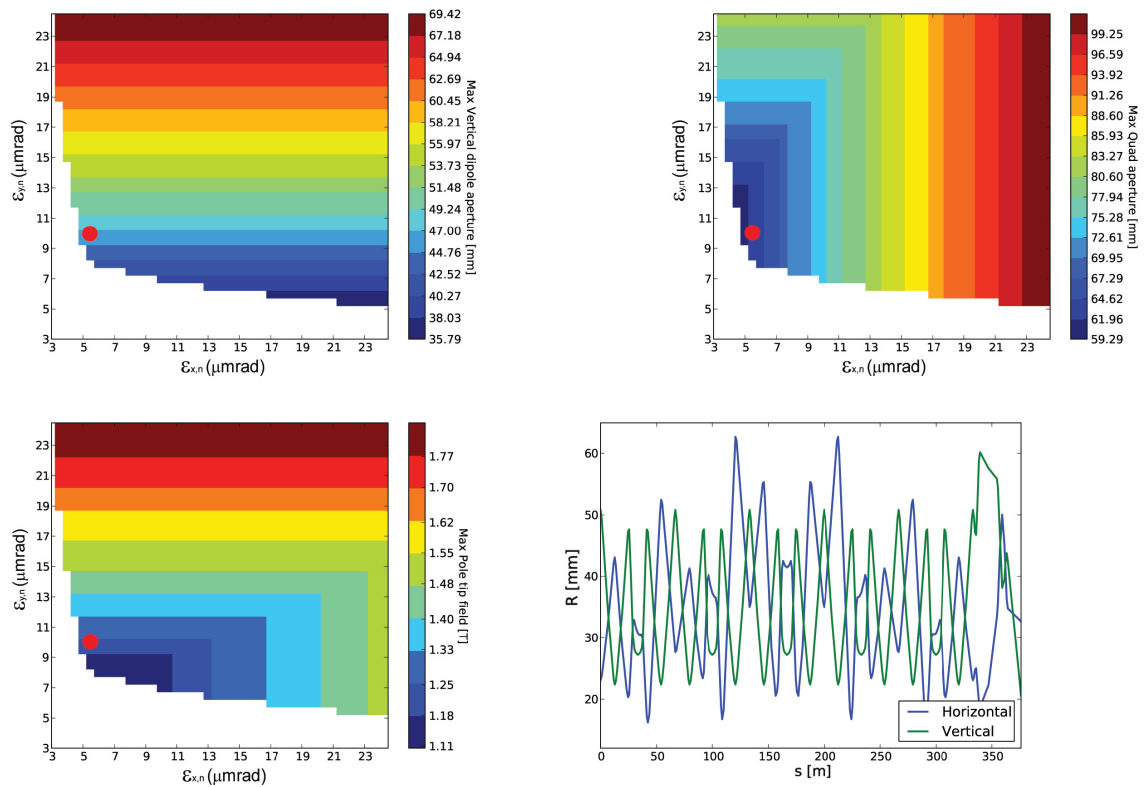
In Fig. 5.4, the horizontal and vertical normalised emittance area is parametrised with the horizontal (top) and vertical (bottom) space charge tune-shift, for the laser injection scheme and the chosen energy spread and bunch length. Both the 50 GeV (left) and the 75 GeV (right) options are presented. The blue colours represent the lower absolute tune-shift whereas the higher values correspond to red colours. The two solid black curves trace the -0.25 space charge limit. The minimum normalised emittances which fulfil the space charge constraint are thus towards the right upper corner of the plot. The white dot represents the chosen emittance working point. The results for the foil injection scheme are very similar and therefore are not presented here.

Fig. 5.5 shows the parametrisation of the dipole half-gap (top, left), the maximum quadrupole radius of the whole lattice (top, right) and the maximum pole-tip field (bottom, left), for the laser injection optics of the 75 GeV ring. Only emittance areas that satisfy the space-charge limit are shown. The apertures are chosen in order to fit a  $4 \sigma$  beam in both planes (bottom, right), including vacuum pipe thickness, mechanical and orbit tolerances. In Fig. 5.5 (bottom right), the apertures for the first sixth of the machine are presented. The vertical emittance mainly affects the dipole acceptance, whereas the quadrupole radius is largely determined by the horizontal beam size. Rounder beams with lower vertical emittances to reduce the dipole gap could be





**Figure 5.4:** Incoherent space charge detuning for the laser injection option. The 50 GeV and 75 GeV versions correspond to the top and bottom plots. The colour code shows the horizontal and vertical detuning (left and right, respectively).



**Figure 5.5:** Parametrisation of maximum dipole half-gap (top left), quadrupole aperture (top right), pole tip field (bottom left) in the plane of the emittances for the 75 GeV HP-PS with laser injection. The bottom right plot shows the radius along one sixth of the lattice.

also envisaged, however the quadrupole radius as well as the maximum pole-tip field would increase beyond the limits.

### 5.2.1.3 Tune working point adjustment

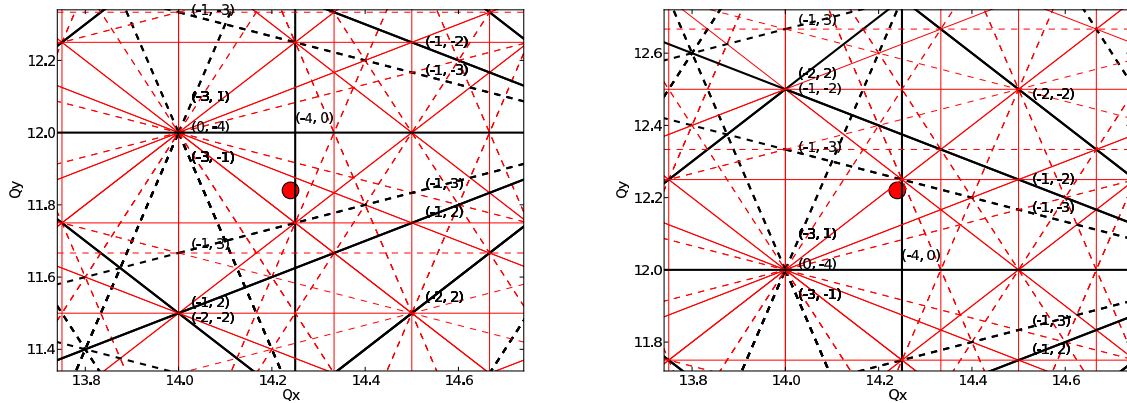


**Figure 5.6:** Working points of the two injection options, foil (left) and laser (right), in the tune map.

In order to keep the achromatic condition in the arcs, the horizontal tuning ability of the ring is provided only by the LSS, whereas the vertical tune is quite flexible. For the foil option the working point is chosen to be  $(Q_x, Q_y) = (14.24, 11.84)$ . For the laser option, the phase advance of the LSS has to be increased, in order to achieve the injection and extraction constraints. The vertical working point is raised, while the horizontal one is kept the same:  $(Q_x, Q_y) = (14.24, 12.22)$ . Fig. 5.6 shows the working points for both injection options in the tune map. Normal resonances are represented by solid lines while skew resonances by dashed. The systematic resonances are shown in black while the non-systematic ones in red.

The ability to tune the ring to different working points is displayed in Fig. 5.7. The parameter space of the independent quadrupoles is scanned by systematically changing their strength in steps between 70% and 130% of their nominal value. Only stable solutions are considered. The HP-PS lattice is tuned this way for several horizontal and vertical working points (from 12 to 16.5 in horizontal and from 10.5 to 13.5 in vertical). The color-code indicates the maximum horizontal and vertical beta functions. Resonances up to third order are shown. For the foil, the horizontal beta function do not depend highly on the vertical tune, and the smaller beta values are found in the working points between 14 and 16 with the exception of 15, the location of the systematic half integer resonance. The vertical beta has a region of low values between 11 and 12 vertical tune. For the laser option there is a low horizontal beta window between 14 and 15 horizontal tune, however for the vertical beta the optimal range is between 11 and 12 vertical tune which is not enough to fullfil the phase advance constraints needed for extraction. The maximum vertical beta in the LSS for our chosen optics is about 65 m.

### 5.2.1.4 Chromaticity correction

Two sextupole families are used for the chromaticity correction, located in dispersive regions in the arcs. In order to minimise their contribution to the non-linear effects they are installed at locations with high dispersion and maximal beta functions, i.e. next to the quadrupoles in the arc. The maximum normalised sextupole strength is  $1.03 \text{ m}^{-3}$  for the 50 GeV option and  $1.09 \text{ m}^{-3}$  for the 75 GeV. As will be discussed later, the dynamic aperture (DA) of the machine is not limited by the sextupoles.

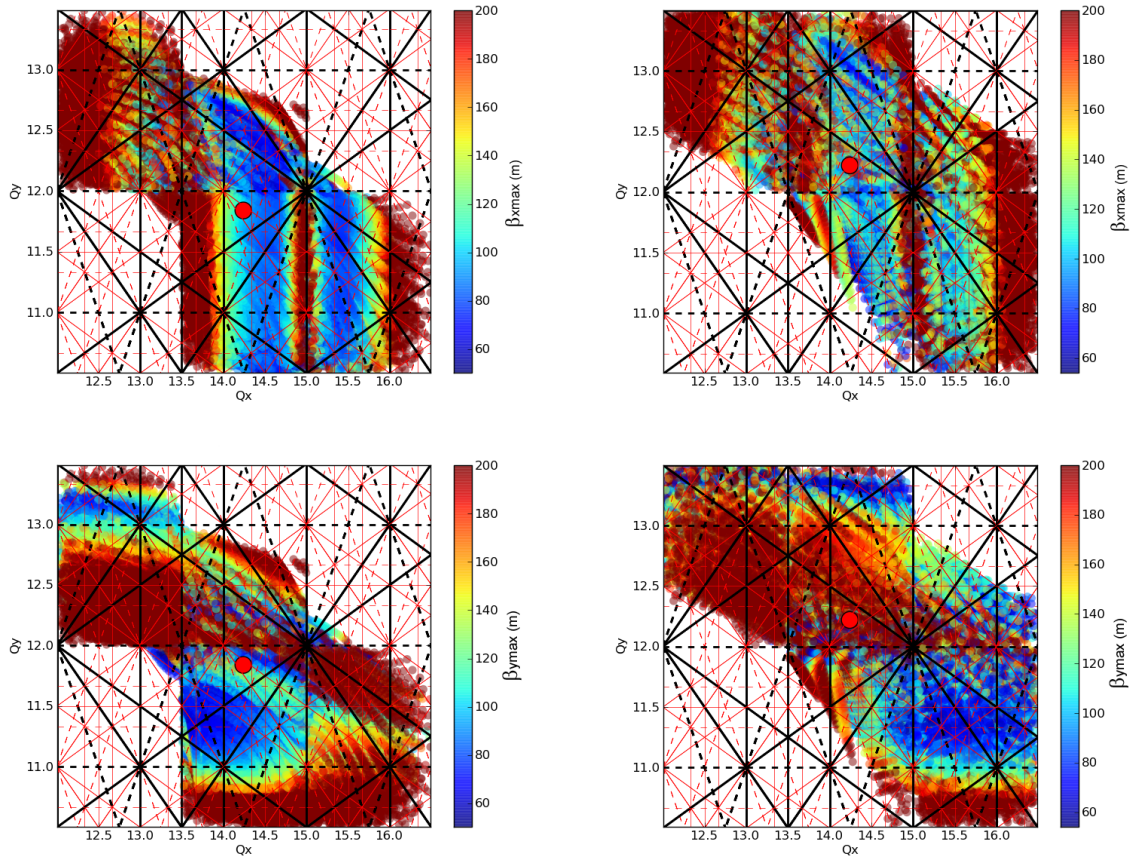


**Figure 5.7:** Tunability plots for the foil injection option (left) and laser injection option (right). The colour code represents the maximum horizontal (top) and vertical (bottom) beta functions.

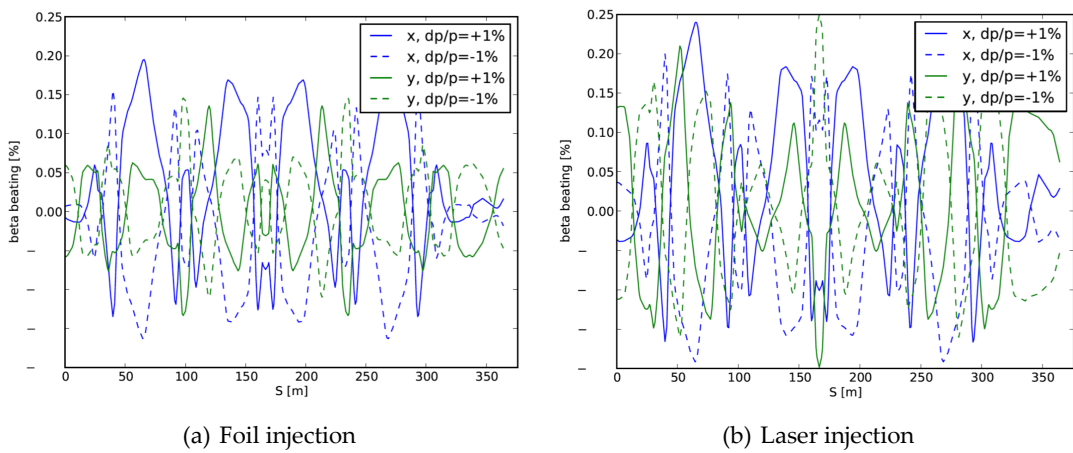


**Figure 5.8:** Off-momentum beta beating along one sixth of the machine for the foil injection scheme (left) and for the laser one (right).

Fig. 5.8 shows the horizontal and vertical off-momentum beta beating along one sixth of the machine for a momentum deviation of  $\pm 1\%$ . The maximum error in the beta functions is around 20% which is the beta beating value considered for the aperture calculations. Although no misalignments have been included here this value is still conservative, as the energy spread value of 1% is quite large and beyond the full rms beam energy spread.

## 5.2.2 Orbit Correction Studies

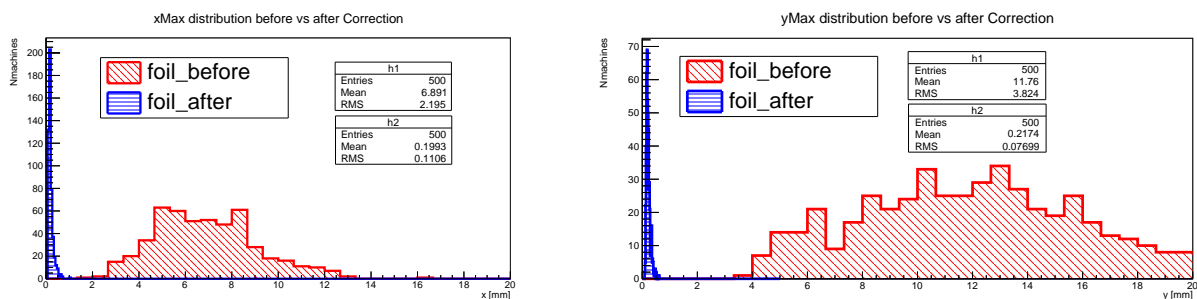
Random field errors and magnet misalignments were introduced in the HP-PS foil and laser optics schemes of 50 GeV, in order to investigate their impact on orbit distortion, and evaluate the efficiency and performance of the HP-PS correction system. The closed orbit errors, summarised in Table 5.11, were distributed with a Gaussian cut at  $3\sigma$ , following the experience gained through the PS2 studies [90, 91]. In the studies described below, the nominal optics were used with the working point at  $(Q_x, Q_y)=(14.24, 11.84)$  for the foil scheme and  $(Q_x, Q_y)=(14.24, 12.22)$  for the laser scheme.

**Table 5.5:** Assumed machine imperfections of the HP-PS lattice (RMS values).

Error	Unit	RMS value
Relative dipole field error	-	$5.0 \cdot 10^{-4}$
Transverse quadrupole shift	[mm]	0.2
Longitudinal dipole shift	[mm]	0.3
Dipole tilt	[mrad]	0.3

73 horizontal and 63 vertical correctors of 20 cm length were placed at local  $\beta_x$  and  $\beta_y$  maxima respectively, for maximum correction efficiency. After distorting the closed orbit, the CORRECT module of MAD-X was used for the orbit correction, with the MICADO algorithm, which provides the most effective correction [92].

The distribution of the maximum horizontal and vertical orbit deviations for 500 random seeds, before and after performing the orbit correction, is shown in Figures 5.9 for the foil optics schemes. The uncorrected orbit distortion exceeds 6 mm in the horizontal and 10 mm in the vertical plane whereas after correction it reduces to as low as  $\sim 0.2$  mm. The mean and RMS values of the maximum distorted orbit before and after correction are summarised in Table 5.6. In both schemes the mean orbit was corrected by a factor of  $\sim 45$  in the horizontal and by a factor larger than 50 in the vertical plane.



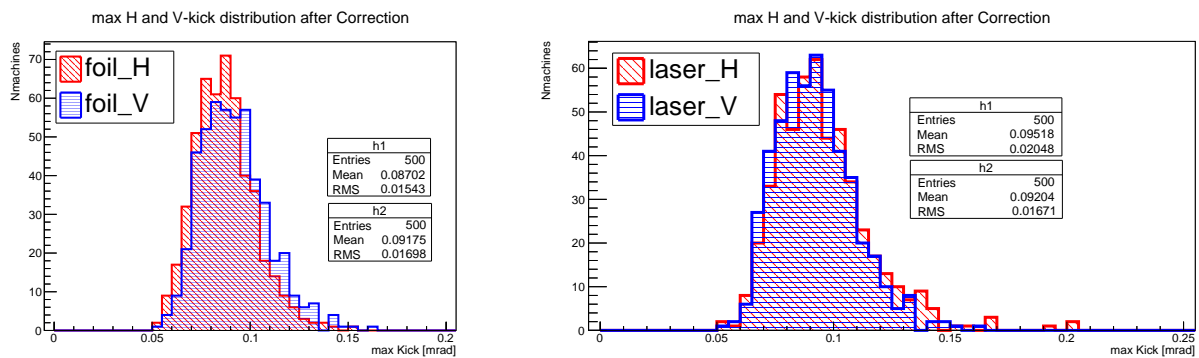
**Figure 5.9:** Distribution of the maximum orbit deviation at the horizontal (left) and vertical (right) planes for the foil optics scheme, before (red) and after (blue) correction.

Figure 5.10 presents the distribution of the maximum required kicker-strength of the 500 random seeds, the mean value of which is  $\sim 0.09$  mrad; this value corresponds to 0.02 T for

**Table 5.6:** Mean maximum closed orbit distortion for the foil and laser optics, before and after correction.

Optics	Plane	Unit	Before correction		After correction	
			Mean	RMS	Mean	RMS
Foil	H	[mm]	6.90	2.20	0.20	0.11
	V	[mm]	11.76	3.82	0.22	0.08
Laser	H	[mm]	9.62	2.63	0.20	3.52
	V	[mm]	10.10	0.12	0.16	0.03

the 50 GeV case, which is well within the magnets' capability limits. The orbits from 50 machines, before (red) and after (blue) correction for both optics schemes are shown in Figures 5.11 and 5.12, demonstrating the good efficiency of the correction system.


**Figure 5.10:** Distribution of the maximum required kicker-strength for 500 random seeds, in the horizontal (red) and vertical (blue) planes, in the foil (left) and laser (right) schemes.

**Table 5.7:** Mean maximum kicker-strength.

Optics	Plane	Unit	Max strength
Foil	H	[mrad]	0.087
	V	[mrad]	0.092
Laser	H	[mrad]	0.095
	V	[mrad]	0.092

It was shown that when 10% of the correctors are switched off (selected randomly), and 5% monitors failure is considered, the obtained orbit deviation is  $\sim 1$  mm in both planes in the foil scheme, and  $\sim 0.5$  mm and  $\sim 0.9$  mm in the horizontal and vertical planes respectively in the laser scheme (see Table 5.8).

Finally, different percentages of working correctors were used (as selected by MICADO), and for each case the maximum horizontal and vertical orbit deviations were calculated. The results, presented in Figure 5.13, show that in the case where 70-80% of the correctors are used, the maximum orbit deviation is  $\sim 0.20$  mm for both planes and both optics schemes, which is considered to be a quite small and sufficient orbit deviation for machine operation.



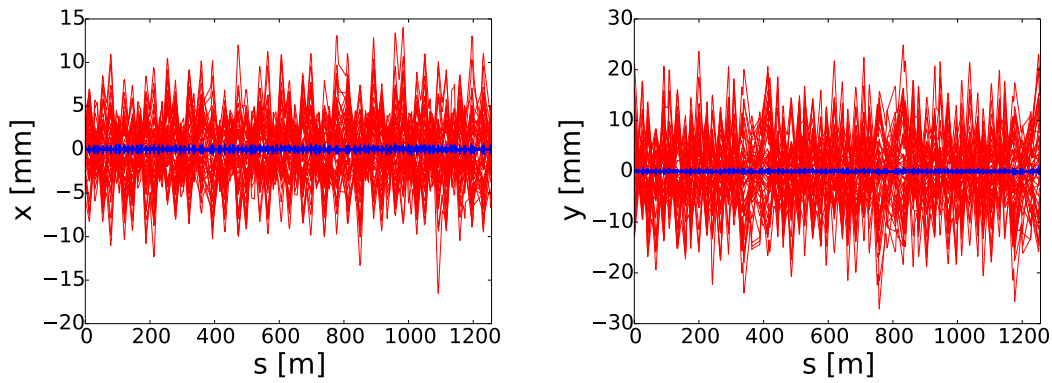


**Figure 5.11:** Horizontal (left) and vertical (right) orbit deviations for the foil scheme, before (red) and after (blue) correction.

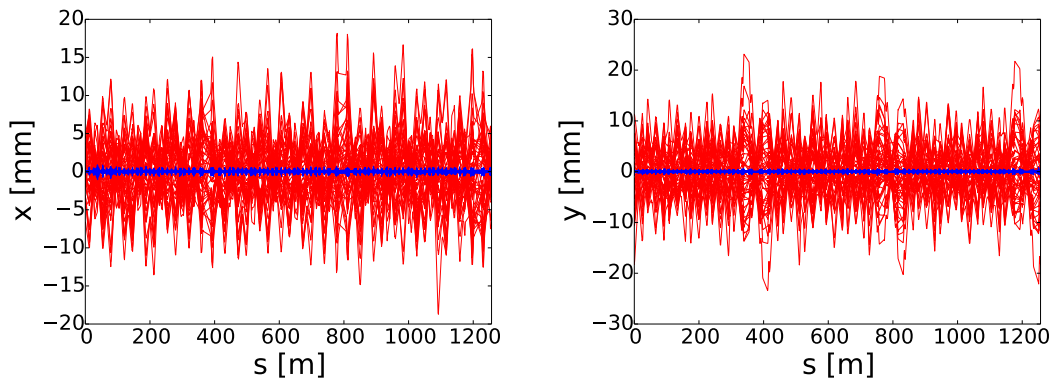


**Figure 5.12:** Horizontal (left) and vertical (right) orbit deviations for the laser scheme, before (red) and after (blue) correction.

**Table 5.8:** Maximum closed orbit distortion for both optics schemes, before and after correction when assuming 10% corrector and 5% monitor failure.

Optics	Plane	Unit	Before correction		After correction	
			Mean	RMS	Mean	RMS
Foil	H	[mm]	5.19	2.17	1.15	0.19
	V	[mm]	12.35	5.51	1.20	0.19
Laser	H	[mm]	9.62	3.81	0.47	0.11
	V	[mm]	10.10	5.20	0.87	0.22

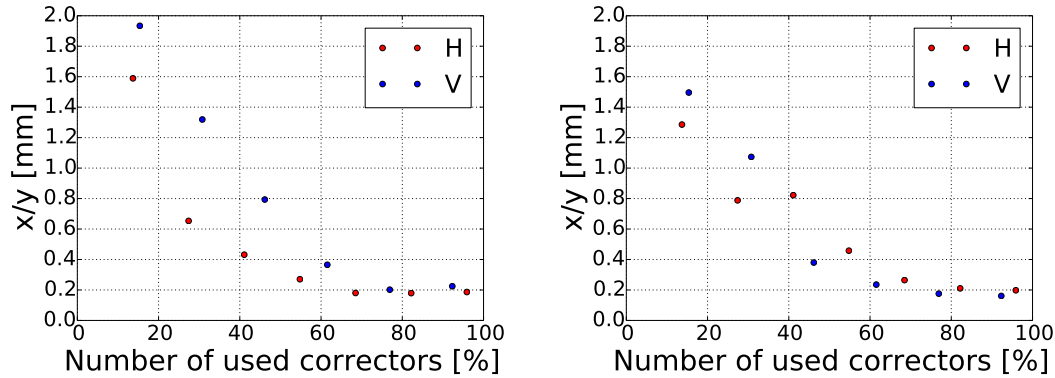


**Figure 5.13:** Maximum orbit deviation for different percentages of used horizontal (red) and vertical (blue) correctors. For each case, a different set of correctors is used by MICADO.

### 5.2.3 Non-linear optics and machine imperfections

Dynamic aperture (DA) simulations were performed in order to evaluate the robustness of the design with respect to single particle non-linear dynamics. As the dispersion is quite high, the two families of chromaticity sextupoles' have quite reduced strengths and the ring's non-linear dynamics performance is not at all limited by them.

The impact of the misalignments and closed orbit errors is studied using the errors in Table 5.11. For this, the errors are first assigned to the lattice after the chromaticity correction. The closed orbit distortion is then corrected, the tunes are rematched to the initial working point and the chromaticity reset to 0. Using the new lattice configuration, particles were tracked for 1000 turns, using the PTC-TRACK module of MADX. Dynamic aperture studies for different momentum offsets were performed and the results are shown in Fig. 5.14 for the two injection options. The nominal lattice is shown in dashed black line. The DA for the misaligned and corrected lattice is shown in green for the on momentum case, in magenta for  $dp/p=0.6\%$  while in blue for  $dp/p=-0.6\%$ . The geometrical acceptance of the ring is shown in solid black. From this we can conclude that the introduction of linear errors and misalignments that distort the orbit have a minor impact in the single particle dynamics in the HPPS lattice.

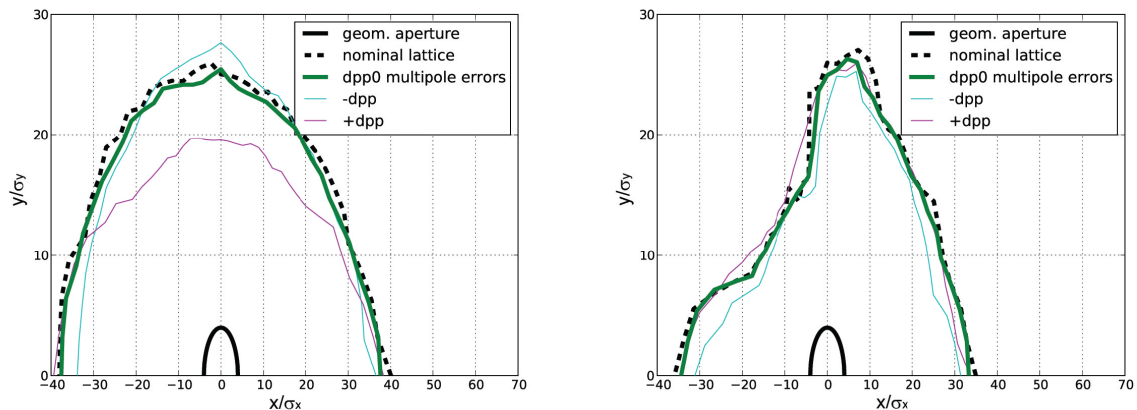


**Figure 5.14:** On and off-momentum average transverse dynamic aperture measured in beam sizes for the HP-PS ring with foil injection (left) and laser injection (right) for 1000-turns tracking, using 100 random seeds of misalignment and correction.



### 5.2.4 Multipole field errors

The impact of the multipole errors of the main magnets on the beam dynamics is also studied. Table 5.9 lists the considered multipoles. Those are similar to the ones used in PS2 [?], which in turn were obtained from the multipoles measured at JPARC Main Ring due to the fact that this machine has parameters comparable to those of the HP-PS. All multipole values in the table are relative to the main component in units  $10^{-4}$ . Their effect is expected to be most severe for low energies where the transverse beam dimensions are much bigger than for high energies.

**Table 5.9:** Relative multipole components in units  $10^{-4}$  at the reference radius  $R$ .

Order n	Dipoles (R=3cm)		Quadrupoles (R=5.95cm)		Sextupoles (R=5.95cm)	
	mean $b_n/b_1$	random $b_n/b_1$	mean $b_n/b_2$	random $b_n/b_2$	mean $b_n/b_3$	random $b_n/b_3$
1	$10^4$	0	0	0	0	0
2	0.15	0.1	$10^4$	5	0	0
3	1	0.5	-2	1	$10^4$	5
4	0.013	0.064	1	1	-0.5	1.5
5	-0.1	0.064	1	1.5	0.5	1.5
6	-0.003	0.003	3	1	-1	0.5
7	-0.026	0.005	0.5	1	1	0.5
8	0.001	0.001	0.5	0.5	0.5	0.5
9	-0.004	0.001	0.1	0.3	-4	0.3
10	-	-	0.5	0.3	0.1	0.5
11	-	-	0.1	0.3	0.1	0.5

Following the same procedure as for the magnet misalignments and closed orbit correction DA calculations, the corrected lattice is used and particles are tracked for 1000 turns using the PTC-track module of MADX, in 5D with momentum offset fixed. DA calculations were performed for different momentum offsets. For each momentum offset, the DA is calculated for 100 error seeds. The results for the foil and laser injection options are shown in Fig. 5.15. The nominal lattice is shown in dashed black line. The DA for the misaligned and corrected lattice including systematic multipole components is shown in green for the on momentum case, in magenta for  $dp/p=0.6\%$  while in blue for  $dp/p=-0.6\%$ . The geometrical acceptance of the ring is shown in solid black. The dynamic aperture is drastically reduced, showing that it is dominated by the multipole magnet errors. The DA is tight but above  $6\sigma$  in both planes, thus 30% higher than the physical aperture.

#### 5.2.4.1 Frequency maps

For the frequency maps analysis, a random seed of a lattice with multipole field errors included was used, after closed orbit, tune and chromaticity corrections. The frequency map analysis (FMA) examines the dynamics in frequency space rather than configuration space. An indication of how much the frequency is changing with time, is measured through the diffusion coefficient, defined by:

$$D = \log \left( \sqrt{|\nu_{x,1} - \nu_{x,2}|^2 + |\nu_{y,1} - \nu_{y,2}|^2} \right) \quad (5.3)$$

where the index 1 refers to a certain number of turns, while, the index 2 to a consecutive same amount of turns. Large negative values of  $D$  denote long term stability while values of  $D$  close to zero denote chaotic motion [?]. Particles were tracked for 1056 turns with the PTC-track module of MADX. The synchrotron motion is neglected and the 5D tracking is made with 3

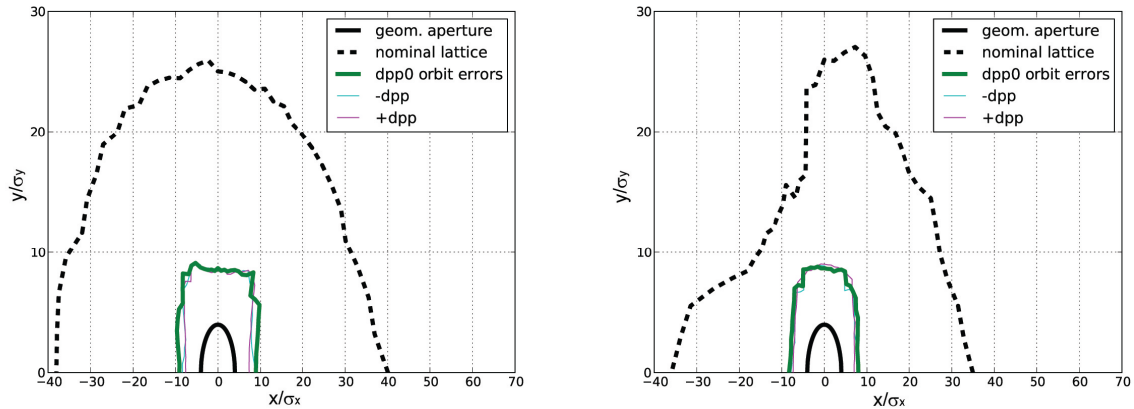


**Figure 5.15:** On and off-momentum average transverse dynamic aperture measured in beam sizes for the HP-PS ring with foil injection (left) and laser injection (right) for 1000-turns tracking, using 100 random seeds of misalignment and correction and applying systematic multipole components.

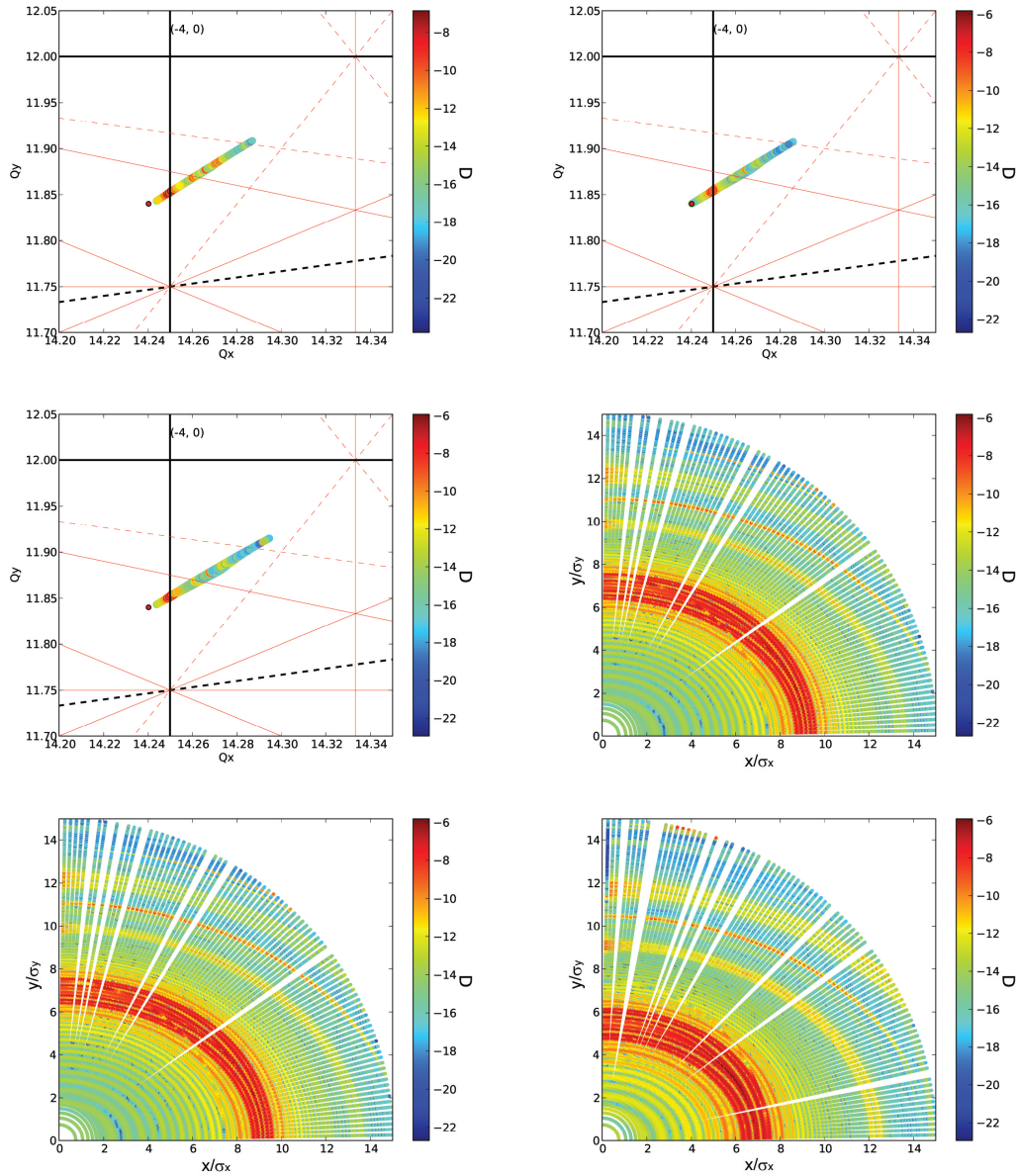
fixed momentum off-sets (0 and  $\pm 1\%$ ). The frequency map analysis was performed with the Numerical Analysis of Fundamental Frequencies (NAFF) algorithm [?].

Fig. 5.16 (left) shows the initial positions of particles survived over 1056 turns, color-coded with the diffusion coefficient of Eq. ??, for on-momentum particles with  $\delta p/p_0=0\%$  (top) and for off-momentum particles with  $\delta p/p_0=1\%$  (middle) and  $\delta p/p_0=-1\%$  (bottom). The particle positions in the horizontal and vertical axis are expressed in units of horizontal and vertical beam sizes at the point of calculation. The frequencies of the particles are presented in the right plots, the frequency maps. The color indicates the regularity of the orbits. Blue regions indicate very regular motion, while dark-red region indicate chaotic motion. The absence of dots means that the particles were lost. Resonance lines in the frequency maps are shown as distorted areas, while the colors allow to relate the resonant features observed, to regions of the physical space. The plots of Fig. 5.16 describe the dynamics of the foil injection scheme. The same is valid for the laser injection option, as shown in Fig. 5.17. For both options, a red area of maximum diffusion at about 8 sigmas corresponds to the DA, presumably corresponding to particles crossing the systematic octupolar resonance. Further optimisation with additional correctors could be subject of future studies to improve the DA.

## 5.2.5 Space-charge studies for the HP-PS

The space-charge tune-spread and the transverse emittance evolution over 5,000 turns were simulated with  $3 \cdot 10^5$  macroparticles using PyORBIT [?]. A pessimistic scenario was considered as Gaussian particle distributions, rather than uniform distributions, were used in both transverse and longitudinal phase-spaces cut at 3 and 2  $\sigma$ , respectively, based on the beam parameters given in Table 5.10. For this study the HP-PS foil optics scheme was used at  $(Q_x, Q_y) = (14.24, 11.84)$  and 4 GeV. The space-charge effect was studied for the ideal lattice without errors and for the case where closed orbit errors due to random field errors and magnet misalignments were included, as summarised in Table 5.11. The assumed error seed results in closed orbit of  $\sim 0.5$  and  $\sim 0.3$  mm maximum excursion in the horizontal and vertical planes respectively, after correction.

Fig. 5.18 shows the tune-spread obtained with PyORBIT in the first turn. The observed space-charge detuning of  $\sim (-0.22)$  is in good agreement with the analytical formula for the



**Figure 5.16:** Frequency and diffusion maps of the HP-PS for the foil injection option. In columns: -0.6% momentum deviation particles, on-momentum particles and 0.6% momentum deviation particles. The diffusion parameter is colour-coded in all plots.

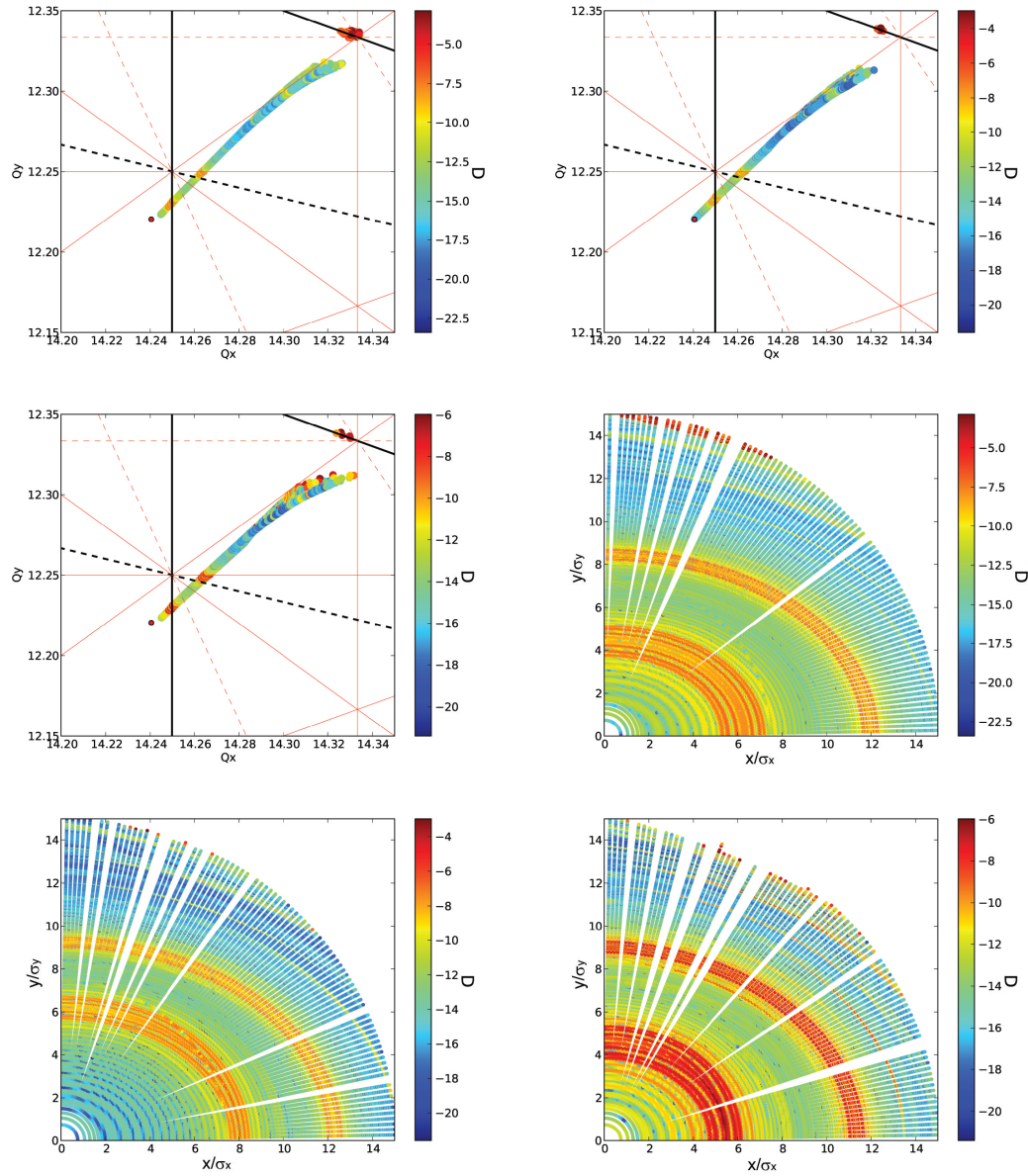


**Figure 5.17:** Frequency and diffusion maps of the HP-PS for the laser injection option. In columns: -0.6% momentum deviation particles, on-momentum particles and 0.6% momentum deviation particles. The diffusion parameter is colour-coded in all plots.

maximum tune-shift due to direct space-charge:

$$\Delta Q_{x,y} = -\frac{N_b r_p}{(2\pi)^{3/2} \gamma^3 \sigma_z} \oint \frac{\beta_{x,y}}{\sigma_{x,y}(\sigma_x + \sigma_y)} ds \quad (5.4)$$

where  $\Delta Q_{x,y}$  is the tune-shift,  $N_b$  is the number of particles per bunch,  $r_p$  is the classical proton radius,  $\gamma$  is the relativistic Lorentz factor,  $\beta_{x,y}$  is the betatron function,  $\sigma_{x,y}$  is the RMS transverse beam size and  $\sigma_z$  the bunch-length.

The emittance evolution, with and without closed orbit errors, is shown in Fig. 5.19; the emittance blow-up is similar in both planes and, as expected, is more pronounced when errors are included due to resonance excitation.

**Table 5.10:** Initial beam parameters

Parameter	Unit	Value
Intensity	[ $10^{12}$ ]	1.6
$\gamma_{rel}$	-	5.26
$\epsilon_{x,rms}$	[ $\mu\text{m}\cdot\text{rad}$ ]	10
$\epsilon_{y,rms}$	[ $\mu\text{m}\cdot\text{rad}$ ]	13
$\epsilon_{z,rms}$	[eV·s]	0.55
Bunch-length	[ns]	11.5
$\Delta p/p(rms)$	[ $\cdot 10^{-3}$ ]	3.3

**Table 5.11:** Assumed machine imperfections of the HP-PS lattice (RMS values)

Error	Unit	RMS value
Relative dipole field error	[ $\cdot 10^{-4}$ ]	5.0
Transverse quadrupole shift	[mm]	0.2
Longitudinal dipole shift	[mm]	0.3
Dipole tilt	[mrad]	0.3

Note that from Fig. 5.19 the expected emittance increase during the injection plateau ( $\sim 2$ - $2.25$  ms, which corresponds to  $\sim 500$  turns) is not significant, even when closed orbit errors are included. Future studies should include multipole errors. Furthermore, a working point optimisation could be performed in order to minimise the emittance blow-up.

### 5.3 Beam transfer

The 4 GeV H<sup>-</sup> ions from SPL have to be transferred via a large bending radius line to avoid Lorentz-stripping. The charge exchange injection system will be based on a foil stripping mechanism, with the upgrade possibility to a laser assisted magnet stripping system.

Two extraction energy options, 50 and 75 GeV, have been studied (see Table 5.3). The beam sizes vary for the two options and so the required kicker deflection angle to reach the minimum clearance at the septum to extract the beam. However, the increased kicker deflection due to possible bigger beam sizes for the 50 GeV synchrotron is overcompensated by the by 1/3 smaller magnetic rigidity compared to the 75 GeV option. The extraction system description focusses on the more challenging 75 GeV option.

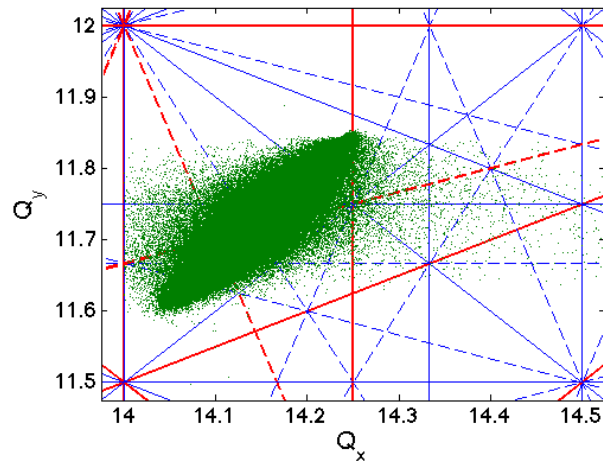


Figure 5.18: Tune-spread (green) of  $\sim(-0.22)$  created due to the space-charge effect

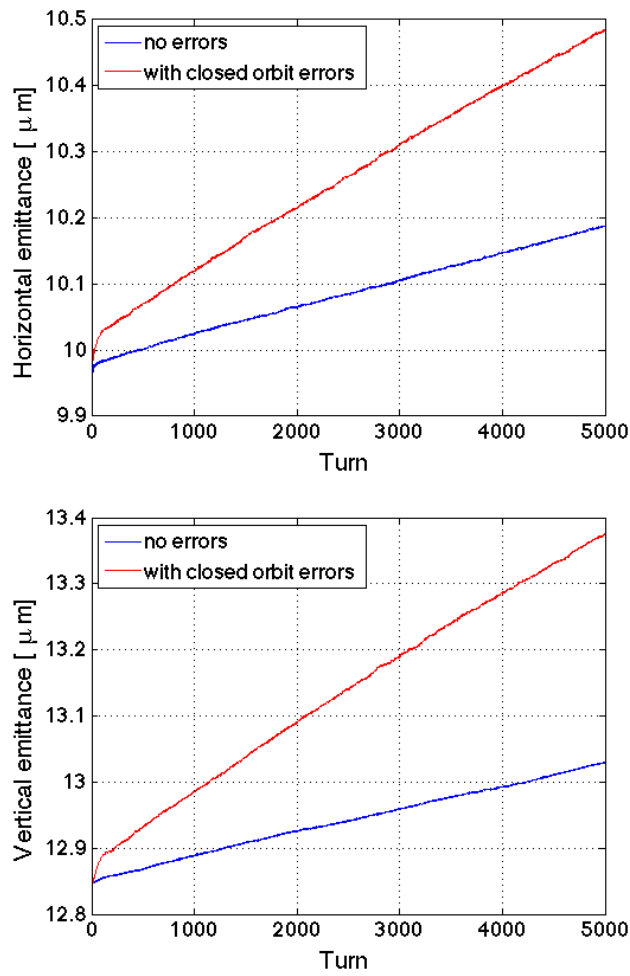


Figure 5.19: Horizontal (top) and vertical (bottom) normalised emittance increase for 5,000 turns due to the space-charge effect, with (red) and without (blue) closed orbit errors.

### 5.3.1 H<sup>-</sup> injection

#### 5.3.1.1 Optics requirements

The optics requirements for foil and laser stripping are contradictory and therefore two lattice versions are prepared, [84]. For the foil stripping scheme, the optics at injection was adapted to the following constraints. Assuming the minimum injected betatron function being fixed due to foil heating, the optimum betatron function at the injection point in the ring is given by matching the incoming and the ring phase space curvatures. The beam divergence  $\alpha$  should be zero at the injection point. With an injected betatron function not smaller than 10 m due to foil heating, the ring betatron function should be around 35 m. A smaller ratio between injected and ring betatron function  $\beta_i/\beta_r$  decreases the number of foil hits and thus emittance blow up but increases the local foil heating.

For the laser stripping scheme it is primarily important to minimise the vertical beam size at the interaction point - if the interaction is in the horizontal plane - since it is proportional to the required laser peak power.

#### 5.3.1.2 Foil Stripping

The long drift space in the center of doublet straight section will house the H<sup>-</sup> injection system. A long 'soft' D2 dipole merges the H<sup>-</sup> and circulating proton beams, with a stripping foil located in the fringe field at the exit. The D3 chicane dipole is strong with B around 1.5 T. The position and strength of these chicane dipoles are adjusted to close the dispersion bump. A second foil between D3 and D4 converts unstripped H<sup>0</sup> to protons to be extracted. Phase space painting kickers can be located inside the straight section. At the stripping foil, the stripping efficiency can be about 95% with a 400  $\mu\text{g}/\text{cm}^2$  foil, Fig. 4. A few percent of H<sup>0</sup> emerges in excited quantum states which will decay to protons in a magnetic field. The H<sup>-</sup> yield will be below 10<sup>-4</sup>, and this H<sup>-</sup> is stripped to H<sup>0</sup> in the first few mm of D3. With the foil located in the D2 fringe field, a field of about 0.07 T will ensure that all states with n=5 and above are immediately field-stripped at the foil, increasing the effective stripping efficiency. With the D3 chicane magnet field of 1.5 T, the n=1 state passes through D3 unchanged and is stripped by a foil at the entrance to D4, and extracted as a waste beam. The state n=2 penetrates deep into the fringe field before stripping, which results in an angular spread of 0.8 to 3 mrad. This would cause halo which might need dedicated collimation. The n=3,4 states have angular errors of up to 0.3 and 0.08 mrad; the n=4 state would therefore remain within the machine acceptance. A reduction in the length of the D3 fringe field by a factor of 5 improves these angular spreads significantly to about 0.3, 0.04 and 0.02 mrad respectively. In this case the n=2 state is the only one which would need more careful evaluation, since the others would remain within the machine acceptance. The effect on halo and emittance is to be evaluated in detail, as does the similar effect for decay of H<sup>0</sup> in D3 and of n $\geq$ 5 at the foil. If such a D3 magnet design with improved fringe field is not feasible an alternative is to reduce the D3 field to about 0.7 T, such that the n=2 states traverse without stripping, and so the waste beam consists of the H<sup>0</sup> states n=1,2 at D4. However, this would simply shift the problem to the n=3 state, which would have a large angular spread - an evaluation of the expected relative yields of the different states is still required to be able to decide on the optimum arrangement. The H<sup>0</sup> stripped at the second foil is deflected outwards by D4 and needs to be transported to an external beam dump. This beam is also composed of the unstripped H<sup>-</sup> fraction, which is normally expected to be very small, but also contains any H<sup>-</sup> which has missed the foil for any reason. This is less easy to evaluate in percentage terms, since it depends on the details of the operational setup and also on any local damage or changes to the foil size, which could evolve during operation. It is therefore assumed that this fraction could reach a few percent, comparable with the unstripped H<sup>0</sup> and requiring similar consideration. Since the H<sup>-</sup> is stripped to H<sup>0</sup> in the first part of D3, an in-



crease in the angular beam spread will also be present - although in this case larger values are probably acceptable since the beam must only be transported through a short line to a beam dump.

The required intensity in the HP-PS is reached for about 600 injected turns or 2 ms. The number of foil hits during this process for a given betatron mismatch at injection can be minimised by adapting the painting function. Here the painting function was chosen to change the position of the injected beam proportional to  $\#turn^{1/4}$  which moves very quickly the beam out of the phase space center and more slowly fills the outer phase space area. The resulting distribution is less dense in the center which will be compensated when taking into account space charge effects, Fig. 5.20.

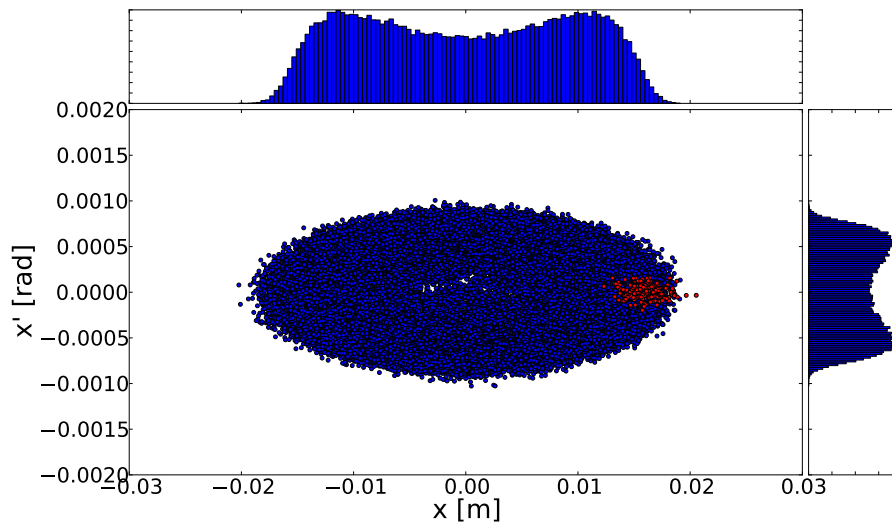


**Figure 5.20:** Phase space distribution after painting over 600 turns. The particles in red represent the last injected bunch.

### 5.3.1.3 Beam loss control

Control of beam losses is an important aspect of the  $H^-$  injection system.  $H^-$  ions may pass the foil unstripped or be partially stripped to excited  $H^0$  states which may be stripped in the subsequent strong-field chicane magnet. Depending on the choice of the magnetic field, atoms in the ground and first excited states can be extracted and dumped. The injected beam power of up to 190 kW is considered to be manageable in view of foil damage; however, losses due to scattering processes in the foil and by deflection of particles with different charge number or state in the chicane dipoles need to be investigated carefully. Laser assisted stripping may offer an attractive alternative with lower beam loss and without the need for a delicate and radioactive stripping foil system.

The following sections will address the different scattering processes with their resulting loss rates and/or emittance growths and the emittance growth and losses due to stripping of different excited states in the fringe fields of the chicane magnets. The stripping efficiency, the absolute yield of  $H^0$  and unstripped  $H^-$  and the yield of the different  $H^0$  excited states depend on the foil thickness and the incident ion energy. Some semi-empirical treatments exist, e.g. [85] which have been adjusted to give reasonable agreement with measured cross-sections at 200 and 800 MeV which can be scaled to the energies of interest here. The different charge state



yields can be written as:

$$y_-(x) = e^{-\rho(\sigma_{-0} + \sigma_{-+})x} \quad (5.5)$$

$$y_0(x) = \frac{\sigma_{-0}}{\sigma_{-0} + \sigma_{-+} - \sigma_{0+}} x \cdot e^{-\rho\sigma_{0+}x} + e^{-\rho(\sigma_{0+} + \sigma_{-+})x} \quad (5.6)$$

$$y_+(x) = 1 - y_-(x) - y_0(x) \quad (5.7)$$

where  $x$  is the foil thickness ( $\mu\text{g}/\text{cm}^2$ ),  $\rho$  is the material density in atoms per  $\mu\text{g}$ , i.e.  $\rho = 1 \cdot 10^{-6} N_A/Z$ , and  $\sigma_{-0}$ ,  $\sigma_{-+}$  and  $\sigma_{0+}$  are the cross sections in  $\text{cm}^2$  for the different stripping processes. The cross-sections used were [ $\cdot 10^{-19} \text{cm}^2$ ]  $\sigma_{-0} = 4.97$ ,  $\sigma_{-+} = 0.09$  and  $\sigma_{0+} = 1.94$ . For a carbon foil with  $400 \mu\text{g}/\text{cm}^2$  a stripping efficiency of 97% percent is expected. 3% of the beam escapes from the foil as  $\text{H}^0$  of which  $\sim 46\%$  occupy the ground state and with decreasing probabilities also higher energy level states. The field of the D3 chicane magnet is chosen to assure the stripping of excited states with  $n > 1$  within the first mm of the fringe field. Fig. 4 shows the lifetime of the excited states with indicated B field of D2 and D3. Between D3 and D4 a second, thicker, stripping foil is placed. Here, any remaining  $\text{H}^-$  and the  $\text{H}^0$  in ground state will be stripped to protons and deflected outwards by the D4 chicane magnet into a dump line.

Three scattering processes have been investigated for a carbon foil.

**5.3.1.3.1 Inelastic nuclear scattering** For inelastic nuclear scattering the attenuation  $N(L)/N_0 = e^{-L/\lambda_i}$  for protons in the carbon foil is characterised by the ratio of foil thickness (L) to inelastic interaction length ( $\lambda_i$ ) for protons at 4 GeV. Since the foil thickness is of the order of  $\mu\text{m}$  and the interaction length  $\sim 50\text{cm}$ , the inelastic nuclear scattering process is negligible.

**5.3.1.3.2 Elastic nuclear scattering** The interaction length for nuclear elastic scattering ( $\lambda_e$ ) is of the order of  $\sim 1.4 \text{m}$ . The angle from a single scattering process can be described by:

$$1/\Theta_{el}^2 = \frac{1}{3} A^{\frac{2}{3}} \left( \frac{p}{0.135} \right)^2 \quad (5.8)$$

where A denotes the atomic number and p the momentum of the scattering particles in GeV/c. This results in an rms angle of 21 mrad. The probability of observing N interactions in a length L with the interaction length  $\lambda_e$  is given by:

$$P\left(\frac{L}{\lambda_e}, n\right) = e^{-L/\lambda_e} \left(\frac{L}{\lambda_e}\right)^n \frac{1}{n!} \quad (5.9)$$

The total angle after n scattering events is distributed about  $(n)^{1/2}\Theta_{el}$ . The probability for one scattering event is  $\sim 1 \cdot 10^{-6}$ , for two events  $\sim 1 \cdot 10^{-13}$  and strongly decreasing for higher numbers of events. Considering the single scattering angle to be Gaussian distributed, the superposition of the angle distributions for higher numbers of scattering processes does not deviate the initial Gaussian. So the rms value is taken to calculate the resulting emittance growth for the elastic scattered particles.

**5.3.1.3.3 Multiple Coulomb Scattering** The angle for multiple scattering is given by:

$$\Theta_{MC} = \frac{0.0136}{\beta c p} z \sqrt{\frac{x}{X_0}} \left[ 1 + 0.038 \ln \left( \frac{x}{X_0} \right) \right] \quad (5.10)$$

with p in GeV the momentum,  $\beta c$  the velocity and z the charge state of the incoming particles.  $x/X_0$  denotes the thickness of the foil in radiation length. For a foil of  $1.7 \mu\text{m}$  thickness the

rms scattering angle results in 0.007 mrad. The second foil creates an angle of 0.025 mrad. The absolute normalised emittance growth is calculated as:

$$\Delta\epsilon = (\beta\gamma)_{rel} \frac{1}{2} \beta \Theta_{rms}^2 \quad (5.11)$$

The corresponding emittance growth for the thin foil amounts to  $0.0012 \pi \cdot mm \cdot mrad$  and 0.0031 for the second foil.

**5.3.1.3.4 Fringe Field Deflection** The yield for  $H^-$  emerging the first stripping foil with  $400 \text{ g/cm}^2$  is about  $1e-4$ . However, it is assumed that the total  $H^-$  fraction can be as high as 2%, to take into account for possible local foil damage and beam missing the foil. Entering the D3 magnet the  $H^-$  ions are deflected in the opposite direction to the fully stripped protons until they are Lorentz stripped to  $H^0$ . The rest frame lifetime for  $H^-$  in a magnetic field is expressed as [86]:

$$\tau = \frac{A_1}{E} e^{\frac{A_2}{E}} \quad (5.12)$$

where  $E = \beta c \gamma B$  the transverse electric field. The coefficients are  $A_1 = 2.47 \cdot 10^{-6} \text{ Vs/m}$  and  $A_2 = 4.49 \cdot 10^9 \text{ V/m}$ . The RMS angular spread for the  $H^-$  stripped in a 1.6 T D3 field was numerically calculated at 0.065 mrad using a simulated fringe field and the field-dependant lifetime. The emittance growth amounts to  $0.25 \pi \cdot mm \cdot mrad$  for the waste  $H^- \rightarrow H^0$  beam.

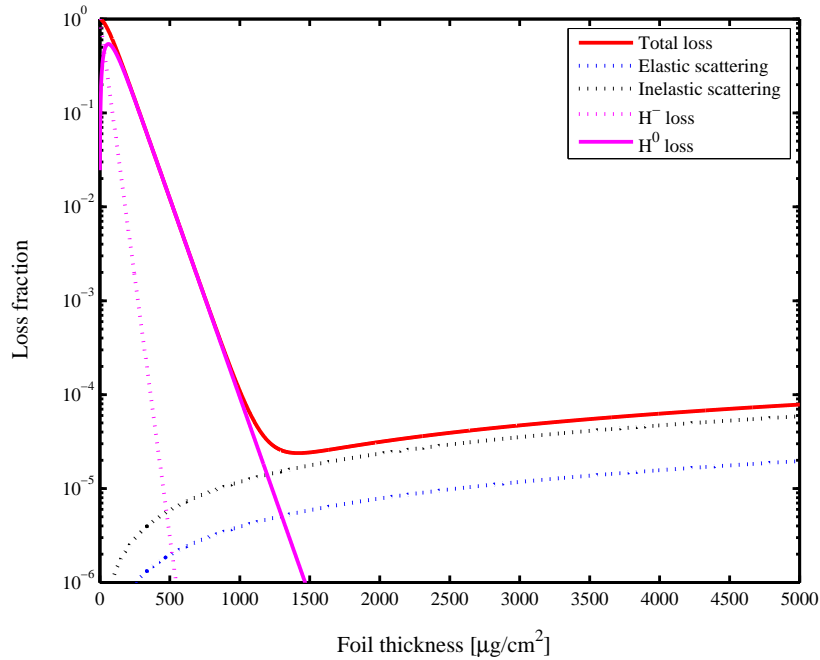


**Figure 5.21:** Total beam loss from stripping inefficiency and scattering. The optimum foil thickness is  $1500 \mu\text{g/cm}^2$

The second foil placed between D3 and D4 aims at stripping all the  $H^0$  originating from  $H^-$  that might have missed the first foil, and the  $H^0$  in the ground state which pass the D3 field without stripping. The thickness of this foil needs to be optimised to minimise the beam loss while controlling emittance increase from scattering. Any  $H^0$  after the foil have to be regarded as uncontrolled losses. An emittance increase determines the acceptance of the dump line and might give rise to uncontrolled losses from large angle scattering. The total beam loss from stripping inefficiency and nuclear scattering was calculated for 4 GeV ions and carbon foil, Fig.

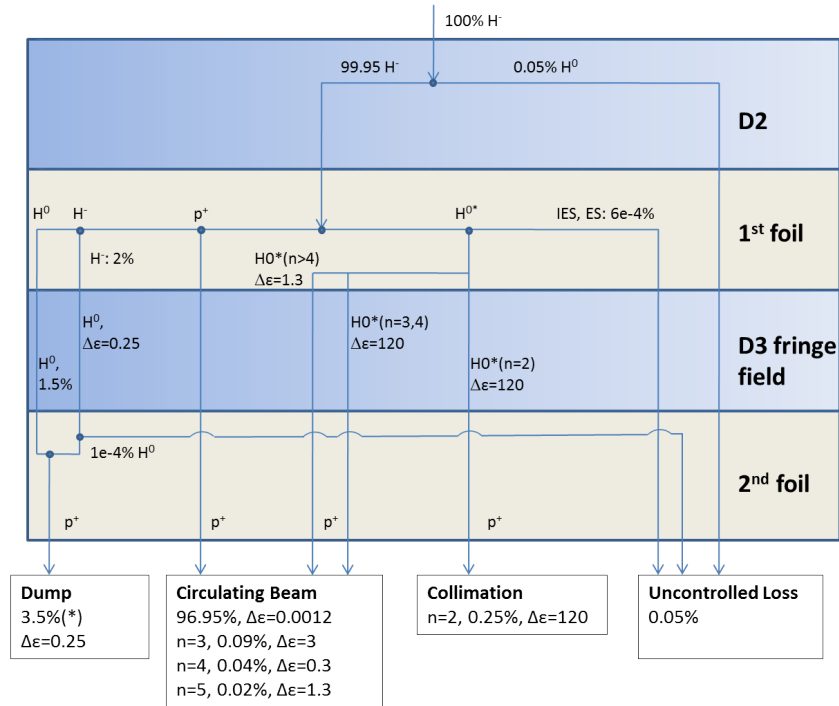
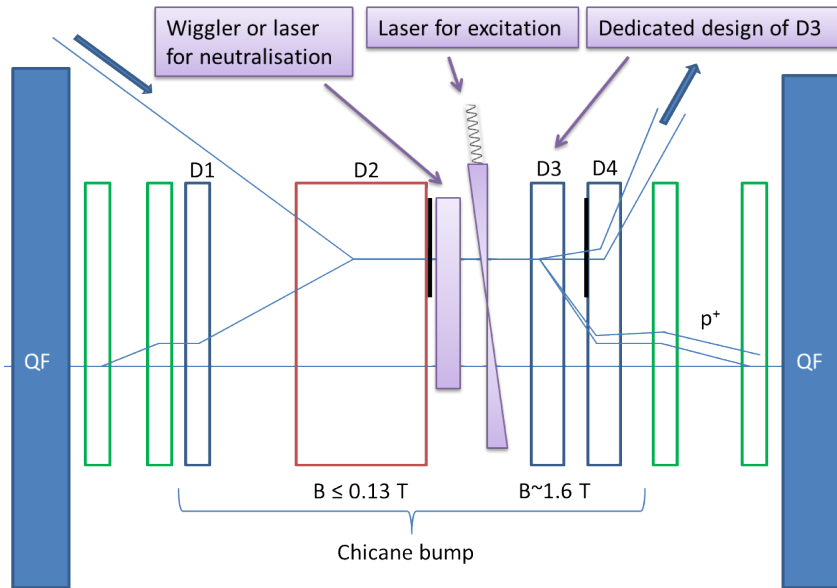


Figure 5.22: Particle flow through the  $H^-$  injection line

5. The optimum foil thickness is at about  $1500 \mu\text{g}/\text{cm}^2$ , where the emittance growth from multiple Coulomb scattering is calculated to be about 0.003. The expected loss levels and emittance growth, for the circulating and different waste beams, is given in Fig. 5.22.

### 5.3.1.4 Laser Stripping

Reduction of beam loss and activation motivate to design the injection system with the possibility to upgrade to a laser assisted magnet stripping scheme. Such a scheme is described in detail for the 4 GeV injection into PS2, which was foreseen to replace the PS in the LHC injector chain [87]. Several parameters differ between the PS2 and HP-PS injection systems. The number of injected turns has to be increased from 200 to 600 in the HP-PS which leads to an increased number of foil hits and emittance blow up. The latter is less critical for the HP-PS since its purpose is not to produce beams for luminosity production, as the aim was for PS2, but for a fixed target beam. However, the target emittance should be reached via controlled painting and not be significantly affected by foil scattering. The 2.6-3.8 times higher injected beam power of the HP-PS with respect to the PS2 is the main motivation for a laser stripping system. A sketch of the injection setup with a combined foil and laser system is shown in Fig. 5.23. Lorentz-stripping in a wiggler magnet or photodissociation by laser light can be used to neutralise the  $H^-$  ions, Fig. 5.24. The advantage of using laser photodissociation for 4 GeV ions is not only to avoid emittance growth originating from the finite stripping length in the magnet, but the possibility to use resonances which leave the  $H^0$  in an already excited state. In a second step, these excited atoms can be pumped onto a higher energy level which has the dual advantage of a longer lifetime for spontaneous decay and shorter lifetime for stripping off the second electron. The required laser parameters to pump the  $H^0$  ions to the excited states  $n=2$  and  $n=3$  are shown in Table 5.12. Due to the Doppler shift of the laser frequency in the ion rest frame, conventionally available laser systems can be frequency tuned to the ion energy by choosing the appropriate geometry between laser and ion beam. Fig. 5.25 shows the required angle between the two beams to reach the respective excitation states of 3.5, 4 and 4.5 GeV ions. It has to be emphasised that the  $n=3$  state cannot be reached for injection energies below 4 GeV.



**Figure 5.23:** Combined foil and laser  $H^-$  injection system. The chicane bumpers are indicated in blue and red, the painting bumpers in green. Two foils are shown, one for the stripping of the injected ions and one for the waste beam. The laser equipment consists of a wiggler, an excitation laser and a specifically designed third chicane magnet.

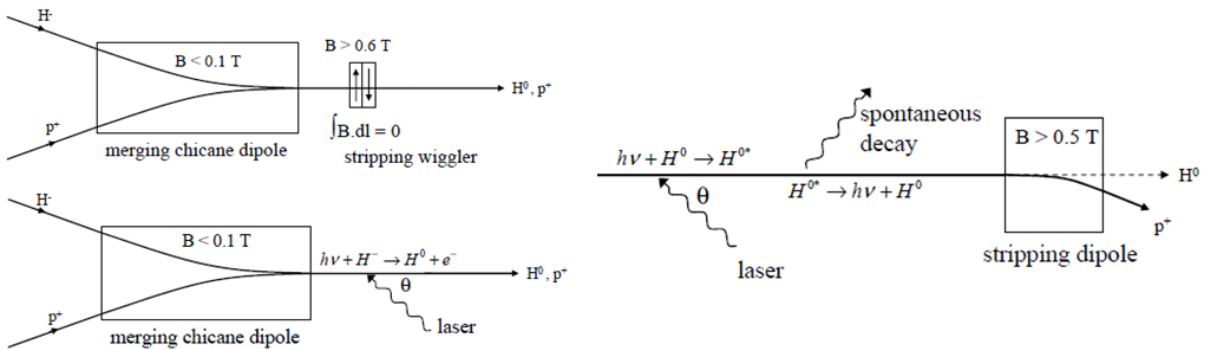


**Figure 5.24:** Stripping scheme with neutralisation in a wiggler magnet or by photodissociation (left) and excitation with final stripping (right).

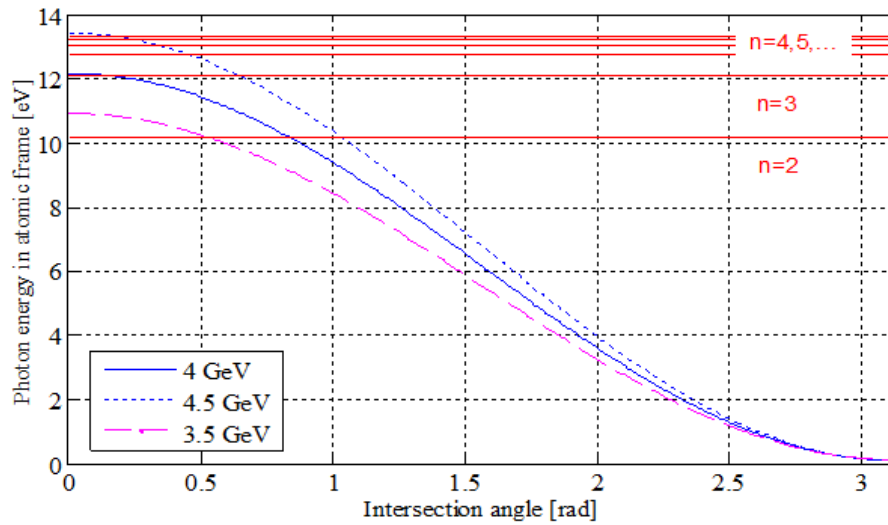


**Figure 5.25:** Required angle between ion and laser beam to reach the respective excited ion states for three different ion energies.

**Table 5.12:** Laser characteristics for  $H^0$  to proton stripping

Parameter	Unit	n=2	n=3
Wavelength	[nm]	1064	1064
Laser/ $H^-$ angle	[deg]	47.50	8.39
Angular spread	[deg]	$\pm 0.10$	$\pm 0.42$
Micropulse energy	[ $\mu$ J]	360	92
Macropulse length	[ms]	2	2
Macropulse energy	[J]	253	65
Peak power (single pass) * 3 (margin)	[MW]	21.6	5.5
Average power	[kW]	127	33
Vertical laser beam height ( $1\sigma$ rms)	[mm]	1.5	1.5
Linac pulse, $1\sigma$ rms separated by 2.84 ns	[ps]	15	15
Microbunch frequency	[MHz]	352	352

One of the lasers for the CLIC test facility CTF3 at CERN is the photo-injector PHIN. After the second amplifier, PHIN delivers a 9 kW average power with 1.5 GHz intra burst repetition rate [88]. Its bunch duration is measured between 8-10 ps. First experiments of a power build up cavity for the SNS stripping scheme at 355 nm resulted in a factor 25 power build up, with further improvements a build up factor of 100 should be achievable [89]. Assuming the n=3 excitation with a required average power of 33 kW, the PHIN output power needs to be enhanced by a factor 4 which can be easily obtained by a cavity. The oscillator for an appropriate pulse rate and pulse duration seems feasible.

### 5.3.2 Longitudinal painting for $H^-$ injection

The longitudinal painting scheme at injection into the HP-PS has the aim to improved the bunching factor and to reduce the space charge effects.

### 5.3.2.1 Basic assumptions

For the HP-PS design a 40 MHz RF system, providing a total voltage of up to 2 MV and working at harmonic number  $h=168$  has been chosen. The injection energy of 4 GeV in combination with the harmonic number and the available RF voltage the synchrotron frequency is sufficiently high to allow for a "passive" painting scheme. The LP-SPL bunches will be injected at a kinetic energy of 4 GeV and with a fundamental RF frequency of  $f_{LP-SPL} = 352.2$  MHz. The energy spread is considered a free parameter and can be adjusted by, changing the settings of the LP-SPL de-buncher. Simulations of longitudinal painting scheme have been achieved using the ESME code [?]. For this the LP-SPL bunch properties have been modelled in ESME, as sketched in Fig. 5.26.

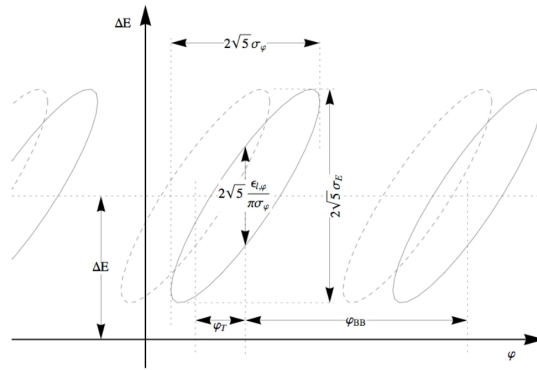


**Figure 5.26:** LP-SPL bunches at injection in the HP-PS. Bunches that are represented by dashed lines are injected one turn later than the bunches represented by solid lines. The ellipses denote the full beam for an elliptical density, hence a parabolic profile is assumed for the simulations.

The distance between consecutive bunches is given by :

$$\varphi_{bb} = (f_{HP-PS}/f_{SPL})360^\circ = 0.23941^\circ \quad (5.13)$$

where  $f_{HP-PS} \simeq 234.249$  kHz is the HP-PS revolution frequency at injection.

The HP-PS circumference can be expressed as :

$$(1/f_{HP-PS})360^\circ = 1503\varphi_{bb} + \varphi_T \quad (5.14)$$

with  $\varphi_T \simeq 0.17^\circ$ .

Therefore the bunch positions are given by :

$$\varphi_B = \varphi_{off} + n_B\varphi_{bb} - (n_T - 1)\varphi_t \quad (5.15)$$

The phase length of an HP-PS bucket is defined by  $360^\circ \div h = 2.14^\circ$ .

As discussed earlier, different extraction energies (50 GeV and 75 GeV) and different injection schemes (foil and laser) have been considered for the HP-PS design. In order to maintain acceptable values for beta functions, phase advance, magnets pole field and vacuum chamber aperture, a set of possible bunch length, beam full momentum spread and transverse emittances have been defined for each options. Bunch length and full momentum spread are presented in table 5.13 for foil injection and in table 5.14 for laser injection.

**Table 5.13:** Bunch length and full momentum spread after injection for the foil injection

Parameter	Unit	50GeV	75GeV
Bunch length, $\tau_b$	[ns]	12.5	14
Full momentum spread, $dp/p$	$[10^{-03}]$	6.6	7.6

**Table 5.14:** Bunch length and full momentum spread after injection for the laser injection

Parameter	Unit	50GeV	75GeV
Bunch length, $\tau_b$	[ns]	13	14
Full momentum spread, $dp/p$	$[10^{-03}]$	7.32	7.6

This leads to a set of longitudinal emittances with corresponding RF voltage after injection detailed in table 5.15 for foil injection and in table 5.16 for laser injection : [?]

**Table 5.15:** Longitudinal emittance and RF voltage after injection for foil injection

Parameter	Unit	50GeV	75GeV
Emittance, $\varepsilon_l$	[eVs]	0.31	0.4
RF voltage	[MV]	0.97	1.02

### 5.3.2.2 Injection with energy offset and single harmonic RF system

For this feasibility study, the most straight forward injection scheme has been chosen for the HP-PS, using a single harmonic RF system. The beam coming from the LP-SPL is chopped such that only bunches within  $0.5^\circ$  are injected, yielding a chopping factor of 0.5. After about 500 turns the required intensity can accumulated. The energy offset and energy spread have been chosen to fulfil the longitudinal emittance requirements with low RF voltage. Then, after injection of the required intensity, the RF voltage is increased up to the values given in tables 5.15 and 5.16 in order to obtain the required bunch length and full momentum spread. An example of results from ESME simulations, without space charge and with initial coordinates, are given in Fig. 5.27 for different steps during injection.

Fig. 5.28 shows the ESME simulation results for the 50 GeV baseline and foil injection, at the end of the painting process (top plots) and at the end of flat-bottom, when the beam fulfils longitudinal emittance, bunch length and full momentum spread requirements, as given in tables 5.13 and 5.15 (bottom plots). Fig. 5.29 shows the same results for the 50 GeV baseline, but now for the Laser injection scheme, complying with the requirements given in tables 5.14 and 5.16 (bottom plots). For the 75 GeV option with foil injection these simulation results are shown in Fig. 5.29 and are based on the requirements given in tables 5.14 and 5.16 (bottom plots). The Fig. 5.31 shows again the ESME simulation results for the 75 GeV option, but now with the laser injection scheme, using the requirements as given in tables 5.14 and 5.16 (bottom plots).

### 5.3.2.3 Summary

The "passive" longitudinal painting using energy offset and single harmonic RF system in the HP-PS works well for all the options considered for the HP-PS design, taking into account a bucket filling factor with enough margin for the reduced bucket area during acceleration and some blowup. The obtained results can be further optimised in terms of peak density, but this will require introducing a higher harmonic RF system or more sophisticated chopping schemes in the LP-SPL, with the aim to de-populate the centre of the HP-PS bunch.

**Table 5.16:** Longitudinal emittance and RF voltage after injection for laser injection

Parameter	Unit	50GeV	75GeV
Emittance, $\epsilon_l$	[eVs]	0.356	0.38
RF voltage	[MV]	1.11	1

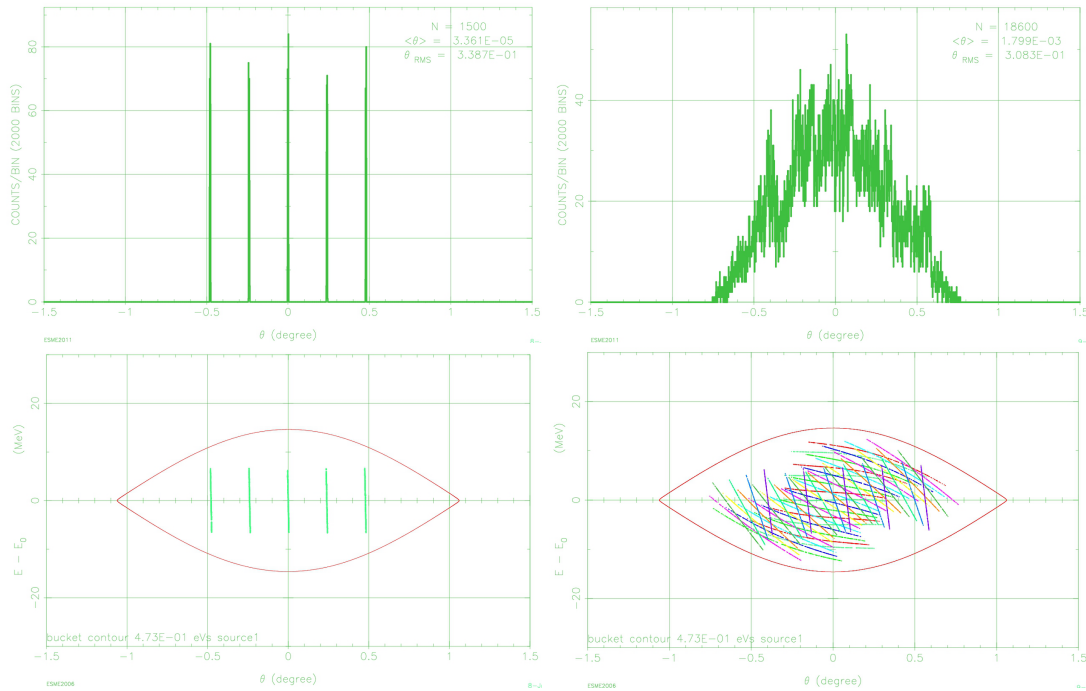


**Figure 5.27:** Example of the longitudinal phase space (bottom) and bunch density (top), for first injected turn (left) and after 10 turns (right) where the filamentation process of the LP-SPL bunches in the HP-PS bucket is clearly visible.

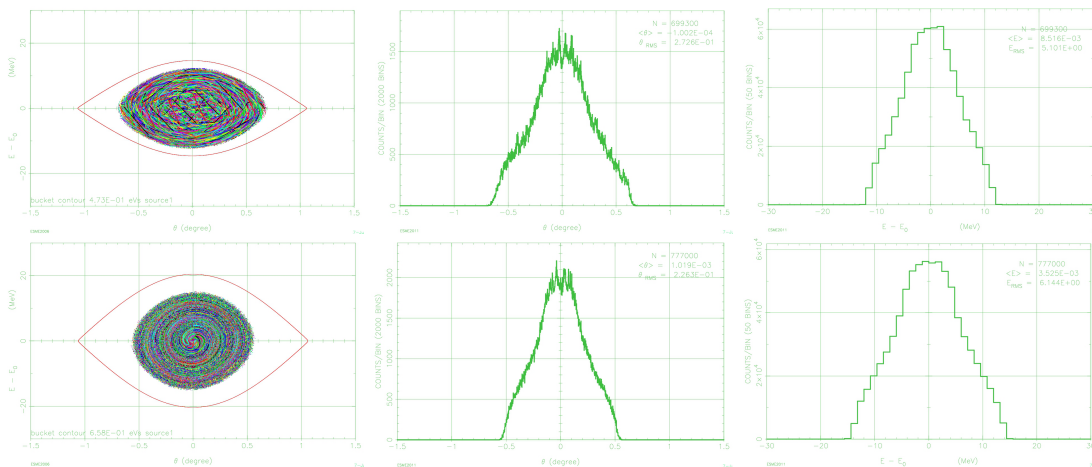


**Figure 5.28:** Longitudinal phase space (left) and bunch density (middle and right) for the 50 GeV baseline and foil injection, at the end of the painting process (top) and at the end of flat-bottom when beam is ready for acceleration (bottom)



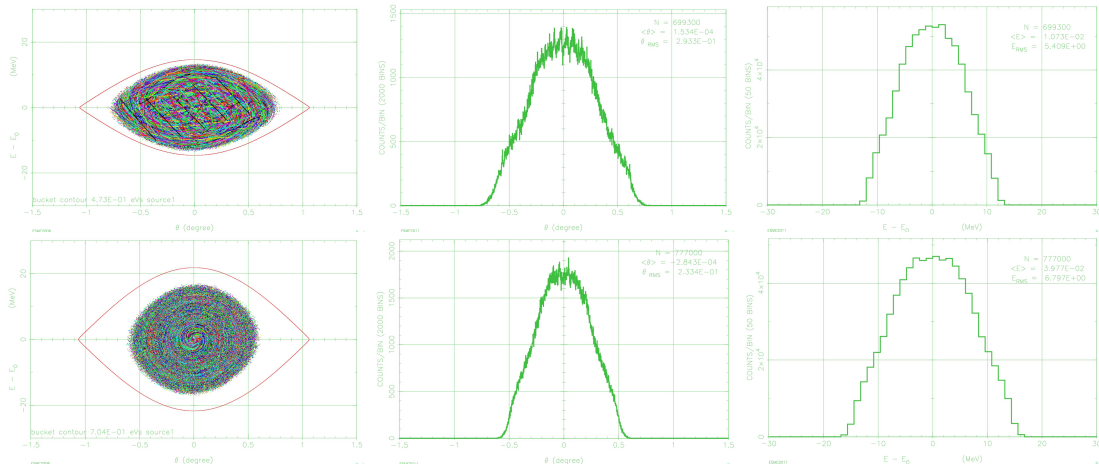


**Figure 5.29:** Longitudinal phase space (left) and bunch density (middle and right) for the 50 GeV baseline and laser injection, at the end of the painting process (top) and at the end of flat-bottom when beam is ready for acceleration (bottom)

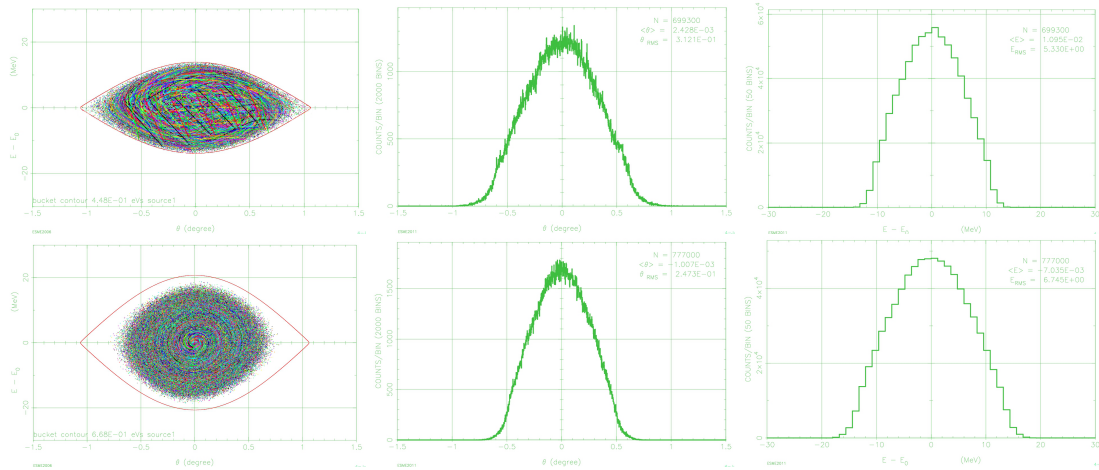


**Figure 5.30:** Longitudinal phase space (left) and bunch density (middle and right) for the 75 GeV option with foil injection, at the end of the painting process (top) and at the end of flat-bottom when beam is ready for acceleration (bottom)

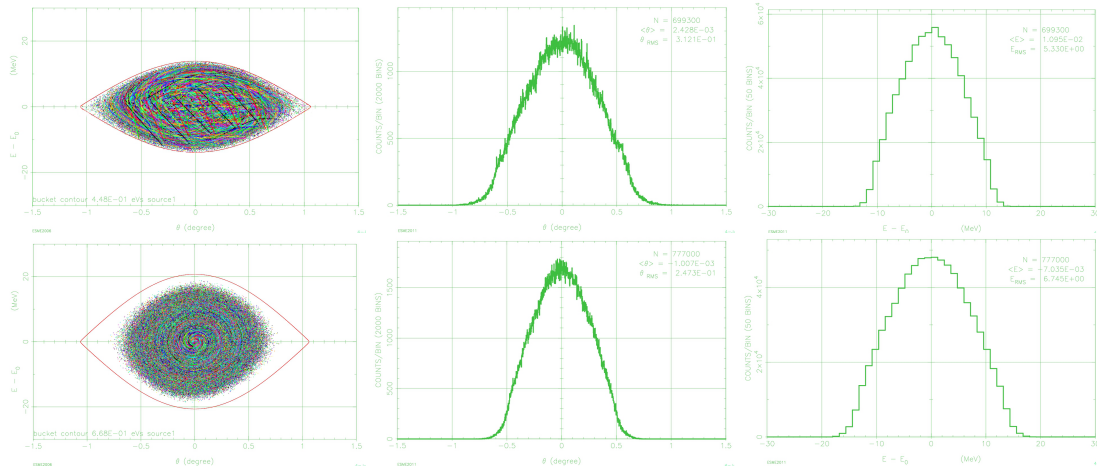


**Figure 5.31:** Longitudinal phase space (left) and bunch density (middle and right) for the 75 GeV option with laser injection, at the end of the painting process (top) and at the end of flat-bottom when beam is ready for acceleration (bottom)

### 5.3.3 Extraction Systems

For the HP-PS a fast extraction system is foreseen. The kicker and septum magnets are placed in two 15 m long drifts on either side of the 24 m long  $H^-$  injection. The lattice does not leave space for a bumper system to reduce the extraction kick angle. In order to estimate the required clearance between the circulating and extracted beam at the septum entrance, the following calculation of half beam sizes is used:

$$A_{x,y} = n_{\sigma} \sqrt{k_{\beta} \beta_{x,y} \frac{\epsilon_{N;x,y}}{\gamma_r \beta_r}} + |k_{\beta} D_{x,y} \sigma_{\delta}| + c.o. + align \quad (5.16)$$

where  $\beta$  and  $D$  denote the betatron and dispersion functions with their uncertainty factor  $k_{\beta}$ ,  $\epsilon$  and  $\sigma_{\delta}$  the distributions of emittance and momentum spread, *c.o.* the trajectory variation and  $\gamma_r$  and  $\beta_r$  the relativistic parameters. The beam sizes are calculated for  $n_{\sigma} = 4$ ,  $k_{\beta} = 1.2$ , *c.o.* = 2 mm and align=4 mm.

#### 5.3.3.1 50 GeV extraction

In case of a 50 GeV machine, a horizontal emittance of 10 and 10.5  $\mu\text{m}$  for foil and laser optics, respectively, have to be acomodated. The required deflection from the kicker system to reach a 5 mm beam clearance at the first septum blade is 3.1 mrad in case of the foil optics, Fig. 5.32. Although the laser optics has the more favourable phase advance between centre of the kickers and septum entrance of  $90^{\circ}$  compared to  $107^{\circ}$  in case of the foil optics, it has lower horizontal betatron functions at the kicker and septa positions and therefore a higher kick of 3.3 mrad is needed, Figures 5.32 and 5.33.

In order to reach this deflection with a maximum rise time of 250 ns, an 80 kV transmission line magnet concept in terminated mode with 7.25 Ohm system impedance is chosen, Table 5.17. The high voltage of 80 kV requires gas filled cables. Since the HP-PS assumes a total intensity of up to  $2.5 \cdot 10^{14}$ , the need of an impedance screen needs to be clarified. In the presented magnet gap, a screen of  $\pm 5$  mm is included. A screen would also delay the rise time of the system which can be compensated by decreasing the cell length of the magnets. The total system length of 13.6 m leaves 1.4 m margin which can be used for additional interconnects in case of shorter magnets.

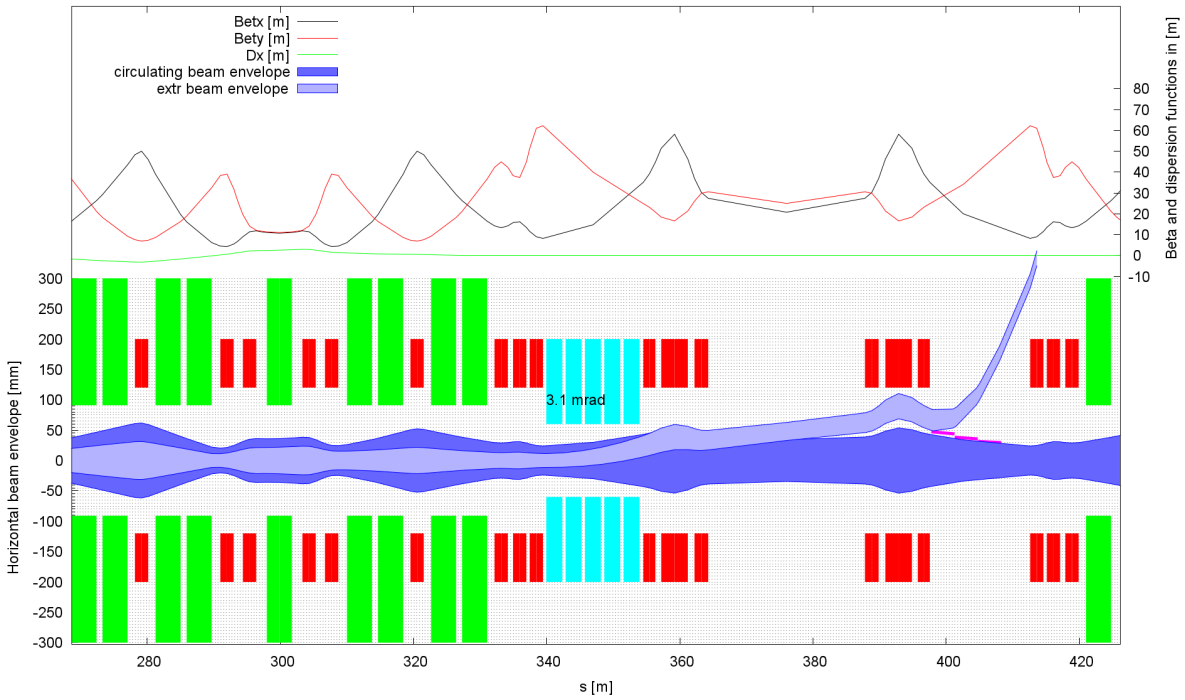


**Figure 5.32:** Betatron and dispersion functions for the 50 GeV foil option of the long straight section in the top plot and beam envelopes at extraction on the bottom. The elements in green denote dipoles, in red quadrupoles and in turquoise the kicker magnets. The septum blades are indicated in magenta.

**Table 5.17:** Kicker and septum parameters for a 50 GeV fast extraction.

Parameter	Unit	Kicker	Septum
Deflection angle	[mrad]	3.3	52
Integrated field	[Tm]	0.561	8.84
Rise time	[ns]	250	-
Impedance	[Ohm]	7.25	-
Voltage	[kV]	80	-
Current	[kA]	5.5	27
Magnet gap/width	[mm]	135/86	34/120
Septum thickness	[mm]	-	5
Magnet length	[m]	2.26	
Number of magnets		5	
Magn./total length	[m]	11.3/13.6	8.8/10.6
Magnetic field	[T]	0.051	1.0

For the septa magnets a total deflection of 52 mrad is required to clear the downstream quadrupoles. A first thin septum with 5 mm thickness is assumed. The central triplet quadrupole in the LSS requires an enlarged aperture of 125 mm.

### 5.3.3.2 75 GeV extraction

In case of a 75 GeV machine, the smaller intensity and thus reduced space charge tune shift allows to reduce the beam emittance in the horizontal plane to  $5.5 \mu\text{m}$ . Therefore, the required deflection to reach a 5 mm clearance for the septum blade is 2.6 mrad for the kicker system for the laser optics, Fig. 5.33. In case of the foil optics an extraction kick of 2.4 mrad is sufficient to extract the beam. A similar kicker system as for the 50 GeV extraction can be chosen since

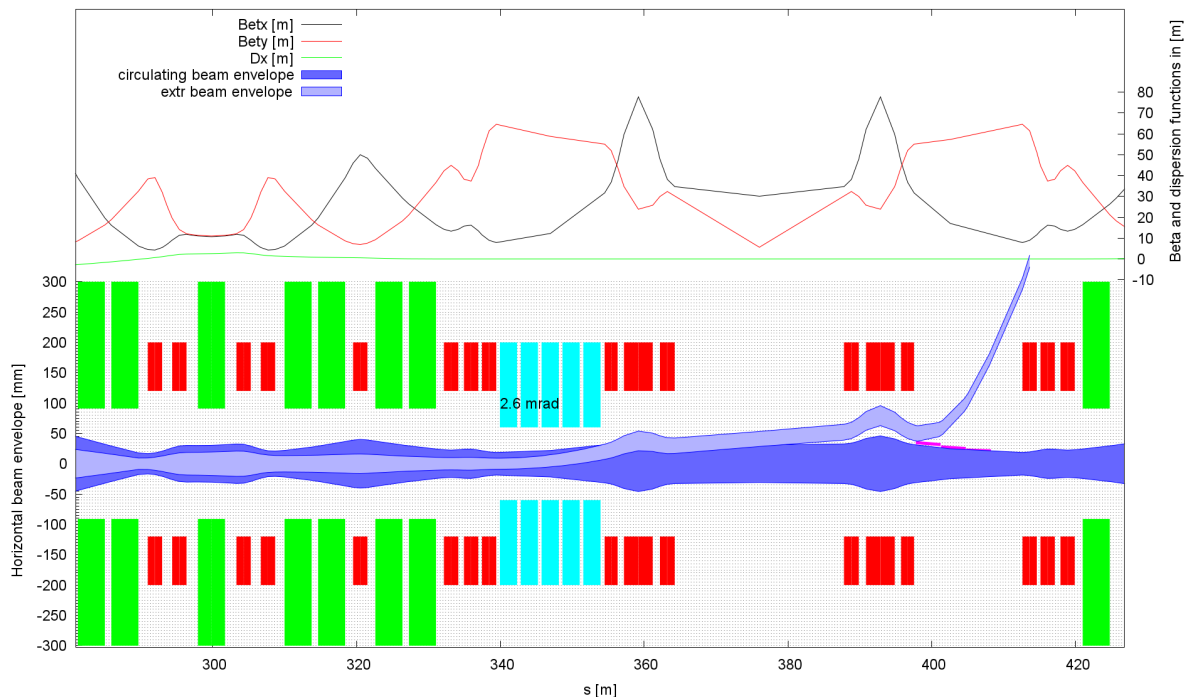


**Figure 5.33:** Betatron and dispersion functions for the 75 GeV laser option of the long straight section in the top plot and beam envelopes at extraction on the bottom. The elements in green denote dipoles, in red quadrupoles and in turquoise the kicker magnets. The septum blades are indicated in magenta.

for 75 GeV the required gap and width are smaller, Table 5.18. Also in this system  $\pm 5$  mm of the magnet gap are reserved for an impedance screen. For the septa the increase in magnetic rigidity is compensated by an increase in magnetic length. The septa system installation length fully covers the available drift. The central triplet quadrupole in the LSS requires an enlarged aperture of 96 mm.

### 5.3.4 The LP-SPL design

The Low-Power Superconducting Proton LINAC (LP-SPL) [83] has been studied as an option for part of the upgrade of the LHC injector chain and is considered as injector for the HP-PS. The main beam characteristics, relevant for the injection into the HP-PS are given in Table 5.19. The LP-SPL design consists of 160 MeV normal conducting LINAC4 front-end, which is presently being built and commissioned at CERN, followed by two families of superconducting cavities, accelerating the beam up to its final energy of 4 GeV.

**Table 5.18:** Kicker and septum parameters for a 75 GeV fast extraction.

Parameter	Unit	Kicker	Septum
Deflection angle	[mrad]	2.6	52
Integrated field	[Tm]	0.659	13.16
Rise time	[ns]	250	-
Impedance	[Ohm]	7.25	-
Voltage	[kV]	80	-
Current	[kA]	5.5	27
Magnet gap/width	[mm]	120/75	34/120
Septum thickness	[mm]	-	5
Magnet length	[m]	2.27	-
Number of magnets		5	-
Magn./total length	[m]	11.3/13.6	13.2/15.0
Magnetic field	[T]	0.063	1.0

**Table 5.19:** Main LP-SPL beam characteristics, relevant for the injection into the HP-PS, based on the present LP-SPL design.

LP-SPL Parameter	Unit	Value
Maximum kinetic energy	[GeV]	4
Average beam current during pulse	[mA]	20
Repetition rate	[Hz]	2
Pulse duration	[ms]	0.9
Resulting number of protons per pulse	[ $10^{14}$ ]	1.13
Beam power	[MW]	0.144

### 5.3.4.1 Fulfilling the HP-PS beam requirements

As previously mentioned the HP-PS is assuming a pulse rate of 1 Hz which is compatible with the LINAC4 and LP-SPL performance reach, one pulse for the existing accelerator complex and one pulse for the HP-PS. However, in order to reach the 2 MW beam power at 50 GeV the LP-SPL will need to inject at least  $2.5 \cdot 10^{14}$  protons per pulse, hence requiring a modification to the LP-SPL performance. An intensity increase from the LP-SPL can be obtained either by increasing the pulse current, but this translates in a higher peak power, which impacts directly on the price of the klystrons that can be come very high, or by increasing the pulse length, which impacts on the modulator stored energy and increases the cryogenic load, but results in little difference for the klystrons and is therefore consider to be more economical. An increase of the pulse length with a factor of 2.5 is feasible and brings the LP-SPL performance to the level required by the baseline design of the HP-PS. For the 75 GeV option an increase of 55% would already be sufficient. A longer linac pulse increases the injection turns into the ring and the charge exchange injection process, through a stripping foil, should be optimised with respect to temperature rise and hitting rate.

**Table 5.20:** The required main LP-SPL beam characteristics.

LP-SPL Parameter	Unit	50 GeV	75 GeV
Maximum kinetic energy	[GeV]		4
Average beam current during pulse	[mA]		20
Pulse rate	[Hz]		2
Pulse duration	[ms]	2.25	1.4
Resulting number of protons per pulse	[ $10^{14}$ ]	2.8	1.8

## 5.4 Longitudinal parameters during acceleration

The longitudinal parameters for the HP-PS are defined during the whole cycle taking into account the aperture and stability requirements. The necessity of continuous longitudinal emittance blow-up is addressed and various emittance blow-up schemes are compared. Finally an "optimum" cycle is presented for all options considered by this feasibility study.

### 5.4.1 Acceleration cycles

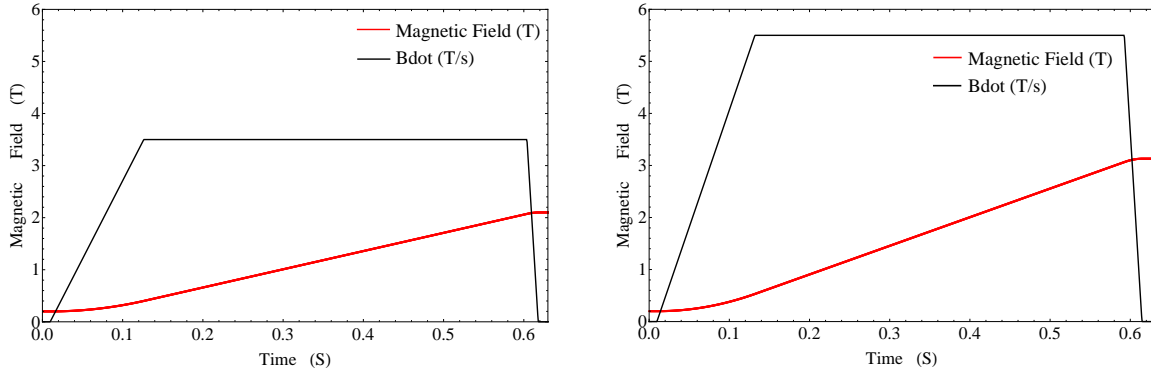
The cycling of the HP-PS is constrained by the repetition rate, as discussed in section 5.1 and imposes a rather fast acceleration time of about 500 to 600 ms, allowing sufficient time (400 to 500 ms) for the magnets to ramp down and be ready at injection for the next cycle. The cycle is composed of the injection plateau, the acceleration ramp, a short extraction flat top and the down ramp. At the end of the injection plateau the acceleration ramps start with a parabolic increase of the field, followed by a linear accretion ramp that rounds off parabolically again before reaching the short extraction flattop. The magnetic field and ramp rate ( $dB/dt$ ) for the main magnets are summarised in Table 5.21. The evolution of the injection plateau, the acceleration ramp and the flat top are illustrated in Fig. 5.34 .

The synchronous momentum evolution during cycle is proportional to the magnetic field variation :

$$p_s \text{ [eV/s]} = ce\rho B \text{ [T]} \quad (5.17)$$

**Table 5.21:** Magnetic field at injection and extraction in the HP-PS together with the maximum  $dB/dt$ .

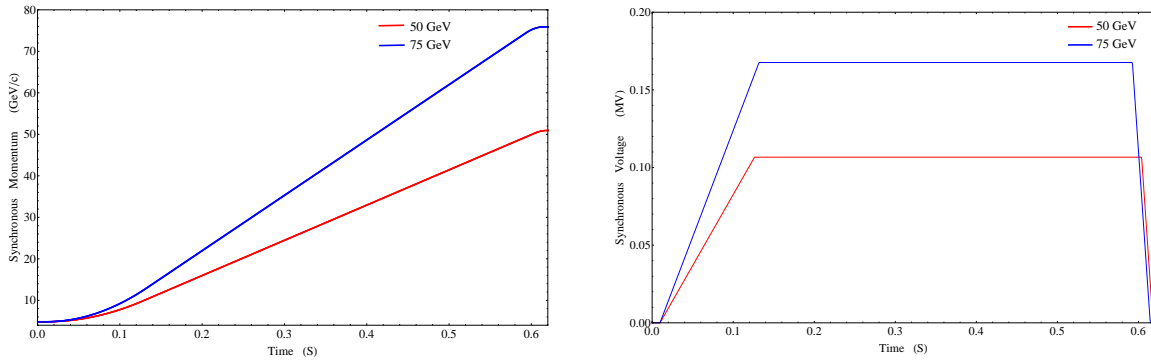
Parameter	Unit	50GeV	75GeV
Injection	[T]	0.19	0.19
Extraction	[T]	2.11	3.13
Maximum $dB/dt$	[T/s]	3.5	5.5


**Figure 5.34:** Magnetic field and  $dB/dt$  during acceleration for the 50 GeV baseline (left) and 75 GeV option (right)

with  $\rho = 80.89$  m the bending radius. The synchronous voltage seen by the particle during acceleration is given by :

$$eV_s \text{ [eV/s]} = 2\pi R \frac{dp_s}{dt} \quad (5.18)$$

The synchronous momentum and voltage for both, the 50 GeV baseline and the 75 GeV option, are shown in Fig. 5.35.


**Figure 5.35:** Synchronous momentum (left) and synchronous voltage (right) for 50 GeV (blue line) and 75 GeV (red line).

The RF voltage during acceleration for a given magnetic field is deduced from the bucket area, which itself is calculated from the longitudinal emittance  $\varepsilon_l$  and filling factor  $q$ , defined as ratio between the bucket area and the longitudinal emittance or as the ratio between the maximum momentum spread of the bucket and the maximum momentum spread in the bunch for a matched bunch. The longitudinal emittance and filling factor are first considered as free parameters to obtain a first estimate of the RF voltage required during acceleration. Fig. 5.36 shows the RF voltage calculated for various values of the longitudinal emittance with a constant filling factor of  $q = 80\%$ . The corresponding beam full momentum spread is shown in Fig. 5.37 while the bunch length is given in Fig. 5.38.

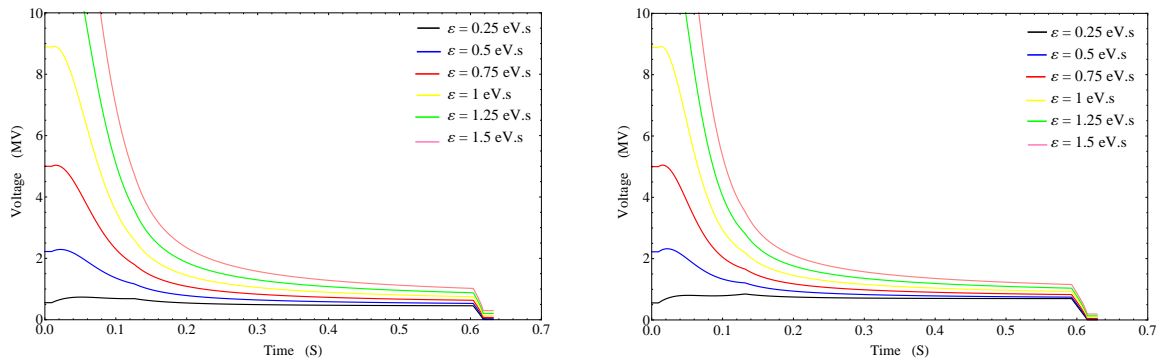


**Figure 5.36:** Accelerating voltage function for a constant filling factor of 80% and various longitudinal emittances for the 50 GeV baseline (left) and the 75 GeV option (right).

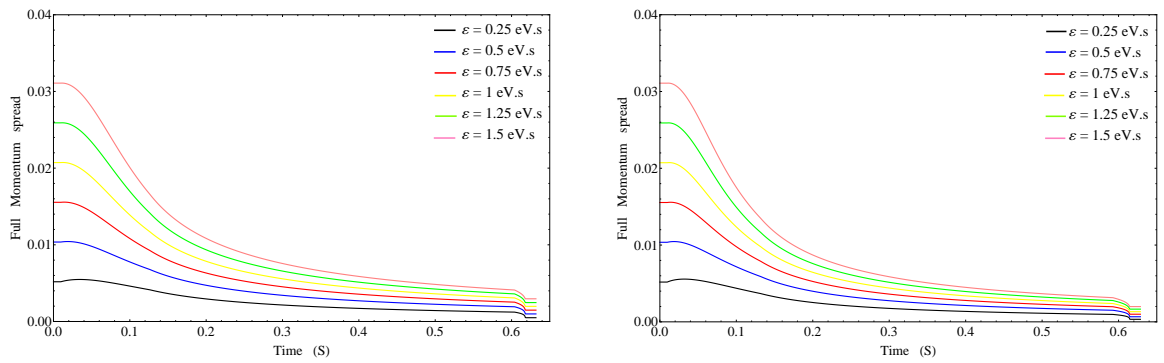


**Figure 5.37:** Full momentum spread for a constant filling factor of 80% and various longitudinal emittances for the 50 GeV baseline (left) and the 75 GeV option (right).

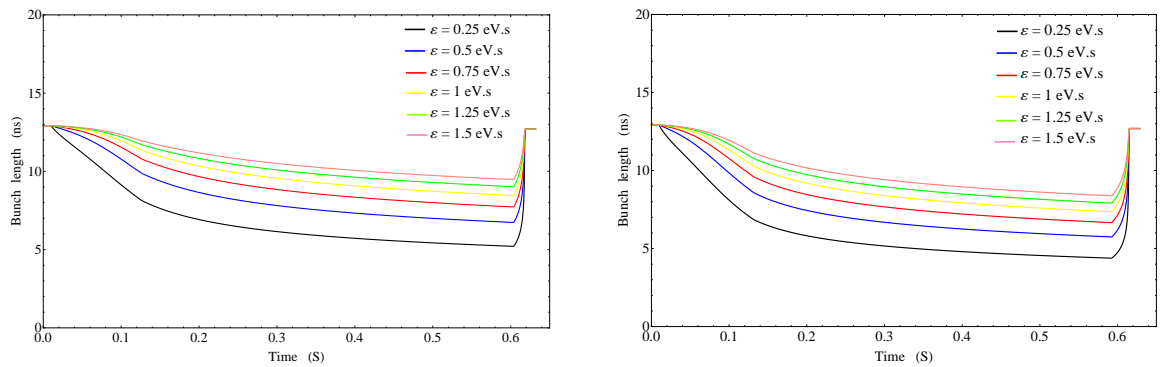


**Figure 5.38:** Bunch length for a constant filling factor of 80 % and various longitudinal emittances for the 50 GeV baseline (left) and the 75 GeV option (right).



Fig. 5.36 shows that the voltage at injection quickly increases with the longitudinal emittance, hence optimisation is required to avoid excessive levels of required RF power. For comparison the 40 MHz RF system that is considered in the PS2 design has a maximum available voltage of 1.5 MV, which results in a maximum longitudinal emittance of around 0.45 eVs at injection. The dynamic aperture of the machine is another important parameter that needs to be taken into account, as the momentum spread ( $dp/p$ ) of the beam is coupled to the transverse beam dimensions through the dispersion function ( $D(s)$ ) and the momentum compaction factor  $\alpha_p$ . The curves for the full momentum spread shown in Fig. 5.37, which each correspond to the voltage programs given in Fig. 5.36, are the minimum values that can be obtained during the cycle for the given emittance, thanks to the high filling factor of 80%.

After these initial estimates for the accelerating voltage, the momentum spread and the bunch length as a function of longitudinal emittance optimisation is necessary, taking into account the instability thresholds both at injection and acceleration.

## 5.4.2 Beam stability

For equally spaced bunches the threshold for coupled-bunched instabilities due to narrow-band impedances with a frequency  $f_r = (pM + n)f_0 + mf_s$  can be approximate with [?], [?]:

$$R_{sh} < \frac{|\eta|E}{eI_0\beta^2} \left(\frac{\Delta E}{E}\right)^2 \frac{\Delta\omega_s}{\omega_s} \frac{F}{f_0\tau} G(f_r\tau) \quad (5.19)$$

where  $f_0$  is the revolution frequency,  $f_s = \omega_s/2\pi$  is the synchrotron frequency,  $p = 0, 1, \dots$ ,  $n = 1, 2, \dots, M - 1$ ,  $m = 1, 2, \dots$  are integers,  $M$  is the number of bunches in the ring,  $\eta = 1/\gamma_t^2 - 1/\gamma^2$ ,  $E$  is the synchronous energy,  $\Delta E/E$  is the relative energy spread in the bunch,  $\Delta\omega_s/\omega_s$  is the relative synchrotron frequency spread in the bunch,  $I_0 = MN_b e f_0$  is the average beam current,  $N_b$  is the bunch intensity, and the form-factor  $F \simeq 0.3$  is defined by the particle distribution, which itself is given by the function  $G(x) = x \min\{J_m^{-2}(\pi x)\}$ , where  $x = f_r\tau$  and  $J_m(x)$  is the Bessel function of order  $m$ .

The Narrow-band thresholds during acceleration for the voltage programs shown in Fig. 5.36 are presented in Fig. 5.39, for both the 50 GeV baseline and the 75 GeV option.

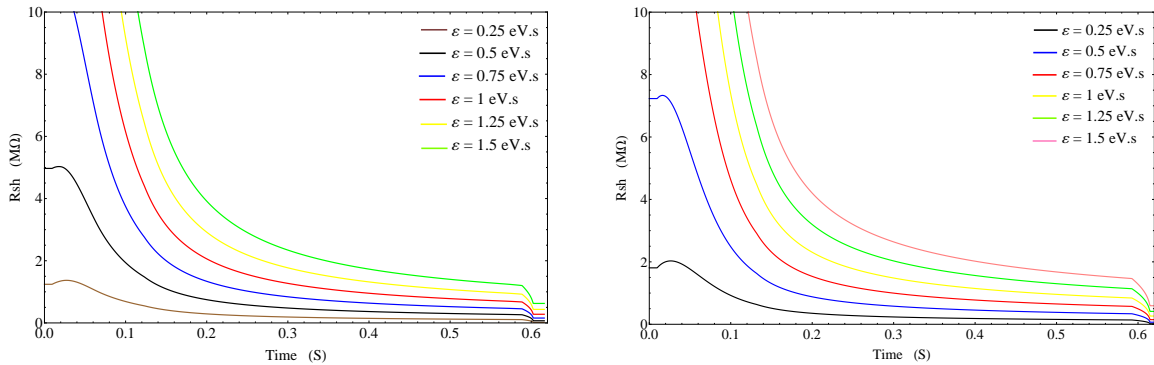


**Figure 5.39:** Narrow-band threshold during acceleration for a constant filling factor of 80% and various longitudinal emittances for the 50 GeV baseline (left) and the 75 GeV option (right).

The threshold value for a reactive part of the broad-band impedance can be expressed by :

$$|\text{Im}Z|/n < \frac{|\eta|E}{eI_b\beta^2} \left(\frac{\Delta E}{E}\right)^2 \frac{\Delta\omega_s}{\omega_s} f_0\tau \quad (5.20)$$

where  $\eta = 1/\gamma_t^2 - 1/\gamma^2$ ,  $E$  is the synchronous energy,  $\Delta E/E$  is the relative energy spread in the bunch,  $\Delta\omega_s/\omega_s$  is the relative synchrotron frequency spread in the bunch,  $I_b = N_b e f_0$  is the bunch current,  $N_b$  is the bunch intensity,  $\tau$  is the full bunch length.

The Broad-band thresholds during acceleration for the voltage programs shown in Fig. 5.36 are presented in Fig. 5.40 together with the space charge impedance, for both the 50 GeV baseline and the 75 GeV option.

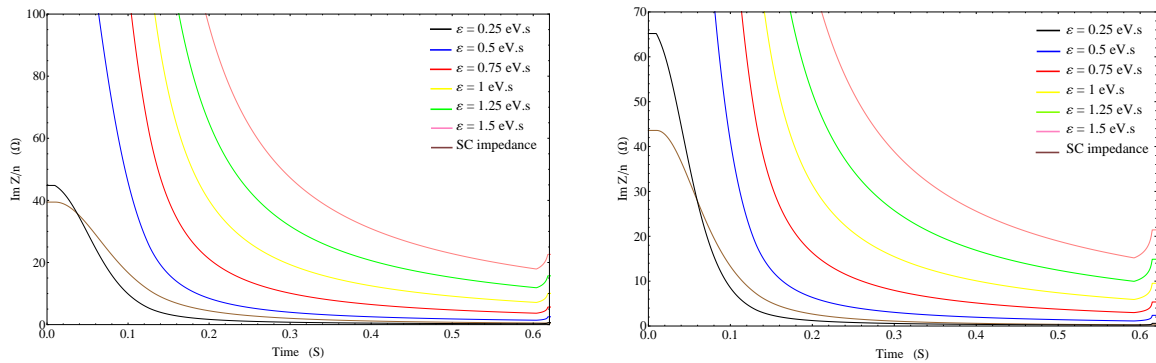


**Figure 5.40:** Broad-band threshold during acceleration for a constant filling factor of 80% and various longitudinal emittances for the 50 GeV baseline (left) and the 75 GeV option (right).

The broad-band threshold for both the 50 GeV baseline and the 75 GeV option and for constant emittance  $\epsilon_l=0.25$  eVs quickly drops below the space charge impedance, leading to the loss of Landau damping. At the flat-top the margin between space charge impedance and broad-band threshold is also quite small for  $\epsilon_l=0.5$  eVs acceleration.

#### 5.4.2.1 Stability at injection

At injection the longitudinal emittance has to be large enough to ensure a high enough the instabilities threshold, but it has also to be small enough to limit the beam full momentum spread as this is limited by the magnet apertures. The final choice of the longitudinal emittance at injection will then be a compromise between these two constraints. For bunches with too small longitudinal emittances Landau damping can be lost due to the HP-PS reactive impedance and the beam can become unstable due to the presence of any resistive impedance. The main contribution to the reactive impedance comes from space charge and can be expressed as :

$$|\text{Im } Z|/n < \frac{Z_0 g_0}{\beta \gamma^2} \quad (5.21)$$

where  $Z_0=377$  Ohm and  $g_0 = \ln(b/a) + 0.5$ ,  $a$  and  $b$  are beam and pipe radius.

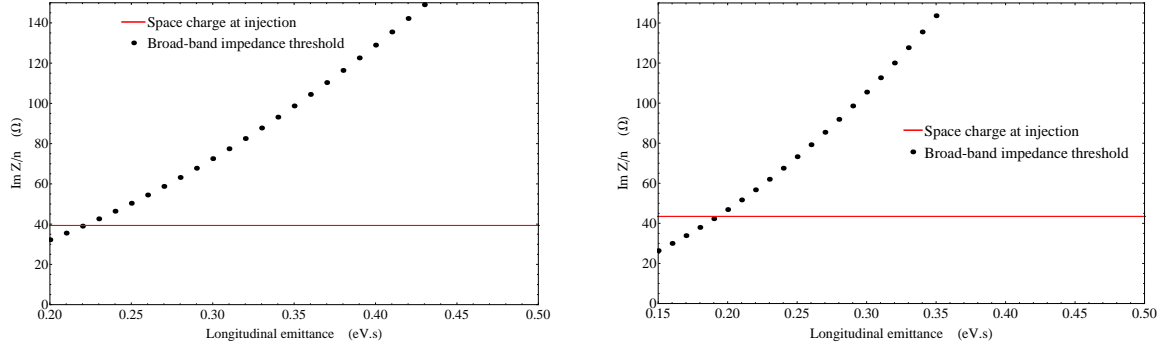
Fig. 5.41 shows the broad-band impedance threshold at injection as a function of longitudinal emittance, together with the space charge impedance at injection for both the 50 GeV baseline and the 75 GeV option.

Fig. F9 shows the lower limit for the longitudinal emittance at injection due to space charge impedance for the HP-PS to be around 0.22 eVs for the 50 GeV baseline and around 0.19 eVs for the 75 GeV option.

#### 5.4.2.2 Constraints from optics

The second group of constraints come from the optics design. In order to maintain reasonable values for the beta functions, phase advance, magnets pole tip field and vacuum chamber aperture, a set of bunch length, beam full momentum spread and transverse emittance has been defined for each option considered (laser and foil injection, for both top energies). This leads to a set of longitudinal emittances at injection that are summarised in Table 5.22 : [?]

All these values satisfy the optics requirements together with stability conditions. However, as shown on the Fig. 5.40, these longitudinal emittances are not sustainable during acceleration.



**Figure 5.41:** Broad-band threshold at injection as a function of longitudinal emittance together with space charge impedance at injection for the 50 GeV baseline (left) and the 75 GeV option (right).

**Table 5.22:** Longitudinal emittances at injection for all options

Parameter	Unit	Foil		Laser	
		50GeV	75GeV	50GeV	75GeV
Emittance, $\varepsilon_l$	[eVs]	0.31	0.4	0.356	0.38

The margin between the impedance and the instability threshold is too small at high energy and could lead to loss of Landau damping. This implies that a controlled emittance blow-up during acceleration is required, which will be addressed in next section with the aim to determine the optimal blow-up program.

### 5.4.2.3 Stability during acceleration

The preservation of Landau damping is especially important in the absence of a longitudinal feedback system. During the cycle the broad-band threshold changes as :

$$|\text{Im}Z|/n \propto \frac{\eta^{5/4} \varepsilon^{5/2}}{\beta^3 E^{5/4} V^{1/4} h^{1/4}} \quad (5.22)$$

The beam is injected in the HP-PS with a kinetic energy of 4 GeV ( $\gamma=5.26$ ) and the transition gamma is  $\gamma_t=15.1i$ . This leads to a non-negligible dependence on  $\beta$  and  $\eta$ , especially during the first half of acceleration. As already discussed and shown, if the longitudinal emittance remains at the injection value during the cycle, the broad-band threshold quickly decreases and beam stability could become critical. For this reason a controlled blow-up during acceleration is necessary to maintain the beam stable. It follows from equation ?? that in order to avoid the decrease of the broad-band threshold during acceleration the emittance should increase according to:

$$\varepsilon \propto \eta^{8/25} \beta^{6/5} E^{1/2} V^{1/10} h^{1/10} \quad (5.23)$$

The dependence on the harmonic number is neglected, as  $h$  remains unchanged during acceleration in the HP-PS, for both top energies. Different possibilities for emittance blow-up dependence have been considered. First a comparison between constant voltage and increasing voltage has been done, without taking into account the dependence on  $\beta$  and  $\eta$ . In this case, for a constant voltage, the emittance changes as :

$$\varepsilon(E) = \varepsilon_{max}(E/E_{max})^{1/2} \quad (5.24)$$

Then, assuming a voltage program :

$$V(E) = V_{max}(E/E_{max})^{1/4} \quad (5.25)$$

the corresponding emittance change, still neglecting the  $\beta$  and  $\eta$  dependence, is :

$$\varepsilon(E) = \varepsilon_{max}(E/E_{max})^{21/40} \quad (5.26)$$

which is not so different than for a constant voltage. The longitudinal emittance and voltage values at injection and extraction for these first two options are summarised in tables 5.23, 5.24, 5.25 and 5.26.

**Table 5.23:** Blow-up parameters at injection and extraction for constant voltage and energy dependence for foil injection

Parameter	Unit	50 GeV		75 GeV	
		Inj.	Extr.	Inj.	Extr.
Emittance, $\varepsilon_l$	[eVs]	0.31	0.99	0.4	1.57
Voltage	[MV]	0.97	0.97	1.02	1.02

**Table 5.24:** Blow-up parameters at injection and extraction for constant voltage and energy dependence for laser injection

Parameter	Unit	50 GeV		75 GeV	
		Inj.	Extr.	Inj.	Extr.
Emittance, $\varepsilon_l$	[eVs]	0.356	1.14	0.38	1.49
Voltage	[MV]	1.11	1.11	1	1

**Table 5.25:** Blow-up parameters at injection and extraction for variable voltage and energy dependence for foil injection

Parameters	Units	50 GeV		75 GeV	
		Inj.	Extr.	Inj.	Extr.
Emittance, $\varepsilon_l$	[eVs]	0.31	1.05	0.4	1.68
Voltage	[MV]	0.97	1.74	1.02	2.02

These voltage and emittance programs do not induce an increase of the momentum spread at the beginning of the ramp, which is beneficial in view of the HP-PS aperture. The blow-up using variable voltage and energy dependence leads to a better threshold, especially for the narrow-band impedance. The minimum difference between the broad-band threshold and the space charge impedance is around  $6\Omega$ . In order to further improve this safety margin the blow-up program should take into account the  $\beta$  and  $\eta$  dependence of the broad-band threshold. In this case, assuming a voltage change given by equation ?? the emittance scales with energy as :

$$\varepsilon \propto \eta^{8/25} \beta^{6/5} E^{21/40} \quad (5.27)$$

assume an emittance blow-up of :

$$\varepsilon = a_0 + a_1(\eta_{max}/\eta)^{8/25} * a_2(\beta/\beta_{max})^{6/5} * a_3(E/E_{max})^{21/40} \quad (5.28)$$

By tuning the weights ( $a_1, a_2, a_3$ ) of the different contributions to the emittance changes, not only different threshold evolutions during acceleration, but also different values of peak momentum spread are obtained. The strategy consists of finding a good compromise between the peak momentum spread, which should be as small as possible in view of the magnet aperture,

**Table 5.26:** Blow-up parameters at injection and extraction for variable voltage and energy dependence for laser injection

Parameters	Units	50 GeV		75 GeV	
		Inj.	Extr.	Inj.	Extr.
Emittance, $\varepsilon_l$	[eVs]	0.356	1.21	0.38	1.59
Voltage	[MV]	1.11	1.97	1	1.98

and the minimum difference between broad-band threshold and reactive impedance. Tables 5.29 and 5.30 present the different combinations of weights which have been considered for the 50 GeV baseline, and tables 5.31 and 5.32 present the different combinations of weights which have been considered for the 75 GeV option. The corresponding peak momentum spread and the minimum difference between broad-band threshold and space charge impedance are also given. All these combinations have been made, assuming a voltage variation during acceleration as given by equation ???. The first combination, called "Blow-up 1", corresponds to the case with only energy dependence of emittance blow-up. The second combination, called "Blow-up 2" has been optimised in order to obtain the broad-band threshold during acceleration as high as possible. This combination leads to an excellent safety margin between the space charge impedance and the broad-band threshold. However it also induces a momentum spread peak at the beginning of the ramp which is not compatible with the machine aperture and bucket acceptance. Following these observations a third combination, called "Blow-up 3" has been studied in order to obtain a safety margin between the broad-band impedance threshold and the space charge impedance as high as possible without compromising the machine aperture at low energy due to momentum spread. The emittance and voltage values at injection and extraction for the "Blow-up 1" scheme are summarised in tables 5.25 and 5.26, while the emittance and voltage values at injection and extraction for the "Blow-up 2" and "Blow-up 3" schemes are summarised in table 5.27 and table 5.28.

**Table 5.27:** Blow-up parameters at injection and extraction for the "Blow-up 2" scheme for both energies and injection options

Parameter	Unit	50 GeV Foil		50 GeV Laser		75 GeV Foil		75 GeV Laser	
		Inj.	Extr.	Inj.	Extr.	Inj.	Extr.	Inj.	Extr.
Emittance, $\varepsilon_l$	[eVs]	0.31	2.2	0.356	2.25	0.4	2.29	0.38	2.27
Voltage	[MV]	0.97	1.74	1.1	1.97	1.02	2.02	1	1.98

**Table 5.28:** Blow-up parameters at injection and extraction for the "Blow-up 3" scheme for both top energies and injection options

Parameter	Unit	50 GeV Foil		50 GeV Laser		75 GeV Foil		75 GeV Laser	
		Inj.	Extr.	Inj.	Extr.	Inj.	Extr.	Inj.	Extr.
Emittance, $\varepsilon_l$	[eVs]	0.31	1.39	0.356	1.44	0.4	1.97	0.38	1.95
Voltage	[MV]	0.97	1.74	1.1	1.97	1.02	2.02	1	1.98

**Table 5.29:** Summary of the emittance blow-up scheme optimisation for the 50 GeV baseline and Foil injection

Parameter	$a_1$	$a_2$	$a_3$	Max dp/p [ $e^{-3}$ ]	Min diff. ( $\Omega$ )
Blow-up 1	0	0	1.05	6.6	5.4
Blow-up 2	6.3	0.35	1.02	7.8	27
Blow-up 3	5.3	0.22	1.1	6.6	11.5

**Table 5.30:** Summary of the emittance blow-up scheme optimisation for the 50 GeV baseline and Laser injection

Parameter	$a_1$	$a_2$	$a_3$	Max dp/p [ $e^{-3}$ ]	Min diff. ( $\Omega$ )
Blow-up 1	0	0	1.05	7.4	6
Blow-up 2	6.3	0.35	1.02	8.2	38.2
Blow-up 3	5.3	0.22	1.1	7.4	12.1

**Table 5.31:** Summary of the emittance blow-up scheme optimisation for the 75 GeV option and Foil injection

Parameter	$a_1$	$a_2$	$a_3$	Max dp/p [ $e^{-3}$ ]	Min diff. ( $\Omega$ )
Blow-up 1	0	0	1.68	7.6	15
Blow-up 2	5.3	0.4	1.02	7.8	33.9
Blow-up 3	5	0.3	1.2	7.6	23.38

Fig. 5.42 and 5.43 show the broad-band threshold variation during acceleration for the 50 GeV baseline and the 75GeV option, respectively, and Fig. 5.44 and 5.45 show the narrow-band threshold variation during acceleration for the 50 GeV baseline and the 75GeV option, respectively. Fig. 5.46 and 5.47 present the longitudinal emittance during acceleration, for all blow-up schemes and for both top energies. Fig. 5.42 shows that the broad-band threshold drops below the space charge impedance in case there is no blow-up for both injection options and 50 GeV baseline and that it is at the limit of stability for both injection options and the 75GeV option. The "Blow-up 1" scheme maintains the threshold always above the space charge impedance, but with a safety margin decreasing to around 5  $\Omega$  in the worst case (Foil injection) for the 50 GeV baseline, and 7  $\Omega$  in the worst case (Laser injection) for the 75GeV option. The "Blow-up 2" scheme maintains high thresholds during acceleration, but leads to a momentum spread peak during acceleration. Finally the "Blow-up 3" scheme does not induce this momentum spread peak while improving the safety margin during acceleration with respect to the "Blow-up 1" scheme. Therefore this is considered the "optimum" scheme.

### 5.4.3 Optimum cycle

In this section the parameters suggested in the previous section are used to define the optimum acceleration parameters for the HP-PS cycle. The voltage and emittance programs are given by the equations ?? and ??, respectively. Their parameters are given in the table 5.28, 5.29, 5.30, 5.31 and 5.32. The voltage programs used for this optimum cycle are presented in Fig. 5.48 and the resulting longitudinal emittance evolutions are presented in Fig. 5.49

The evolution of the momentum spread together with the synchrotron tune is given in Fig. 5.50. The applied voltage program and evolution of the longitudinal emittance do not lead to an increase in the momentum spread at the beginning of acceleration.

The thresholds impedances  $R_{sh}^{min}$  (minimum value at  $f_r = f_r^{min}$ ) and  $ImZ/n$  corresponding to this voltage program and emittance evolution are presented in Fig. 5.51. As explained

**Table 5.32:** Summary of the emittance blow-up scheme optimisation for the 75 GeV option and Laser injection

Parameter	$a_1$	$a_2$	$a_3$	Max dp/p ( $e^{-3}$ )	Min diff. ( $\Omega$ )
Blow-up 1	0	0	1.68	7.4	13.7
Blow-up 2	5.3	0.4	1.02	7.6	33.3
Blow-up 3	5	0.3	1.2	7.4	22.8

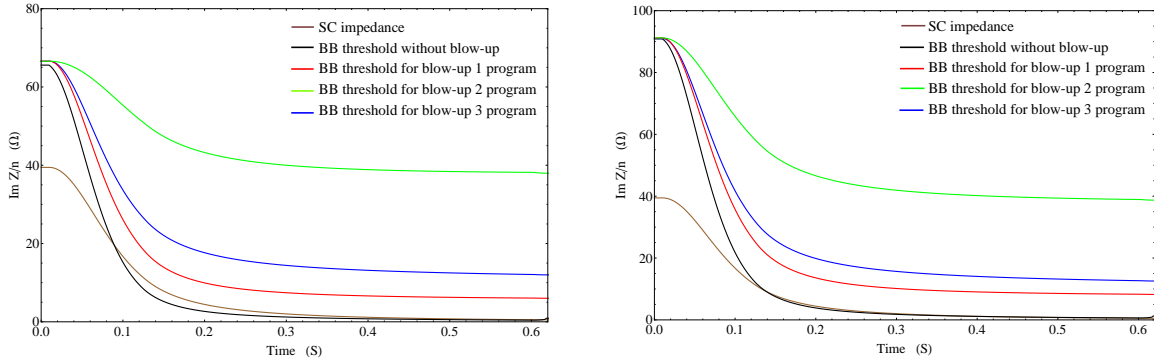


**Figure 5.42:** Broad-band threshold during acceleration for various longitudinal emittances blow up schemes together with the space charge impedance for the 50 GeV baseline in case of foil injection (left) or laser injection (right).

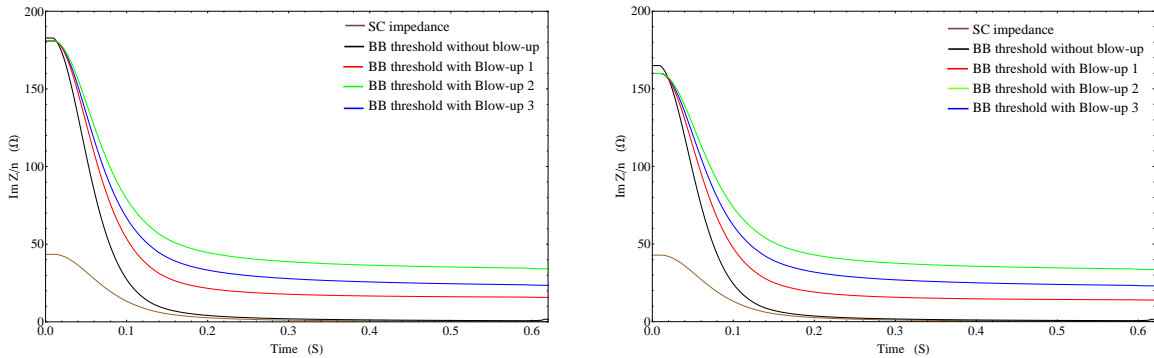


**Figure 5.43:** Broad-band threshold during acceleration for various longitudinal emittances blow up schemes together with the space charge impedance for the 75 GeV option in case of foil injection (left) or laser injection (right).

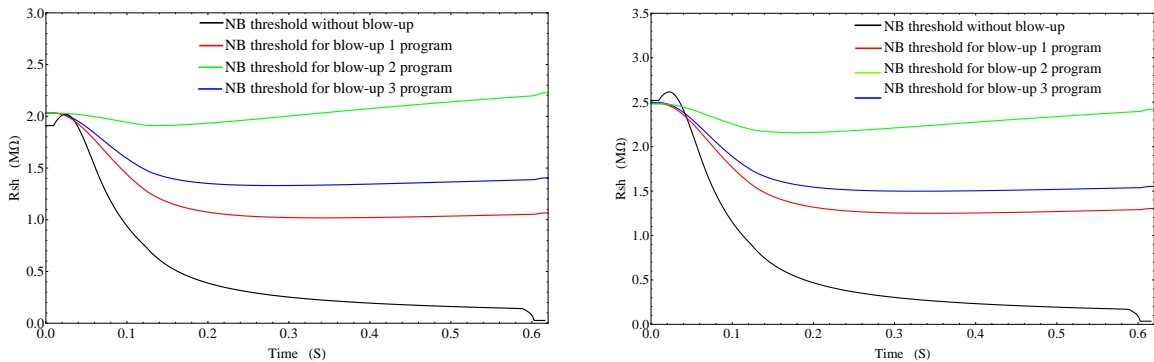


**Figure 5.44:** Narrow-band threshold during acceleration for various longitudinal emittances blow up schemes together with the space charge impedance for the 50 GeV baseline in case of foil injection (left) or laser injection (right).

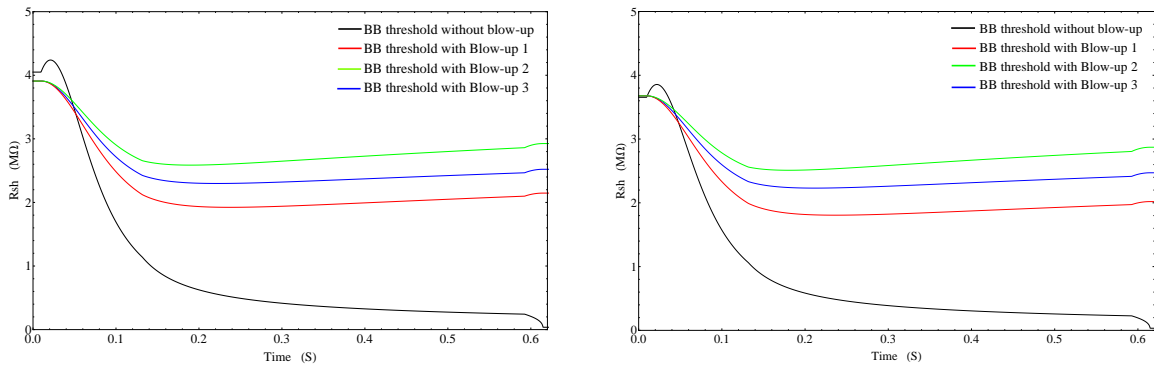


**Figure 5.45:** Narrow-band threshold during acceleration for various longitudinal emittances blow up schemes together with the space charge impedance for the 75 GeV option in case of foil injection (left) or laser injection (right).

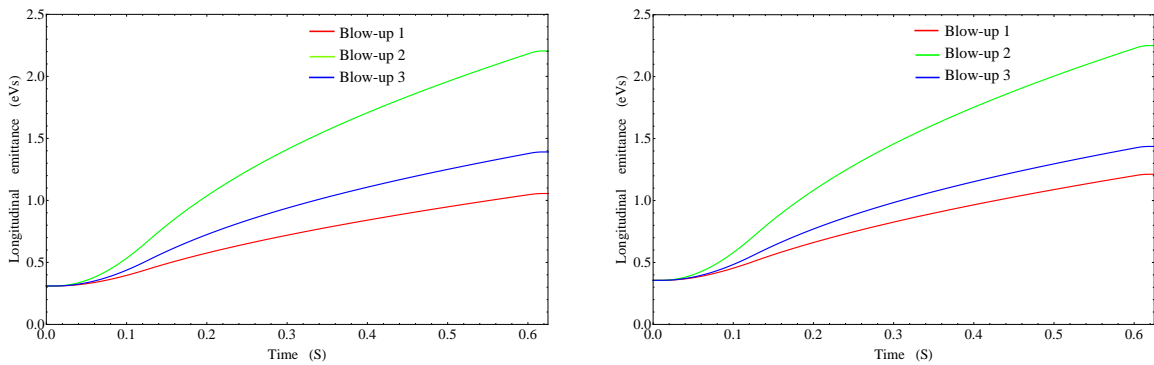


**Figure 5.46:** Emittance blow-up during acceleration corresponding to values given in table 5.29 for the 50 GeV baseline in case of foil injection (left) or table 5.30 for laser injection (right).

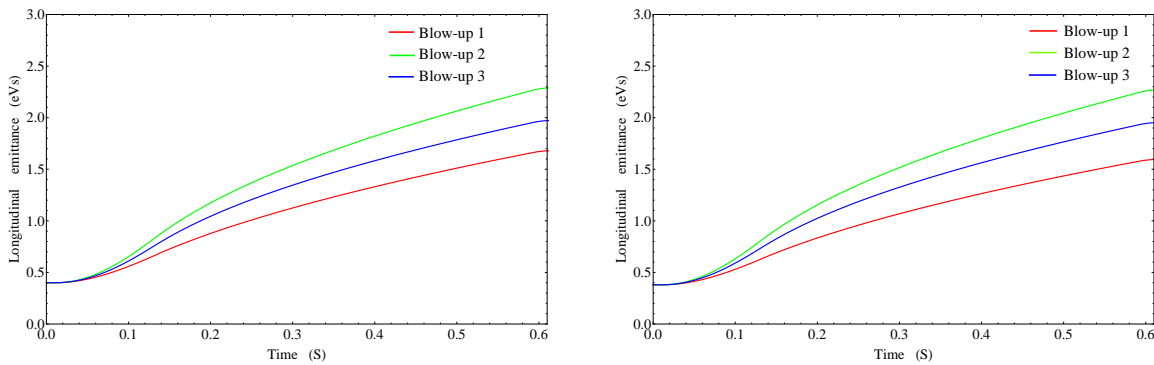


**Figure 5.47:** Emittance blow-up during acceleration corresponding to values given in table 5.31 for the 75 GeV option in case of foil injection (left) or table 5.32 for laser injection (right).



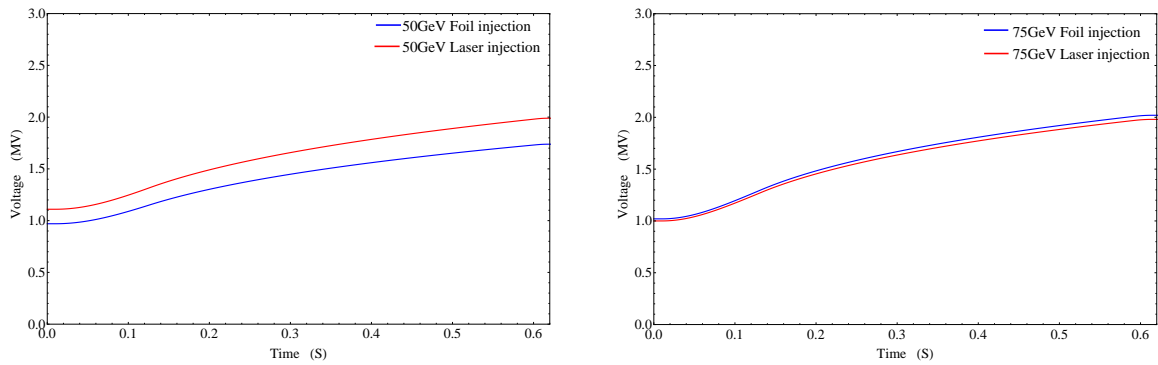


**Figure 5.48:** Voltage program and emittance program during the optimum cycle, both calculated for the 50 GeV baseline (left) and the 75 GeV option (right).

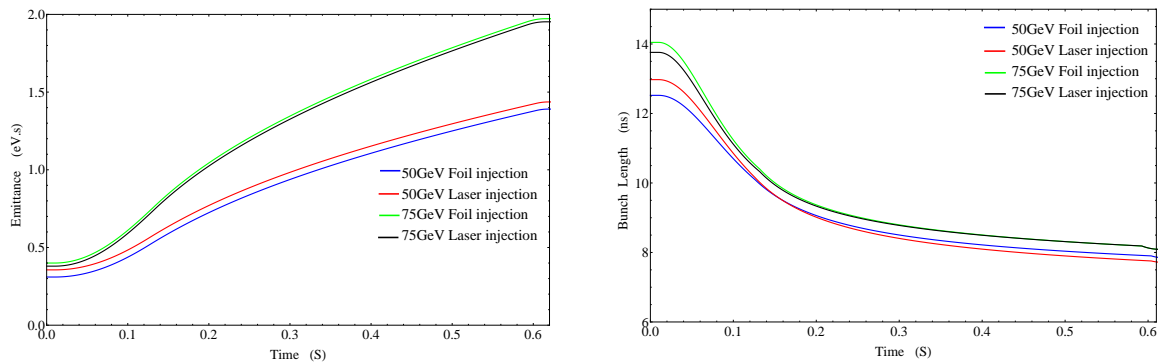


**Figure 5.49:** Longitudinal emittance evolution and corresponding bunch length for all options considered (50 GeV, 75 GeV, laser and foil injection).

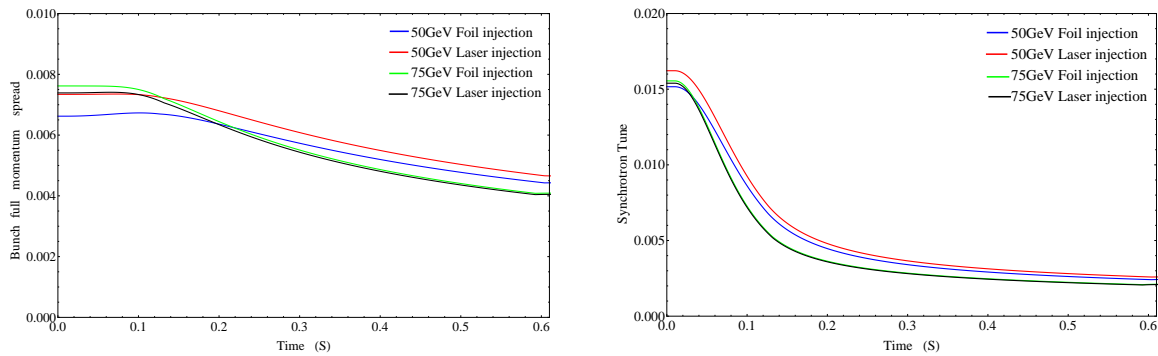


**Figure 5.50:** Bunch full momentum spread (left) and synchrotron tune (right) during the optimum cycle, both calculated for all options considered (50 GeV, 75 GeV, laser and foil injection).

earlier a compromise has been found between minimising the threshold degradation during acceleration and minimising the momentum spread peak at the beginning of acceleration.

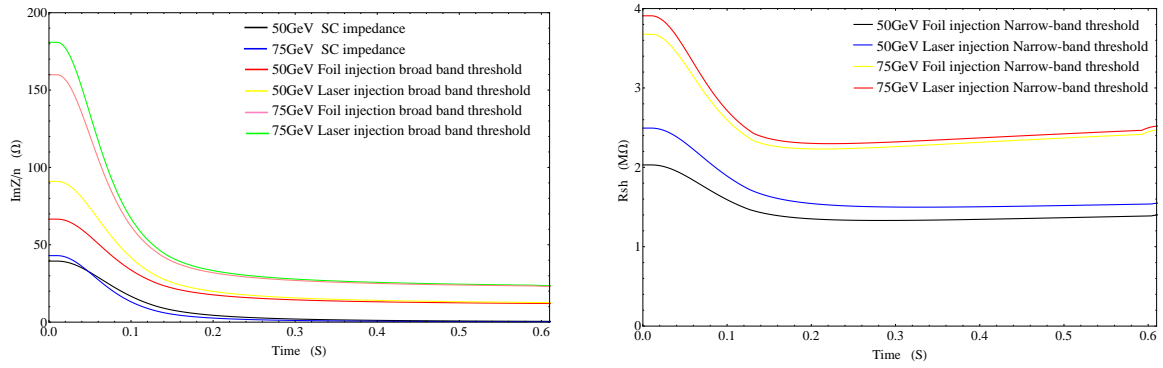


**Figure 5.51:** Broad-band threshold together with the space-charge impedance (left) and the narrow-band threshold (right) during the optimum cycle both calculated for all options considered (50 GeV, 75GeV, laser and foil injection).

#### 5.4.4 Injection into SPS

As mentioned in section 5.1, the possibility of injecting beams into SPS has been taken into account. In fact the size of the HP-PS has been optimized, slightly increased, to allow proper synchronisation with and filling of the SPS. In addition the bunch parameters at extraction of the HP-PS must satisfy the SPS requirements:

- Bunch length of 4ns at extraction
- A longitudinal emittance higher than 0.35 eVs but not too high due to the limited RF voltage in the SPS
- A bunch intensity limited to  $2.5 * 10^{11}$  ppb.

The required bunch length is obtained by tuning the voltage at extraction in the HP-PS. The required voltage corresponding to a given longitudinal emittance and bunch length is given by :

$$V = \frac{16 \varepsilon_l C^2 \eta}{\beta^4 2\pi h c^2 q E \Delta t^4 \cos \varphi_s} \quad (5.29)$$

where  $\varepsilon_l$  is the longitudinal emittance,  $C$  the ring circumference,  $\eta$  the slip factor,  $\beta$  the Lorentz factor,  $c$  the speed of light,  $q$  the particle charge,  $E$  the total energy,  $\Delta t$  the bunch length and  $\varphi_s$  is the synchronous phase.

The compression voltage, for both the 50 GeV baseline and the 75 GeV option and for a maximum bunch length of 4 ns as a function of the longitudinal emittance at extraction is shown in Fig. 5.52.

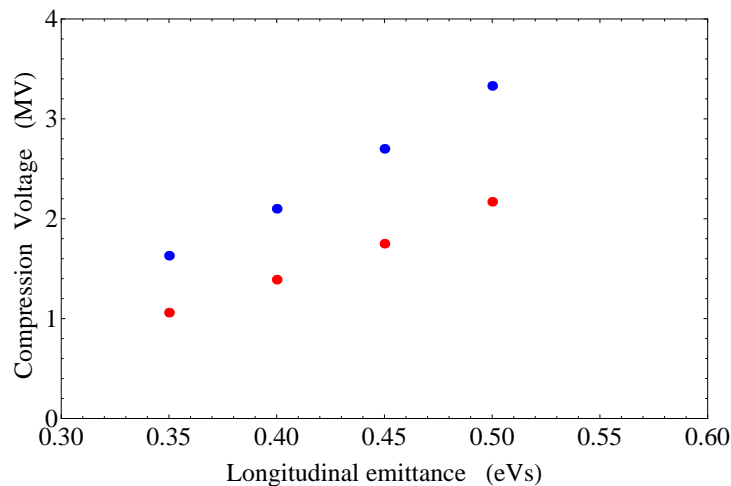


**Figure 5.52:** Required voltage to compress the bunch to 4 ns as a function of the longitudinal emittance at extraction for the 50 GeV baseline (blue dots) and the 75 GeV option (red dots)

The compression voltage quickly increases with the longitudinal emittance. The upper limit of this compression voltage has been fixed at the same value than for LAGUNA-LBNO beams ( $\sim 2$  MV in both cases). This leads to a maximum longitudinal emittance at extraction of 0.4 eVs for the 50 GeV baseline and more than 0.5 eVs for the 75 GeV option. However, as mentioned before the longitudinal emittances at injection into SPS should be around 0.35 eVs in order to limit the required RF voltage in SPS. They are already higher than 0.35 eVs at injection in the HP-PS in all cases, except for the 50 GeV baseline with Foil injection (see table 5.22). There they are maintained at their initial value during acceleration and blown-up to around

0.38 eVs. The voltage programs are deduced from the compression voltage at extraction and the required voltage at injection to fill the stability and aperture requirements. The voltage programs and emittance evolutions for SPS injection are shown in Fig. 5.53, while the bunch full momentum spread and the bunch length evolutions are shown in Fig. 5.54.

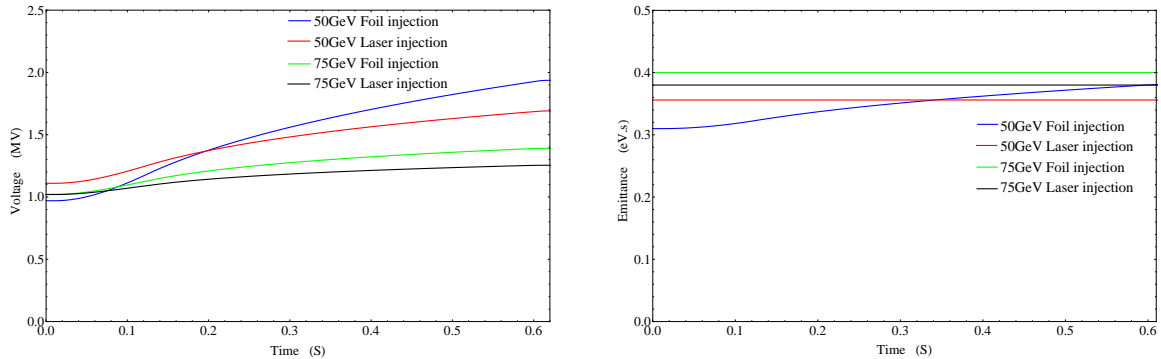


**Figure 5.53:** Voltage program (left) and emittance program (right) during the cycle for injection into SPS, both calculated for all options under consideration.

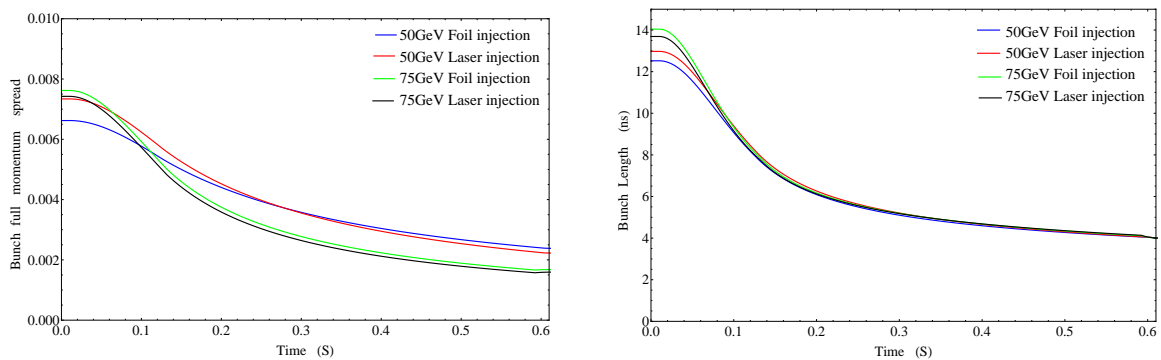


**Figure 5.54:** Full bunch momentum spread (left) and full bunch length (right) during the cycle for injection into SPS, both calculated for all options under consideration.

The Narrow-band threshold together with the Broad-band and Space Charge impedance for both top energies are shown in Fig. 5.55.

As shown on Fig. 5.55 the most critical part is at the flat-top when the threshold is at it's minimum, which have been calculated, using a bunch intensity of  $2.5e^{11}$ ppb. Fig. 5.56 shows the evolution of the minimum difference between the broad-band threshold and the space charge impedance as a function of the bunch intensity.

### 5.4.5 Summary

The presented cycle and voltage program together with the longitudinal emittance evolution fulfil the constraints imposed by the optics and the machine aperture and provide the required beam stability. Without any controlled longitudinal emittance blow-up during acceleration the danger of loss of Landau damping become important, hence a controlled longitudinal emittance blow up program has to be foreseen. During the study several scenarios have been investigated and one has been retained, as it provides a good safety margin for the instability threshold without compromising the dynamic aperture of the machine. In order to keep the option open to inject into the SPS the voltage program and longitudinal emittance evolution have been studied and optimised to satisfy the SPS injection requirements.

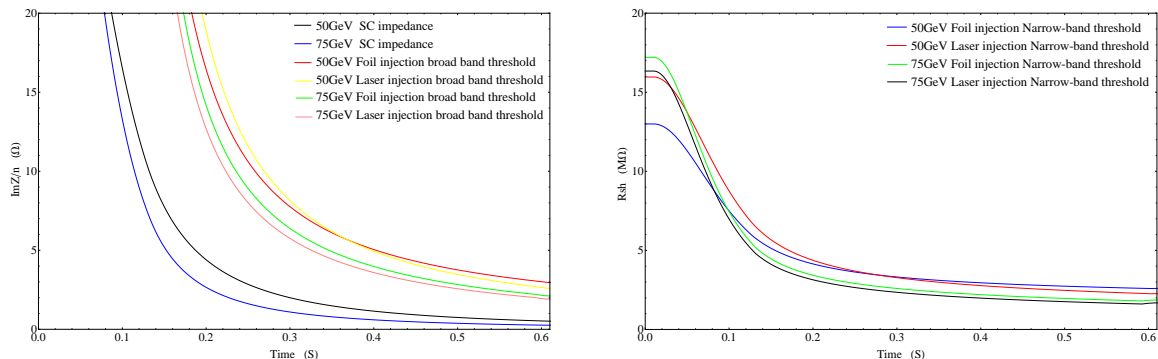


**Figure 5.55:** Narrow-band and broad-band thresholds during acceleration together with space charge impedance for SPS injection calculated for 50GeV top energy (left) and 75GeV top energy (right).

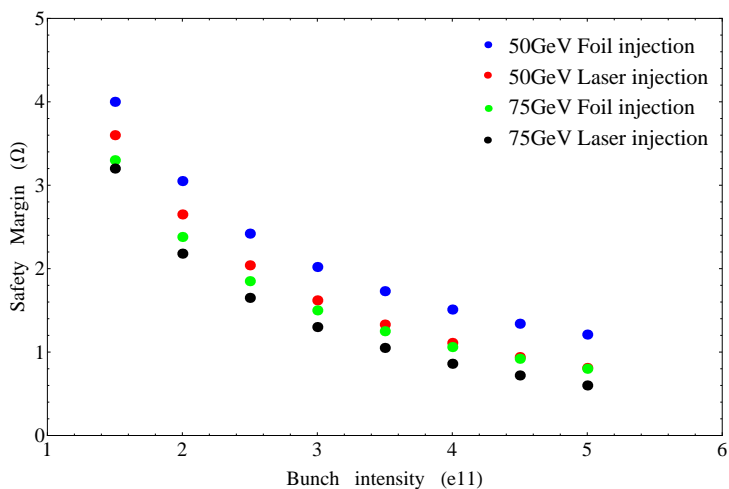


**Figure 5.56:** Variation of the minimum difference between the broad-band threshold and the space charge impedance at extraction for injection into the SPS as a function of the beam intensity.

## 5.5 Collimation

### 5.5.1 Introduction

A collimation system, in general, is essential to:

- prevent halo particles from impacting the superconducting magnets of the machine that could otherwise lead to quenching of the magnets
- protect sensitive equipment of the ring
- limit the irradiation of equipment close to the beam, which could restrict the maintenance of the facility and pose health risks
- avoid secondary electron emission, which could create an electron cloud

A collimation system is vital for the HP-PS, in order to protect the beamline by absorbing the halo particles before they reach the high power of 2 MW. It is hosted in a long straight section (LSS) dedicated for beam collimation, and uses a two-stage collimation approach: a thin primary collimator (scatterer/scraper) gives an angle to the impacting halo particles, increasing the possibility that they will be absorbed by a secondary collimator (absorber). The secondary collimator, located downstream the primary collimator, has a larger jaw opening than that of the primary (in units of  $\sigma$ , the r.m.s. beam size) to ensure it will never be treated as a primary one (see Fig. 5.57).

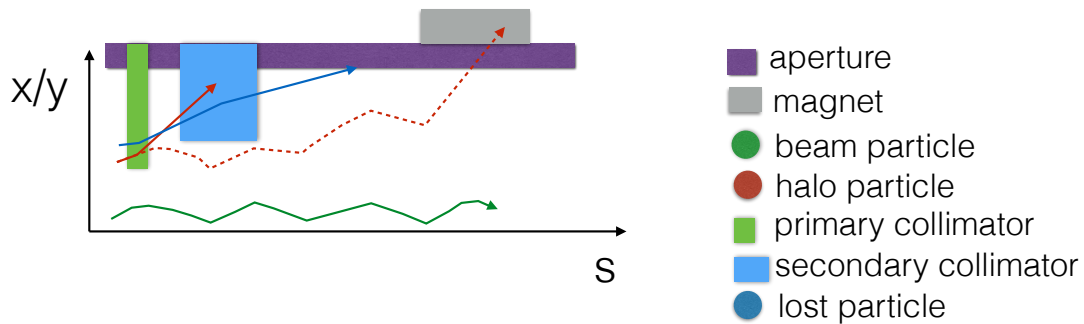


**Figure 5.57:** Halo particles could impact the magnets (grey rectangle), depositing energy that could lead to quenching (red dashed arrow). At a two-stage collimation system the halo particles (red arrow) will get a kick from a thin primary collimator (green rectangle) which will increase the possibility that they will subsequently impact a thick secondary collimator (blue rectangle) where they could get absorbed. The blue arrow represents the case of halo particles that escaped the collimation system and deposited their power in the aperture (purple colour).

At least two secondary collimators should be used since the new maximum amplitude of the scattered particle can be reached for two different phase advance values,  $\Delta\mu_1$  and  $\Delta\mu_2$  (see Fig. 5.58) [?]. The optimum positions of the secondary collimators are described in equation ?? [?], where  $\mu_{s,1}$  and  $\mu_{s,2}$  are the phase advances of the first and second secondary collimators with respect to the primary, and  $N_p$  and  $N_s$  are the jaw opening sizes of the primary and secondary collimators respectively, in units of  $\sigma$ .

$$\begin{aligned}\mu_{s,1} &= a \cos(N_p/N_s) \\ \mu_{s,2} &= \pi - \mu_{s,1}\end{aligned}\tag{5.30}$$

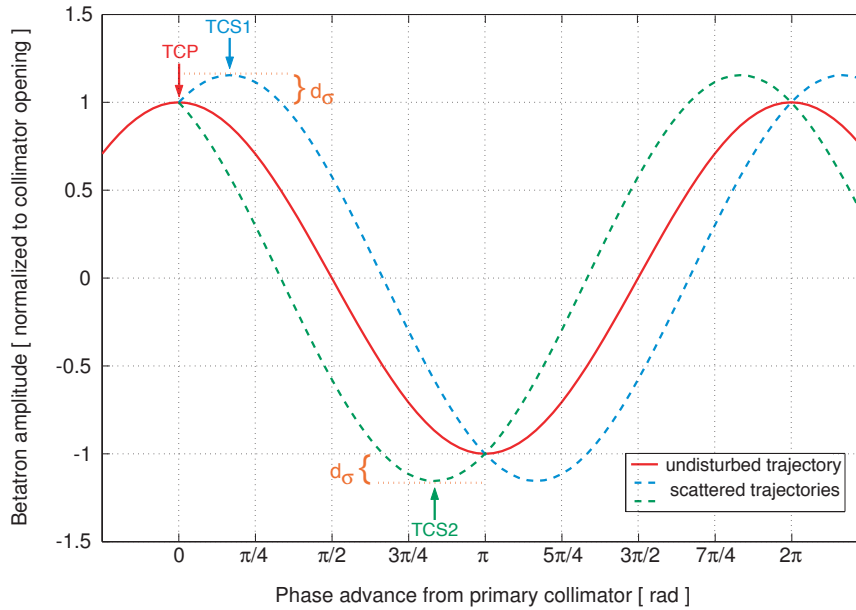


**Figure 5.58:** Secondary collimators location (TCS1 and TCS2) as a function of the phase advance from the primary collimator (TCP). The dashed lines represent the extremum scattered trajectories that reach their maximum amplitude at the location of the two secondary collimators, and  $d_\sigma$  stands for the relative retraction between the primary and secondary collimators' jaws. Figure taken from [?].

## 5.5.2 Collimators and halo settings

### 5.5.2.1 Collimator-placement and jaw opening size

Many parameters can be taken into account when optimising a collimation system: the thickness and material of the primary and secondary collimators, the size of their jaw openings, their relative  $s$ -positioning, the number of secondary collimators used etc. All these parameters are also affected by the halo parameters such as its size, thickness (smear) and type (horizontal/vertical).

Taking into account that the magnets and equipment we want to protect are at  $4\sigma$  (geometrical aperture), the openings of the collimators jaws were chosen to be  $N_p = 3\sigma$  and  $N_s = 3.5\sigma$ , resulting in  $\mu_{s,1} = 31^\circ$ , and  $\mu_{s,2} = 149^\circ$ . Both horizontal (H) and vertical (V) collimators are necessary as after impacting the primary collimators there is coupling between the two planes.

Although Eq. ?? describes the optimum collimation-positioning of the secondary collimators with respect to the primary collimator, it should be emphasised that the optics of the HP-PS sequence imposed in many cases the location and thickness of the secondary collimators. Furthermore, throughout the HP-PS collimation system studies it has been shown that the collimation system performance is significantly enhanced when there are no quadrupoles between the primary and secondary collimators. For the above reasons the locations of the collimators were not necessarily at the theoretical optimum locations. The optimum and used locations and phase advances of the secondary collimators, with respect to the primaries, are shown in Table 5.33.

As described in [?] additional collimators placed at  $\mu_{add} = 90^\circ$  can have a positive impact on the collimation efficiency. The positions and phase advances of these additional collimators in the HP-PS ring are shown in Table 5.34. For the results presented in this report, the additional collimators had the same length and were made of the same material as the secondary collimators.

Table 5.35 summarises the values of  $\sigma_x$  and  $\sigma_y$  at the location of the collimators and the sizes of their geometrical jaw-openings. Figures 5.59 and 5.60 show the location of the collimators (red: horizontal, blue: vertical) within the collimation-LSS, and the beta and alpha functions; the upstream and downstream arcs are shown in yellow.

**Table 5.33:** Positions and phase advances (H: Horizontal, V: Vertical, P: Primary, S: Secondary; phase advances are given with respect to the primary collimators)

Name	s [m]	$\mu_x$ [deg]	$\mu_y$ [deg]
HP	339.47	0.00	0.00
VP	339.50	0.00	0.00
HS1	344.50	31.83	5.35
VS1	352.61	58.93	18.31
HS2	398.67	149.82	129.02
VS2	410.00	192.68	146.33

**Table 5.34:** Positions and phase advances of the additional 90% collimators; phase advances are given with respect to the primary

Name	s [m]	$\mu_x$ [deg]	$\mu_y$ [deg]
HS90	370.10	90.00	61.50
VS90	383.40	123.5	90.10

**Table 5.35:** Collimator jaw opening-size and  $\sigma_{x,y}$  at the centre of the collimators

Collimator	Half-gap [mm]	$\sigma_x$ [mm]	$\sigma_y$ [mm]
HP	13.499	4.4990	4.052
VP	42.166	4.4986	14.040
HS1	18.281	5.2224	12.146
VS1	32.968	8.4029	9.4142
HS90	25.995	7.4284	9.1128
VS90	32.359	7.5806	9.2552
HS2	30.637	8.7534	9.2075
VS2	45.803	4.6846	13.075

### 5.5.2.2 Collimator-material

Ideally, the material of the collimators should be one with high conductivity to reduce impedance, present high robustness when impacted by high power particles, and absorb a high number of particles (if secondary collimator) to obtain a better cleaning efficiency [?]. However, these three conditions cannot be fulfilled simultaneously by the same material, and therefore different steps were followed in order to decide which material should be used for primary and which for secondary collimators (described in section 5.5.3).

Several scattering processes occur when halo particles impact a collimator, the main one of which is the Multiple Coulomb Scattering (see [?] and [?] for a summary of the scattering



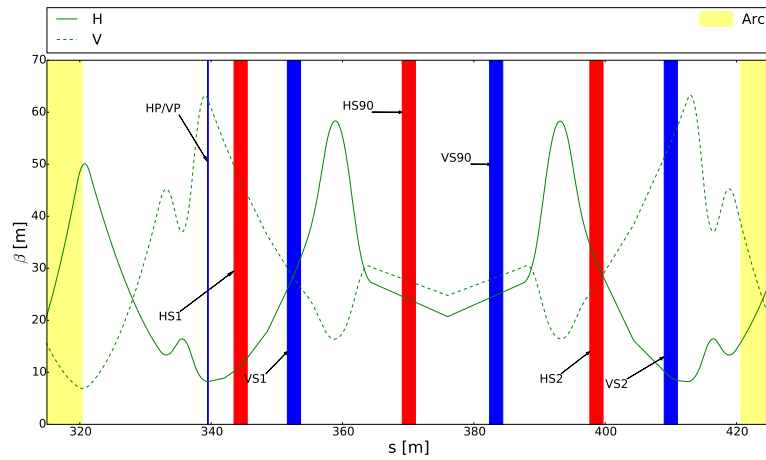


**Figure 5.59:**  $\beta(s)_x$  (continuous line) and  $\beta(s)_y$  (dashed line) in the collimation-LSS. The location of the collimators is indicated (red: horizontal, blue: vertical)

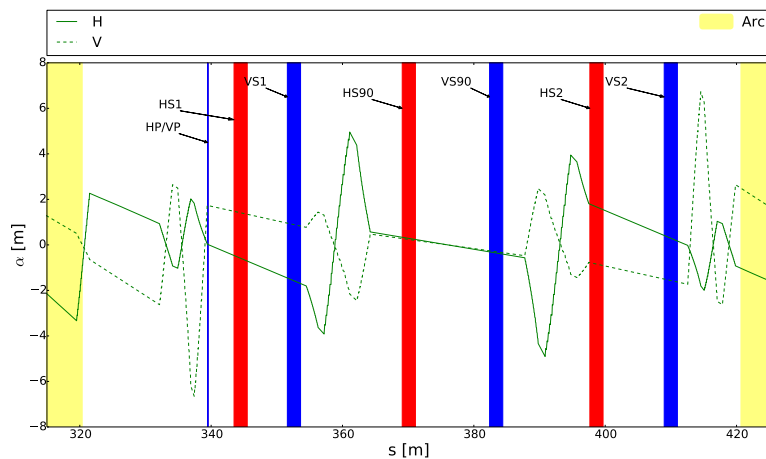


**Figure 5.60:**  $\alpha(s)_x$  (continuous line) and  $\alpha(s)_y$  (dashed line) in the collimation-LSS. The location of the collimators is indicated (red: horizontal, blue: vertical)

processes that can take place in a collimation system). Using a Gaussian approximation for the central 98% of the projected angular distribution, the r.m.s. angle  $\theta$  after traversing  $s$  length of material is given by:

$$\theta(s) = \frac{13.6 \text{ MeV}}{\beta_{rel} c p} \cdot \sqrt{\frac{s}{\chi_0}} [1 + 0.038 \cdot \ln(\frac{s}{\chi_0})] \quad (5.31)$$

where  $\theta(s)$  is the scattering angle,  $\beta_{rel}c$  and  $p$  are the velocity and momentum of the incident particle, and  $s/\chi_0$  is the thickness of the scattering medium in radiation lengths [?]. The r.m.s. scattering angle for Graphite (red), Tungsten (green) and Copper (blue), calculated using Equation ??, is shown in Fig. 5.61 and gives an indication of the minimum length that the primary collimators should have in order to ensure the particles impacting them will reach the secondary collimators. The SixTrack tracking code was used for the collimation simulations, halo production and tracking.

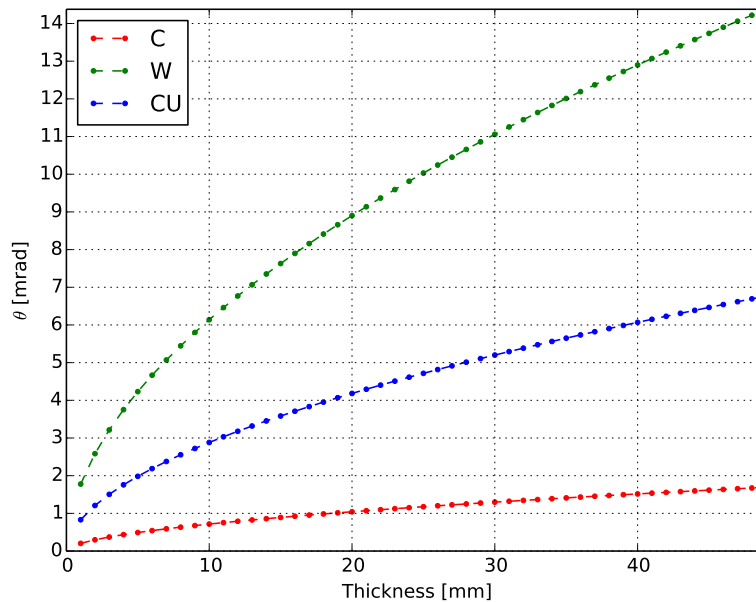


**Figure 5.61:** Scattering angle (r.m.s.) for Graphite (red), Tungsten (green), and Copper (blue) collimators at injection energy (4 GeV).

### 5.5.2.3 Halo settings

In order to understand better the behaviour of the collimation system, a purely horizontal and purely vertical halo of 2,000 particles with reference energy of 4 GeV, were generated directly upstream the horizontal primary collimator at  $3\sigma$ , with a smear (thickness) of  $0.01\sigma$ . The energy was set to 4 GeV as it was assumed that the majority of losses will occur at injection. The phase-space of the horizontal and vertical halos are shown in Fig. 5.62. Figures 5.63 show the initial  $x$ ,  $y$  and  $x'$ ,  $y'$  of the generated halos. The higher density of particles at the end of the distributions is due to the smear (thickness) of halo.

Note that the halo thickness is an arbitrary number that could only be set precisely after performing diffusion studies. For the studies presented in this report, the halo thickness was chosen to be  $0.01\sigma$  as this value corresponds to an impact parameter of  $\sim 50 \mu\text{m}$  at the horizontal primary collimator and  $\sim 150 \mu\text{m}$  at the vertical primary collimator, i.e. values larger

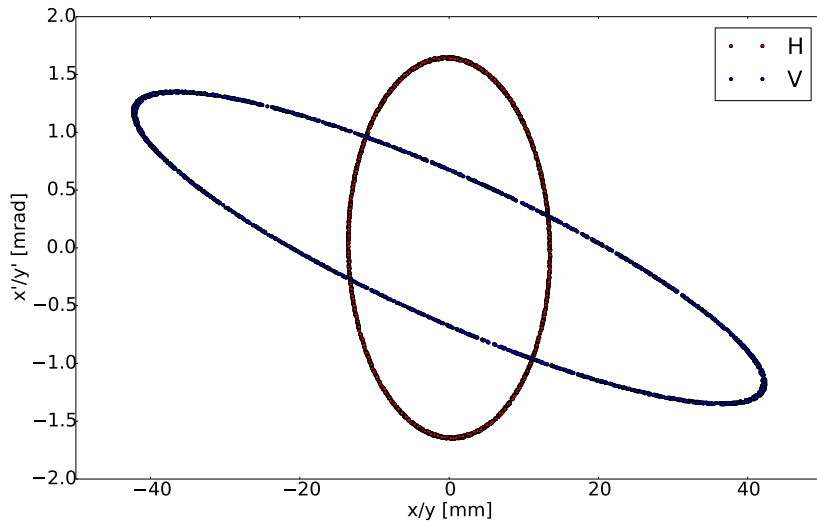


**Figure 5.62:** Halo horizontal (red) and vertical (blue) phase-space when generating only horizontal or only vertical halos respectively.

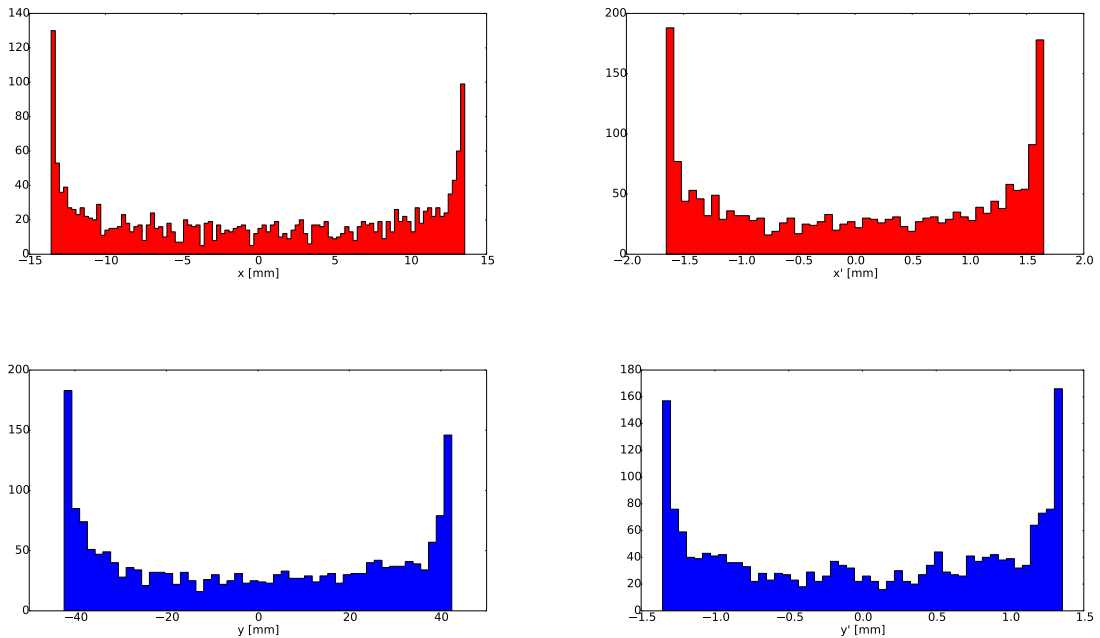


**Figure 5.63:** Initial distribution of  $x, x'$  (red) and  $y, y'$  (blue) of generated H/V halos.

than  $25 \mu\text{m}$ , the mechanical precision needed to flatten the collimators' surface<sup>1</sup>. The impact parameter,  $b_{x,y}$ , is defined as the transverse offset between the impact location of a halo particle on the primary collimator and the edge of its jaw (see Figure 5.64). The impact parameter of the horizontal and vertical halos is shown in Fig. 5.78. Note that although the same number of halo particles is generated for both halo types (H/V), fewer particles interact with the primary collimators in the case of vertical halo due to the value of  $\alpha_y$  directly upstream the horizontal primary collimator (see Fig. 5.62). In addition, the impact parameter reaches values up to  $\sim 100 \mu\text{m}$  in the case of vertical halo, whereas when a horizontal halo is generated the maximum impact factor is  $\sim 40 \mu\text{m}$ .

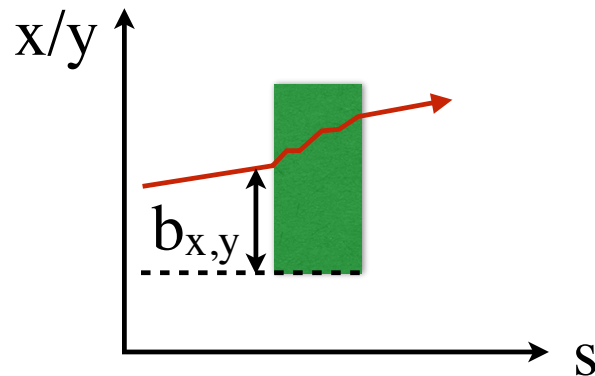


**Figure 5.64:** The impact parameter,  $b_{x,y}$  is defined as the transverse offset between the impact location of a halo particle (red arrow) on the primary collimator (green rectangle) and the edge of its jaw.

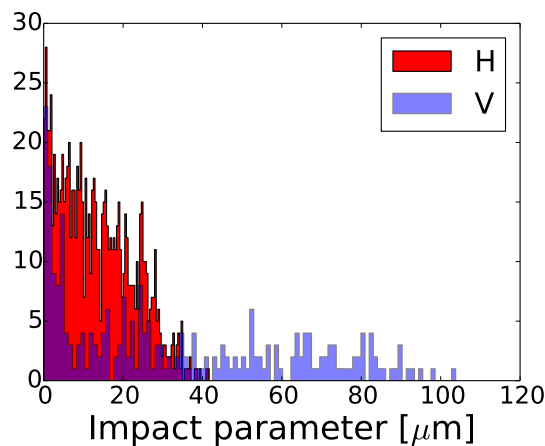


**Figure 5.65:** Impact parameter on the primary collimators when generating a purely horizontal (red) or vertical (blue) halo at  $3\sigma$  with  $0.01\sigma$  thickness. Fewer particles interact with the primary collimators when a vertical halo is generated due to the value of  $\alpha_y$  directly upstream the primary collimators.

<sup>1</sup>This value was found during the manufacturing process of the LHC collimators [?].

### 5.5.3 Length and material of primary collimators

#### 5.5.3.1 Inefficiency

The efficiency of the collimation system and the number of particles absorbed by each collimator were examined for different materials and thicknesses of the primary collimators. The generated halos (only H or only V) were at  $3\sigma$  with  $0.01\sigma$  smear, and the secondary collimators were chosen to be 2 m long Tungsten blocks.

Figure 5.66 presents the global inefficiency,  $\eta_{inef}$  for both horizontal and vertical halos, as a function of the primary collimators' length. The global inefficiency is defined as:

$$\eta_{inef} = N_{lost}/N_{tot} \quad (5.32)$$

where  $N_{lost}$  is the number of particles that impacted the aperture (lost) and  $N_{tot}$  the number of particles that impacted a collimator at least once. The inefficiency does not change significantly with the increase of the primary collimator length when using Tungsten or Copper, for neither of the generated halo types, since for this order of magnitude of primary thickness the scattering angle is sufficient for the halo particles to impact the secondary collimators (see Fig. 5.61). On the other hand the global inefficiency drops with the increase of thickness, when the primary collimator is Graphite and the generated halo is horizontal, whereas it is observed that when a vertical halo is generated the inefficiency is not affected by the length of the graphite primary collimator. This behaviour can be explained when looking at the distribution of the impact parameters of the horizontal and vertical halos (shown in Fig. 5.78).

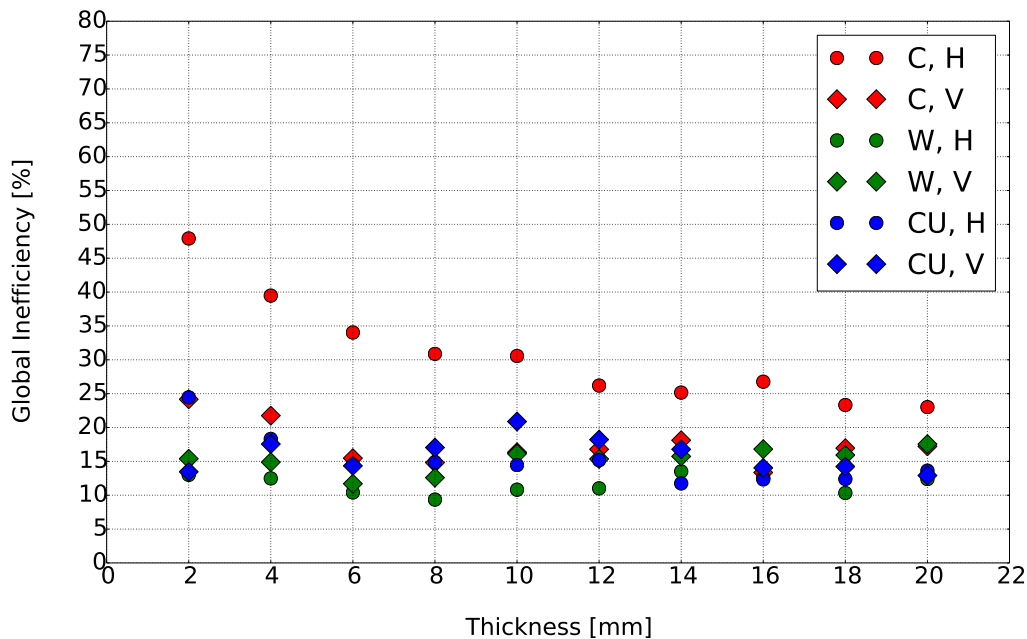


**Figure 5.66:** Global inefficiency with respect to the thickness of the primary collimators for horizontal (round markers) and vertical (diamond markers) halos, for Graphite (red), Tungsten (green) and Copper (blue) primaries.

Figure 5.67 shows the inefficiency when generating horizontal halo is reduced by a factor of two for all the thicknesses of Tungsten and Copper when using additional collimators at  $90^\circ$  phase advance, and for Graphite length above 10 mm. When generating vertical halo the inefficiency improves by a factor of  $\sim 1.5$  for Tungsten and Copper, however the improvement

is not obvious when Graphite is used as a similar number of particles impact the collimators, get absorbed or get lost in the aperture, regardless of whether or not the 90° collimators are included.

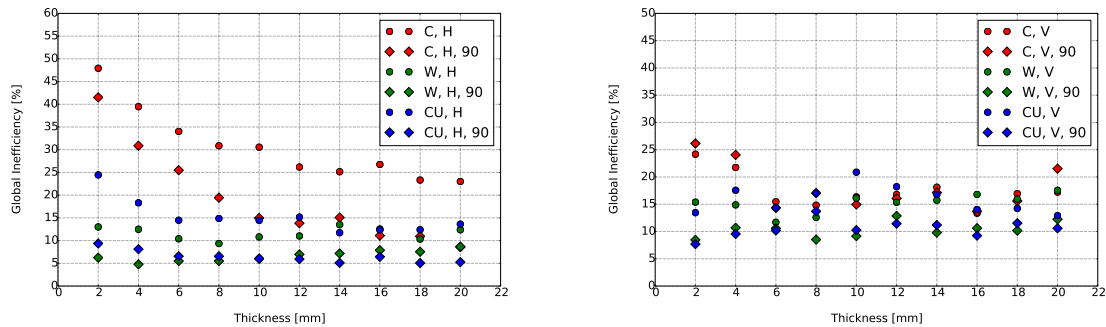


**Figure 5.67:** Global inefficiency with respect to the thickness of the primary collimators for horizontal (left) and vertical (right) halo, for Graphite (red), Tungsten (green) and Copper (blue), with and without additional 90° collimators (round and diamond markers respectively).

### 5.5.3.2 Absorptions

The number of particles absorbed by each collimator, when no additional collimators are used, are shown in Fig. 5.68. Figure 5.69(a) shows there are almost zero absorptions of vertical halo particles in HP, whereas for all three materials the absorptions of horizontal halo particles increase with the material-thickness. Similarly, fig. 5.69(b) shows there are very few absorptions of horizontal halo particles in VP and a similar increase of absorbed particles with thickness. For a thickness of 2 mm the three materials absorb similar number of particles in the primary collimators, however due to the high atomic number of Copper and Tungsten the rise in number of particles absorbed with the increase of thickness is more rapid than in the case of Graphite.

Although from Fig. 5.66 it can be seen that the inefficiency of the collimation system is smaller when using Tungsten or Copper primary collimators, it should be noted that from Figs 5.69(a) and 5.69(b) the absorptions in the primary collimators when using these materials is increasing significantly with the length of the primary collimator and can result in high power deposition and damage of the material. From the above it can be concluded that the collimation system performance will be more effective when Graphite primaries are used; however it is interesting to see how the absorptions in the secondary collimators are affected by the choice of primary collimator-material.

Similar number of particles are absorbed by HS1, regardless of the generated halo type, when Tungsten is used as the primary collimator material. In the case of Copper primaries, the number of orthogonally scattered particles increases with thickness (see fig. 5.69(c)); at 20 mm almost the same percentage of horizontal and vertical halo particles is absorbed by HS1. On the other hand, there seems to be smaller orthogonal scattering when Graphite is used, as with the increase of thickness the number of vertical halo particles absorbed by HS1 is <5%. The above observations regarding orthogonal scattering are confirmed in fig. 5.69(d) where in the case of Tungsten, excluding the first point at 2 mm, a similar number of horizontal and vertical halo particles are absorbed by VS1. The absorbed horizontal halo particles increase with thickness, more rapidly between 2-6 mm of Copper and more smoothly from 6-20 mm, whereas a drastic decrease with thickness in absorbed vertical halo particles is notable, from ~43% at 2 mm to ~21% at 20 mm. There are as little horizontal halo absorptions as ~10% when using Graphite primaries, whereas the vertical halo absorptions oscillate around 35-40%.

A smooth increase on the number of horizontal halo particles absorbed by HS2 is noticed with the increase of thickness of the Graphite primary collimators, whereas a stable behaviour, and a smooth reduction is shown when Tungsten or Copper are used respectively. The absorptions of vertical halo particles by HS2 are close to zero for all three materials (see Fig. 5.69(e)). Finally, Fig. 5.69(f) shows that a higher percentage of both halo types is absorbed by VS2 when Graphite is used. There is a smooth decrease in the absorbed vertical halo particles when using Copper or Tungsten whereas only a small percentage ( $\sim 0-5\%$ ) of the horizontal halo is absorbed.

A comparison between the absorptions in each collimator when the additional  $90^\circ$  are included (diamond markers) or not (round markers), is shown in Figs. 5.69 and 5.70, for horizontal and vertical halos respectively.

In the horizontal halo case, a similar number of particles is absorbed by HP, VP, HS1 and VS1, regardless of whether or not the additional collimators are used. The difference in absorptions appears at HS2 and VS2; there is an increase in the number of particles absorbed by HS2 with thickness, when Graphite primaries are used and no additional collimators are included, whereas the number of absorptions when the  $90^\circ$  collimators are present smoothly decreases. When Tungsten or Copper are used as primary collimators there is a similar difference in the absorbed particles with the increase of thickness;  $<5\%$  of particles are absorbed by HS2 and VS2 when the additional collimators are present. Fig. 5.70(e) shows that more particles are absorbed by HS90 when Tungsten or Copper are used as primary collimators, whereas it seems there are more absorptions by VS90 of orthogonally scattered particles when Graphite is used (see Fig. 5.70(f)).

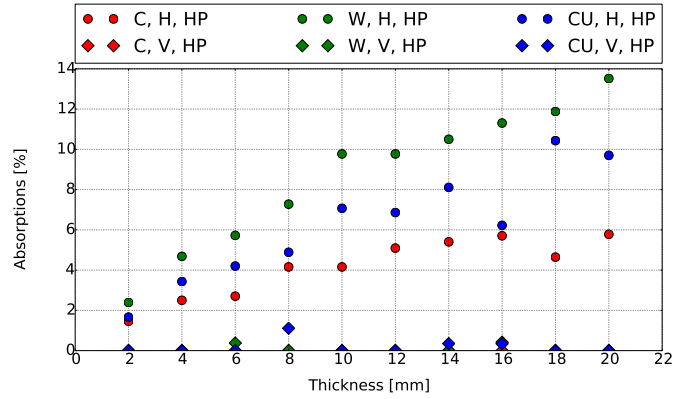
When generating a vertical halo, again there are similar absorptions in HP, VP, HS1 and VS1, regardless of whether the  $90^\circ$  collimators are used or not. Only a small percentage of particles ( $<5\%$ ) is absorbed by HS2, with or without the additional collimators, and  $>2$  times more particles are absorbed by VS2 when no additional collimators are included (see Figs. fig:HS2-Vhalo and 5.71(g)). In the case of Graphite this can explain why the inefficiency when generating a vertical halo was not improved with the additional collimators (see Fig. 5.67). More orthogonally scattered particles are absorbed by HS90 when Tungsten or Copper are used as primary collimators (see Fig. 5.71(e)); more particles are absorbed by VS90 as the thickness of the Graphite primary collimator increases, whereas the opposite behaviour is observed, but not as rapid, when increasing the thickness of the Tungsten and Copper primaries.

### 5.5.3.3 Losses in the collimation-LSS

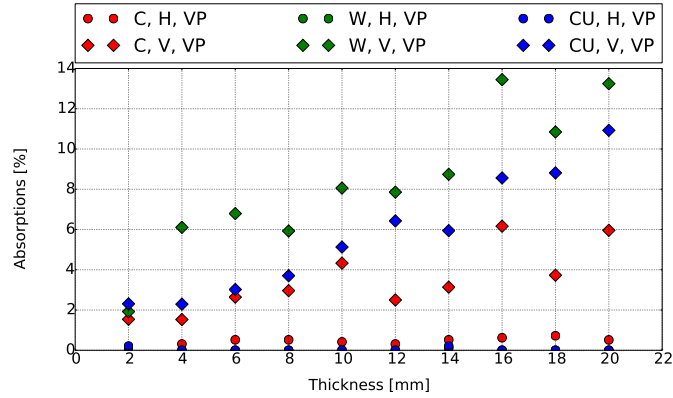
Figures 5.71, 5.72 and 5.73 show the number of particles lost per m within the collimation-LSS, for different thicknesses of Graphite, Tungsten and Copper primary collimators respectively. The figures include the cases where only horizontal or only vertical halos are generated, and when including or not the additional  $90^\circ$  collimators.

When a horizontal halo is generated, and no additional collimators are included, there is a maximum of  $\sim 40-60$  particles lost within 1 m for all primary materials, whereas when the generated halo is vertical there are maximum of  $\sim 10-20$  particles lost within 1 m of the LSS. As soon as the additional collimators are included the maximum losses within 1 m drop to  $\sim 10$  particles for both the horizontal and vertical halo cases.

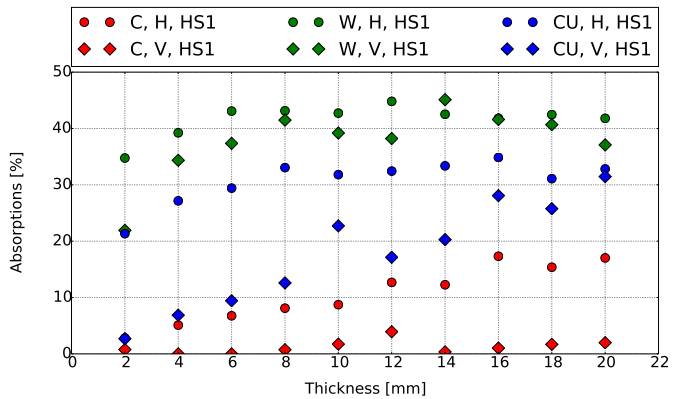
Regardless of what material is used for the primary collimators, there is a peak of losses at  $\sim 50$  m that reduces significantly in all cases where the  $90^\circ$  collimators are included, except for when a horizontal halo is generated and Graphite is used as the primary collimator. Figure 5.74 shows the distribution in  $x$ - and  $y$ -coordinates of particles lost per m between the first 45-51 m of the collimation-LSS when no additional collimators are used, and shows that the losses are mainly in the vertical direction which explains why by including an additional vertical



(a) Absorptions in HP, H and V halo

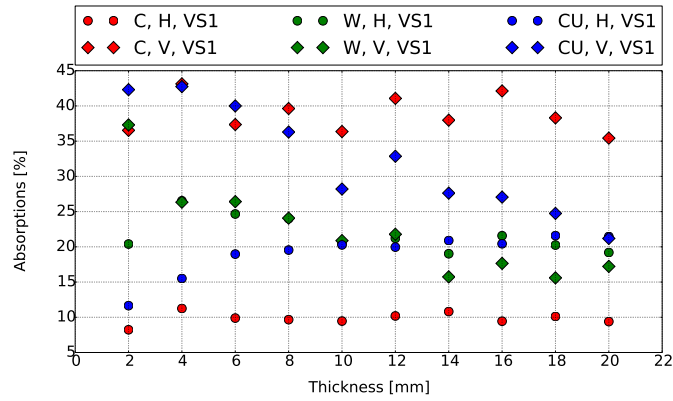


(b) Absorptions in VP, H and V halo

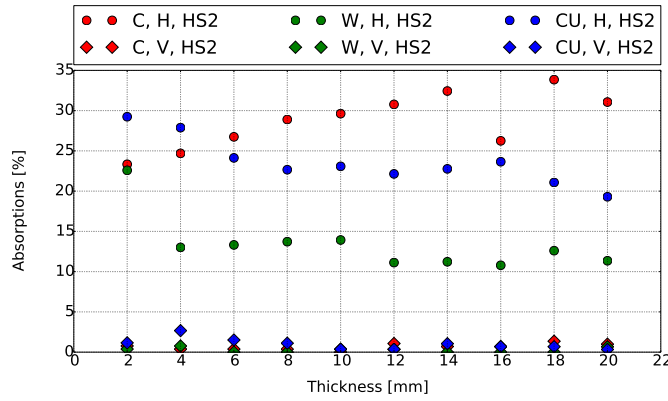


(c) Absorptions in HS1, H and V halo

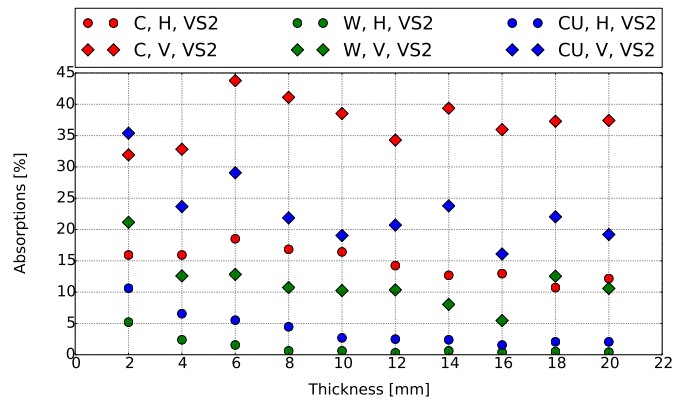




(d) Absorptions in VS1, H and V halo

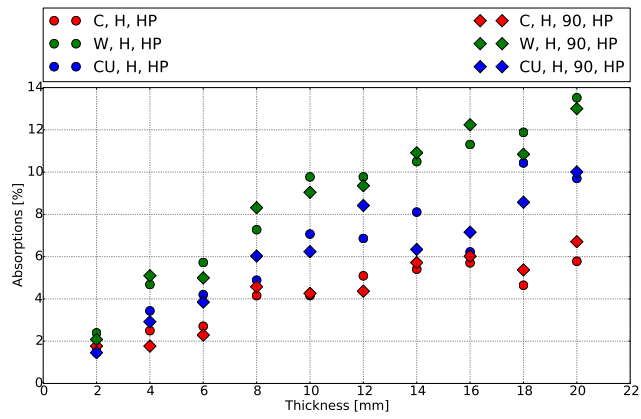


(e) Absorptions in HS2, H and V halo

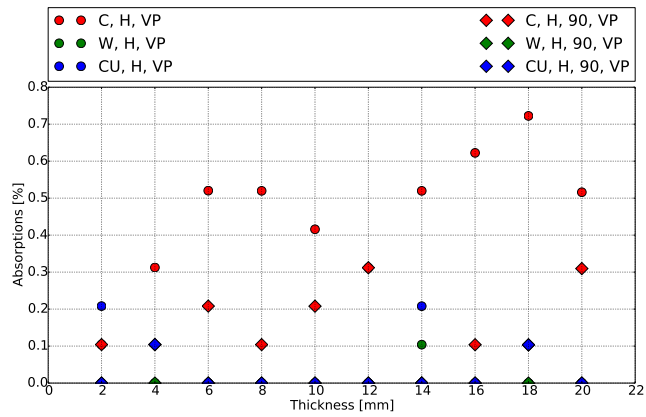


(f) Absorptions in VS2, H and V halo

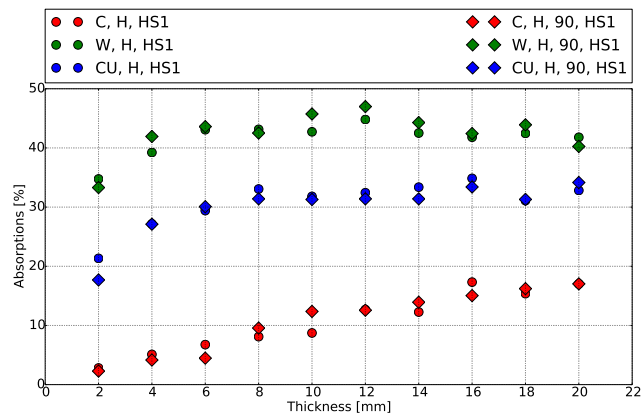
**Figure 5.68:** Number of halo particles absorbed by each collimator over the the total number of particles that impacted at least once a collimator (in percentage), for different primary collimator material and thickness. . H: Horizontal, V: Vertical, P: Primary, S: Secondary.



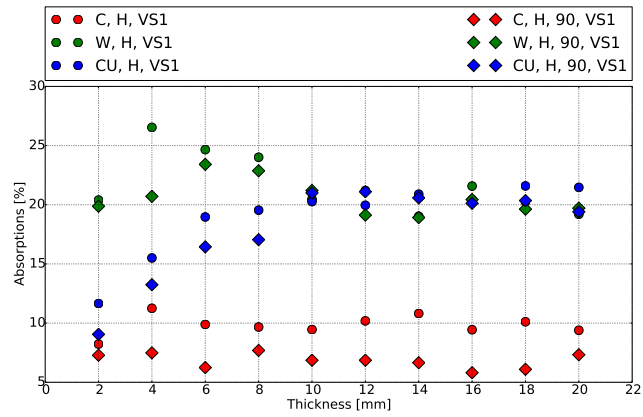
(a) Absorptions in HP, H halo



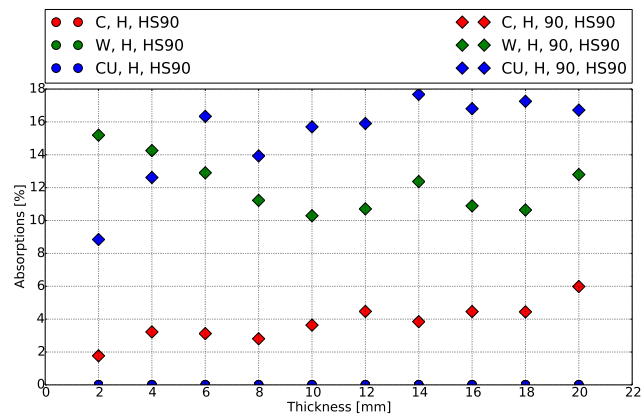
(b) Absorptions in VP, H halo



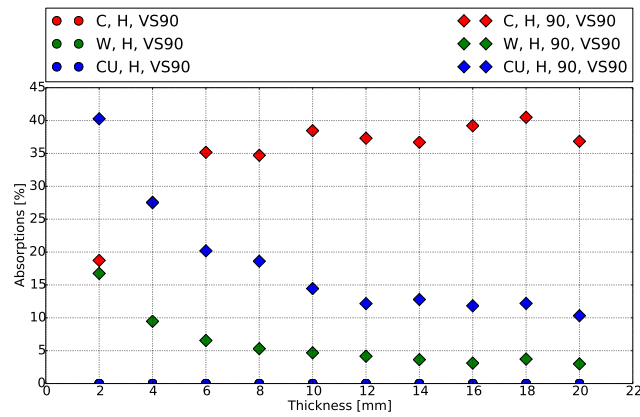
(c) Absorptions in HS1, H halo



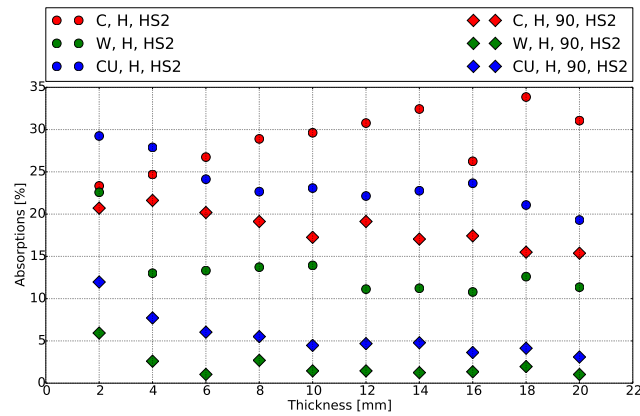
(d) Absorptions in VS1, H halo



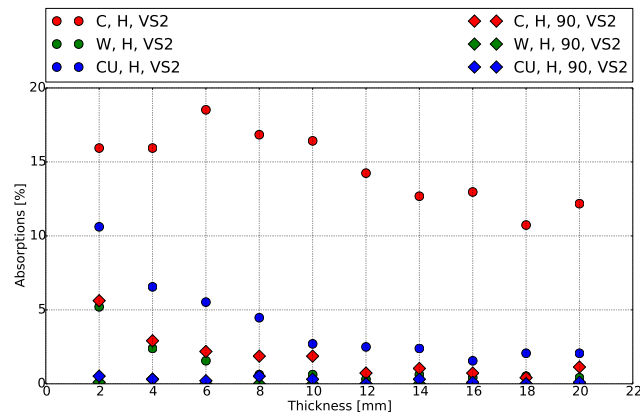
(e) Absorptions in HS90, H halo



(f) Absorptions in VS90, H halo

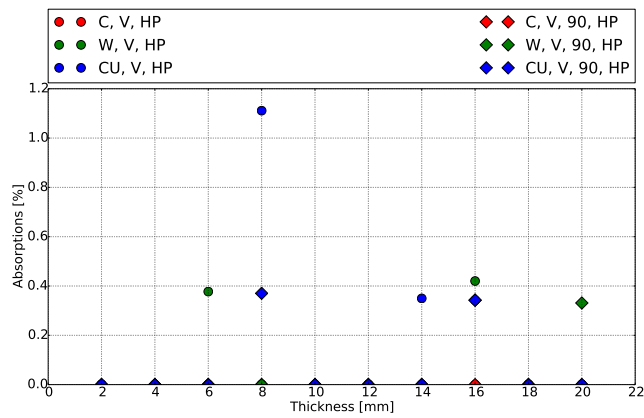


(g) Absorptions in HS2, H halo

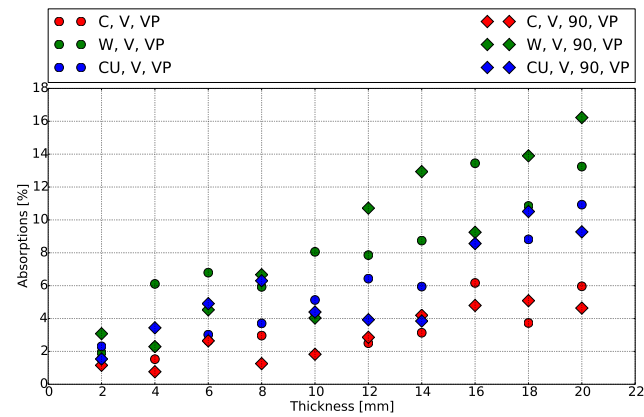


(h) Absorptions in VS2, H halo

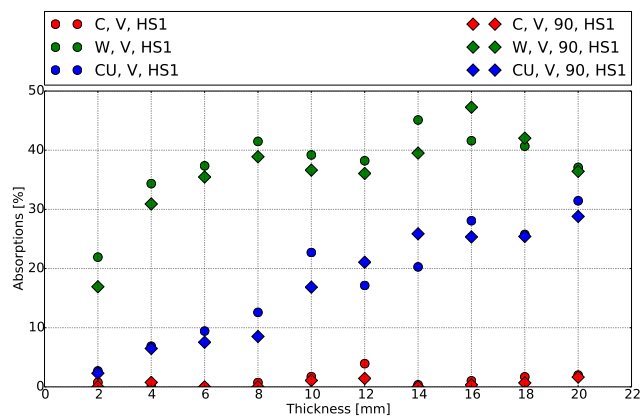
**Figure 5.69:** Number of horizontal halo particles absorbed by each collimator over the the total number of particles that impacted at least once a collimator (in percentage), with and without additional 90° collimators (round and diamond markers respectively), for different primary collimator material and thickness. H: Horizontal, V: Vertical, P: Primary, S: Secondary.



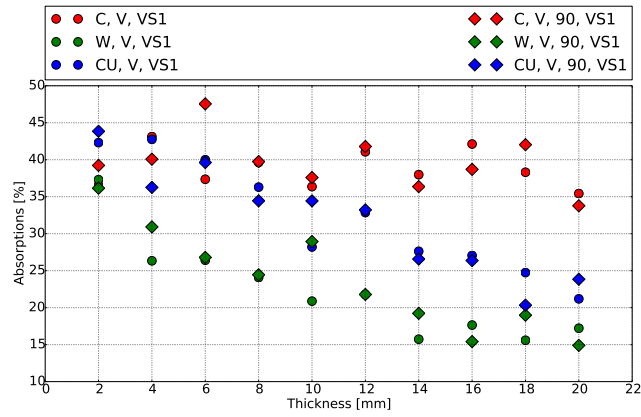
(a) Absorptions in HP, V halo



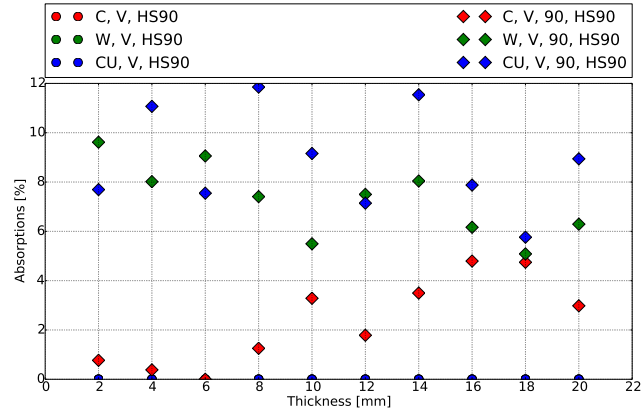
(b) Absorptions in VP, V halo



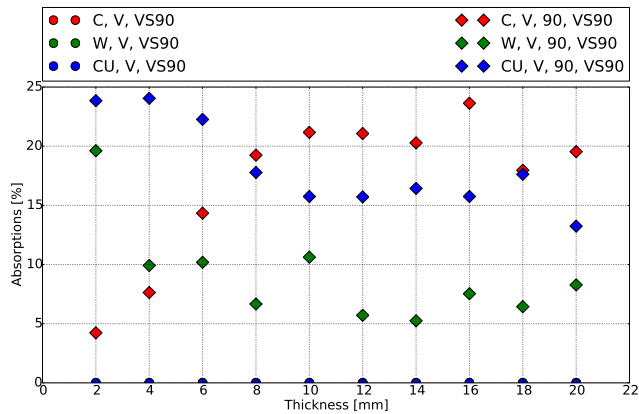
(c) Absorptions in HS1, V halo



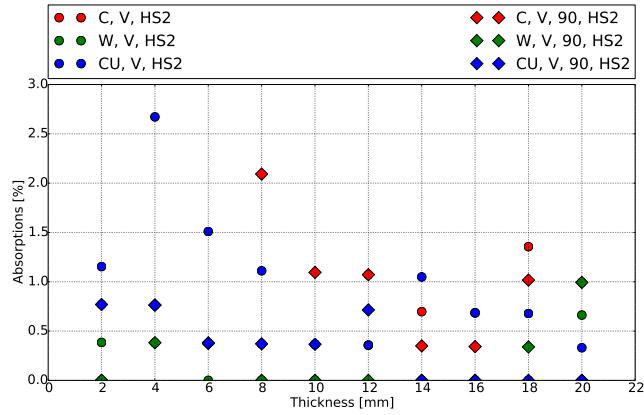
(d) Absorptions in VS1, V halo



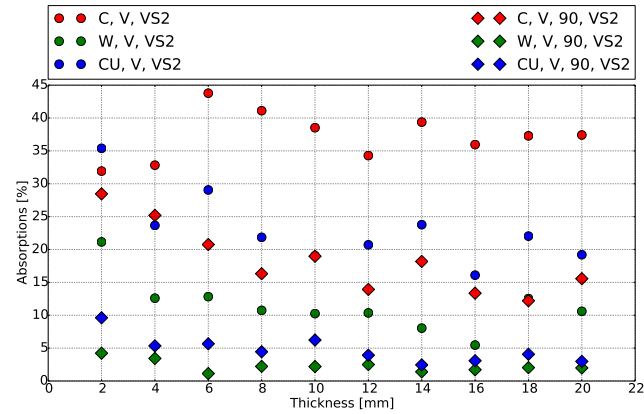
(e) Absorptions in HS90, V halo



(f) Absorptions in VS90, V halo

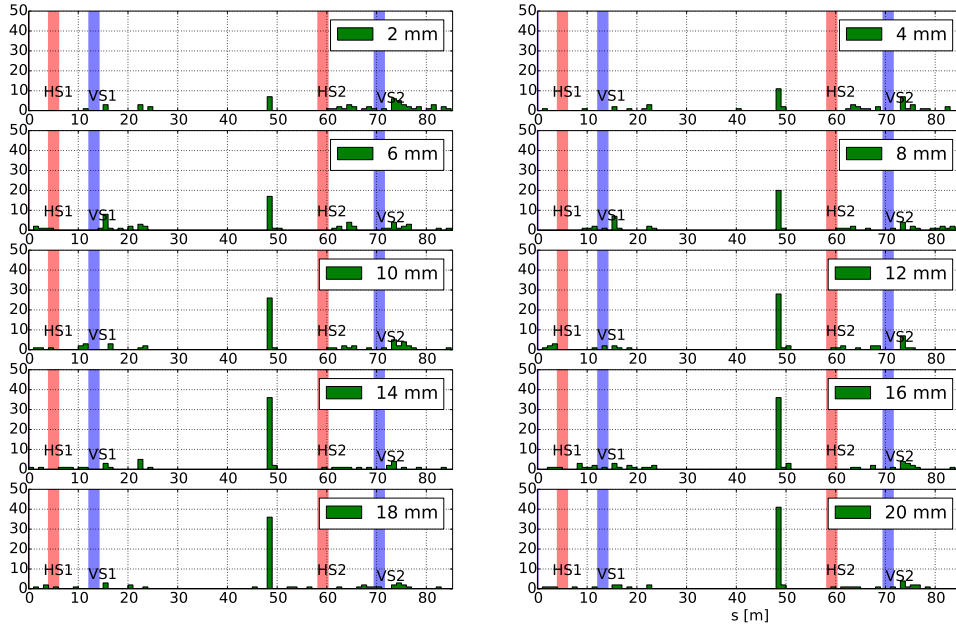


(g) Absorptions in HS2, V halo

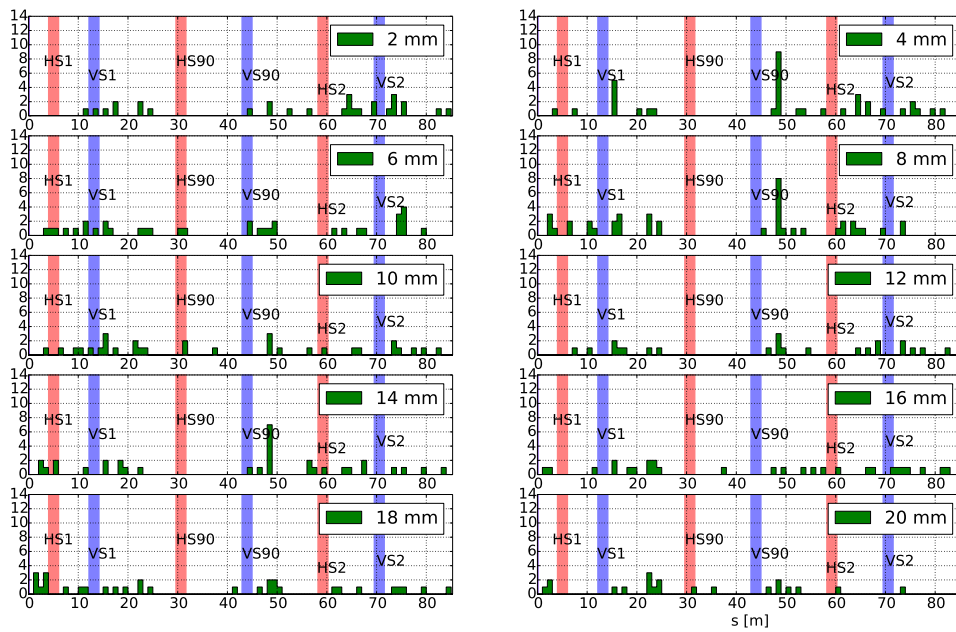


(h) Absorptions in VS2, V halo

**Figure 5.70:** Number of vertical halo particles absorbed by each collimator over the the total number of particles that impacted at least once a collimator (in percentage), with and without additional 90° collimators (round and diamond markers respectively), for different primary collimator material and thickness. . H: Horizontal, V: Vertical, P: Primary, S: Secondary.

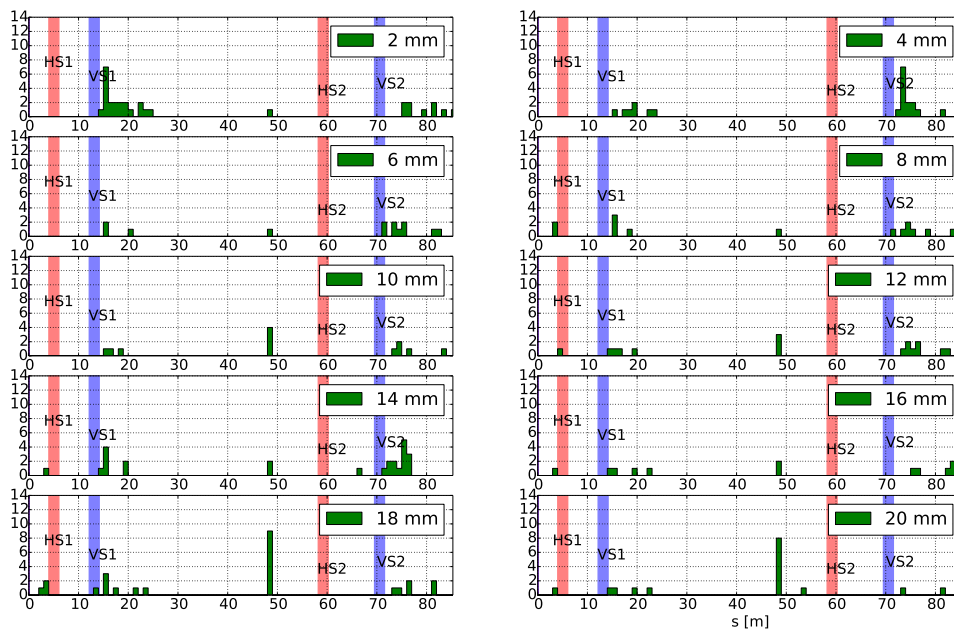


(a) H halo

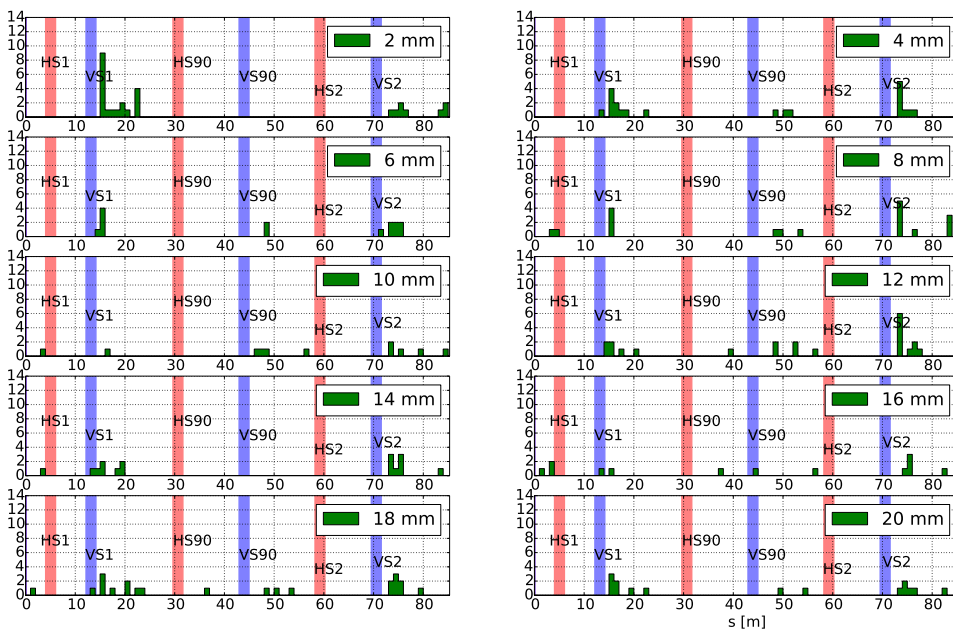


(b) Including additional 90° collimators, H halo



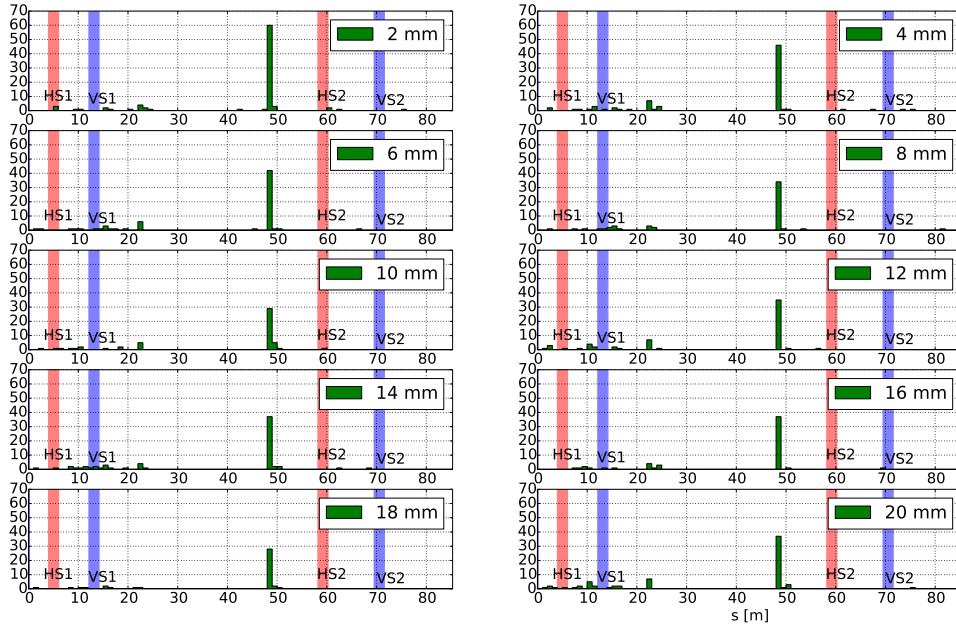


(c) V halo

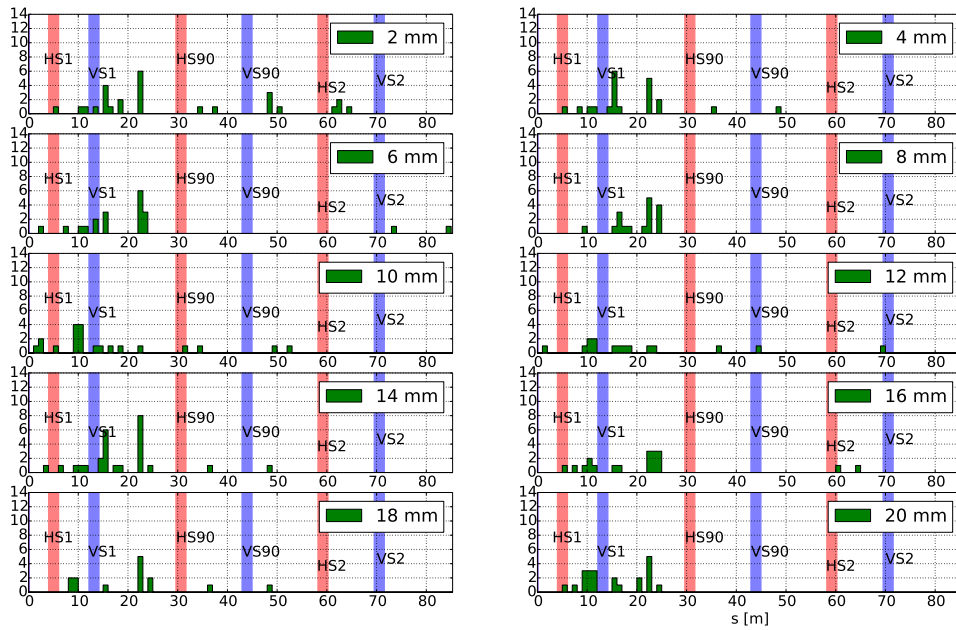


(d) Including additional 90° collimators, V halo

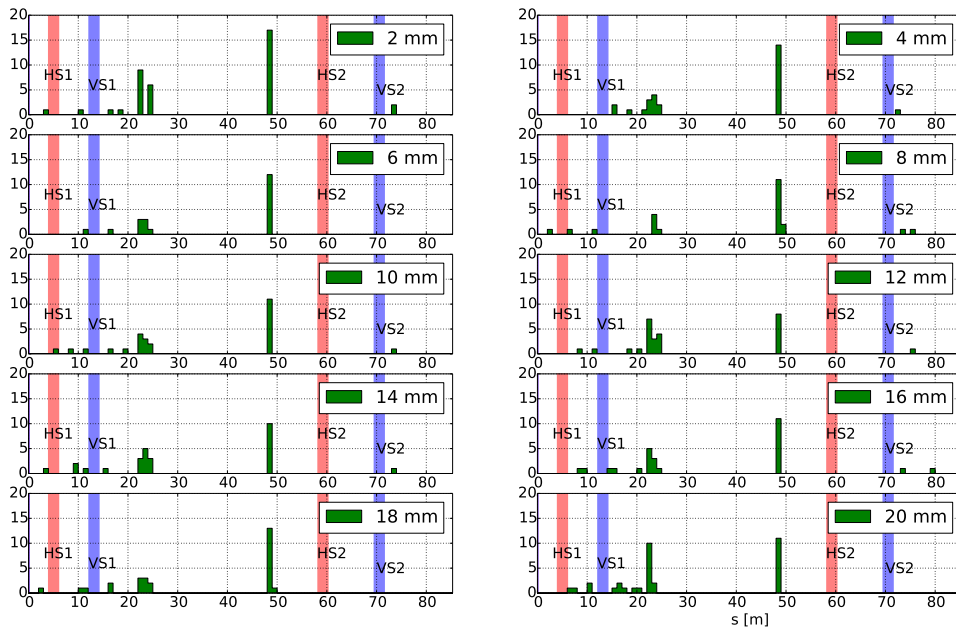
**Figure 5.71:** Number of particles lost per m in the collimation-LSS, when using Graphite primary collimators



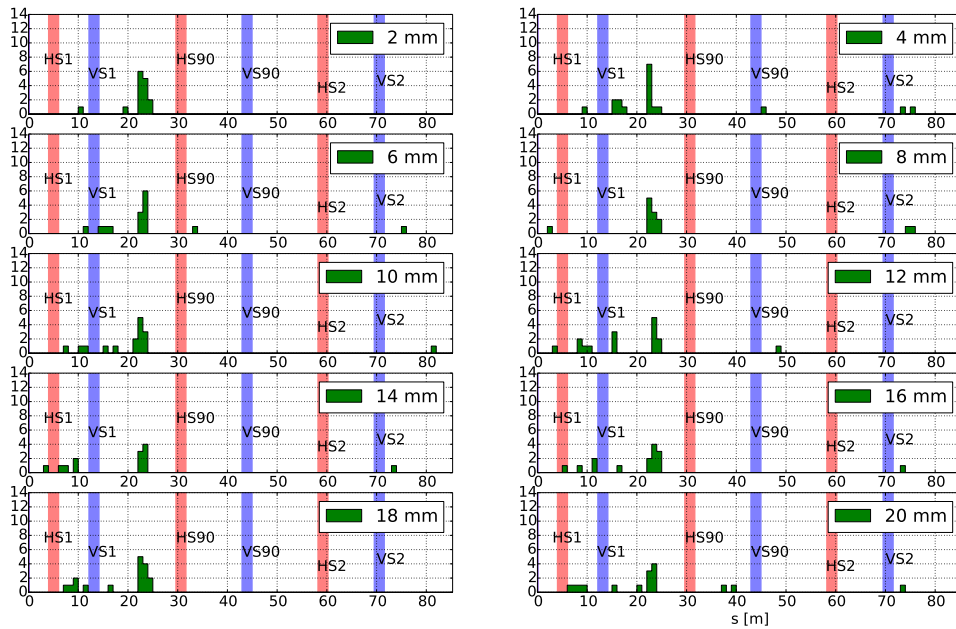
(a) H halo



(b) Including additional 90° collimators, H halo

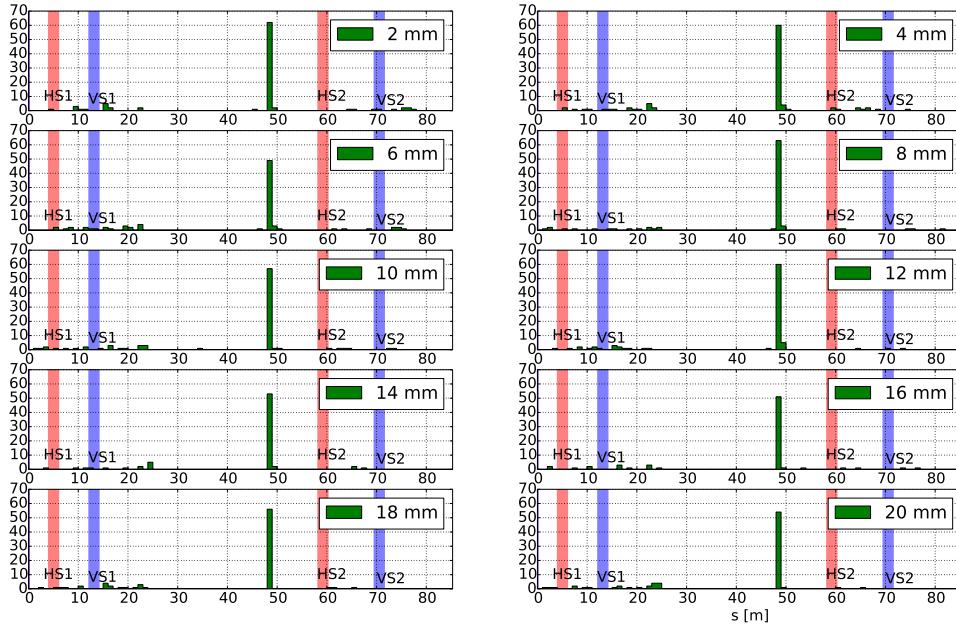


(c) V halo

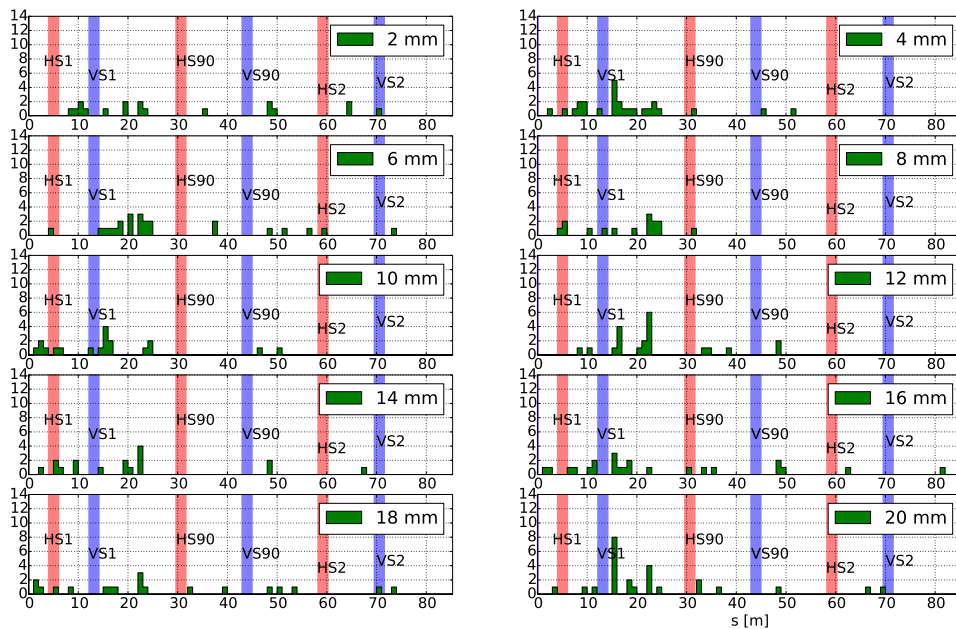


(d) Including additional 90° collimators, V halo

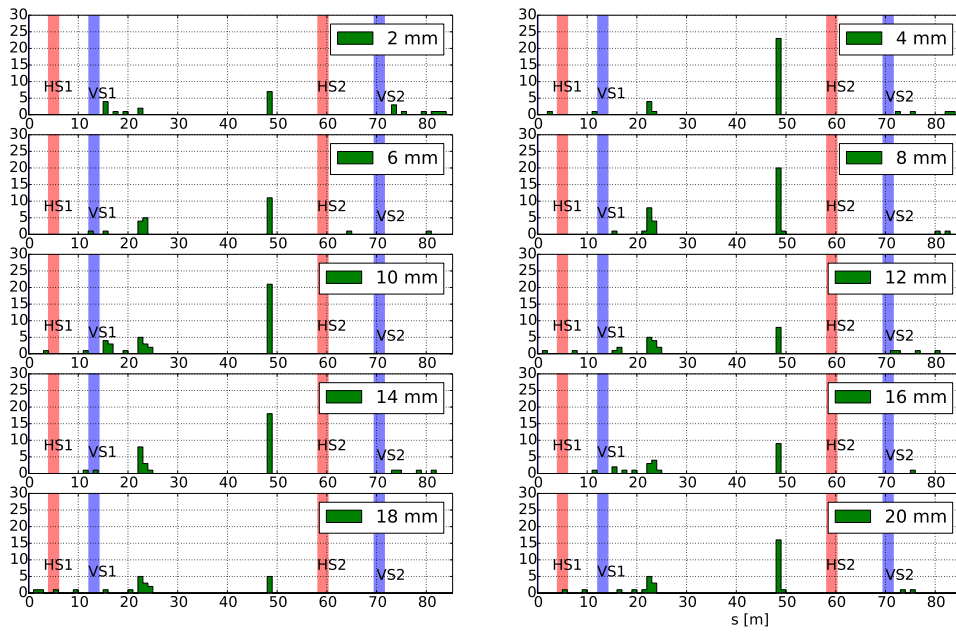
**Figure 5.72:** Number of particles lost per m in the collimation-LSS, when using Tungsten primary collimators



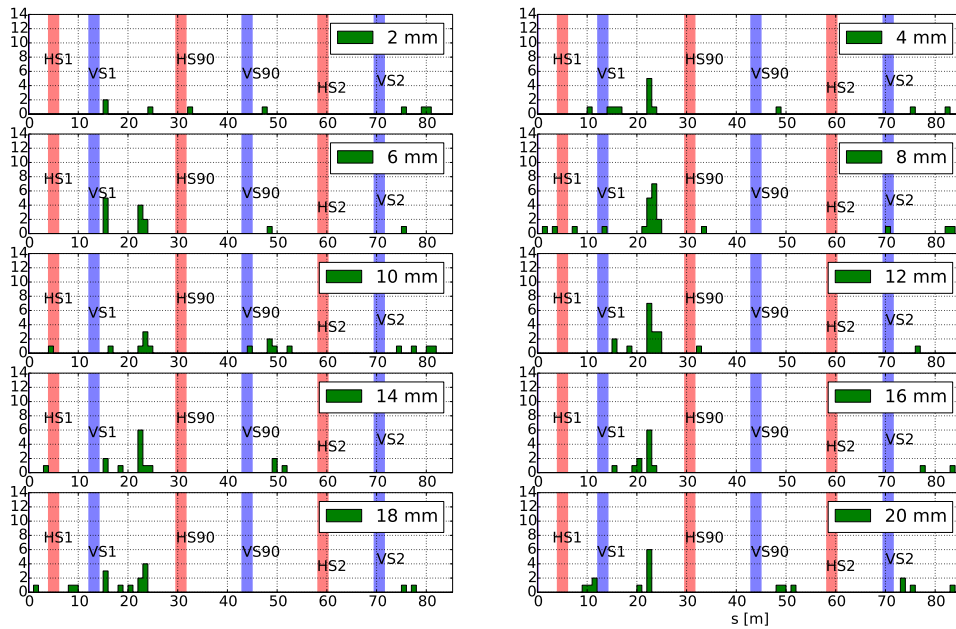
(a) H halo



(b) Including additional 90° collimators, H halo



(c) V halo



(d) Including additional 90° collimators, V halo

**Figure 5.73:** Number of particles lost per m in the collimation-LSS, when using Copper primary collimators

collimator at  $\sim 44$  m this losses-peak reduces significantly or is even completely removed.

It should be emphasised that the losses within the collimation-LSS are important only regarding the efficiency of the collimator system, since  $\eta_{inef} = N_{lost}/N_{tot}$ . What is of high importance is the number of particles lost outside the collimation-LSS, and especially the arcs, where the superconducting magnets are placed.

#### 5.5.3.4 Losses downstream the collimation-LSS

Figures 5.75, 5.76 and 5.77 show the number of particles lost per m outside the collimation-LSS (i.e.  $s > 81.5$  m). When Graphite primaries are used and a horizontal halo is generated the losses per m can be as high as  $\sim 30$  particles per m within the first 30 m after the end of the collimation-LSS, whereas when Copper or Tungsten is used the maximum losses per m are  $\sim 15$  and 6 particles per m respectively. The x-y coordinates of the losses occurring between 81.5 and 110.0 m when horizontal halo is generated and Graphite is used as a primary collimator, are plotted in Fig. 5.78 demonstrating they are mainly vertical. As soon as the additional collimators are included the losses drop to less than  $\sim 1-2$  particles per m for all the materials (in the case of Graphite this is true for thicknesses of  $\sim 8$  mm and above). When a vertical halo is generated there are in general fewer particles lost per m in all cases ( $\sim 6$  for Graphite and  $\sim 2$  for Tungsten and Copper). After including the additional collimators only 1-2 particles are lost per m for all materials (above  $\sim 6$  mm in the case of Graphite). Note there are almost no losses after 300 m from the end of the collimation-LSS; the majority of losses occur in the first 50 m from this point.

### 5.5.4 Impact parameter and material of secondary collimators

While using Graphite primary collimators of 14 mm length, the efficiency of the collimation system was then examined for different halo sizes, and different material of the secondary collimators. The generated halo was varied from  $3.0$  to  $3.8\sigma$ , while the smear size was kept constant at  $0.01\sigma$ . In these simulations the additional  $90^\circ$  collimators were included, located at the positions shown in Table 5.34. As shown in Fig. 5.79 the impact parameter changes drastically with the vertical halo size, which is not the case for the horizontal halo. Note that the change is uncorrelated to the material of the secondary collimators.

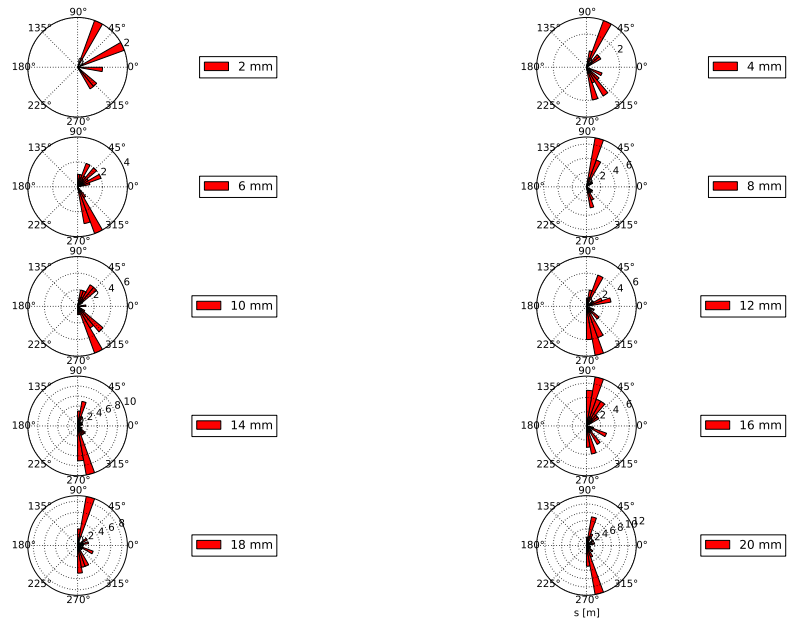
#### 5.5.4.1 Inefficiency

When generating a horizontal halo of different sizes, that correspond to different impact parameters on the primary collimators, the inefficiency is smaller when Copper or Tungsten, rather than Graphite, are used as the material of the secondary collimators. When Graphite is used, the inefficiency does not change significantly with the increase of the impact parameter, whereas it reduces by more than 1.5 times when Tungsten or Copper are used: the inefficiency drops from  $\sim 15\%$  at  $\sim 10\mu\text{m}$  impact parameter to  $\sim 9\%$  for these two materials.

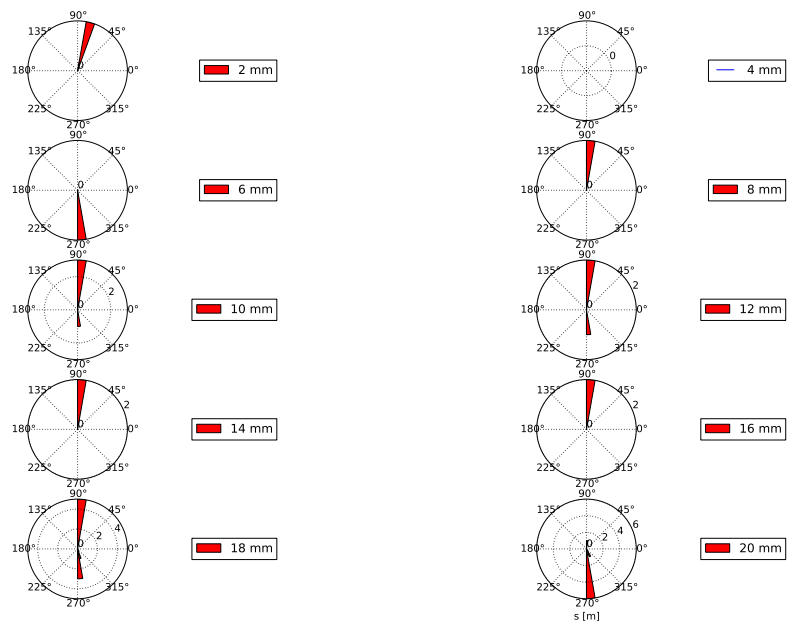
Similarly when a vertical halo is generated a smooth decrease of inefficiency is observed for both Tungsten and Copper with the increase of impact parameter; compared to the case where horizontal halo was generated, there is also a higher fluctuation with the vertical halo when Graphite is used as the secondary collimator.

#### 5.5.4.2 Absorptions

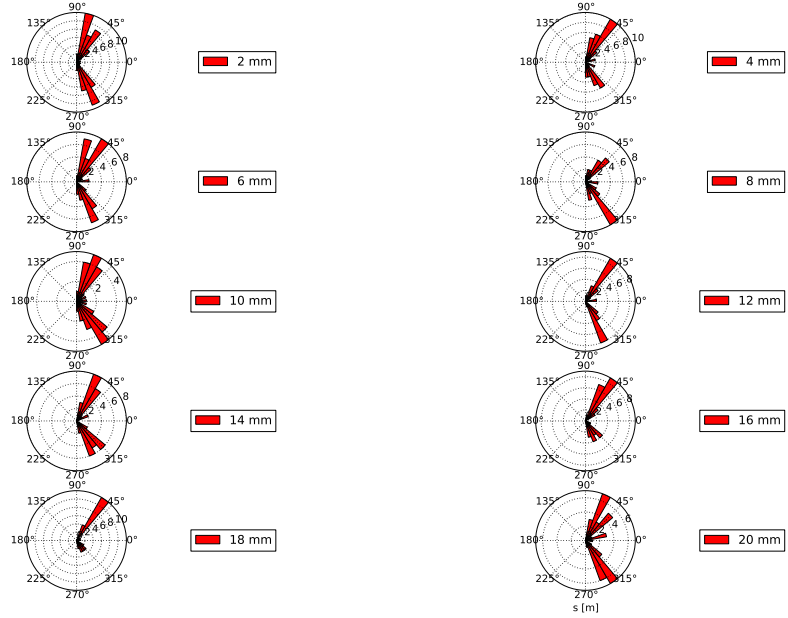
When a horizontal halo is generated the absorptions in all collimators do not change significantly for different impact parameters (see Fig. 5.82). On the other hand, when a vertical halo is created the absorptions in VP and VS1 increase smoothly with the impact parameter; in all



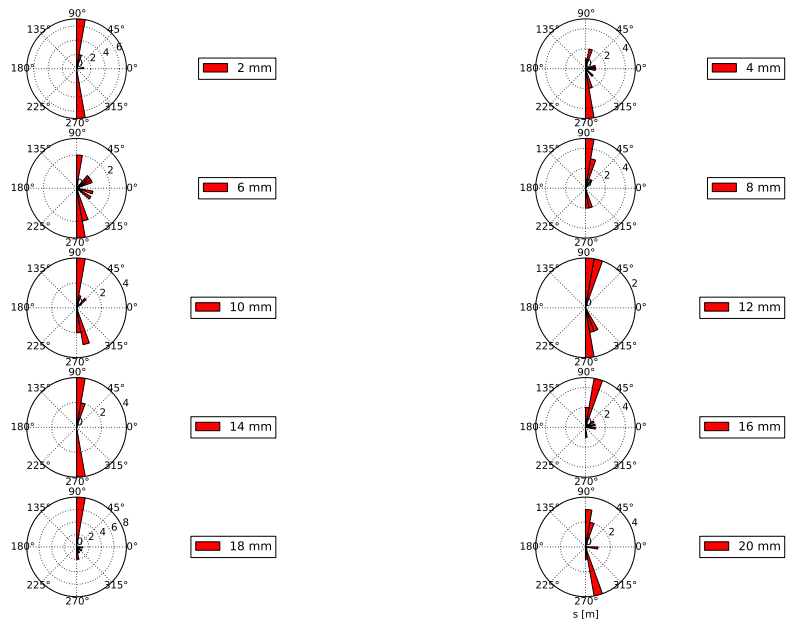
(a) H halo, Graphite



(b) V halo, Graphite

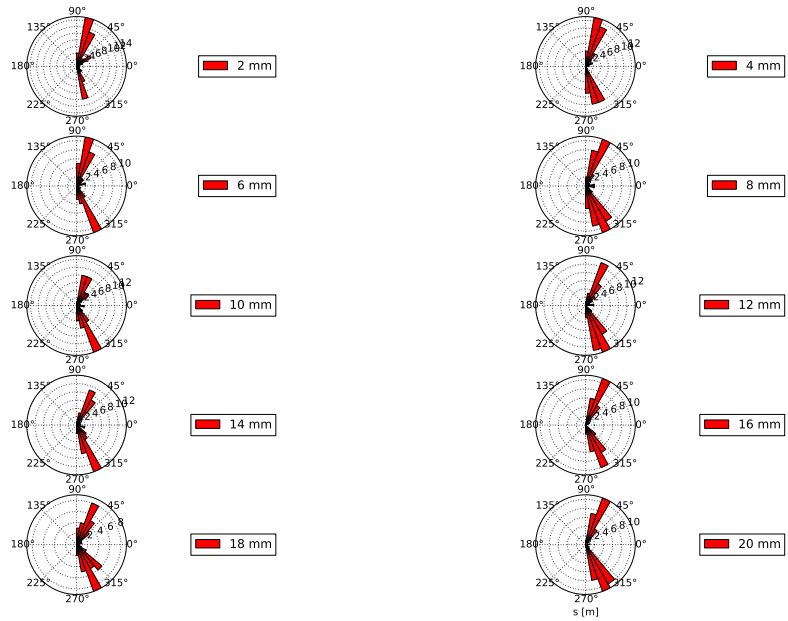


(c) H halo, Tungsten

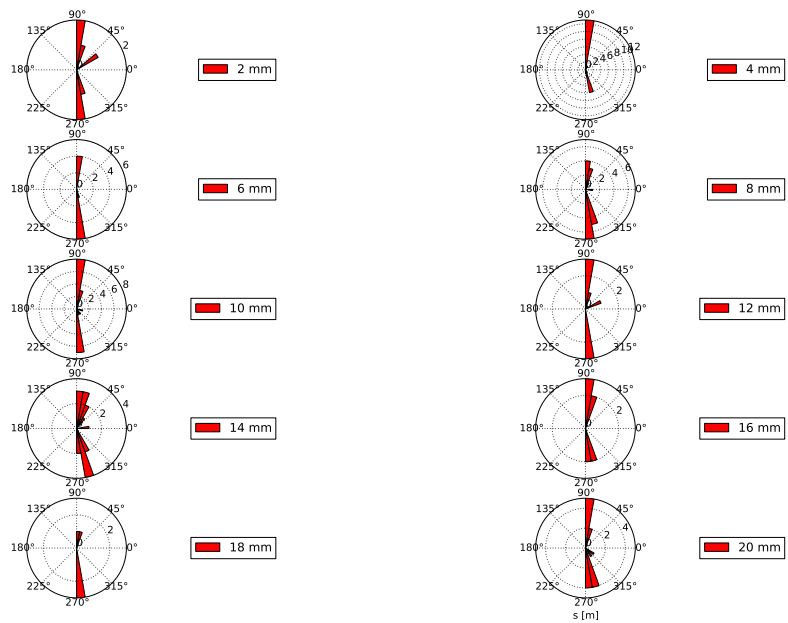


(d) V halo, Tungsten



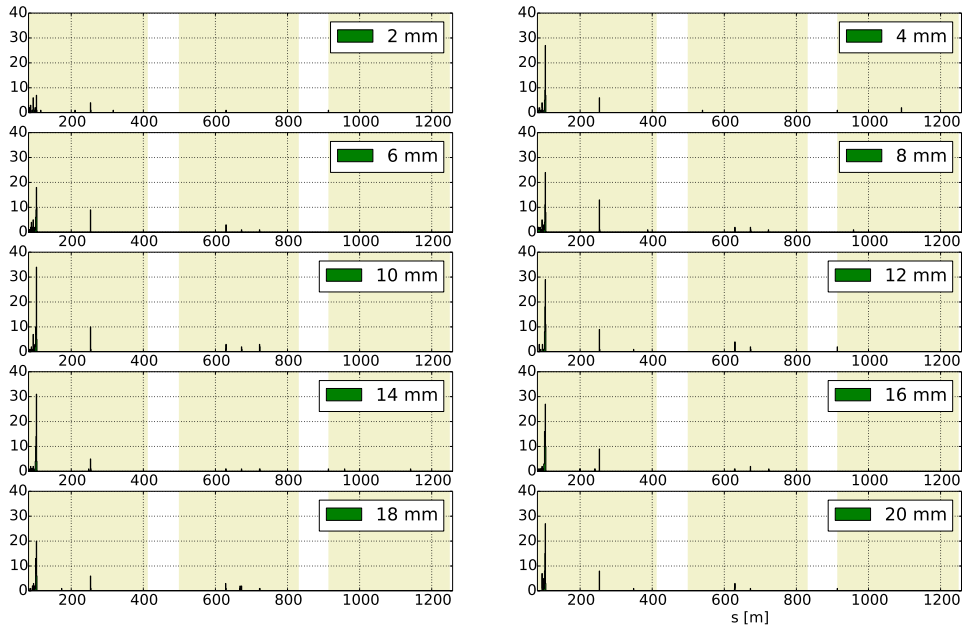


(e) H halo, Copper

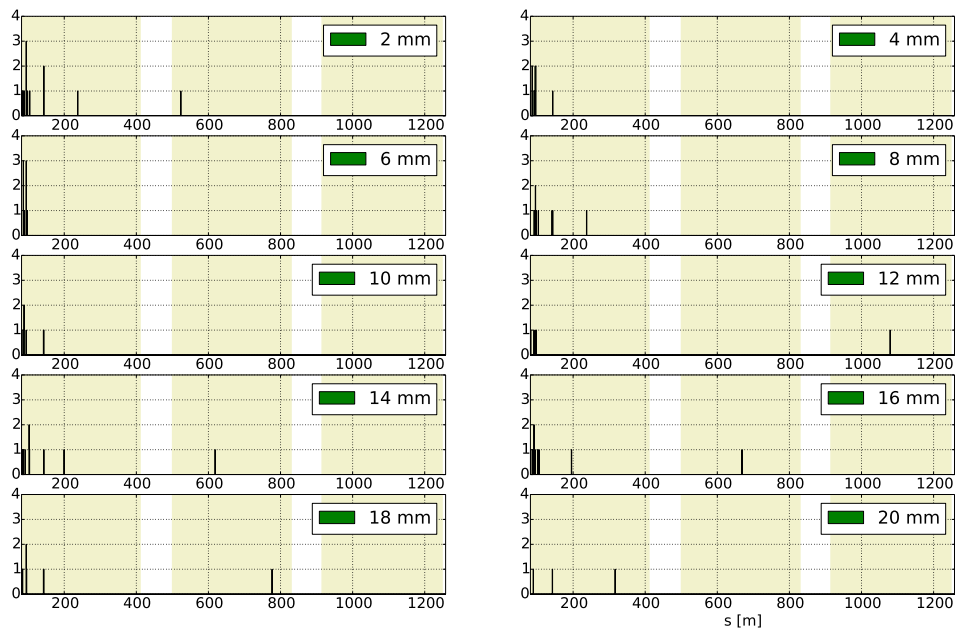


(f) C halo, Copper

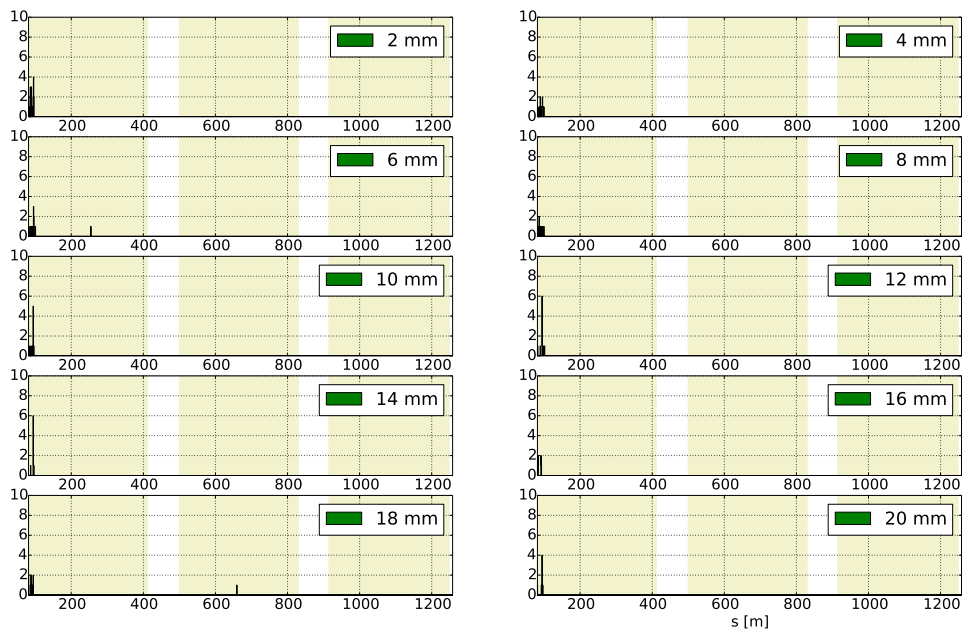
**Figure 5.74:**  $x$ - and  $y$ -coordinates of particles lost per m between the first 45-51 m of the collimation-LSS when no additional collimators are used.



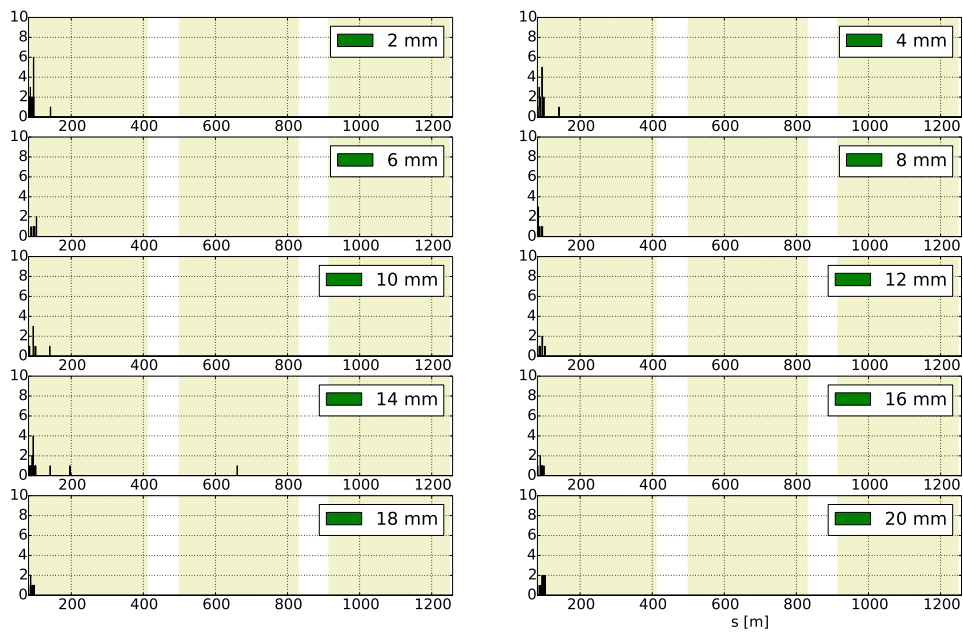
(a) H halo



(b) Including additional  $90^\circ$  collimators, H halo

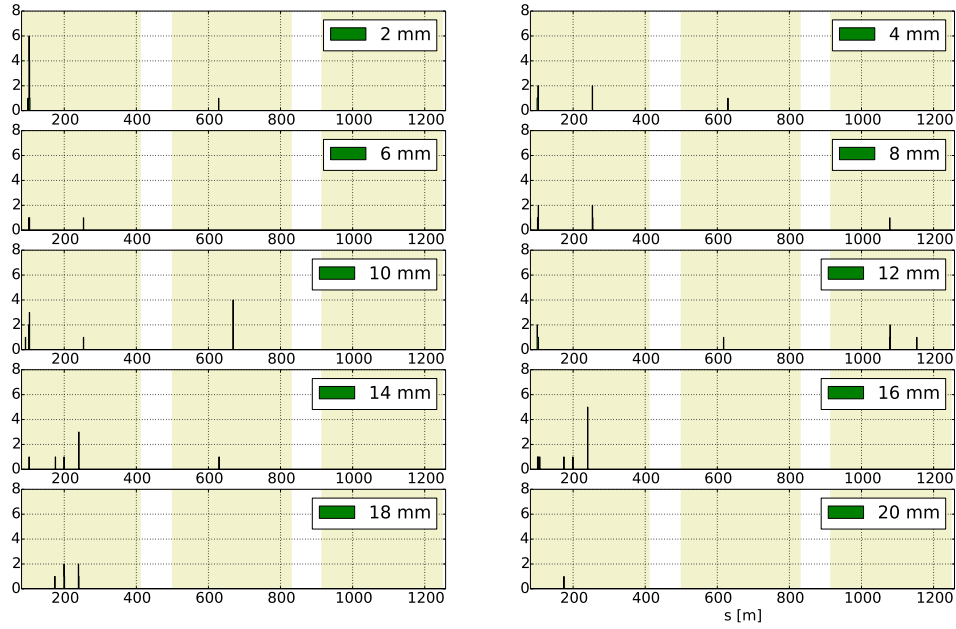


(c) V halo

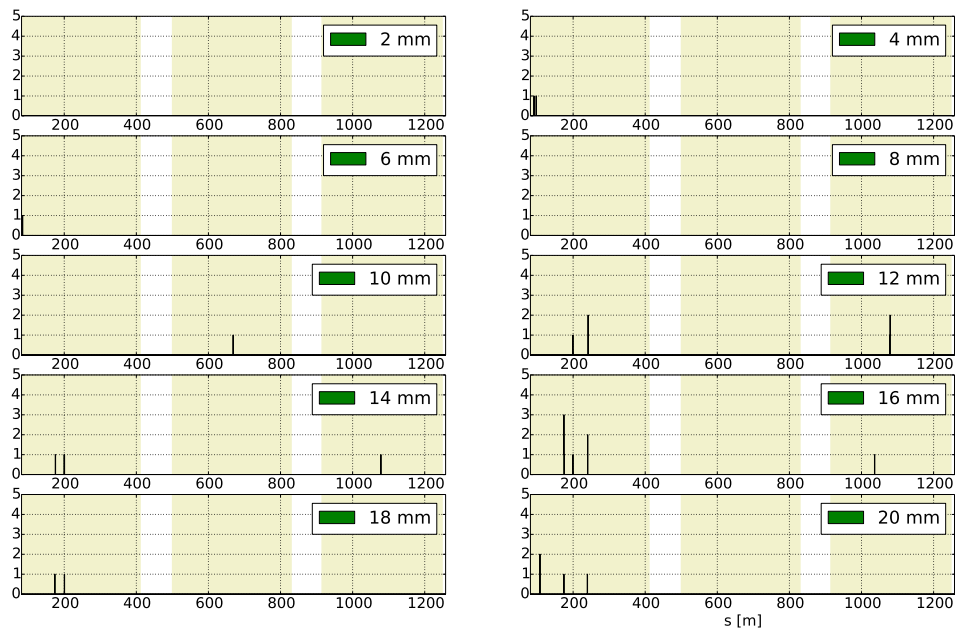


(d) Including additional 90° collimators, V halo

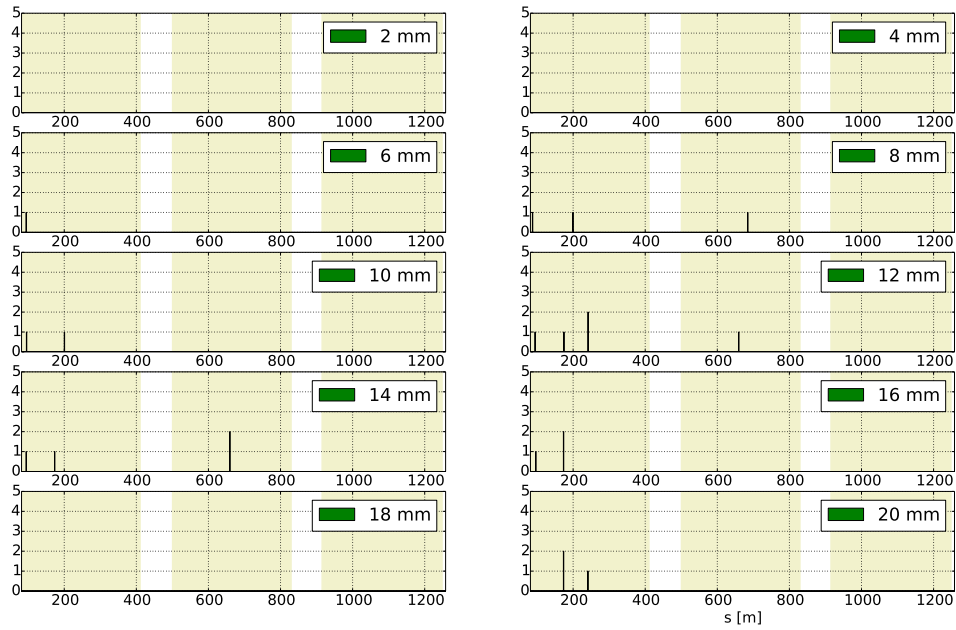
**Figure 5.75:** Number of particles lost per m outside the collimation-LSS, when using Graphite primary collimators; the arcs are the areas in yellow colour and the horizontal axis starts at 81.5 m.



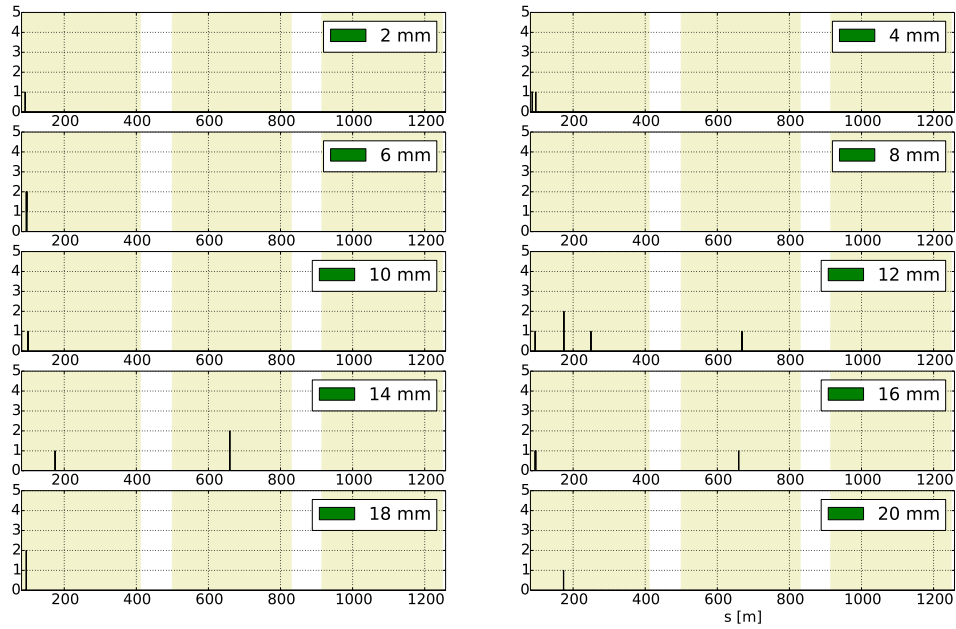
(a) H halo



(b) Including additional  $90^\circ$  collimators, H halo. The arcs are the areas in yellow colour.

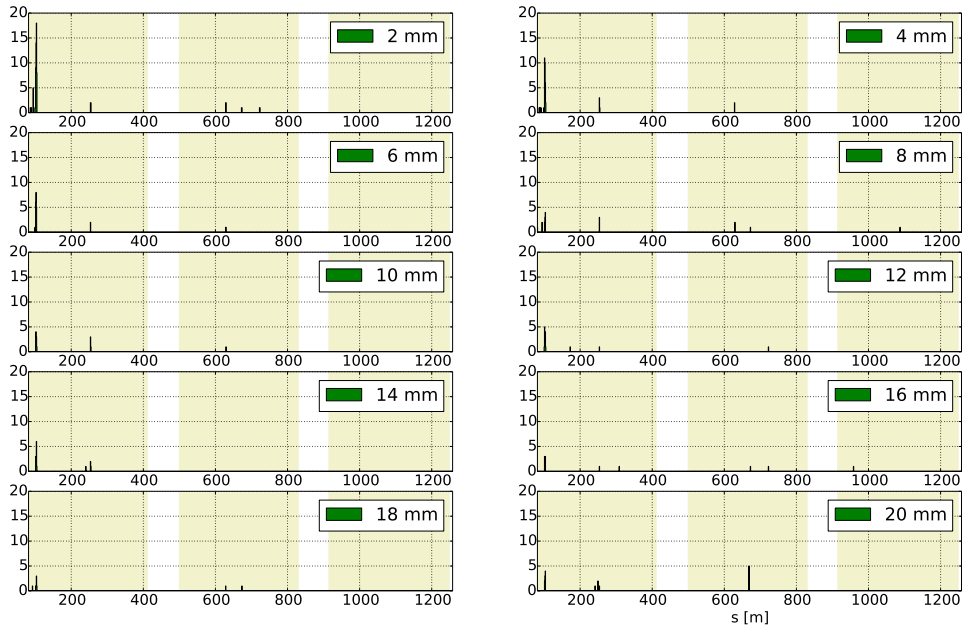


(c) V halo

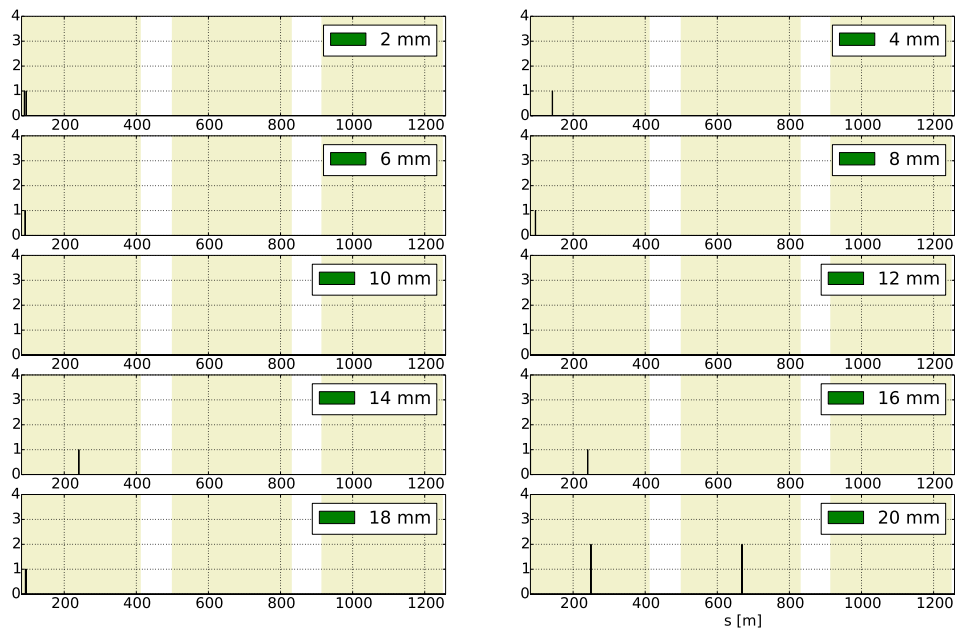


(d) Including additional 90° collimators, V halo

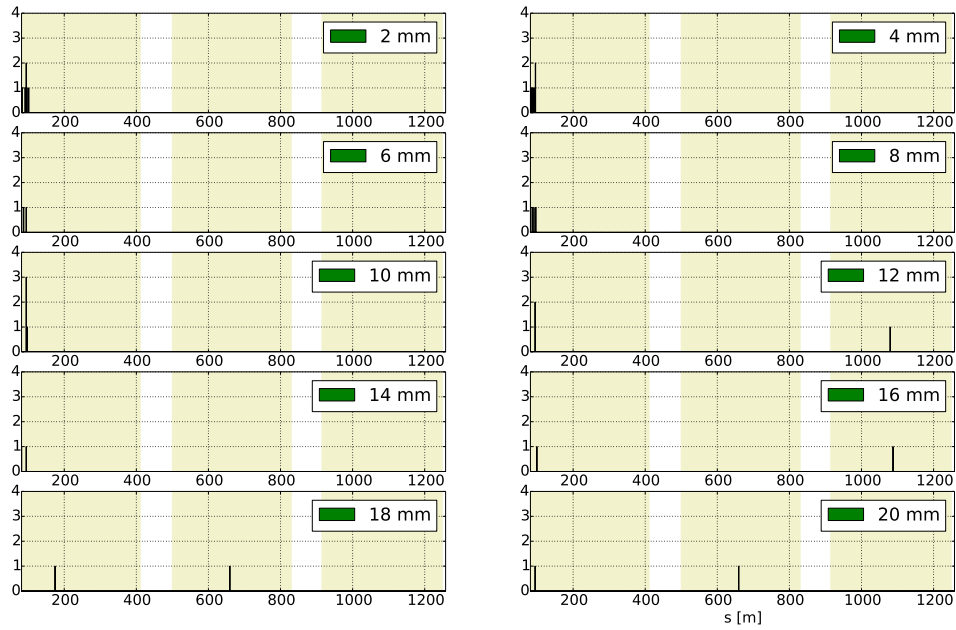
**Figure 5.76:** Number of particles lost per m outside the collimation-LSS, when using Tungsten primary collimators; the arcs are the areas in yellow colour and the horizontal axis starts at 81.5 m.



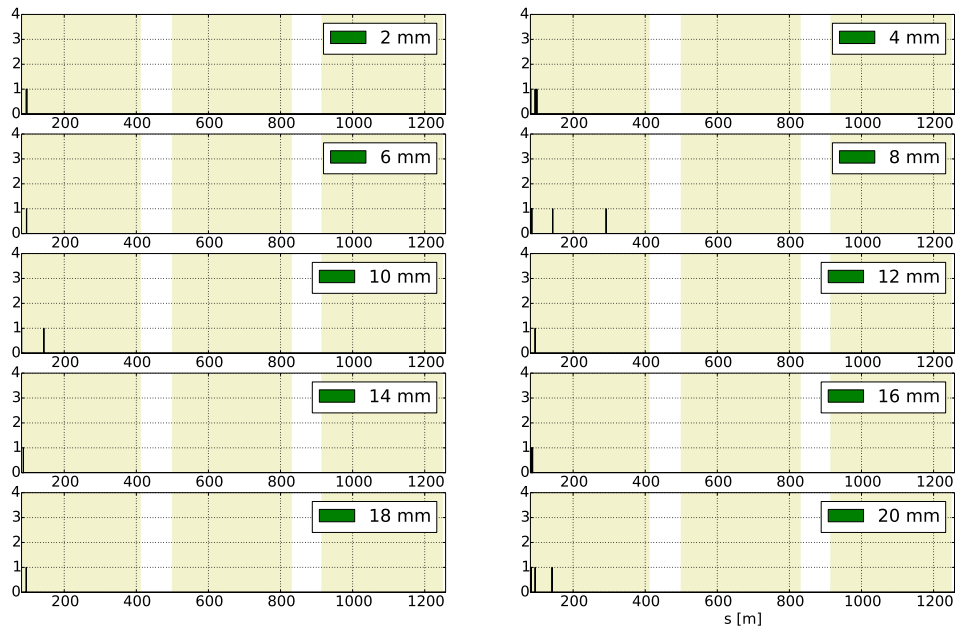
(a) H halo



(b) Including additional  $90^\circ$  collimators, H halo



(c) V halo



(d) Including additional 90° collimators, V halo

**Figure 5.77:** Number of particles lost per m outside the collimation-LSS, when using Copper primary collimators; the arcs are the areas in yellow colour and the horizontal axis starts at 81.5 m.

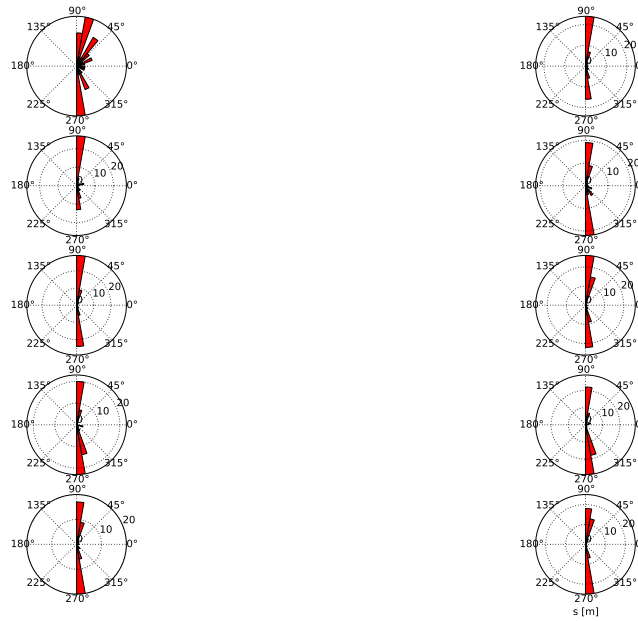


**Figure 5.78:** *x*- and *y*-coordinates of particles lost per *m* between the first 81.5-110.0 *m* from the primary collimator.

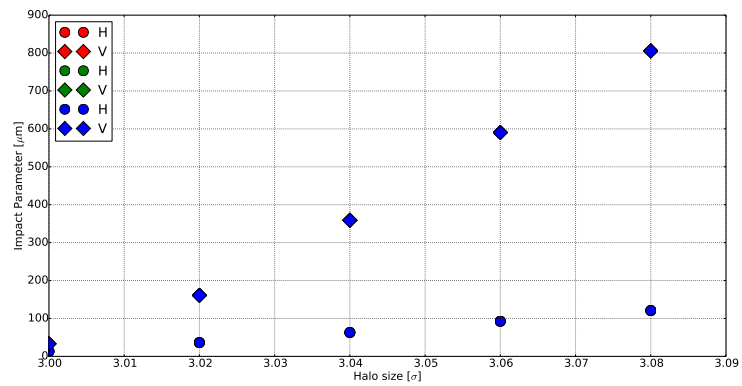
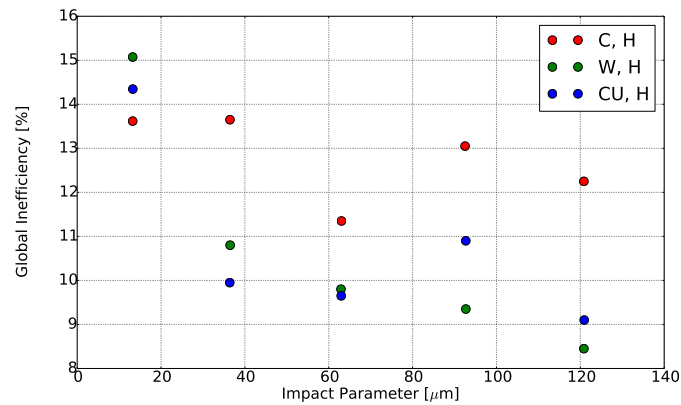
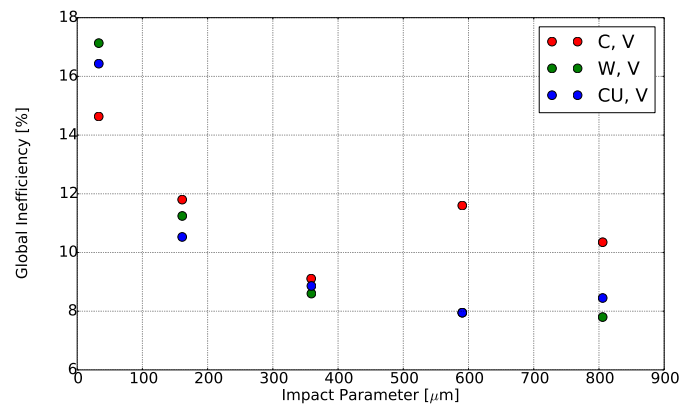


**Figure 5.79:** Change of impact parameter with the halo size for both horizontal and vertical halos (round and diamond markers respectively).





(a) H halo



(b) V halo

**Figure 5.80:** Global inefficiency with respect to the impact parameter of horizontal (top) and vertical (bottom) halo, for Graphite (red), Tungsten (green) and Copper (blue) secondaries.

other collimators it appears that the impact parameter does not affect the number of absorptions.

### 5.5.4.3 Losses in the collimation-LSS

When Graphite secondary collimators are used and horizontal halo is generated, peak-losses at  $\sim 45\text{-}50$  m increase with the increase of the halo size, and for halo  $>3.02\sigma$  the loss-peak at  $\sim 10\text{-}20$  m increases to up to 24 particles. When Tungsten or Copper secondaries and horizontal halo is generated the losses along the collimation-LSS do not change significantly with the increase of impact parameter, whereas the loss-peak at  $\sim 10\text{-}20$  m increases by up to 8 times when vertical halo is created (see Figs. 5.83, 5.84 and 5.85). The different behaviour with respect to losses between the horizontal and vertical halos was expected since the increase of impact parameter with halo size is more drastic in the vertical halo case (see Fig. 5.79).

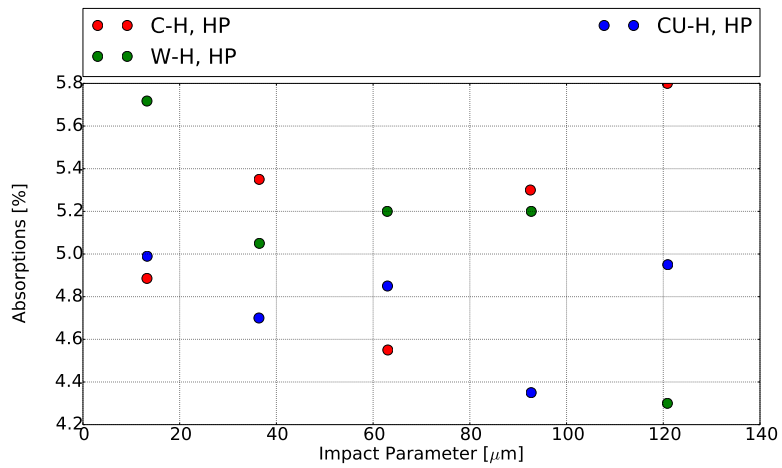
Note that also in the case where a horizontal halo is generated, for all halo sizes except for  $3.0\sigma$ , the whole halo impacts a primary collimator, whereas at  $3\sigma$  only  $\sim 50\%$  of the beam interacts at least once with a primary. When a  $3\sigma$  vertical halo is generated only 15% of the particles impact a primary. At  $3.02\sigma$  already  $\sim 75\%$  of the halo interacts whereas for halos  $>3.02\sigma$  the whole halo beam impacts a primary collimator. This can explain why in the vertical halo case there are very small changes in losses for halo-sizes between  $3.04$  and  $3.08\sigma$ . As mentioned in section 5.5.2.1 the difference between horizontal and vertical halo behaviour for small halo sizes is a result of the different  $\alpha$  functions at the point where the halos are generated (see Fig. 5.60).

### 5.5.4.4 Losses downstream the collimation-LSS

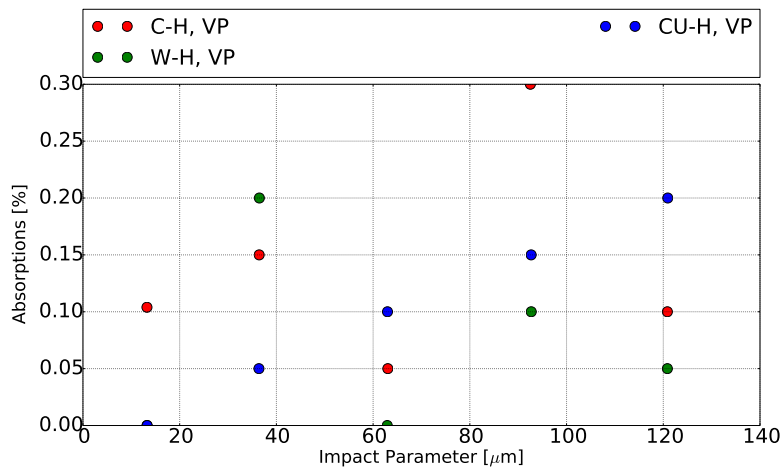
There are few losses outside the collimation-LSS (less than 4 losses per m) when a horizontal halo is generated, regardless of the impact parameter and of what material is used for the secondary collimators. On the contrary, the losses in the first  $\sim 30$  m from the end of the collimation-LSS increase more than two times when generating a  $>3.0\sigma$  vertical halo for all secondary-materials. Fig. 5.89 shows the distribution in  $x - y$  of losses between 81.5-110 m when vertical halos are generated; the majority of the losses are in the vertical direction which indicates that an additional vertical collimator would be beneficial.

## 5.5.5 Power deposition

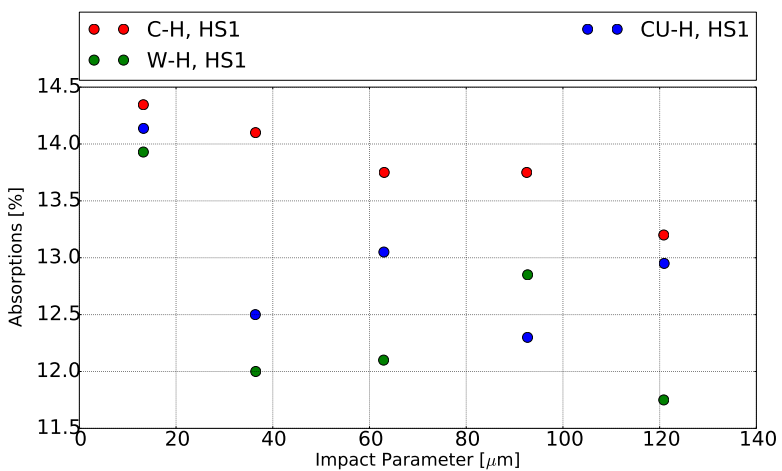
It is important to calculate the power deposited outside the collimation-LSS from particles that impact the aperture, as the radiation limit is  $\sim 1$  W/m. Assuming the generated halo is 1% of the injected beam, which is of 0.16 MW, the power carried by the halo is 1.6 kW. If this corresponds to 2,000 particles (the number of generated halo particles in the results presented above) then each particle carries 0.8 W. From Figs. 5.75, 5.76 and 5.77 it is shown that regardless of what material is used as a primary collimator, when additional  $90^\circ$  collimators are used, the losses outside the collimation-LSS are as low as 1-2 particles (in the case of Graphite, this is true for  $>8$  mm thickness). This corresponds to power that is below, or slightly exceeds the 1 W/m radiation limit. Diffusion studies including space-charge should be combined with the collimation studies in the future to ensure the losses in the arcs will remain at acceptable levels, since as seen in Section 5.5.4.4 the losses become important when vertical halo of  $>3.00\sigma$  is generated. For the losses that slightly exceed the radiation limit, Special masks can be used, or the aperture of the magnets can increase in the locations where the limit is exceeded.



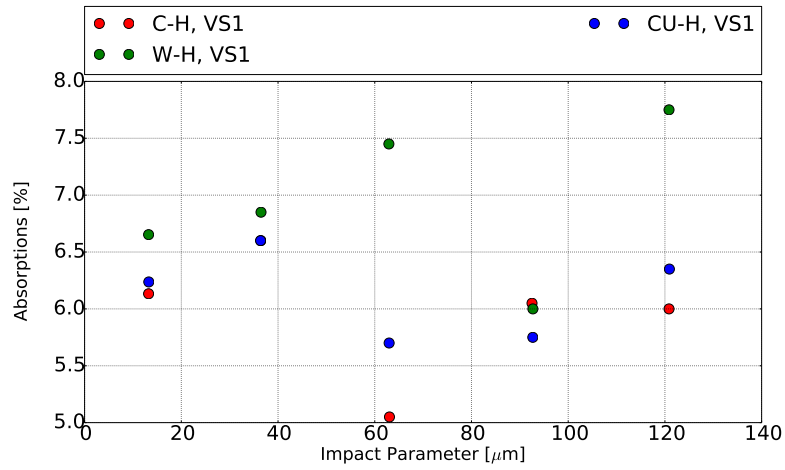
(a) Absorptions in HP, H halo



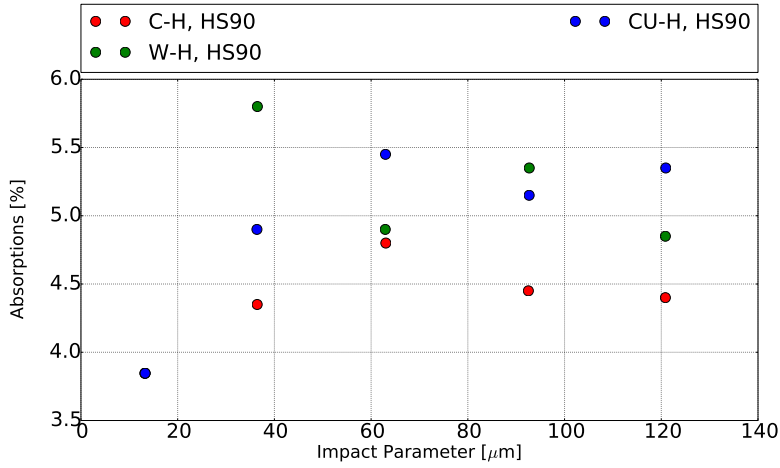
(b) Absorptions in VP, H halo



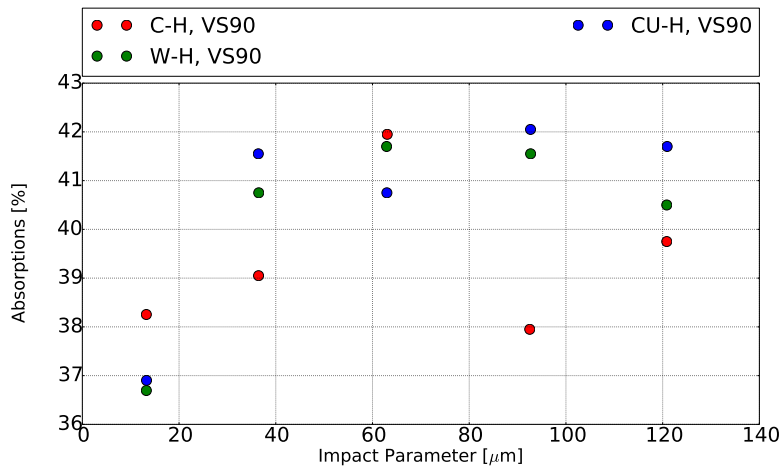
(c) Absorptions in HS1, H halo



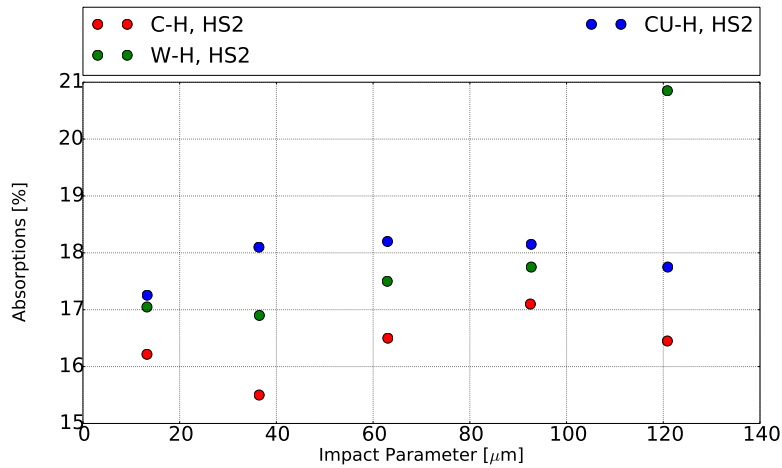
(d) Absorptions in VS1, H halo



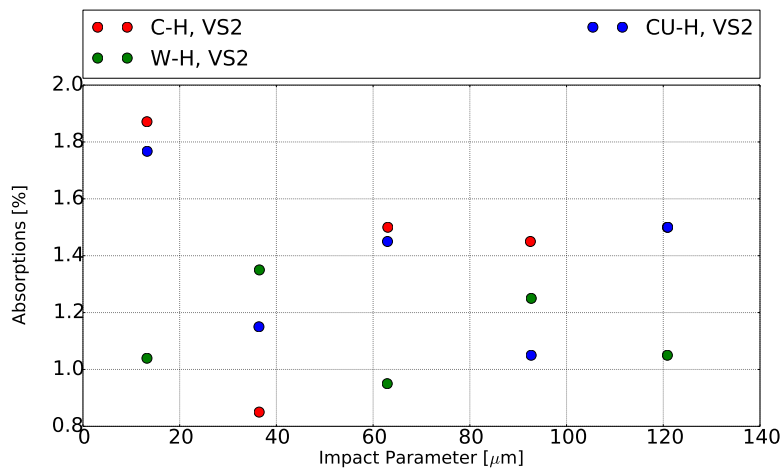
(e) Absorptions in HS90, H halo



(f) Absorptions in VS90, H halo

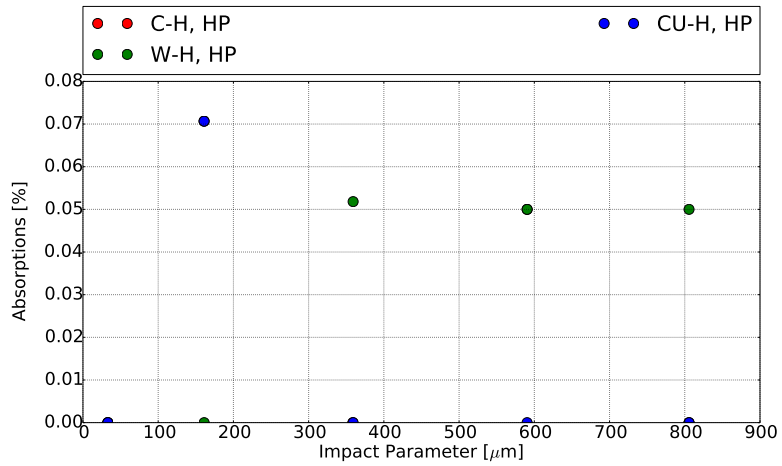


(g) Absorptions in HS2, H halo

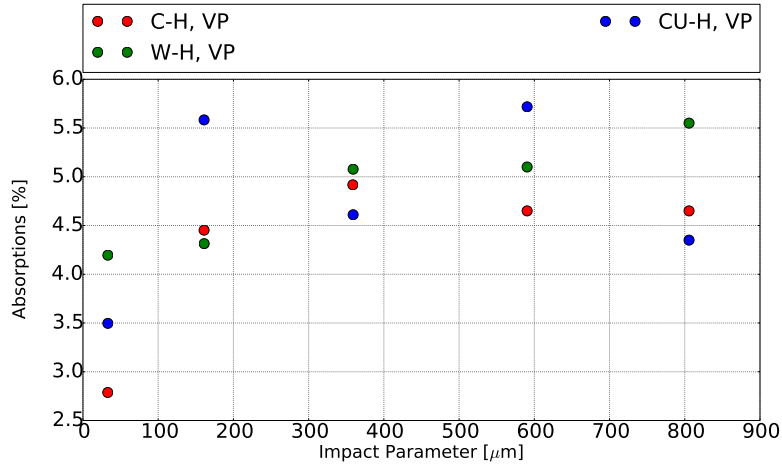


(h) Absorptions in VS2, H halo

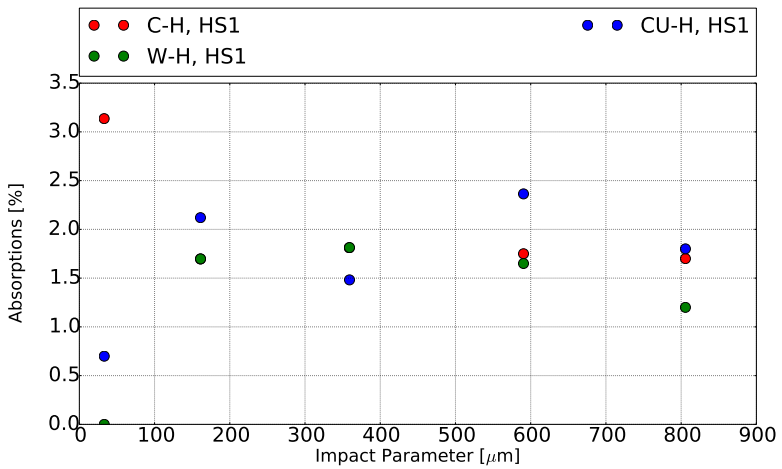
**Figure 5.81:** Number of horizontal halo particles absorbed by each collimator over the the total number of particles that impacted at least once a collimator (in percentage), for different secondary collimator material and impact parameters. H: Horizontal, V: Vertical, P: Primary, S: Secondary.



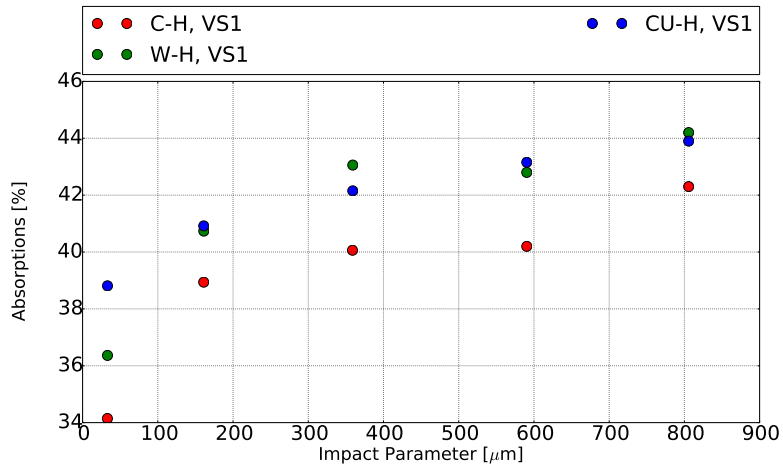
(a) Absorptions in HP, V halo-sec



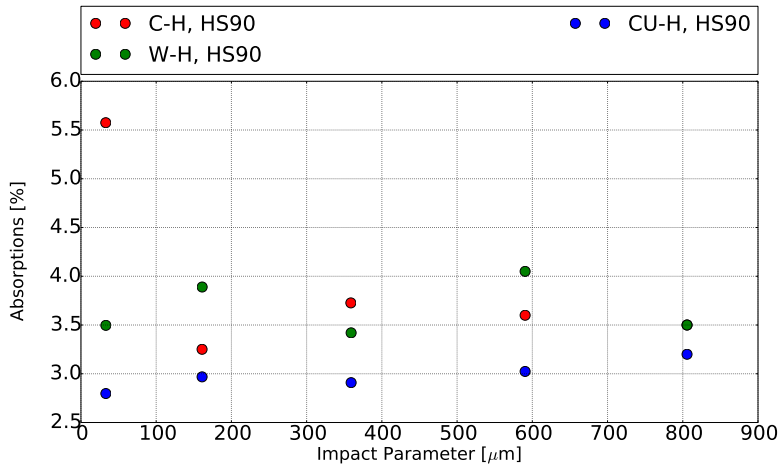
(b) Absorptions in VP, V halo-sec



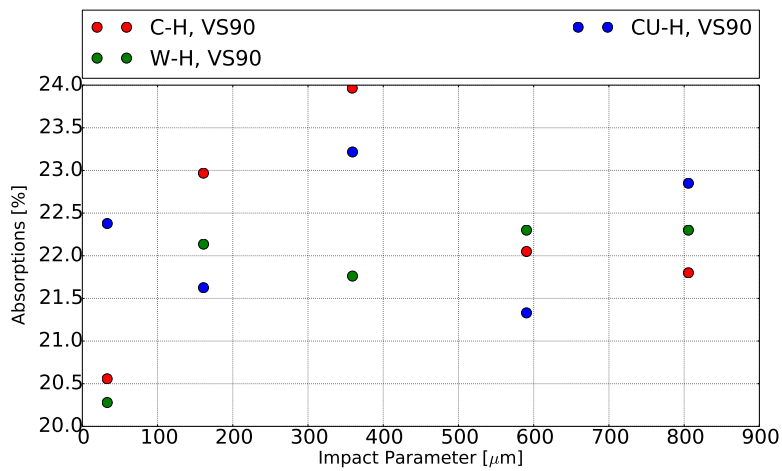
(c) Absorptions in HS1, V halo



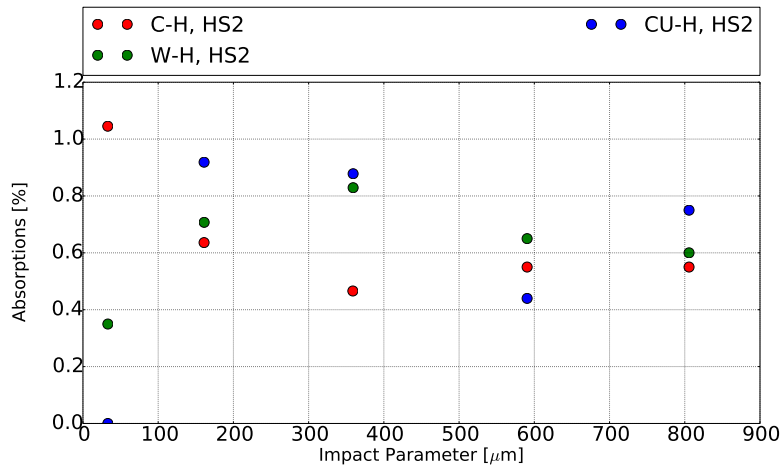
(d) Absorptions in VS1, V halo



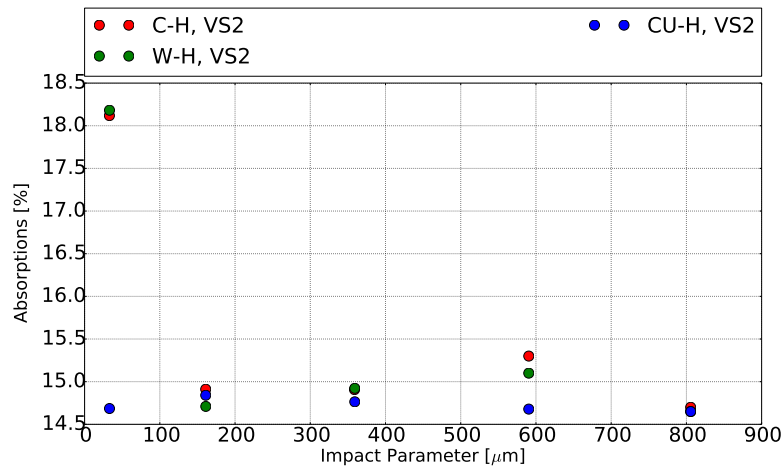
(e) Absorptions in HS90, V halo



(f) Absorptions in VS90, V halo



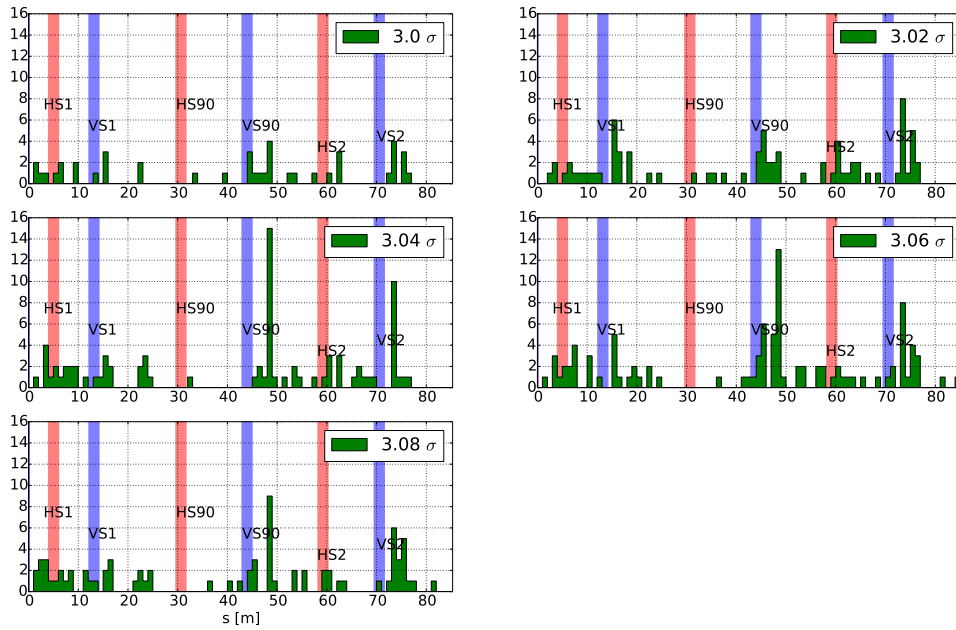
(g) Absorptions in HS2, V halo



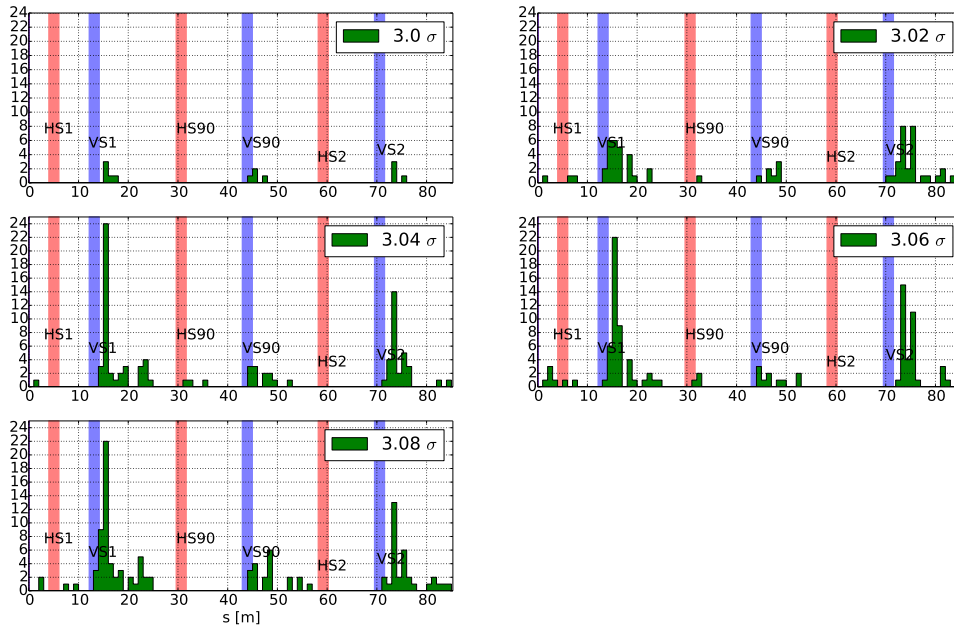
(h) Absorptions in VS2, V halo

**Figure 5.82:** Number of vertical halo particles absorbed by each collimator over the the total number of particles that impacted at least once a collimator (in percentage), for different secondary collimator material and impact parameters. H: Horizontal, V: Vertical, P: Primary, S: Secondary.



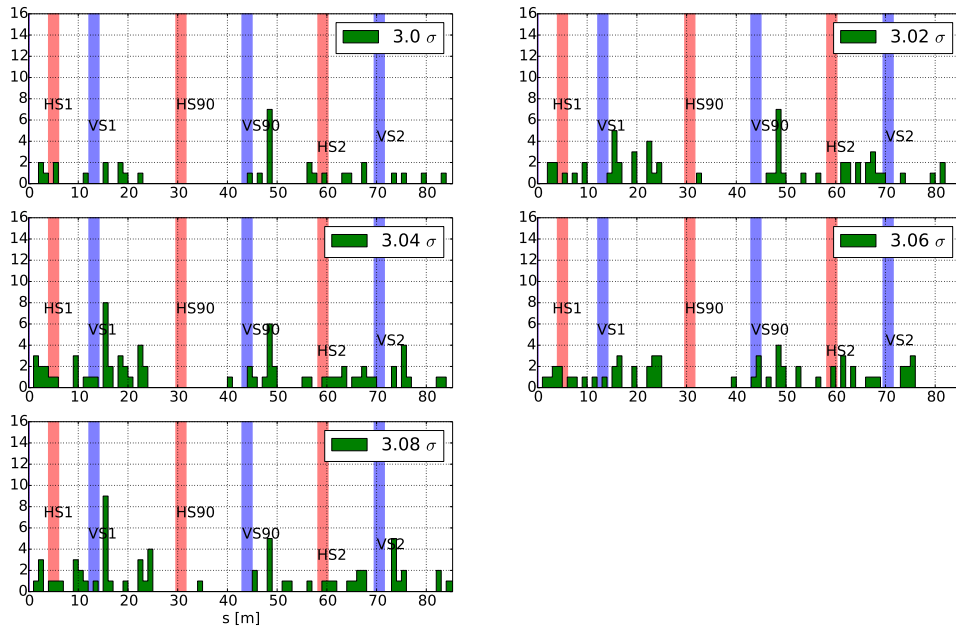


(a) C, H halo

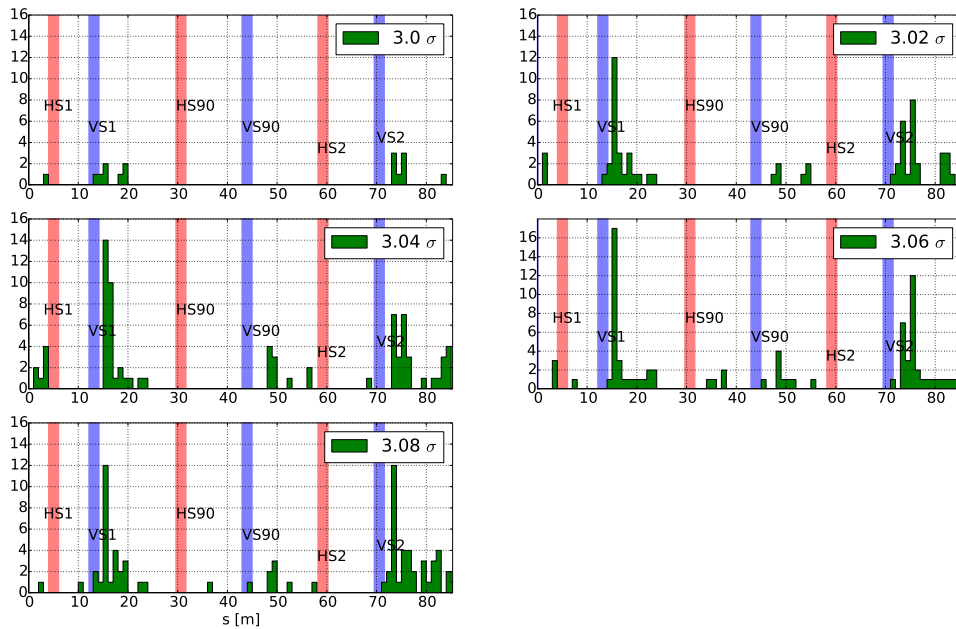


(b) C, V halo

**Figure 5.83:** Number of particles lost per m in the collimation-LSS, when using Graphite primary collimators

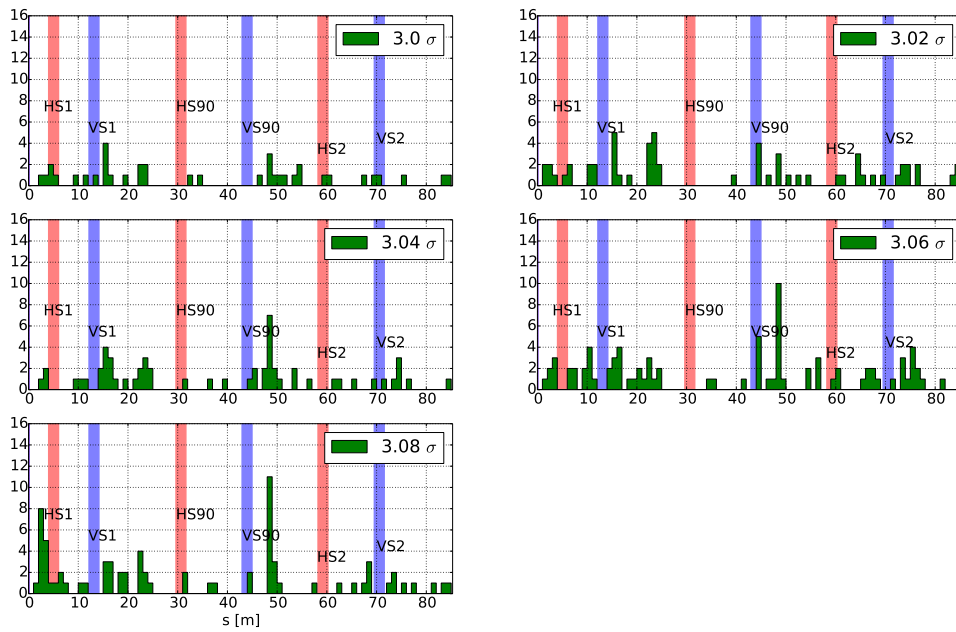


(a) W, H halo

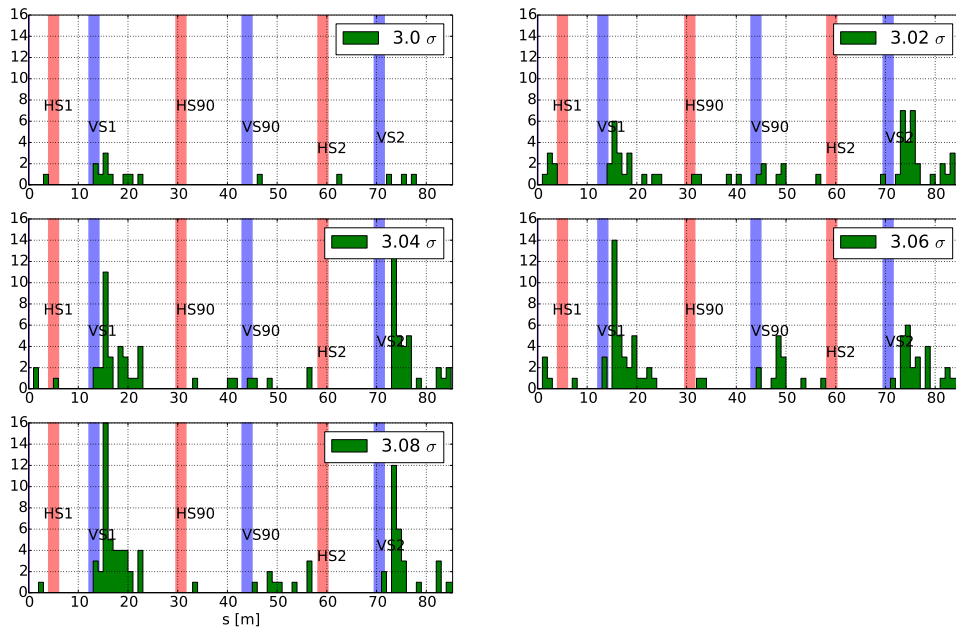


(b) W, V halo

**Figure 5.84:** Number of particles lost per m in the collimation-LSS, when using Tungsten primary collimators

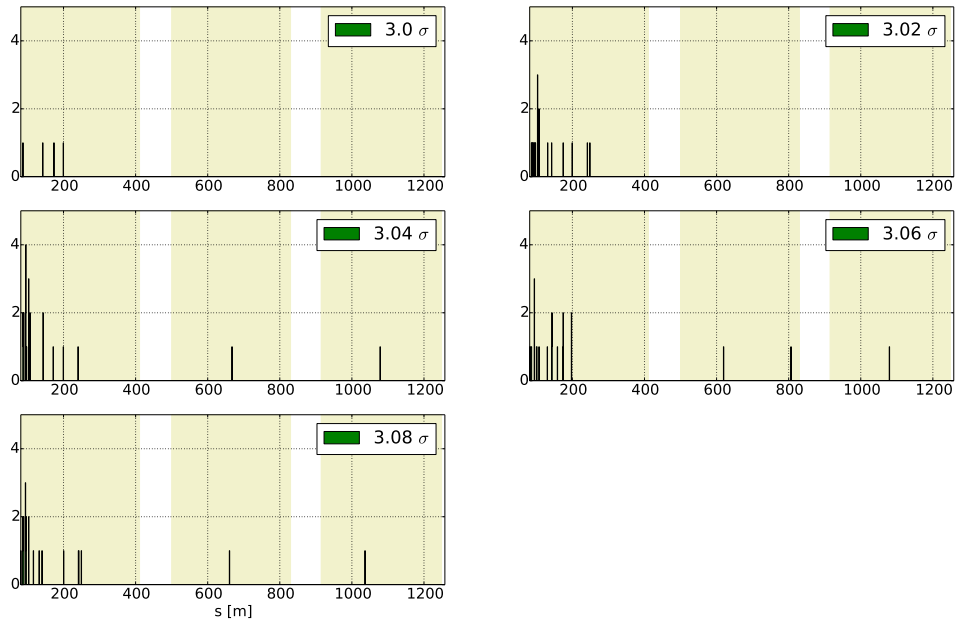


(a) CU, H halo

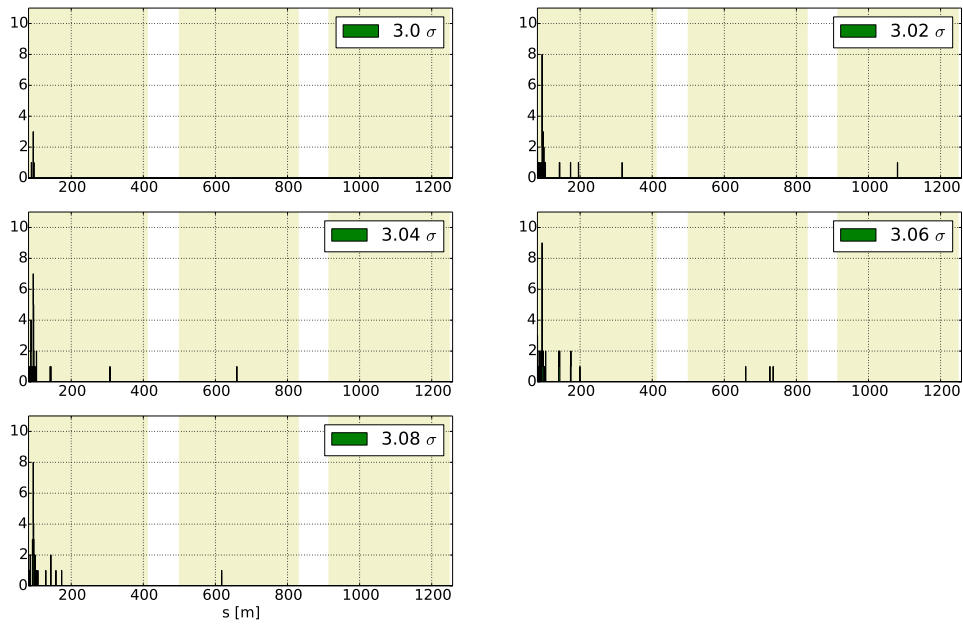


(b) CU, V halo

**Figure 5.85:** Number of particles lost per m in the collimation-LSS, when using Copper primary collimators

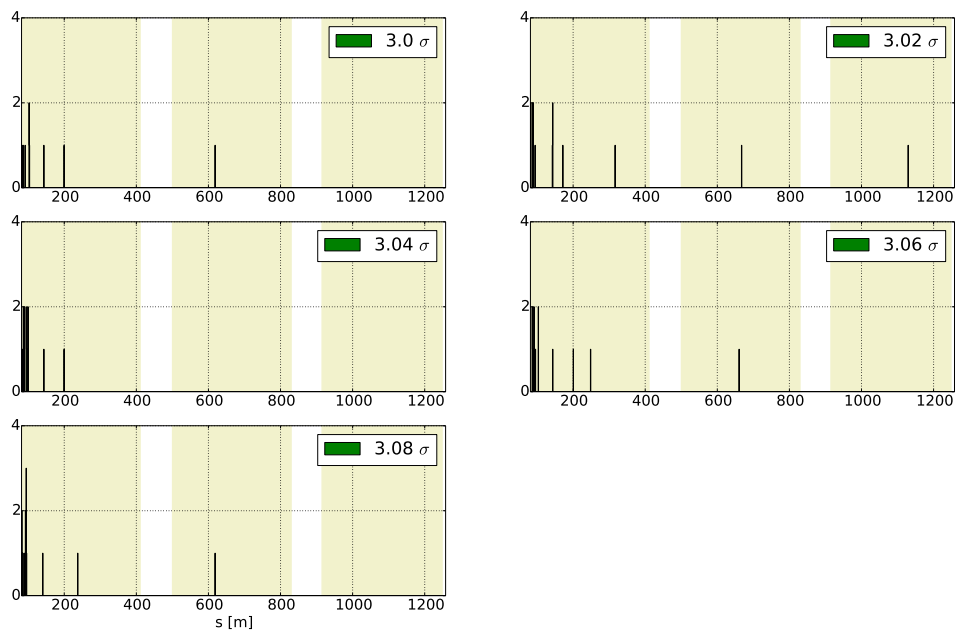


(a) C, H halo

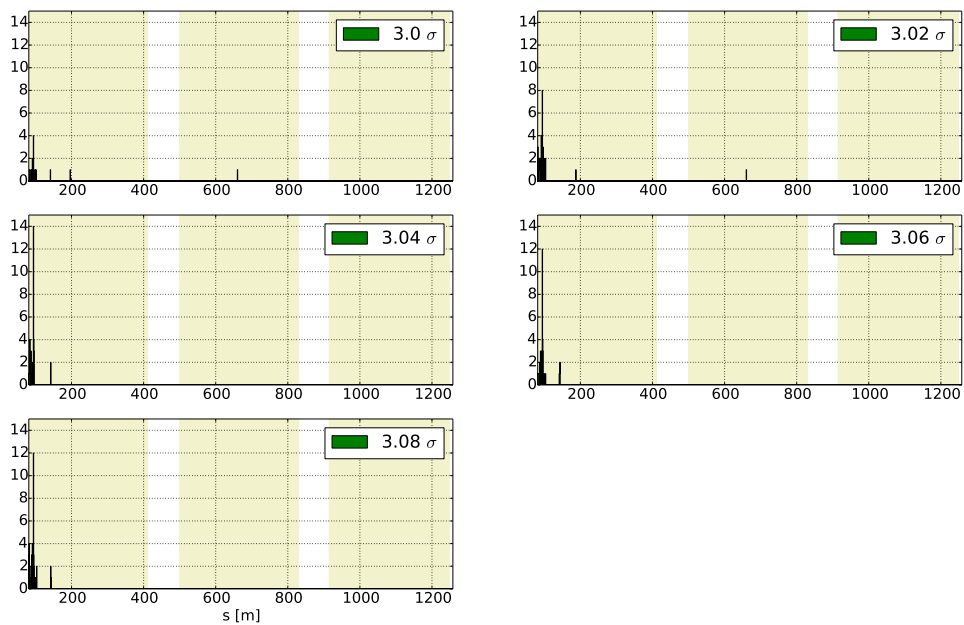


(b) C, V halo

**Figure 5.86:** Number of particles lost per m outside the collimation-LSS, when using Graphite secondary collimators; the arcs are the areas in yellow colour and the horizontal axis starts at 81.5 m.

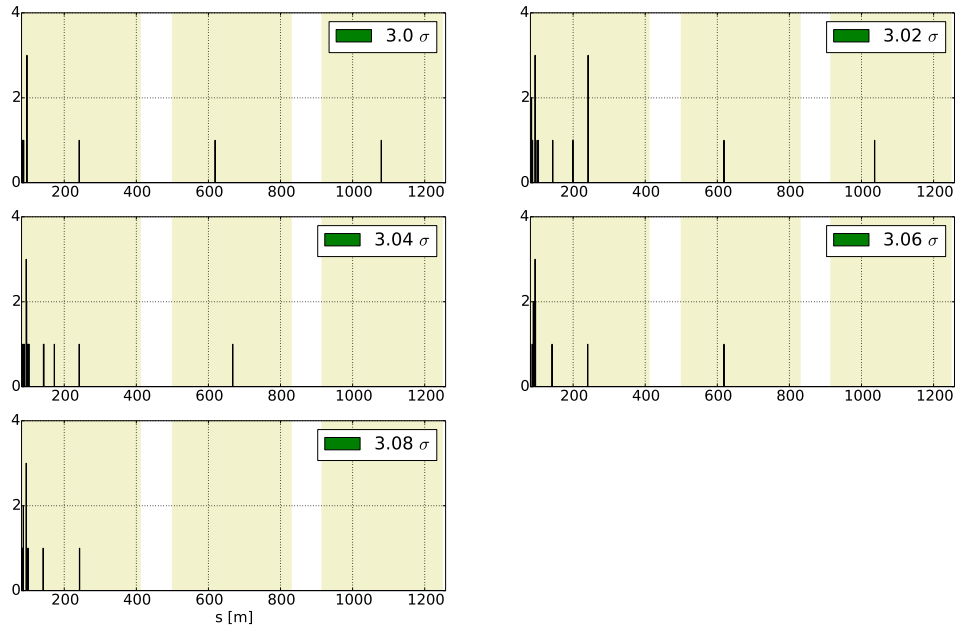


(a) W, H halo

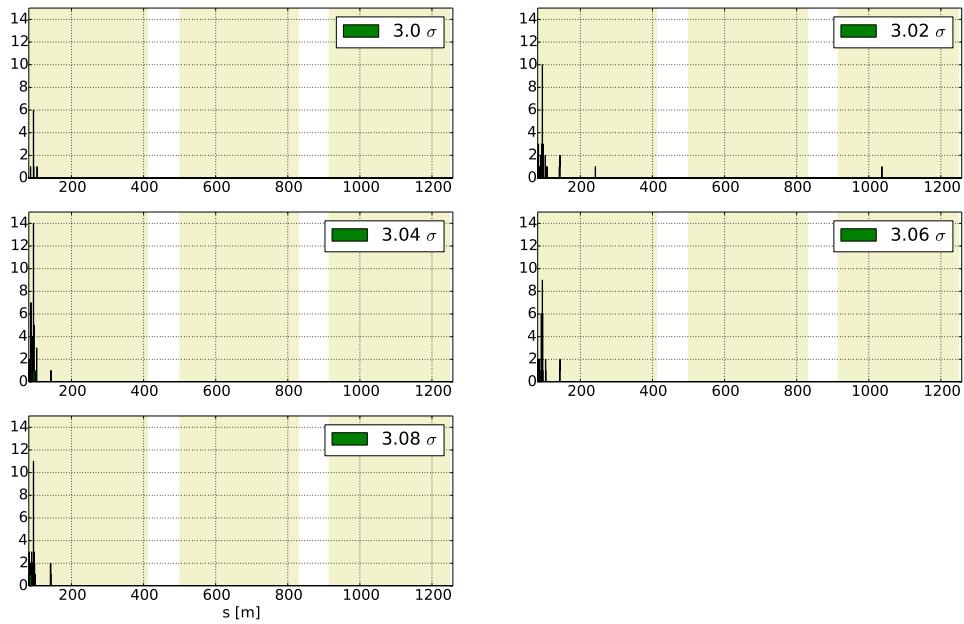


(b) W, V halo

**Figure 5.87:** Number of particles lost per m outside the collimation-LSS, when using Tungsten secondary collimators; the arcs are the areas in yellow colour and the horizontal axis starts at 81.5 m.

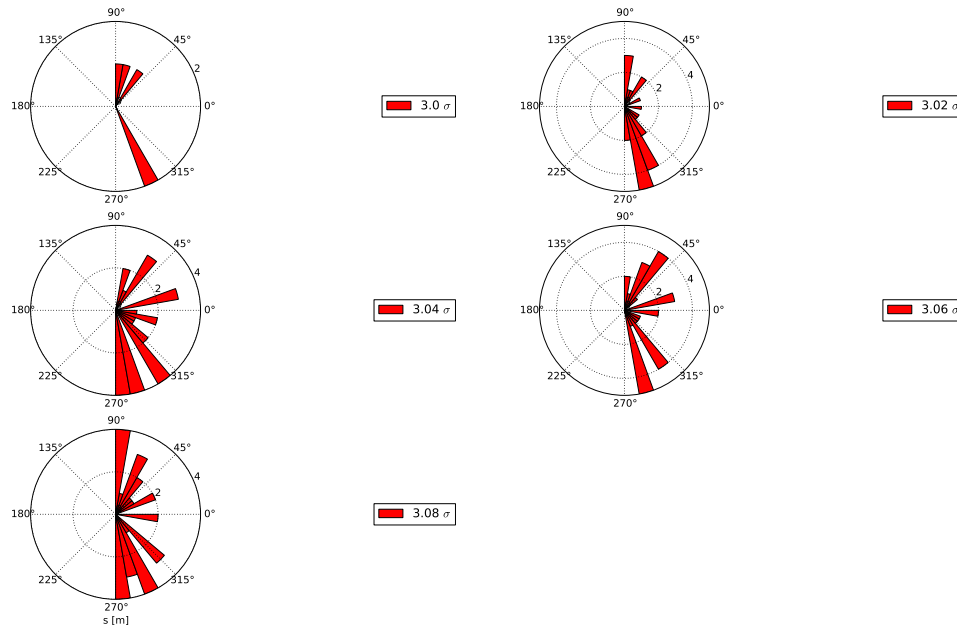


(a) CU, H halo

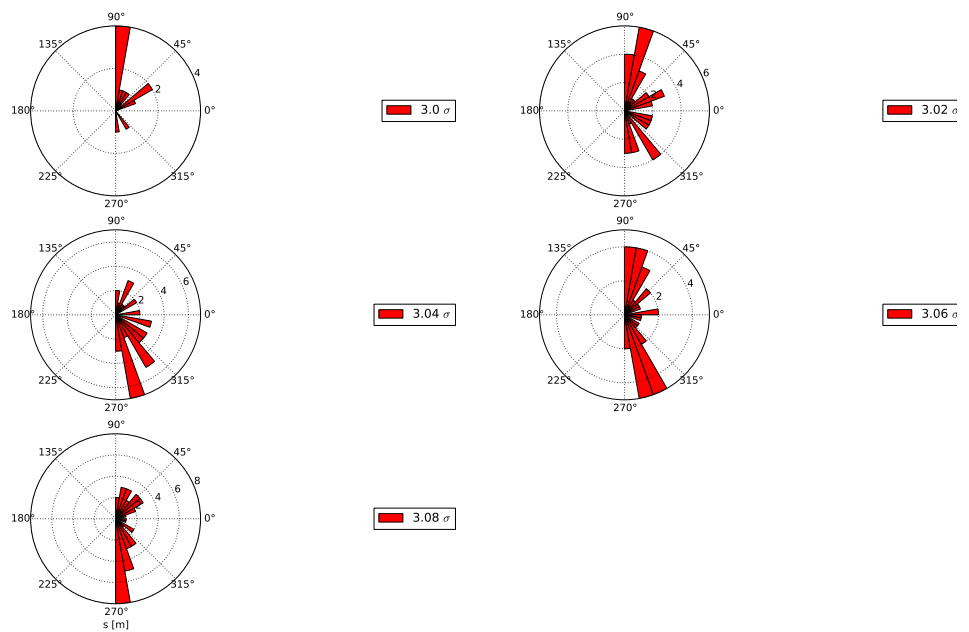


(b) CU, V halo

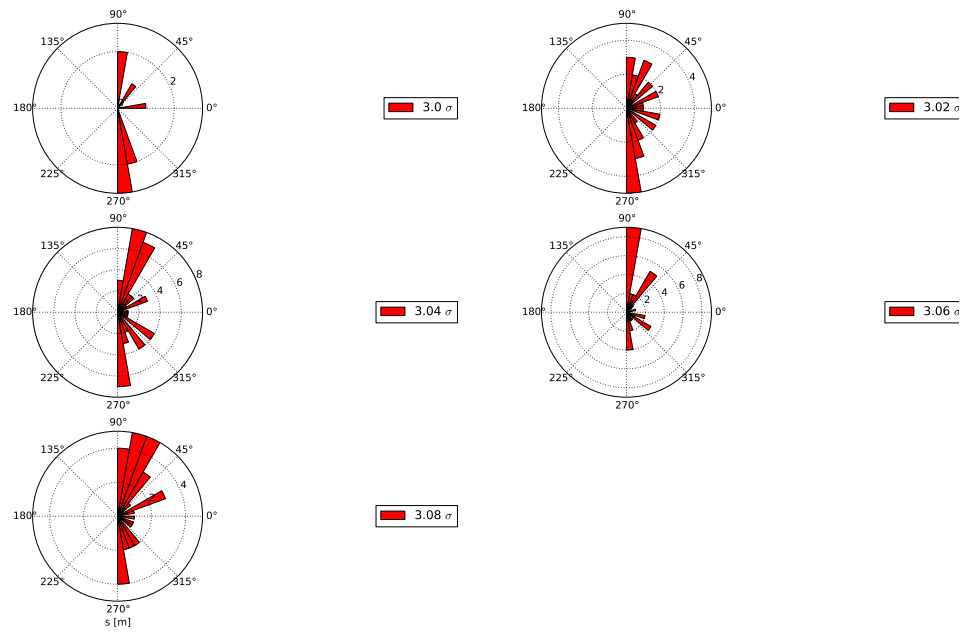
**Figure 5.88:** Number of particles lost per m outside the collimation-LSS, when using Copper secondary collimators; the arcs are the areas in yellow colour and the horizontal axis starts at 81.5 m.



(a) V halo, Graphite



(b) V halo, Tungsten



(c) V halo, Copper

**Figure 5.89:**  $x$ - and  $y$ -coordinates of particles lost per m within the first  $\sim 30$  m from the end of the collimation-LSS when vertical halo is generated.

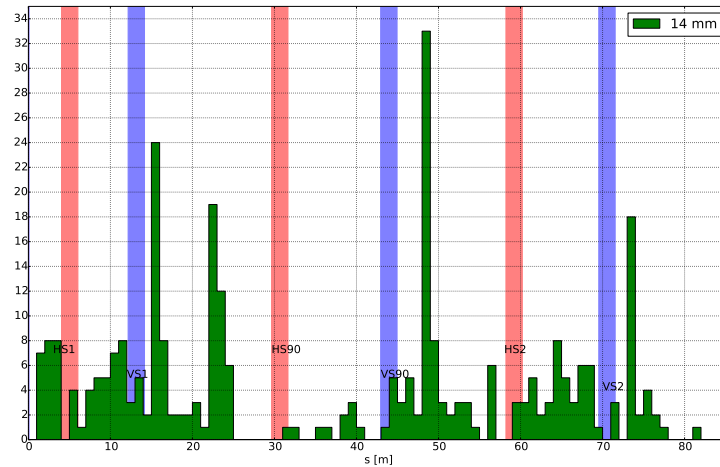
### 5.5.6 Higher statistics

Since the precision of the results presented above can be affected by statistical fluctuations, a purely horizontal and purely vertical halo were generated consisting of 20,000 particles, aiming for a better precision of the power deposited outside the collimation-LSS, and of the global collimation efficiency. Graphite primary collimators of 14 mm and 2 m long Tungsten secondary collimators were used, including the additional  $90^\circ$  collimators. Table 5.36 summarises the total number of particles that impacted at least once a collimator, the total number of lost and absorbed particles, and the inefficiency of the system for both halo types. Figs. 5.90 and 5.91 show the number of losses per m in the collimation-LSS and the rest of the ring respectively; each lost particle corresponds to a maximum power of 0.08 W. Finally, Fig. 5.92 shows the power deposition in W/m downstream the collimation-LSS for the horizontal and vertical halos; the red line corresponds to the 1 W/m radiation limit. As can be seen there is only one narrow area in which this limit is slightly exceeded (at  $\sim 95$  m from the primary collimator), where, as mentioned above, special masks can be used or the aperture of the magnet at that location can increase.

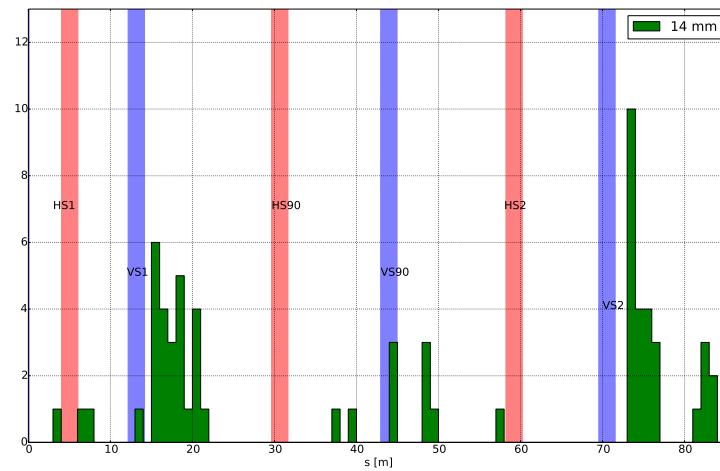
**Table 5.36:** Summary of results for higher statistics

Parameter	H	V
Tot.	9204	1507
Abs.	7996	1243
Los.	1163	257
Inef. (global) [%]	12.64	17.05





(a)

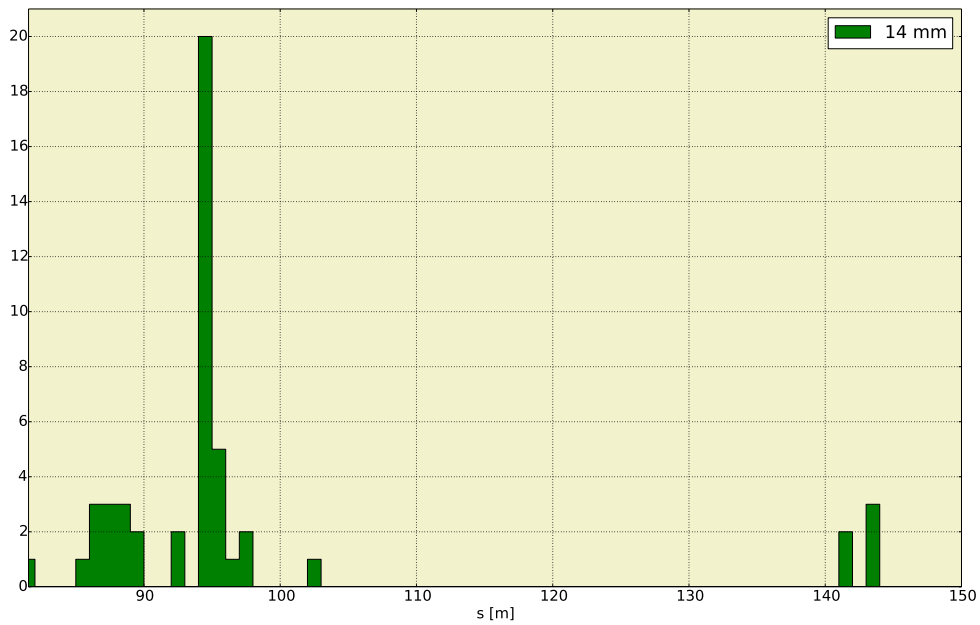


(b)

**Figure 5.90:** Number of particles lost per m within the collimation-LSS, when 20,000 horizontal (top) and vertical (bottom) halo particles were generated; each lost particle corresponds to a maximum power of 0.08 W.

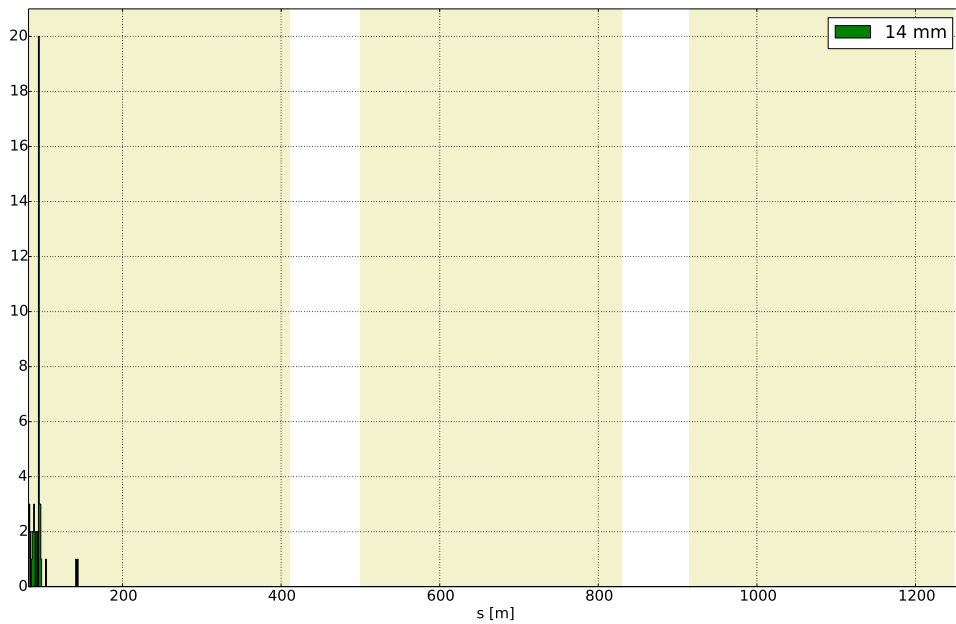


(a)

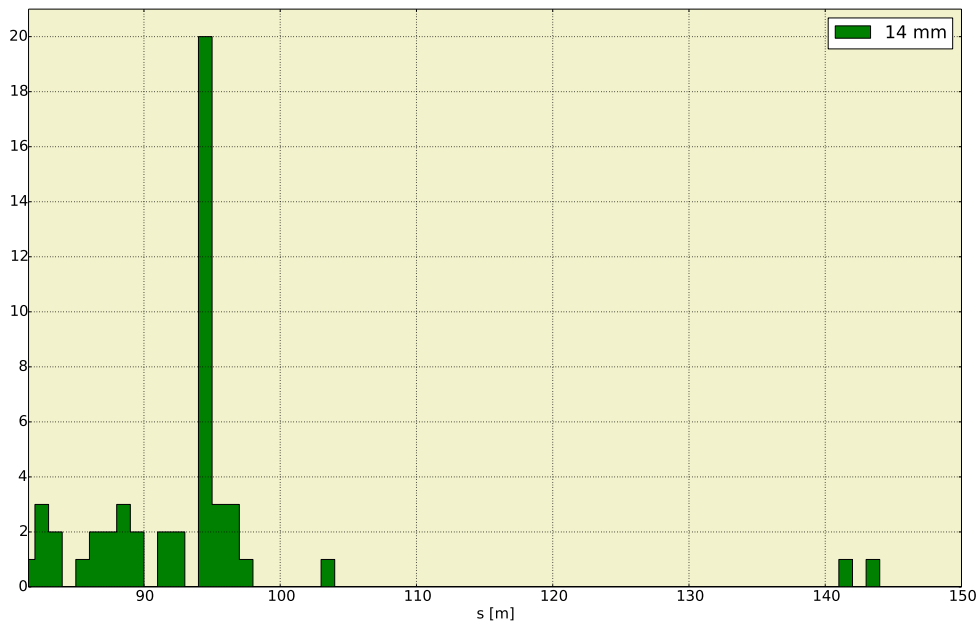


(b)

**Figure 5.91:** *H* halo, first ~70 m from the end of the collimation-LSS

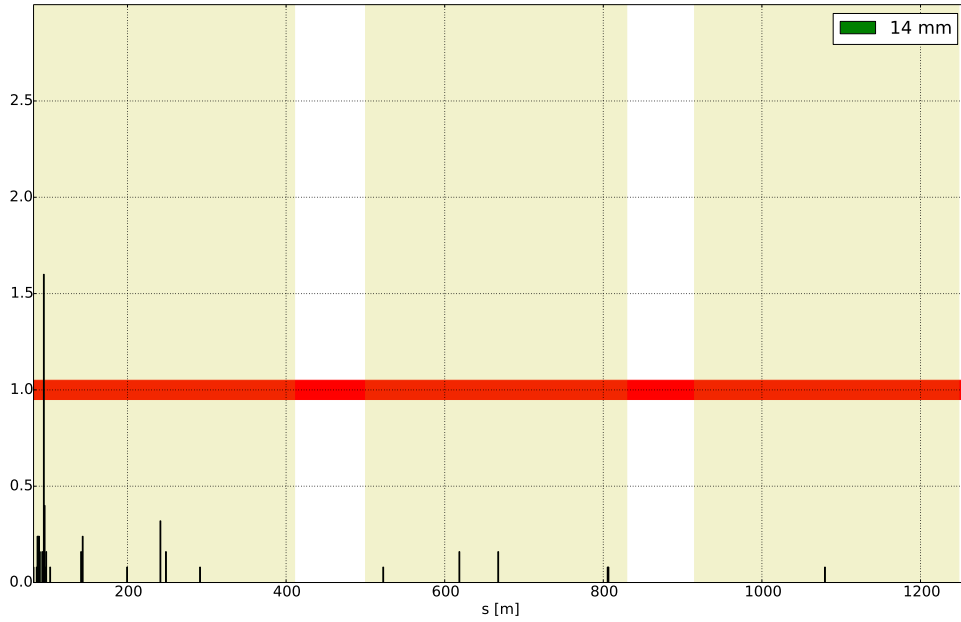


(c)

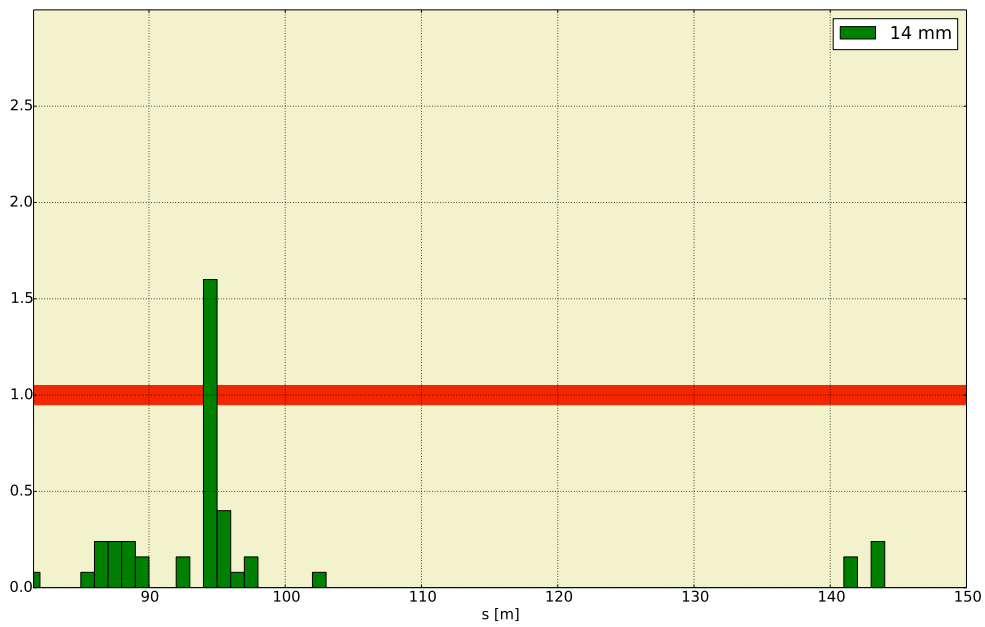


(d) V halo, first ~70 m from the end of the collimation-LSS

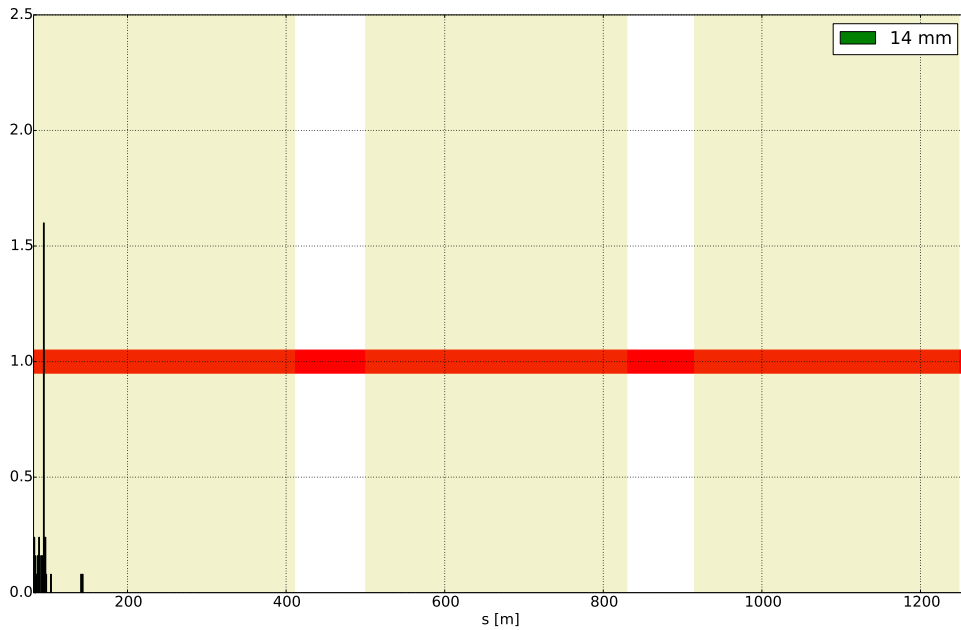
**Figure 5.91:** Number of particles lost per m downstream the collimation-LSS, when 20,000 horizontal and vertical halo particles were generated (bottom plot: first ~70 m from the end of the collimation-LSS); each lost particle corresponds to a maximum power of 0.08 W. The arcs are the areas in yellow colour; top two plots are for horizontal halo, and bottom two plots for vertical halo.



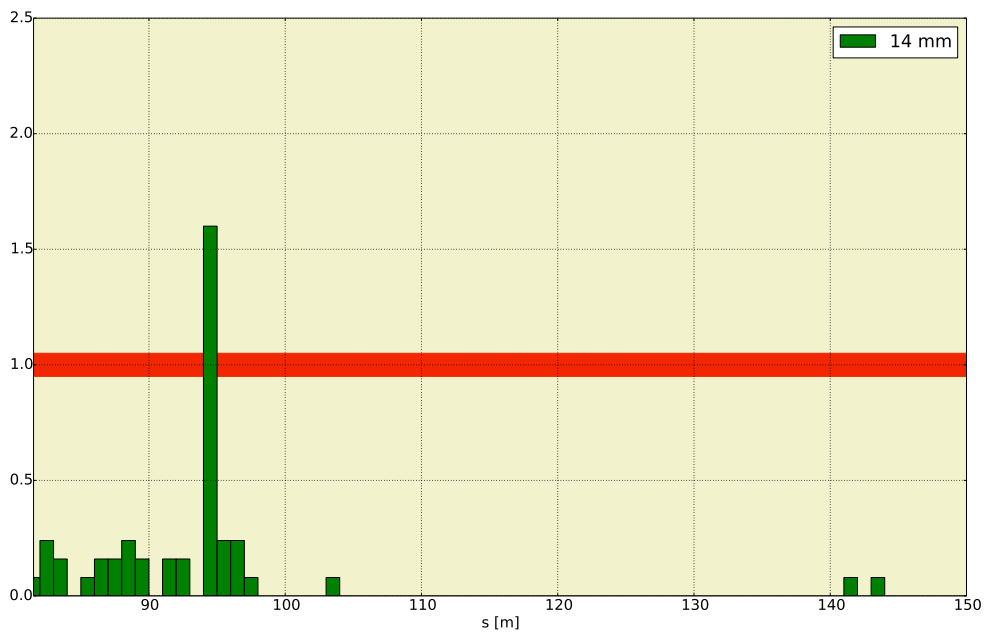
(a)



(b)



(c)



(d)

**Figure 5.92:** Losses of halo in  $W/m$  outside the collimation-LSS, given that each lost particle corresponds to 0.08 W. The red line corresponds to the 1  $W/m$  radiation limit and the arcs are the areas in yellow colour; top two plots are for horizontal halo, and bottom two plots for vertical halo.

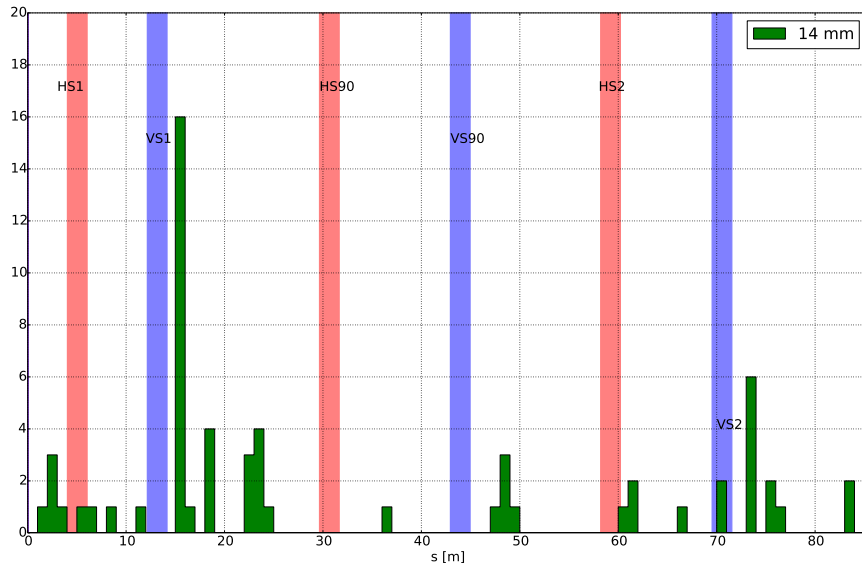
### 5.5.7 Both H and V halo

Finally a worst case scenario, in which both horizontal and vertical halos with particles occupying the largest possible horizontal and vertical phase-space was studied (2,000 particles were generated for this study). Table 5.37 summarises the total number of particles that impacted at least once a collimator, the total number of lost and absorbed particles, and the global inefficiency of the system. The losses-locations within and downstream the collimation-LSS are shown in Fig. 5.93.

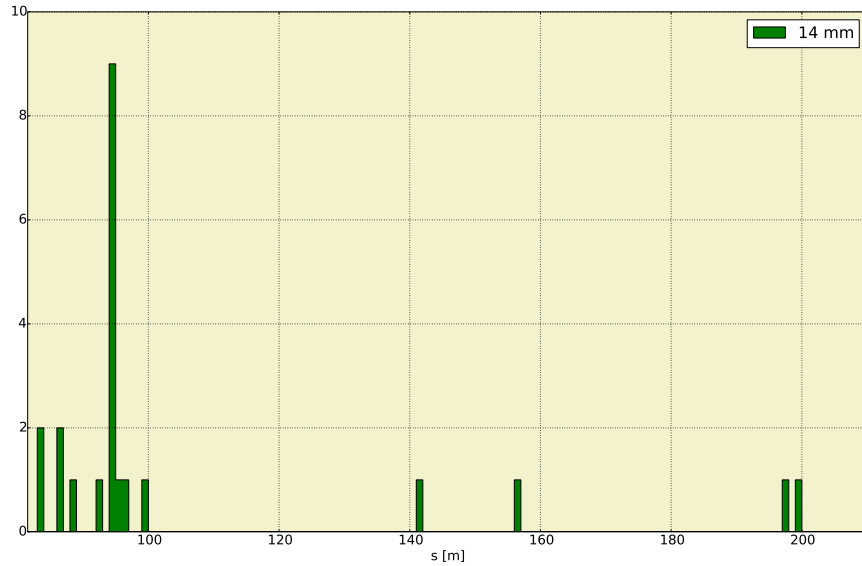
**Table 5.37:** Summary of results when generating H and V halos

Parameter	H and V
Tot.	1542
Abs.	1349
Los.	184
Inef. (global) [%]	11.93

Figure 5.94 shows the  $x$ - and  $y$ -coordinates of the particles lost within 93-98 m from the primary collimator (i.e. at the beginning of the arc downstream the collimation-LSS). Note that the first dipoles of the arc are at  $\sim 83.4$ , 88.1, 96.0 and 100.7 m from the primary collimator. As each particle carries a maximum of 0.8 W, it is essential that the loss-peak at the entrance of the arc downstream the collimation-LSS is reduced. Future studies can include additional collimators (tertiary collimators) at locations that will result in a minimisation of this losses-peak. In order to understand at which locations the placement of tertiary collimators would be beneficial, the tracks of the lost and absorbed particles have been plotted, shown in Fig. 5.95 and 5.96 respectively. Note that the number of additional collimators should be optimised to minimise the impedance issues.



(a)



(b)

**Figure 5.93:** Number of particles lost per m within and downstream the collimation-LSS, when both H and V halos were generated (bottom plot only extends to  $s \approx 200$  m as there were no losses downstream this position); the yellow colour represents the arc.

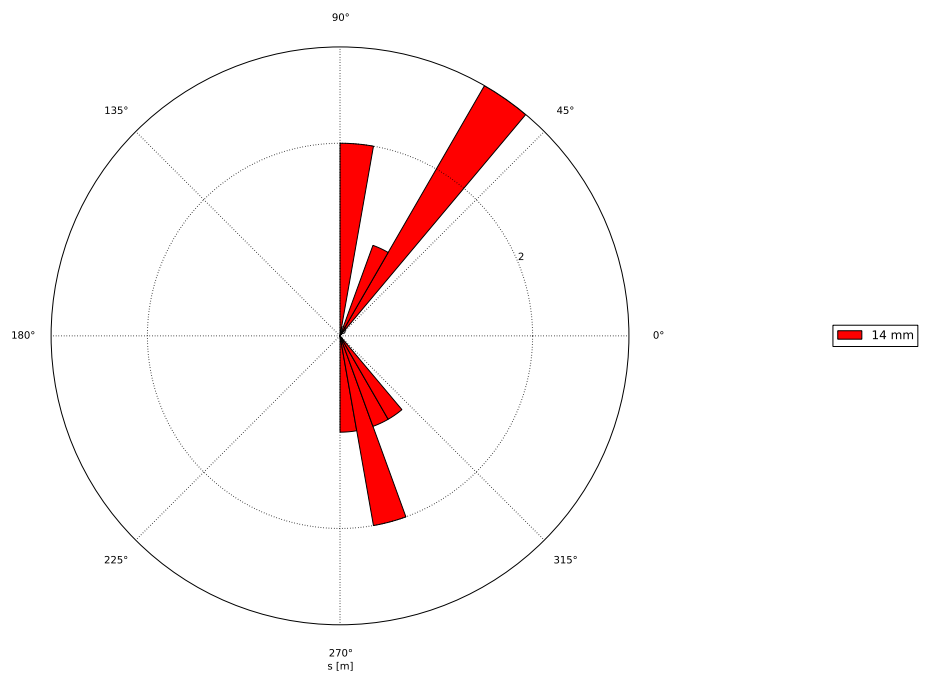


**Figure 5.94:** *x- and y-coordinates of particles lost per m between the first 93-98 m from the primary collimator.*



### 5.5.8 Summary

A collimation system is necessary in general to a beamline and is essential for HP-PS in order to absorb the halo particles at injection, before reaching the 2 MW beam power. A two-stage collimation system has been designed to protect the superconducting magnets of the HP-PS, and to ensure the power deposited in the arcs is less than the radiation limit (1 W/m). The efficiency of the system was studied for different lengths and materials (Graphite, Tungsten and Copper) of the collimators, and different halo sizes. The results of the global inefficiency and the absorptions at each collimator, together with histograms showing the local inefficiency in losses per m, and the  $x, y$  coordinates of the lost particles at specific  $s$ -locations, were provided.

For purely horizontal or vertical halos of 2,000 particles and different materials and thicknesses of the primary collimators it was found that the inefficiency of the system is smaller when Tungsten or Copper are used as primary collimators. However these two materials also result in slightly higher absorptions in the primaries due to their high atomic number. The collimation system was greatly benefited when additional  $90^\circ$  collimators were used; with these collimators in place the local losses outside the collimation-LSS resulted in power smaller, or slightly above the radiation limit, for all the primary collimators materials.

Graphite primaries of 14 mm and 2 m long secondary collimators of different materials were used to study the efficiency of the collimation system for different halo-sizes. Regardless of the secondary collimator material and halo size the losses are acceptable when horizontal halo is produced whereas for  $>3\sigma$  the losses outside the collimation-LSS increase drastically when a vertical halo is generated.

When generating 20,000 particles and 14 mm of Graphite and 2 m of Tungsten are used as primary and secondary collimators respectively, the radiation limit is exceeded only at one specific location ( $\sim 94$  m) where  $\sim 1.7$  W/m are deposited (in both cases where horizontal or vertical halos are generated).

Finally one of the worst case scenarios has been examined in which both horizontal and vertical halos of 2,000 particles in total were generated simultaneously occupying the largest possible horizontal and vertical phase-space; at 94 m the power limit was exceeded by almost 7 times. The tracks of lost and absorbed particles were provided since tertiary collimators could be added in the future in areas that could result a minimisation of the losses at the beginning of the arc; however as additional collimators will effect negatively the impedance, special masks can be used or the aperture of the magnets can increase, at locations where the radiation limit is exceeded.

FLUKA studies can be performed in the future in order to examine the heat deposition and secondary particle emission for different materials. Furthermore, diffusion studies in combination with the space-charge effect should be implemented as the inefficiency seems to change significantly for vertical halo sizes larger than the primary collimator opening.

## 5.6 Magnetic Elements

With the fixed optics and the aperture calculations previously discussed, the main characteristics of the linear magnetic elements for the different energy and injection options have been summarised.

The dipole specifications are presented in table 5.38. Iron dominated dipoles have a peak field limit of about 1.7 T, which means a maximum HP-PS achievable energy of 41 GeV. Superferric (SF) magnets, i.e. warm iron yoke magnets with superconducting coils, have to be considered for higher peak fields and ramp rates. SF magnets are low power compared with normal-conducting ones, because yoke AC losses do not account in the power balance of the cryogenic plant since the yoke is not at cryogenic temperature. The average density in the coil winding

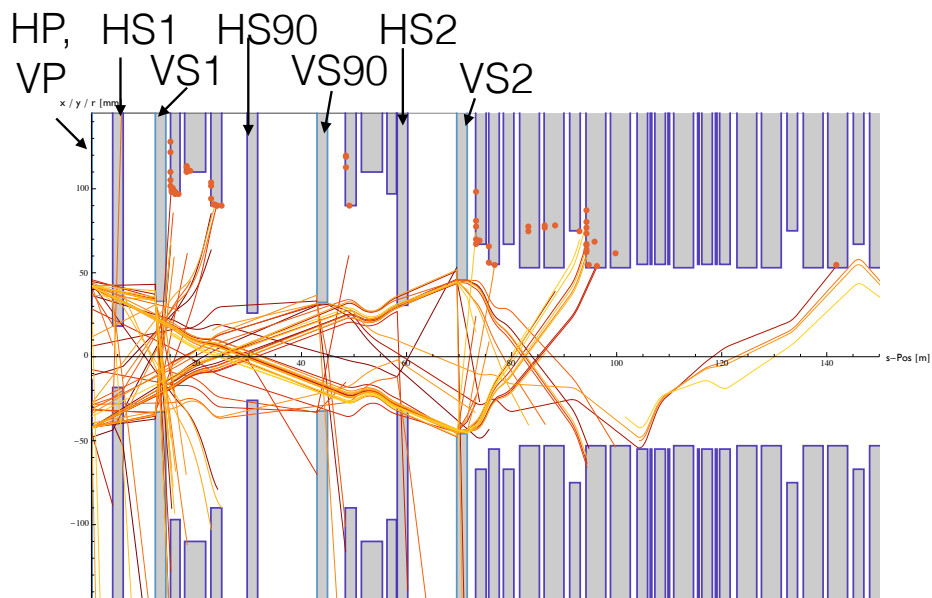
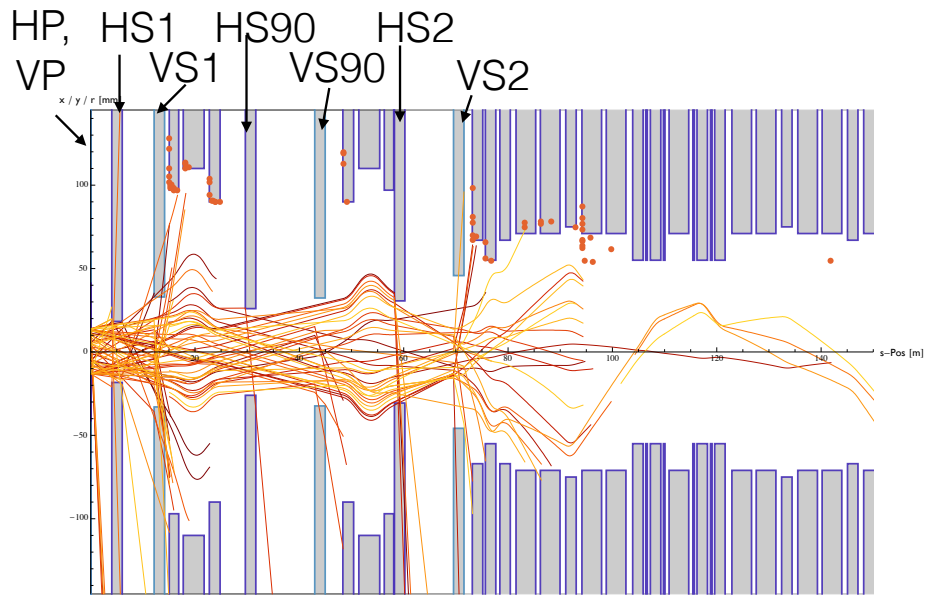


**Figure 5.95:** Horizontal (top) and vertical (bottom) tracks of particles lost within 150 m from the primary collimator.

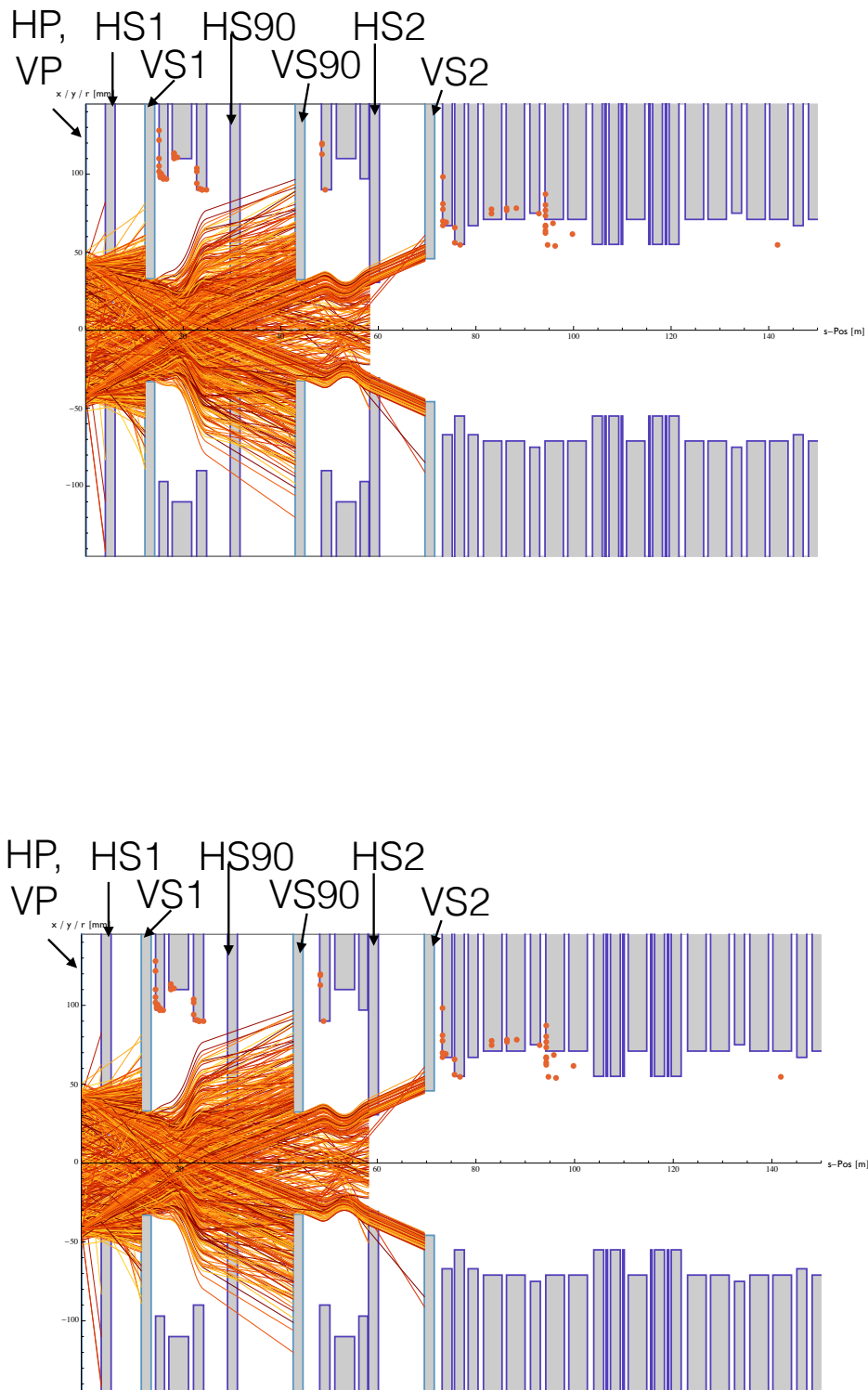


Figure 5.96: Horizontal (top) and vertical (bottom) tracks of the absorbed particles.

is of the order of  $50 \text{ A/mm}^2$  compared to  $1\text{-}5 \text{ A/mm}^2$  in the resistive case. This implies the coil needs less space and the yoke size can be reduced. Moreover, it can be taken out of the magnet mid-plane and therefore out of beam particle losses exposition and heat load. Previous studies [?] have shown that an SF dipole with similar parameters to those of the HP-PS could be built, sparing about a 50% of yoke metal and limiting AC losses to about  $1 \text{ W/m}$  of magnet.

Table 5.39 summarises the main characteristics of the HP-PS quadrupoles grouped in families. For every combination of energy and injection scheme the more pushed elements in terms of pole tip field and aperture are those of the triplet in the middle of the LSS (corresponding to families 4 to 6). This is due to the fact that in order to have enough clearance for the extracted beam, their aperture should be almost twice the aperture of the circulating beam. The high energy version and the laser injection option (due to the low vertical betas) are more demanding in terms of magnetic field.

**Table 5.38:** Dipole parameters for every HP-PS option.

	50 GeV option	75 GeV option
Field at injection, [T]	0.19	0.19
Field at extraction, [T]	2.11	3.13
Dipole ramp rate, $\frac{dB}{dt}$ [T/s]	3.5	5.5
Gap height [mm]	53	46
Length [m]	3.765	3.765

Table 5.39: Quadrupole parameters for every HP-PS option.

Family	Number	Length [m]	Radius [mm]	$B_{pt}$ [T]
<b>Foil injection, 50 GeV</b>				
1	66	2	55	0.97
2	24	2	67	0.83
3	30	2	75	0.73
4	6	1.81	97	0.33
5	6	4	110	0.79
6	6	2.06	90	0.79
<b>Laser injection, 50 GeV</b>				
1	66	2	55	0.97
2	24	2	66	0.70
3	30	2	75	0.73
4	6	1.81	99	1.04
5	6	4	124	1.22
6	6	2.06	99	1.13
<b>Foil injection, 75 GeV</b>				
1	66	2	48	1.26
2	24	2	59	1.09
3	30	2	63	0.92
4	6	1.81	75	0.38
5	6	4	84	0.91
6	6	2.06	70	0.92
<b>Laser injection, 75 GeV</b>				
1	66	2	48	1.26
2	24	2	59	0.93
3	30	2	63	0.92
4	6	1.81	80	1.27
5	6	4	100	1.47
6	6	2.06	80	1.37

# Chapter 6

## Implementation

### 6.1 Civil engineering considerations

#### 6.1.1 Overview

Infrastructure costs for the projects such as LAGUNA-LBNO, typically represent approximately one third of the overall budget. For this reason, particular emphasis has been placed on Civil Engineering (CE), to ensure a cost efficient conceptual design. This chapter provides an overview of the designs adopted for the key infrastructure cost driver, namely, civil engineering. The civil engineering requirements for the Far Detector are not discussed in this Chapter.

Two different solutions to host the LAGUNA-LBNO facilities at CERN have been investigated and presented in the following chapter. The two options, highlighted in red, are shown in Figure 6.1.

TT69 Meyrin Option A. A schematic layout of the CE complex is shown on Figure 6.2.

TT20 Preveessin Option B. A schematic layout of the CE complex is shown on Figure 6.3.

It is foreseen that the new SPL and HP-PS underground facilities could be adapted for both options. The civil engineering requirements for the SPL and HP-PS are not discussed in this report.

The main difference between the two options is actually the beam extraction (end of TCC6 for Option A, end of TT20 for Option B). The Target Area, Decay Pipe, Hadron Stop and the Near Detector, located downstream of the beam line extraction point, are the same for both options. The global depth of these new facilities and the Extraction Tunnel geometry are different for the two options.

The key features for the Option A layout, only considering the structures downstream of the beam line extraction point, are:

- X m long machine Extraction Tunnel (3.65 m wide by 3.5 m high)
- Access Shafts (143 m deep for the Target Area, 215 m deep for the Hadron Stop Area and 300 m deep for the Near Detector Area), connect the underground structures to the surface and allow access for transportation and maintenance work
- X m long by X m wide Target Area on surface
- 298 m long Decay tunnel split in two parts
- 110 m long Hadron Stopper tunnel
- X m long by X m wide Hadron Stopper Area on surface
- X m long by Xm wide Near Detector Area on surface



**Figure 6.1:** Overall CERN environmental view with the two Options foreseen



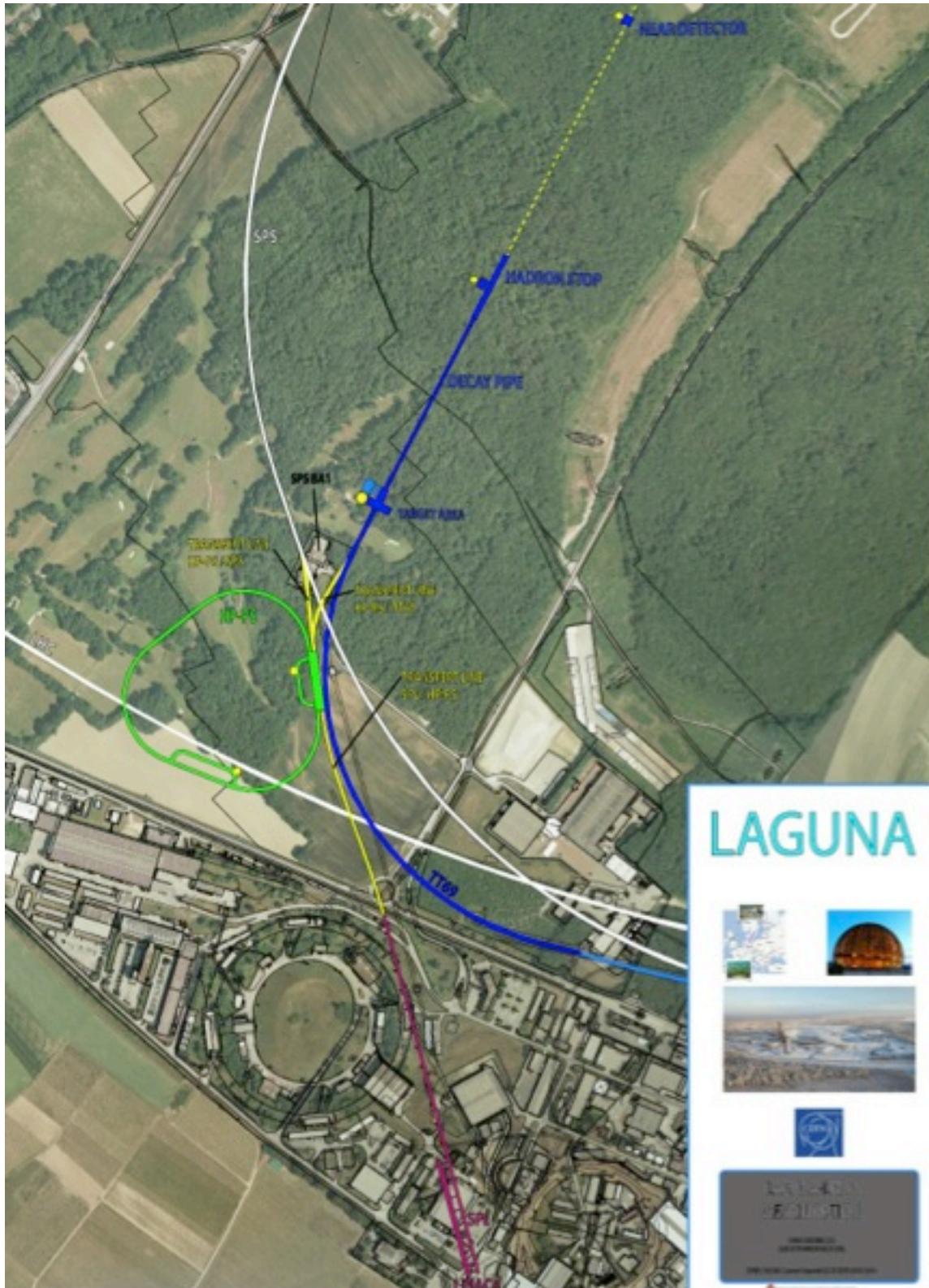
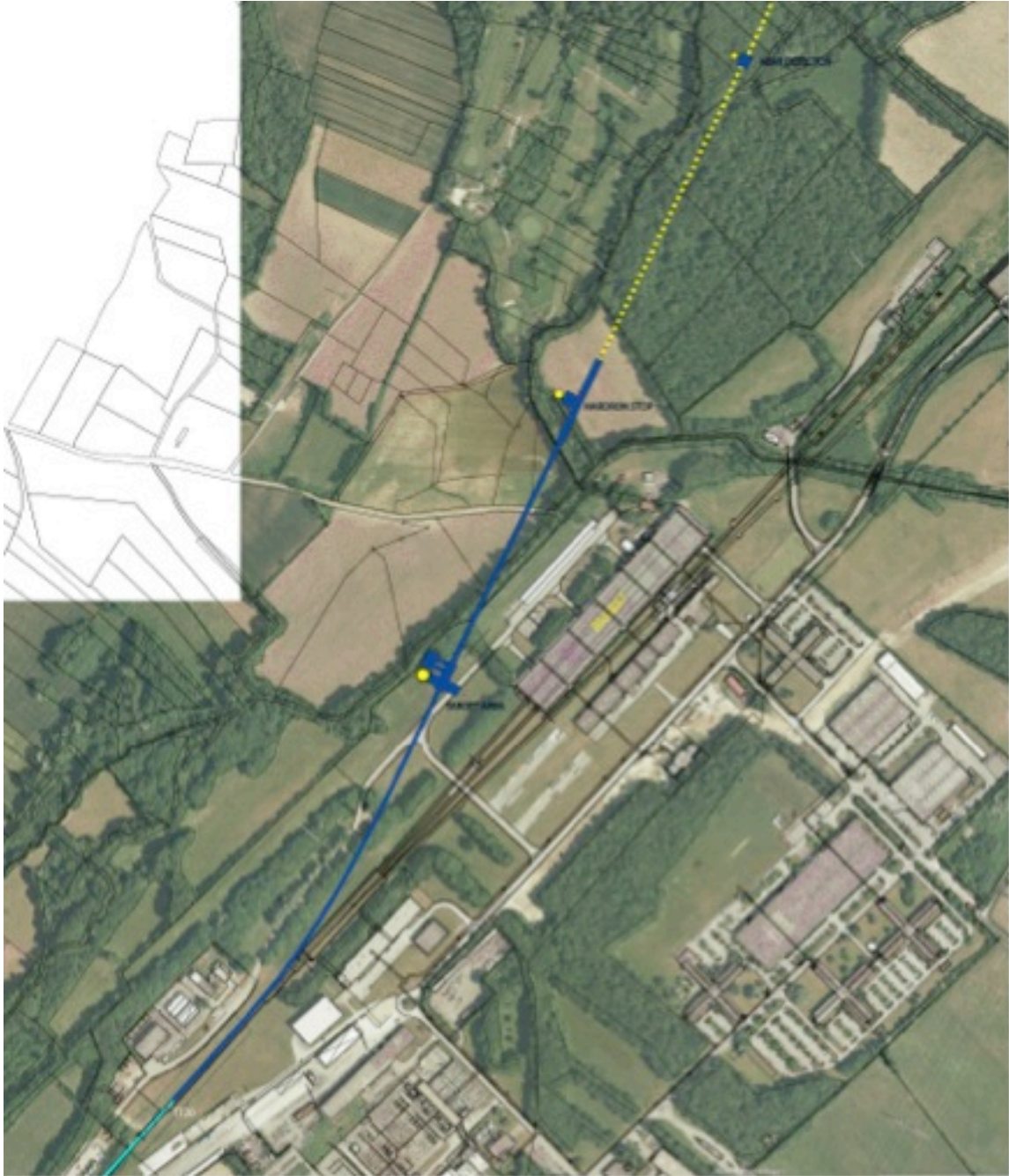


Figure 6.2: Schematic layout of the civil engineering complex for the Meyrin Option A





**Figure 6.3:** Schematic layout of the civil engineering complex for the Preveessin Option B

All underground works are within the Molasse rock, the depth of tunnels being between 35 m and 300 m. All underground works will use *®Roadheader®* excavation techniques.

The key features for the Option B layout, only considering the structures downstream the beam line extraction point, are:

- X m long machine Extraction Tunnel (3.65 m wide by 3.5 m high)
- Access Shafts (X m deep for the Target Area, X m deep for the Hadron Stop Area and X m deep for the Near Detector Area), connect the underground structures to the surface and allow access for transportation and maintenance work
- X m long by X m wide Target Area on surface
- 298 m long Decay Pipe split in two parts
- 110 m long Hadron Stopper tunnel
- X m long by X m wide Hadron Stopper Area on surface
- X m long by X m wide Near Detector Area on surface

All underground works, in this case, are within the Molasse rock with the exception of the first part of the Extraction Tunnel, which is located close to the surface, and would be constructed in the Moraine glacial deposits. Excavation in the Moraines will be executed using the *®Cut-and-Cover®* technique.

## 6.1.2 Civil Engineering

This section describes the civil engineering envisaged both on surface and underground for the LAGUNA-LBNO Projects (Option A and B).

### 6.1.2.1 Location

The proposed site for the LAGUNA-LBNO-Option A facilities are located on or near the CERN Meyrin Campus, northwest of Geneva along the French/Swiss border. Part of the envisaged structures extend in NE direction from the Meyrin (out of the existing CERN land) towards the CERN Prevezin site. This area is unpopulated and consists mainly of farmland and LHC excavation stockpiles, housing high-tension power lines.

On the other hand LAGUNA-LBNO-Option B facilities are mostly located on CERN Prevezin Site (on its northwest side). In this case only the Near Detector region is out of existing CERN land.

The CERN area is extremely well suited to housing such a large project, with the very stable and well understood ground conditions having several particle accelerators in the region for over 60 years. The civil engineering works for the most recent machine, the LHC were completed in 2005, so excellent geological records exist and have been utilised for this study to minimise the costs and risk to the project.

CERN and the Geneva region have all the necessary infrastructure at their disposal to accommodate such a project. Due to the fact that Geneva is the home of many international organizations excellent transport and communication networks already exist. Geneva Airport is only 5km from the CERN site, with direct links and a newly constructed tramway, shown in Figure 6.5, gives direct access from the Meyrin Site to the city centre.

The governments of France and Switzerland have long standing agreements concerning the support of particle accelerators in the CERN region, which make it very likely that the necessary planning permissions could be granted in a relatively short timeframe.



**Figure 6.4:** Tram stop outside CERN Meyrin Site

### 6.1.2.2 Land Features

The proposed location for the accelerator is situated within the Swiss midlands embedded between the high mountain chains of the Alps and the lower mountain chain of the Jura. CERN is situated at the feet of the Jura mountain chain in a plain slightly inclined towards the lake of Geneva. The surface terrain was shaped by the Rhone glacier which once extended from the Alps to the valley of the Rhone. The water of the area flows to the Mediterranean Sea. The absolute altitude of the surface ranges from 430 to 500 m with respect to sea level.

The physical positioning for the project has been developed based on the assumption that the maximum underground volume possible should be housed within the Molasse Rock and should avoid as much as possible any known geological faults or environmentally sensitive areas. The shafts leading to any on-surface facilities have been positioned in the least populated areas, however, as no real discussions have taken place with the local authorities, the presented layouts can only be regarded as indicative, for costing purposes only.

### 6.1.2.3 Geology

The LAGUNA-LBNO project is within the Geneva Basin, a sub-basin of the large North Alpine Foreland (or Molasse) Basin. This is a large basin which extends along the entire Alpine Front from South-Eastern France to Bavaria, and is infilled by Molasse deposits of Oligocene and Miocene age. The basin is underlain by crystalline basement rocks and formations of Triassic, Jurassic and Cretaceous age. The Molasse comprises alternating sequences of horizontally bedded sedimentary deposit layers of marls, limestone, sandstones and formations of intermediate compositions. The formations have varying strengths, material properties and layer thickness and are known to be relatively dry. Quaternary water-bearing Moraines, containing mainly gravels and sands with varying amount of clay and silt from the Würmian and Rissien glaciations, cover the Molasse.

The region is generally considered to be a "low risk" seismic area.

Figure ?? shows a simplified layout of the LHC.

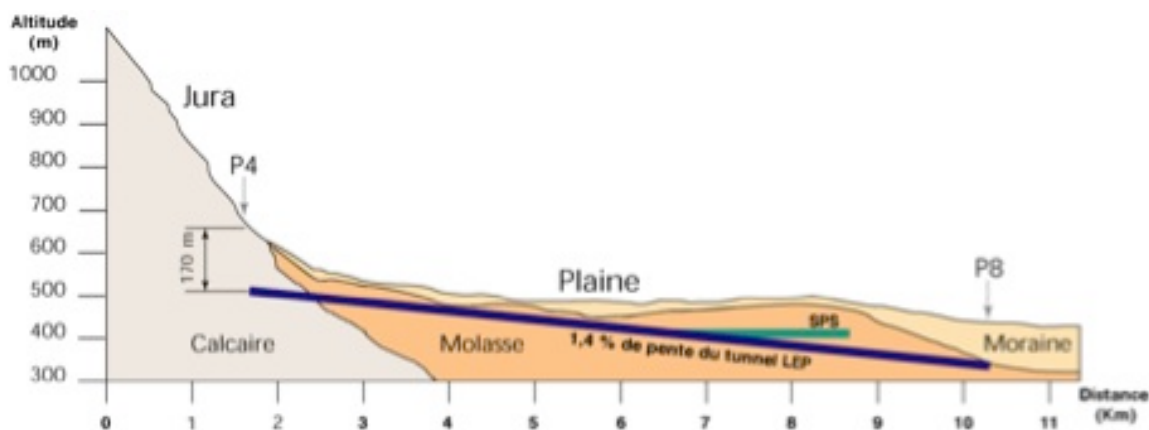


Figure 6.5: Simplified cross section of the LHC housed mostly in Molasse Rock

Figure 6.7 shows a typical geological borehole log for the Moraines nearby the LAGUNA-LBNO-Option B area (extract from the CENF geotechnical report source).

Figure ?? shows a typical geological borehole log that highlights the typical alternating sequences of horizontally bedded sedimentary within the Molasse deposit layers. The borehole is located on the LAGUNA-LBNO-Option A area, nearby the SPS BA1 (extract from SPS geotechnical report source).

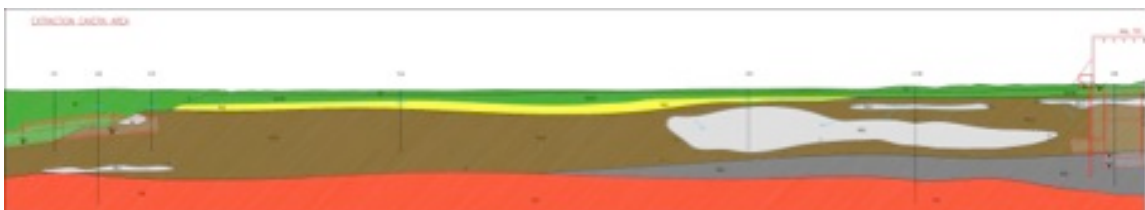
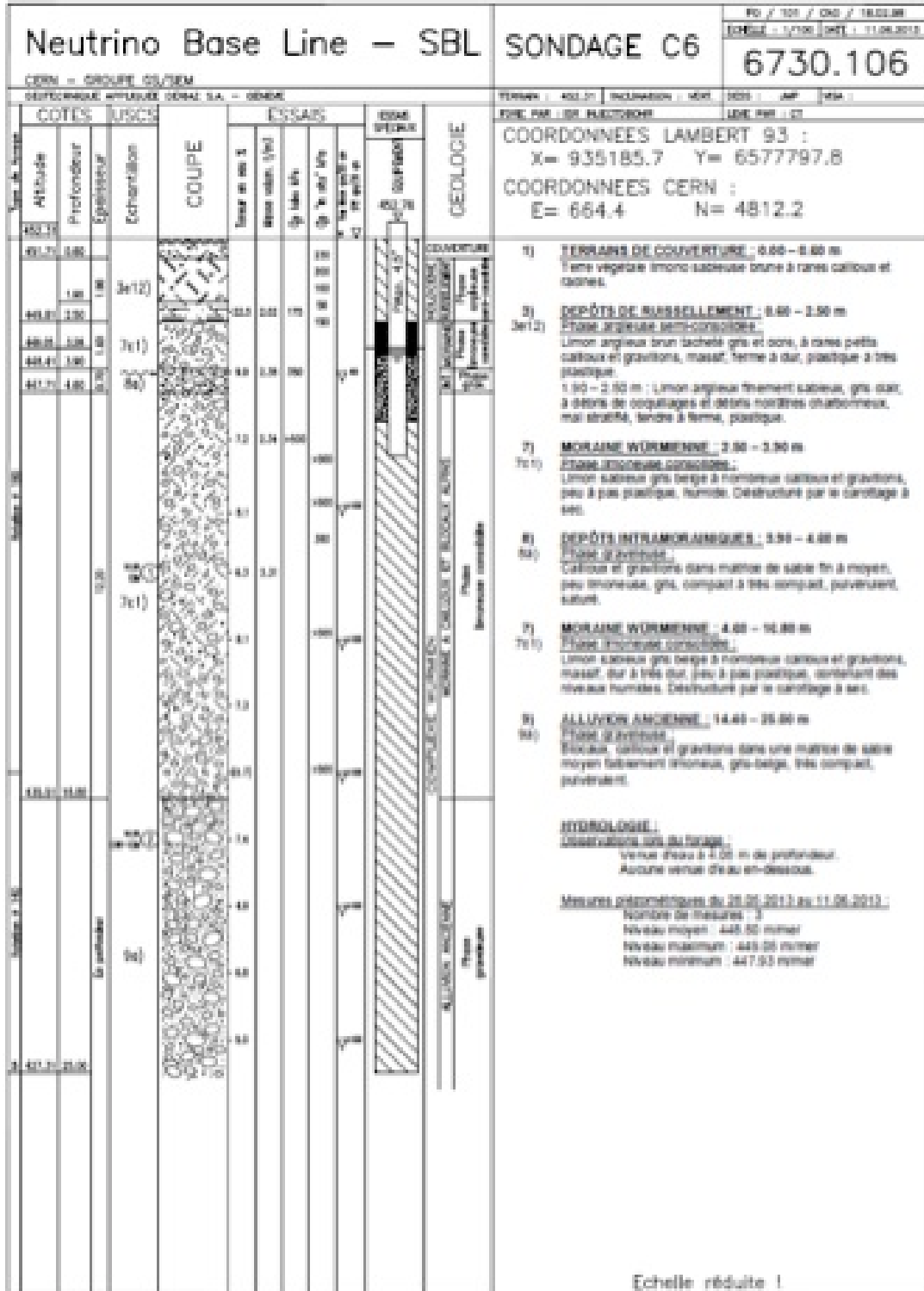
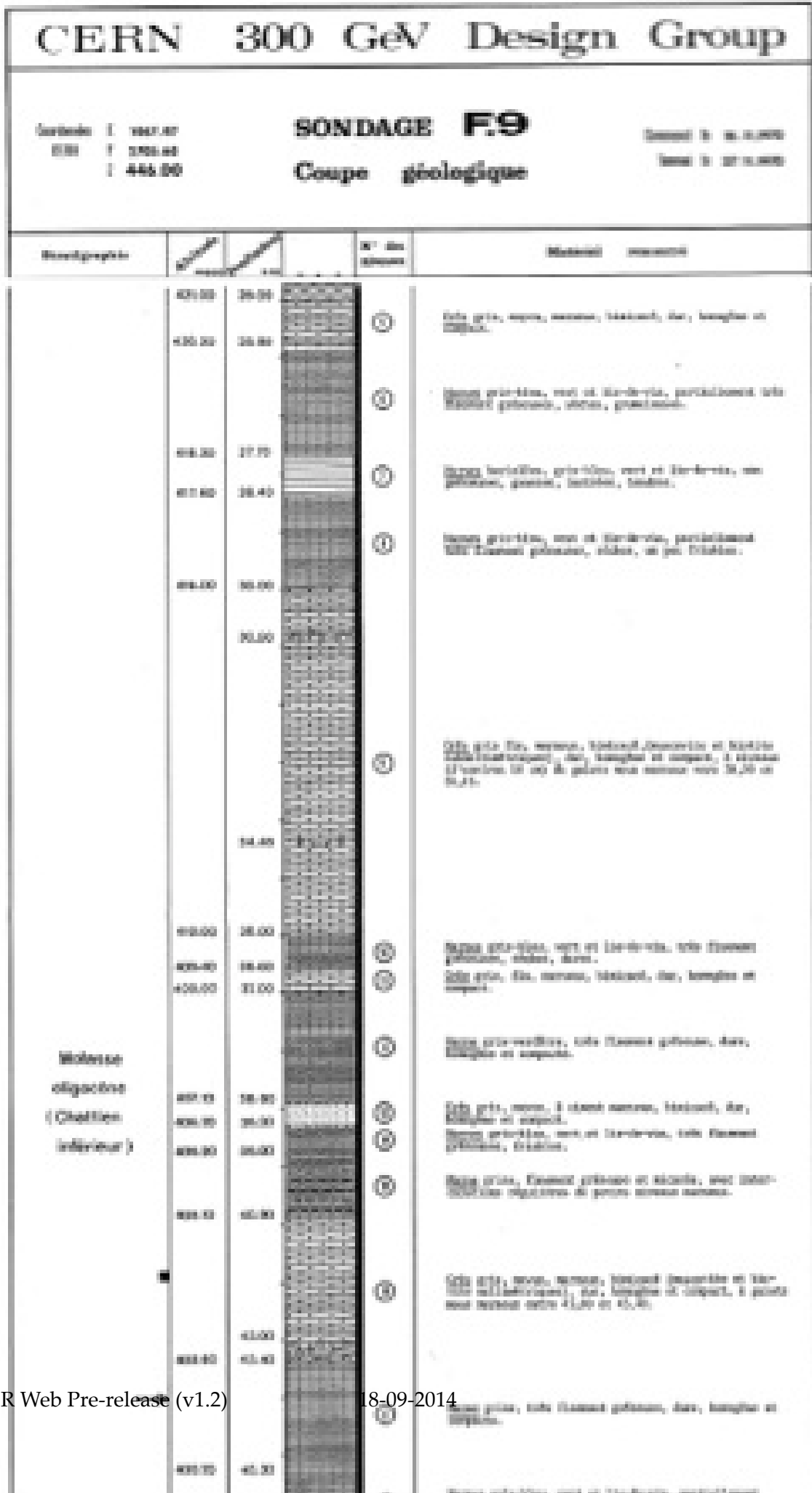


Figure 6.6: Typical geological borehole log and long profile for the area.





#### 6.1.2.4 Site Development

As most of the new works are on a close to existing facilities, it is assumed for the CDR that the existing facilities such as restaurant, main access, road network etc are sufficient and have not been costed. However, for the parts located outside the existing fence line, but within CERN property, the following items will have to be included in the costs:

- Roads and car parks
- Drainage networks
- Landscaping and planting
- Spoil dumps
- Temporary facilities needed for construction works

#### 6.1.2.5 Construction Methods

Excavation of the underground complex will mostly be executed by road header type machines. Where appropriate (Extraction tunnel first part within Option B), the undergrounds tunnels will be excavated using the *cut-and-cover* technique. This construction method was recently used for the construction of the 100m long LINAC4 injector for the LHC (see figure ??).



**Figure 6.8:** *Cut-and-Cover* excavation technique at LINAC4 (left) and the road header machine (right)

Any new shafts that have to pass through substantial layers of water bearing moraines (for example at CMS) will have to utilize the ground freezing technique. This involves freezing the ground with a primary cooling circuit using ammonia and a secondary circuit using brine at  $-23^{\circ}\text{C}$ , circulating in vertical tubes in pre-drilled holes at 1.5 metre intervals. This frozen wall allows excavation of the shafts in dry ground conditions and also acts as a retaining wall.

Figure 6.9 shows this method being utilized for LHC shaft excavation at CMS.



**Figure 6.9:** ↗Cut-and-Cover↖ excavation technique at LINAC4 (left) and the road header machine (right)

#### 6.1.2.6 Junction Cavern

The Junction Cavern provides the starting point for the new extraction tunnel. Two different considerations can be made about the two options envisaged. For the Meyrin Option A, the existing TT61 and TN facilities can be adapted, as shown in Figure ??, with the aim to provide the required space to install the new machines for the LAGUNA-LBNO Project. Approximately X m length of existing machine and services will have to be removed to allow demolition works to be executed.

For the Preveessin Option B the Junction Cavern consists of Xm long new facility, as shown in Figure 6.11. Even in this case, the existing machine and services will have to be removed, for a total length of Xm, to allow the construction of this new facility.

In both cases the potential risk of the existing concrete and surrounding earth being radioactively contaminated still needs to be assessed. This could potentially have a major impact on the cost of the LAGUNA-LBNO project.

#### 6.1.3 Proton Beam Tunnel

It has been assumed for costing purposes that the internal dimensions of the X m long Extraction Tunnel for Option A and X m long for Option B, will be 3.65 m wide by 3.5 m high. This size has been determined by inserting all known machine components / services into a 2D drawings while maintaining free space for transport vehicles and safe passage of personnel.

A machine lattice file was used to determine the alignment of the new tunnels. It remains to be seen if intermediate access or ventilation shafts are required.

For both options the Extraction Tunnel slope will change along the path reaching the 18% in the final part. Consequently the floor level of the Extraction Tunnel will decrease from X masl (above sea level) to X masl for Option A and from X masl to X masl for Option B. A typical Cross Section for the machine Extraction Tunnel is shown in Fig 6.12.





Figure 6.10: New Junction Cavern in the existing TN-TT61 complex.

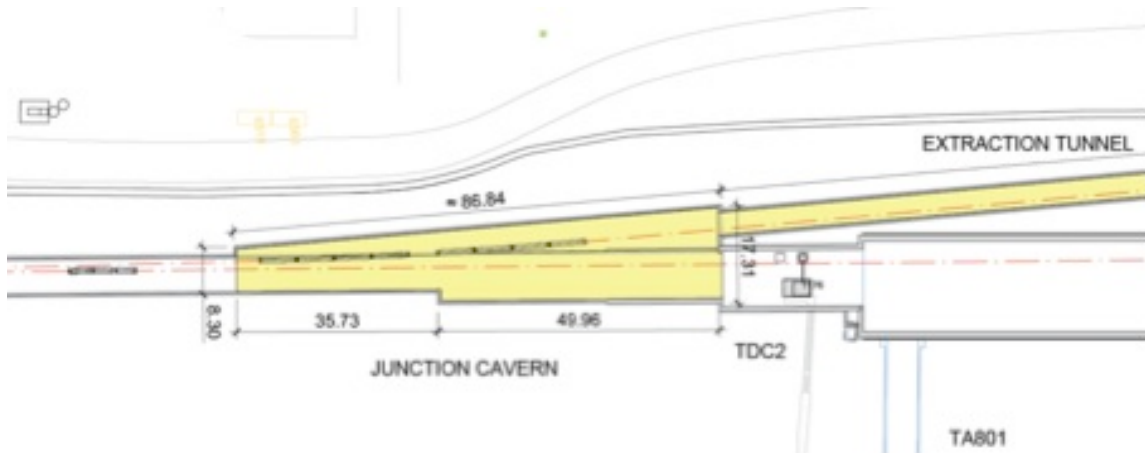


Figure 6.11: New Junction Cavern in the existing TDC2 complex (SHIP Project source).

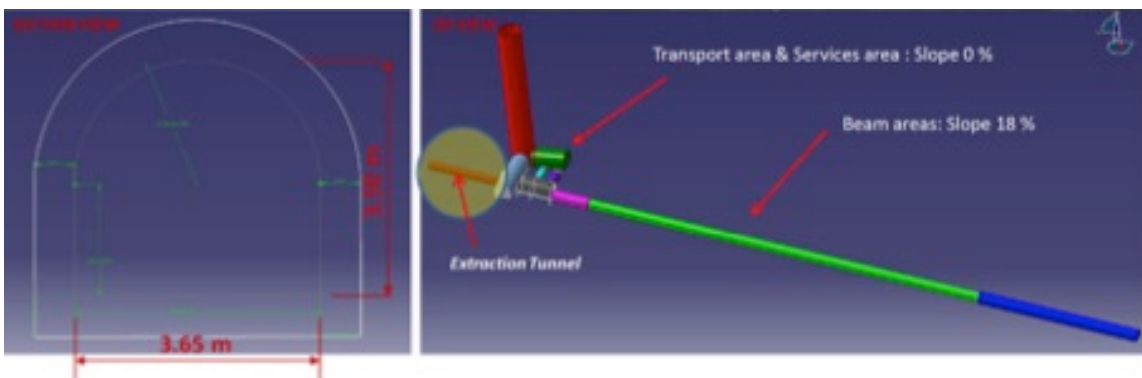


Figure 6.12: Typical machine Extraction Tunnel cross section.

### 6.1.4 Neutrino Beam Tunnels

The neutrino beam complex on surface will have approximate plan dimensions of X<sub>m</sub> by X<sub>m</sub> as shown in Figure 6.13.



**Figure 6.13:** Plan view of surface buildings for the target cavern.

The underground structures of the neutrino beam include: the target cavern, the decay pipe and hadron stop and the near detector cavern. They are all underground covering a total of 650.2 m of tunnels and 647.2 m of access shafts (see Figure ?? For the civil engineering studies

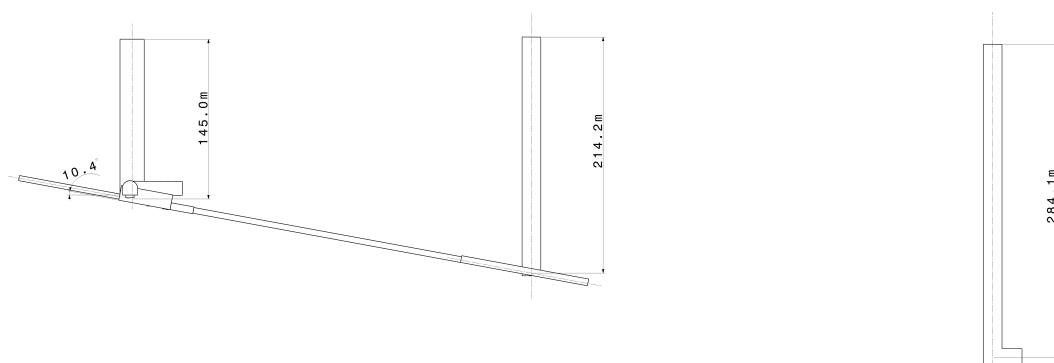


**Figure 6.14:** General 3D view of the neutrino beam underground structures.

the assembly of the structures is divided into six parts:

1. **The Transfer Area** All the objects e.g. target, horn, reflector, will be transferred through this area. This area can be subdivided in the following tunnels :

- The main access shaft - PMNU
  - The transport cavern - TCT
2. **The Service Cavern:** It will host all the services e.g. cooling and ventilation systems, vicinity electronics, water stations etc. This area is further subdivided in the following tunnels:
    - the main connection tunnel - TSG1
    - the service cavern - TCV
    - the connection Tunnel 1 - TSG2
    - the ditch 1 - TSD2
    - the connection Tunnel 2 - TSG3
    - the ditch 2 - TSD3
  3. **The Morgue Area:** The area will be used as a transient cool down zone for activated components before they are evacuated as radioactive waste. It contains the morgue tunnel with three pits for storing targets, horn and reflector assemblies.
  4. **The Beam Tunnel Area:** It is the beam part of the facility. This area includes the neutrino beam elements (the target, horn and reflector) the decay pipe, the hadron stopper and all the secondary technical infrastructure such as concrete blocks, cooling pipes, helium vessel etc. This area can be subdivided in the following tunnels :
    - the Proton Beam Tunnel - TTX
    - the target Chamber Tunnel - TCC
    - the upstream Decay Pipe Tunnel - TCD1
    - the downstream Decay Pipe Part Tunnel - TCD2
    - the Hadron Stop Tunnel - TNM
    - the Hadron Stopper Access Shaft - PMHS
    - the Connection Tunnel - TSGN
  5. **The Hot Cell Area:** - TCHS that includes the hot cell where remote operations on the target unit and the horns can take place.
  6. **The Near Detector Area:** - TCND A separate zone with its own access shaft that hosts the near detector assembly.

All the tunnels in the Transfer Area, Service Area, Morgue Area and Near Detector Area are horizontal, conversely to all the tunnels in the beam areas that are following a slope of 18% which is the slope determined by the bending of the beam in order to point to the far detector at Pyhäsalmi. In Table ?? the key parameters for the civil engineering tunnels are summarised.

In the following sections a short description of the underground areas of the facility is given.

#### 6.1.4.1 The transfer area

##### The main access shaft

It is a 20.0 m diameter shaft 140.0 m deep (for Option-A) that connects the underground structures at the bottom to the surface hall and allows access for transportation and maintenance work as well as the passage of the required services for the underground facilities. The shaft

Table 6.1: default

Underground Structures	Length or Inner Diameter (m)	Inner Floor Width or Diameter (m)	Inner Height (m)
<i>Transfer Area</i>			
Main Access Shaft	20.0	-	140.0
Transport Tunnel	40.2	12.0	11.0
<i>Service Area</i>			
Main Connection Tunnel	46.6	5.0	5.0
Service Tunnel	27.7	12.0	10.5
Connection Tunnel 1	14.3	3.0	3.0
Ditch 1	5.0	-	4.8
Connection Tunnel 2	14.3	3.0	3.0
Ditch 2	5.0	-	6.5
<i>Morgue Area</i>			
Morgue Tunnel	22.0	12.0	11.0
<i>Beam Areas</i>			
Proton Beam Tunnel	-	3.66	3.50
Target Chamber Tunnel	45.4	8.8	11.6
Decay Pipe Part One Tunnel	22.0	5.04	5.04
Decay Pipe Part Two Tunnel	248.6	4.04	4.04
Hadron Stopper Tunnel	115.5	7.0	5.0
Hadron Stopper Access Shaft	15.0	-	215.7
Connection Tunnel	3.4	3.0	3.0
<i>Hot Cell Area</i>			
Hot Cell Tunnel	9.0	12.0	10.5
<i>Near Detector Area</i>			
Near Detector Access Shaft	15.0	-	291.5
Near Detector Tunnel	21.5	10.06	14.37

**Table 6.2:** Region volumes for the underground structures. The units are in m<sup>3</sup>.

Area	Excavation volume	Internal volume	Concrete volume
<i>Access shafts:</i>			
Target cavern	53571.54	43960.0	9611.54
Hadron stop	49162.73	38099.10	11063.63
Near detector :	66359.47	51487.64	14871.83
<i>Caverns:</i>			
Transport tunnel and morgue	10009.85	7131.02	2878.82
Service tunnel and hot cell	6326.52	4321.33	1928.19
Connection tunnel	2038.05	1039.88	998.17
Access gallery 1	319.10	114.90	204.20
Access gallery 2	319.10	115.90	204.20
Ditch 1	175.04	94.22	70.27
Ditch 2	226.35	127.59	98.75
Hadron stop access gallery	75.87	27.32	49.55
Target cavern	6901.58	4699.03	2102.34
target trench		936.36	
R-concrete shielding		696.51	
L-concrete shielding		1030.92	
Decay tunnel (part 1)	729.83	453.42	584.82
Decay tunnel (part 2)	6091.64	3621.06	4289.30
Hadron stop tunnel	5080.56	3434.39	1646.71
Near detector tunnel	3456.60	2441.74	1014.86
<b>Total</b>	<b>210843.87</b>	<b>161167.56</b>	<b>53343.11</b>

**Table 6.3:** Air or He volumes in the underground structures.

Area	Volume m <sup>3</sup>
<i>Air:</i>	
Target cavern	2099.03
Secondary areas	6350.34
<b>Helium</b>	
Target cavern	120
Decay pipe	2050.0

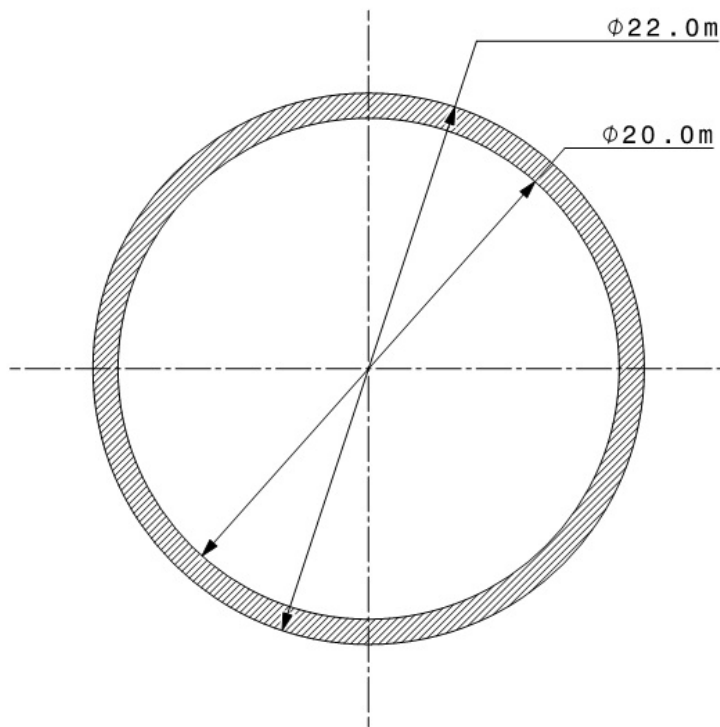


**Figure 6.15:** 2D cross-section of the main access shaft.

will host a crane, stairs, elevator, air, water and helium pipes and cables required for the installed equipment and general services underground. The typical Cross Sections of the underground facilities are shown in Figure ??.

The control cubical for the remotely operated cranes will also be installed at the bottom of the shaft.

### The transport tunnel

This tunnel will be used for the transportation of all the equipment during installation and operation of the experiment. It is the connection tunnel between the main access shaft and the beam areas. Inside the tunnel after all the objects are installed there will be two ventilation doors. The tunnel will host a crane, as well as air pipes. The width of the tunnel floor slab is 12.0 m, and it has a height of 11.0 m. The total length of it is 40.2 m.

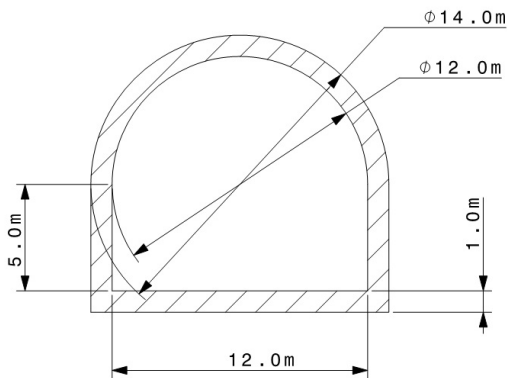


Figure 6.16: 2D cross-section of the transport and morgue tunnels.

#### 6.1.4.2 The service cavern - TCV

##### The connection tunnel

This tunnel connects the main access shaft with the service cavern. The tunnel will host mainly pipes for water, helium, electricity etc. The width of the tunnel floor slab is 5.0 m, and it has a height of 5.0 m. The total length of it is 46.6 m. the crane remote control room.

### **The service cavern**

The service cavern will be divided in two parts, to separate the services related to the radioactive areas from the general ones. A metallic structure would allow installation in two floors. In particular, the cavern will host:

1. the air handling units for: the target cavern, the proton beam tunnel, the hot cell
2. the He handling units for the target cavern and decay pipe vessel,
3. the cooling water units for the: shielding blocks, the horn and reflector, and the decay pipe,

Space is foreseen for electronics racks for the various equipment and beam instrumentation. The width of the tunnel floor slab is 12.0 m and it has a height of 10.5 m. The total length of it is 27.7 m.

### **The hot cell**

The hot cell is adjacent to the service cavern. It has a width of 12.0 m, a height of 10.5 m and is 9.0 m long sufficient to accommodate the horn/reflector and allow insertion or extraction of the target unit.

### **The connection galleries**

The service tunnel is connected with the beam area with two service galleries. Due to the steep slope the two galleries are at variable depth; the first at -4.8 and at -6.5 m. The two service galleries are 3.0 m height and 3.0 m wide and have a length of 14.3 m each.

### **The morgue area**

This tunnel will be used as a cool down zone (morgue) for all the radioactive objects before starting transporting them to the surface. The width of the tunnel floor slab is 12.0 m and it has a height of 11.0 m. The total length of it is 22.0 m. Three pits are foreseen dimensioned to accommodate a horn/reflector each. The pits will be covered with concrete shielding blocks to provide the necessary shielding.

### **The proton beam tunnel**

The last part of the proton beam tunnel will be constructed at 18% slope, pointing to the far detector direction. The tunnel will be 3.66 m wide and 3.5 m height. It will be equipped with either a rail system or an overhead gantry crane to allow for the installation of the beam magnets and other components.

### **The target cavern**

The target cavern hosts the main components of the neutrino beam. The width of the tunnel floor slab is 8.8 m and it has a height of 11.6 m. The total length of it is 45.4 m (see Figure 6.17). After the installation of the decay pipe, the side walls of the cavern will be filled with concrete to provide the necessary shielding for the radiation, and form the trench where the neutrino beam elements and iron shielding will be installed.



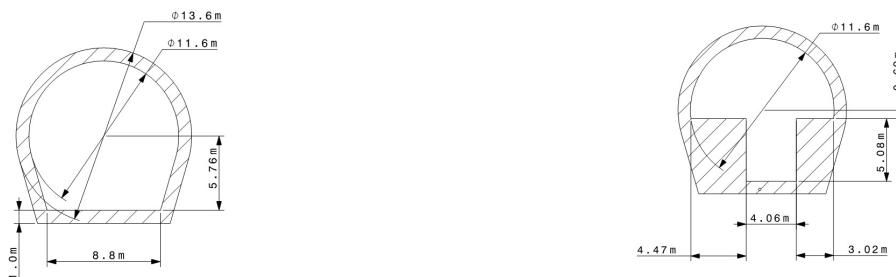


**Figure 6.17:** 2D cross-section of the target cavern before (left) and after the side concrete walls are constructed (right).

### 6.1.5 Decay and Hadron Stop tunnels

The decay tunnel follows the target cavern and is also constructed at 18% slope and has a total length of 270.6 m ending at the hadron stop cavern. The tunnel hosts the 3.0 m diameter decay pipe that is embed in 0.8 m of concrete all around. The construction of the decay pipe tunnel is similar to CNGS [?] following the same requirements and constraints. To cope with the high radiation levels, the first 22.0 m of the tunnel have a thicker (1.5 m wide) concrete shielding.

Two 200 mm diameter pipes are also embedded in the concrete shielding all along the decay pipe.

#### 6.1.5.1 The hadron stop tunnel

The Hadron stop tunnel (7.0 m wide, 5.0 m height, 115.5 m long) completes the complex. It is also build following the 18% slope of the beam tunnels. The 100 m of the iron shielding are separated in four parts each approx. 25 m long. A concrete wall separates the first part of the iron shielding from the rest. This to keep the air activation contained and allow easy access in the rest of the areas.

The gap at the end of the first and second part of the shielding is larger in order to accommodate the two muon statins (see Figure 6.18).

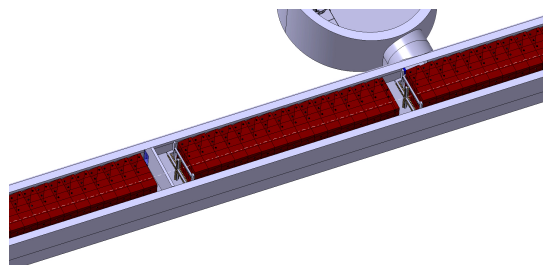


**Figure 6.18:** 3D top view of the hadron stop with the position of the muon detectors.

Access to the hadron stop is done with a dedicated shaft (215.7 m deep, 15.0 m inner diameter) connected at approx. 50 m from the front face of the hadron stop. The tunnel will be

equipped with a crane, stairs and elevator for personnel access.

### 6.1.6 Near Detector Area

Access to the near detector cavern is done with a 291.5 m deep, 15.0 m inner radius shaft. The shaft will host a crane, stairs, and an elevator for personnel access. The detector cavern is 10.06 m wide and has a height of 14.37 m to accommodate the overhead crane. The length of the cavern is 21.5 m. A metallic structure at the bottom of the shaft will provide the necessary surface area to install the services and proximity electronics of the detector.

### 6.1.7 Civil Engineering Cost Considerations

The cost estimate for LAGUNA-LBNO Project will be prepared, based on the layouts presented in this chapter. The estimate includes all aspects of construction, final engineering designs and construction management. Many of the rates used to formulate this estimate will be based on real construction costs from LHC experience (1998-2005).

### 6.1.8 Civil Engineering Scheduling and Resource Considerations

A preliminary schedule, shown in Table 6.19, has been studied for the construction of the LAGUNA-LBNO Project using the knowledge acquired from the construction of previous similar schemes at CERN. A lot more work will be needed to clarify the details of this schedule but the current sequence seems to indicate 3 years civil engineering during normal machine operations, followed by a one year period to demolish and rebuild the junction cavern. Two years are needed for pre-construction activities (design studies, building permits, tendering) after formal approval of the project.

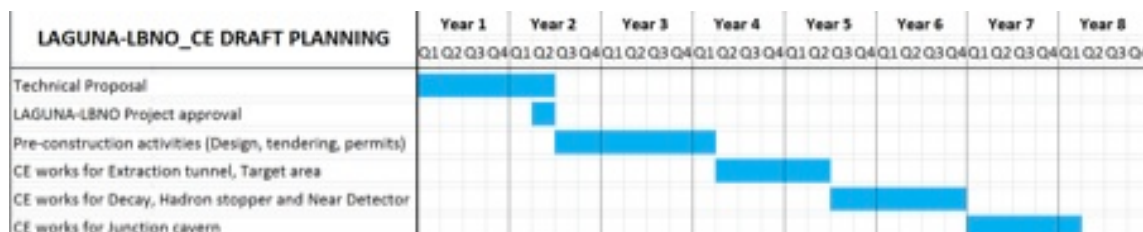


Figure 6.19: CE planning.

## 6.2 Handling and transport

For the handling and transport activities in the facility during installation, operation and future dismantling, a set of cranes will be installed, divided in two categories:

- Standart

**Standard cranes** used when no particular radiation constraints apply. These cranes can be operated remotely from a fixed or portable control unit. Redundancy levels as of normal industrial cranes apply.

**Remotely operated cranes** used in areas where increased radiation levels are expected. They will be operated remotely from a fixed control unit and will be equipped with cameras and other instruments to facilitate the operations.

A detailed description of the foreseen cranes and installation sequences is described in the next sections.

## 6.2.1 Standard cranes

### 6.2.1.1 Main access shaft crane

This crane is located at the surface building on top of the main access shaft of the target cavern. It is a double-girder overhead crane that will be installed on rails at approximately 10 m above the floor. The 40 t hoist will be used for handling items and to transport them to the cavern.

Crane characteristics were defined to accommodate the handling requirements of the major components of the experiments (see Table 6.4). Speeds values were chosen to guarantee that average duration time of each handling operations will be appropriated, delicate assembly work will be carried out operating the crane at its minimum speeds.

**Table 6.4:** Key design parameters for the Target Cavern access shaft crane.

Parameter	Unit	Value
Span	mm	25000
Clearance between girder and the floor	m	10
Long travel speed	m/min	0.4 - 8
<i>Main hoist</i>		
Capacity	tonnes	40
Lifting height	m	150
Min Lifting speed	m/min	0.25
Max Lifting speed with load	m/min	30
Max lifting speed without load	m/min	0.25
Cross travel speed	m/min	0.4 - 8
Maximum lifting / braking acceleration	m/s <sup>2</sup>	1
Hook size (according to DIN 15402)		20

In Figures 6.24 and 6.23 show the foreseen installation of this crane. The design will consider that the crane will not be used frequently during its whole lifetime and not always at its full capacity (light-medium duty crane). Crane will be equipped with one additional brake acting directly on the hoisting drum in the event of failure of any elements of the hoisting drive chain (emergency brake).

### 6.2.1.2 The near detector shaft surface crane

Similar to the target cavern shaft crane, it is a double-girder overhead crane will be installed on rails at approximately 10 m above the floor. It is equipped with a 50 t hoist that will be used to transport the components of the detectors to the cavern. Crane characteristics were defined to accommodate the handling requirements of the major components of the experiments. Speeds values were chosen to guarantee that average duration time of each handling operations will be appropriated, delicate assembly work will be carried out operating the crane at its minimum speeds. In Figures ?? and ?? show the foreseen installation of this crane. The design will consider that the crane will not be used frequently during its whole lifetime and not always at its full capacity (light-medium duty crane). Crane will be equipped with one additional brake acting directly on the hoisting drum in the event of failure of any elements of the hoisting drive chain (emergency brake).

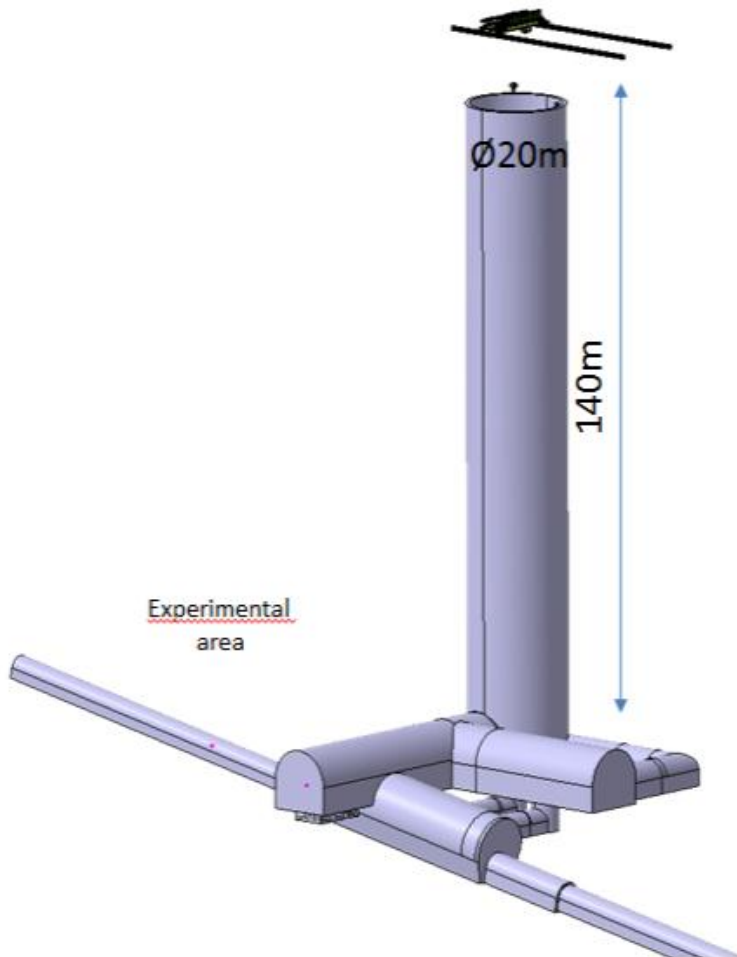


**Figure 6.20:** *The target cavern shaft and the surface crane.*

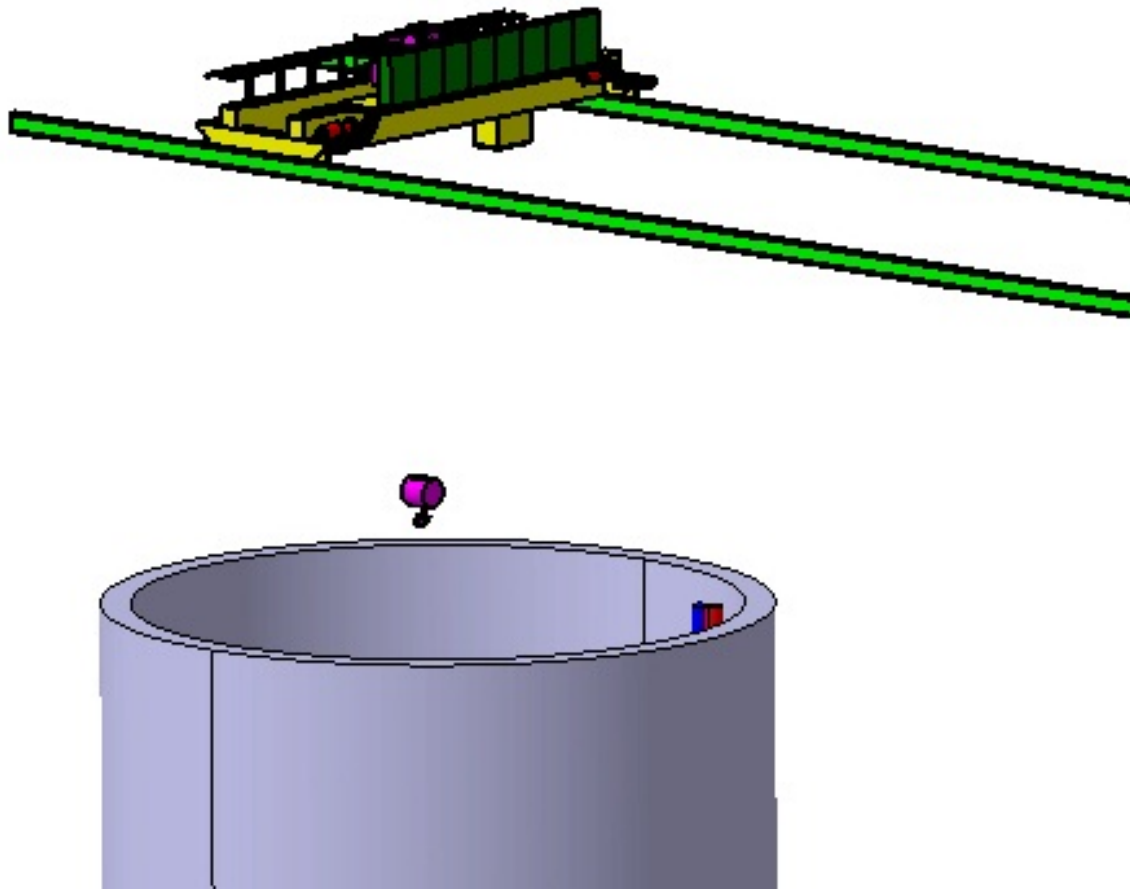
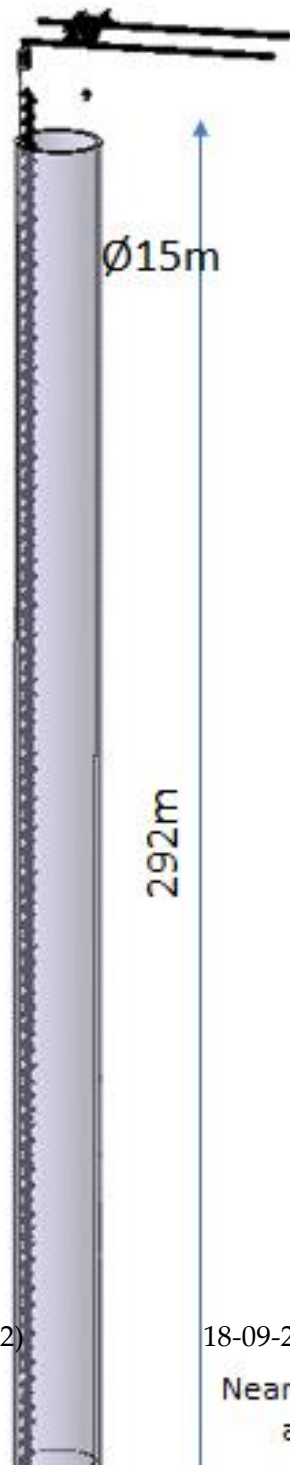
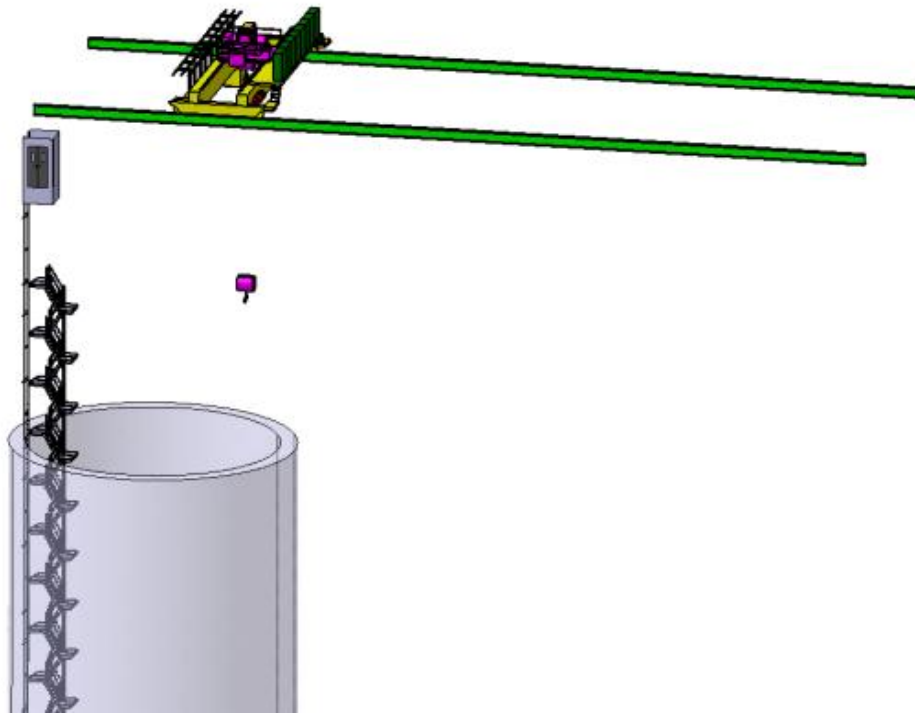


Figure 6.21: Detail on the target cavern access shaft crane.

Table 6.5: Key design parameters for the ND shaft crane.

Parameter	Unit	Value
Span	mm	17000
Clearance between girder and the floor	m	10
Long travel speed	m/min	0.4 - 8
<i>Main hoist</i>		
Capacity	tonnes	50
Lifting height	m	310
Min Lifting speed	m/min	0.25
Max Lifting speed with load	m/min	30
May lifting speed without load	m/min	0.25
Cross travel speed	m/min	0.4 - 8
Maximum lifting / braking acceleration	m/s <sup>2</sup>	1
Hook size (according to DIN 15402)		20





**Figure 6.23:** Detail of the ND access shaft crane.

### 6.2.1.3 The near detector tunnel overhead crane

A double-girder overhead crane will be installed on rails at approximately 9 m above the floor; the 50 t hoist will be used for handling items. Crane characteristics were defined to accommodate the handling requirements of the major components of the experiments. Speeds values were chosen to guarantee that average duration time of each handling operations will be appropriated, delicate assembly work will be carried out operating the crane at its minimum speeds. The key design parameters are summarised in Table 6.6. In Figures ?? shows the foreseen installation of this crane and use for the ND installation and operations. The design will consider that the crane will not be used frequently during its whole lifetime and not always at its full capacity (light-medium duty crane).

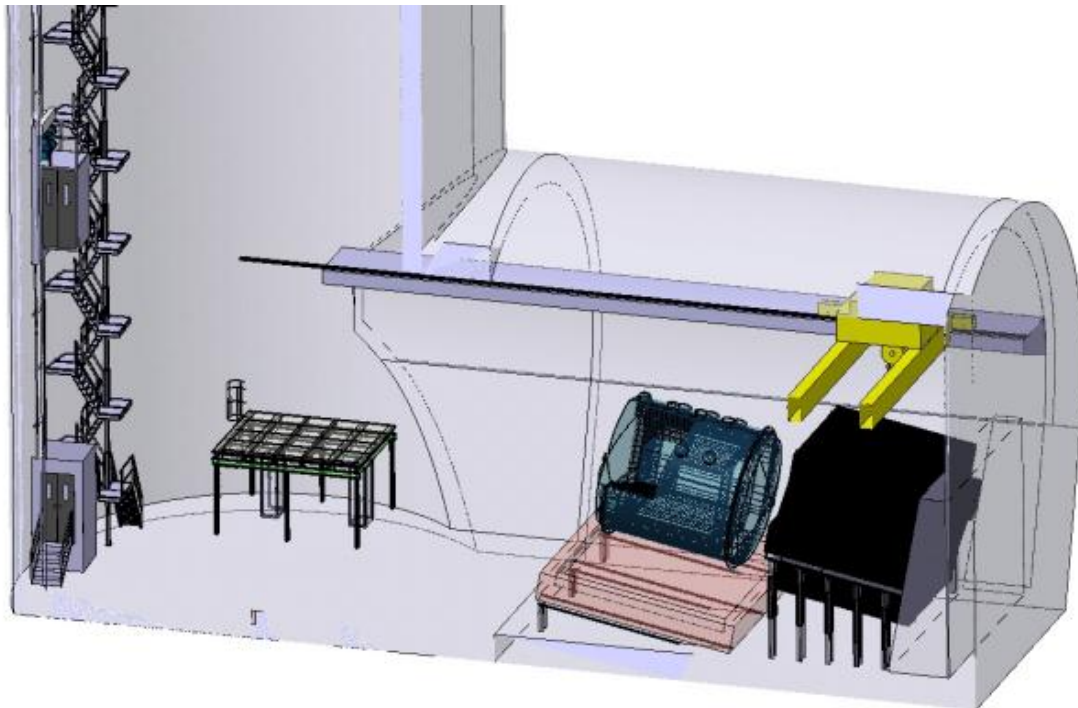
## 6.2.2 Remotely operated cranes

### 6.2.2.1 Transport tunnel overhead crane

A double-girder overhead crane will be installed on rails at approximately 7.5 m above the floor; the 40 T hoist will be used for handling the heaviest and most sensible items while a 5 T auxiliary hoist sliding on the side of one girder will be used for handling smaller objects. Crane characteristics were defined to accommodate the handling requirements of the major components of the experiments. Speeds values were chosen to guarantee that average duration time of each handling operations will be 10-15 minutes, delicate assembly work will be carried out operating the crane at its minimum speeds. The key design parameters for this crane are summarised in Table 6.7. Figure 6.25 and Figure 6.26 shows the foreseen installation of this crane and use for the ND installation and operations. The design will consider that the crane

**Table 6.6:** Key design parameters for the ND overhead crane.

Parameter	Unit	Value
Span	mm	9500
Clearance between girder and the floor	m	9
Long travel speed	m/min	0.4 - 8
<i>Main hoist</i>		
Capacity	tonnes	50
Lifting height	m	10
Lifting speed	m/min	0.25-5
Cross travel speed	m/min	0.4 - 8
Maximum lifting / braking acceleration	m/s <sup>2</sup>	1
Hook size (according to DIN 15402)		20

**Figure 6.24:** The ND access shaft surface crane.



**Table 6.7:** Key design parameters for the ND overhead crane.

Parameter	Unit	Value	
Span	mm	11500	
Clearance between girder and the floor	m	7.5	
Long travel speed	m/min	0.4-8	
Hoist		<i>Main</i>	<i>Auxiliary</i>
Capacity	tonnes	40	5
Lifting height	m	20	20
Lifting speed	m/min	0.25-5	1-10
Cross travel speed	m/min	0.4 - 8	1-10
Maximum lifting / braking acceleration	m/s <sup>2</sup>	1	
Hook size (according to DIN 15402)		20	

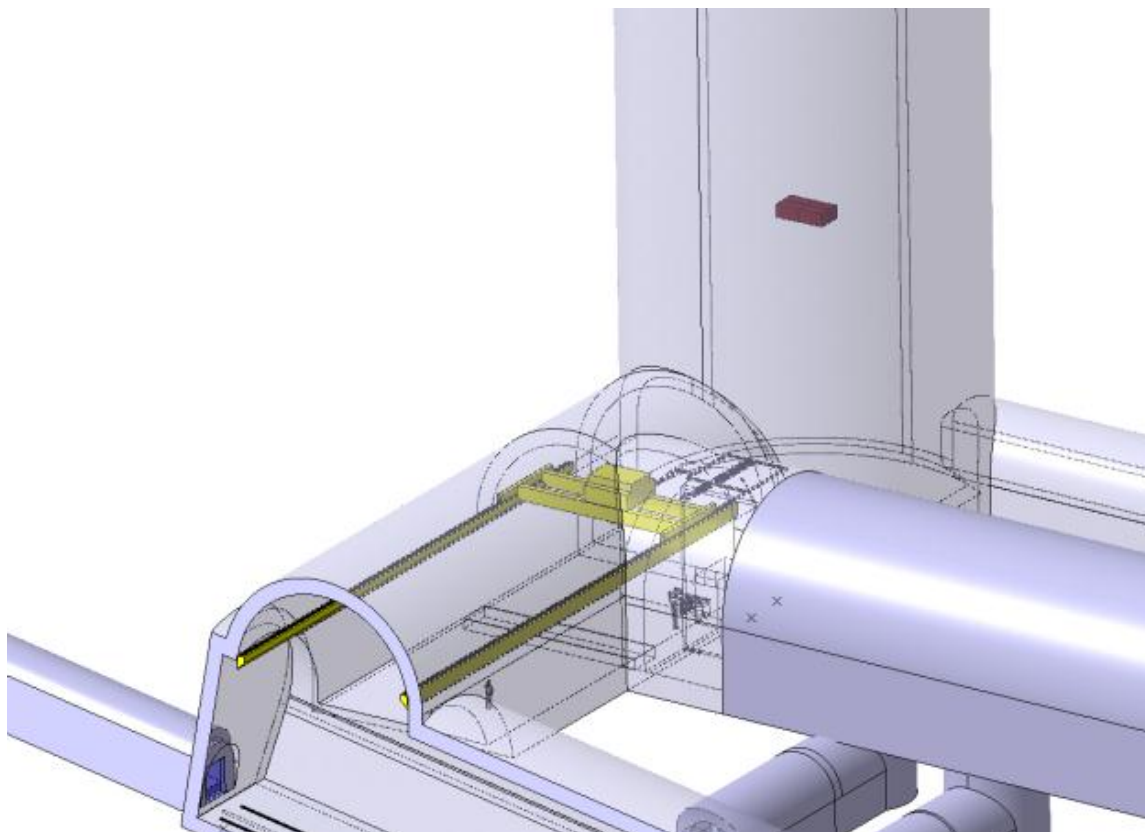


**Figure 6.25:** The transport tunnel overhead crane.

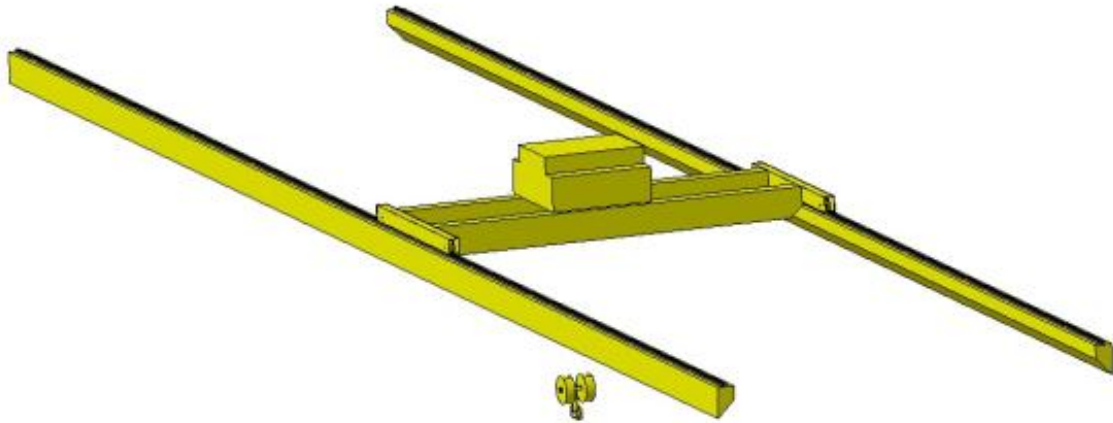


**Figure 6.26:** Detail of the transport tunnel overhead crane.

will not be used frequently during its whole lifetime and not always at its full capacity (light-medium duty crane). In addition the following points will be considered:

1. Hoist will be conceived so that the hook will be lifted or lowered without any horizontal drift (pure vertical lifting); motorized hook will allow rotation of the items during handling.
2. Electrical motors will be driven by frequency converters to obtain smooth accelerations thus limiting the stress in the components.
3. The crane will have a precision of positioning in the three directions of 1 mm.
4. Cables descending from the crane to the hook will bring electrical power and command signals to the spreader for the twist locks lock-unlock movements as well as information coming from the camera installed on the spreader; cables will be manually connected to the spreader through a plug-socket.
5. Crane will be equipped with proper instruments (lasers, encoders) giving the possibility to measure the position of the hook along the three directions and to set-up predefined points where the hook can position automatically when the crane is operated from remote.
6. Through PLC it will be possible to define multiple areas where access of the hook is forbidden thus avoiding risk of crash with sensible objects in case operator view of the area will be limited.
7. Personnel will operate the crane through joysticks installed on a remote desk in the control room; screens will provide images of the whole operating area as well as close-ups on the interactions between the hook, the spreader and the objects being handled.
8. Radio remote controls will be used instead whenever personnel are allowed to access the operating area.

### 6.2.2.2 Beam tunnel crane

This is a remotely operated gantry crane with vision system and electrically operated hook will be installed on a cable driven trolley. Rails will be buried in the floor. The rails will be installed

inside the transport tunnel, inside the morgue tunnel, and in the target chamber tunnel. The gantry crane can be loaded on the cable driven trolley to move up and down the chamber tunnel. When the beam is on, the gantry crane is stored at the far end of the transport cavern to avoid exposure to radiation of the electronic and motors.

The above described system is a result of the fact that no electronics or motors can be left inside the experimental cavern during operation of the beam (constraints as a result from the radiation protection study). All wheels of the gantry crane will be motorized so that, in case of fault of any motor or gearbox, the other motors will be able to complete the operation and move the crane in an area with lower radiation dose rate. The winches for the cable driven trolley will be installed in the far end of the morgue tunnel to be protected from radiation damages. The key parameters of this crane and the movable trolley are summarised in Table 6.9 and Table 6.10. In Figure 6.27 and Figure 6.28 the arrangement of the gantry crane and the travelling

**Table 6.8:** Key design parameters for the beam tunnel crane.

Parameter	Unit	Value
Span	mm	7000
Clearance between girder and the floor	m	2.5
Long travel speed <i>Gantry crane hoist</i>	m/min	0.4 - 8
Capacity	tonnes	40
Lifting height	m	10
Lifting speed	m/min	0.25 - 5
Cross travel speed	m/min	0.4 - 8
Maximum lifting / braking acceleration	m/s <sup>2</sup>	1
Hook size (according to DIN 15402)		20

**Table 6.9:** Key design parameters for the beam tunnel trolley.

Parameter	Unit	Value
Span	mm	7000
Clearance between girder and the floor	m	2.5
Long travel speed <i>Trolley winch</i>	m/min	0.4 - 8
Capacity	tonnes	40
Travelling distance	m	45
Travelling speed	m/min	0.25 - 5
Cross travel speed	m/min	0.4 - 8
Maximum lifting / braking acceleration	m/s <sup>2</sup>	1

trolley is shown. The dimensions of the traveling trolley and the gantry crane are such to allow manipulation of all objects inside the beam area. This in particular involves the handling of the horn - target assembly and of the shielding blocks, as shown in Figure 6.29. The design will consider that the crane will be used frequently during the installation and operation. As this device is capital for the availability of the facility it will be designed according to highest standards of quality to maximise its reliability. In particular:

- Hoist will be conceived so that the hook will be lifted or lowered without any horizontal drift (pure vertical lifting); motorized hook will allow rotation of the items during

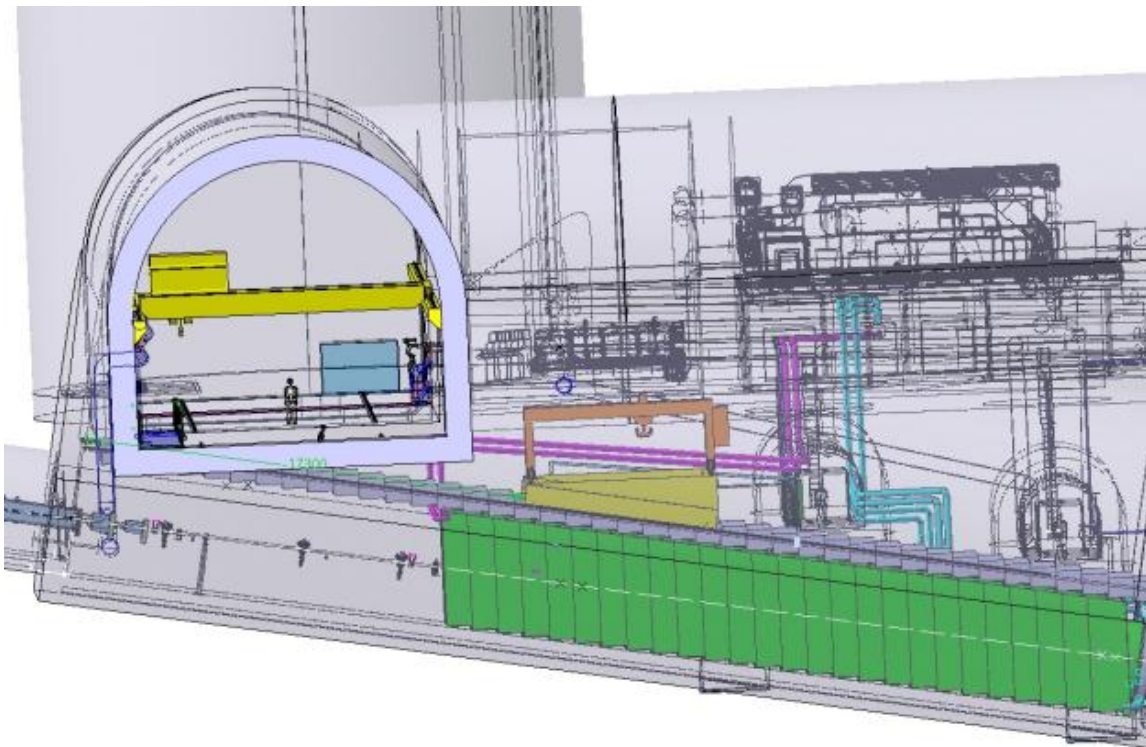


Figure 6.27: Layout of the gantry crane in the beam tunnel.

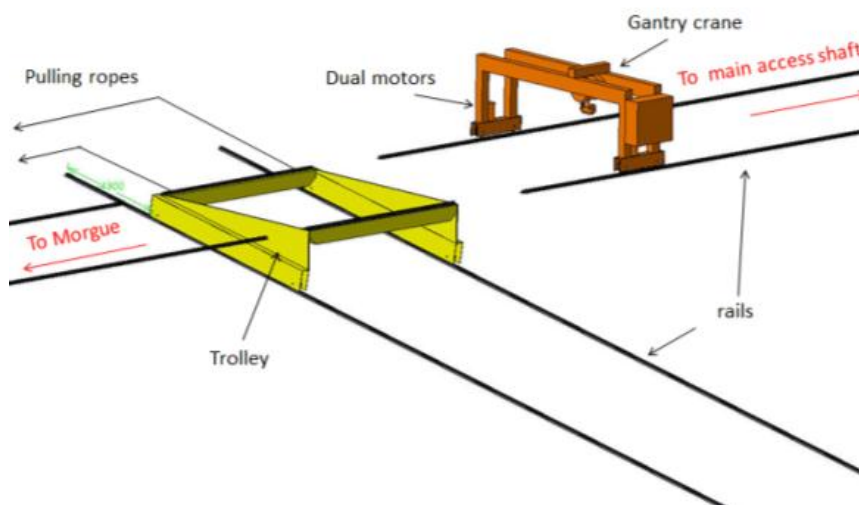


Figure 6.28: Detail of the layout and coupling of the gantry crane to the travelling trolley.

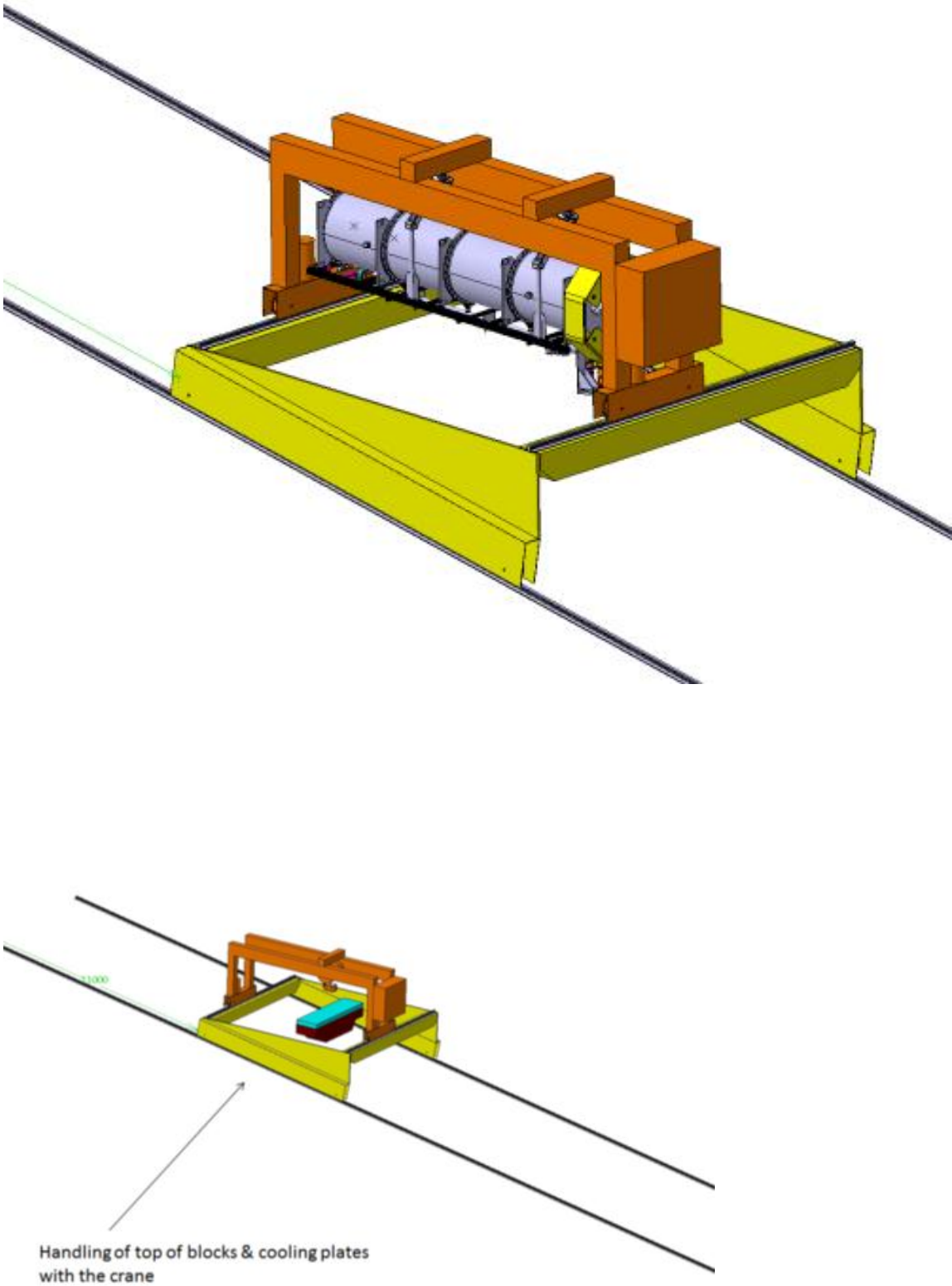


Figure 6.29: Detail of the handling of the horn and shielding blocks with the gantry crane.

handling.

- The crane will be equipped with one additional brake acting directly on the hoisting drum in the event of failure of any elements of the hoisting drive chain (emergency brake).
- Electrical motors will be driven by frequency converters to obtain smooth accelerations thus limiting the stress in the components.
- The crane will have a precision of positioning in the three directions of 1 mm.
- Cables descending from the crane to the hook will bring electrical power and command signals to the spreader for the twistlocks lock-unlock movements as well as information coming from the camera installed on the spreader; cables will be manually connected to the spreader through a plug-socket.
- Crane will be equipped with proper instruments (lasers, encoders) giving the possibility to measure the position of the hook along the three directions and to set-up predefined points where the hook can position automatically when the crane is operated from remote.
- The vision system will be conceived in a way that the cameras of the gantry cranes shall allow a precise positioning of the crane itself and of the trolley by reading distances on markers installed alongside the rails.
- Through PLC it will be possible to define multiple areas where access of the hook is forbidden thus avoiding risk of crash with sensible objects in case operator view of the area will be limited.
- Personnel will operate the crane through joysticks installed on a remote desk in the control room; screens will provide images of the whole operating area as well as close-ups on the interactions between the hook, the spreader and the objects being handled.
- Radio remote controls will be used instead whenever personnel are allowed to access the operating area. A radiation hard leaky feeder cable will be installed in the target chamber tunnel for data transfer, vision control, and communication with the remotely operated equipment.
- Power feeding rails will be installed alongside the rails. The power feeding rails shall be radiation hard.
- The gantry crane will be equipped with a hard wired emergency control system for recovery. It will be made of a redundant festoon with Harting type connector that will be installed permanently in the cavern and connected in case of failure on the main control system. The connector on the gantry crane shall be positioned in an area that minimizes the exposure of the maintenance technician to radiation.
- Special work procedure including systematic test of the equipment before operation shall be setup. Crane manufacturer shall supply special test bench to connect to the Harting socket to check the correct behaviour of the lifting and transport equipment before any operation in the radioactive zone.

### 6.2.2.3 Remote operations

After the beam startup all handling operations in the target cavern will be done remotely. At CERN sufficient experience is available from existing facilities like the CNGS and HiRadMat areas. Special tools, like the electrically driven hook shown in Figures 6.30 and 6.31 developed



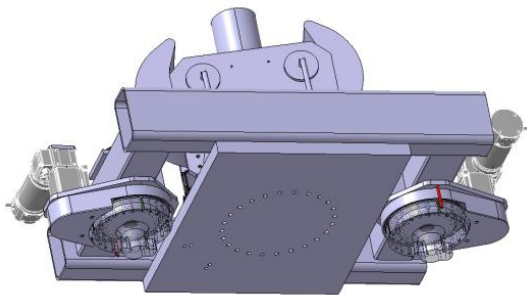


**Figure 6.30:** 3D drawing (left) and photo (right) of the electrical double twist lock hook used for the handling of shielding blocks.

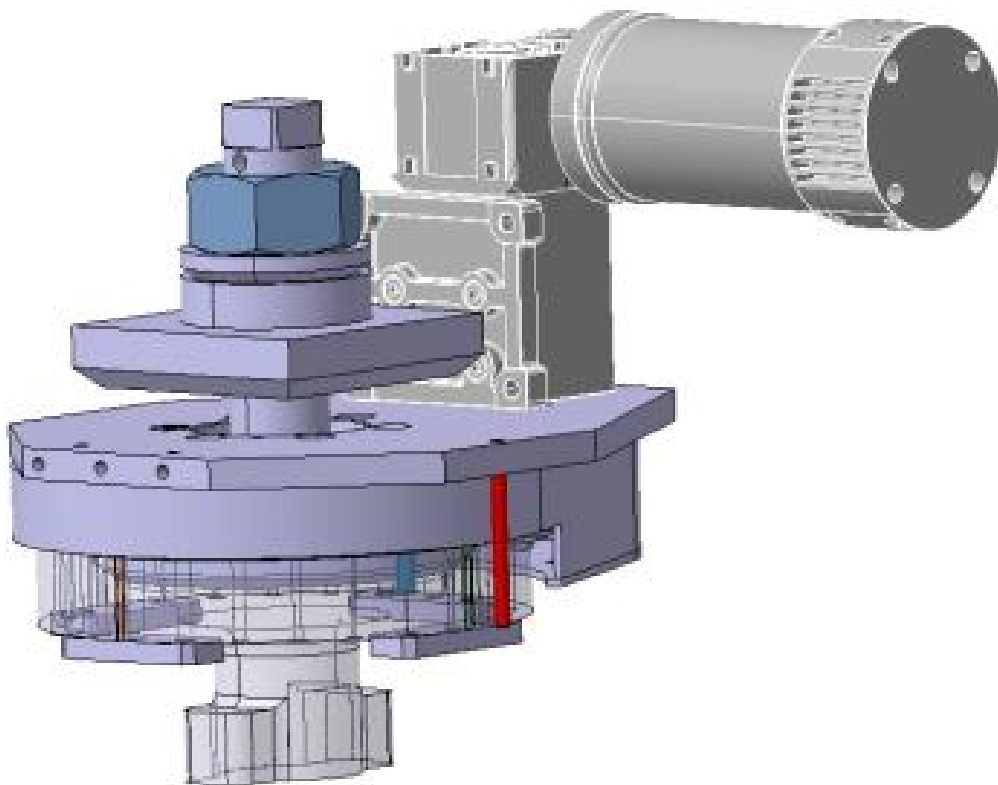


**Figure 6.31:** 3D drawing of the electrical single twist lock hook used for the handling of shielding blocks.

for the handling of highly radioactive blocks in the HiRadMat and ex-WANF area. The remote operations will be done from a control cubical installed at the bottom of the main access shaft as shown in Figure 6.32. All the remotely operated cranes will be equipped with high-resolution

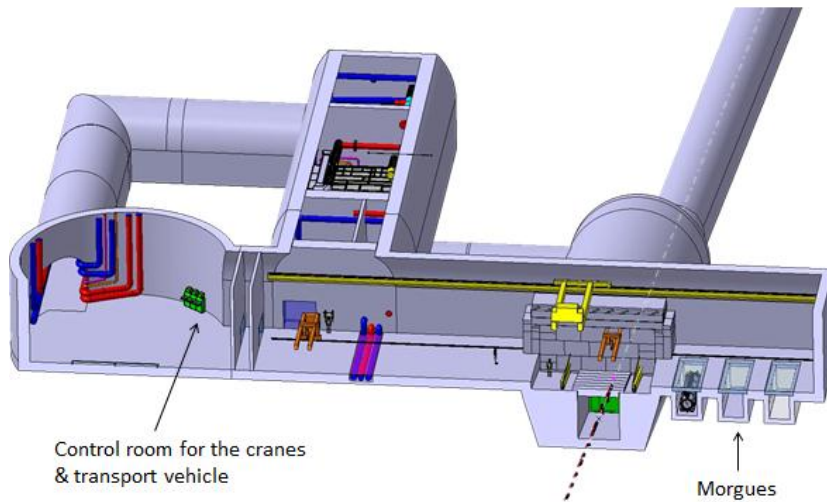


**Figure 6.32:** 3D drawing indicating the location of the remote control operations cubical.

cameras with zoom and orientation possibility as well as powerful lighting. Examples of such installations for CNGS following a recent upgrade is shown in Figures ?? and 6.34.

The desing of the target cavern crane should comply with the the requirements of the following European Directives:

- 2006/42/EC on machinery;
- 2004/108/EC on the approximation of the laws of the Member States relating to electromagnetic compatibility;
- 2006/95/EC on the harmonisation of the laws of Member States relating to electrical equipment designed for use within certain voltage limits.

As well as the following CERN safety codes:

- SR-M: Mechanical equipment;
- GSI-M1: Standard lifting equipment.

Since the crane will be required to handle activated objects, interventions of personnel shall be avoided when the load is still suspended or, at least, their duration kept to a minimum; design will therefore foresee measures that either reduce the risk of fault or, in case of breakdown, guarantee the possibility to lay down the load without intervention (single-failure proof), or to reduce the intervention duration. Following a fault analysis, the following additional features have been therefore identified (valid for all remotely operated cranes):

- The hoist motor will be backed up, in case of failure, by an emergency motor which will allow completing the operation; the two motors will be installed on two input shafts of a differential unit which guarantees their independence;





**Figure 6.33:** Photo showing the CNGS remotely operated overhead crane after the onboard camera and lighting upgrade.



**Figure 6.34:** Photo showing the CNGS remotely operated overhead crane after the onboard camera and lighting upgrade.

- Hoisting gearbox will be oversized, i.e. it will be designed as if it were installed on a heavy-duty crane thus reducing the probability of failure;
- All wheels will be motorized so that, in case of fault of any motor or gearbox, the other motors will be able to complete the operation and move the crane in an area with lower radiation dose rate;
- Electrical cubicles will be located in a separate room; cables connecting the crane to the cubicles will be grouped in one festoon and be installed on one of the two walkways at the sides of the crane;
- Only electrical components whose failure won't affect the crane operation will be installed on-board;
- Spare wires will be left inside electrical cables so that intervention time in case of defect on wiring will be limited.

### 6.2.3 Remotely operated Omni-wheel platform

An autonomous omni-wheel platform equipped with automatic guidance system (laser scanners and buried wire guidance system) will be used to transport the horn and the reflector. The device will be operated remotely by an operator located in the control room. The sequence of the operations for the handling of the target-horn assembly is briefly described below. The Omni wheel platform is equipped with a lifting table. The operator drives it under the equipment to be transported that has been previously installed on a specially designed 'table'. The table is then lifted and driven to the hot cell for maintenance. The vehicle automatically follows the buried wire and the laser scanners prevent any collision with the environment. Example of similar equipment can be found on internet [?]. The load capacity of the Omni wheel is 2.5 T.

The Omni wheel platform is available from the industry as a commercial 'off the shelf product'. For LAGUNA, this equipment will handle highly radioactive components of the experience (horn, reflector) and will be specified accordingly. To avoid having to expose the maintenance personnel to radiation, the omni wheel lifting platform will integrate specific features such as:

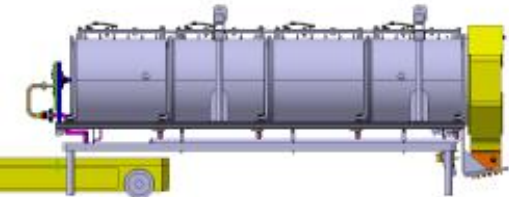


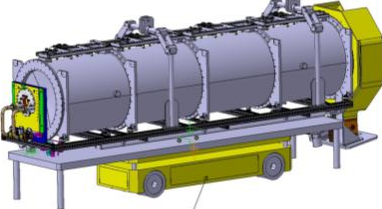
- wireless recovery control system with procedure
- vision control system
- hard wired Recovery control system
- fail safe lifting mechanism (in case of failure of the control system, the load is made free so the platform can be recovered for repair without the load).
- brake release mechanism (in case of failure, the platform can be recovered for repair without the load).

### 6.2.4 Lifts

Stairs and lifts will be installed inside the three access shafts: the main access shaft for the target chamber, the hadron stop tunnel access shaft, and the near detector access shaft. The relevant depths are summarised in Figure 6.35.

For the near detector shaft, due the large depth a special lift is foreseen. The lift will be rack and pinion worksite lift for permanent access purposes. The lift will be used for passengers and can be used to carry loads up to 1000 kg. The size of the lift is small, compared to other lifts in shafts, to dedicate a bigger area for handling operations in the bottom of the shaft. Stairs

**Table 6.10:** Sequence of operations for the Omni-wheel platform for the handling of the horn.

Step	Actions	Image
1	enters under the table with the horn	
2	positioned under the table	
3	raising the lifting table	
4	moving around	 <p data-bbox="842 1912 1082 1939">Horn &amp; target transported using remotely operated "lifting table" vehicle - omnidirectional.</p>

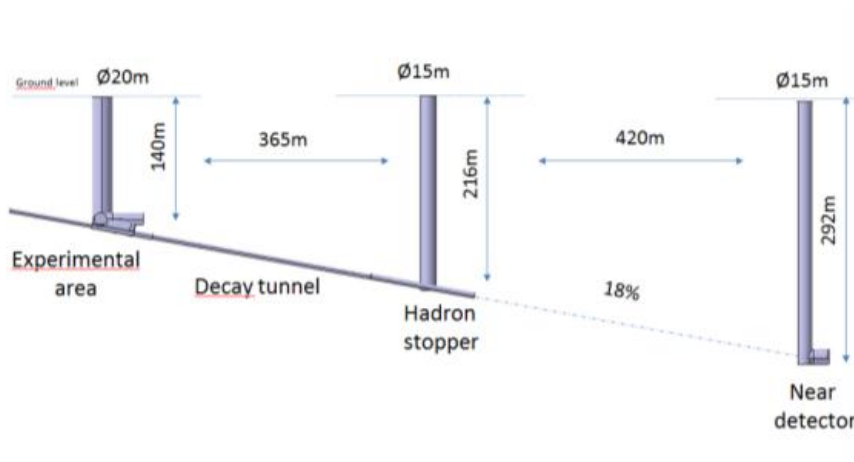


**Figure 6.35:** Cut view showing the access shafts and corresponding depths.

will be next to the lift in case of a breakdown of the lift and there are escape areas in different levels of the stairs. The lift guiding rails will be fixed to the walls of the shaft; hence no civil engineering work is required for the lift itself. The implementation is shown in Figure 6.36 and the key parameters in Table ??.

**Table 6.11:** Key parameters of the ND shaft lift.

Characteristic	Unit	Value
Capacity	kg	1000
Type		Worksite lift
Travel height	m	320
Stories		2
Cabin doors		1
Speed	m/s	1.20
Cabine size		
Inner Dimensions:		
Width	mm	1400
Depth	mm	1500
Height	mm	2800
Cabine doors		
Free width	mm	1200
Free height	mm	2600

### 6.3 Installation scenarios

Installation scenarios for the facility are presented, using the above defined cranes and handling equipment. After excavation, the installation of the facility will start from the hadron stop working backwards up to the target cavern.

The following design guidelines are considered for defining the installation scenarios:

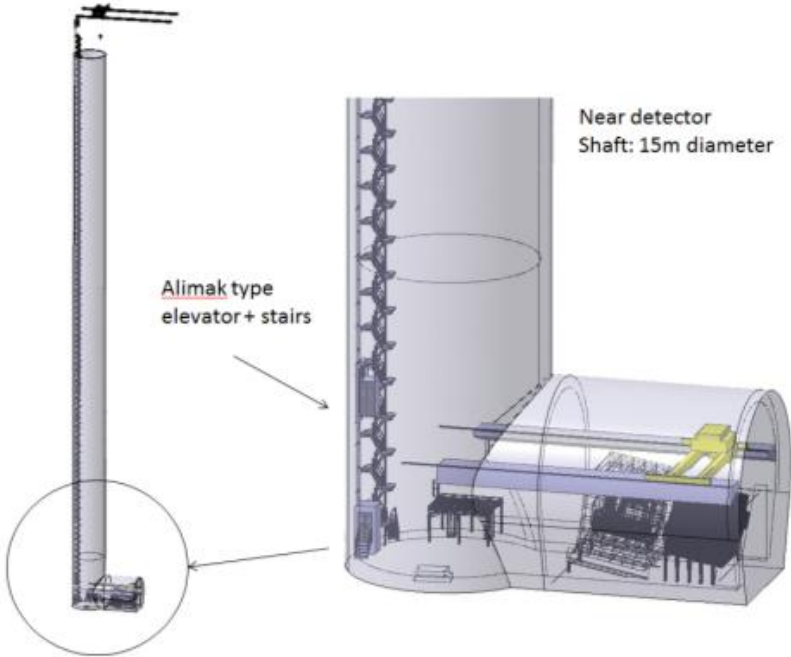


**Figure 6.36:** 3D drawing showing the access shaft lift for the near detector site.

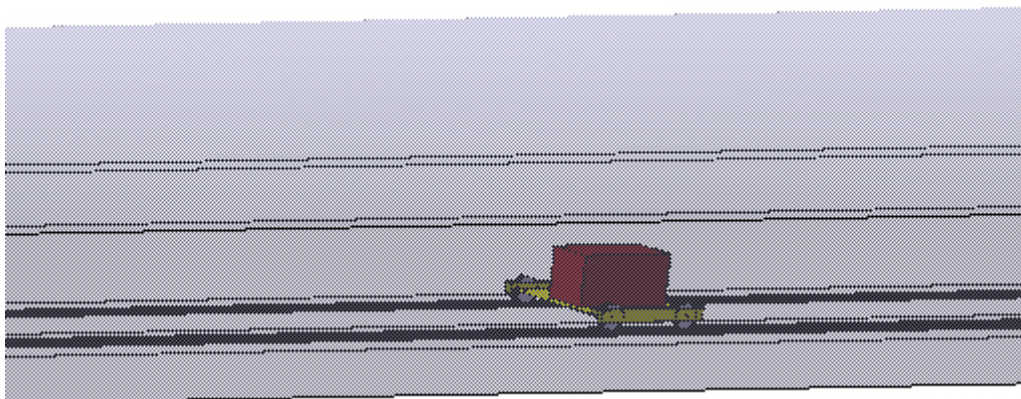
- Lifting and handling equipment shall be compatible with the 18% slope. The use of overhead cranes is preferred for handling of the equipment in such steep slopes.
- To comply with radiation protection requirements, no electronics or motors are left inside the experimental cavern during operation due to high radiation level.
- Equipment shall be remotely operated during maintenance of the horn or of the reflector using cameras for supervising the operation.
- Equipment shall be left available for decommissioning.

### 6.3.1 Hadron stop

The key element to install is the 100 m (115.5 m exactly) long pipe of cast iron blocks. Each block has dimensions  $1.6 \times 0.8 \times 0.8$  m and weights 8.06 t. For the full 115.5 m length of the hadron stop there will be 1575 blocks.

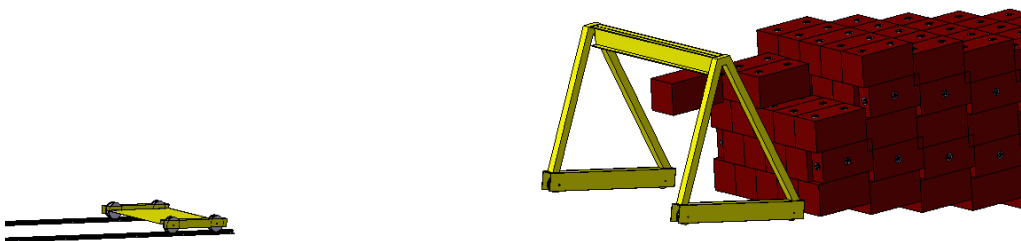
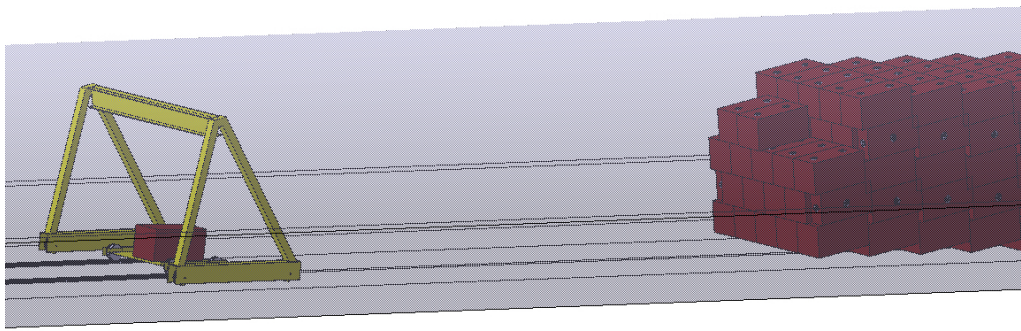
The following sequence of operations is foreseen:

1. Lowering the iron blocks through the main access shaft using the surface crane. The blocks are lowered down in packs of  $4 \times 4$  to the bottom of the access shaft.
2. The blocks are individually pick up by the cavern crane (no remote operation at that stage) and lowered on a wagon on the floor of the target chamber tunnel.
3. The blocks are transported through the empty decay pipe tunnel to the hadron stopper tunnel. Temporarily rails are installed during the installation phase inside the chamber and the decay pipe tunnel down to the hadron stopper tunnel. These rails have to be removed after installation. The wagons are drum cable driven, and is pulled back with a winch once unloaded.



4. Inside the hadron stopper tunnel, the blocks are handled with a portable gantry crane.





This crane will be dismantled after the installation.

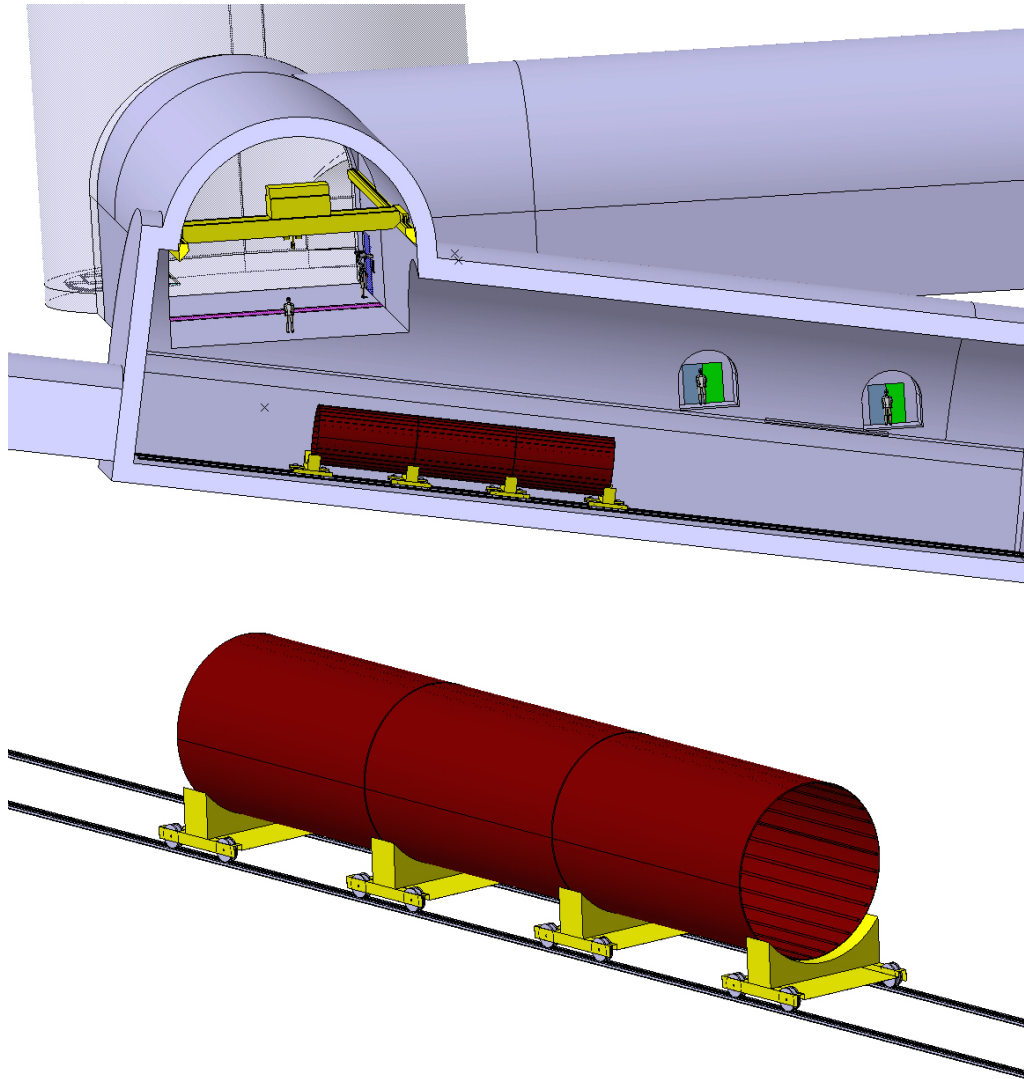
5. The top layer of blocks is not accessible with the gantry crane and a diesel telescopic crane used in the mine industry for example shall be lowered down for these operations. These machine are capable of handle the 18% slope.

6. The

### 6.3.2 Decay pipe

A similar procedure as for CNGS [?] will be used, adopted to the steep 18% slope of the tunnel. The key operations include:

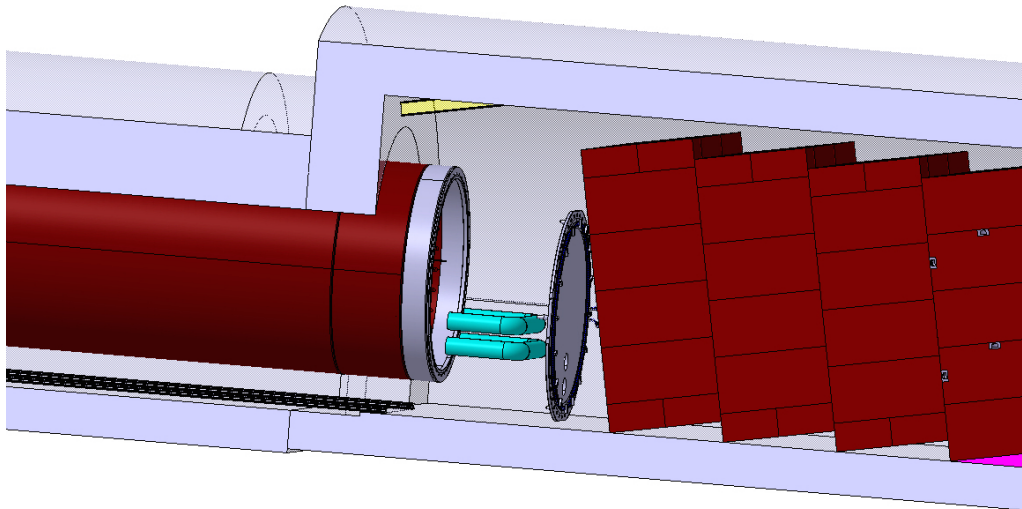
1. The decay pipe tubes are lowered from the access shaft in pieces of 5 m long (7.37 t of weight), and with the overhead crane are positioned into the target cavern on specially designed wagons.
2. Three tubes are positioned on wagons and welded together to form an assembly.



This wagons are connected together and the assembly is lowered down to the decay pipe tunnel using rails. The convoy is cable drum driven.

3. Once in position, the new set of tubes are aligned and anchored to the tunnel walls.
4. The new tubes are welded to the previous ones, and all the piping connections are welded as well from the inside. The wagons retracted,
5. The He tubes running on the outside of the decay pipe is lowered for the corresponding meters before, welded and positioned in place.
6. After installing the special insulation liners for all tubes, the assembly is concreted, for approx. 13 m.
7. The sequence continues until all the 270 m of the decay pipe (18 assemblies of 15 m) is installed.
8. The downstream window that has been lowered before the installation of the decay pipe is put in place and the He supply lines are connected.





### 6.3.3 Target cavern installation

The target cavern installation follows that of the decay pipe. In Figure 6.37 the finished target cavern and service area is shown. The major installation sequence steps are:

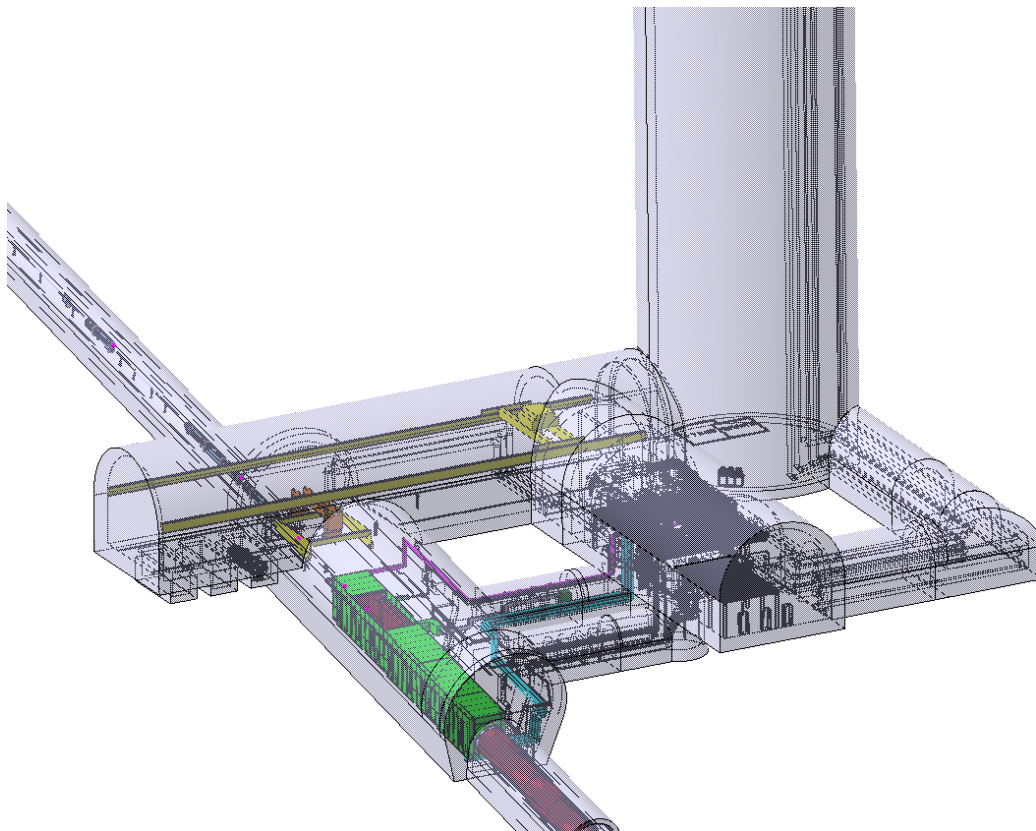
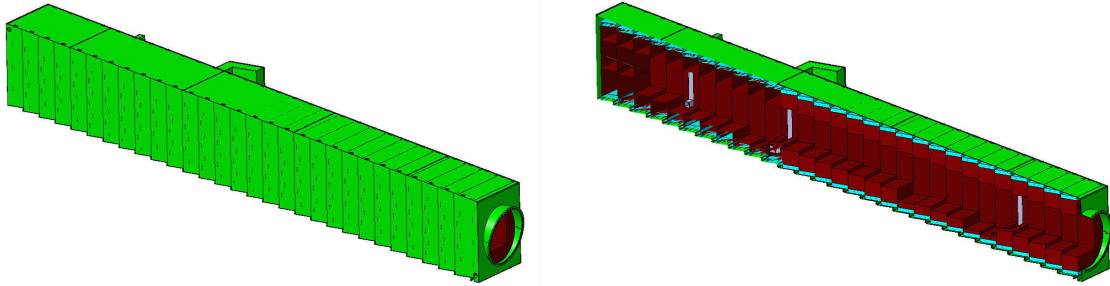


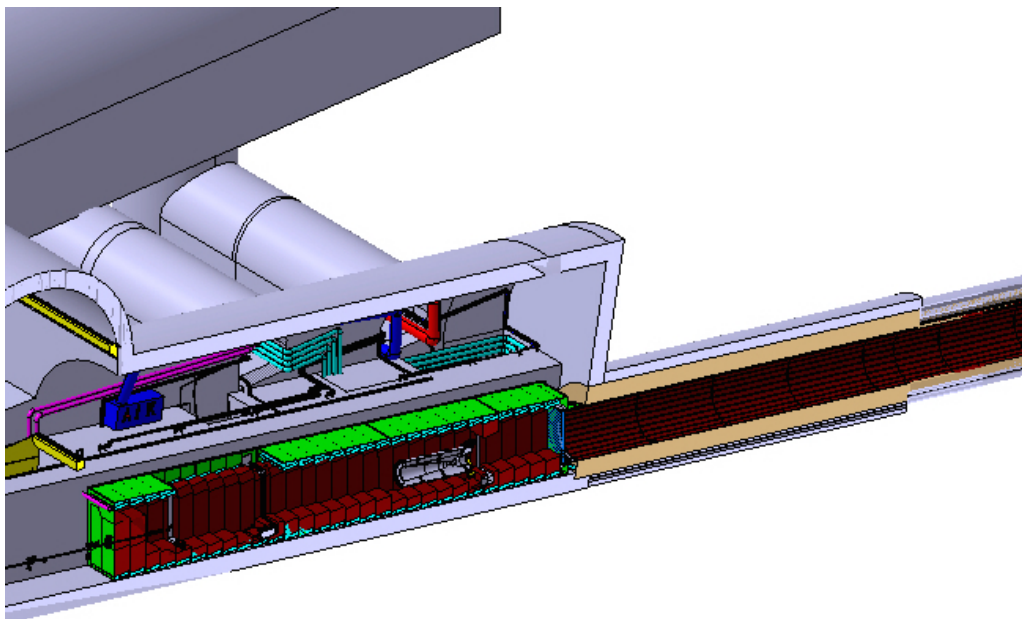
**Figure 6.37:** 3D drawing showing the completed target cavern and service area.

1. The drainage and horn and reflector water collection tanks are lowered and installed in their locations at the downstream end of the target cavern.

2. The side shielding walls are constructed and the rails of the gantry crane are installed. This crane will be used for the installation of the shielding blocks and the other equipment in the cavern.
3. The He tank is constructed first. The 1 m long pieces are lowered and positioned in place using special wedge supports that compensate for the slope. The pieces are welded together to form the full container. The He container is also connected to the decay pipe and the separation window is also installed.



4. The iron and aluminium cooling blocks are installed next. All the blocks are lowered with the gantry crane and installed in place are pushed against the He tank lateral walls to allow good thermal contact. The flexible pipes for the bottom and side cooling blocks are installed up to the top of the He-tank, that later one will be connected to the distribution manifolds.

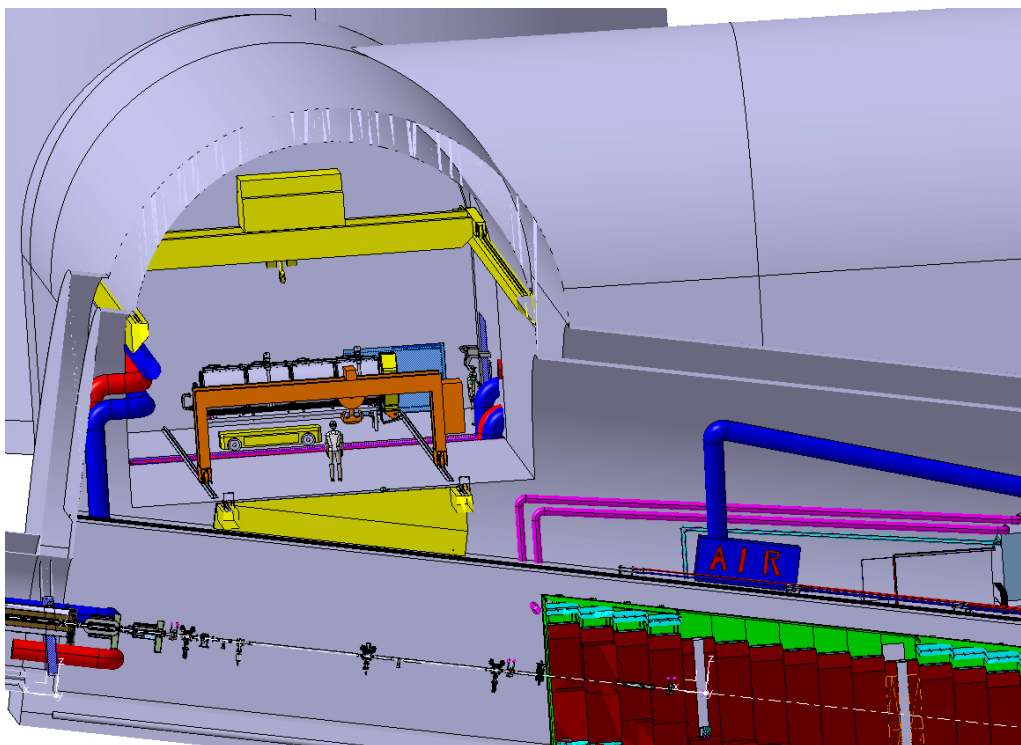


5. The fixed supports and base table for the horn, reflector and other beam elements are installed and aligned.
6. The fixed top shielding blocks, He tank cover and top concrete shielding blocks are installed. The part on top of the horn and reflector positions will be closed once the elements are in place.

### 6.3.3.1 Horn (Refelctor) installation and exchange

The installation and exchange of the horn and reflector will be done remotely using the gantry crane and the omni-wheel table. The sequence of operations is outlined below.

1. The top concrete shielding blocks in the target cavern are removed. The blocks are stored further downstream in the target cavern.
2. The He vessel cover is removed. This operation is done remotely using a special tool to unscrew the few bolts, as explained in Section ???. The covers are stored in the upstream part close to the morgue.
3. The top iron blocks are removed and stored in the target cavern. The services to the top shielding blocks are disconnected at the beginning of the operation before step-1, i.e. before removing the top concrete shielding. With sufficient cool-down time, the expected radiation levels in the target cavern would be such to allow short interventions when the full shielding is in place, as the one required here. Alternatively, the operation could be further optimised to be done fully remotely, or a mechanical solution could be envisaged to displace the top iron shielding blocks using rails and sufficiently long flexible cooling pipes that would also have the additional advantage not to disconnect and thus require to purge the system each time.
4. The horn is removed from its position using the gantry crane. It is positioned on a support table in a specially prepared area in the upstream access tunnel.
5. The omni-wheel vehicle moves the horn into the hot cell or into the morgue.



### 6.3.3.2 Installation of Near Detector

Two options considered for the installation of the near detector.

- The detector is assembled at the surface and lowered down as a single piece where it is put in position using jacks and winches.
- The detector is lowered piece-by-piece and it is assembled in-situ.

At CERN sufficient experience is available of the first option, that was the adopted solution for the installation of the LHC CMS Detector: 5'000 t × 120 m. For the ND case, the weight is

much smaller but the dept bigger that compensates. Although such a solution could be feasible, in this CDR a mixed solution is adopted, where the detectors are assembled in big pieces at the surface and then lowered into the cavern with the shaft crane and then assembled into position with the cavern overhead crane. The sequence of operations is outlined in the pictures below.

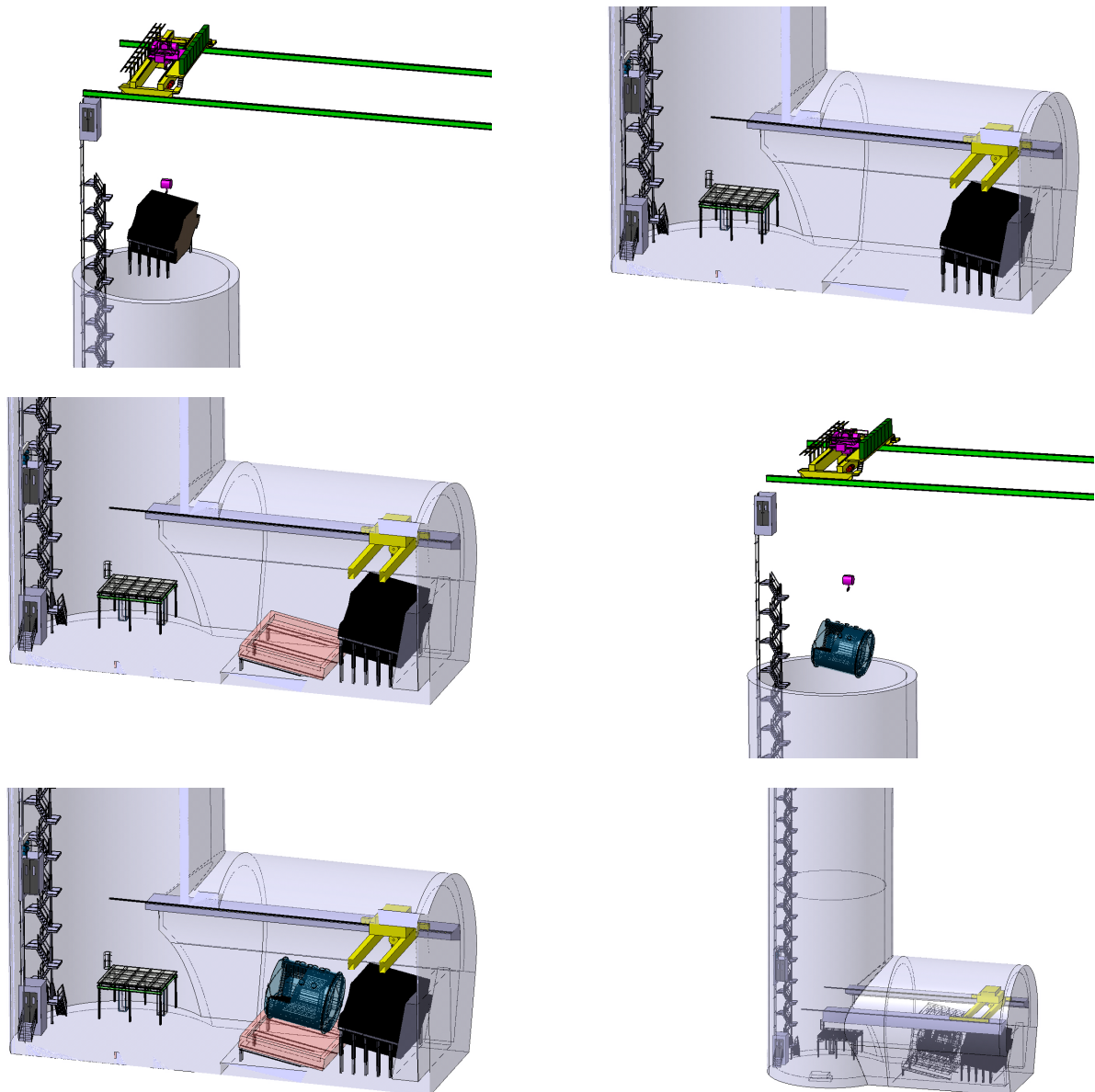


**Figure 6.38:** *Sequence of operations for the Near Detector installation.*



# Chapter 7

## The Near Detector

### 7.1 General Considerations

The LBNO ND design work consists of several iterations. The composition of the  $\nu$  beams at the ND location was provided by the beamline study carried out at CERN. From these  $\nu$  beams, the energy spectra of the secondaries resulting from interactions in the ND were estimated, and required functionalities of various sub-detectors were defined in a first iteration. The main assumptions for the sub-detectors are the following:

- The argon gas TPC is used primarily as a vertex detector for  $\nu$  interactions occurring within its fiducial volume. It is also proposed to perform momentum measurements;
- The T ASD and ECAL are only used to reconstruct secondaries from  $\nu$  interactions taking place in the fiducial volume of the argon gas TPC;
- The MIND is used to both:
  - reconstruct  $\nu$  interactions taking place in the fiducial volume of the argon gas TPC;
  - as a standalone detector, collecting an independent sample of  $\nu$  events.

### 7.2 Beam at the ND

The primary goal of the beam line optimisation is to maximise the flux of the 1st and 2nd oscillation maxima at the Far Detector location (no optimisation for the ND!), see Figure 7.1. The optimisation is through a multi parametric scan of all possible configurations of the horn inner shape (and external radius), reflector inner shape (and external radius), horn/reflector current, horn/reflector length and relative distances. The latest baseline is to have one configuration of the horns, with 2 horns, and to change the positioning of the target depending on the available beam energy:

- 50 GeV protons on target: target inside horn;
- 400 GeV protons on target: target outside horn (the default).

Requirements for the optimisation of the ND neutrino spectra are not formulated. These could be submitted as requests at a later stage if they do not affect the far detector spectra which have first priority. The impact of the ND spectra on the overall oscillation physics analysis has not been investigated (near/far flux extrapolation, impact on this extrapolation of differences in spectra at near and far locations).



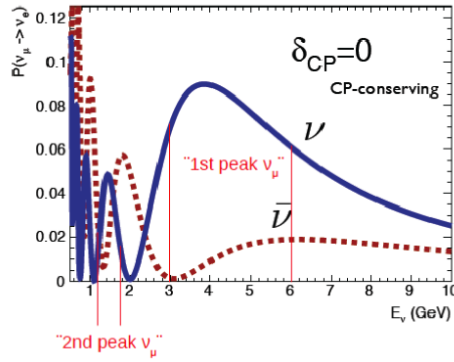


Figure 7.1: Oscillation probabilities at the LBNO far detector and beam optimisation for  $\nu_\mu$ .

### 7.2.1 ND Placement

The ND placement from the beam target is an important factor to the experimental requirements. Due to cost restrictions and engineering difficulties this is limited to 1000 m. Beam requirements also cause heavy restrictions on the ND placement, incurring a lower bound of 500 m from the target. The LBNO beamline group have investigated in some detail the muon background at the ND location, with several configurations of muon shields to reduce the muon background to below  $9 \mu/\text{m}^2/\text{spill}$ , considered acceptable for TPC operation. Their studies conclude that the lower limit should be set to 800 m from the target. Given these limitations, 800 m is favourable (and default), but 900 and 1000 m remain as candidate distances.

### 7.2.2 Spectra at the ND for a $\nu_\mu$ Run

The  $\nu_\mu$ ,  $\bar{\nu}_\mu$ ,  $\nu_e$  and  $\bar{\nu}_e$  spectra for horns set to a  $\nu_\mu$  beam configuration are given for near (800 m) and far detector locations for both the default 400 GeV beam and alternative 50 GeV beam normalized to equivalent power,  $10^{20}$  p.o.t and  $8 \times 10^{20}$  pot respectively, see Figures 7.2 and 7.3.

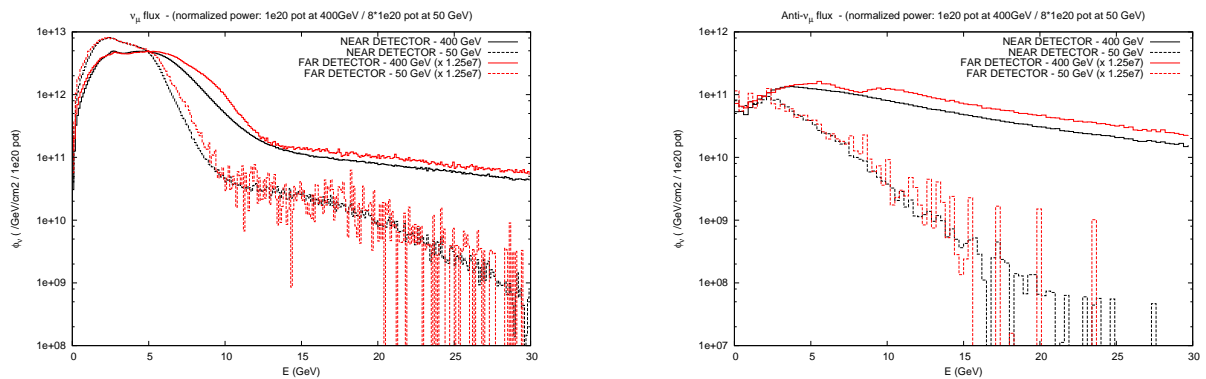
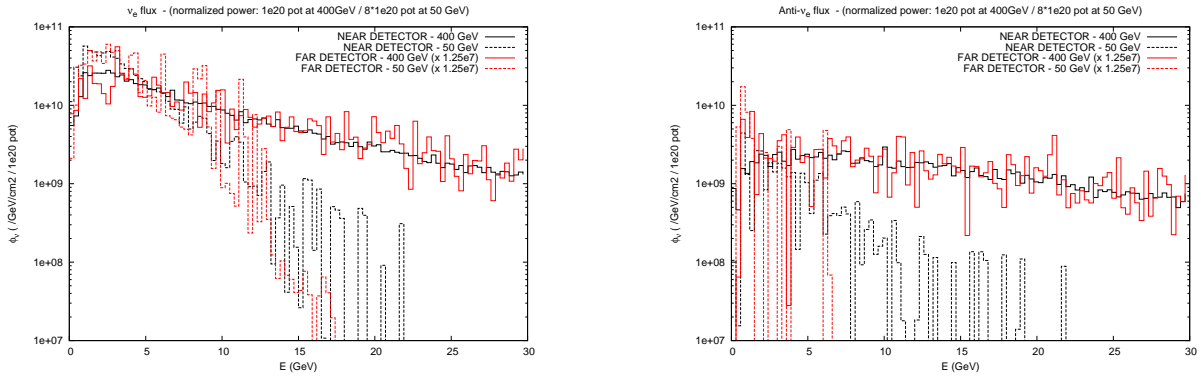


Figure 7.2:  $\nu_\mu$  and  $\bar{\nu}_\mu$  spectra for horns set to  $\nu_\mu$  run. Two primary proton beam configurations are given: the 400 GeV option operates with the target outside the horn, the 50 GeV option operates with the target inside the horn. Both beams are normalized to equivalent beam power.

## 7.3 LBNO ND Layout

The proposed layout is shown schematically in figure 7.4. The assumption is that the angular distribution of secondary leptons will be peaked in the forward direction since the energy



**Figure 7.3:**  $\nu_e$  and  $\bar{\nu}_e$  spectra spectra for horns set to  $\nu_\mu$  run. Two primary proton beam configurations are given: the 400 GeV option operates with the target outside the horn, the 50 GeV option operates with the target inside the horn. Both beams are normalized to equivalent beam power.

spectra extends to 10 GeV, whereas secondary  $\pi$  and protons have much lower energies and will be largely contained in the argon gas and a few layers of TASD. Therefore the forward direction should be instrumented with an ECAL and a MIND, whereas the barrel section of the "air magnet" do not need to be covered by an ECAL and MIND.

A few planes of TASD could be placed in front of the argon gas TPC to detect muons from  $\nu$  interactions in the surrounding rock.

The number of layers for the TASD, ECAL and MIND are to be defined, the main parameters serving as a starting point are listed in Table 7.1.

## 7.4 Sub-detectors

The optimisation of sub-detectors is carried out as a function of the type of particles and information required. Table 7.2 lists expected secondaries from  $\nu$  interactions in the gas TPC.

### 7.4.1 The Argon Gas Time Projection Chamber: TPC

The main motivation for having a Gas Argon (GAR) TPC is to measure cross-sections in argon, the same material as the far detector. Its characteristics as a vertex detector are well suited to this task, as is illustrated in Figure 7.6 which compares liquid with gas.

As a starting point, only neutrino interactions occurring in the argon gas TPC will be recorded. Any other interactions outside of the TPC but resulting in secondaries that either stop or traverse the TPC will be considered as background. This applies for example to:

- Leptons arising from neutrino interactions in the rock or the other subdetectors,
- Gammas from  $\pi^0$ 's created in interactions in the rock or the other subdetectors.

### 7.4.2 The Totally Active Scintillating Detector: TASD

The TASD will instrument the volume outside the TPC. It is a complement to the TPC measurements and is currently only envisaged to contribute to the reconstruction of neutrino interactions in the TPC. Its function is to reconstruct low energy particles such as low energy neutral pions decaying to gammas which are likely to stop in the TASD. The acceptance is to be determined from simulations, we think it will not be necessary to cover the full barrel region



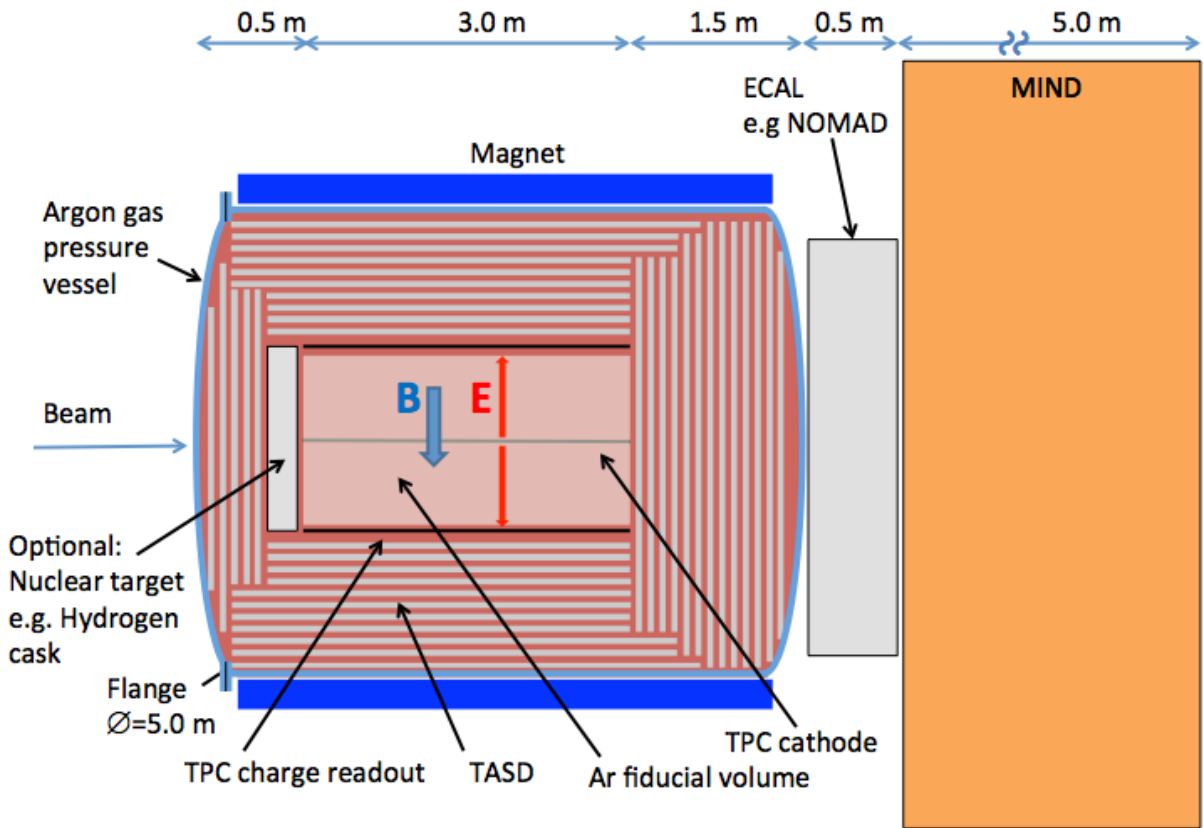


Figure 7.4: Schematic layout of the LBNO ND.

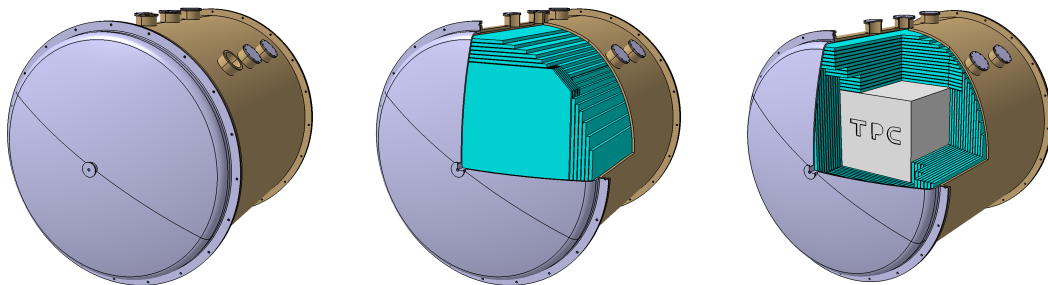


Figure 7.5: Plastic scintillator coverage within the pressure vessel.

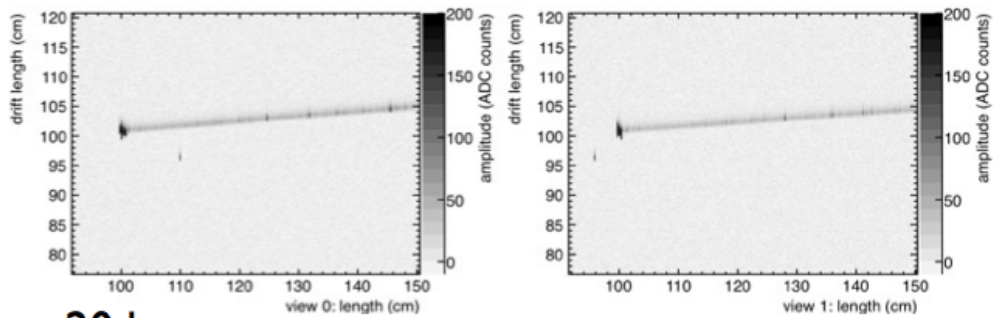
**Table 7.1:** Geometrical preliminary parameters for the detector layers.

Item description	Number	Thickness [mm]	Width [m]	Height (radi.) [m]	Depth [m]	Mass [t]
<i>Air magnet inner volume</i>						
Air magnet	1	1000	-	(3.5 outer)	5.0	440
<i>Argon gas TPC</i>						
TPC	1	-	2.4	2.4	3.0	0.6
Anode/Cathode plates	3	13.2	2.3	2.3	-	-
<i>Pressure vessel</i>						
Barrel	1	20	-	(2.5)	5	-
Ends (semi-hemis.)	2	20	-	(1.5)	-	-
Fiducial volume	1	-	-	(0.5)	5	-
Steel envelope	1	10	-	-	-	-
<i>TASD</i>						
Scintillator bars	150000	7	0.03	-	-	162
Plane (X or Y or U or V)	200	7.5	-	-	-	-
Module (X+Y)	100	15	-	-	-	-
<i>ECAL</i>						
Lead (or steel) plates	50	10	-	-	-	160
Scintillator bars	20000	7	0.03	-	-	23
Module (X+Y)	50	15	-	-	-	-
Structure (Pb + Scint)	50	25	-	-	-	-
<i>MIND</i>						
Iron plates	150	30	10	10	-	3600
Scintillator bars	100000	7	0.03	-	-	245
Module (X+Y)	150	15	10	10	-	-
Structure (Fe + Scint)	150	45	-	-	-	-

**Table 7.2:** Particle parameters relevant to the LBNO ND. Interactions in the sub-detectors are shown with a \*.

Particle type	$\bar{E}$ [GeV]	$E_{min}$ [GeV]	$E_{max}$ [GeV]	Argon gas TPC	TASD	ECAL	MIND
Beamline parent particles							
$\pi^+$ (1 <sup>st</sup> peak)	10	7	50	-	-	-	-
$\pi^+$ (2 <sup>nd</sup> peak)	5	2.5	25	-	-	-	-
Neutrinos at the ND							
$\nu_\mu$	1.5	0	10	*	*	*	*
$\bar{\nu}_\mu$	2	0	10	*	*	*	*
$\nu_e$	5	0	10	*	*	*	*
$\bar{\nu}_e$	6	0	10	*	*	*	*
Secondaries from $\nu$ interactions in Gas argon TPC (no background)							
protons	1	tbc	tbc	*	*	-	-
$\pi^{+/-}$	0.5	0.1	5	*	*	-	-
$\pi^0$	0.5	0.1	5	*	*	-	-
neutrons	-	tbc	tbc	*	-	-	-
$e$	3	0.1	10	*	*	*	-
$\mu$	3	0.1	10	*	*	*	*
$\gamma$	tbc	0.1	10	*	*	-	-

## liquid Ar



## Ar gas 20 bar

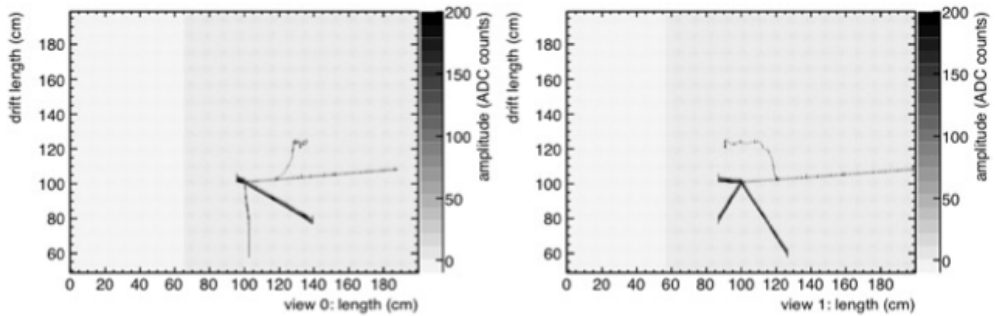


**Figure 7.6:** Comparing quasi-elastic charged current interactions in liquid and gas argon. The three protons from the interaction vertex are apparent in the GAr TPC, but cannot be resolved in the LAr.

of the TPC. A secondary function to be confirmed at a later stage would involve cross-section measurements for neutrino interactions in plastic, in combination with the ECAL and MIND.

### 7.4.3 The Electromagnetic Calorimeter: ECAL

The ECAL will provide energy measurements for the high energy electrons which are expected to be produced in the forward direction. It does not necessarily need to surround the barrel region of the TPC, but will occupy the region downstream of the TPC, after the TASD. It is a complement to the TPC measurements. It is currently only envisaged to reconstruct neutrino interactions in the TPC.

### 7.4.4 The Magnetised Iron Neutrino Detector: MIND

The MIND will measure escaping muons from interactions in the TPC, and will therefore complement the TPC measurements, i.e. it is an integral part of the reconstruction of neutrino events occurring in the TPC. The MIND will also be used as a standalone detector. Considering its mass for the geometry proposed here  $10 \times 10 \times 5 \text{ m}^3$ , 8 kton compared with 1 ton of argon, the number of events scales roughly to  $\sim 10^5$  more neutrino interactions in the MIND compared with the argon. These numbers will be refined with a clearer description of the neutrino beam from the target+horn assembly.

### 7.4.5 The Air Magnet Around the Pressure Vessel

The magnet has not been considered in detail. It is assumed to be a solenoid magnet. This is imposed by the fact that the field has to be parallel to the drift direction for charge carriers in the TPC. The feasibility of the magnet, especially with respect to its size, and compatibility with

the nearby MIND magnet, is to be checked. Investigations of engineering aspects concerning the pressure vessel are outside the scope of these studies. They would have to include choice of suitable material, optimisation of pressure vessel thickness, number of feedthroughs, large flange for insertion of TPC and plastic scintillator slabs.

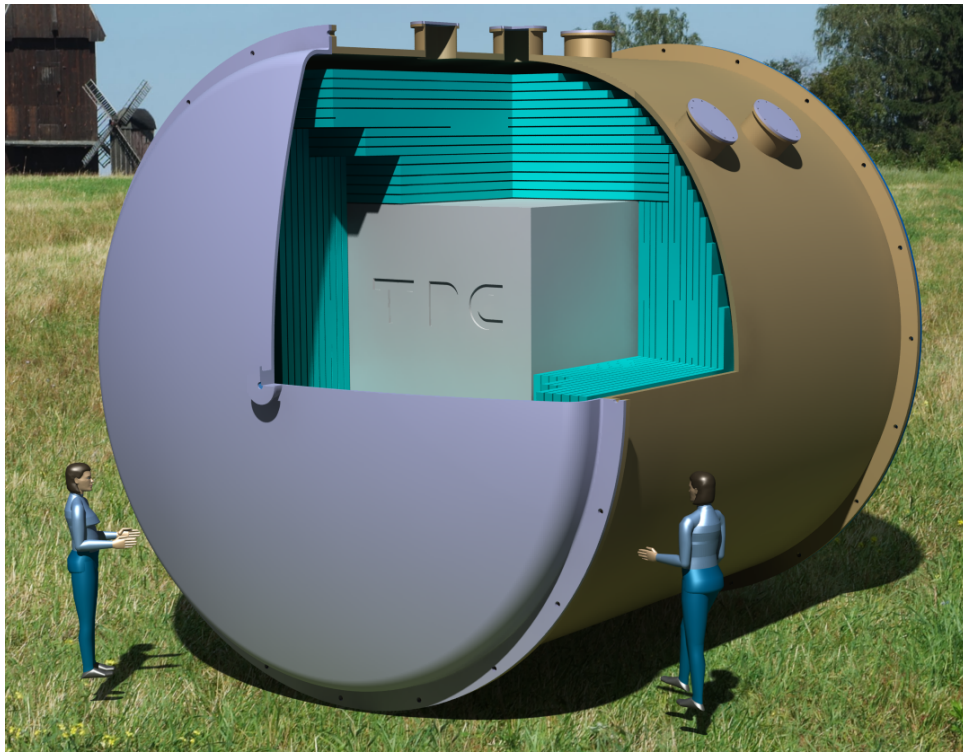


**Figure 7.7:** Sketch of the LBNO ND pressure vessel, showing its main features: the TPC, plastic scintillator modules surrounding the TPC, large flanges, feedthroughs.

## 7.5 LBNO ND Study Plan

### 7.5.1 Phase 0

- B-field calculation: Estimate analytically a value for the B-field which is appropriate for momentum resolution inside the TPC.

### 7.5.2 Phase 1

- Only consider instrumented TPC: Simulate neutrino events inside the TPC only.
- Determine particle fluxes out of each TPC face: Record energy spectra for secondaries exiting the six faces of the TPC. This is in order to estimate analytically the number of plastic scintillator layers required around the TPC, especially upstream of the TPC.

### 7.5.3 Phase 2

- Consider pressure vessel layer: Take into account pressure vessel. More generally, take into account neutrino interactions outside the TPC, in the outlying layers of plastic scintillator, the pressure vessel, the magnet steel, the rock in the ND cavern.

- Determine particle fluxes: Simulate particle fluxes from the different sources mentioned above, to estimate whether pile-up could be an issue.

#### 7.5.4 Phase 3

- Introduce scintillator/radiator: Describe scintillator in the detector geometry.
- Introduce rock environment. The rock environment is required to study the effects of background on the reconstruction of events in the TPC.

#### 7.5.5 Phase 4

- Detector optimisation. General optimization of the detector, including some event reconstruction in the TPC and the plastic scintillator. For high energy muons ( $>3$  GeV), include the ECAL and the MIND in the simulations.

#### 7.5.6 Phase 5

- Pit optimization within rock: Phase 5 is to be considered once a clear technical description of the ND is available. The pit optimization would then be carried out to determine appropriate lengths between the cavern edge and the detector for all sides of the detector.
- Magnet optimisation: The magnet optimization is a task to be carried out by specialist magnet designers for the specific application of the LBNO ND. Once the optimization is done, the resulting B-field can serve as a new input to the simulation process.

### 7.6 Software framework

The complexity of the task of simulating a ND for a neutrino beam experiment puts strong requirements on the necessary software framework. The experimental setup consists of relatively independent elements working cohesively, but having different requirements for simulation. It is therefore natural to subdivide the process of the simulation into several steps. For example:

1. Simulation of the target station, the focusing system and the decay pipe;
2. Simulation of the neutrino interactions in different material;
3. Tracking of the secondary particles inside the detector;
4. Digitization of the detector response;
5. Reconstruction of the neutrino events;
6. Analysis of the results.

Having this in mind, along with the fact that some of the steps, listed above, require usage of the external third party libraries like Root, Geant4, Fluka, Genie, etc., we have designed a framework which is flexible and adaptable, but in the same time is easy to use and maintain.

The framework provides:

- Scripts for automatic installation of the third party libraries;
- Build system based on CMAKE;
- Data structure and data recording in Root files.

- Process management that provides standardised data flow between the different steps of the simulation and allows to run all these steps into a single program.

The current status of the software covers some of the steps discussed but is far from a complete simulation package. Steps 2 and 3 are extensively covered while areas 4,5 and 6 are still in early development. With fairly primitive reconstruction implementation and basic detector effects modeled. No simulation of the beam is included, step 1, this is currently done externally by the beam group in LAGUNA.

The code of the project is available at <https://launchpad.net/lbno-nd>

### 7.6.1 Third Party Dependency Software Versions

The currently implemented software uses the following versions of third party software shown in table 7.3.

Third party software	Version
ROOT [95]	5.34.05
GENIE [96]	2.6.6
Geant4 [97]	4.9.6.p01
CLHEP	2.1.3.1
Pythia	v6.424
LHAPDF	5.8.7
Xerces	3.1.1
g4vmc	2.13a

**Table 7.3:** An extensive table showing all third party software and versions used for current simulation studies

## 7.7 Simulations

The following sections relate to Monte Carlo (MC) studies using the software described in the previous section.

### 7.7.1 The Near Detector Implementation in the Software

The current Near Detector (ND) design is implemented in ROOT [95] and GEANT4 [97]. Dimensions and parameters are at a preliminary stage but can be easily altered in the software to fit users requirements. The geometry displayed in ROOT is shown in figure 7.8. Detector effects are not modelled in the software and only detector mass and orientation are of concern for the current design study. The geometry in root is not a detailed and precise model of the actual design proposed but is designed to be a very close representation of it.

The code for the geometry construction is available at <https://launchpad.net/lbno-nd/geomconstruct>.

#### 7.7.1.1 The Time Projection Chamber

The Gas Argon Time Projection Chamber (TPC) is the primary target of the detector, shown in purple, consisting of a gas mixture of 95% Ar<sup>40</sup>, 3% CH<sub>4</sub> and 2% Isobutane (C<sub>4</sub>H<sub>10</sub>). The gas pressure is 20 atm, which is contained in a volume of  $2.4 \times 2.4 \times 3.0 \text{ m}^3$ . The corresponding density of the gas for this pressure is  $0.035 \text{ gcm}^{-3}$ , yielding a target mass of 605 kg. The introduction of cathode and anode plates (red in figure) in the TPC reduces this active volume by

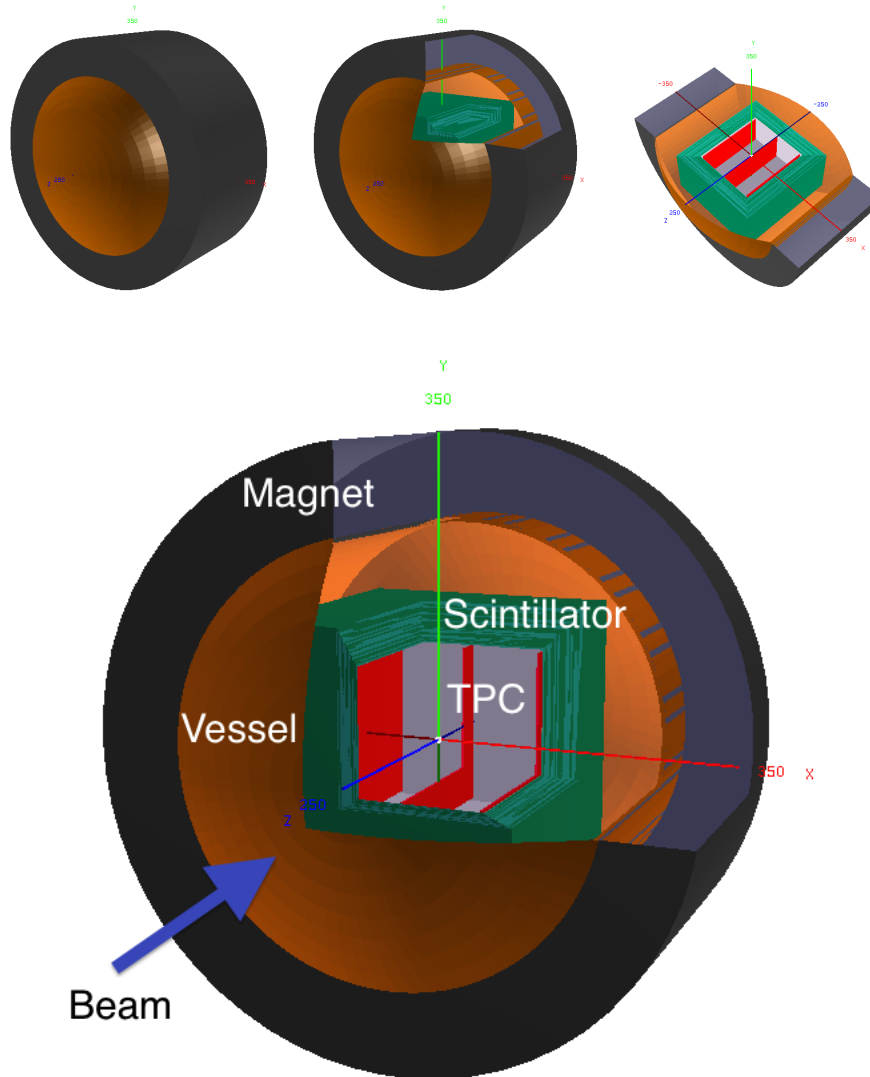


**Figure 7.8:** Top: Images of the ND geometry in the ROOT display for closed (left), partly open (middle) and cross section (right). Bottom: A fully labelled image showing dimensions in cm with detector chambers labelled.

$\sim 7$  kg. Each plate has a thickness of 13.2 mm with length and width of 2.3 m, based on the T2K ND280 detector design.

### 7.7.1.2 The Scintillator Bars

The scintillator bars are simulated as plastic planes ( $C_5O_2H_8$ ), of density  $1.18 \text{ gcm}^{-3}$ , placed to surround the TPC, with each layer increasing in size to fully enclose the previous layer. These planes are 10 mm thick, with 31 layers on each side of the TPC. The number of layers is limited by the inner pressure vessel dimensions. The total mass is then 18600 kg.

No radiator is implemented until further studies suggest their need for inclusion.

### 7.7.1.3 The Vessel

The pressure vessel is 20 mm thick Aluminium, with a vessel diameter of 5 m and total length of 5 m, including the curved ends. The gas inside the vessel matches the TPC.

### 7.7.1.4 The Magnetic Field

The magnetic field is simulated as a dipole of constant magnetic field strength of 0.5 T. Requiring  $\delta p/p \sim 5\%$  for a 3 GeV muon, given  $\delta s \sim 300 \mu\text{m}$  (T2K ND280), yields  $\sim 0.5$  T. The magnetic field is only implemented across the TPC as for current studies we are only concerned with this area of the detector.

### 7.7.1.5 The Magnet

In order to maintain a magnetic field strength of 0.5 T a 1 m thick Iron Magnet surrounds the pressure vessel. With a length of 3 m, the magnet mass is considerable at 440 tonnes.

### 7.7.1.6 The Surrounding Environment

Similar to the T2K near detector (ND280), the cavity is a topless pit, composed of Air. The detector is then situated on the bottom of this pit which is excavated in the rock environment. The rock is modelled as sandstone ( $SiO_2$ ) with a constant density of  $2.3 \text{ gcm}^{-3}$ . At least 30 m of rock surrounds the ND, to allow for highly energetic muons of up to 20 GeV to reach the ND.

Materials are summarised in table 7.4.

**Table 7.4:** Material Parameters.

Item description	Composition (%)	Density [ $\text{kgm}^{-3}$ ]
TPC Gas Mixture [20 bar]	Ar(95), $CH_4$ (3), Isobutane(2)	35
Scintillator	$C_5O_2H_8$ (100)	1180
Vessel	Al (100)	2700
Magnet	Fe (100)	7870
Cavity	N (78),O (22)	1.29
Rock	O (53), Si (47)	2323



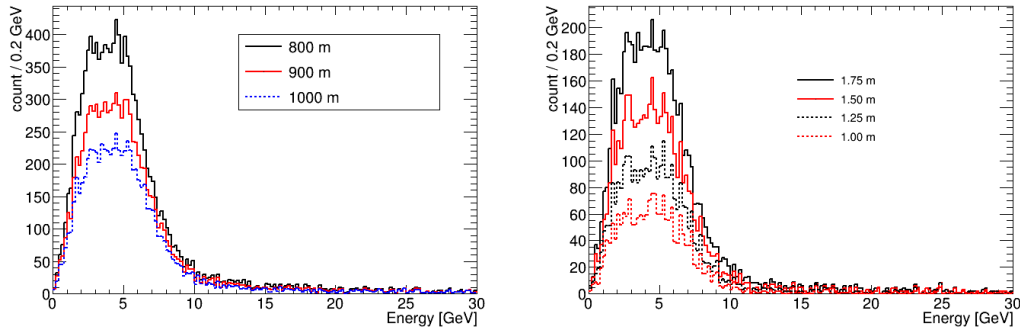


**Figure 7.9:** Left: The muon neutrino energy spectra expected at the ND for placements of 800, 900 and 1000 m from the target. Right: The muon neutrino energy spectra expected at the ND for various radius cuts.

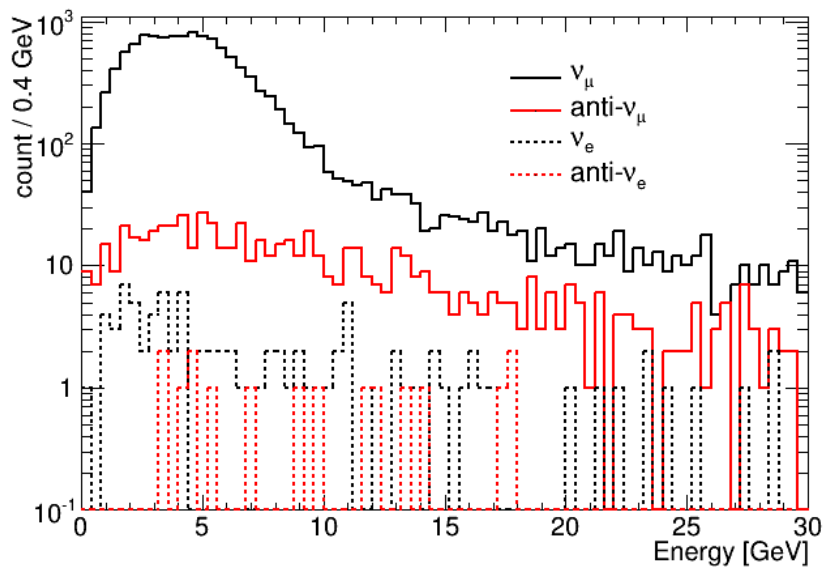


**Figure 7.10:** The neutrino energy spectra, for flavour breakdown, expected at the ND of 800 m. Showing 4 flavours,  $\nu_\mu$  in solid black,  $\bar{\nu}_\mu$  in solid red,  $\nu_e$  in dashed black and  $\bar{\nu}_e$  in dashed red.

### 7.7.2 Simulation of the Beam

FLUKA [98] simulations have been conducted to model the beam to be used within the ND software framework. Neutrino vertices are output from the beam simulation and are used as primary input for the ND software. Figure 7.9 shows a comparison of these distances for the  $\nu_\mu$  energies expected at the ND, produced exclusively from the beam target. The dependence on the TPC size is also shown in figure 7.9, with the current dimensions of  $2.4 \times 2.4 \times 3.0 \text{ m}^3$ , a beam radius of 1.75 m corresponds to full TPC coverage. At  $\sim 1 \text{ m}$  radius, the  $\nu_\mu$  energy peak is dramatically reduced, resulting in a TPC with  $2.0 \times 2.0 \text{ m}^2$  or less cross sectional area having a dramatically reduced interaction rate.

It must be noted that the ND in LAGUNA is on-axis in order to cover the energy range required for oscillation measurements. Fixing the detector at 800m from the target the resulting flavour beam composition is shown in figure 7.10, excluding tau neutrinos. The composition of the beam is  $\sim 94\% \nu_\mu$ ,  $5\% \bar{\nu}_\mu$ ,  $>1\% \nu_e$  and  $>0.1\% \bar{\nu}_e$ .

### 7.7.3 Expected TPC Rates

Estimations of acceptable rates for the TPC were derived in the context of LBNO to ensure the detector is operational in a regime where pile-up is not an issue, although it is unavoidable. The main criteria are those that are relevant to vertex reconstruction in the presence of multiple tracks. The assumptions on the beam were set for the SPS operating in double extraction mode:

- SPS pulse = 2 spills, each  $3.5 \times 10^{13}$  protons;
- Spill duration =  $10.5 \mu\text{s}$ ;
- Separation between spills within pulse = 50 ms.

For a TPC drift length of 1.25m, 20 bar Ar, 1 kV/cm ( $E/p = 0.05 \text{ kV/cm/bar}$ ) which is considered feasible, a drift velocity in the range  $1\text{-}3 \text{ cm}/\mu\text{s}$  can be expected [99]. This in turn leads to a drift time of order  $100 \mu\text{s}$ . Based on the beam time structure, further assumptions were made for the TPC:

- The TPC will integrate all events within an SPS spill;
- Second spill events are not affected by first spill events;
- Event reconstruction is not possible if a track crosses within a  $5 \times 5 \times 5 \text{ cm}^3$  volume of the vertex.

A limit to the muon background from the target was imposed as a constraint for the optimization of the beam, set to  $2.5 \text{ muons/m}^2/1.0 \times 10^{13}$  protons. This leads to 52 tracks per spill in the TPC, or 2% of the TPC detector cross-section perpendicular to the beam.

Given the wide energy range of the incident neutrino flux, the ND can expect a large muon rate. This will be composed of 3 main components, beam induced muons, sand muons and signal muons. Distinguishing the latter from the former two is crucial for measurements. The beam design must be concerned with minimising the high energy beam muons that persist through the rock and the ND design must consider minimising the sand muon rate. Sand muons refer to muons that are produced from interactions in the surrounding detector environment. The largest contribution being from the rock but also including interactions that occur inside the ND components except the TPC. Figure 7.11 shows the potential tracks that could pass the TPC.

For a beam spill of  $3.5 \times 10^{13}$  protons, an upper limit of  $9 \mu/\text{m}^2$  per spill has been established. This considers muons arising from the beam target, focusing horns and decay pipe. Using the software framework, estimates have been established for sand muon rates. The neutrino

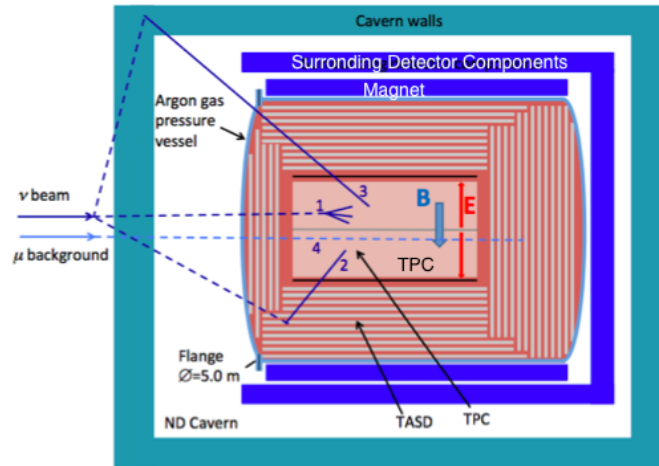


**Figure 7.11:** An illustration of the ND in the rock environment showing the potential muon tracks that would reach the TPC. The beam is incident from the left and the detector cross section is perpendicular to the beam axis.

rates for interaction inside the TPC are also calculated, in order to give an estimate for the background to signal muons. This is summarised in table 7.5.

distance [m]	800	900	1000
$\nu$ inside TPC [ $\mu/m^2/spill$ ]	$0.0250 \pm 0.0004$	$0.0204 \pm 0.0003$	$0.0159 \pm 0.0002$
$\nu$ outside TPC [ $\mu/m^2/spill$ ]	$6.11 \pm 0.05$	$4.92 \pm 0.04$	$3.98 \pm 0.04$
outside/inside ratio	$244.4 \pm 4.4$	$241.2 \pm 3.1$	$250.3 \pm 4.0$

**Table 7.5:** A table showing the number of muons per spill reaching the TPC from neutrino interactions inside and outside the TPC. Inside the TPC corresponds to a signal muon and outside corresponds to a sand muon. Errors are statistical only.

From these  $\sim 98\%$  occur in the rock, with  $\sim 2\%$  originating from the magnet, coherent with the rock to magnet mass ratio. Other parts of the detector contribute  $< 1\%$ .

The ratio of muons originating from outside to inside the TPC is large, 244 for 800 m from the target and remains constant for the other distances. At this distance it can be expected  $\sim 15 \mu/m^2/spill$  in the TPC for both beam and sand muons. In addition the signal muons contribute  $\sim 0.03 \mu/m^2/spill$ . This corresponds to 1 signal muon track for every 500 beam and sand muons.

The muon kinetic energies are shown for both sand and signal muons in figure 7.12. It can be noticed that the spectra are similar in shape, with slightly more lower energy muons originating from the outside. Around the energies of interest, 2 to 5 GeV, there is little difference between the two spectra.

### 7.7.4 Neutrino Interactions in the TPC

The particle types emitted from the neutrino vertices in the TPC are shown in table 7.6. This follows for an exposure of  $1.22 \times 10^{20}$  p.o.t yielding a total of 457039 neutrino interactions in the volume with 75% of these occurring in the active volume. With an average multiplicity of 6.5 particles / event it is paramount that the TPC can distinguish between these particle tracks.

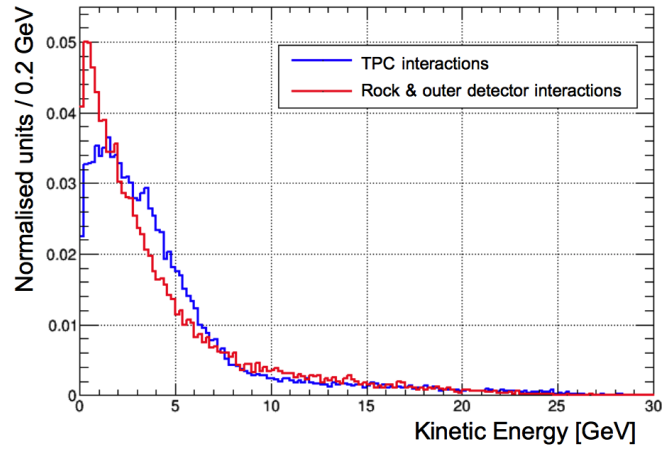


**Figure 7.12:** The kinetic energy spectrum for muons in the TPC for neutrino interactions originating in (blue) and outside (red) the TPC.

particle	count
p	647631 (28.9%)
n	533868 (23.9%)
$\pi^+$	277825 (12.4%)
$\pi^0$	265408 (11.9%)
$\mu^-$	243577 (10.9%)
$\pi^-$	144379 (6.5%)
$\gamma$	23000 (1.0%)
$\mu^+$	11953 (0.5%)
$e^-$	2981 (0.1%)
$e^+$	439 (<0.1%)
other	86120 (3.8%)
<b>Total</b>	<b>2237481</b> (excluding $\nu$ )

**Table 7.6:** A table showing the number of primary particles generated at in the TPC from neutrino interactions.

### 7.7.5 Particles leaving the TPC

In order to optimize the detector layers outside the TPC, it must be understood what particles are leaving the primary target. Since the TPC is of cube shape, each face of the cube can be used to monitor particle flux. Defining the beam direction in the z axis, the downstream and upstream faces are perpendicular to this axis at positive and negative z respectively. The faces perpendicular to the magnetic field are defined as top and bottom, positive and negative y respectively. The remaining faces are then defined as positive and negative x for left and right.

Defining  $\cos\theta = p_z/|p|$ , each face can be projected onto the z momentum (in the beam direction) of the particles leaving the TPC. The kinetic energies as a function of the angular distribution are shown in figure 7.14. It can be seen that the muons are very forward going with the peak energy around 4 GeV, making the need for a MIND a necessity. The pions have a large angular distribution, with energies  $> 1$  GeV, requiring the scintillator layer to contain them. Particles other than forward going (positive z plane) have kinetic energies below 5 GeV, with many  $< 1$  GeV.

The particle numbers leaving the TPC for an exposure of  $1.77 \times 10^{20}$  protons on target (p.o.t), are shown in table 7.7. The majority of the particles are photons, with 38% leaving the volume which includes all photons originating from  $\pi^0$  decays.

particle	$\mu^-$	p	$\pi^+/\pi^-$	$e^-$	$\gamma$	n
leaving TPC	441775 (5.6%)	801459 (10.1%)	727786 (9.2%)	314400 (4.0%)	2996796 (37.9%)	2148620 (27.2%)
downstream	382015 (86%)	319162 (40.0%)	429119 (58.9%)	91056 (29.0%)	940483 (31.4%)	465392 (21.7%)

**Table 7.7:** A table showing the number of muons per spill reaching the TPC from neutrino interactions inside and outside the TPC. Inside the TPC corresponds to a signal muon and outside corresponds to a sand muon. Errors are statistical only.

### 7.7.6 TPC Momentum Reconstruction Techniques

It is possible to reconstruct the neutrino momentum from a measurement of the track sagitta, using equation ??.

$$p = \frac{BL^2}{26.7} \frac{1}{s} \quad (7.1)$$

The magnetic field, B is measured in Tesla, the length, l, and sagitta, s, are measured in m, yielding a value of the momentum in GeV/c. To measure the sagitta, no track reconstruction is implemented in the software, instead a smearing technique is employed. Using the truth value for the particle momentum, the sagitta value is then calculated using equation ?. Smearing this value over a Gaussian distribution a new value is taken for the sagitta and the momentum is recalculated to yield a reconstructed momentum measurement. A resolution of  $\delta s = 300 \mu\text{m}$  is used, following from previous assumptions. For an event, each track is reconstructed using this technique and summed to give a reconstructed neutrino momentum,  $p_\nu$ , equation ??

$$p_\nu = \sum_i^{\text{tracks}} p_i \quad (7.2)$$

In the software a requirement of at least 3 'hit points' per track is enforced for an event to be a candidate for reconstruction. A hit point is defined in GEANT as a point in which the particle deposited energy in the gas, set to a user specific threshold. Only events are reconstructed when all tracks meet this requirement. To further enforce this condition applying fiducial cuts on the TPC volume are used.

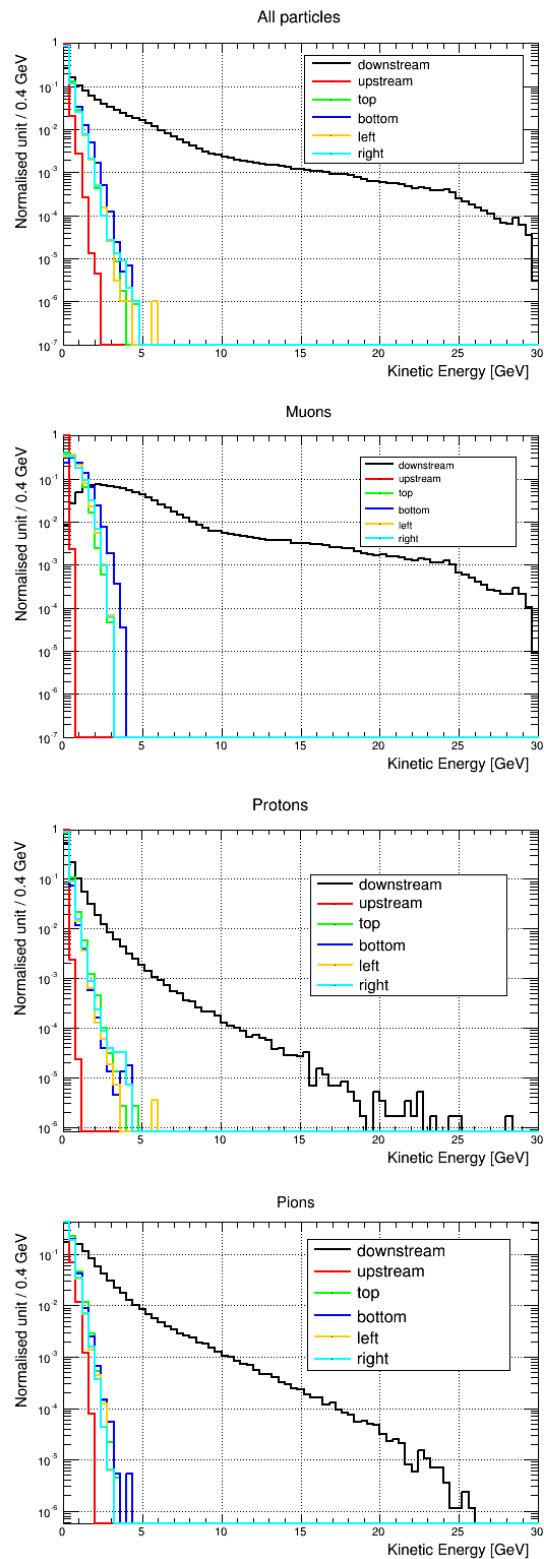


**Figure 7.13:** The kinetic energies for particles leaving the TPC are shown for each face of the TPC. Upper left shows all types, upper right shows protons, lower left shows muons and lower right shows pions.

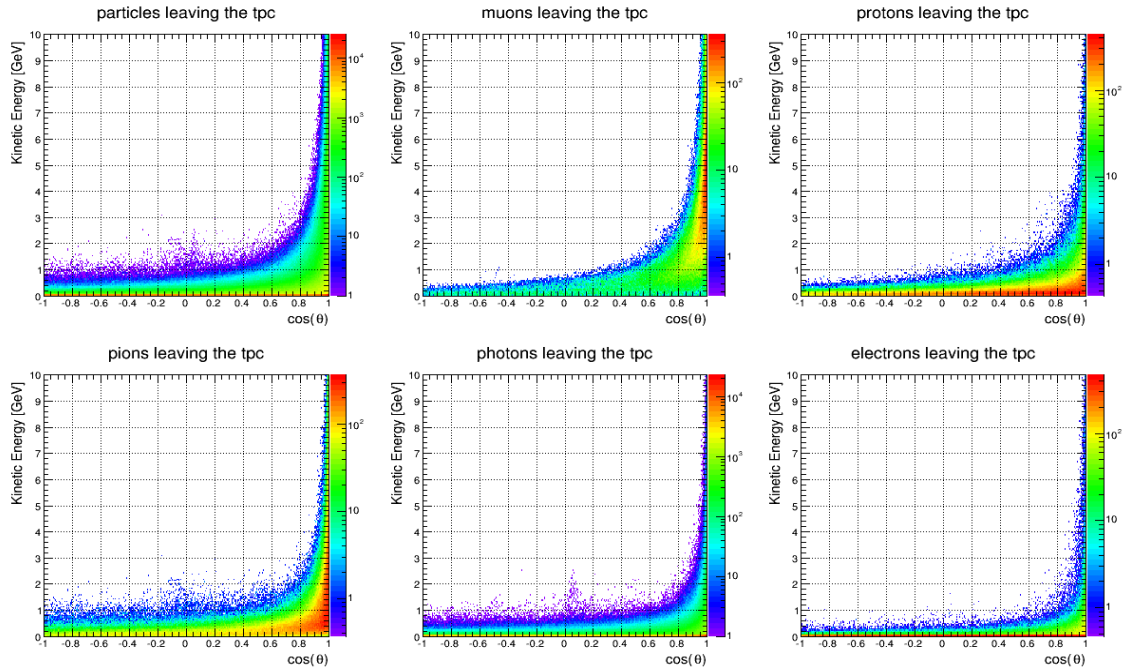


**Figure 7.14:** The kinetic energy as a function of angular distribution for particle type breakdown. Clockwise from the top left we have all particles, muons, protons, electrons, gammas and pions.

For an exposure of  $1.77 \times 10^{20}$  p.o.t,  $1.09 \times 10^6$  neutrino interactions in the TPC can be expected. Employing a fiducial cut of 20 cm,  $6.7 \times 10^5$  (61%) events remain that can be used for momentum reconstruction. Of these events  $3.8 \times 10^4$  (5.7%) are Charged Current Quasi-Elastic (CCQE) events. Using equation ?? figure 7.16 shows the result from event by event reconstruction for all neutrino interaction and for CCQE only. It is expected that the reconstruction is poor for all event types as many neutral particles will not show in the TPC. However for CCQE interactions the proton and muon should show in the TPC, meaning the neutrino momentum should be well reconstructed. Figure 7.15 shows two event displays from the simulation, both show a CCQE interaction, one well reconstructed and one poorly reconstructed.

It is also possible to use only the muon momentum to fully reconstruct the neutrino momentum for CCQE interactions. Equation ?? is used to see if the reconstruction can be improved, so the smearing on the proton is not used. Using the mass of the muon,  $m_\mu$ , proton,  $m_p$  and assuming the beam is incident from the z axis, the energy of the muon,  $E_\mu = \sqrt{m_\mu^2 + p_\mu^2}$  is calculated and then the neutrino momentum is known.

$$E_{\nu_\mu} = \frac{E_\mu m_p - m_\mu^2}{m_p - E_\mu + p_\mu \cos\theta} \quad (7.3)$$

This benefit of using equation ?? instead of a simple momentum sum of  $p_\mu + p_p$  is highlighted in the lower plot of figure 7.17.

Using these various techniques and event types, the resultant reconstructed neutrino momentum at the ND is shown in figure 7.18. The truth values are shown in black, with reconstructed values for all neutrino interaction events are shown in red. Reconstructing CCQE events only are in blue and the green is CCQE with only the muon momentum used.

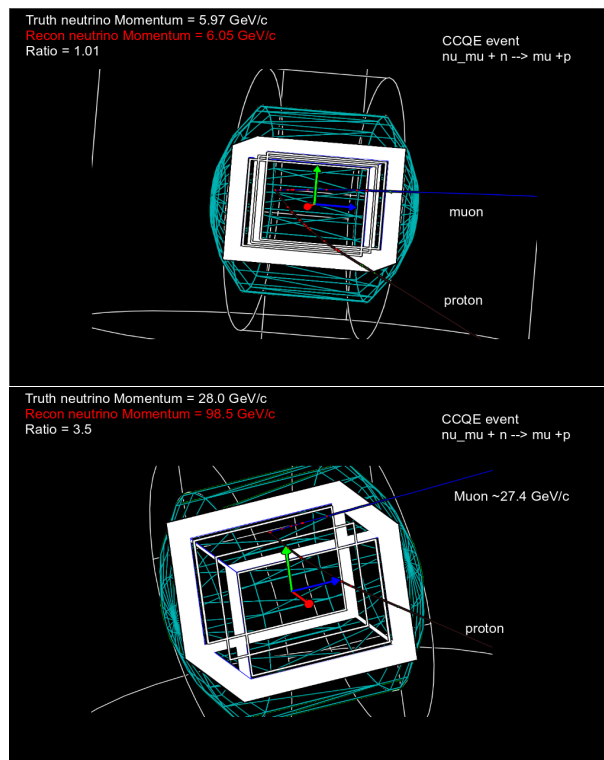


**Figure 7.15:** Event displays output from the simulation. Left image shows a well reconstructed CCQE event, while the right shows a poorly reconstructed CCQE event.



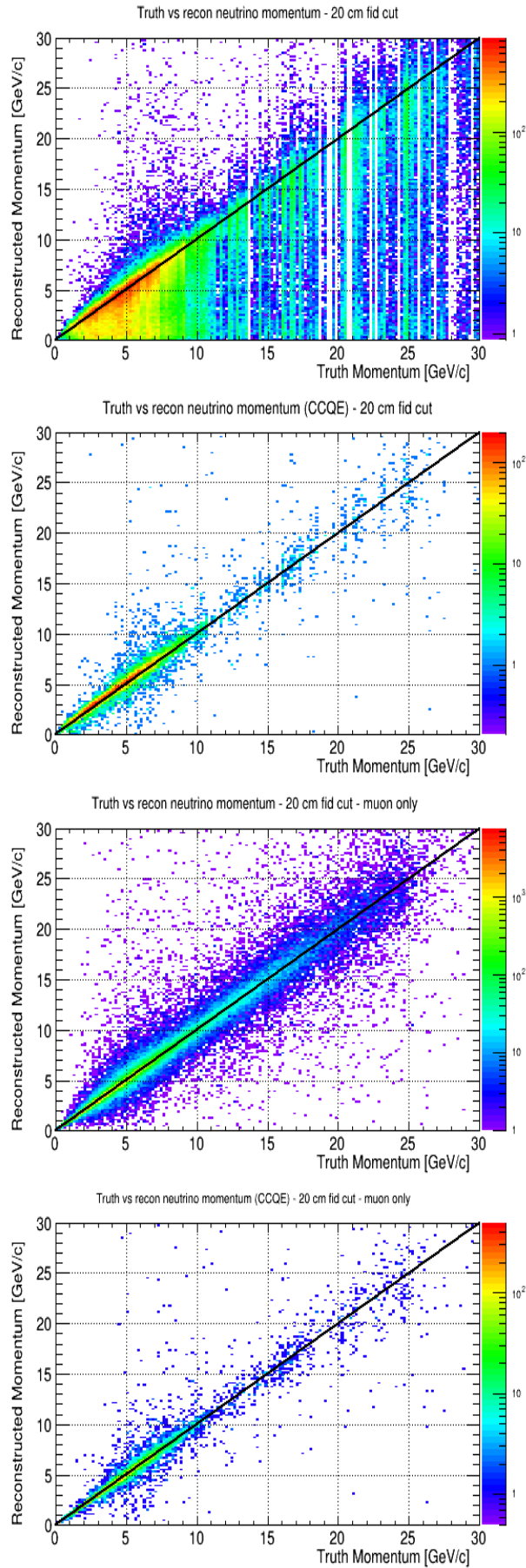


**Figure 7.16:** Left: The comparison of truth vs reconstructed muon neutrino momentum on an event by event binning. Right: The comparison of truth vs reconstructed muon momentum on an event by event binning. Upper plots show all neutrino interaction types, with only CCQE events shown in the lower plots.

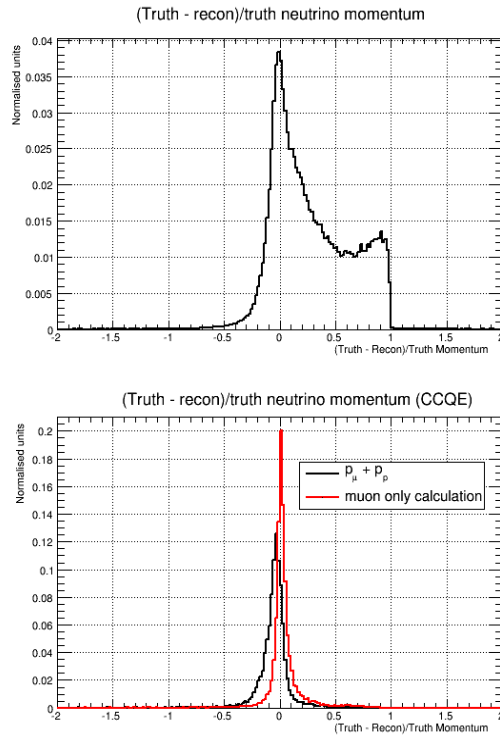


**Figure 7.17:** Upper: The (truth - reconstructed)/truth neutrino momentum for all interaction types. Lower: The (truth - reconstructed)/truth neutrino momentum for CCQE events only, with equation ?? used in black histogram and equation ?? for the red histogram. For neutrino truth energies  $\leq 10$  GeV

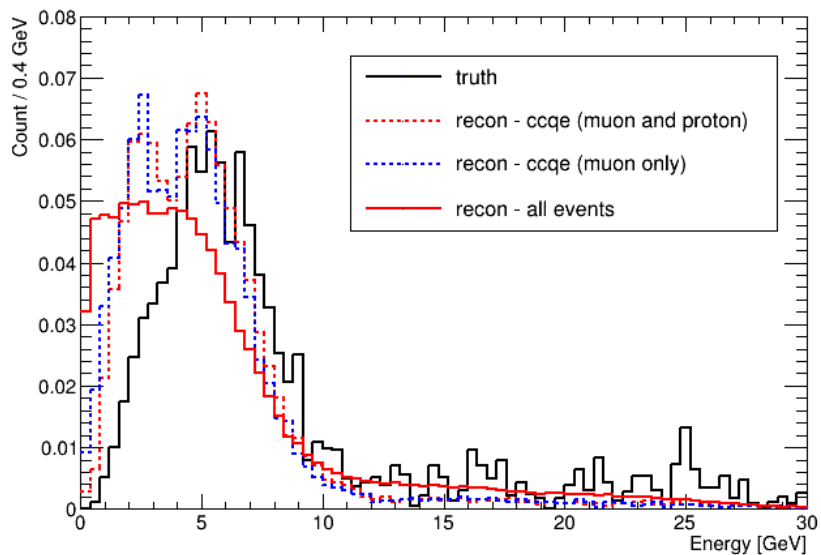


**Figure 7.18:** The comparison of reconstructed neutrino momentum with truth values. The black histogram corresponds to truth values while the red histogram is for all reconstructed events. Using only CCQE events, the dotted red is using the momentum sum of the proton and muon and the dotted blue is using only the muon momentum.



## Chapter 8

# Radiation and Environmental Aspects

### 8.1 Radiological aspects

As LAGUNA – LBNO aims at pushing the primary proton beam to a power of up to 2 MW, radiation protection considerations strongly determine the design of the facility. In particular extremely high prompt and residual dose rates call for considerable shielding and access restrictions allowing only remote interventions in some of the areas. Also the risk due to highly activated air and the impact of its release into the environment heavily influence the design. A few general radiation protection guidelines for the design of such a high powered facility are specified in Section 4.2.1. The most important aspects, which were studied in more detail and will be discussed later on, involve the following:

- **Prompt radiation:** Just as previous high power deep-underground facilities at CERN, LAGUNA – LBNO was designed under the condition that there is no access to its underground infrastructure<sup>1</sup> during beam operation. Considerable shielding is nevertheless required to reduce the prompt radiation and thus the resulting activation levels of the surrounding infrastructure and molasse. The prompt radiation was therefore studied to investigate the effectiveness of the various shielding components. Furthermore the prompt dose was evaluated for a given accident scenario.
- **Residual radiation:** The target area as well as the upstream part of the hadron stopper area will become highly activated. Studies were performed to assess the expected residual dose rates in these areas and the adjacent ones. The residual dose rates originating from the removable shielding as well as the target were further evaluated standalone. This information is essential for situations where these components must be handled, e.g. in case of a target failure.
- **Air and helium activation:** The air volumes in the high-radiation areas of the facility were minimised in order to reduce the production and releases of airborne radioactivity. In the most critical regions the air was furthermore replaced by a helium environment. The remaining production of radionuclides in air and helium and the consequent effective dose rates to workers and the reference group were evaluated. The impact of the releases to the environment and the resulting effective dose to members of the public are furthermore discussed in Section 8.2.
- **Molasse activation:** Thanks to the placement of the most activated elements of the facility in deep impermeable molasse that is not in contact with shallower aquifers in moraine located above, the radiological hazard arising from the activation of molasse is expected to be negligible. The geological structure is not suitable for exploitation of drinking water.

---

<sup>1</sup>It is assumed that the neutrino production target of LAGUNA – LBNO is located at a depth of about 80 - 100 m.

The activation of the molasse surrounding the facility has nevertheless been investigated. Owing to the magnitude of the activation, the environmental impact expected from it shall be investigated in combination with a hydrogeological study. It is discussed in more details in Section 8.2.

To assess the above-mentioned radiation protection aspects, extensive simulations were performed with the FLUKA Monte Carlo particle transport code [100, 101]. The details of these studies and their results as well as their impact on the design of the LAGUNA – LBNO neutrino production facility will be presented in this chapter.

Additional radiation protection studies like the production of radioactive waste, waste disposal, dismantling of the facility, etc. have not been investigated to date. These will however be required at a later stage of the project.

### 8.1.1 FLUKA studies

The Monte Carlo particle code FLUKA was used to evaluate the radiation protection requirements for the LAGUNA-LBNO neutrino production facility. The FLUKA model of the facility was developed in collaboration with EN-STI [104] and run under the latest version of the code (2011.2b.5). Figures 8.1 - 8.4 depict, from a radiation protection point of view, the most critical areas of the facility: the target chamber, its connecting tunnels and the hadron stopper area. The coordinate system used in the model is a right-handed Cartesian coordinate system with origin in the centre of the target front. The orientation of the coordinate system is defined by the width (x) and height (y) of the target chamber and the beam direction (z).

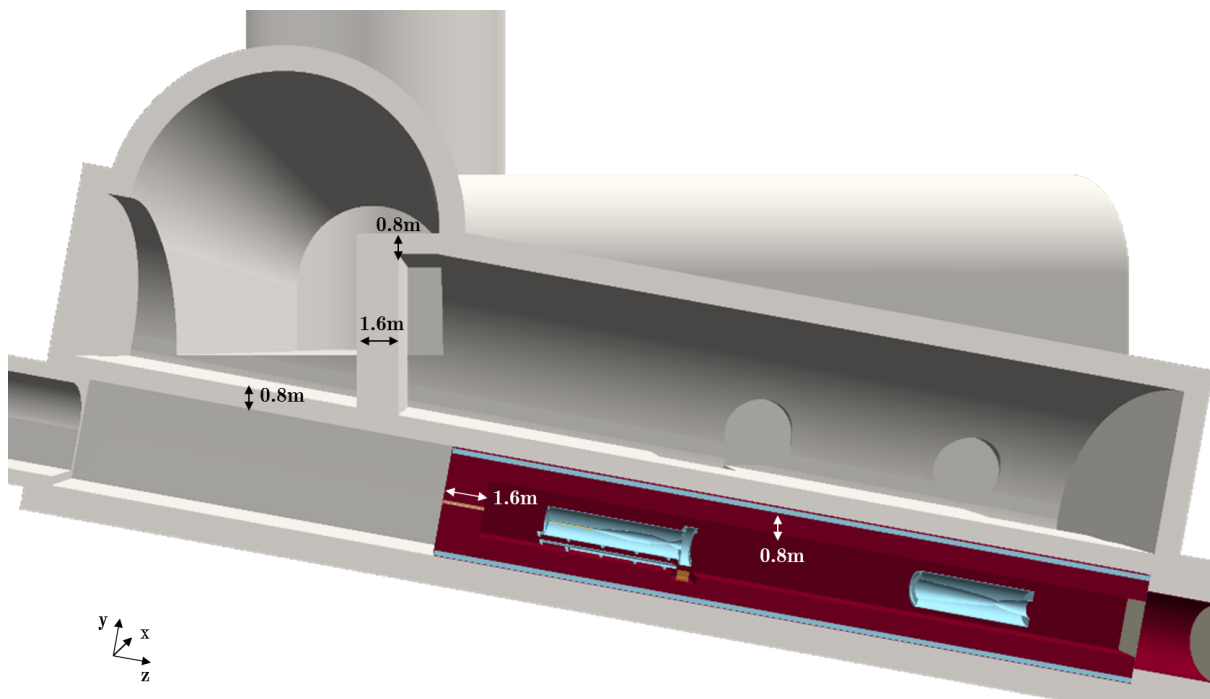


**Figure 8.1:** Side view of the LAGUNA – LBNO target chamber as implemented in FLUKA showing the He-vessel with the secondary beam-line elements and the central shielding blocks. Iron is displayed in red, concrete in grey, aluminium in light blue and graphite in yellow.

As mentioned before, LAGUNA – LBNO was designed under the condition that there is no access to the underground infrastructure during operation. Although this principally relaxes shielding requirements for personnel protection regarding prompt dose rates, massive shielding is nevertheless required to keep residual dose rates of the infrastructure reasonably low.

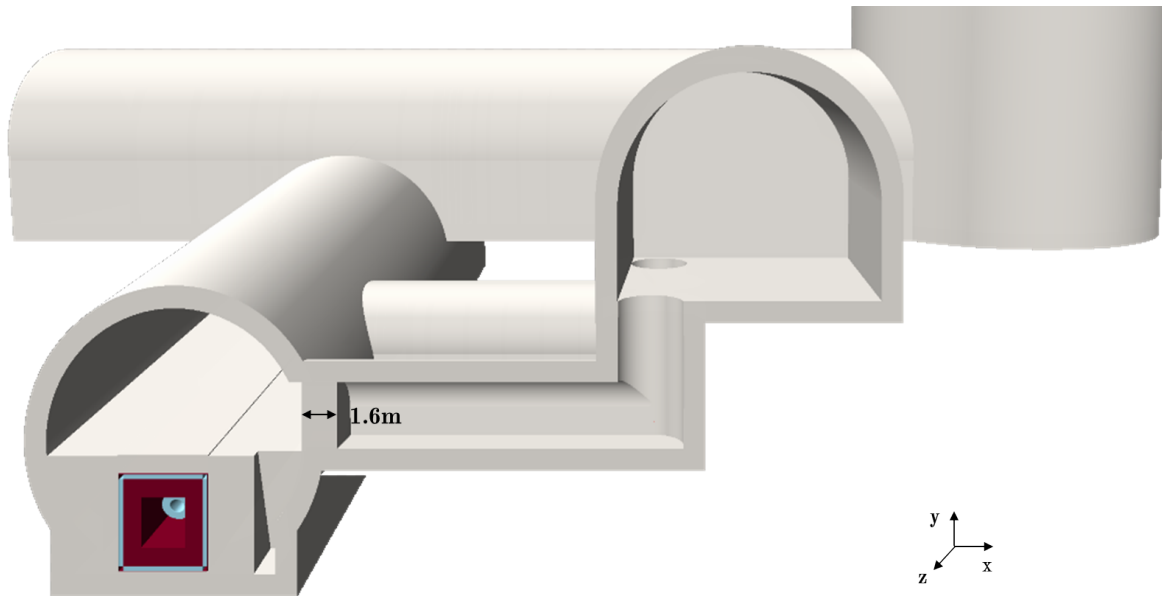


**Figure 8.2:** Back view of the LAGUNA – LBNO target chamber, the connection tunnels and the service gallery as implemented in FLUKA. Iron is displayed in red, concrete in grey, aluminium in light blue.

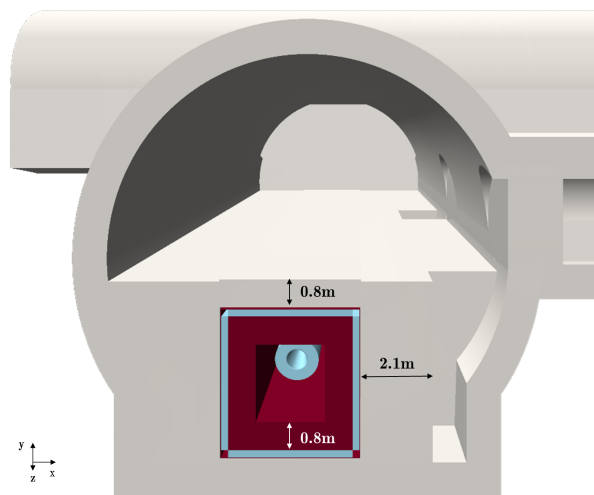


**Figure 8.3:** Back view of the LAGUNA – LBNO target chamber showing the shielding inside and around the He-vessel, the connection tunnels and the access shafts to the water sumps. Iron is displayed in red, concrete in grey, aluminium in light blue.

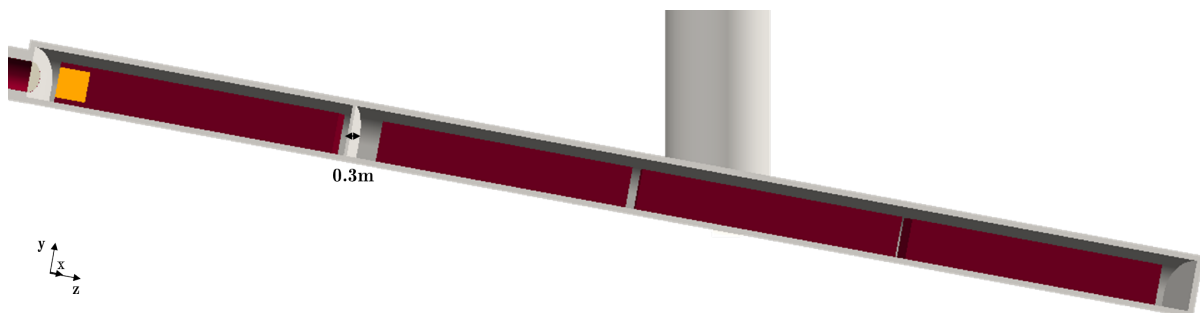


**Figure 8.4:** Side view of the LAGUNA – LBNO hadron stopper area as implemented in FLUKA. Iron is displayed in red, concrete in light grey and graphite in yellow.

Next to the personnel protection aspects, considerable shielding is also indispensable to lower the environmental impact from activated air and molasse activation as well as to relax radiation stresses on equipment (see Chapters 8.2). The shielding was consequently designed with the objective to keep prompt and residual dose levels as well as airborne radioactivity as low as reasonably possible, while taking the constraints from the different stages of the experiment, that is the construction, operation, maintenance and dismantling, into account.

The shielding in the target area was modeled with 80 cm thick iron blocks (160 cm upstream of the target) surrounded by 20 cm of aluminium blocks, which will include water cooling pipes for heat removal. They are embedded in a 2 cm thick He-vessel made out of iron, which is further enclosed by at least 80 cm of concrete. The opening in the shielding upstream of the target was minimized to 2 cm in diameter to avoid a “back splash” of particles into the primary beam area, which would increase the activation of the upstream beam-line components and the surrounding air. To reduce streaming of radiation from the target area into the neighbouring compartments, additional concrete shielding blocks of 160 cm thickness were foreseen for the beginning of the connection tunnels to the service gallery as well as to the transport tunnel. To account for possible weak points in the shielding, that may result from imperfect alignment, ducts for cooling, electronics etc., gaps of 1 cm and 4 cm thickness were introduced next to and above the He-vessel, respectively. These will be reviewed at a later stage of the experiment when a more detailed layout of the geometry is available. Note that any feed-throughs in the shielding should be implemented in a way that the shielding efficiency is not decreased (e.g. chicanes, additional shielding elements, etc.).

The material properties employed for the shielding components were chosen such that they result in rather conservative prompt and residual dose rate estimates. The composition of the shielding materials is given in Table 8.1. Note that for cast iron the self-shielded low energy neutron cross-sections were utilized in order to correct for self-shielding effects. A density of 7.2 g/cm<sup>3</sup> and 2.42 g/cm<sup>3</sup> was furthermore assumed for the iron and concrete components, respectively.

Material	Element	Weight percentage
<b>Cast iron</b>	Iron (self-shielded)	94.3%
	Carbon	3.4%
	Silicon	1.8%
	Manganese	0.5%
<b>Concrete</b>	Oxygen	52.9%
	Silicon	33.7%
	Calcium	4.4%
	Aluminium	3.4%
	Sodium	1.6%
	Iron	1.4%
	Potassium	1.3%
	Hydrogen	1.0%
	Magnesium	0.2%
	Carbon	0.1%

**Table 8.1:** Elemental composition of the shielding materials as defined in the FLUKA studies.

The air volumes of the facility were minimized to lower the production of airborne radioactivity. In the most critical area, that is the central region along the secondary beam-line, the air was further replaced by a helium environment. This is motivated by the fact that helium gives only rise to the formation of tritium, which has a significantly lower radiological impact than the radionuclides arising from air (see Section 8.1.5). Compartments like the target

chamber and the hadron stopper tunnel, in which considerable air activation is expected (see Section 8.1.4), are further separated from the accessible areas of the facility to avoid unjustified exposure to personnel. Therefore, airtight doors are foreseen between the target chamber and the access and service tunnels and a 30 cm thick concrete wall after the first 32 m of the hadron stopper tunnel. The activated air in the target chamber and the first part of the hadron stopper tunnel should only be released into the environment in case of access to these areas.

Two different beam scenarios, which assume operation with a 50 GeV and 400 GeV proton beam, were employed in the FLUKA studies. To obtain pessimistic dose rate estimates, the maximum of the expected beam power, intensity and operation time was used for each scenario. The various parameters are listed in Table 8.2. Figure 8.5 shows the comparison of the prompt and residual dose rates for the two different scenarios. It can clearly be seen that the most critical scenario is the one of 50 GeV due to its high beam power. As the 50 GeV scenario was also observed to be worse with respect to air and helium activation, the results presented in the following are limited to the 50 GeV scenario. One should note that the 400 GeV scenario however still effects other issues concerning the design of the facility such as the beam dump design.

	50 GeV	400 GeV
Beam energy	50 GeV	400 GeV
Beam power	2 MW	750 kW
Beam intensity	$2.5 \times 10^{14}$ p/s	$1.17 \times 10^{13}$ p/s
Beam profile	Gaussian FWHM 0.8 cm	
Duration	180 days continuous operation per year	

**Table 8.2:** Parameters of the two standard beam scenarios as employed in the FLUKA studies.

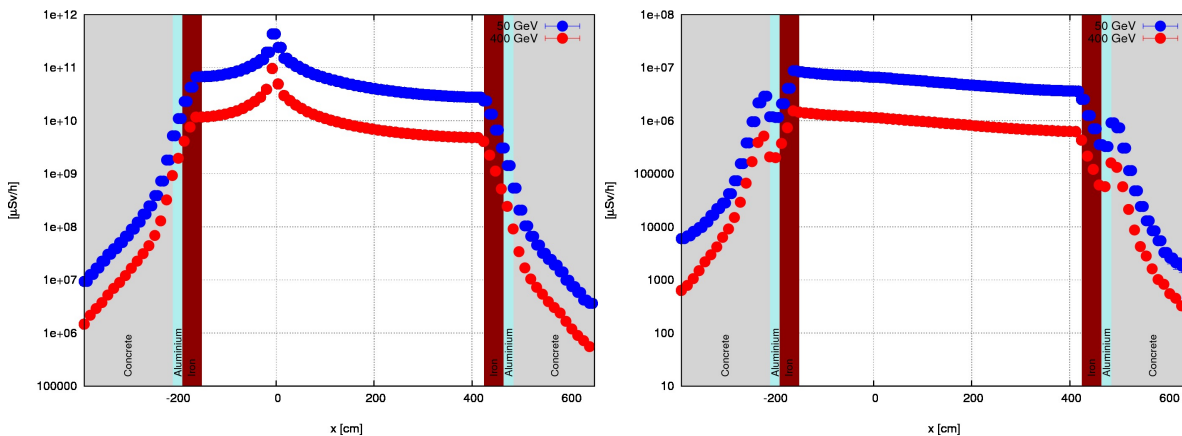


**Figure 8.5:** Prompt (left) and residual (right) dose rates (in  $\mu\text{Sv/h}$ ) for the 50 GeV (blue) and 400 GeV (red) beam scenario. Note that the given results were based on a preliminary version of the LAGUNA – LBNO target chamber geometry and are only shown for comparative purposes.

Next to the standard beam scenarios, also an accident scenario with beam loss in the upstream part of the target chamber was studied. Therefore, a loss of  $2.5 \times 10^{14}$  protons of 50 GeV onto a copper target (radius - 5 cm, length - 1 m) positioned in the primary beam-line below the transport tunnel was assumed.

### 8.1.2 Prompt dose rates

As previously mentioned, LAGUNA – LBNO was designed under the condition that there is no access to the underground infrastructure during operation. The prompt dose rates ex-



pected were nevertheless studied for the standard beam operation and the accident scenario, as they demonstrate the effectiveness of the various shielding components and allow for a further risk analysis of the facility. The prompt dose rates were calculated in a three-dimensional mesh covering the whole target chamber and the connecting tunnels. They were obtained by convoluting the fluence of neutrons, protons, charged pions and muons with the respective energy-dependent fluence-to-dose equivalent conversion coefficients [108]. Note that the contribution from photons, electrons and positrons was neglected for saving computing time. It has however been verified that it should be smaller than 15%.

Figures 8.6 and 8.7 show the prompt ambient dose equivalent rates in the target chamber predicted for the 50 GeV beam scenario. As expected, the highest dose rates can be found in the region of the target and the horn reaching up to  $10^{12}$   $\mu\text{Sv/h}$ . They are reduced by a few orders of magnitude in the surrounding iron, aluminium and concrete shielding. Outside of the shielding, the prompt dose rates amount up to a few  $10^7$   $\mu\text{Sv/h}$ . Note that the dose rates outside of the shielding can in reality be locally increased, as the simulation does not take possible weak points in the shielding like feed-throughs for cooling and cabling into account.

The radiation streaming from the target chamber into the duct, which is connecting the target chamber and the service gallery, is illustrated in Figure 8.8. It can be seen that the dose rates are significantly reduced with the help of the concrete shielding block located at the beginning of the duct, leaving dose rates of the order of a few  $\text{mSv/h}$  behind the shielding. The radiation further attenuates while traveling through the duct leading to dose rates of 30  $\mu\text{Sv/h}$  at the bottom end of the duct and of about 1  $\mu\text{Sv/h}$  at the beginning of the above service gallery.

The upstream part of the target chamber is furthermore connected to the morgue room and the transport tunnel. The expected dose rates in these regions are illustrated in Figure 8.9. They reach up to a few  $10^4$   $\mu\text{Sv/h}$  in the central region above the shielding however decrease with the length of the morgue room and transport tunnel. At the end of the transport tunnel the dose rates lie below 10  $\mu\text{Sv/h}$ .

The dose rates at the surface level can further be estimated by multiplying the dose rates observed at the end of the transport tunnel by an attenuation estimate in the access shaft [110]. Assuming an access shaft length of 80 m, the dose rates are expected to drop down to a level of about 0.05  $\mu\text{Sv/h}$  at the end of the shaft. Depending on the layout and the position of the above-ground infrastructure of the facility, the prompt radiation at the surface level and the stray radiation in the surrounding experimental and public areas are expected to decrease even further. A more precise analysis of it should be performed once the above-ground infrastructure has been designed, but the first estimate suggests acceptable radiation levels.

The prompt dose rates expected in case of the accident scenario with beam loss in the upstream part of the target chamber is shown in Figure 8.10. The dose rates reach up to the order of  $\text{Sv/h}$  in the target chamber above the shielding and still amount to a few  $\text{mSv/h}$  at the end of the transport tunnel. Note that additional weak points in the shielding may further increase the expected dose rates.

### 8.1.3 Residual dose rates

The residual dose rates were calculated in a three-dimensional mesh covering the whole target chamber and the hadron stopper tunnel. They were obtained by convoluting the fluence of photons, electrons and positrons from  $\gamma$ - and  $\beta$ -decays with the respective energy-dependent fluence-to-dose equivalent conversion coefficients [108]. Note that the air-filled regions were selectively set to vacuum when producing and transporting the radioactive decay products. In that way, radioactive decay products originating from the activated air were ignored. This is useful since the activated air inside of the target chamber is to be released into the environment in case of access and will therefore no longer contribute to the respective residual dose rates. The committed effective dose due to activated air was evaluated separately (see Section 8.1.4).

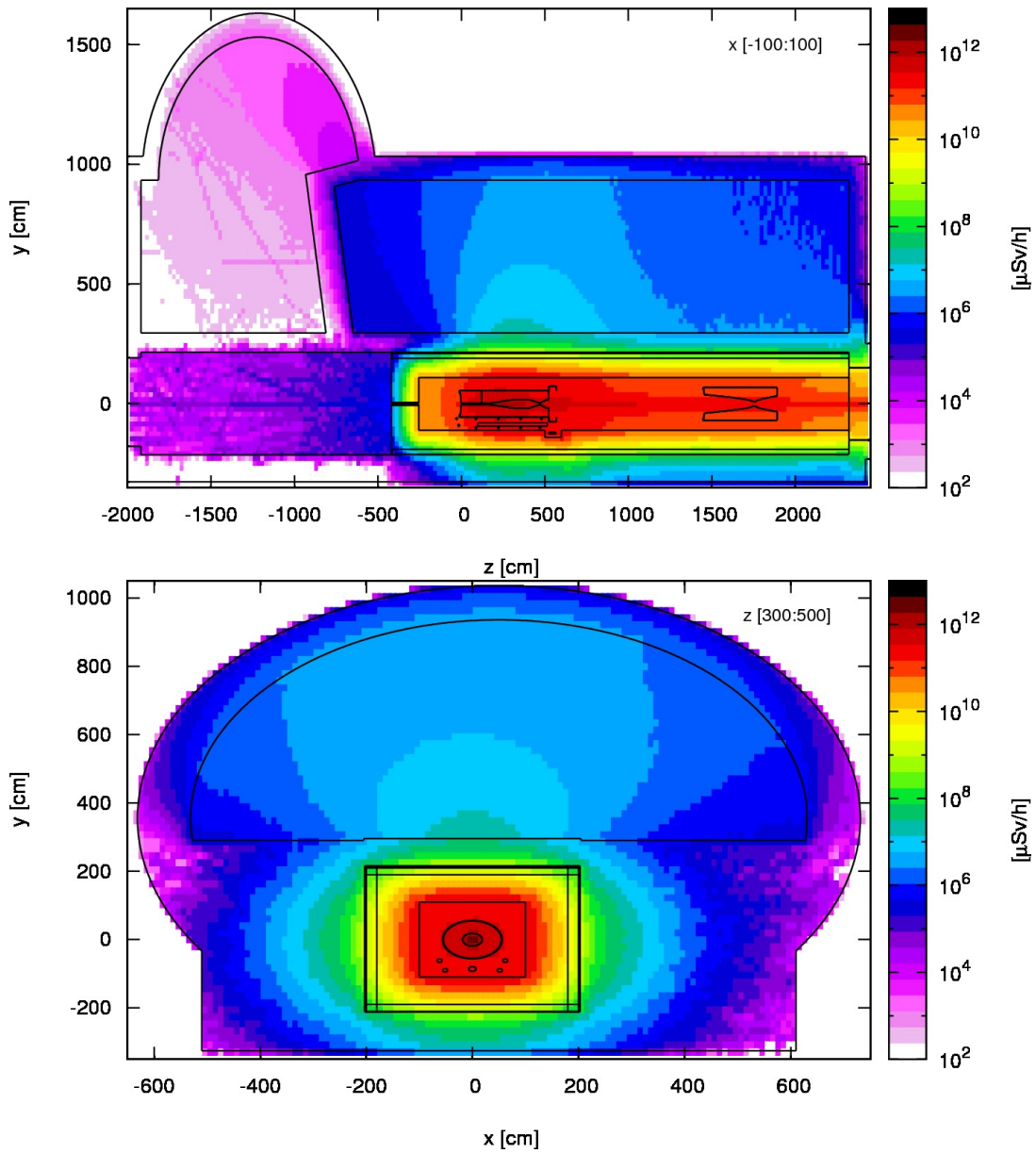


**Figure 8.6:** Prompt ambient dose equivalent rates (in  $\mu\text{Sv/h}$ ) in the target chamber (top: side view, bottom: front view at horn).

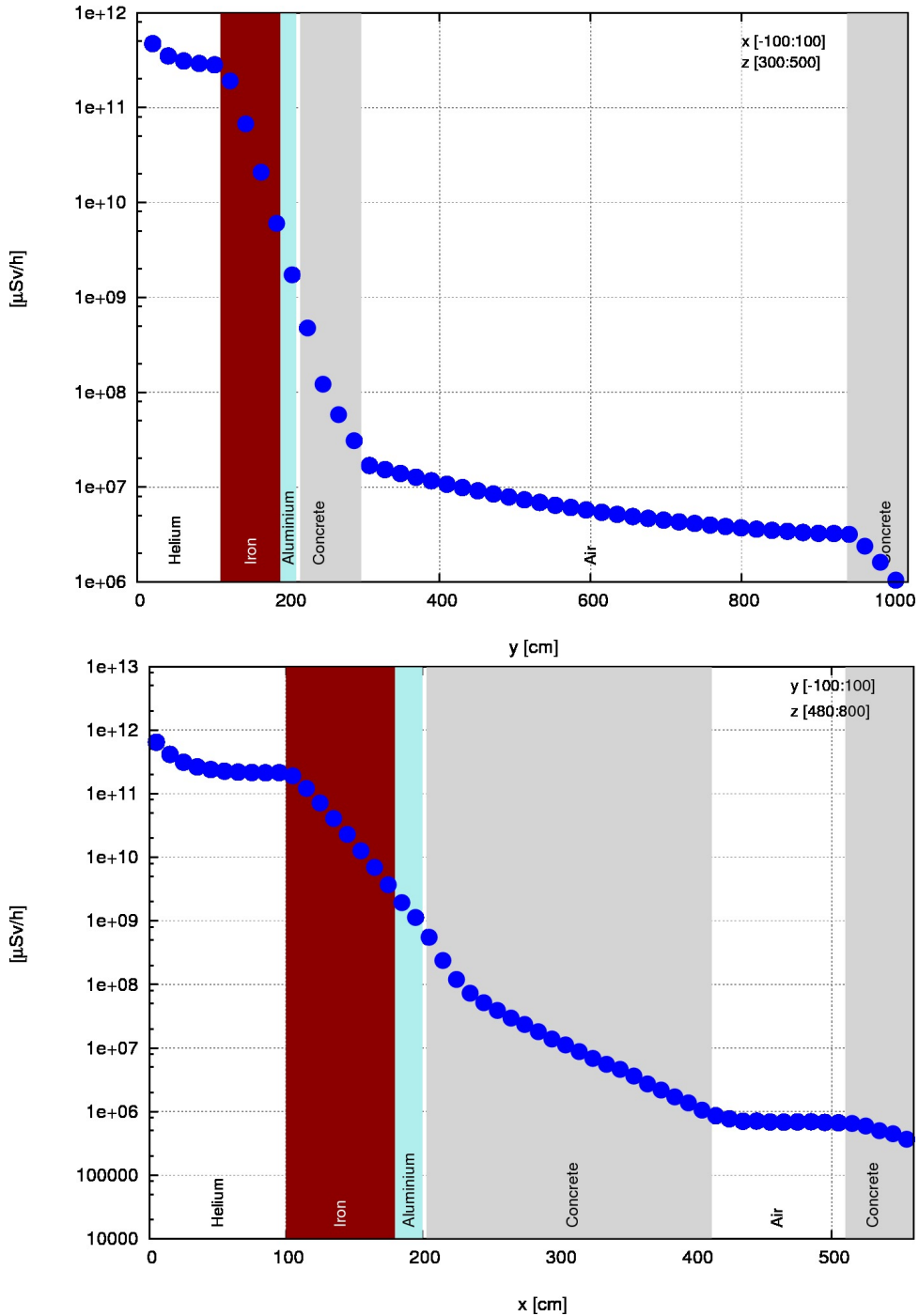


**Figure 8.7:** Prompt ambient dose equivalent rates (in  $\mu\text{Sv/h}$ ) in the target chamber (top: along the y-axis at the horn, bottom: along the x-axis at the access to the first sump).

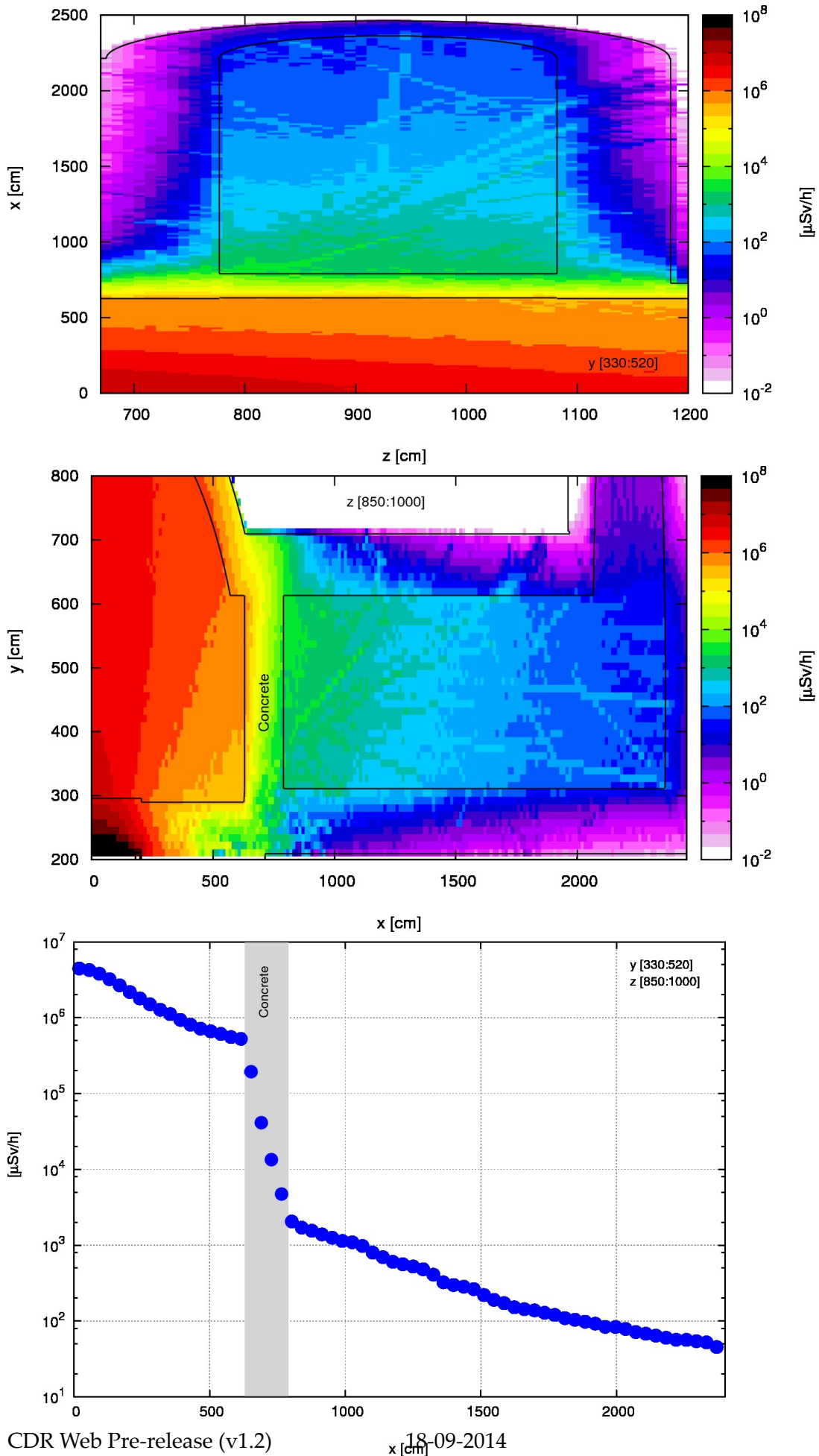


**Figure 8.8:** Prompt ambient dose equivalent rates (in  $\mu\text{Sv/h}$ ) in the duct connecting the target chamber and the service gallery (top: top view, middle: side view, bottom: along the x-axis).

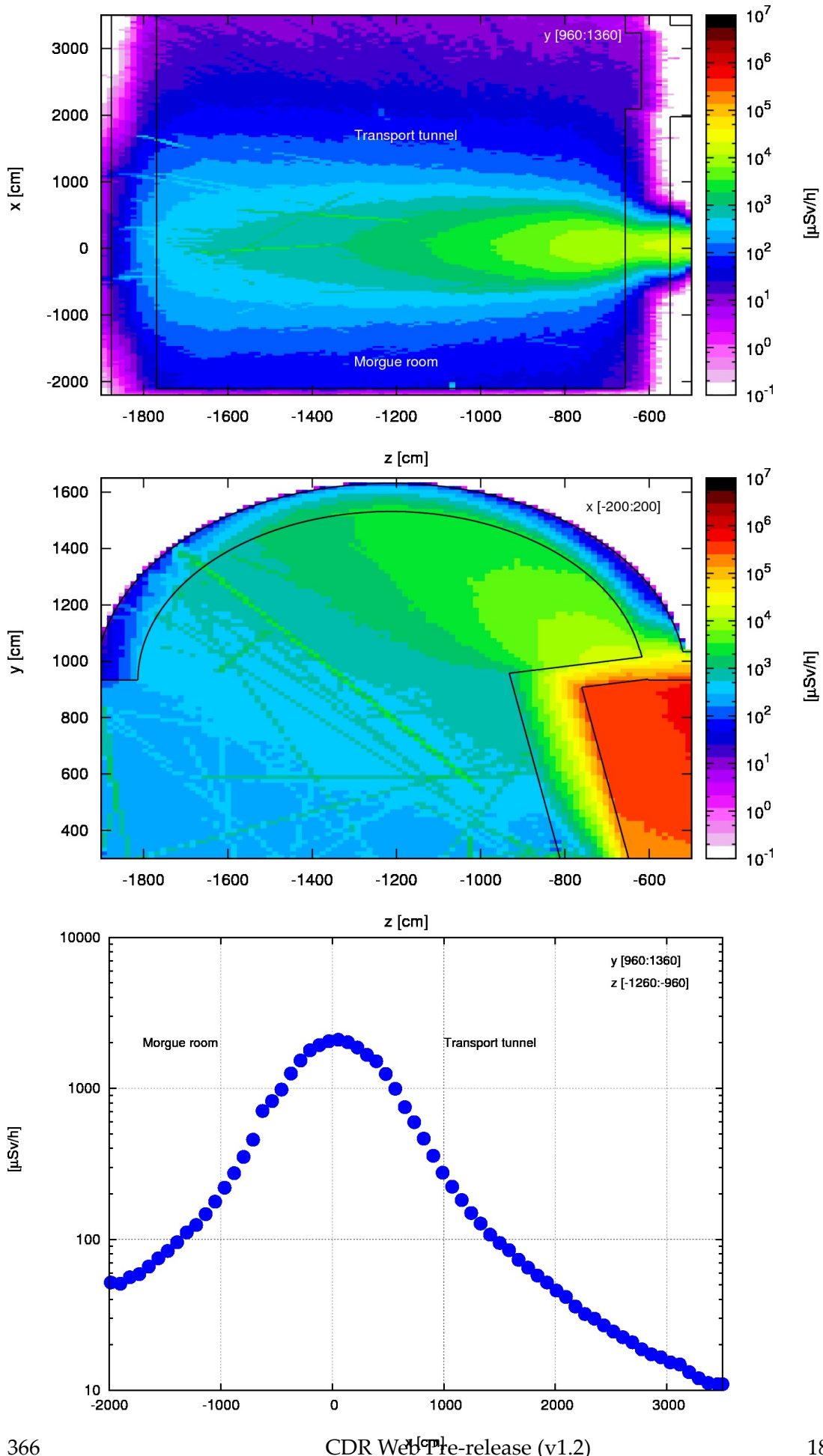


**Figure 8.9:** Prompt ambient dose equivalent rates (in  $\mu\text{Sv/h}$ ) in the morgue room and the transport tunnel (top: top view, middle: side view, bottom: along the x-axis).



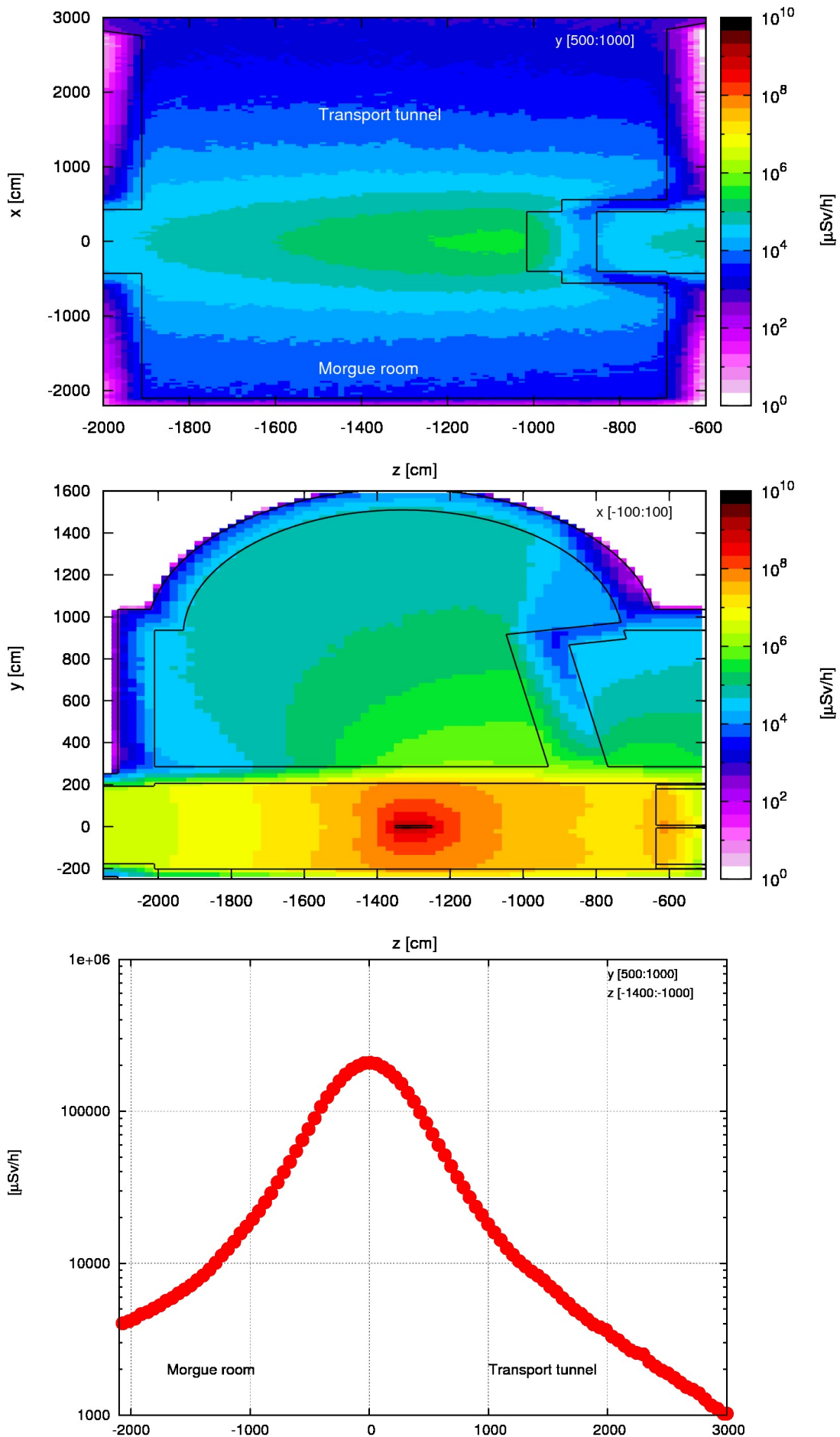


**Figure 8.10:** Prompt ambient dose equivalent rates (in  $\mu\text{Sv/h}$ ) in the morgue room and the transport tunnel for the case of an accidental beam loss in the upstream part of the target chamber (top: top view, middle: side view, bottom: along the  $x$ -axis).

Figures 8.11 - 8.15 show the expected residual dose rates in the target chamber for five different cooling times (1 hour, 1 day, 1 week, 1 month and 6 months) after continuous operation for 180 days with  $2.5 \times 10^{14}$  p/s of 50 GeV (i.e.  $4 \times 10^{21}$  pot). Naturally, values are the highest around the horn reaching 10-100 Sv/h after short cooling times. Outside of the shielding above the horn, the residual dose rates amount to about 100  $\mu$ Sv/h after 1 week of cooling. The dose rates upstream of the target chamber can be considered as negligible. However, one should take into account, that any additional equipment located in the target chamber will become activated and further contribute to the residual dose. Note that in the concrete the high contribution of residual dose for short cooling times mainly comes from  $^{24}\text{Na}$ , which has a half-life of 15 h. A concrete composition with low sodium content or an additional marble layer should therefore be utilized. These studies show that all operations connected to accessing the Helvessel (e.g. for exchanging the horn) and removing the shielding around it can only be done remotely due to the very high residual dose rates in this area.

The residual dose rates originating from the removable shielding as well as the target were further evaluated standalone. This information is essential for situations where these components must be removed, e.g. when the target needs to be replaced. Therefore, all regions other than the object of interest were selectively set to vacuum when transporting the radioactive decay products, such that only the radioactive decay products originating from the object were taken into account.

Figure 8.16 illustrates the distribution of the residual dose rates originating from the removable iron shielding above the target, horn and reflector. It can be seen that the dose rates strongly vary depending on the position. While after one day of cooling they are of the order of 10 Sv/h in the bottom part of the shielding located close to the horn, they drop along the height of the shielding by about two orders of magnitude. This trend can also be observed for longer cooling times. Only for the short cooling time of 1 hour the decline turns out slightly less steep. The results show that even after 1 year of cooling, dose rates reach up to the level of 1 Sv/h. The iron shielding should therefore be kept in the non-accessible downstream part of the target chamber in case they are removed from the helium vessel.

The residual dose rates originating from the concrete shielding are illustrated in Figure 8.17. Similarly to what has been observed for the iron shielding, the concrete is mostly activated at the bottom part located close to the horn. However, here the dose rates are only of the order of a few mSv/h after 1 week of cooling time. Note that significantly higher dose rates are reached after shorter cooling times, which can mainly be traced back to the short-lived radio-nuclide  $^{24}\text{Na}$ .

Figure 8.18 shows the residual dose rates resulting from the graphite target. After one week of cooling time the surface dose rate reaches up to the order of 100 Sv/h in the downstream part of the target and falls by about one order of magnitude along the length of the target. Note that the dose rates are even expected to be higher due to additional support structure and equipment fixed to the target which are so far missing in the studies. These studies should therefore be refined once a detailed target design is available. Nevertheless, it becomes clear that any handling of the target will become an intervention with high radiological risks requiring remote handling only. Assuming the target to be handled in the hot cell, a shielding thickness of 160 cm of concrete or 30 cm of lead for the walls of the hot cell is considered the minimum for the moment.

Figures 8.19 and 8.20 show the residual dose rates in the hadron stopper tunnel for five different cooling times (1 hour, 1 day, 1 week, 1 month and 6 months). The results demonstrate that the highly activated part of the hadron stopper is enclosed in the non-accessible part of the tunnel, which is separated by a concrete wall from the rest of the tunnel. The activation in the accessible part of the tunnel is expected to be lower than 100  $\mu$ Sv/h after 1 hour of cooling dropping down to negligible values after 1 week of cooling. Here again, any additional equipment located in the hadron stopper tunnel will become activated and will further contribute

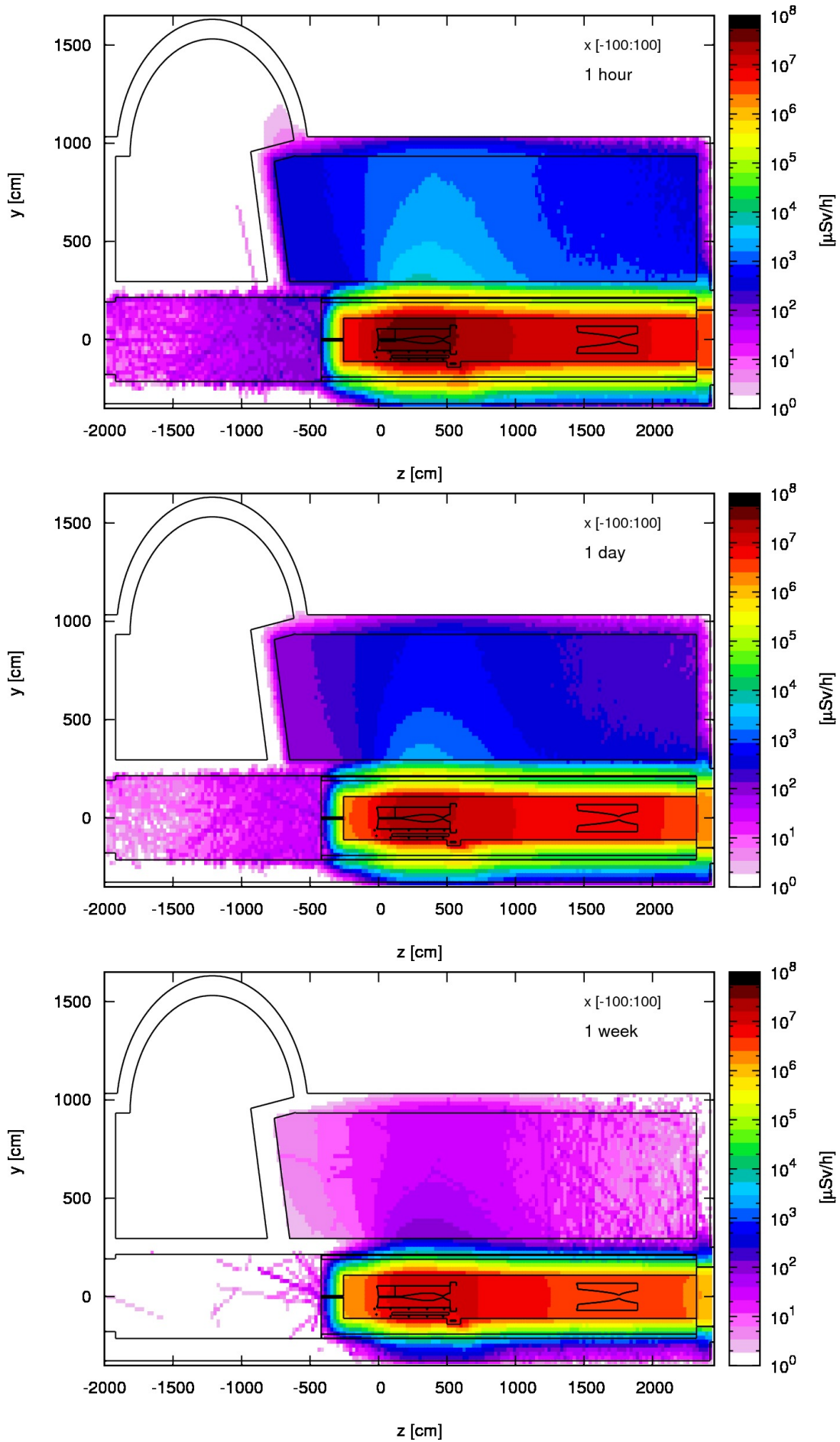
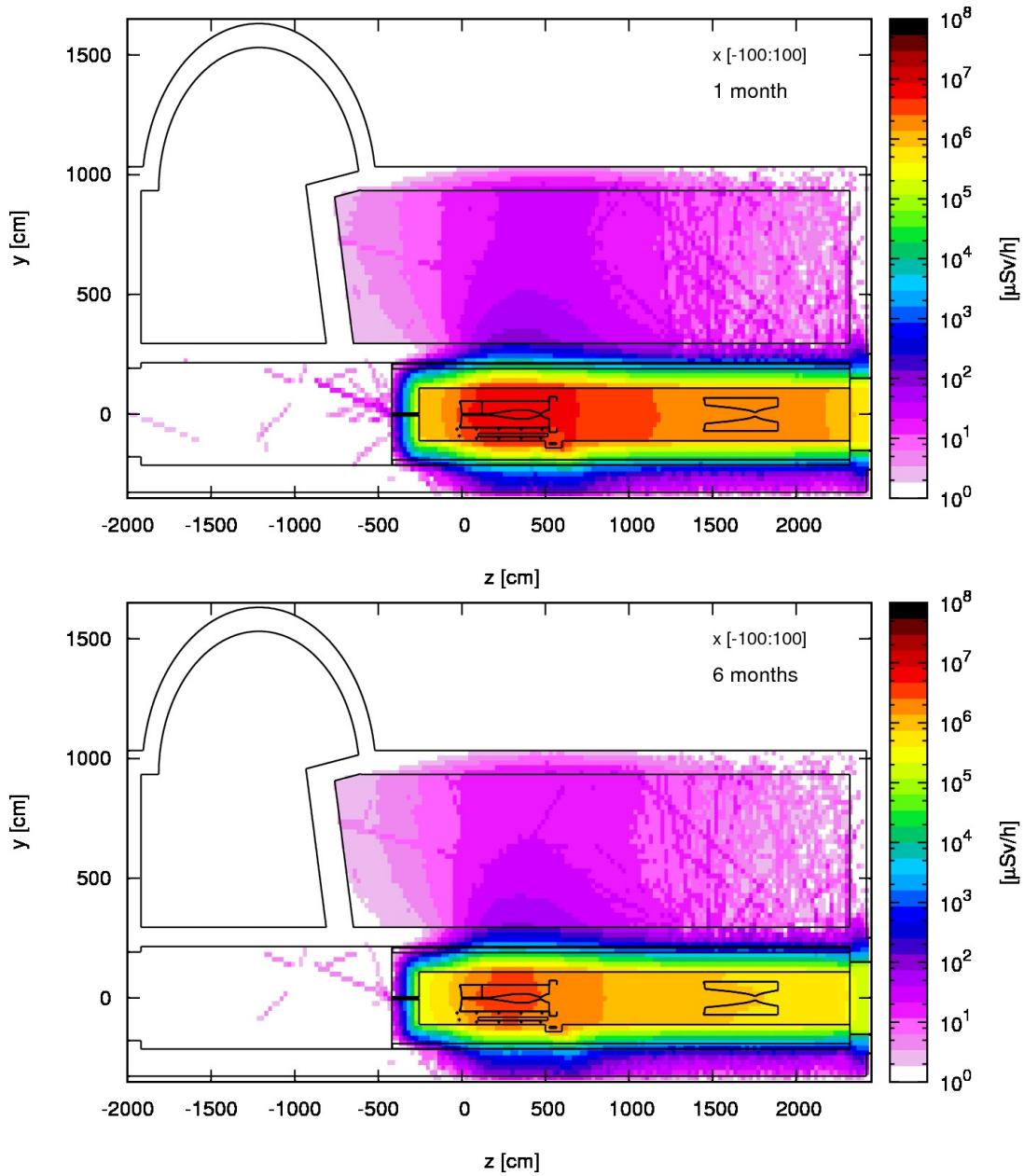


Figure 8.11: Side view of the residual dose rates (in  $\mu\text{Sv/h}$ ) in the target chamber for different cooling times (1 hour, 1 day, 1 week).





**Figure 8.12:** Side view of the residual dose rates (in  $\mu\text{Sv/h}$ ) in the target chamber for different cooling times (1 month, 6 months).

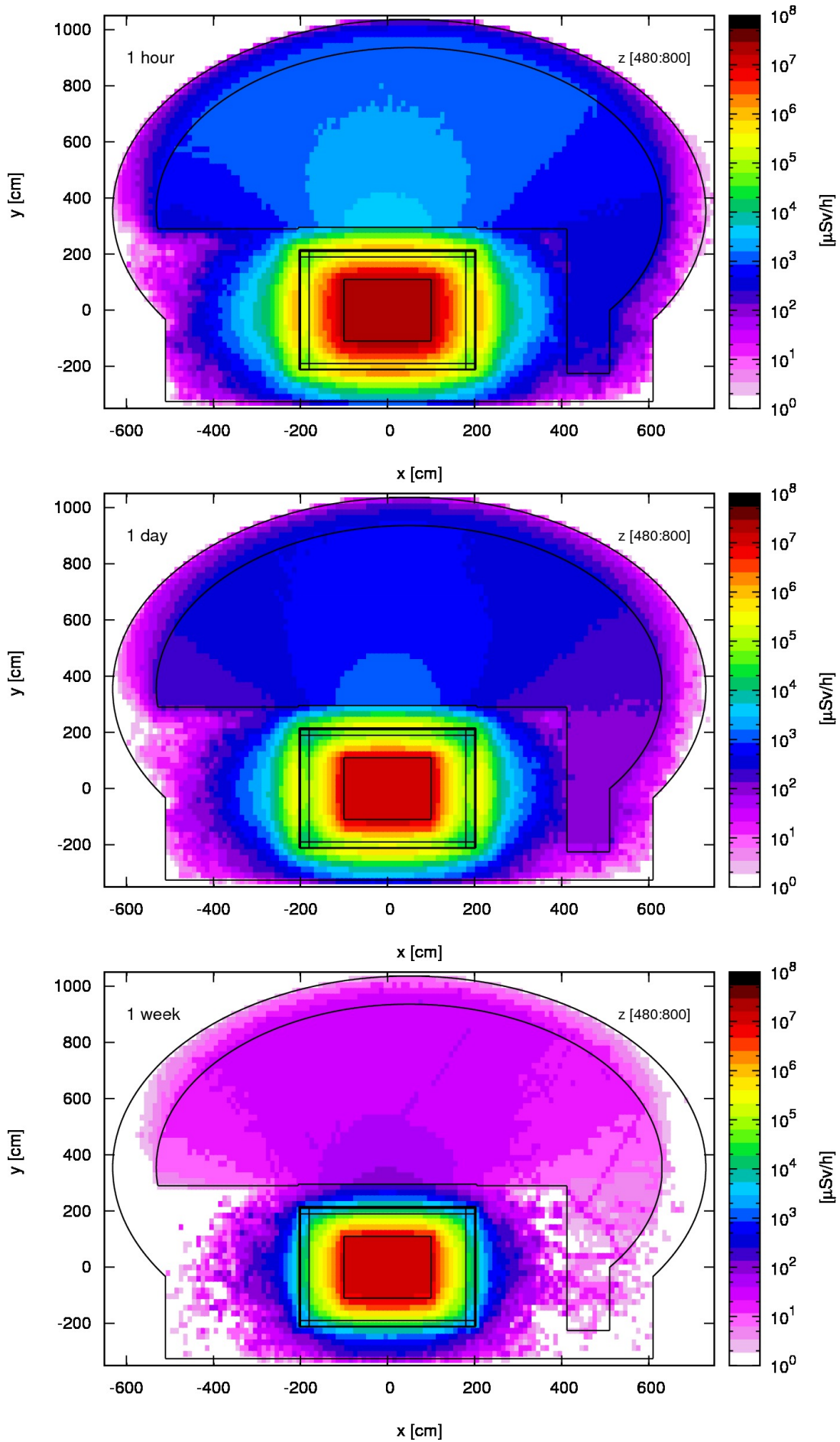
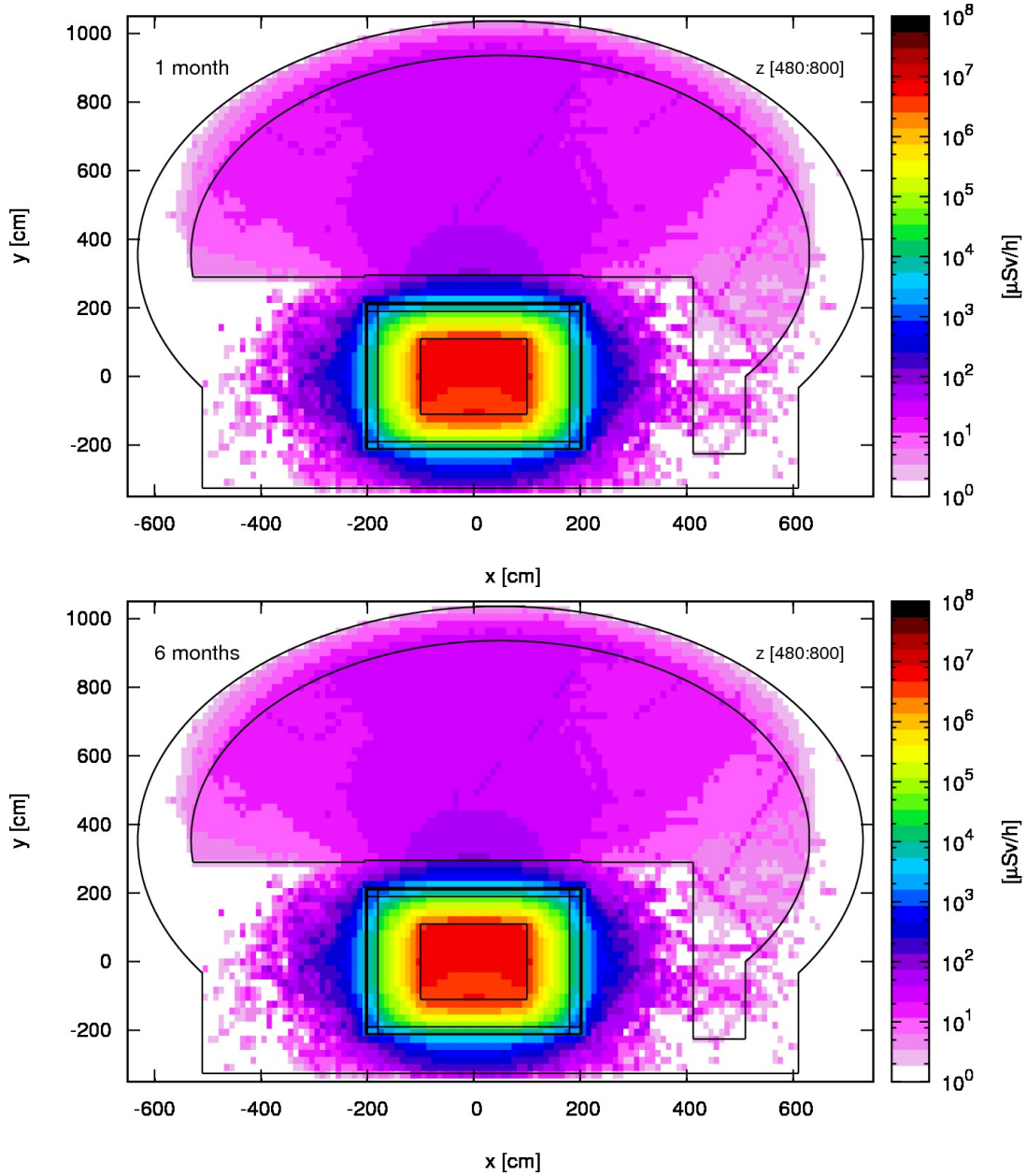


Figure 8.13: Front views of the residual dose rates ( $\mu\text{Sv/h}$ ) at the level of the horn for different cooling times (1 hour, 1 day, 1 week).



**Figure 8.14:** Front view of the residual dose rates (in  $\mu\text{Sv/h}$ ) at the level of the horn for different cooling times (1 month, 6 months).

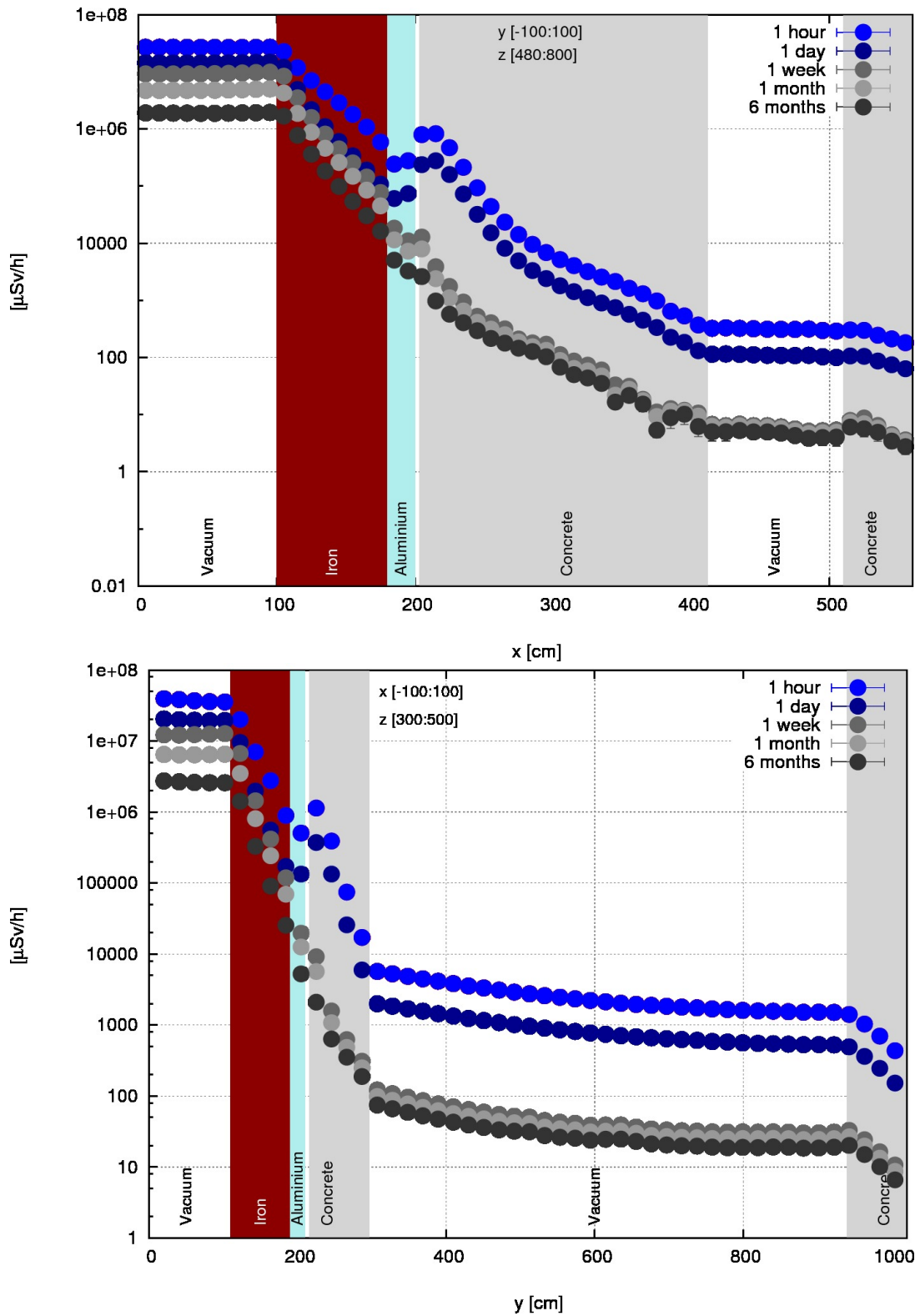
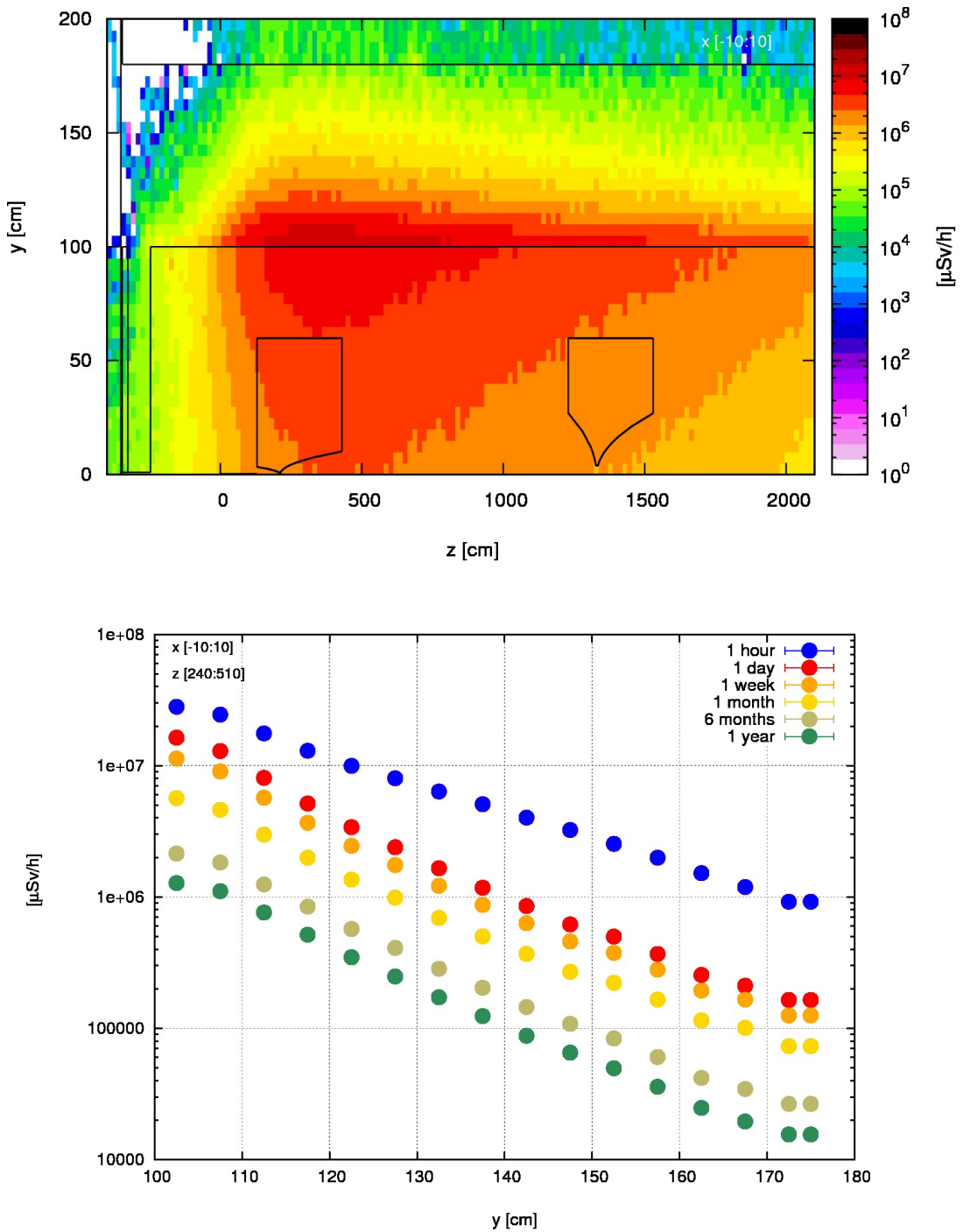
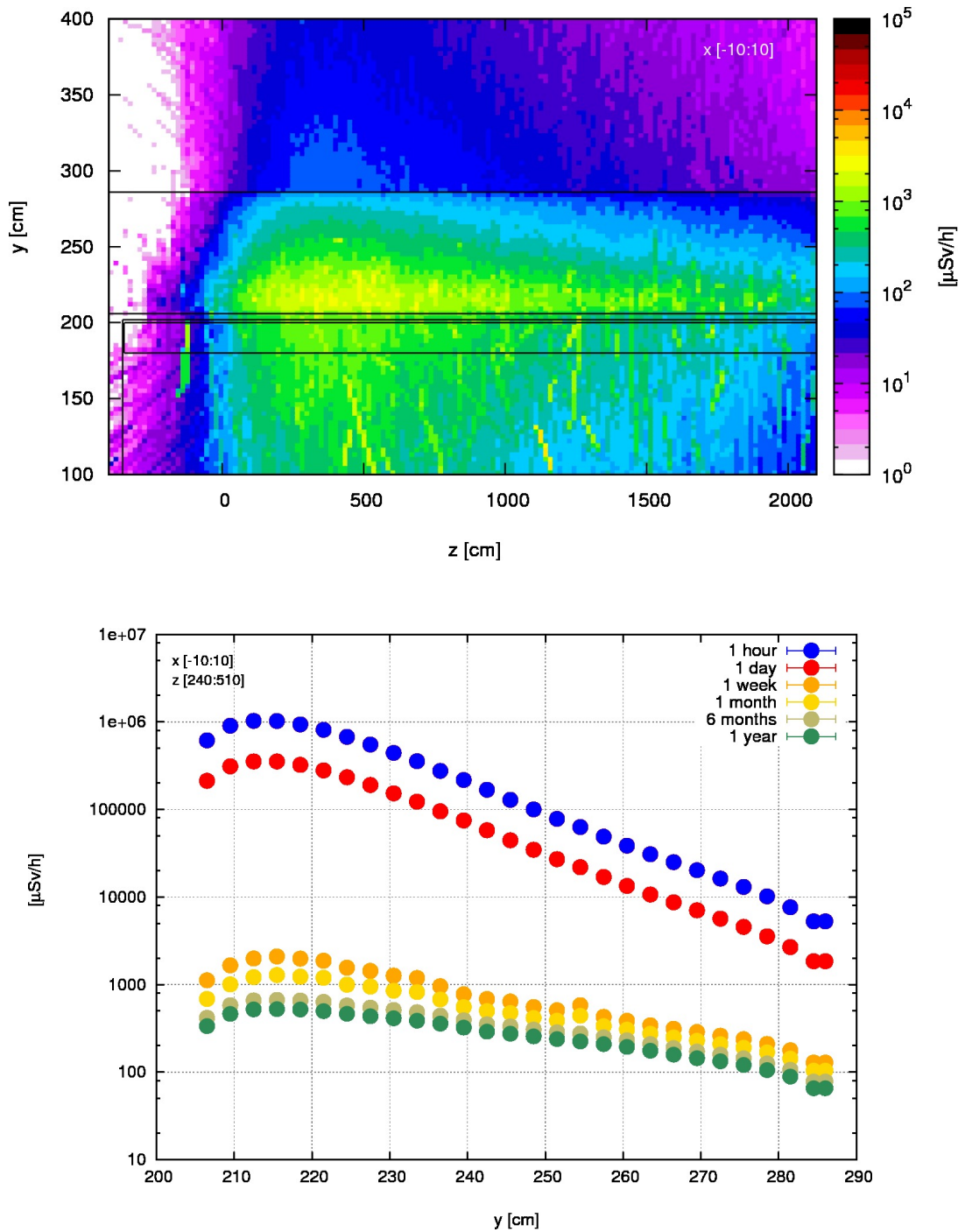


Figure 8.15: Residual dose rates (in  $\mu\text{Sv/h}$ ) along the x- (top) and the y-axis (bottom) at the level of the horn for different cooling times (1 hour, 1 day, 1 week, 1 month, 6 months).



**Figure 8.16:** Residual dose rates (in  $\mu\text{Sv/h}$ ) around the iron shielding located inside of the He-vessel for 1 week of cooling time (top) and along the height of the iron shielding above the horn for different cooling times (1 hour, 1 day, 1 week, 1 month, 6 months, 1 year) (bottom).





**Figure 8.17:** Residual dose rates (in  $\mu\text{Sv/h}$ ) around the concrete shielding located above the He-vessel for 1 week of cooling time (top) and along the height of the concrete shielding above the horn for different cooling times (1 hour, 1 day, 1 week, 1 month, 6 months, 1 year) (bottom).

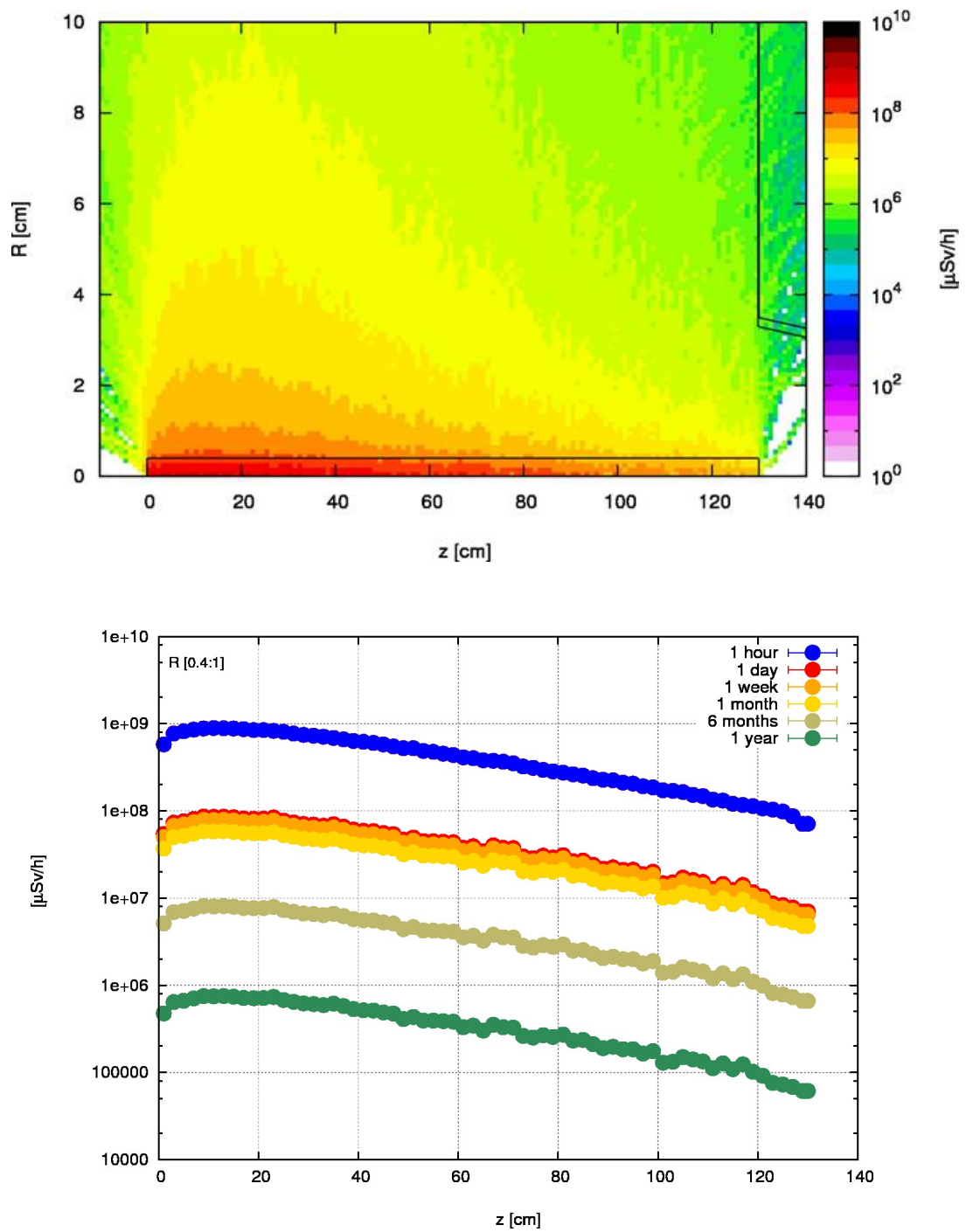


**Figure 8.18:** Residual dose rates (in  $\mu\text{Sv/h}$ ) around the graphite target for 1 week of cooling time (top) and along the length of the graphite target for different cooling times (1 hour, 1 day, 1 week, 1 month, 6 months, 1 year) (bottom).

to the residual dose. The activation of the muon detectors, which are foreseen to be installed upstream of the second hadron stopper, should therefore be investigated once its design has been determined.

The residual dose studies show that all operations connected to accessing the He-vessel or the first part of the hadron stopper can only be done remotely due to the very high residual dose rates in these areas after beam stop. For example in case of a target failure the handling of the horn and target as well as the shielding blocks above the He-vessel will have to be done remotely. Thus, an exchange of a broken target will become an intervention with high radiological risks requiring further studies and optimisation.

#### 8.1.4 Air activation

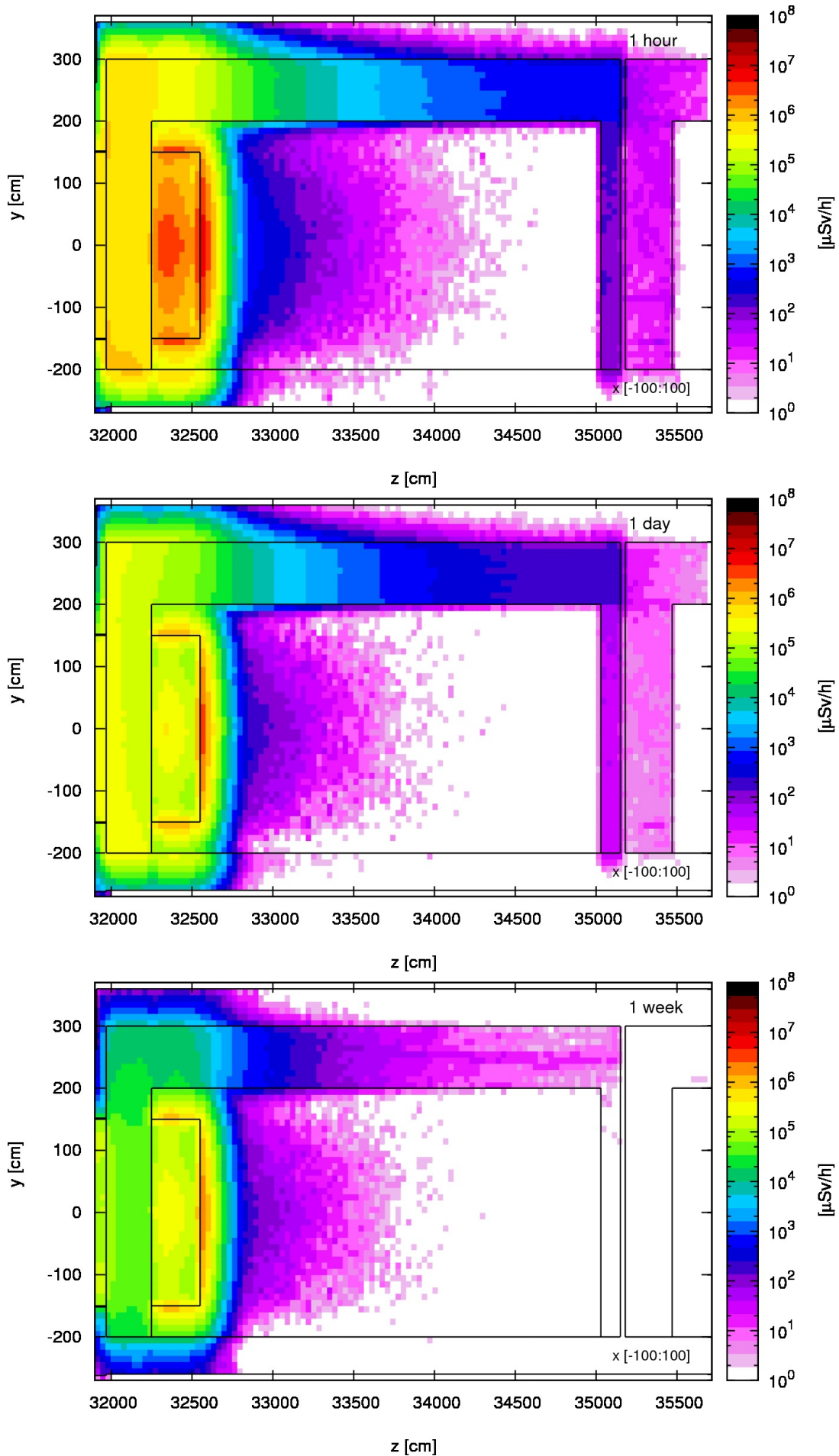
Another important aspect which has not only to be taken into account from a personnel protection but also environmental point of view is the activation of the air in the facility. The production of radionuclides in the air and the resulting activity and effective dose rates were therefore evaluated for the critical regions of LAGUNA-LBNO, which are the ones of high particle fluences like the target chamber and the beginning of the hadron stopper tunnel. A total of 39 isotopes were considered in the study, including the radiologically most relevant short-lived isotopes  $^{11}\text{C}$ ,  $^{13}\text{N}$ ,  $^{14}\text{O}$ ,  $^{15}\text{O}$  and  $^{41}\text{Ar}$  as well as  $^3\text{H}$ ,  $^7\text{Be}$ ,  $^{14}\text{C}$ ,  $^{32}\text{P}$ ,  $^{33}\text{P}$  and  $^{35}\text{S}$  among those with long half-lives. The production yields of interest were obtained by scoring the track length spectra for neutrons, protons and charged pions and folding them with the respective production cross sections [105, 106]. The results for the air activation in the target area and the first part<sup>2</sup> of the hadron stopper area are presented in Tables 8.3 and 8.4, respectively.

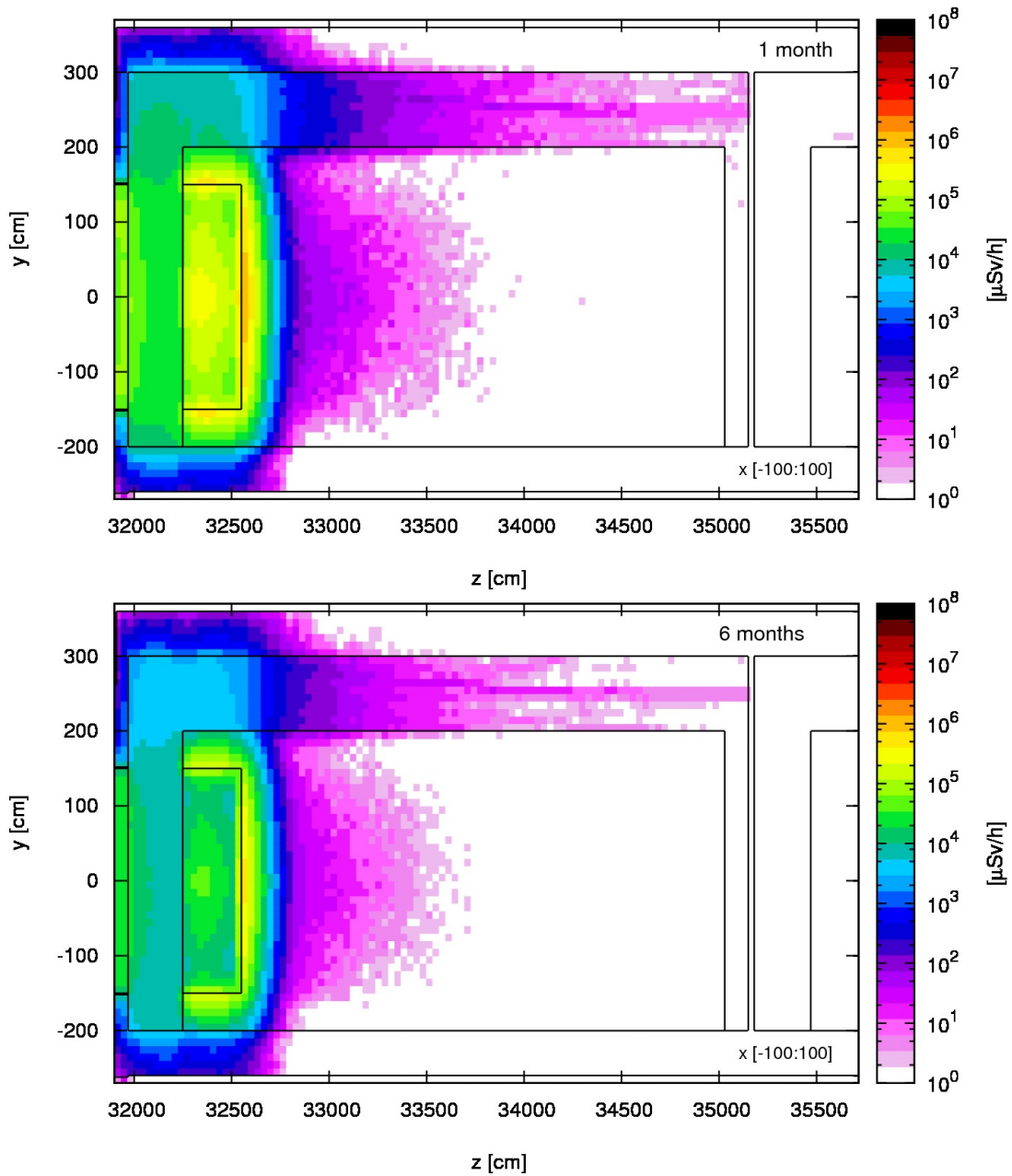
The obtained radionuclide yields were used to calculate the expected radioactivity in the air of the target chamber and the beginning of the hadron stopper tunnel after one operational year. The results give a very conservative estimation due to the fact that a continuous operation for 180 days with  $2.5 \times 10^{14}$  p/s of 50 GeV (i.e.  $4 \times 10^{21}$  pot) was assumed. The calculations were conducted with the help of a simple build-up formula not accounting for the decay chains. To compare the results to the CA values of the Swiss legislation [103], the resulting total activity was divided by the volume of the respective air region. An air volume as implemented in the FLUKA model and estimated with the help of SimpleGeo [107] of  $2740 \text{ m}^3$  for the target chamber and  $500 \text{ m}^3$  for the first part of the hadron stopper area was assumed. The results are given in Tables 8.3 and 8.4. Note that they were obtained under the assumption that there is no air flow inside or in between any of the air compartments. The comparison shows that the activity concentration exceeds the CA values by a factor of about 14 for the target chamber and 3670 for the hadron stopper area. The given values correspond to an effective dose per hour of stay of approximately  $75 \mu\text{Sv}$  and  $20 \text{ mSv}$  due to immersion and inhalation of the activated air in the target chamber and the hadron stopper area, respectively. Note that these are conservative estimates, due to the fact that no cooling time and air extraction has been assumed for the calculations. According to CERN's design guidelines access to an area with activated air can only be given if the committed effective dose per hour of stay originating from the activated air is lower than  $1 \mu\text{Sv}$ . Thus, in case of access to these areas, the contained air would have to be extracted to the environment to avoid unjustified exposure of personnel entering the area or a neighbouring one. The impact of the releases to the environment and the resulting effective dose to members of the public are discussed in Section 8.2.

Figure 8.21 illustrates the activity per radionuclide as a function of half-life, which one would expect for the target chamber and the first part of the hadron stopper tunnel after one operational year and no cooling time. It can clearly be seen that for both air compartments a significant contribution comes from the short-lived radionuclides  $^{11}\text{C}$ ,  $^{13}\text{N}$ ,  $^{14}\text{O}$ ,  $^{15}\text{O}$  and  $^{41}\text{Ar}$ , resulting in a total activity of 2 GBq for the target chamber and 90 GBq for the hadron stopper

<sup>2</sup>The first 32 m of the hadron stopper tunnel are separated by a wall from the rest of the tunnel







**Figure 8.20:** Side view of the residual dose rates (in  $\mu\text{Sv/h}$ ) in the hadron stopper tunnel for different cooling times (1 month, 6 months).

Radionuclide	Production yield (nucl./pp)	Total activity (Bq)	CA (Bq/m <sup>3</sup> )	Activity conc. / CA
H-3	3.27E-06	2.23E+07	2.00E+05	4.08E-02
Be-7	5.80E-07	1.31E+08	1.00E+05	4.79E-01
Be-10	1.41E-06	7.53E+01	9.00E+01	3.06E-04
C-11	1.26E-06	3.15E+08	7.00E+04	1.64E+00
C-14	1.08E-03	1.61E+07	1.00E+04	5.89E-01
N-13	2.99E-06	7.48E+08	7.00E+04	3.90E+00
O-14	6.90E-08	1.73E+07		
O-15	1.65E-06	4.13E+08	7.00E+04	2.15E+00
O-19	7.88E-12	1.97E+03		
F-18	3.84E-10	9.60E+04	7.00E+04	5.01E-04
Ne-23	3.78E-11	9.45E+03		
Ne-24	5.17E-12	1.29E+03		
Na-22	2.49E-10	7.66E+03	4.00E+03	7.00E-04
Na-24	4.31E-10	1.08E+05	3.00E+04	1.31E-03
Na-25	9.79E-11	2.45E+04		
Mg-27	2.15E-10	5.38E+04		
Mg-28	1.43E-10	3.58E+04	6.00E+03	2.18E-03
Al-26	3.03E-10	3.61E-02	4.00E+02	3.30E-08
Al-28	1.25E-09	3.13E+05	6.00E+03	1.90E-02
Al-29	6.11E-10	1.53E+05		
Si-31	8.57E-10	2.14E+05	1.00E+05	7.83E-04
Si-32	6.49E-10	1.23E+02	3.00E+01	1.50E-03
P-30	1.90E-10	4.75E+04		
P-32	1.46E-08	3.65E+06	2.00E+03	6.67E-01
P-33	1.38E-08	3.42E+06	1.00E+04	1.25E-01
P-35	1.46E-09	3.65E+05		
S-35	1.87E-08	3.55E+06	1.00E+04	1.30E-01
S-37	5.91E-09	1.48E+06		
S-38	4.01E-09	1.00E+06		
Cl-34	3.61E-10	9.03E+04		
Cl-36	5.43E-08	1.54E+01	1.00E+03	5.63E-06
Cl-38	4.63E-08	1.16E+07	4.00E+04	1.06E-01
Cl-39	7.20E-08	1.80E+07	2.00E+05	3.29E-02
Cl-40	1.26E-08	3.15E+06		
Ar-37	1.01E-07	2.45E+07	1.00E+11	8.97E-08
Ar-39	2.21E-07	7.01E+04	7.00E+06	3.66E-06
Ar-41	2.31E-06	5.78E+08	5.00E+04	4.22E+00
K-38	1.18E-10	2.95E+04		
K-40	7.51E-10	5.01E-05	3.00E+03	6.10E-12
Sum		2.31E+09		1.41E+01

**Table 8.3:** Target area: Radionuclide yield (nuclide per primary proton), total activity at the end of an operational year (in Bq), CA values (in Bq/m<sup>3</sup>) and ratio of the activity concentration to the CA values. Note, that the Swiss legislation does not include the CA values for some of the short-lived radionuclides, which are however irrelevant for the given studies.

Radionuclide	Production yield (nucl./pp)	Total activity (Bq)	CA (Bq/m <sup>3</sup> )	Activity conc. / CA
H-3	2.52E-04	1.72E+09	2.00E+05	1.72E+01
Be-7	5.48E-05	1.24E+10	1.00E+05	2.47E+02
Be-10	3.09E-05	1.65E+03	9.00E+01	3.66E-02
C-11	6.73E-05	1.68E+10	7.00E+04	4.80E+02
C-14	6.82E-02	1.02E+09	1.00E+04	2.03E+02
N-13	9.08E-05	2.27E+10	7.00E+04	6.47E+02
O-14	3.79E-06	9.48E+08		
O-15	5.36E-05	1.34E+10	7.00E+04	3.83E+02
O-19	1.45E-08	3.61E+06		
F-18	2.23E-07	5.57E+07	7.00E+04	1.59E+00
Ne-23	2.95E-08	7.37E+06		
Ne-24	7.16E-09	1.79E+06		
Na-22	6.83E-08	2.10E+06	4.00E+03	1.05E+00
Na-24	1.02E-07	2.55E+07	3.00E+04	1.70E+00
Na-25	4.70E-08	1.17E+07		
Mg-27	5.59E-08	1.40E+07		
Mg-28	1.49E-08	3.72E+06	6.00E+03	1.24E+00
Al-26	9.61E-08	1.15E+01	4.00E+02	5.72E-05
Al-28	2.01E-07	5.03E+07	6.00E+03	1.67E+01
Al-29	9.26E-08	2.32E+07		
Si-31	1.17E-07	2.93E+07	1.00E+05	5.85E-01
Si-32	6.16E-08	1.17E+04	3.00E+01	7.78E-01
P-30	6.21E-08	1.55E+07		
P-32	5.81E-07	1.45E+08	2.00E+03	1.45E+02
P-33	4.36E-07	1.08E+08	1.00E+04	2.16E+01
P-35	4.71E-08	1.18E+07		
S-35	5.38E-07	1.02E+08	1.00E+04	2.04E+01
S-37	1.28E-07	3.19E+07		
S-38	9.83E-08	2.46E+07		
Cl-34	2.22E-08	5.55E+06		
Cl-36	1.25E-06	3.55E+02	1.00E+03	7.09E-04
Cl-38	9.69E-07	2.42E+08	4.00E+04	1.21E+01
Cl-39	1.84E-06	4.60E+08	2.00E+05	4.59E+00
Cl-40	2.06E-07	5.16E+07		
Ar-37	4.74E-06	1.15E+09	1.00E+11	2.30E-05
Ar-39	6.01E-06	1.91E+06	7.00E+06	5.44E-04
Ar-41	1.46E-04	3.66E+10	5.00E+04	1.46E+03
K-38	1.46E-08	3.65E+06		
K-40	3.98E-08	2.65E-03	3.00E+03	1.77E-09
Sum		1.08E+11		3.67E+03

**Table 8.4:** Hadron stopper area (first 32 m): Radionuclide yield (nuclide per primary proton), total activity at the end of an operational year (in Bq), CA values (in Bq/m<sup>3</sup>) and ratio of the activity concentration to the CA values. Note, that the Swiss legislation does not include the CA values for some of the short-lived radionuclides, which are however irrelevant for the given studies.

tunnel. This demonstrates that delaying the releases of the activated air into the environment allows to significantly reduce the committed effective dose rates. The leakage and extraction rates of the activated air should thus be kept as low as reasonably possible with a maximum delay time before being released into the environment. The design of the ventilation system should furthermore take into account that the air pressure should be the lowest in the area with the highest radiological risk, higher in adjacent areas and highest outside of the facility such that the air flows from low to high contaminated areas only.

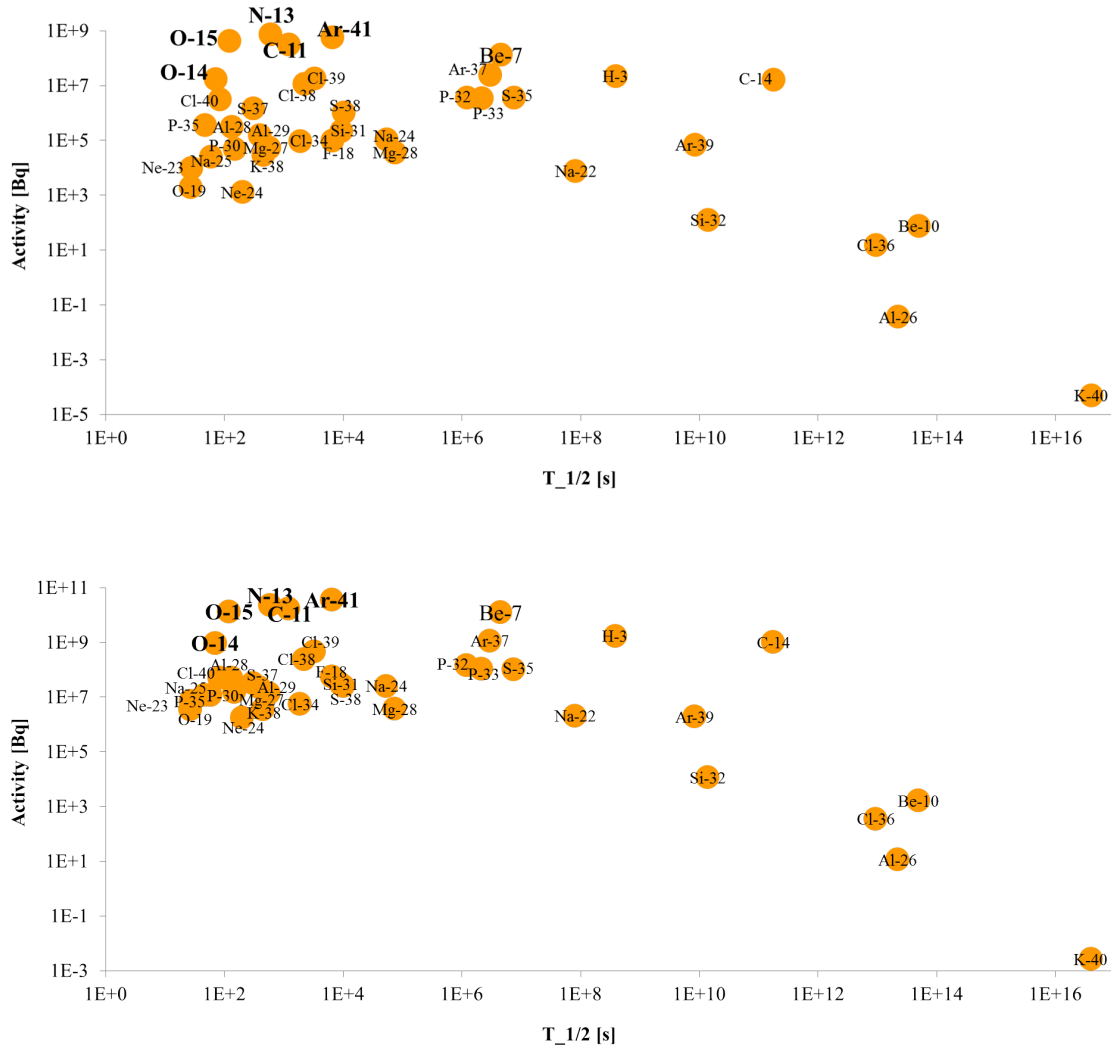


**Figure 8.21:** Activity (in Bq) per radio-nuclide in the air of the target chamber (above) and the first part of the hadron stopper area (below) at the end of an operational year and no cooling time as a function of half-life (in s). Note that no air exchange was assumed.

The radionuclide production in the hadron stopper tunnel was also studied as a function of the length of the tunnel. As expected, the highest radionuclide production was found at the beginning of the tunnel, which continuously decreases with the length of the tunnel. As the air in front of the hadron stopper currently accounts for about 90% of the overall produced activity in the hadron stopper tunnel, we strongly recommend to further reduce the air volume between the end of the decay pipe tunnel and the beginning of the hadron stopper. It was furthermore seen that the production rates behind the concrete wall were more than five orders of magnitude lower than the ones observed in the upstream part of the tunnel. The results show that the separation wall at 32 m sufficiently confines the highly activated part of the air in the

hadron stopper tunnel and that only air with minor activation will have to be extracted into the environment when the downstream part of the tunnel is accessed.

### 8.1.5 Helium activation

The region close to the secondary beam-line was embedded in a helium environment in order to reduce the production of airborne radioactivity. Helium however still gives rise to the formation of tritium, whose radiological impact has to be taken into account when the helium compartments are opened and the helium is being released into the environment. The expected helium activation was therefore studied for the He-vessel as well as the decay pipe. The results are presented in the following. To demonstrate that the radiological impact of helium is significantly lower than the one which would arise in case of air, the production of radionuclides in helium and air and the resulting activities are further compared to each other. The results were moreover used to define an acceptable level of air contamination in the helium-filled regions. For details see Section 8.2.

Tables 8.5 and 8.6 summarize the expected tritium production in the helium of the He-vessel and the decay pipe. A total activity of 89 GBq in the He-vessel and 134 GBq in the decay pipe after one operational year was found. The results give a very conservative estimation due to the fact that a continuous operation for 180 days with  $2.5 \times 10^{14}$  p/s of 50 GeV (i.e.  $4 \times 10^{21}$  pot) was assumed. Note that the helium inside of the He-vessel will have to be released each time the target, horn or reflector has to be accessed, while releases from the decay pipe are only relevant for the dismantling of the facility as well as accidental risk analyses.

The results of the helium activation are further compared to the radionuclide production for the case that the He-vessel and the decay pipe are filled with air. It can be seen that for both media the level of the tritium production is comparable, even though the underlying production mechanisms<sup>3</sup> differ. However, next to tritium, there is a bulk of other radionuclides produced in the air which dominate the airborne radioactivity. As a result, the air-filling yields a total activity which is roughly two orders of magnitude higher than the one for the helium-filling. Also the activity concentration with respect to the Swiss CA values is approximately two orders of magnitude higher in case of the air-filling. The results clearly demonstrate that the production of radionuclides and the resulting radiological impact is significantly lower for the helium than for the air. This is why even small contaminations of air inside of the helium vessel have to be taken into account for the releases. The impact from the releases of the activated helium into the environment as well as the acceptable level of air contamination in the He-vessel are discussed in Section 8.2.

## 8.2 Environmental aspects

Owing to the high beam power dissipated in the target area and the resulting production of radioactive substances in air, water and soil, radiological environmental aspects need to be considered carefully already at the stage of the conceptual design. As various supporting systems, like HVAC, are not yet designed to details, some generic calculations are presented and constraints given for the design of such systems so that the radiological impact of the facility would remain acceptable.

The measure of the radiological environmental impact of an accelerator facility is the effective dose received by a member of the public belonging to a reference group of the population, usually a group consisting of the most exposed persons; due to their residence place and/or due to their behaviour. The dose objective for members of the public sought by CERN is  $10 \mu\text{Sv}$  per year and lower from all CERN's facilities, which is the *de minimis* value defined in CERN's

<sup>3</sup>Tritium is mainly produced in the air via the spallation of N and O.

Filling	Radio-nuclide	Prod. yield (nucl./pp)	Total activity (Bq)	CA (Bq/m <sup>3</sup> )	Activity conc./CA
<b>He</b>	H-3	1.31E-02	8.94E+10	2.00E+05	3.55E+03
<b>Air</b>	H-3	1.41E-02	9.62E+10	2.00E+05	3.83E+03
	Be-7	5.13E-03	1.16E+12	1.00E+05	9.22E+04
	Be-10	1.89E-03	1.01E+05	9.00E+01	8.92E+00
	C-11	6.89E-03	1.72E+12	7.00E+04	1.96E+05
	C-14	9.45E-02	1.41E+09	1.00E+04	1.12E+03
	N-13	7.58E-03	1.90E+12	7.00E+04	2.15E+05
	O-14	5.58E-04	1.40E+11		
	O-15	7.08E-03	1.77E+12	7.00E+04	2.01E+05
	O-19	9.96E-07	2.49E+08		
	F-18	1.77E-05	4.43E+09	7.00E+04	5.03E+02
	Ne-23	2.16E-06	5.40E+08		
	Ne-24	5.04E-07	1.26E+08		
	Na-22	5.72E-06	1.76E+08	4.00E+03	3.50E+02
	Na-24	8.39E-06	2.10E+09	3.00E+04	5.56E+02
	Na-25	3.59E-06	8.98E+08		
	Mg-27	3.91E-06	9.78E+08		
	Mg-28	1.34E-06	3.35E+08	6.00E+03	4.44E+02
	Al-26	8.52E-06	1.02E+03	4.00E+02	2.02E-02
	Al-28	2.02E-05	5.05E+09	6.00E+03	6.69E+03
	Al-29	7.29E-06	1.82E+09		
	Si-31	1.16E-05	2.90E+09	1.00E+05	2.31E+02
	Si-32	6.28E-06	1.19E+06	3.00E+01	3.16E+02
	P-30	6.43E-06	1.61E+09		
	P-32	6.17E-05	1.54E+10	2.00E+03	6.13E+04
	P-33	4.22E-05	1.05E+10	1.00E+04	8.33E+03
	P-35	4.99E-06	1.25E+09		
	S-35	5.42E-05	1.03E+10	1.00E+04	8.19E+03
	S-37	1.11E-05	2.78E+09		
	S-38	8.92E-06	2.23E+09		
	Cl-34	2.84E-06	7.10E+08		
	Cl-36	1.21E-04	3.43E+04	1.00E+03	2.73E-01
	Cl-38	7.53E-05	1.88E+10	4.00E+04	3.74E+03
	Cl-39	1.51E-04	3.78E+10	2.00E+05	1.50E+03
	Cl-40	9.71E-06	2.43E+09		
	Ar-37	8.25E-05	2.00E+10	1.00E+11	1.59E-03
	Ar-39	3.95E-04	1.25E+08	7.00E+06	1.42E-01
Ar-41	1.26E-04	3.15E+10	5.00E+04	5.01E+03	
K-38	2.28E-06	5.70E+08			
K-40	6.92E-06	4.62E-01	3.00E+03	1.22E-06	
	Sum		6.96E+12		8.06E+05

**Table 8.5:** Activation of helium (top) vs. air (bottom) in the He-vessel: Radionuclide yield (nuclide per primary proton), total activity at the end of an operational year (in Bq), CA values (in Bq/m<sup>3</sup>) and ratio of the activity concentration to the CA values. Note, that the Swiss legislation does not include the CA values for some of the short-lived radionuclides, which are however irrelevant for the given studies.

Filling	Radio-nuclide	Prod. yield (nucl./pp)	Total activity (Bq)	CA (Bq/m <sup>3</sup> )	Activity conc./CA
<b>He</b>	H-3	1.96E-02	1.34E+11	2.00E+05	3.18E+02
<b>Air</b>	H-3	3.79E-02	2.58E+11	2.00E+05	6.15E+02
	Be-7	9.61E-03	2.17E+12	1.00E+05	1.03E+04
	Be-10	2.46E-03	1.31E+05	9.00E+01	6.93E-01
	C-11	1.07E-02	2.67E+12	7.00E+04	1.81E+04
	C-14	1.24E-01	1.85E+09	1.00E+04	8.80E+01
	N-13	1.12E-02	2.79E+12	7.00E+04	1.89E+04
	O-14	6.00E-04	1.50E+11		
	O-15	7.62E-03	1.91E+12	7.00E+04	1.29E+04
	O-19	2.77E-06	6.93E+08		
	F-18	4.26E-05	1.07E+10	7.00E+04	7.24E+01
	Ne-23	5.64E-06	1.41E+09		
	Ne-24	1.37E-06	3.44E+08		
	Na-22	1.28E-05	3.94E+08	4.00E+03	4.69E+01
	Na-24	1.91E-05	4.78E+09	3.00E+04	7.57E+01
	Na-25	8.93E-06	2.23E+09		
	Mg-27	1.00E-05	2.51E+09		
	Mg-28	2.69E-06	6.73E+08	6.00E+03	5.33E+01
	Al-26	1.88E-05	2.24E+03	4.00E+02	2.66E-03
	Al-28	3.89E-05	9.72E+09	6.00E+03	7.70E+02
	Al-29	1.65E-05	4.14E+09		
	Si-31	2.15E-05	5.36E+09	1.00E+05	2.55E+01
	Si-32	1.11E-05	2.10E+06	3.00E+01	3.34E+01
	P-30	1.19E-05	2.98E+09		
	P-32	9.12E-05	2.28E+10	2.00E+03	5.42E+03
	P-33	6.21E-05	1.54E+10	1.00E+04	7.33E+02
	P-35	6.91E-06	1.73E+09		
	S-35	7.28E-05	1.38E+10	1.00E+04	6.58E+02
	S-37	1.10E-05	2.76E+09		
	S-38	1.29E-05	3.22E+09		
	Cl-34	3.92E-06	9.79E+08		
	Cl-36	1.50E-04	4.26E+04	1.00E+03	2.03E-02
	Cl-38	9.92E-05	2.48E+10	4.00E+04	2.95E+02
	Cl-39	2.20E-04	5.49E+10	2.00E+05	1.31E+02
	Cl-40	7.85E-06	1.96E+09		
	Ar-37	9.40E-05	2.28E+10	1.00E+11	1.09E-04
	Ar-39	4.83E-04	1.53E+08	7.00E+06	1.04E-02
	Ar-41	2.32E-04	5.81E+10	5.00E+04	5.52E+02
K-38	2.74E-06	6.86E+08			
K-40	6.38E-06	4.26E-01	3.00E+03	6.75E-08	
	Sum		1.02E+13		6.99E+04

**Table 8.6:** Activation of helium (top) vs. air (bottom) in the decay pipe: Radionuclide yield (nuclide per primary proton), total activity at the end of an operational year (in Bq), CA values (in Bq/m<sup>3</sup>) and ratio of the activity concentration to the CA values. Note, that the Swiss legislation does not include the CA values for some of the short-lived radionuclides, which are however irrelevant for the given studies.



Code F [?] below which a practice is deemed to be justified and optimized. As there are multiple facilities contributing to the exposure near CERN's sites, the objective for a single facility must be even lower, in fact a few  $\mu\text{Sv}$  per year. The following aspects will be discussed below:

- Releases of radioactive substances to the ambient air
- Releases of radioactive substances to the surface watercourses
- Stray radiation at the surface around the facility
- Activation of soil, rock and groundwater

### 8.2.1 Releases of radioactive substances to the ambient air

In Section ??, yields of a number of radionuclides were calculated for the most activated air-filled and He-filled regions: The Target Chamber, Hadron Stopper (first 32 m), He Vessel and Decay Pipe.

There are several radionuclide categories with specific properties that allow for release minimization by various techniques.

First, the most active are the short-lived radioactive gases produced by spallation of oxygen, and nitrogen nuclei in air, namely  $^{11}\text{C}$ ,  $^{13}\text{N}$ ,  $^{14,15}\text{O}$ , and short-lived radioactive gases or volatile elements produced from Ar in the air, which are dominated by  $^{41}\text{Ar}(n,\gamma)$  and spallation products  $^{19}\text{O}$ ,  $^{18}\text{F}$ ,  $^{23,24}\text{Ne}$ ,  $^{34,38,39,40}\text{Cl}$ . As the gases cannot be retained by filters or by other methods at reasonable effort, the only way of reducing their activity is by a delayed release, either through a long tunnel, or from a semi-closed ventilation system providing a long mean residence time compared with the half-life of the most active nuclides from this category. Certain small extraction (leak) is usually needed to guarantee dynamic confinement.

The second group are radionuclides attaching to aerosols, out of which the radiologically most important are the phosphorus isotopes  $^{32,32}\text{P}$  and  $^{35}\text{S}$  for which the most important exposure pathway is ingestion. Important aerosol-bound radionuclides are also  $^7\text{Be}$  and  $^{22}\text{Na}$ . Such radionuclides can be retained by high-efficiency particle and aerosol (HEPA) filters. Experience shows that the best results can be obtained by recirculation in a semi-closed ventilation system that removes aerosol-bound radioactivity continuously, in the process of air cleaning, and finally by HEPA filters during the final air extraction. Besides radionuclides calculated by FLUKA under ideal conditions there are activated dust particles and corrosion fragments that contain, for example, Mn and Co radioisotopes, e.g.  $^{60}\text{Co}$ . These radionuclides are efficiently removed by HEPA filters as well. Third, there are long-lived gases or volatile elements that cannot be efficiently removed by any of the above-mentioned methods:  $^3\text{H}$  (HT, HTO),  $^{14}\text{C}$  ( $^{14}\text{CO}_2$ ),  $^{36}\text{Cl}$ ,  $^{37,39}\text{Ar}$ . Their releases may provide a serious limitation for the facility performance at very high beam powers. Tritium in the form of tritiated water (HTO) may condensate inside the experimental halls and HVAC units. There are also other sources of tritium in air that will be discussed at the end of this Section.

#### 8.2.1.1 Generic dose coefficients for atmospheric releases

At the stage of the conceptual design, the detailed layout of the ventilation systems, and location and parameters of the air extraction stacks are not known yet. Similarly, the characteristics of the reference population groups can only be assumed. However, to assess the dosimetric impact of the expected releases, dose coefficients that link the released activity with effective doses to members of the public are needed for each radionuclide. Based on the experience and judgments, a generic set of dose coefficients for long-term releases was derived using the models described in Ref [?]. The set is reasonably conservative and covering all exposure pathways although in reality one pathway may exclude the other one. Namely, a generic stack of 10 m

height and 1 m diameter was assumed with an air exhaust speed of 10 m/s ( $28 \times 10^3$  m<sup>3</sup>/h). For long-term releases, the weather data of 2011 and 2012 from an anemometer located in Maisonnex, about 1.5 km easterly, was used. The residence places, with 100% occupancy, were located 200 m away from the stack at three azimuths with the most frequent winds from the stack position: 25° (NE), 175° (S) and 247.5° (SW). All consumed vegetables, meat and milk were produced in the area of concern. For every radionuclide, the maximal value from the age-dependent and place-dependent values was taken.

In some scenarios, a short-term release is assumed (flushing) that may happen during adverse atmospheric dispersion and deposition conditions. The maximum dispersion coefficient was found for the stability class D with the wind speed of 1.5 m/s. A precipitation rate of 2 mm/h was assumed as recommended in Ref [?]. Table ?? lists the dose coefficients for each investigated receptor place to assess their spatial variability and, in the last two columns, the generic dose coefficients used further on for long-term releases and short-term releases respectively.

### 8.2.1.2 Target Chamber

The Target Chamber will very likely be ventilated by a semi-closed ventilation system keeping the desired air quality (temperature, humidity, etc.) in the compartment with static and dynamic confinement. The dynamic confinement will be ensured by air extraction towards outside with a small flow rate. From the point of view of releases of short-lived radioactivity, the mean residence time of air inside the compartment is crucial. It is defined by a ratio of the compartment volume  $V$  and the extraction rate  $E$ :

$$\tau = \frac{V}{E} \quad (8.1)$$

For the annual released activity of a given radionuclide,  $Q$ , an equation can be derived by solving a differential equation describing the temporal change of the total activity inside the compartment as a function of a source  $\odot$  production by radiation, and sinks  $\odot$  radioactive decay and removal by air extraction. The initial condition is assumed that the total activity at the beginning of the operation is zero. Namely:

$$Q = \frac{P'}{\lambda} \cdot \frac{1}{\tau} \left[ 1 - \frac{1}{\lambda' T} (1 - e^{-\lambda' T}) \right] \quad (8.2)$$

where

$P'$  is the total radioactivity production =  $\lambda Y N_{pp}$ , with  $\lambda$  being the radioactive decay constant,  $Y$  being the radionuclide yield per primary proton and  $N_{pp}$  being the number of primary protons delivered on the target per year ( $3.89 \times 10^{21}$ ).

$\lambda'$  is the effective removal constant =  $\lambda + 1/\tau$ .

$T$  is the annual operation time = 180 days or  $1.56 \times 10^7$  s.

Table 8.8 shows the produced and released activities as well as the estimated effective doses to members of the public provided the mean residence time of air in the Target Chamber would be 3600 s. The annual effective dose due to releases of radioactive substances from the Target Chamber would be 1.35  $\mu$ Sv out of which as much as 1.09  $\mu$ Sv would be caused by gaseous radioactivity that cannot be filtered. Such dose is acceptable and the calculation gives a tentative constraint on the leak extraction rate that should not exceed a value leading to a mean residence time of air inside the compartment shorter than 3600 s.

**Table 8.7:** Dose coefficients for atmospheric releases at three receptor places with the most probable wind directions from the source location and the generic set used in dose calculations for long-term releases and short-term releases

Nuclide	25° NE	175° S	247.5° SW	Long-term	Short-term
	Sv/Bq				
H-3	1.30E-19	2.15E-19	1.19E-19	2.15E-19	2.12E-18
BE-7	1.30E-17	2.14E-17	1.18E-17	2.14E-17	1.74E-16
BE-10	4.29E-16	7.08E-16	3.91E-16	7.08E-16	1.07E-14
C-11	9.82E-20	2.27E-19	1.20E-19	2.27E-19	1.79E-18
C-14	6.17E-17	1.02E-16	5.62E-17	1.02E-16	1.00E-15
N-13	8.60E-20	1.88E-19	9.99E-20	1.88E-19	1.61E-18
O-14	1.02E-19	1.23E-19	8.93E-20	1.23E-19	1.46E-18
O-15	5.07E-20	7.68E-20	4.99E-20	7.68E-20	9.10E-19
O-19	1.20E-20	9.64E-21	9.72E-21	1.20E-20	8.52E-20
F-18	5.50E-19	9.75E-19	5.32E-19	9.75E-19	1.18E-17
NE-23	3.57E-21	3.14E-21	2.71E-21	3.57E-21	3.96E-20
NE-24	3.26E-20	6.20E-20	3.57E-20	6.20E-20	6.41E-19
NA-22	3.23E-14	5.33E-14	2.95E-14	5.33E-14	4.99E-13
NA-24	2.90E-17	4.81E-17	2.66E-17	4.81E-17	7.08E-16
NA-25	1.30E-20	1.45E-20	1.13E-20	1.45E-20	1.94E-19
MG-27	1.12E-18	1.68E-18	9.86E-19	1.68E-18	1.87E-17
MG-28	1.23E-16	2.03E-16	1.12E-16	2.03E-16	3.16E-15
AL-26	5.32E-14	8.77E-14	4.84E-14	8.77E-14	5.28E-14
AL-28	1.81E-18	1.92E-18	1.40E-18	1.92E-18	2.54E-17
AL-29	1.35E-19	2.52E-19	1.43E-19	2.52E-19	2.60E-18
SI-31	3.34E-19	5.46E-19	3.03E-19	5.46E-19	7.09E-18
SI-32	2.85E-16	4.70E-16	2.59E-16	4.70E-16	6.71E-15
P-30	1.03E-19	1.39E-19	9.07E-20	1.39E-19	1.75E-18
P-32	4.11E-15	6.78E-15	3.74E-15	6.78E-15	1.12E-13
P-33	5.40E-16	8.91E-16	4.92E-16	8.91E-16	1.54E-14
P-35	2.92E-18	1.51E-18	1.81E-18	2.92E-18	2.37E-17
S-35	3.90E-16	6.43E-16	3.55E-16	6.43E-16	1.15E-14
S-37	2.06E-19	3.71E-19	2.16E-19	3.71E-19	3.83E-18
S-38	1.88E-18	3.19E-18	1.76E-18	3.19E-18	3.97E-17
CL-34M	5.02E-19	9.26E-19	5.10E-19	9.26E-19	1.01E-17
CL-36	5.28E-13	8.71E-13	4.81E-13	8.71E-13	1.39E-13
CL-38	4.08E-19	7.40E-19	4.07E-19	7.40E-19	8.28E-18
CL-39	4.81E-19	8.73E-19	4.78E-19	8.73E-19	9.97E-18
CL-40	1.34E-19	1.74E-19	1.25E-19	1.74E-19	2.13E-18
AR-37	6.64E-26	1.09E-25	6.05E-26	1.09E-25	2.70E-24
AR-39	2.52E-22	4.15E-22	2.29E-22	4.15E-22	1.02E-20
AR-41	1.23E-19	2.90E-19	1.55E-19	2.90E-19	2.11E-18
K-38	5.49E-19	9.04E-19	5.25E-19	9.04E-19	9.82E-18
K-40	2.46E-13	4.06E-13	2.24E-13	4.06E-13	2.84E-13

**Table 8.8:** Production and releases of radioactivity from the Target Chamber as well as resulting effective doses for the mean residence time of air inside the compartment of 3600 s.

Nuclide	Yield /pp	$\lambda$ [s <sup>-1</sup> ]	$P$ [Bq/y]	$\lambda'$ [s <sup>-1</sup> ]	$Q$ [Bq/y]	Sv/Bq	Sv
H-3	3.27E-06	1.78E-09	2.26E+07	2.78E-04	2.26E+07	2.15E-19	4.86E-12
Be-7	5.80E-07	1.51E-07	3.39E+08	2.78E-04	3.39E+08	2.14E-17	7.26E-09
Be-10	1.41E-06	1.37E-14	7.53E+01	2.78E-04	7.53E+01	7.08E-16	5.33E-14
C-11	1.26E-06	5.67E-04	2.78E+12	8.45E-04	9.13E+11	2.27E-19	2.07E-07
C-14	1.08E-03	3.84E-12	1.61E+07	2.78E-04	1.61E+07	1.02E-16	1.64E-09
N-13	2.99E-06	1.16E-03	1.35E+13	1.44E-03	2.60E+12	1.88E-19	4.90E-07
O-14	6.90E-08	9.76E-03	2.62E+12	1.00E-02	7.25E+10	1.23E-19	8.91E-09
O-15	1.65E-06	5.67E-03	3.64E+13	5.95E-03	1.70E+12	7.68E-20	1.30E-07
O-19	7.88E-12	2.56E-02	7.84E+08	2.59E-02	8.42E+06	1.20E-20	1.01E-13
F-18	3.84E-10	1.05E-04	1.57E+08	3.83E-04	1.14E+08	9.75E-19	1.11E-10
Ne-23	3.78E-11	2.48E-02	3.64E+09	2.50E-02	4.04E+07	3.57E-21	1.44E-13
Ne-24	5.17E-12	3.42E-03	6.87E+07	3.70E-03	5.16E+06	6.20E-20	3.20E-13
Na-22	2.49E-10	8.44E-09	8.17E+03	2.78E-04	8.17E+03	5.33E-14	4.35E-10
Na-24	4.31E-10	1.28E-05	2.15E+07	2.91E-04	2.06E+07	4.81E-17	9.89E-10
Na-25	9.79E-11	1.16E-02	4.40E+09	1.18E-02	1.03E+08	1.45E-20	1.50E-12
Mg-27	2.15E-10	1.22E-03	1.02E+09	1.49E-03	1.89E+08	1.68E-18	3.18E-10
Mg-28	1.43E-10	9.21E-06	5.12E+06	2.87E-04	4.95E+06	2.03E-16	1.01E-09
Al-26	3.03E-10	3.07E-14	3.61E-02	2.78E-04	3.61E-02	8.77E-14	3.17E-15
Al-28	1.25E-09	5.16E-03	2.51E+10	5.44E-03	1.28E+09	1.92E-18	2.46E-09
Al-29	6.11E-10	1.75E-03	4.16E+09	2.03E-03	5.69E+08	2.52E-19	1.44E-10
Si-31	8.57E-10	7.34E-05	2.45E+08	3.51E-04	1.94E+08	5.46E-19	1.06E-10
Si-32	6.49E-10	4.88E-11	1.23E+02	2.78E-04	1.23E+02	4.70E-16	5.79E-14
P-30	1.90E-10	4.62E-03	3.41E+09	4.90E-03	1.94E+08	1.39E-19	2.69E-11
P-32	1.46E-08	5.61E-07	3.19E+07	2.78E-04	3.18E+07	6.78E-15	2.16E-07
P-33	1.38E-08	3.16E-07	1.69E+07	2.78E-04	1.69E+07	8.91E-16	1.51E-08
P-35	1.46E-09	1.46E-02	8.30E+10	1.49E-02	1.55E+09	2.92E-18	4.52E-09
S-35	1.87E-08	9.17E-08	6.67E+06	2.78E-04	6.67E+06	6.43E-16	4.29E-09
S-37	5.91E-09	2.28E-03	5.25E+10	2.56E-03	5.69E+09	3.71E-19	2.11E-09
S-38	4.01E-09	6.71E-05	1.05E+09	3.45E-04	8.42E+08	3.19E-18	2.69E-09
Cl-34	3.61E-10	3.61E-04	5.07E+08	6.39E-04	2.20E+08	9.26E-19	2.04E-10
Cl-36	5.43E-08	7.30E-14	1.54E+01	2.78E-04	1.54E+01	8.71E-13	1.34E-11
Cl-38	4.63E-08	3.10E-04	5.59E+10	5.88E-04	2.64E+10	7.40E-19	1.95E-08
Cl-39	7.20E-08	2.08E-04	5.82E+10	4.86E-04	3.33E+10	8.73E-19	2.90E-08
Cl-40	1.26E-08	8.25E-03	4.04E+11	8.53E-03	1.32E+10	1.74E-19	2.29E-09
Ar-37	1.01E-07	2.29E-07	9.00E+07	2.78E-04	8.99E+07	1.09E-25	9.80E-18
Ar-39	2.21E-07	8.17E-11	7.02E+04	2.78E-04	7.01E+04	4.15E-22	2.91E-17
Ar-41	2.31E-06	1.05E-04	9.47E+11	3.83E-04	6.86E+11	2.90E-19	1.99E-07
K-38	1.18E-10	1.51E-03	6.94E+08	1.79E-03	1.08E+08	9.04E-19	9.73E-11
K-40	7.51E-10	1.72E-17	5.01E-05	2.78E-04	5.01E-05	4.06E-13	2.03E-17
Total							<b>1.35E-06</b>
Gases							<b>1.09E-06</b>

### 8.2.1.3 Hadron Stopper

The Hadron Stopper is supposed to be air-tight and closed completely. No access will be needed to the Hadron Stopper during the operation period. The production of radioactivity in this compartment is much higher than in the Target Chamber. A complete tightness of the compartment may not be guaranteed all the time, hence, at first, the shortest acceptable mean residence time for air was sought to set a constraint on the tightness of this compartment. It was supposed that the leaking air would pass through the Target Chamber and that it will be cleaned and evacuated by its ventilation system. For the sake of simplicity, the removal of short-lived radioactivity by radioactive decay inside the Target Chamber was not considered because the mean residence time in the Target Chamber would be much shorter. This approach is conservative. Equation ?? was applied with the corresponding radionuclide yields and other variables and acceptable results were obtained with a mean residence time longer than 2 days ( $1.73 \times 10^5$  s). The detailed results are listed in Table 8.9. The activities released annually in this way are named as  $Q_{leak}$  and the resulting effective doses are labelled as  $E_{leak}$ . Although the total annual effective dose would be as much as  $11.1 \mu\text{Sv}$ , the major part is due to  $^{32}\text{P}$  ( $7.76 \mu\text{Sv}$ ) that could be removed efficiently by HEPA filters. The effective dose due to gaseous radioactivity, which cannot to be removed by HEPA filters, is  $1.89 \mu\text{Sv}$ . Carbon-14, in the form of very long-lived radioactive gas, presumably  $^{14}\text{CO}_2$ , would contribute by about  $0.10 \mu\text{Sv}$  @ an acceptable value.

An opposite case would be a completely tight Hadron Stopper in which the radioactivity could build up during a long time, e.g. during the annual operation period  $T$ . A prolonged cooling time would not help to decrease the resulting effective dose essentially. The detailed results are shown in Table 8.10 for a zero cooling time. The activities built-up and released just after the end of an annual run are named as  $Q_t$  and the resulting effective doses calculated by using the short-term dose coefficients are labelled as  $E_t$ . The total effective dose would be  $16.5 \mu\text{Sv}$ , out of which  $11.6 \mu\text{Sv}$  would be caused by  $^{32}\text{P}$  that could be removed efficiently by HEPA filters. The gaseous radioactivity would contribute by  $0.33 \mu\text{Sv}$ , with  $0.14 \mu\text{Sv}$  due to  $^{14}\text{CO}_2$ .

### 8.2.1.4 Helium volumes

To keep the air activation at low level, the horn and the reflector as well as the interior of the Decay Pipe will be kept in a helium atmosphere at a slight overpressure. In reality, helium may contain air as impurity. Therefore radionuclide yields were calculated for the He Vessel housing the horn and the reflector and their supporting systems and for the Decay Pipe filled both with pure He and pure air (Table ?? and Table ??). Before filling with helium, the two volumes will be evacuated down to a few mb of air. Hence, the maximum initial air admixture would be about 1% vol. The volumes will be then kept under slight overpressure by adding pure helium. One can investigate two extreme scenarios with a mixture of 1% vol. of air in He: (a) Both volumes will continuously leak with a leak rate of 1% per hour. Although adding high purity helium continuously should gradually decrease the initial content of air, for the sake of simplicity, let us conservatively assume a mixture of 1% vol. of air in He all the time. (b) Totally tight He volumes that would be open at the end of the annual operation period  $T$  (180 days). Radioactivity will build up during the operation period to its maximum level and then it will be released to the atmosphere. The production of radioactivity in the He-air mixture can be calculated from the yields of the radionuclides given in Table ?? and Table ??,  $Y_a$  for pure air and  $Y_{He}$  for pure He:

$$P = \lambda N_{pp} [p Y_a + (1 - p) Y_{He}] \quad (8.3)$$

where  $p$  is the volumic fraction of air in He (0.01 for 1% vol.), and the other symbols have the same meaning as in the text above.

The results for the case of a continuous leak from the He volumes are listed in Table 8.11.

**Table 8.9:** Production and releases of radioactivity from the Hadron Stopper as well as resulting effective doses for a leak with the mean residence time of air inside the compartment of 2 days.

Nuclide	Yield/pp	$P$ [Bq/y]	$Q_{leak}$ [Bq/y]	Sv/Bq	$E_{leak}$ [Sv]
H-3	2.52E-04	1.74E+09	1.72E+09	2.15E-19	3.71E-10
Be-7	5.48E-05	3.21E+10	3.09E+10	2.14E-17	6.62E-07
Be-10	3.09E-05	1.65E+03	1.63E+03	7.08E-16	1.16E-12
C-11	6.73E-05	1.48E+14	1.50E+12	2.27E-19	3.40E-07
C-14	6.82E-02	1.02E+09	1.01E+09	1.02E-16	1.03E-07
N-13	9.08E-05	4.09E+14	2.03E+12	1.88E-19	3.82E-07
O-14	3.79E-06	1.44E+14	8.52E+10	1.23E-19	1.05E-08
O-15	5.36E-05	1.18E+15	1.21E+12	7.68E-20	9.26E-08
O-19	1.45E-08	1.44E+12	3.25E+08	9.64E-21	3.14E-12
F-18	2.23E-07	9.11E+10	4.75E+09	9.75E-19	4.63E-09
Ne-23	2.95E-08	2.84E+12	6.63E+08	3.14E-21	2.08E-12
Ne-24	7.16E-09	9.52E+10	1.61E+08	6.20E-20	9.97E-12
Na-22	6.83E-08	2.24E+06	2.21E+06	5.33E-14	1.18E-07
Na-24	1.02E-07	5.10E+09	1.58E+09	4.81E-17	7.59E-08
Na-25	4.70E-08	2.11E+12	1.06E+09	1.45E-20	1.53E-11
Mg-27	5.59E-08	2.64E+11	1.25E+09	1.68E-18	2.10E-09
Mg-28	1.49E-08	5.33E+08	2.05E+08	2.03E-16	4.16E-08
Al-26	9.61E-08	1.15E+01	1.13E+01	8.77E-14	9.94E-13
Al-28	2.01E-07	4.03E+12	4.52E+09	1.92E-18	8.68E-09
Al-29	9.26E-08	6.30E+11	2.08E+09	2.52E-19	5.23E-10
Si-31	1.17E-07	3.34E+10	2.44E+09	5.46E-19	1.33E-09
Si-32	6.16E-08	1.17E+04	1.16E+04	4.70E-16	5.43E-12
P-30	6.21E-08	1.12E+12	1.39E+09	1.39E-19	1.94E-10
P-32	5.81E-07	1.27E+09	1.14E+09	6.78E-15	7.76E-06
P-33	4.36E-07	5.36E+08	5.03E+08	8.91E-16	4.48E-07
P-35	4.71E-08	2.68E+12	1.06E+09	1.51E-18	1.60E-09
S-35	5.38E-07	1.92E+08	1.87E+08	6.43E-16	1.20E-07
S-37	1.28E-07	1.13E+12	2.86E+09	3.71E-19	1.06E-09
S-38	9.83E-08	2.56E+10	2.03E+09	3.19E-18	6.49E-09
Cl-34	2.22E-08	3.12E+10	4.92E+08	9.26E-19	4.55E-10
Cl-36	1.25E-06	3.55E+02	3.51E+02	8.71E-13	3.06E-10
Cl-38	9.69E-07	1.17E+12	2.14E+10	7.40E-19	1.58E-08
Cl-39	1.84E-06	1.49E+12	4.02E+10	8.73E-19	3.51E-08
Cl-40	2.06E-07	6.62E+12	4.64E+09	1.74E-19	8.07E-10
Ar-37	4.74E-06	4.22E+09	4.02E+09	1.09E-25	4.38E-16
Ar-39	6.01E-06	1.91E+06	1.89E+06	4.15E-22	7.83E-16
Ar-41	1.46E-04	6.00E+13	3.12E+12	2.90E-19	9.05E-07
K-38	1.46E-08	8.59E+10	3.27E+08	9.04E-19	2.96E-10
K-40	3.98E-08	2.66E-03	2.63E-03	4.06E-13	1.07E-15
				Total	1.11E-05
				Gases	1.89E-06

**Table 8.10:** Production and releases of radioactivity from the Hadron Stopper as well as resulting effective doses for a flush of the compartment after the annual operation period (a short-term release scenario).

Nuclide	Yield /pp	$P$ [Bq/y]	$Q_t$ [Bq/y]	Sv/Bq	$E_t$ [Sv]
H-3	1.74E+09	1.74E+09	1.72E+09	2.15E-19	5.06E-10
Be-7	3.21E+10	3.21E+10	1.24E+10	2.14E-17	1.76E-06
Be-10	1.65E+03	1.65E+03	1.65E+03	7.08E-16	1.21E-11
C-11	1.48E+14	1.48E+14	1.68E+10	2.27E-19	3.40E-08
C-14	1.02E+09	1.02E+09	1.02E+09	1.02E-16	1.41E-07
N-13	4.09E+14	4.09E+14	2.27E+10	1.88E-19	4.08E-08
O-14	1.44E+14	1.44E+14	9.48E+08	1.23E-19	9.95E-10
O-15	1.18E+15	1.18E+15	1.34E+10	7.68E-20	1.04E-08
O-19	1.44E+12	1.44E+12	3.61E+06	9.64E-21	1.62E-13
F-18	9.11E+10	9.11E+10	5.57E+07	9.75E-19	5.39E-10
Ne-23	2.84E+12	2.84E+12	7.37E+06	3.14E-21	1.26E-13
Ne-24	9.52E+10	9.52E+10	1.79E+06	6.20E-20	1.12E-12
Na-22	2.24E+06	2.24E+06	2.10E+06	5.33E-14	7.58E-07
Na-24	5.10E+09	5.10E+09	2.55E+07	4.81E-17	1.38E-08
Na-25	2.11E+12	2.11E+12	1.17E+07	1.45E-20	1.35E-12
Mg-27	2.64E+11	2.64E+11	1.40E+07	1.68E-18	6.36E-11
Mg-28	5.33E+08	5.33E+08	3.72E+06	2.03E-16	8.45E-09
Al-26	1.15E+01	1.15E+01	1.15E+01	8.77E-14	4.84E-13
Al-28	4.03E+12	4.03E+12	5.03E+07	1.92E-18	1.88E-10
Al-29	6.30E+11	6.30E+11	2.32E+07	2.52E-19	5.56E-11
Si-31	3.34E+10	3.34E+10	2.93E+07	5.46E-19	1.01E-10
Si-32	1.17E+04	1.17E+04	1.17E+04	4.70E-16	4.60E-11
P-30	1.12E+12	1.12E+12	1.55E+07	1.39E-19	1.61E-11
P-32	1.27E+09	1.27E+09	1.45E+08	6.78E-15	1.16E-05
P-33	5.36E+08	5.36E+08	1.08E+08	8.91E-16	1.19E-06
P-35	2.68E+12	2.68E+12	1.18E+07	1.51E-18	1.70E-11
S-35	1.92E+08	1.92E+08	1.02E+08	6.43E-16	8.39E-07
S-37	1.13E+12	1.13E+12	3.19E+07	3.71E-19	1.16E-10
S-38	2.56E+10	2.56E+10	2.46E+07	3.19E-18	6.66E-10
Cl-34	3.12E+10	3.12E+10	5.55E+06	9.26E-19	4.79E-11
Cl-36	3.55E+02	3.55E+02	3.55E+02	8.71E-13	3.62E-11
Cl-38	1.17E+12	1.17E+12	2.42E+08	7.40E-19	1.57E-09
Cl-39	1.49E+12	1.49E+12	4.60E+08	8.73E-19	3.79E-09
Cl-40	6.62E+12	6.62E+12	5.16E+07	1.74E-19	7.94E-11
Ar-37	4.22E+09	4.22E+09	1.15E+09	1.09E-25	4.32E-16
Ar-39	1.91E+06	1.91E+06	1.91E+06	4.15E-22	2.71E-15
Ar-41	6.00E+13	6.00E+13	3.66E+10	2.90E-19	9.15E-08
K-38	8.59E+10	8.59E+10	3.65E+06	9.04E-19	2.20E-11
K-40	2.66E-03	2.66E-03	2.66E-03	4.06E-13	5.44E-16
				Total	1.65E-05
				Gases	3.26E-07

In the case of the leaking He Vessel, the maximum effective dose could reach  $9.2 \mu\text{Sv}$  (the main contribution by  $^{32}\text{P}$ ) out of which the gaseous radioactivity would account for  $0.44 \mu\text{Sv}$ . In the case of the leaking Decay Pipe, the maximum effective dose would amount to  $13.9 \mu\text{Sv}$  (the main contribution by  $^{32}\text{P}$ ), while the gaseous radioactivity would contribute by  $0.63 \mu\text{Sv}$ .

Table 8.12 lists the annual production of radioactivity in the two He volumes as well as its build-up at the end of the annual operation period T in case of the perfectly tight volumes. The maximum effective doses to members of the public resulting from a release of the built-up radioactivity after the end of the operation period are listed as well. For the He Vessel, the total effective dose should not exceed  $23.3 \mu\text{Sv}$ ; the major part is due to  $^{32}\text{P}$  that could be removed by the HEPA filters. The gaseous radioactivity would contribute only by  $0.29 \mu\text{Sv}$ . The situation is similar for the Decay Pipe: The total effective dose shall be smaller than  $35.7 \mu\text{Sv}$ , with the greatest contribution by  $^{32}\text{P}$ . The gaseous radioactivity would contribute only by  $0.43 \mu\text{Sv}$ .

### 8.2.1.5 Summary and constraints

The annual effective doses to members of the public resulting from releases of radioactive substances to the ambient air from the four most activated compartments are summarized in Table 1.r.

The following pessimistic assumption were made that, at the same time, serve as constraints for the design of the ventilation system:

1. The primary target will receive  $3.89 \times 10^{21}$  50 GeV/c protons per year within 180 days.
2. The extraction rate of air from the Target Chamber will be such that the mean residence time of air in the compartment will be at least 1 hour.
3. The Hadron Stopper will be so tight that the maximum residence time of air in the compartment will be at least 2 days. A flush of the compartment after one 180-day operation period is allowed.
4. The maximum admixture of air in helium in the helium volumes during periods with the primary beam will be 1% vol.
5. The helium volumes can leak (due to overpressure) with a maximum rate of 1% per hour.
6. The helium volumes can be flushed after one 180-day operation period.

Although the assumptions may seem to be too pessimistic, they provide large engineering margins for technical solutions for the ventilation system. One can see from Table 8.14 that the dose objective of a few  $\mu\text{Sv}$  per year cannot be achieved without a performing aerosol retention system. However, considering an overall high-efficiency particle and aerosol retention system, one would attain an annual effective dose below  $5 \mu\text{Sv}$  by releasing essentially only radioactive gases. This dose can be further minimized by prolonging the mean residence time of air or helium in the compartments and by decreasing the contamination of helium with air.

Tritium in the form of tritiated water can be also released by two other processes than the direct activation of air or helium/air mixture as mentioned above:

1. The concrete and other solid materials containing hydrogen are activated as well. Due to the process of isotopic exchange, originally tritium-free water molecules in the water vapour can get a tritium atom at the place of a stable hydrogen atom from such materials. The magnitude of this process is difficult to predict but it can be mitigated by two measures: (a) To avoid wet concrete by reducing any kind of groundwater infiltration (e.g. by use of geo-membranes) and by avoiding as much as possible water leaks and open water bodies (e.g. sumps) in zones with a high material activation. (b) To dry air from outside



**Table 8.11:** Production and releases of radioactivity from the He volumes as well as the resulting annual effective doses for the scenario of leaking volumes for one annual operation period.

Nuclide	P [Bq/y]		Q [Bq/y]		Sv/Bq	E [Sv/y]	
	He Vessel	Decay Pipe	He Vessel	Decay Pipe		He Vessel	Decay Pipe
H-3	9.07E+10	1.37E+11	8.86E+10	1.34E+11	2.15E-19	1.90E-08	2.87E-08
Be-7	3.00E+10	5.62E+10	2.79E+10	5.22E+10	2.14E-17	5.96E-07	1.12E-06
Be-10	1.01E+03	1.31E+03	9.86E+02	1.28E+03	7.08E-16	6.98E-13	9.07E-13
C-11	1.52E+14	2.35E+14	7.40E+11	1.15E+12	2.27E-19	1.68E-07	2.60E-07
C-14	1.41E+07	1.85E+07	1.38E+07	1.81E+07	1.02E-16	1.40E-09	1.84E-09
N-13	3.42E+14	5.03E+14	8.17E+11	1.20E+12	1.88E-19	1.54E-07	2.26E-07
O-14	2.12E+14	2.28E+14	6.02E+10	6.48E+10	1.23E-19	7.41E-09	7.97E-09
O-15	1.56E+15	1.68E+15	7.64E+11	8.23E+11	7.68E-20	5.87E-08	6.32E-08
O-19	9.90E+11	2.76E+12	1.08E+08	2.99E+08	1.20E-20	1.29E-12	3.59E-12
F-18	7.24E+10	1.74E+11	1.86E+09	4.48E+09	9.75E-19	1.81E-09	4.37E-09
Ne-23	2.08E+12	5.43E+12	2.33E+08	6.09E+08	3.57E-21	8.33E-13	2.17E-12
Ne-24	6.70E+10	1.83E+11	5.44E+07	1.48E+08	6.20E-20	3.37E-12	9.19E-12
Na-22	1.88E+06	4.21E+06	1.83E+06	4.10E+06	5.33E-14	9.75E-08	2.18E-07
Na-24	4.19E+09	9.53E+09	7.42E+08	1.69E+09	4.81E-17	3.57E-08	8.12E-08
Na-25	1.61E+12	4.01E+12	3.88E+08	9.64E+08	1.45E-20	5.62E-12	1.40E-11
Mg-27	1.85E+11	4.74E+11	4.21E+08	1.08E+09	1.68E-18	7.08E-10	1.82E-09
Mg-28	4.80E+08	9.63E+08	1.11E+08	2.22E+08	2.03E-16	2.24E-08	4.51E-08
Al-26	1.02E+01	2.24E+01	9.93E+00	2.19E+01	8.77E-14	8.71E-13	1.92E-12
Al-28	4.05E+12	7.79E+12	2.18E+09	4.19E+09	1.92E-18	4.19E-09	8.05E-09
Al-29	4.96E+11	1.13E+12	7.86E+08	1.78E+09	2.52E-19	1.98E-10	4.49E-10
Si-31	3.31E+10	6.12E+10	1.21E+09	2.23E+09	5.46E-19	6.59E-10	1.22E-09
Si-32	1.19E+04	2.10E+04	1.16E+04	2.06E+04	4.70E-16	5.47E-12	9.66E-12
P-30	1.16E+12	2.14E+12	6.94E+08	1.29E+09	1.39E-19	9.65E-11	1.79E-10
P-32	1.35E+09	1.99E+09	1.10E+09	1.62E+09	6.78E-15	7.45E-06	1.10E-05
P-33	5.18E+08	7.63E+08	4.56E+08	6.71E+08	8.91E-16	4.06E-07	5.97E-07
P-35	2.84E+12	3.93E+12	5.39E+08	7.46E+08	2.92E-18	1.57E-09	2.18E-09
S-35	1.93E+08	2.60E+08	1.83E+08	2.46E+08	6.43E-16	1.18E-07	1.58E-07
S-37	9.85E+11	9.80E+11	1.20E+09	1.19E+09	3.71E-19	4.44E-10	4.42E-10
S-38	2.33E+10	3.35E+10	9.24E+08	1.33E+09	3.19E-18	2.95E-09	4.25E-09
Cl-34	3.99E+10	5.50E+10	3.04E+08	4.20E+08	9.26E-19	2.82E-10	3.89E-10
Cl-36	3.43E+02	4.26E+02	3.35E+02	4.17E+02	8.71E-13	2.92E-10	3.63E-10
Cl-38	9.09E+11	1.20E+12	8.06E+09	1.06E+10	7.40E-19	5.96E-09	7.86E-09
Cl-39	1.22E+12	1.77E+12	1.61E+10	2.34E+10	8.73E-19	1.40E-08	2.04E-08
Cl-40	3.12E+12	2.52E+12	1.05E+09	8.48E+08	1.74E-19	1.82E-10	1.47E-10
Ar-37	7.35E+08	8.37E+08	6.64E+08	7.57E+08	1.09E-25	7.24E-17	8.25E-17
Ar-39	1.25E+06	1.53E+06	1.22E+06	1.50E+06	4.15E-22	5.08E-16	6.22E-16
Ar-41	5.16E+11	9.51E+11	1.33E+10	2.44E+10	2.90E-19	3.84E-09	7.08E-09
K-38	1.34E+11	1.61E+11	2.46E+08	2.96E+08	9.04E-19	2.22E-10	2.67E-10
K-40	4.62E-03	4.26E-03	4.51E-03	4.16E-03	4.06E-13	1.83E-15	1.69E-15
Total						9.17E-06	1.39E-05
Gases						4.35E-07	6.28E-07

**Table 8.12:** Production and releases of radioactivity from the He volumes as well as the resulting annual effective doses for the scenario of the perfectly tight volumes flushed at the end of the annual operation period (a short-term release).

Nuclide	P [Bq/y]		Q [Bq/y]		Sv/Bq	E [Sv/y]	
	He Vessel	Decay Pipe	He Vessel	Decay Pipe		He Vessel	Decay Pipe
H-3	9.07E+10	1.37E+11	8.95E+10	1.35E+11	2.12E-18	1.90E-07	2.86E-07
Be-7	3.00E+10	5.62E+10	1.16E+10	2.17E+10	1.74E-16	2.02E-06	3.78E-06
Be-10	1.01E+03	1.31E+03	1.01E+03	1.31E+03	1.07E-14	1.08E-11	1.40E-11
C-11	1.52E+14	2.35E+14	1.72E+10	2.67E+10	1.79E-18	3.08E-08	4.77E-08
C-14	1.41E+07	1.85E+07	1.41E+07	1.85E+07	1.00E-15	1.41E-08	1.85E-08
N-13	3.42E+14	5.03E+14	1.90E+10	2.79E+10	1.61E-18	3.05E-08	4.49E-08
O-14	2.12E+14	2.28E+14	1.40E+09	1.50E+09	1.46E-18	2.04E-09	2.19E-09
O-15	1.56E+15	1.68E+15	1.77E+10	1.91E+10	9.10E-19	1.61E-08	1.73E-08
O-19	9.90E+11	2.76E+12	2.49E+06	6.93E+06	8.52E-20	2.12E-13	5.90E-13
F-18	7.24E+10	1.74E+11	4.43E+07	1.07E+08	1.18E-17	5.22E-10	1.26E-09
Ne-23	2.08E+12	5.43E+12	5.40E+06	1.41E+07	3.96E-20	2.14E-13	5.58E-13
Ne-24	6.70E+10	1.83E+11	1.26E+06	3.44E+06	6.41E-19	8.08E-13	2.20E-12
Na-22	1.88E+06	4.21E+06	1.76E+06	3.94E+06	4.99E-13	8.78E-07	1.97E-06
Na-24	4.19E+09	9.53E+09	2.10E+07	4.78E+07	7.08E-16	1.49E-08	3.38E-08
Na-25	1.61E+12	4.01E+12	8.98E+06	2.23E+07	1.94E-19	1.74E-12	4.33E-12
Mg-27	1.85E+11	4.74E+11	9.78E+06	2.51E+07	1.87E-17	1.83E-10	4.69E-10
Mg-28	4.80E+08	9.63E+08	3.35E+06	6.73E+06	3.16E-15	1.06E-08	2.13E-08
Al-26	1.02E+01	2.24E+01	1.02E+01	2.24E+01	5.28E-14	5.37E-13	1.18E-12
Al-28	4.05E+12	7.79E+12	5.05E+07	9.72E+07	2.54E-17	1.28E-09	2.47E-09
Al-29	4.96E+11	1.13E+12	1.82E+07	4.14E+07	2.60E-18	4.74E-11	1.08E-10
Si-31	3.31E+10	6.12E+10	2.90E+07	5.36E+07	7.09E-18	2.06E-10	3.80E-10
Si-32	1.19E+04	2.10E+04	1.19E+04	2.10E+04	6.71E-15	7.99E-11	1.41E-10
P-30	1.16E+12	2.14E+12	1.61E+07	2.98E+07	1.75E-18	2.81E-11	5.21E-11
P-32	1.35E+09	1.99E+09	1.54E+08	2.28E+08	1.12E-13	1.73E-05	2.55E-05
P-33	5.18E+08	7.63E+08	1.05E+08	1.54E+08	1.54E-14	1.61E-06	2.37E-06
P-35	2.84E+12	3.93E+12	1.25E+07	1.73E+07	2.37E-17	2.96E-10	4.09E-10
S-35	1.93E+08	2.60E+08	1.03E+08	1.38E+08	1.15E-14	1.18E-06	1.59E-06
S-37	9.85E+11	9.80E+11	2.78E+07	2.76E+07	3.83E-18	1.06E-10	1.06E-10
S-38	2.33E+10	3.35E+10	2.23E+07	3.22E+07	3.97E-17	8.85E-10	1.28E-09
Cl-34	3.99E+10	5.50E+10	7.10E+06	9.79E+06	1.01E-17	7.17E-11	9.89E-11
Cl-36	3.43E+02	4.26E+02	3.43E+02	4.26E+02	1.39E-13	4.77E-11	5.93E-11
Cl-38	9.09E+11	1.20E+12	1.88E+08	2.48E+08	8.28E-18	1.56E-09	2.05E-09
Cl-39	1.22E+12	1.77E+12	3.78E+08	5.49E+08	9.97E-18	3.76E-09	5.47E-09
Cl-40	3.12E+12	2.52E+12	2.43E+07	1.96E+07	2.13E-18	5.17E-11	4.18E-11
Ar-37	7.35E+08	8.37E+08	2.00E+08	2.28E+08	2.70E-24	5.41E-16	6.17E-16
Ar-39	1.25E+06	1.53E+06	1.25E+06	1.53E+06	1.02E-20	1.28E-14	1.56E-14
Ar-41	5.16E+11	9.51E+11	3.15E+08	5.81E+08	2.11E-18	6.65E-10	1.22E-09
K-38	1.34E+11	1.61E+11	5.70E+06	6.86E+06	9.82E-18	5.60E-11	6.73E-11
K-40	4.62E-03	4.26E-03	4.62E-03	4.26E-03	2.84E-13	1.31E-15	1.21E-15
Total						2.33E-05	3.57E-05
Gases						2.90E-07	4.27E-07

**Table 8.13:** Summary of the maximum annual effective doses incurred to a member of the public due to releases of radioactive substances to the ambient air from the four most activated compartments.

Compartment	Ventilation mode	Effective dose [ $\mu\text{Sv/y}$ ]	
		All radionuclides	Gases
Target Chamber	Leaking	1.35	1.09
Hadron Stopper	Leaking	11.1	1.89
	Tight/Flush	16.5	0.33
He Vessel	Leaking	9.2	0.44
	Tight/Flush	23.3	0.29
Decay Pipe	Leaking	13.9	0.63
	Tight/Flush	35.7	0.43
Maximal Total		76.9	4.05

before supplying it to zones with a high material activation. Such HTO releases usually continue also during the time without a particle beam.

- As will be shown later, there is no receiving river with a sufficient baseline flow rate, which could safely absorb releases of activated or contaminated water. Such water will have to be cleaned from other radionuclides than tritium (ion exchangers, filters) and continuously evaporated to the atmosphere through the ventilation duct(s). Obviously, tritium in the form of HTO cannot be eliminated in other way on the site. Care shall be taken to prevent condensation of evaporated water on cold ventilation ducts.

Assuming the generic long-term dose coefficient for HTO of  $2.15 \times 10^{719}$  Sv/Bq, to keep the annual effective dose to members of the public due to these supplementary tritium releases below  $1 \mu\text{Sv}$ , one would be allowed to release 4.6 TBq of HTO per year in addition.

The effective dose due to  $^{14}\text{CO}_2$  shall remain below  $0.2 \mu\text{Sv/year}$  even in the most pessimistic scenarios. The most critical operation would be flushing of the Hadron Stopper that could be carried out outside the photosynthesis time of plants, for example during the night to prevent the assimilation of  $^{14}\text{C}$  into the plant tissues.

#### 8.2.1.6 Releases of radioactive substances to surface water

There is no river with a sufficient flow rate nearby to absorb safely activated and contaminated water. At this stage, cooling circuits were not yet designed but, following the experience with other high beam-power facilities, two or even three staged cooling circuits will have to be used.

Water exposed to hadron cascades is activated with tritium and other spallation products of oxygen  $^{10,14,15}\text{O}$ ,  $^{6,11,14}\text{C}$ ,  $^{13}\text{N}$ ,  $^{7,10}\text{Be}$ . Except for tritium,  $^{14}\text{C}$ ,  $^7\text{Be}$  and  $^{10}\text{Be}$ , short-lived radionuclides decay inside the closed circuits unless they need to be outgassed with excessive oxygen to keep certain chemical properties of the circulating water. The water in the most activated primary and secondary circuits will have to be cleaned by ion-exchangers to remove longer-lived radionuclides, namely  $^7\text{Be}$  and  $^{10}\text{Be}$ , although the latter will be produced in small activities thanks to its very long half-life. Besides spallation products of pure water, there are other activation products frequently present; isotopes of sodium,  $^{22,24}\text{Na}$ , and radioactive isotopes of Co, Fe and Mn @ the corrosion products. With such a high beam power, certain attention should be devoted to the production of  $^{14}\text{C}$  that could outgas from the water cooling circuits as  $^{14}\text{CO}_2$  and contribute to the airborne exposure.

Highly activated water shall be evaporated on the site after cleaning. The residues shall be then temporary stored and finally eliminated as radioactive waste. This method allows for

certain dispersion of tritiated water (HTO) in the atmosphere compared to releases in a highly concentrated form to local rain collectors.

The tunnels of the facility must remain dry by minimizing water infiltration by civil engineering means, for example by external geo-membranes. A thorough geotechnical and hydrogeological studies are necessary before the detailed design of the tunnels. In particular, seeping of natural hydrocarbons known to be present at these depths must be avoided. Evaporation of water and elimination of radioactive residues contaminated with hydrocarbons are particularly difficult.

Sumps in high activation areas, which are constantly filled with water, shall be avoided because they would capture HTO from activated air. However, some sumps will be needed as collectors for cases of rupture of water circuits when they will serve as buffers to be emptied locally, if the specific activity of water collected in them will be low or evaporated and cleaned from dirt and radioactive residues.

#### 8.2.1.7 Stray radiation at the surface of the facility

The facility is placed sufficiently deep so that stray radiation can penetrate on the surface and to the environment only through vertical shafts or openings. The access shaft has the worst position relative to the primary target. The estimated dose rate at the top of the access shaft of  $0.05 \mu\text{Sv/h}$  (Section 1.9.2) is equivalent to about 200  $\mu\text{Sv}$  per one 180-day operating period, which is far above the dose objective of less than a few  $\mu\text{Sv}$  per year from all sources.

More studies are needed once the ground-level infrastructure will be designed. In particular, sky-shine shall be investigated, as back-scattering of neutrons from air to long distances beyond the fenced part of the site. Eventually a concrete cover of the access shaft would be needed to reduce the exposure to the stray radiation to acceptable levels.

#### 8.2.1.8 Activation of soil, rock and groundwater

The radionuclides produced in the concrete structures of an accelerator facility are relatively immobile. However, the radionuclides produced in the shield of groundwater are free to move. The radionuclides produced in the groundwater might pass into the general groundwater system and therefore potentially into the public water supplies extracted from the area. In addition, the possibility that activity induced in the earth may be leached into the groundwater system must be also considered. A review of the processes taking place is given in Ref. [?]. A large number of radionuclides may be produced in the earth and groundwater by high energy accelerator beams. However, the ultimate concentration of radionuclides in the groundwater will then be controlled by the half-life of the radioactive species, solubility of the radionuclide, its possible dilution, re-adsorption of diluted ions, and the site hydrology. Radionuclides with too short a half-life will decay so rapidly as to be of no potential hazard when they would reach a public water supply. Conversely, if the half-life is too long, saturation activities will not be approached [?]. In practice, the production of  $^3\text{H}$ ,  $^{22}\text{Na}$ ,  $^{54}\text{Mn}$  and  $^{45}\text{Ca}$  merits a detailed study [?]. While many studies indicate a high mobility of  $^3\text{H}$  in groundwater, Hoyer showed that, in molasse from around CERN, the only other mobile radionuclide was  $^{22}\text{Na}$  [?]. Production of more than 400 radionuclides in molasse was calculated by FLUKA. Table ?? shows the production of the four above-mentioned radionuclides during one 180-day operation period with  $2.4 \times 10^{14}$  p/second.

The most activated parts of the facility are in deep layers of molasse. This rock contains some 10% of water but it is almost impermeable, which makes it unsuitable for exploitation of drinking water. This deep water is not in contact with the shallower layers of water [?] in moraine. By contrast to the deep groundwater in molasse, the relatively shallow moraine placed above forms aquifers and has been used as drinking water source.

**Table 8.14:** Production of the four radionuclides most relevant for groundwater pollution during one 180-day operation period with  $2.4 \times 10^{14}$  p/second.

Radionuclide	Bq	Half-life
$^3\text{H}$	$2.38 \times 10^{11}$	12.32 y
$^{22}\text{Na}$	$2.18 \times 10^{11}$	2.060 y
$^{45}\text{Ca}$	$6.03 \times 10^{11}$	162.6 d
$^{54}\text{Mn}$	$3.53 \times 10^{11}$	312.05 d

The activities listed in Table ?? are impressive and although it is assumed that the radioactivity remains quite immobile deeply underground, a hydrogeological study will have to be carried out to confirm this assumption and to exclude a contact with moraine in upper layers. Another aspect is the use of geothermal energy. It shall be proven that the spatial distribution of the rock and groundwater activation will be narrow enough to avoid a contact of geothermal drillings with activated zones underground.

It cannot be excluded that massive concrete layers around the most activated elements will have to be built to keep the larger part of the produced activity immobilized stronger than would be the case in the molasse alone.

## Chapter 9

# Acknowledgements

The design study reported here is the summary of the work of all people involved in the Work-Package 4 (WP4) of the LAGUNA-LBNO FP7 Design Study, from CERN, RAL and UniGe.

This report summarizes the studies done which for some parts go well beyond the conceptual level, thanks to the enthusiasm and motivation of all participants.

The section on the transfer line from SPL to HP-PS is essentially a synopsis of the detailed and thorough work on the 4 GeV/c  $H^-$  injection line for PS2 performed by Christophe Hessler. The layout of the HP-PS and lines to the targets have been drawn up in close collaboration with Laurent Faisandel and John Osborne. The non-local extraction studies and tests were conducted together with many colleagues from the SPS, too numerous to mention individually. The overall impetus and coordination of the study has been managed by Ilias Efthymiopoulos, who also made much valuable technical input for the transfer lines.

For the validation of the non-local fast extraction concept at SPS, as well as specific measurements with the CNGS beam to understand the limitations of the machine were done during MD slots in the 2012 operation, also made possible thanks to the support of the CCC SPS operation team and K. Cornelis in particular.

The section of the civil engineering is greatly inspired from the work done for CNGS. We thank A. Luz Lopez-Hernandez for giving access to the technical drawings, the fruitful discussions and guidance during the studies.

For the engineering solutions of the handling and installation scenarios, addressing in particular the challenging 18% slope, the input and experience from the colleagues in the Handling Group of CERN was very valuable. We thank D. Lafarge, G. Roche, JP. Granchelli, R. Rinaldesi, JL. Grenard and K. Kershaw for the fruitful discussions and feedback.

The discussions and feedback from the colleagues in the LAGUNA-LBNO Consortium given during the general meetings is greatly acknowledged.



## **Appendix A**

# **LAGUNA-LBNO Parameter List**





# Appendix B

## Engineering drawings

3-D and 2-D Drawings for the CN2PY Beam & LAGUNA-LBNO Experiment in CERN SmarTeam and EDMS systems.

### B.1 3-D model references in SmarTeam

For each drawing the SmarTeam reference number is given

D/N	Model Description	SmarTeam Number
1	Total Civil Engineering Model	ST0583672
2	Total Final Laguna Model	ST0585508

**Table B.1:** Total Model of CN2PY facility

D/N	Model Description	SmarTeam Number
3	Main Access Shaft	ST0583688
4	Transport Tunnel	ST0583694

**Table B.2:** Part Model - CN2PY Target Area.

D/N	Model Description	SmarTeam Number
5	Main Connection Tunnel	ST0619321 ST0623110
6	Service Tunnel	ST0583689
7	Connection Tunnel 1	ST0583686
8	Ditch 1	ST0583690
9	Connection Tunnel 2	ST0583687
10	Ditch 2	ST0583691

**Table B.3:** Part Model - CN2PY Service Area.

### B.2 2-D model references in SmarTeam and EDMS

D/N	Model Description	SmarTeam Number
11	Morgue Tunnel	ST0583694

**Table B.4:** Part Model - CN2PY Morgue Area.

D/N	Model Description	SmarTeam Number
12	Proton Beam Tunnel	ST0583692
13	Target Chamber Tunnel	ST0583694
14	Decay Pipe Part One Tunnel	ST0583988
15	Decay Pipe Part Two Tunnel	ST0583683
16	Hadron Stopper Tunnel	ST0583684
17	Hadron Stopper Access Shaft	ST0594041
18	Connection Tunnel	ST0594040

**Table B.5:** Part Model - CN2PY Beam Areas.

D/N	Model Description	SmarTeam Number
19	Hot Cell Tunnel	ST0583694

**Table B.6:** Part Model - CN2PY Hot Cell Area.

D/N	Model Description	SmarTeam Number
20	Near Detector Access Shaft	ST0594459
21	Near Detector Tunnel	ST0600481
22	Mind	ST0614518
23	Metallic Structure + Racks	ST0621851
24	Near Detector + Iron Blocks	ST0600502

**Table B.7:** Part Model - CN2PY Near Detector Area.

D/N	Model Description	SmarTeam Number
25	Passage(bridge) from transport area to the morgue	ST0597263
26	Air Ducts for the Target Chamber Tunnel	ST0598603
27	Ventilation doors + Concrete wall shielding inside the connection tunnels 1 and 2	ST0617506
28	Overhead crane beginning of Hadron Stopper Tunnel	ST0618078
29	Shutter for the Helium Vessel + Decay pipe	ST0617629
30	Ventilation System + Metallic Structures	ST0618755
31	Ladders for the water sumps	ST0618867
32	Remote Control Crane Area	ST0619093
33	Racks	ST0621146
34	Water System	ST0621362
35	He System	ST0621491
36	Ventilation System for Hadron Stopper Tunnel	ST0621317
37	Stairs for the Ditches	ST0623111
38	Aluminium + Iron Shielding Blocks for the Target Chamber Tunnel	ST0586654
39	Helium Vessel for the Target Chamber Tunnel	ST0586840
40	Horn + Support Table	ST0621082
41	Reflector + Support Table	ST0621556
42	Concrete Shielding Blocks for the Target Chamber Tunnel	ST0586745
43	Concrete shielding wall to separate the Target Chamber Tunnel from the Transport Tunnel	ST0590144
44	Water + He Pipes + Strip lines	ST0590452
45	Manipulator for the hot cell	ST0600435
46	Beam line (magnets)	ST0592744
47	Decay pipe	ST0621966
48	Iron Blocks for the Hadron Stopper Tunnel	ST0623323
49	Overhead Crane inside the Transport Tunnel	ST0594122
50	Crane for the Target Chamber Tunnel + the Transport Tunnel	ST0594245
51	Shielding wall + Muon Detector for the Hadron Stopper Tunnel	ST0617302
52	LAGUNA Meyrin option	ST0619814
53	LAGUNA Preveessin option	ST0618454

Table B.8: 3-D Part Model - CN2PY Area.

D/N	Drawing Description	SmarTeam Number
1	Laguna Meyrin Option	ST0623705
2	Laguna Preveessin Option	ST0618454
3	Horn	ST0621082
D/N	Drawing Description	EDMS Number
4	Laguna Meyrin Option	1385398
5	Laguna Preveessin Option	1387244

Table B.9: 2-D Total Model - CN2PY Layouts



# Bibliography

- [1] LAGUNA reference.
- [2] LAGUNA reference.
- [3] A. Stahl et al., Expression of Interest for a very long baseline neutrino oscillation experiment (LBNO), CERN, CERN-SPSC-2012-021, SPSC-EOI-007 (2012).
- [4] T. Bohl, T.P. Linnecar, E. Shaposhnikova, RF studies of the high intensity CNGS beam in the SPS, CERN, AB-Note-2005-034 (2005)
- [5] E. Regenstreif, The CERN Proton Synchrotron, pt.1, CERN-59-29.
- [6] S. Gilardoni and D. Manglunki (eds.), CERN-2011-004.
- [7] M. Giovannozzi et al., Possible improvements to the existing pre-injector complex in the framework of continued consolidation, Proceedings of the Chamonix 2010 LHC Performance Workshop.
- [8] J. Barranco, S. Gilardoni, Simulation and optimization of beam losses during continuous transfer extraction at the CERN Proton Synchrotron, Phys. Rev. ST Accel. Beams 14 (2011) 030101
- [9] M. Giovannozzi (ed.), CERN-2006-11
- [10] K. Elsener, ed., CERN Report No. CERN-SL/99-034-DI (1999)
- [11] G. Arduini et al., Recent Intensity Increase in the CERN Accelerator Chain, CERN-AB-2005-029
- [12] <http://blrwg.web.cern.ch/blrwg/>
- [13] L. Bruno et al., Final Report of the PS Radiation Working Group, CERN-ATS-2011-007
- [14] S. Gilardoni (ed.), PS Upgrade Technical design report, to be published.
- [15] E. Radermacher, ed., CERN Report No. CERN-INTC- 2000-004 (2000)
- [16] I. Efthymiopoulos, Opportunities for  $\nu$ -beams at CERN, Presented at Neutrino Town Meeting, CERN, 2012.
- [17] S. Aumon, High Intensity Beam Issues in the CERN Proton Synchrotron, CERN-THESIS-2012-261
- [18] A. Huschauer et al., paper submitted to PRSTAB
- [19] A. Blas et al., Beam Tests and Plans for the Cern PS Transverse Damper System, CERN-ACC-2013-0215

- [20] H.-Ch. Grassmann, R. Jankovsky, W. Pirkl, New RF System for the 28 GeV Proton Synchrotron at CERN, *Siemens Review*, 44, 1977, p. 166.
- [21] G. Favia, Measurements and potential improvements of the amplifier for the 10 MHz cavities, unpublished presentation, LIU-PS Working Group Meeting, CERN, Geneva, Switzerland, 2013.
- [22] H. Damerau, S. Hancock, M. Schokker, Longitudinal Performance with High-density Beams for the LHC in the CERN PS, HB2010, Mohrschach, Switzerland, 2010, p. 193.
- [23] H. Damerau, S. Hancock, Update on Longitudinal Performance of LHC Beams in the PS, unpublished presentation, Machine Studies Working Group Meeting, CERN, Geneva, Switzerland, 2011.
- [24] M. Fujieda et al., Magnetic Alloy Loaded RF Cavity for Barrier Bucket Experiment at the AGS, PAC99, New York, USA, 1999, p. 857.
- [25] E. Metral, Fast High-Intensity Single-Bunch Transverse Coherent Instability in Synchrotrons due to a Broad-Band Resonator Impedance, Technical Report CERN-PS-2001-035-AE, CERN, Geneva, Jul 2001
- [26] M. Migliorati, private communication
- [27] R. Cappi et al., Beam Breakup Instability in the CERN PS near Transition, Proc. 7th EPAC, Vienna, Austria, 26-30 June 2000.
- [28] M. J. Barners et al., Injection and extraction magnets: kicker magnets, arXiv:1103.1583 [physics.acc-ph]
- [29] V. Kornilov et al., MD at the PS: Beam Break-Up Instability Near Transition, CERN-ATS-Note-2013-038 MD
- [30] J. M. Cesaratto et al., SPS Wideband Transverse Feedback Kicker: Design Report, SLAC-R-1037
- [31] M. Giovannozzi, Status of MTE, presentation at the CERN-IEFC meeting held on 25 of May 2010.
- [32] C. Bertone et al., Studies and implementation of the PS dummy septum to mitigate irradiation of magnetic septum in straight section 16, CERN-ACC-2014-0043
- [33] E. Shaposhnikova, E. Ciapala, E. Montesinos, Upgrade of the 200 MHz RF System in the CERN SPS, CERN-ATS-2011-042
- [34] S. Gilardoni et al., First observations of intensity-dependent effects for transversely split beams during multiturn extraction studies at the CERN Proton Synchrotron, *Phys. Rev. ST Accel. Beams* 16 (2013) 051001
- [35] M. Giovannozzi et al., Generating Unstable Resonances for Extraction Schemes Based on Transverse Splitting, *Phys. Rev. Spec. Top. Accel. Beams* 12 (2009) 024003
- [36] A. Franchi et al., Progresses in the studies of adiabatic splitting of charged particle beams by crossing nonlinear resonances, *Phys. Rev. ST Accel. Beams* 12 (2009) 014001
- [37] E. Shaposhnikova et al., Recent intensity increase in the CERN SPS, Proc. PAC05, Knoxville, USA, (2005).

- [38] T. Bohl, T. Linnecar, E. Shaposhnikova, RF studies of the high intensity CNGS beam in the SPS, CERN AB-Note-2005-034 (2005).
- [39] M. Meddahi, E. Shaposhnikova, Analysis of the maximum potential proton flux to CNGS, CERN-AB-2007-013 PAF (2007).
- [40] Summary of the beam collimation review, CERN, 2014
- [41] C. Lazaridis et al., Recent CNGS-type Beam Studies in the SPS, CERN-ACC-NOTE-2014-, to be published
- [42] LIU project: website
- [43] E. Shaposhnikova, E. Ciapala, E. Montesinos, Upgrade of the 200 MHz RF system in the CERN SPS, Proceed, IPAC11, San-Sebastian, Spain (2011)
- [44] G. Rumolo, *HL-LHC beam parameters*, CERN EDMS document 1296306, <https://edms.cern.ch/document/1296306/1>
- [45] ALICE Collaboration, *The Zero Degree Calorimeters for the ALICE Experiment*, CERN-ALICE-PUB-99-17, 1999.
- [46] V.Kain et al., *The expected performance of the LHC injection protection system*, Presented at EPAC'04; 9th European Particle Accelerator Conference 2004.
- [47] O. Brüning, J. B. Jeanneret, *Optics constrains imposed by the injection in IR2 and IR8*, CERN/LHC Project Note 141 1998.
- [48] LHC Design Report, <http://ab-div.web.cern.ch/ab-div/Publications/LHC-DesignReport.html>
- [49] M.J. Barnes et al., *Upgrade of the LHC Injection Kicker Magnets*, proc. of IPAC'13, MOPWA030; <http://www.JACoW.org>
- [50] M.J. Barnes, F. Caspers, L. Ducimetière, N. Garrel, T. Kroyer, *The Beam Screen for the LHC Injection Kicker Magnets*, Proc. EPAC'06, TUPLS011; <http://www.JACoW.org>
- [51] PhD Thesis, H. Day, to be published.
- [52] H. Day et al., *Evaluation of the Beam Coupling Impedance of New Beam Screen Designs for the LHC Injection Kicker Magnets*, Proc. IPAC'13, TUPME033; <http://www.JACoW.org>
- [53] M.J. Barnes et al., *Beam Induced Ferrite Heating of the LHC Injection Kickers and Proposals for Improved Cooling*, Proc. IPAC'13, MOPWA031; <http://www.JACoW.org>
- [54] T. Baer et al., *UFOs: Observations, Statistics and Extrapolations*, Proc. LHC Beam Operation workshop, Evian, 17-20 December 2012.
- [55] Priv. comm., G. Rumolo and G. Iadarola, 16 April 2013.
- [56] T.S. Sudarshan, J.D. Cross, *The Effect of Chromium Oxide Coatings on Surface Flashover of Alumina Spacers in Vacuum*, IEEE Trans. on Electrical Insulation, Vol. EI-11, No. 1, March 1976, pp32-35.
- [57] B. Goddard et al., *Transient Beam Losses in the LHC Injection Kickers from Micron Scale Dust Particles*, IPAC'12, TUPPR092; <http://www.JACoW.org>



- [58] M.J. Barnes, L. Ducimetière, N. Garrel, B. Goddard, V. Mertens, W. Weterings, *Analysis of Ferrite Heating of the LHC Injection Kickers and Proposals for Future Reduction of Temperature*, Proc. IPAC'12, TUPPR090; <http://www.JACoW.org>
- [59] J. B. Jeanneret, R. Ostojic, *Geometrical acceptance in LHC version 5.0*, CERN-LHC-Note-111, 1997.
- [60] B. Goddard et al., *Beamloss Control at Injection into the LHC*, CERN-ATS-2011-274, 2011.
- [61] L. Drosdal et al., *Analysis of LHC Transfer Line Trajectory Drifts*, IPAC'13, MOPWO033; <http://www.JACoW.org>
- [62] W. Bartmann et al., *LHC abort gap cleaning studies during luminosity operation*, IPAC'12, MOPPD058; <http://www.JACoW.org>
- [63] A. Boccardi et al., *Summary of Injection pre-cleaning tests performed on October 27, 2010*, CERN-ATS-Note-2010-050 PERF. 2010.
- [64] C. Bracco et al., *Injection and lessons for 2012*, Chamonix 2012 Workshop on LHC Performance, pp.65-68.
- [65] T. Antonakakis, C. Maglioni, *Upgrade of the TCDQ: A dumping protection system for the LHC*, sLHC Project Note 0041, 2013.
- [66] R. Versaci, B. Goddard, V. Vlachoudis, *LHC Asynchronous Beam Dump: Study of new TCDQ model and effects on downstream magnets*, CERN-ATS-Note-2012-084 MD, 2012.
- [67] A. Antoine, E. Carlier, N. Voumard, *The LHC Beam Dumping System Trigger Synchronisation and Distribution System*, ICALEPCS2005, Geneva, 2005.
- [68] R. Filippini, *Dependability analysis of a safety critical system : the LHC beam dumping system at CERN*, CERN-THESIS-2006-054 - Pisa U., 2006.
- [69] J. Zazula and S. Péraire, *LHC beam dump design study; 1, simulation of energy deposition by particle cascades; implications for the dump core and beam sweeping system*, CERN-LHC-Project-Report-80, 1996.
- [70] R. Versaci, B. Goddard, V. Vlachoudis, V, *LHC Asynchronous Beam Dump: Study of new TCDQ model and effects on downstream magnets*, CERN-ATS-Note-2012-084 MD, 2012.
- [71] V. Senaj, L. Ducimetiere, *Attempt to a non-destructive single event burnout test of high current thyristors*, Pulsed Power Conference, 2011 IEEE, ISBN 978-1-4577-0629-5.
- [72] A dummy reference.
- [73] <https://cds.cern.ch/record/1635961/files/CERN-ACC-2013-0271.pdf>
- [74] CES selector 2012, Cambridge University/
- [75] T2K Experiment, T2K collaboration, *Nuclear Instruments and Methods in Physics Research A*, Volume 659, Issue 1, p. 106-135. <http://arxiv.org/abs/1106.1238>
- [76] FLUKA: a multi-particle transport code, A. Ferrari, P.R. Sala, A. Fassio', and J. Ranft, CERN-2005-10 (2005), INFN/TC\_05/11, SLAC-R-773
- [77] IG-43 High Temperature Characteristics, Unknown source.
- [78] ANSYS® CFX, Release 15.0

- [79] ANSYS<sup>®</sup> Mechanical, Release 15.0
- [80] Toyo Tanso property data [http://www.toyotanso.co.jp/Products/Special\\_graphite/data\\_en.html](http://www.toyotanso.co.jp/Products/Special_graphite/data_en.html) accessed on 20/08/2014.
- [81] HTGR Graphite Core Component Stress Analysis Research Program © Task 1 Technical Letter Report, ANL-11/04, Argonne National Laboratory, September, 2011, Page 111
- [82] J.M. Cravero, G. Maire, and J.-P. Royer, ©High current capacitor discharge power converters for the magnetic lenses of a neutrino beam facility,© in Power Electronics and Applications, 2007 European Conference on, Sept. 2007, pp. 1©8.
- [83] F Gerigk (editor) et al, “Conceptual design of the SPL II, A high-power superconducting H<sup>-</sup> linac at CERN”, Geneva, CERN, 2006. <http://cds.cern.ch/record/975366?ln=en>
- [84] Y. Papaphilippou et al., ““Optics Design of the High-power Proton Synchrotron for LAGUNA-LBNO””, these proceedings.
- [85] A.H. Mohagheghi et al., “Interaction of relativistic H<sup>-</sup> ions with thin foils, Phys. Rev. A43, 1345, (1991).
- [86] L. Scherk, “An Improved Value for the Electron Affinity of the Negative Hydrogen Ion”, Dan. J.Phys. 57, 558 (1979).
- [87] B. Goddard et al., ““Laser Stripping for the PS2 Charge-Exchange Injection System””, PAC09, Vancouver, TU6RFP028, (2009) <http://epaper.kek.jp/PAC2009/papers/tu6rfp028.pdf>
- [88] M. Petrarca et al., ““Study of the Powerful Nd:YLF Laser Amplifiers for the CTF3 Photoinjectors””, IEEE Journal of Quantum Electronics, VOL. 47, NO. 3, MARCH 2011, p. 306-313
- [89] M. Notcutt et al., ““First experiments with a Power Buildup cavity at 355 nm””, 3rd mini-Workshop on H- Laser Stripping and Accelerator Applications, Fermilab, Batavia, US, 2013 <https://indico.fnal.gov/getFile.py/access?contribId=27&sessionId=3&resId=0&materialId=slides&confId=6855>
- [90] H. Bartosik. *Beam dynamics and optics studies for the LHC injectors upgrade*. PhD thesis, Vienna University of Technology, 2013.
- [91] Y. Papaphilippou et al. Orbit, optics and chromaticity correction for PS2 negative momentum compaction lattices. *TH6PFP043, Proceedings of PAC09, 2009*.
- [92] <http://mad.web.cern.ch/mad/>.
- [93] A dummy reference
- [94] A. Stahl, C. Wiebusch, A. M. Guler, M. Kamiscioglu, R. Sever, A. U. Yilmazer, C. Gunes and D. Yilmaz *et al.*, CERN-SPSC-2012-021.
- [95] R. Brun and F. Rademakers, Nucl. Instrum. Meth. A **389** (1997) 81.
- [96] C. Andreopoulos, A. Bell, D. Bhattacharya, F. Cavanna, J. Dobson, S. Dytman, H. Gallagher and P. Guzowski *et al.*, Nucl. Instrum. Meth. A **614** (2010) 87 [arXiv:0905.2517 [hep-ph]].
- [97] J. Allison, M. Asai, G. Barrand, M. Donszelmann, K. Minamimoto, S. Tanaka, E. Tcherniaev and J. Tinslay, Comput. Phys. Commun. **178** (2008) 331.

- [98] A. Ferrari, P.R. Sala, A. Fasso', and J. Ranft, CERN-2005-10 (2005).
- [99] A. Andronic, S. Biagi, P. Braun-Munzinger, C. Garabatos, G. Tsileidakis arXiv:physics/0402044v1 [physics.ins-det].
- [100] A. Ferrari, P. R. Sala, A. Fasso and J. Ranft, "FLUKA: A multi-particle transport code," CERN-2005-010 (2005).
- [101] G. Battistoni, S. Muraro, P. R. Sala, F. Cerutti, A. Ferrari, S. Roesler, A. Fasso and J. Ranft, "The FLUKA code: Description and benchmarking," AIP Conf. Proc. **896**, 31 (2007).
- [102] A. Fasso, A. Ferrari, J. Ranft, P.R. Sala, "FLUKA2011 MANUAL" (2011).
- [103] Bundesamt fuer Arbeit und Gesundheit, "Swiss ordinance for radiation protection" (2010).
- [104] P. Velten, Private communication.
- [105] M. Huhtinen, "Determination of cross-sections for assessments of air activation at LHC," CERN Internal Report CERN/TIS-RP/TM/97-29 (1997).
- [106] M. Brugger, D. Forkel-Wirth, S. Roesler, P. Vojtyla, "Effective Dose to the Public from Air Releases at LHC Point 7," CERN-SC-2004-064-RP-TN, EDMS 493681 (2004).
- [107] C. Theis, K.H. Buchegger, M. Brugger, D. Forkel-Wirth, S. Roesler, H. Vincke, "Interactive three dimensional visualization and creation of geometries for Monte Carlo calculations," Nuclear Instruments and Methods in Physics Research A 562, pp. 827-829 (2006).
- [108] S. Roesler, G.R. Stevenson, "deq99.f - A FLUKA user-routine converting fluence into effective dose and ambient dose equivalent," Technical Note CERN-CS-2006-070-RP-TN, EDMS 809389 (2006).
- [109] R. Froeschl et al., "Radiological Hazard classification of materia in CERN,Äôs accelerators," EDMS 1184236 (2012).
- [110] J.D. Cossairt, "Radiation Physics for Personnel and Environmental Protection," Fermilab Report TM-1834 (2007).